# Using a human induced pluripotent stem cell model to investigate the role of perlecan in cardiovascular development and disease.

By

Benjamin Blakeley Johnson, BSc, MSc

100294802

A thesis submitted for the degree:

**Doctor of Philosophy**

The University of East Anglia, Norwich, UK

School of Medicine

Date of submission: 31st January 2023

## Declaration

I declare that the contents of this thesis entitled “Using a human induced pluripotent stem cell model to investigate the role of perlecan in cardiovascular development and disease.” was undertaken and completed by myself, unless otherwise acknowledged and has not been submitted in an application for another degree or qualification in this or any other university or institution.

This thesis is approximately 55,000 words in length, excluding references.

Parts of this research have been published prior to submission and are referenced in the List of Publications.

Benjamin B Johnson

## Acknowledgements

Firstly, I want to thank my fantastic supervisor, James Smith for his unfaltering support during my project. With your positive enthusiasm, knowledge, and friendship I truly enjoyed my PhD and will miss deciphering your doodles. Through your guidance I feel I have become a strong scientist and hopefully will continue to work with you in the future. I also want to thank Stuart Rushworth and Linda Troeberg, and their lab members, for their support and passion throughout the whole process. Many thanks to Andreia Bernardo, Lorenza and Elisa at the Francis Crick Institute for their techniques, knowledge, and support.

Many thanks to the support staff of BCRE, Catherine, Jaz, and Chris. You are all amazing and keep everything running smoothly, despite having to look after us PhD students. I will miss all the entertainment you brought to the labs, the stories, talks and occasional boxing sessions with Catherine.

I want to thank the friends I made here for keeping me sane throughout the whole process. Both friends from BCRE and those I met through my time here have made my stay in Norwich better than I could have imagined, and I would have struggled without your love. Extra love to Tom, Scott, Dan, Reuben, Josh and Magda. Special thanks to Terri for often being my voice of reason and helping me out whenever you could. I also want to thank my long-distance friends, Jordan and Alice for their intelligence and wit, Simon for the “je ne sais quoi”, Sam and Evers for their support. I can’t finish this section without thanking Oli, honestly couldn’t have asked for a better friend, thank you for all your support and wisdom throughout this journey.

Finally, I want to thank my family for their never-ending love, support and curiosities into my work. I want to dedicate this thesis to my grandparents who never got to see my finish my PhD, I know how proud you would have been.

## Abstract

Heparan sulfate proteoglycans (HSPGs) contribute to structural integrity and signalling regulation during cardiac development, healing, and wound repair, one such HSPG being perlecan (*HSPG2*). Perlecan is a large basement membrane protein known for the binding of growth factors and extracellular matrix, highlighted as essential in innate cardiac function. A *HSPG2* knock-out (KO) causes embryonic lethality in mice due to 'leaky' hearts, this KO in rescued mice show perlecan has a role in metabolic output in a cell specific manner. During cardiomyocyte (CM) development, a metabolic switch from glycolysis to fatty acid metabolism is essential for developmental maturation. I aimed to investigate the role of perlecan in cardiac cell populations.

Perlecan deficient hiPSC-Cardiac fibroblasts (CFs) showed higher levels of myofibroblast activation, and a reduced mitochondrial function compared to WT. Transcriptomic analysis of a differentiation time course to hiPSC-CMs highlighted 11 genes consistently dysregulated due to perlecan deficiency, including *HSPG2, NNAT, SLC15A4, KCNC3, RBM46, GLT1D1, TMSB4Y, ZNF676, SVIL-AS1, MGMT* and *TRIM61*. Perlecan deficient hiPSC-CMs have an increased reliance of glycolysis, are prone to cardiac remodelling when in 3D and show increased genetic differences during the stages of CM maturation. Our results show how hiPSC-CMs with attenuated perlecan have an immature cardiac phenotype when compared to WT hiPSC-CMs, confirmed via the use of metabolic assays and gene expression. While culturing of hiPSC-CMs on a synthetic perlecan surface induced enhanced multinucleation, suggestive of hyperplastic to hypertrophic development.

The lack of perlecan in our cardiac populations has detrimental effects on metabolism of both hiPSC-CMs and CFs. The metabolic switch in hiPSC-CMs is essential to maturation, it is attenuated in our perlecan deficient hiPSC-CMs, indicative of a less mature CM. Understanding perlecans role in cardiac populations could lead to improved maturation of hiPSC-CMs for drug screening and disease modelling, as well as further insights into cardiac wound recovery.

# Table of Contents

## List of publications and conference presentations

### Publications

Hellmich, C., Wojtowicz, E., Moore, J.A., Mistry, J.J., Jibril, A., **Johnson, B.B.**, Smith, J.G., Beraza, N., Bowles, K.M. and Rushworth, S.A., 2022. p16INK4A dependent senescence in the bone marrow niche drives age-related metabolic changes of hematopoietic progenitors. Blood Advances.

**Johnson, B.B.,** Reinhold, J., Holmes, T.L., Moore, J.A., Cowell, V., Bernardo, A.S., Rushworth, S.A., Vassiliou, V. and Smith, J.G., 2021. Modelling metabolic shifts during cardiomyocyte differentiation, iron deficiency and transferrin rescue using human pluripotent stem cells. Metabolites, 12(1), p.9.

James, V., Nizamudeen, Z.A., Lea, D., Dottorini, T., Holmes, T.L., **Johnson, B.B**., Arkill, K.P., Denning, C. and Smith, J.G., 2021. Transcriptomic analysis of cardiomyocyte extracellular vesicles in hypertrophic cardiomyopathy reveals differential snoRNA cargo. Stem Cells and Development, 30(24), pp.1215-1227.

Hellmich, C., Mistry, J.J., Jibril, A., Moore, J.A., **Johnson, B.B.,** Smith, J.G., Wojtowicz, E., Beraza, N., Bowles, K.M. and Rushworth, S.A., 2021. BCL-Xl Driven Accumulation of Dysfunctional Mitochondria in Aged Stromal Cells Impairs the Haematopoietic Stem Cell Response to Stress. Blood, 138, p.1097.

Bhagwan, J.R., Collins, E., Mosqueira, D., Bakar, M., **Johnson, B.B.,** Thompson, A., Smith, J.G. and Denning, C., 2019. Variable expression and silencing of CRISPR-Cas9 targeted transgenes identifies the AAVS1 locus as not an entirely safe harbour. F1000Research, 8.

Rushworth, S.A., **Johnson, B.B.**, Ashurst, K., Davidson, R., Paddy, P., Mistry, J.J., Moore, J.A., Hellmich, C., Edwards, D.R., Afonso, D.D.L. and Xydopoulos, G., 2020. Performance and health economic evaluation of the

Mount Sinai COVID-19 serological assay identifies modification of thresholding as necessary to maximise specificity of the assay. medRxiv.

**Presentations**

International Society for Stem Cell Research, 2022, San Francisco, Poster Presentation

International Society for Stem Cell Research, 2020, Boston-Virtual, Poster Presentation

UEA Postgraduate Research Faculty of Medicine and Health Conference, 2020, University of East Anglia-Virtual, Poster Presentation

**Short Talks**

UK Proteoglycans, 2022, Virtual, Short Talk

British Society of Matrix Biology - Proteoglycans Meeting, 2020, Virtual, Short Talk

## List of Figures

## List of Tables

## List of Abbreviations

| | |
|---|---|
| A.U. | Arbitrary Units |
| aDGC | Alpha Dystroglycan Complex |
| AngII | Angiotensin II |
| ANP | Atrial Natriuretic Peptide |
| ATP | Adenosine Triphosphate |
| AV | Atrioventricular |
| BMP | Bone Morphogenic Protein |
| BNP | Brain Natriuretic Peptide |
| cAMP | Cyclin AMP |
| CCD | Charge-Coupled Device |
| cDNA | Complementary DNA |
| CF | Cardiac Fibroblast |
| CM | Cardiomyocyte |
| CPCs | Cardiac Progenitor Cells |
| CRISPR | Clustered Regularly Interspaced Short Palindromic Repeats |
| CS | Chondroitin Sulfate |
| DDSH | Dyssegmental Dysplasia, Silverman-Handmaker type |
| DEG | Differentially Expressed Gene |
| DMEM | Dulbecco's Modified Eagle's Medium |
| DMSO | Dimethyl Sulfoxide |
| DNA | Deoxyribonucleic Acid |
| E8 | Essential 8 |
| EC | Endothelial Cell |
| ECAR | Extracellular Acidification Rate |
| ECM | Extracellular Matrix |
| EDTA | Ethylenediaminetetraacetic Acid |
| EHT | Engineered Heart Tissue |
| EMT | Epithelial to Mesenchymal Transition |
| EPCs | Epicardial Progenitor Cells |
| EPDCs | Epithelial-Derived Cells |
| FBS | Foetal Bovine Serum |
| FGF | Fibroblast Growth Factor |
| FHF | First Heart Field |
| GAGs | Glycosaminoglycans |
| gDNA | Genomic DNA |
| GFP | Green Fluorescent Protein |
| GO | Gene Ontology |
| GO:BP | Gene Ontology Binding Protein |
| GO:CC | Gene Ontology Cellular Components |
| GO:MF | Gene Ontology Molecular Function |
| GSK3β | Glycogen Synthase Kinase 3 Beta |

| | |
|---|---|
| HA | Hyaluronan |
| HDM | High Density Matrix |
| HIF1a | Hypoxia Induced Factor 1a |
| hiPSCs | Human Induced Pluripotent Stem Cells |
| HM1/2/3 | Heart Media 1/2/3 |
| HS | Heparan Sulfate |
| HSPG | Heparan Sulfate Proteoglycan |
| iCMs | Induced Cardiomyocytes |
| IGF | Insulin Growth Factor |
| IL | Interleukins |
| KEGG | Kyoto Encyclopaedia of Genes and Genomes |
| KO | Knockout |
| KS | Keratin Sulfate |
| LDL | Low-Density Lipoprotein |
| MF | Myofibroblast |
| MI | Myocardial Infarction |
| MMP | Matrix Metalloproteinase |
| mRNA | Messenger RNA |
| MSCs | Mesenchymal Stem Cells |
| NEB | New England Biolabs |
| NMJ | Neuromuscular Junction |
| NO | Nitric Oxide |
| OCR | Oxygen Consumption Rate |
| ORF | Open Reading Frame |
| OXPHOS | Oxidative Phosphorylation |
| PAM | Protospacer-Adjacent Motif |
| PBS | Phosphate-Buffered Saline |
| PCA | Principal Component Analysis |
| PCR | Polymerase Chain Reaction |
| PDGF | Platelet-Derived Growth Factor |
| PER-P | Perlecan Synthetic Peptide |
| PFA | Paraformaldehyde |
| PG | Proteoglycan |
| qRT-PCR | Real Time Quantitative Polymerase Chain Reaction |
| RA | Retinoic Acid |
| REAC | Reactome |
| RNA | Ribonucleic Acid |
| RPM | Revolutions Per Minute |
| SDS | Sodium Dodecyl Sulfate |
| SEA | Sperm, Enterokinase and Agrin |
| SEM | Standard Error of Mean |
| sfGFP | Super Fold GFP |
| SFs | Skin Fibroblasts |

| | |
|---|---|
| sgRNA | Single Guide RNA |
| SHF | Second Heart Field |
| SJS | Schwartz-Jampel Syndrome |
| SLRPs | Small Leucine Rich Proteoglycans |
| SMC | Smooth Muscle Cell |
| SOC | Super Optimal Catabolite |
| T3 | Thyroid Hormone Triiodothyronine |
| TAE | Tris-Acetate-EDTA |
| TAZ | Transcriptional Co-Activator |
| TCA | Trichloroacetic Acid |
| TGBβ | Transforming Growth Factor |
| TIMP | Tissue Inhibitors of Metalloproteinase |
| TWOMBLI | The Workflow of Matrix Biology Informatics |
| VEGF | Vascular Endothelial Growth Factor |
| VTN | Vitronectin |
| WP | WikiPathways |
| WT | Wild Type |
| WTN | Wingless-Related Integration Site Family |
| YAP | Yes-Associated Protein |
| α-SMA | Alpha Smooth Muscle Actin |

# 1. Introduction

## 1.1. Heart Development

### 1.1.1. Overview of Heart Development

The heart is one of the first organs to undergo development in the embryo (Günthel et al., 2018). During early stages of embryonic development, the mesoderm layer forms between the ectoderm and endoderm. Within the mesoderm layer, the precardiac mesoderm forms from the anterior primitive streak. Cells from the anterior primitive streak migrate to form the cardiac crescent, which differentiates and remodels to eventually form the heart tube (de Sousa Lopes et al., 2006). Cells found within the cardiac crescent display a cardiogenetic expression profile and are capable of initiating calcium transients (Tyser and Srinivas, 2020). Throughout embryogenesis the heart tube undergoes a series of folds to form a primitive heart (Figure 1.1) (Günthel et al., 2018; Lindsey et al., 2014).

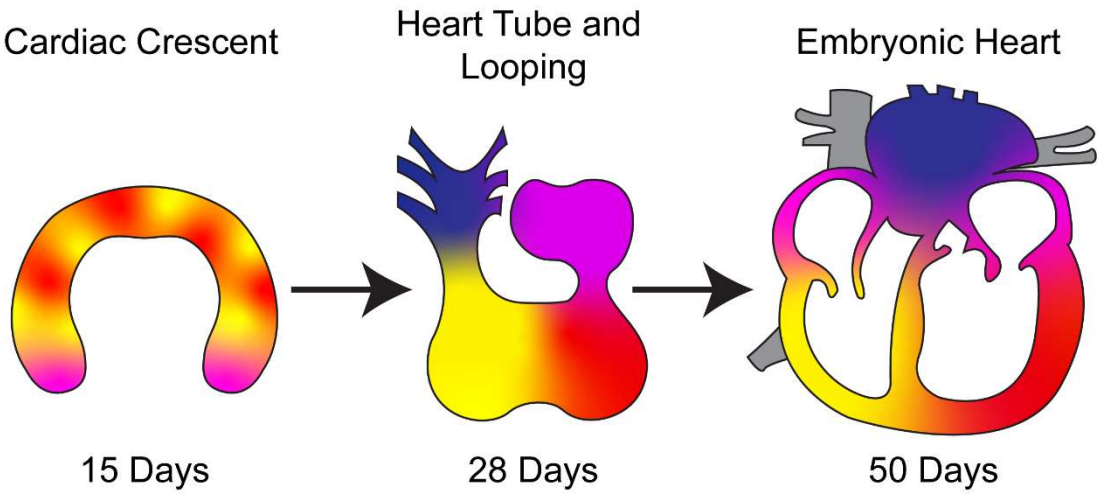


***Figure 1.1 – Stages of early heart development.*** *Schematic shows morphological changes of the developing human heart, colour coded for each structural region. Left (yellow) and right (red) ventricular, and atrial (pink) populations are found in the developing cardiac crescent. Following heart tube formation and looping the ventricular populations are separated and the aortic sac (blue) is found developing the future aorta. Further development separates each chamber giving rise to the embryonic heart. Adapted from Lindsey SE et al., 2014.*

During this stage, calcium transients are initiated, causing heart contractions that pump developing blood throughout the embryo (Tyser and Srinivas, 2020). The heart tube further differentiates into the four chambers that make up the adult heart (left and right atria and ventricles). Creation of isolated chambers allows the heart to pump both oxygenated and deoxygenated blood throughout the developing foetus (Combs and Yutzey, 2009; J. Patterson and Zhang, 2010).

During embryogenesis the coronary circulation network develops, with arteries and veins branching off the aorta and pulmonary artery. The coronary arteries carry oxygenated blood from the aorta to the heart, while the veins take deoxygenated blood from the heart to the right atria (de Boer et al., 2012; Tomanek, 2016). As the foetus develops, the circulatory system and heart mature, becoming more efficient, with thickening of the septa and valves forming between the chambers (Kloesel et al., 2016). The heart will eventually become proficient, delivering oxygenated blood to all emerging organs and tissues withing the developing foetus.

### 1.1.2. Cellular composition of the heart

In the human heart, there are five major resident cell types (Figure 1.2); smooth muscle cells (SMCs), macrophages, endothelial cells (ECs), cardiac fibroblasts (CFs) and cardiomyocytes (CMs) (Porter and Turner, 2009; Souders et al., 2009). CMs occupy between 70-85% the total volume of the heart, although only 30-40% of the total cell number (Zhou and Pu, 2016). ECs are amongst the most abundant cell type found, compared to CFs which are three-fold less than ECs (Giacomelli et al., 2020).

CMs, also known as myocardial cells, are responsible for the contraction and relaxation of the hearts chambers, pumping blood through the circulatory system. CMs show an elongated physiology, approximately 100 μm long, but only 10 μm wide. Highly developed sarcoplasmic reticulum and mitochondria provide calcium storage and ATP production for contraction. CMs develop myosin and actin filaments into a basic contractile unit, known as the sarcomere (Karbassi et al., 2020). Contraction is stimulated by release of

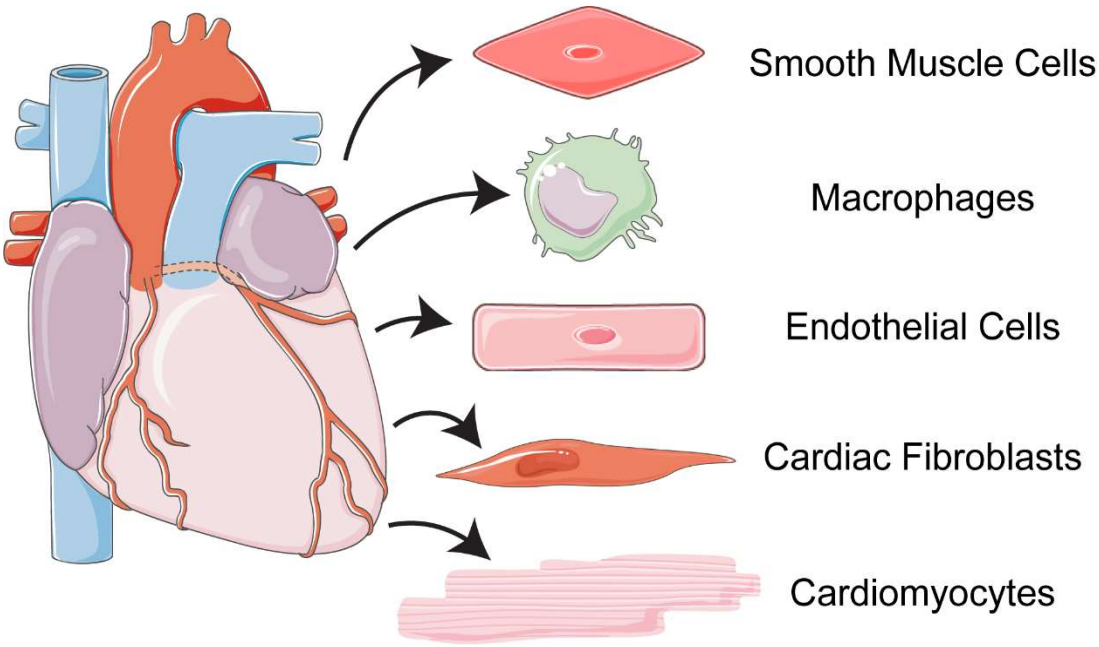


***Figure 1.2 – Cellular composition of the heart.*** *Five key cell types of the heart highlighted here, including smooth muscle cells, macrophages, endothelial cells, cardiac fibroblasts, and cardiomyocytes. These cell types forming the majority of the hearts cellular population and are crucial for maintaining the hearts functions through both health and disease.*

calcium ions from the sarcoplasmic reticulum, activating the myosin-actin interaction, initiating contraction. Calcium ions are actively transported back to the sarcoplasmic reticulum, deactivating the myosin-actin interaction and allowing relaxation to occur (Eisner et al., 2017). Through electrocoupling, the CMs contract in waves of unison, causing complete contraction of the heart muscle, allowing the pumping of blood to effectively occur (Padala et al., 2021).

CFs reside between muscle fibres acting as a scaffold, producing and maintaining the extracellular matrix (ECM) of the heart (Fan et al., 2012). The ECM is essential to maintain the myocardial structure. CFs control this by regulating ECM production and turnover, through the regulation of matrix metalloproteinases (MMPs) and tissue inhibitors of metalloproteinases (TIMPs) (Porter and Turner, 2009; Spinale, 2002). CFs assist development and growth via secretion of cytokines such as transforming growth factor beta (TGFβ), platelet-derived growth factor (PDGF) and vascular endothelial

growth factor (VEGF) (Snider et al., 2009). Following cardiac damage, the CF is responsible for tissue repair and cardiac remodelling through ECM composition changes, (Valiente-Alandi et al., 2016) and further forms the pro ECM secretory myofibroblast (MF). The CF also plays a crucial role in cardiac electrophysiology, gap junctions between the CF and CM allow the maintenance of electrical conductance generated by CMs over a longer distance, assisting in efficient contraction of the heart (Zhang et al., 2012).

ECs line the inner layer of blood vessels and the heart; these thin flat cells are involved in the regulation of blood vessels. ECs maintain the structural integrity of blood vessels through ECM maintenance and turnover. The EC is also responsible for regulation of blood vessel permeability through tight junctions. ECs communicate to SMCs regulating the diameter of vessels, controlling blood flow and blood pressure (Ishii et al., 2009; Lother et al., 2018; Montecucco and Marzo, 2012).

SMCs are found within the walls of blood vessels, maintaining the elasticity required in an artery, and with collaboration with ECs are responsible for controlling blood flow through signalling cascades. SMCs are also responsible for maintaining ECM of vessels alongside the ECs (Qi et al., 2021; Zhuge et al., 2020).

The role of macrophages in the heart is linked to tissue repair and remodelling. After cardiac damage macrophages are activated to remove necrotic tissue and initiate wound healing signalling cascades (Krzyszczyk et al., 2018). The signalling released from macrophages encourages activation and migration of CFs followed by transdifferentiation to a MF (Wynn and Barron, 2010).

In this thesis I focus on the roles played by CMs and CFs in the heart, and as such further detail into the origins of these two cell types is described below.

### 1.1.3. Origins of Cardiomyocytes

During the early stages of cardiac development, the mesoderm specifies towards the cardiac mesoderm, controlled by families of signalling molecules: wingless-related integration site (WNT), fibroblast growth factors (FGFs), TGFβ, bone morphogenic proteins (BMPs), Nodal and activin A (Noseda et al., 2011; Payan et al., 2020a; Später et al., 2014). Within the cardiac mesoderm two precursor populations of cells form. These can be distinguished through marker expression, consisting of the first heart field (FHF) [*TBX5* and *HCN4*] and second heart field (SHF) [*TBX1, FGF8* and *FGF10*, *ISL1*] (Black, 2007; Pezhouman et al., 2021; Tampakakis et al., 2019). The FHF cell populations fuse the midline of the cardiac crescent, forming the heart tube, separating the myocardial layer from the now enclosed endocardial layers.

The separation of these layers is maintained by a layer of ECM called the cardiac jelly (Männer and Yelbuz, 2019). Once the heart tube has been formed, the primitive CMs stop proliferation, the heart tube continues development via migration of SHF precursor cells (Brade et al., 2013). SHF cells undergo rapid proliferation mediated by the canonical WNT/β-catenin signalling. SHF populations then undergo cardiac specific differentiation at the arterial and venous poles of the heart tube, whereby the SHF CMs stop proliferating (Fan et al., 2018; Ruiz-Villalba et al., 2016). FHF cells will form the definitive left ventricle, while the SHF cells contribute to the formation of the right ventricle (Figure 1.3), both FHF and SHF contribute to the atria (Black, 2007; Buckingham et al., 2005).

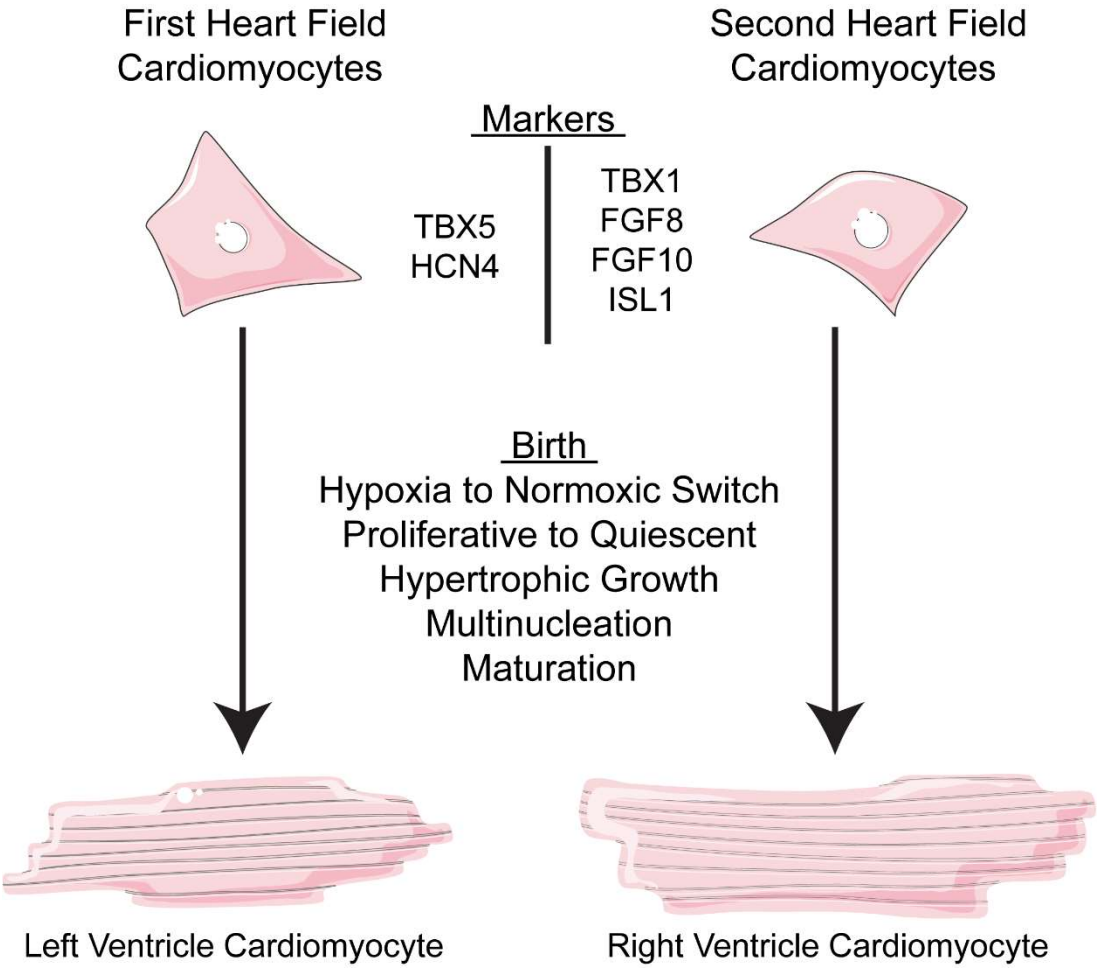


***Figure 1.3 – Origin of ventricular cardiomyocytes.*** *Both first and second heart field populations separated by markers. Following birth cardiomyocytes environment switches to normoxic, encouraging cardiomyocyte maturation through quiescent, hypertrophic growth.*

The FHF and SHF are the main source of CMs, although there is a minor contribution from the proepicardium (Zhou et al., 2008). As well as WNT, insulin growth factor (IGF) signals are involved in controlling the CM proliferation (Huang et al., 2013; Li et al., 2011). Both WNT and IGF can act through glycogen synthase kinase 3 beta (GSK3β), stabilising β-catenin, and are linked to Hippo signalling pathways through Yes-associated protein (YAP) (Jiang L et al., 2020; Wu and Pan, 2010). Other families of signalling factors including BMPs, FGFs and Notch, have been identified to cause CM proliferation during development. Both FHF and SHF CMs undergo a second wave of proliferation following the remodelling process of the heart tube, whereby the chambers become developed (Galdos and Wu, 2019).

After birth, (Figure 1.3) the CMs begin transitioning from a proliferative to quiescent cell, maturing CMs are unable to undergo cytokinesis during mitosis, leading to multinucleated cells (Naqvi et al., 2014; Velayutham et al., 2020). Hyperplastic CM growth is shown to continue in humans up to 20 years of age, although this only accounts for a 1% increase in CM number per year (Bergmann et al., 2015). The main cause of postnatal heart expansion is due to CM hypertrophy, whereby CMs substantially increase in size (M. T. Zhao et al., 2020). Following birth, the human heart loses its regenerative ability as the proliferative capability of CMs is attenuated, this is due to several influences. The heart is switched from a hypoxic to normoxic environment, this switch reduces hypoxia induced factor 1a (*HIF1a*) nuclear localisation, a transcription factor linked to foetal CM proliferation, thereby attenuating hyperplastic growth (J. Patterson and Zhang, 2010). Other transcription factors such as *FOXO1* and *FOXO3* mRNA levels decrease following birth, while *MEIS1* expression increases and localises to the nucleus by P7 (Mahmoud et al., 2013). Expression of YAP is attenuated following birth, declining with age, and lost after 12 weeks, aligning with the reduction of proliferative CMs (Payan et al., 2020).

### 1.1.4. Origins of Cardiac Fibroblasts

During embryonic development the CF derives mainly from the pro-epicardial organ, a source of cardiovascular progenitor cells (Deb and Ubil, 2014; Souders et al., 2009). The cardiac progenitor cells found in the pro-epicardial organ are also able to differentiate to SMCs (Mikawa and Gourdie, 1996). After the heart tube has looped, the pro-epicardial cells undergo migration, creating a single cell layer over the entire embryonic heart forming the embryonic epicardium (Männer et al., 2001). From within the embryonic epicardium a subset of cells undergo epithelial to mesenchymal transition (EMT), migrating to the myocardium. These migrating cells are referred to as epicardial-derived cells (EPDCs) and undergo further differentiation to interstitial and adventitial CFs (Smith et al., 2011). Transcription factor 21 (*TCF21*) is fundamental in directing the fate of cells in the embryonic epicardium to undergo EMT and differentiation to a CF (Acharya et al., 2012). Mouse hearts lacking Tcf21 are unable to generate CFs due to EMT being unable to occur (Acharya et al.,

2012). Although most CFs are derived from the epicardium, a small subset is formed from the endocardium (Doppler et al., 2017). The endocardium if found to line the inner lumen of the heart, here a subset of cells will undergo endothelial-to-mesenchymal transition. The mesenchymal cells derived here will generate the valves of the heart, whereby the fibroblasts contribute to the interventricular system (Harris and Black, 2010; Monaghan et al., 2016).

### 1.1.5. Cellular communications between cardiac fibroblasts and cardiomyocytes

Cardiomyocytes and cardiac fibroblasts communicate through an array of different methods, including ECM interactions, electrical interactions, mechanical junctions, and paracrine signalling (Figure 1.4) (Pellman et al., 2016). The ECM secreted by CFs is 'stretch-sensitive' and signals to neighbouring cells via multiple pathways when under mechanical stress.

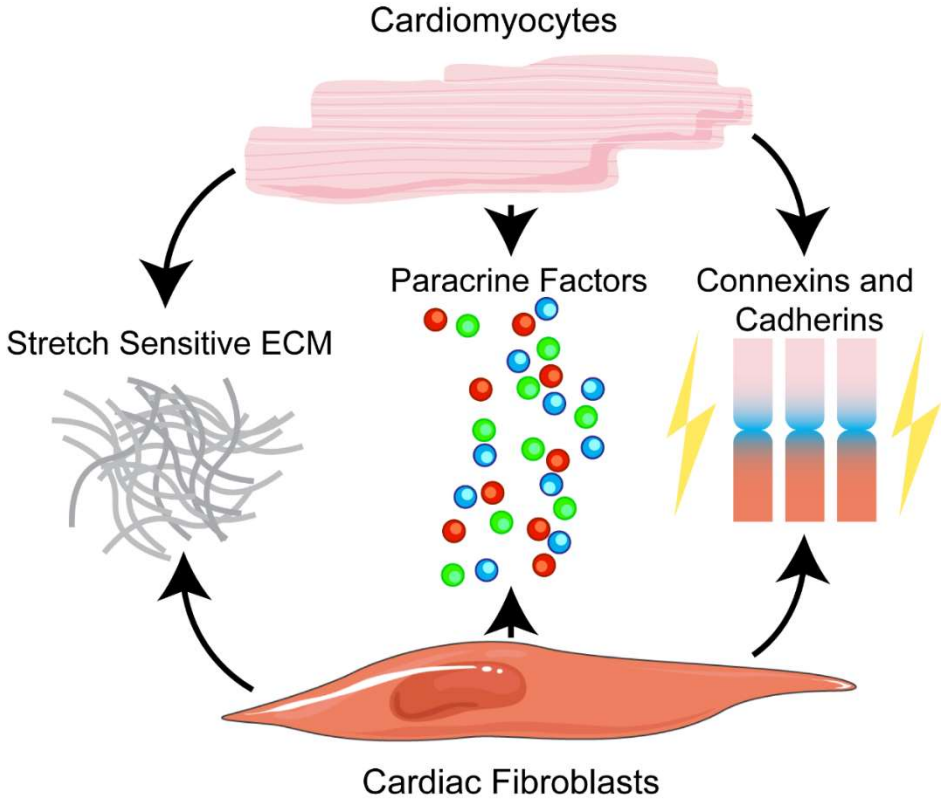


***Figure 1.4 - Communications between cardiomyocytes and cardiac fibroblasts.*** *Methods of communication between cardiac fibroblasts and cardiomyocytes include secretion of a stretch sensitive ECM, paracrine factors, and interactions on cellular surface junctions involving connexins and cadherins. Adapted from Pellman et al., 2016.*

These mechanical stress pathways can induce signal transductions inducing proliferation, ECM deposition and growth factor release (Camelliti et al., 2005; MacKenna et al., 2000). The CF is also known to assist in electrical conductance via cell surface protein families, including connexins [Cx40, Cx43 (Louault et al., 2008), Cx45 (Camelliti et al., 2004)] and cadherins [cadherin-11 (Orlandini and Oliviero, 2001), cadherin-13 and N-cadherin (Barcelona-Estaje et al., 2021)], creating connections between CMs and other fibroblasts (Souders et al., 2009). While CFs may be electrically unexcitable, they still contribute to the electrophysiology of the myocardium (Porter and Turner, 2009). CFs have also been shown to assist in the maturation of *in vitro* CMs, occurring through elevated cyclic AMP (cAMP) signalling, enhancing the assembly of CX43 gap junctions (Giacomelli et al., 2020). TGFβ, WNT, interleukins (IL) and angiotensin II (AngII) have all been implemented as major paracrine factors involved in signalling between CMs and CFs. These signalling factors are often released in response to cardiac injury, inducing a healing response in both cell types, hypertrophy in CMs, and a pro-fibrotic response in CFs. Loss of communication between CMs and CFs is thought to play a central role in heart disease, exacerbated in disorders such as cardiac fibrosis and arrhythmias (Hall et al., 2021; Pellman et al., 2016). This is linked to the overproduction of ECM and fibroblast accumulation, altering the ratio of CM to CFs, causing decoupling of CMs (Hall et al., 2021; Xie et al., 2009).

### 1.1.6. Metabolism in heart development

Contraction of CMs is energy demanding, and therefore requires high ATP production. As such, metabolism plays an important role in the growth and differentiation of CMs in the developing heart. The metabolism of the foetal heart relies mainly on glucose, although capable of metabolising all substrates for ATP production (Piquereau and Ventura-Clapier, 2018). CMs with suppressed glycolytic activity are unable to migrate and form the trabeculae of the developing heart (Fukuda et al., 2019; Leung and Shi, 2022). The reliance on glycolysis comes from the foetus forming in a hypoxic environment, with low levels of circulating fatty acids (J. Patterson and Zhang, 2010). Along with glycolysis, lactate oxidation is a major source of ATP in the foetal heart, lactate

hinders the oxidation of lipids, reducing fatty acid metabolism (Xu, 2009). As the heart develops, the substrate preference and metabolic reliance shifts from glucose to fatty acids (J. Patterson and Zhang, 2010). As well as a source of ATP, fatty acids are essential for the synthesis of structural proteins, collagens, and elastin, that are required to mature the ECM of the developing heart. The metabolic switch from glycolytic, to fatty acid reliance, correlates with the reduction of CM proliferation and loss of regenerative ability (Günthel et al., 2018; Piquereau and Ventura-Clapier, 2018). This transition is triggered by changes occurring following birth, with the environment switching from hypoxic to normoxic, and the intake of enriched lipids from maternal milk (Berhrsin and Gibson, 2011; Mei et al., 2020) (Figure 1.5).

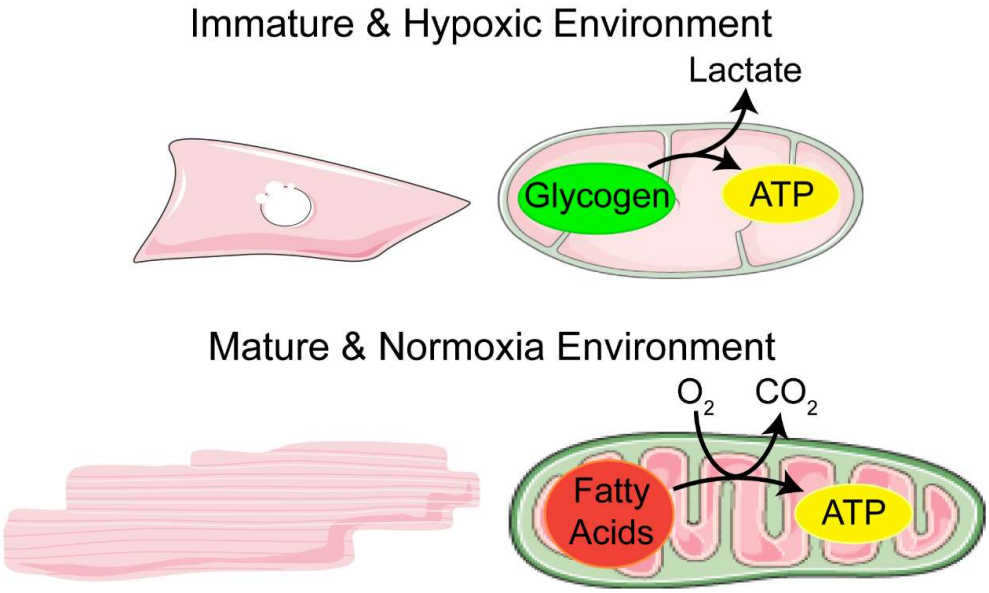


***Figure 1.5 – Maturation switch in cardiomyocytes.*** *Following birth, the hearts environment switches from hypoxic and glycogen rich, to normoxic and fatty acid rich. This switch is essential for the maturation of cardiomyocytes and allows a higher ATP production through the mitochondria metabolising a more efficient metabolite.*

*HIF1a* is known to regulate pro-glycolytic energy metabolism, cell proliferation and maturation, initiated via a hypoxic environment (Kierans and Taylor, 2021). *HIF1a* has been shown to control the metabolic shift from glycolysis to oxidative phosphorylation (OXPHOS). After birth, in a normoxic environment,

*HIF1a* localisation and expression is attenuated, promoting OXPHOS metabolism (Goda and Kanai, 2012). One third of the total CM volume is occupied by mitochondria, producing the majority of the CMs energy requirements through OXPHOS (Piquereau et al., 2013). Prenatal CM mitochondria are disorganised, containing a reduced mass compared to the adult CM mitochondria. Mitochondrial fusion and biogenesis are some of the key signs a CM is undergoing maturation to maintain the energy requirement for adult contraction (A. Li et al., 2020).

## 1.2. Cardiac Extracellular Matrix

### 1.2.1. ECM in heart development

A crucial component of regulating heart development is the ECM, in the initial form the cardiac jelly, which forms the developing atrioventricular (AV) junction. The ECM composition changes through development, creating spatial changes that allow remodelling and formation of the functional heart (Lockhart et al., 2011). The developing ECM consists of proteoglycans, collagens, and other structural proteins such as elastin, fibronectin, and laminins (Figure 1.6) (Frantz et al., 2010; Lockhart et al., 2011). A knockout of ECM components often leads to embryonic lethality highlighting how essential the maintenance of the ECM is.

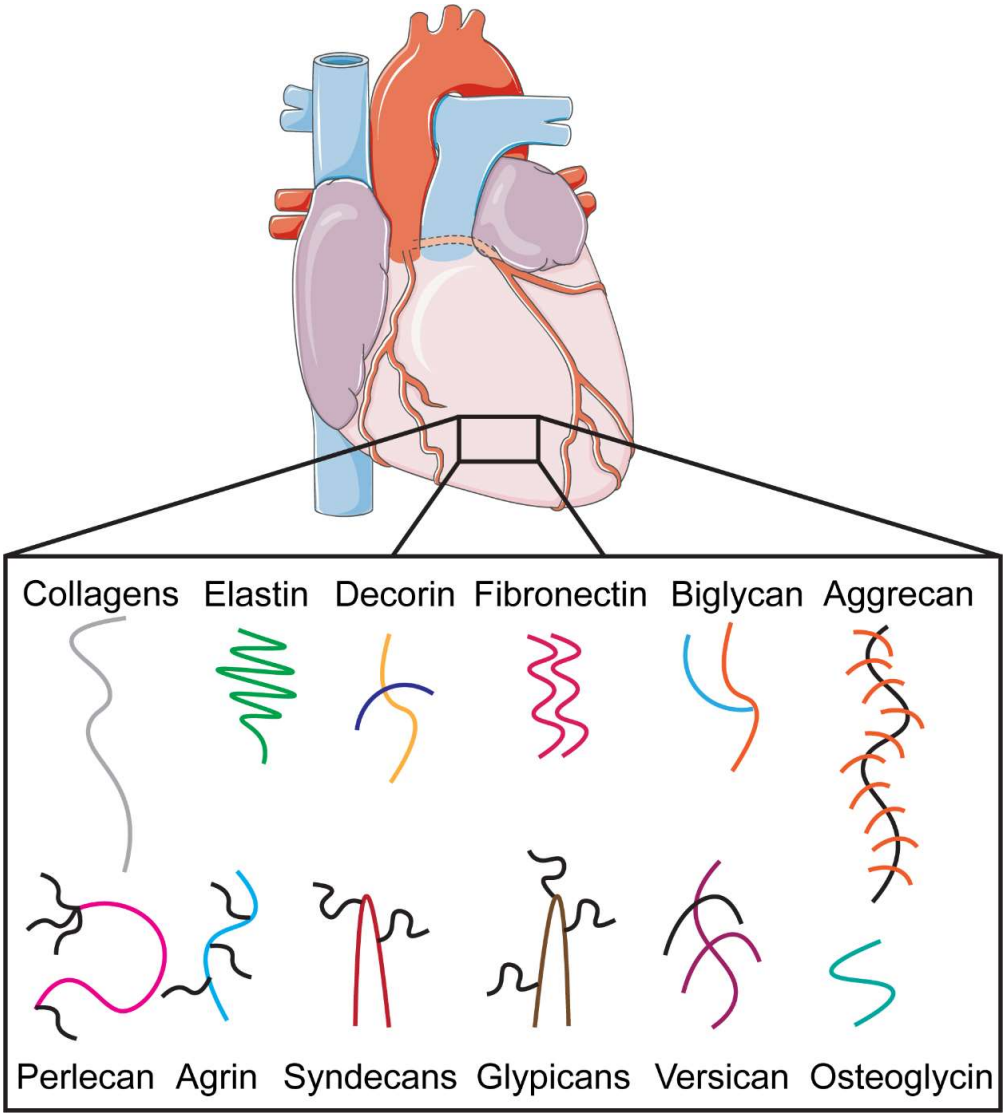


***Figure 1.6 - ECM components of the heart.*** *Several of the ECM components of the heart essential for maintaining function and structure through both health and disease.*

### 1.2.2. Collagens in the Heart

Of the 28 different variants of collagens, several are found in the developing heart. Collagens I, III and V are considered fibrillar collagens, these collagens are found within the ventricles and AV valves (Lockhart et al., 2011). Both collagens I and III knockouts allow initial survival of mice to adulthood, although these mice show an increased risk of cardiac and vessel rupturing (Liu et al., 1997; Rahkonen et al., 2004). While a collagen V KO is embryonic lethal, due to reduced collagen fibril formation (Wenstrup et al., 2004). These collagens provide the elasticity that is required to maintain the high mechanical stresses the heart undergoes.

Collagen VI is found within the developing aortas, myocardium, epicardium and AV valves of the heart (Lockhart et al., 2011). Collagen VI is considered a network forming collagen, its involvement focuses on linking of microfilaments, providing structure and stability to the ECM (Klewer et al., 1998.). Collagen XI is found in the developing AV valves and ventricle trabeculae, regulating collagen fibril assembly. Collagen XI deficient mice die at birth, analysis reveals an increased compensatory expression of collagen I in the AV valve leaflets and interventricular septum (Lincoln et al., 2006; Lockhart et al., 2011).

Finally, collagens XV and XVIII are expressed throughout the basement membranes of the myocardium during development. Knockouts of these collagens show cardiac morphological changes and defects, although these do not appear to be lethal (Eklund et al., 2001; Utriainen et al., 2004). Collagens XV and XVIII are nonfibrillar collagens and contain binding sites for attachment of glycosaminoglycan (GAG) side chains, due to this these collagens are also classified as members the proteoglycan (PG) family.

### 1.2.3. Proteoglycans and HS/CS in the Heart

PGs consist of a core protein with four potential classes of attached GAG side chains. These four classes are chondroitin sulfate (CS), keratin sulfate (KS), hyaluronan (HA) and heparan sulfate (HS) (Figure 1.7) (Lockhart et al., 2011). Consisting of HS chains covalently bound to a PG core, heparan sulfate proteoglycans (HSPGs) are crucial regulators of development (Iwamoto et al., 2010). HS chains bind growth factors families such as FGFs (Aviezer et al., 1994), VEGF (Uchimura et al., 2006), TGFβ and BMPs (Rider, 2006), depending on the HS sulfation pattern. Along with HS chains binding essential developmental growth factors, they also create morphogen gradients for WNT and hedgehog developmental signalling pathways (Lin and Perrimon, 2002).

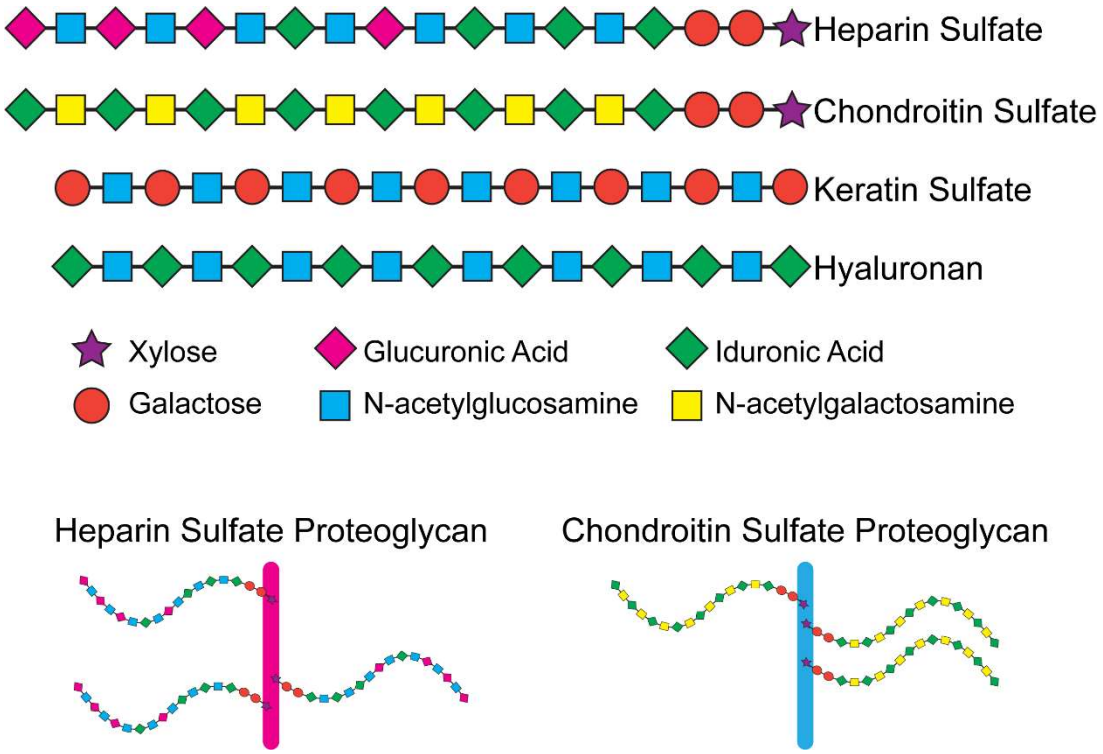


***Figure 1.7 – Structure of GAGs.*** *Heparin sulfate, chondroitin sulfate, keratin sulfate and hyaluronan are constructed from a selection of 6 components. These GAGs are then attached to a proteoglycan creating the ECM components HSPGs or CSPGs. Adapted from* Couchman and Pataki, 2012

Versican, a chondroitin sulfate proteoglycan (CSPGs), is essential in cardiac development. Cleavage of versican by MMPs matures the AV region (Kern et al., 2006), while deletion leads to embryonic lethality around day 11, due to cardiac defects (Yamamura et al., 1997).

HSPGs such as perlecan (*HSPG2*), agrin (*AGRN*), glypicans and syndecans also play an important role in cardiac development (Lockhart et al., 2011). Among the family of glypicans (1-6), glypican-3 and -4 are important in cardiac development. Glypican-3 is widely expressed in vertebrate development, deletion leads to congenital cardiac malformation effects, like Simpson-Golabi-Behmel syndrome in humans (Ng et al., 2009). Glypican-4 knockout has been linked to severe cardiac defects during embryonic development, associated with a reduction in CM numbers (Strate et al., 2015). The syndecan family (1-4) show expression throughout the myocardium. Syndecans-1 and -2 are lowly expressed in the heart (Asundi et al., 1997), while syndecans-3 and -4 are

highly expressed in the myocardium, more specifically CFs (Cornelison et al., 2004; Lockhart et al., 2011; Tkachenko et al., 2005).

Proteoglycans have been shown to have essential roles in cardiac remodelling and fibrosis, suggesting they are potential therapeutic targets and have yet to be fully explored (Christensen et al., 2019; Herum et al., 2017). Small leucine rich proteoglycans (SLRPs) are a family of proteoglycans that organise matrix structure and have been studied in the heart, in response to cardiac remodelling. These include lumican, fibromodulin, biglycan, decorin and osteoglycin (Figure 1.8) (Christensen et al., 2019). Lumican and fibromodulin expression in the heart increases after myocardial infarction, suggesting roles in remodelling (Engebretsen et al., 2013). Lumican knockout reduces systolic function after cardiac remodelling has occurred, promoting downstream heart failure (Chen et al., 2016). Biglycan is highly expressed in CFs compared to other cardiac cells, deletion reduced hypertrophy and fibrosis, leading to increased cardiac rupture after MI (Beetz et al., 2016). Biglycan is found within the tightly packed scar tissue formed by collagen bundles after a myocardial infarction, reinforcing its requirement in heart remodelling (Westermann et al., 2008). Interestingly decorin, like biglycan, has anti-fibrotic properties, and its overexpression reduced fibrotic effects (Yan et al., 2009). Osteoglycin is essential for collagen cross-linking in remodelling, a knockout increased the risk of cardiac rupture following remodelling after a MI (van Aelst et al., 2015), due to a lack of collagen bridging (Zhang et al., 2011). Both syndecan-1 and -4 are linked to collagen crosslinking, knockout mice have diminished fibrosis post-MI, leading to increased risk of cardiac rupture (Lunde et al., 2016; Schellings et al., 2010). Initial studies have been performed looking at the role of glypican PGs in cardiac remodelling. These showed that both glypican-3 and -6 are important and upregulated *in vivo* in MI responses (Melleby et al., 2016). Although more work is required to establish the role of both syndecan and glypican PG families in cardiac fibrosis (Christensen et al., 2019).

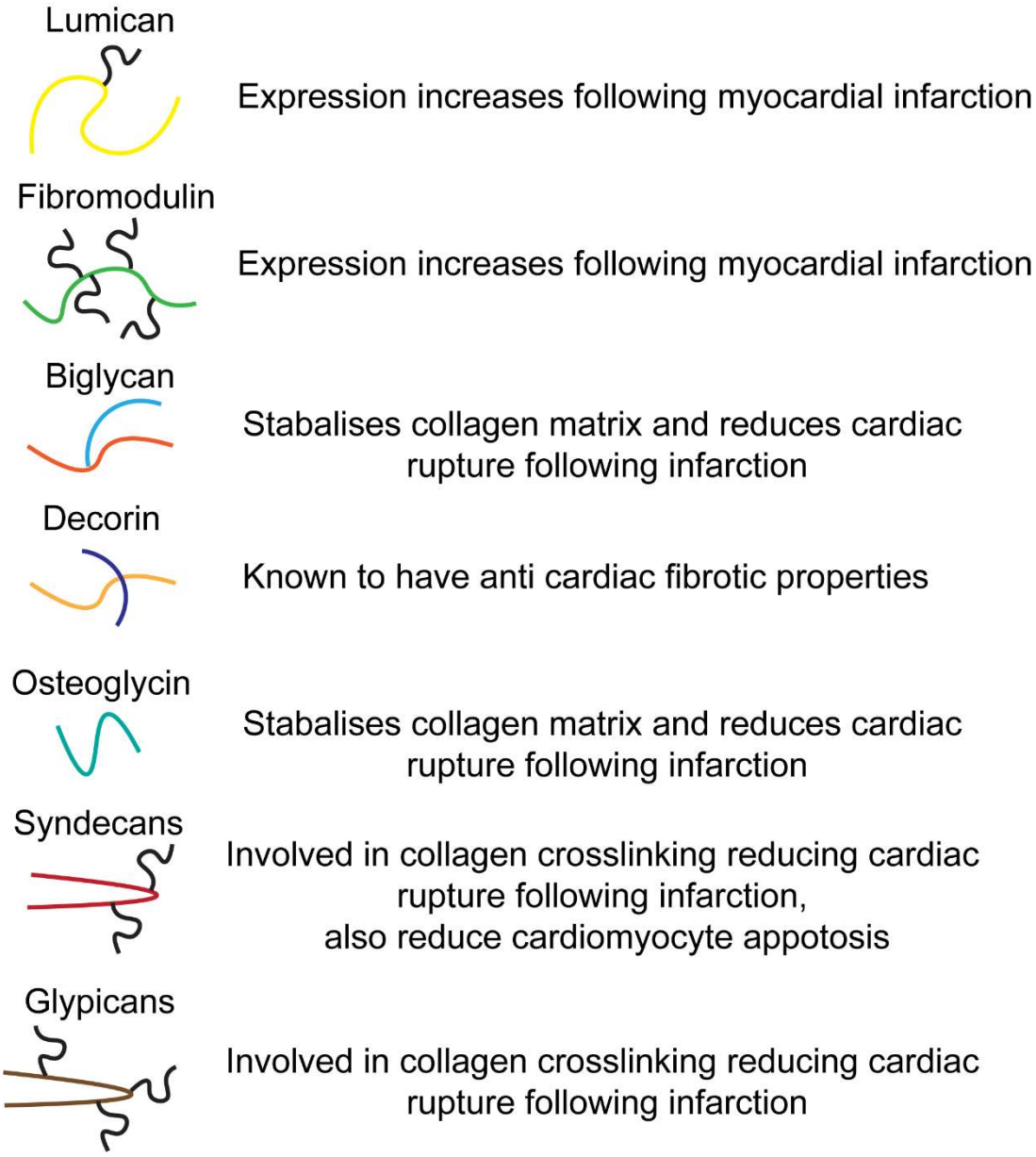


***Figure 1.8 - Roles of proteoglycans of the heart following disease.*** *Post myocardial infarction recovery requires co-operation of ECM proteoglycans including lumican, fibromodulin, biglycan, decorin, osteoglycin, syndecans and glypicans. Adapted from Lockhart et al., 2011.*

### 1.2.4. Agrin in the heart

One of the major ECM HSPGs, agrin is primarily known for its essential role in recruiting and clustering of acetylcholine receptors at the neuromuscular junction (NMJ) (Weston et al., 2000). During development, agrin is required for the correct formation of the NMJ in the heart, coordinating differentiation and migration of neurons and CMs, and formation of synaptic junctions

(Daniels, 2012). Agrin maintains the NMJs, regulating muscle contractility and blood flow (Tezuka et al., 2014). Agrin is also involved in cancer progression, regulating YAP and transcriptional co-activator (TAZ), through a mechanotransductive link between the ECM, enabling unregulated proliferation (Cai et al., 2021).

In the heart, agrin is an essential HSPG for proliferation of foetal CMs, with its deletion leading to embryonic lethality. Upregulation of agrin has recently been recognised in promoting proliferation of CMs, while attenuating CM maturation capabilities (Bassat et al., 2017). Administration of agrin was performed on infarcted pig hearts, showing agrin could reduce ischemia-reperfusion injury and improve heart function (Baehr et al., 2020). When the HSPG agrin was knocked out in mice, reduced proliferation of CMs and enhanced fibrosis was observed, suggesting agrin may have anti-fibrotic properties (Bassat et al., 2017). The α-dystroglycan complex (aDGC) is a cellular binding site for agrin, acting as both a receptor, and part of the mechanotransductive link between the ECM and transcription factors YAP and TAZ (Morikawa et al., 2017). Aggregation of agrin to the aDGC promotes epicardial EMT, an essential process of cardiac development (Sun et al., 2021). This complex also binds other ECM components, including laminins and perlecan (Montanaro et al., 1999). The regulation of the agrin-aDGC is largely undefined, although one suggested explanation is other aDGC binding ECM components may reduce the affinity of agrin binding (Bigotti et al., 2020). As ECM in the heart is developed, the agrin-aDGC binding affinity could be lowered though binding of other higher affinity ECM components. The c-terminus of agrin, which binds to the aDGC, is structurally similar to the c-terminus of perlecan. Of the ECM components that bind to aDGC, perlecan has a higher binding affinity compared to agrin (Dempsey et al., 2019). Therefore, an increase in perlecan would outcompete binding of aDGC against agrin.

### 1.3. *HSPG2* and Perlecan

#### 1.3.1. *HSPG2* and its structure

Perlecan is one of the major HSPGs found in basement membranes (Martinez et al., 2018), and consists of 5 domains (Figure 1.9), (Lord et al., 2018; A. D. Murdoch et al., 1992) created by 97 exons transcribing a ~460kDa protein core (Lord et al., 2014a).

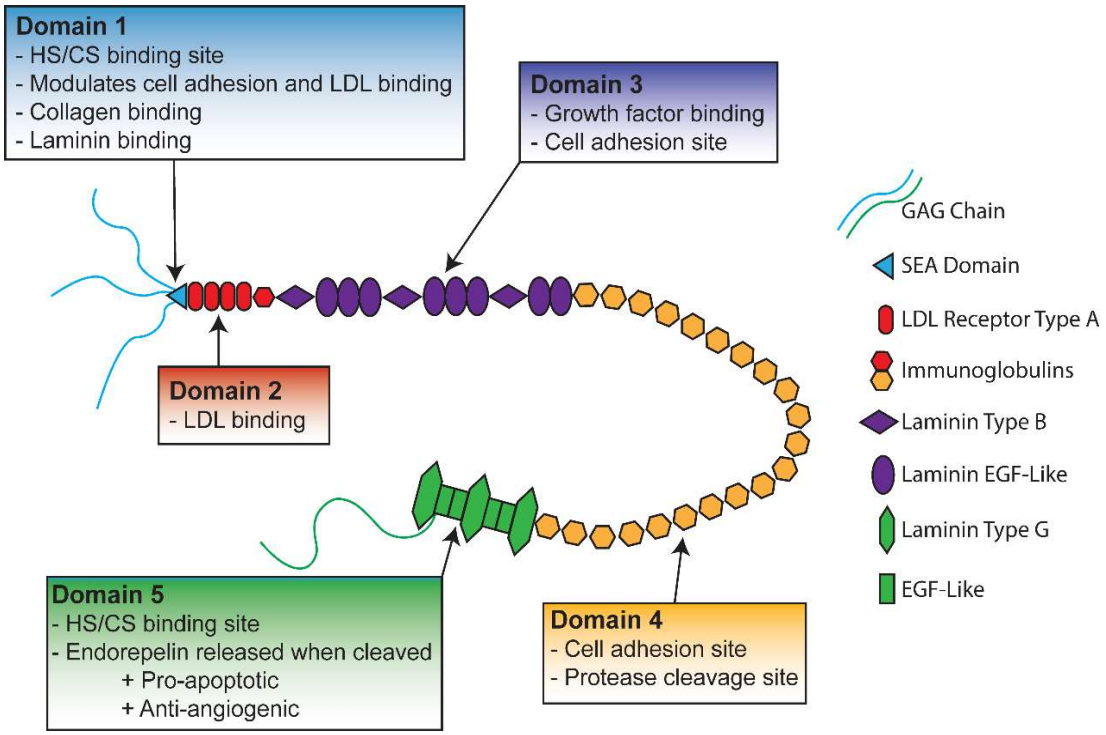


***Figure 1.9 – Schematic of HSPG2.*** *HSPG2 labelled domains 1-5 including brief function of each domain. Details of individual fragments keyed to HSPG2s structure.*

Each domain has individual functions, with the first domain of *HSPG2* (domain I) containing a sperm, enterokinase and agrin (SEA) module, followed by 3 GAG attachment sites that can be substituted with either HS or CS chains (Bork and Patthy, 1995). Domain II of perlecan contains four low-density lipoprotein receptor motifs, linked to calcium signalling (Costell et al., 1996) and potentially WNT signalling, contributing to perlecans role during development (Kamimura et al., 2013). Domain III of perlecan has binding sites for FGF, consisting of laminin epidermal growth factor and laminin B repeats,

forming the main core inflexible structure of perlecan (Smith et al., 2007b). The fourth domain of *HSPG2*, domain IV, is known for its interactions with ECM surface proteins such as fibronectin and nidogen. These help perlecan to provide mechanical stability to tissues, like proteins found in cartilage and muscle tissues (Hopf et al., 2001; Wijeratne et al., 2016). The final domain, domain V, can be cleaved from full length *HSPG2* to form a soluble protein known as endorepellin (Mongiat et al., 2003). Endorepellin, containing the fourth GAG binding site, is known to have opposite effects to full-length perlecan, i.e., endorepellin is pro-autophagic (Gubbiotti et al., 2017) and anti-angiogenic (Zoeller et al., 2009a). In total, perlecan including its bound GAG sidechains can interact with growth factors (FGFs), cellular signalling (calcium and WNT), cell surface receptors (integrins), and ECM molecules (collagen and laminin), making perlecan an essential matrix scaffold and mediator of growth factor activity (Iozzo et al., 1994).

There are two known genetic disorders caused by a perlecan deficiency in humans, these include Schwartz-Jampel syndrome (SJS) and dyssegmental dysplasia, Silverman-Handmaker type (DDSH) (Arikawa-Hirasawa et al., 2002). DDSH is the result of a complete perlecan KO, leading to a lethal form of neonatal short-limbed dwarfism, along with multiple other skeletal malformities (Arikawa-Hirasawa et al., 2002; Vadukkut et al., 2021). In DDSH the *HSPG2* mutation causes truncated forms of perlecan that are unable to be secreted into the matrix (Castellanos et al., 2021). SJS also causes skeletal deformations, but to a milder extant that DDSH. Despite the *HSPG2* mutations involved in SJS also creating truncated forms of perlecan, these can be secreted into ECM. Multiple mutations of SJS have been discovered, most notably a mutation that causes perlecan formation without domain 5, and one that causes a complete reduction in full length *HSPG2* (Arikawa-Hirasawa et al., 2002; Lin et al., 2021).

Several mechanistic pathways have been identified in regulating the expression of *HSPG2.* In pancreatic tumour cells and breast cancer induced macrophage polarisation HSPG2 regulation was identified through NF-κB-dependant pathways (De Paolis et al., 2022; Vennin et al., 2019). Through

notch signalling *HSPG2* is regulated in ECs, controlling the formation of adhesion junctions (Zhao et al., 2022). Furthermore, mechanical forces are capable of inducing *HSPG2* expression in ECs, requiring activation through autocrine TGFβ and ERK signalling pathways (Baker et al., 2008; Verrecchia et al., 2001).

### 1.3.2. *HSPG2* Splice variants

It has been reported that *HSPG2* mRNA can undergo splicing in domains I and IV, leading to variants of *HSPG2* that are lacking domains IV and V (Lord et al., 2014b). Jung and colleagues show mast cells produce a novel short form of perlecan corresponding to domain I and V, although lacking domain III (MoonSun Jung et al., 2013). Using a *Caenorhabditis elegans* model, complex splicing of *HSPG2* has identified several genes involved in interacting with *HSPG2* mRNA. These genes include *smu-1* and *smu-2*, nuclear proteins that form a complex to regulate activity of *mec-8* (C. A. Spike et al., 2002). A mutation of *smu-2* leads to unregulated *mec-8*, creating an increased accumulation of *unc-52* (*HSPG2* in mammals) transcripts lacking exon 17 (Martinez et al., 2018). Another gene, *hrp-2*, has been identified to cause alternate splicing in *unc-52*, with inhibition of *hrp-2* causing increased cassette exon skipping (Kabat et al., 2009). The regulation of *hrp-2* is theorised to be balanced by alternate splicing factor *mec-8,* implying that this splicing regulator is not tissue specific (Kabat et al., 2009; C. Spike et al., 2002). Further interactions with *hrp-2* have identified *ccar-1* as a physical interactor with *hrp-2*, leading to increased removal and splicing of exon 17 in the presence of *ccar-1* (Fu et al., 2018). Splicing of *HSPG2* may explain why *HSPG2* has been shown to have cell and tissue-specific roles.

### 1.3.3. *HSPG2* in the heart

Perlecan is highly expressed in the cardiac jelly, throughout pericellular matrixes and smooth muscle walls (Costell et al., 1996; Handler et al., 1997). Perlecan knockout mice show severe embryonic cardiac defects leading to embryonic death at day 10.5 in 70-80% of mice, due to a leaky heart created by basement membrane defects (Sasse et al., 2008a). Indeed, a similar response was seen in cardiovascular development of perlecan null zebrafish.

Zoeller and colleagues identify severe defects in cardiovascular system development, somatic muscle development and cardiovascular angiogenesis, highlighting perlecan as a key regulator in these processes (Zoeller et al., 2009b). In gestational week 6/7 perlecan is present in the basement membrane of the endo/pericardium, but not CMs. From gestational week 8/9 onwards domains III and V of perlecan are both expressed in all cardiac basement membranes, including CMs (Roediger et al., 2009a). These studies confirm not only perlecans presence is essential for cardiac development, but perlecan expression develops at later stages of CM development. Not only has perlecans role in development been identified, but also involvement in cardiac damage.

Perlecan ECM is found in the 'infarct zone' after a MI, with similar kinetics to type IV collagen and laminin, suggesting perlecan interacts with these ECM molecules (Nakahama et al., 2000). A key role of perlecan is to control growth factor activity by regulating their sequestration, stabilisation, binding, and signalling (Vlodavsky et al., 1996). Therefore, perlecan may play a larger role in cardiovascular disease than simply as an ECM component, although this requires further investigation.

### 1.3.4. *HSPG2* in other tissues

*HSPG2* has been extensively studied in other tissues, and has cell and tissue-specific functions, here insights reveal findings that may alter functions also found in a cardiac environment. A study by Yamashita *et.al* shows *HSPG2* KO adult mice have reduced white adipose tissue, due to an increased lipid metabolism. Further to this, the *HSPG2* KO mice had increased oxidative metabolism in smooth muscle cells (Yamashita et al., 2018a). As such, defining the role of perlecan is cardiac metabolism, within specific cell populations, may lead to interesting insights.

In osteoporosis, a lack of perlecan reduces calcium signalling, with osteoblasts unable to co-localise with calcium sensitive channels (Pei et al., 2020a). CMs are extremely reliant on calcium signalling, lack of signalling is a critical step in heart failure (Lukyanenko et al., 2009). Both CM metabolism (Bray et al.,

2008) and autophagy (Ucar et al., 2012) play essential roles in the heart. Therefore, these factors are worth investigating further in relation to the roles of perlecan in the cardiac environment, under both homeostasis and fibrotic stress.

## 1.4. Heart Disease and Cardiac Fibrosis

### 1.4.1. Heart Disease

Cardiovascular disease and heart failure are ranked as one of the leading causes of death worldwide, with its prevalence increasing (Gheorghe et al., 2018). Heart failure is the result of the cardiovascular damage, leading to the ability to pump blood hindered, and the hearts output not able to meet its demand (Murphy et al., 2020). Risk factors, such as hypertension, diabetes and obesity are known to increase the likelihood of heart failure. High reliance is placed upon early treatment strategies as these are the current most effective strategies for reducing the risk of future myocardial infarction (Artham et al., 2009). Despite the advances in treatments and prevention strategies, mortality and morbidity remain high, with a predicted increase towards the future (Gheorghe et al., 2018).

### 1.4.2. Cardiac Fibrosis

Cardiac fibrosis is the process in which excess extracellular matrix (ECM) is accumulated within the myocardium, a key feature of heart failure (Berk et al., 2007) leading to dysfunction of the heart (Kong et al., 2013). Accumulation of ECM following injury is part of the natural process of wound healing and tissue repair. In a normal response to injury, the first stage of wound healing involves inflammation, occurring immediately after damage to tissue has occurred (Figure 1.10, A) (Gurtner et al., 2008). This is initiated in response to molecular signals released by dying resident cells (Wynn and Vannella, 2016; Zhang et al., 2010). Monocytes migrate to the wound site and differentiate into macrophages (Gurtner et al., 2008) regulating the inflammation process. Macrophages produce profibrotic mediators, assist in regulation of matrix metalloproteinases (MMPs) and tissue inhibitors of metalloproteinases

(TIMPs) (Wynn and Barron, 2010) and remove tissue debris (Wynn, 2007). The next stage involves migration, recruitment, and activation of leukocytes which in turn proliferate and secrete profibrotic cytokines (Wynn, 2007). The release of profibrotic factors enhances proliferation and activates resident fibroblast populations (Gurtner et al., 2008), along with recruited fibroblasts and epithelial cells (Wynn, 2007).

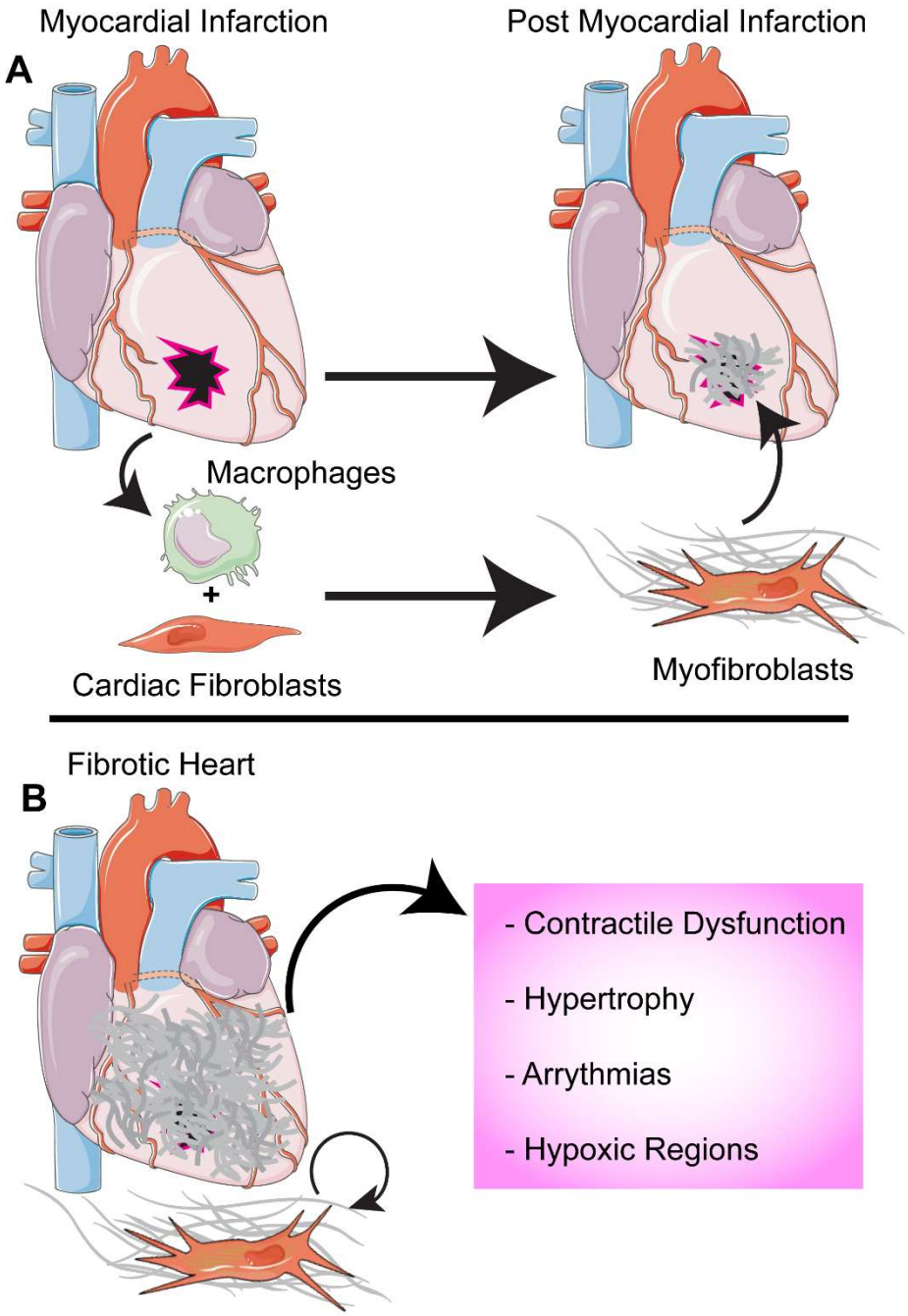


***Figure 1.10 - Wound healing response following myocardial infarction.*** *(A) Following myocardial infarction macrophages and fibroblasts migrate to*

*the wound site to initiate the wound healing response. Cardiac fibroblasts are activated to myofibroblasts secreting ECM to close the cardiac wound. (B) Persistence of myofibroblasts leads to an overproduction of ECM causing cardiac dysfunction.*

Fibroblasts are activated by increased ECM rigidity and tension (Hinz and Gabbiani, 2003), along with chemokines and peptides, such as TGFβ and endothelin-1, which encourage differentiation into an alpha smooth muscle actin (α-SMA) expressing myofibroblasts (Werner et al., 2007). Myofibroblasts are initially in a proto-myofibroblast form, which can be identified by the presence of microfilament bundles known as stress fibres, lacking α-SMA expression (Tomasek et al., 2002). When the proto-myofibroblast is exposed to a prolonged environment with increased tension, TGFβ and endothelin-1, it transitions to a fully differentiated α-SMA expressing myofibroblast (Tomasek et al., 2002; van den Borne et al., 2010). The role of myofibroblasts is to facilitate ECM synthesis and create wound contraction and closure (Wynn and Vannella, 2016). Myofibroblasts shift the repair process into a state where the synthesis of collagen exceeds its rate of degradation. Although initially essential to wound healing, persistence of myofibroblasts leads to out-of-control ECM synthesis, also known as fibrosis (Figure 1.10, B) (Wynn, 2007). Under normal conditions in the wound healing process the collagen-secreting myofibroblasts undergo apoptosis leaving behind a mature scar tissue, but the persistence of myofibroblasts accelerates the tissue towards a fibrotic state (Travers et al., 2016). Myofibroblasts themselves secrete cytokines that encourage a persistent inflammatory response, thereby maintaining the pro-fibrotic environment and inflammatory response (Baum and Duffy, 2011).

There are two main outcomes of the tissue repair process: regeneration, whereby the injured cells are replaced with similar cells, or fibrosis where ECM replaces the normal resident cells (Wynn, 2007). Heart disease is one of biggest killers in the world (Balakumar et al., 2016) with cardiac fibrosis progressing the heart towards failure with excessive build-up of ECM deposition (Hinderer and Schenke-Layland, 2019). There is currently no effective treatment for cardiac fibrosis, or other fibrotic conditions, such as

idiopathic pulmonary fibrosis and renal fibrosis, that also experience a persistent fibrotic process leading to organ failure (Vancheri et al., 2010). Research and models of cardiac fibrosis is thus of significant clinical importance.

## 1.5. Models of heart development and disease

### 1.5.1. Animal models

The development of the heart is a delicately regulated process, highly conserved across vertebrate species, this conservation allows the use of animal models to simulate human development for investigation (Xia et al., 2020). Mouse models are ideal mammalian models, with rapid development and relatively simple genetic manipulation techniques, they can be used for lineage tracing through cardiac development (Zaruba and Field, 2008). While non-mammalian models such as zebrafish and chicken are ideal for real-time imaging, as cardiac development is undergone rapidly, in a more observable environment and at a reduced cost to mouse models (Kemmler et al., 2021; Wittig and Münsterberg, 2020).

Large animals were initially the gold standard for modelling heart disease due to their increased heart size, but the field has now shifted to mouse models, due to their ease of access and use, lower maintenance cost and availability of genetically modified mice lines (Lin et al., 1995; Rai et al., 2017). Methods such as ischemic reperfusion are used to stimulate microvascular dysfunction and initiate cardiac necrosis in a healthy heart, creating a model whereby the heart would respond in a similar way as it does to cardiac assault (Rai et al., 2017; Xia et al., 2016). Pressure overload models work by stimulating cardiac hypertrophy, which is a response to infarctions and heart failure (Borgdorff et al., 2015) which in turn trigger downstream fibrosis (Hirata et al., 2015). These methods were then applied to transgenic mice containing knockout, knock-in and overexpression systems to focus on the roles of specific proteins (Rai et al., 2017).

Mutant mice lines have been generated to simulate fibrosis resulting in different disorders (Rai et al., 2017), such as an imbalance in collagen synthesis and degradation (Bujak and Frangogiannis, 2007), and diabetic models (Wu et al., 2011). Mice models are also extremely powerful for tracking the origin of recruited cells and establishing the function of resident cells in response to cardiac assault (Kanisicak et al., 2016). Some of the main problems and limitations with studying fibroblasts and fibrosis *in vivo* arise from the lack of available markers for cardiac-specific fibroblasts and myofibroblasts (Travers et al., 2016), along with species differences between mice and humans (Musunuru et al., 2010).

### 1.5.2. Human cell models and hiPSCs

Due to the limited ability to gain access to and propagate human cardiac tissue for disease modelling, cell models provide an alternative solution. HEK293 cells are widely used within the cardiovascular field, due to their ease of maintenance and transfection capabilities (Lippi et al., 2020). HEK293 cells express low levels of cardiac ion channels that can be overexpressed, for use of patch clamp and investigation into ion channel related disorders (Vatta et al., 2006). Investigation into the roles of gap junctions via proteins such as Cx43 can be performed on buccal mucosa cell models. The expression of Cx43 follows a similar trend as seen in the hearts of arrhythmogenic cardiomyopathy patients (W. Liu et al., 2020). Although useful in a specialised focus, they lack capabilities required for disease modelling or development.

The discovery that human-induced pluripotent stem cells (hiPSCs) can be generated from fibroblasts (Takahashi et al., 2007) opened a whole new avenue for disease modelling (Musunuru et al., 2010), with their ability to proliferate and differentiate into cells of all 3 germ layers (Chen et al., 2021). Using 4 transcription factors (*Oct-4, Sox-2, c-Myc* and *Klf4*), fibroblasts are reprogramed to a pluripotent state (Takahashi et al., 2007). hiPSCs generated are comparable to embryonic stem cells (hESCs), with similarities in morphology, expression of pluripotency markers and lineage differentiation (Toivonen et al., 2013). Indeed, the hiPSCs retain the genetic identity of the donor (Takahashi et al., 2007), although unlike hESCs, hiPSCs also retain

DNA methylation patterns resulting in an ‘epigenetic memory’ (Lister et al., 2011). Generation and use of hiPSCs removed the ethical concerns surrounding hESCs and the destruction of human embryos. Although, some ethical concerns remain over the use of hiPSCs, including improper reprogramming, tumour formation in therapies and cloning (Zheng, 2016). hiPSCs can alleviate species differences arising from murine models, further including possibilities of modelling not only diseases *in vitro*, but also studying the roles of specific cell types within those diseases (Yoshida and Yamanaka, 2010).

hiPSC derived cardiac populations are currently used in *in vitro* models of cardiac disease and fibrosis. Many *in vitro* models focus on CMs and lack the other crucial cell types known to regulate fibrosis (Polonchuk et al., 2017). Use of primary human CMs are limited by their inability to proliferate, and difficulties in accessing heart tissue for research. Therefore, differentiation of hiPSCs to CMs has become an increasingly popular avenue of research, with several optimised methods being developed (Burridge et al., 2012; Lian et al., 2012). Models now being developed contain a mixture of endothelial cells, CFs and CMs differentiated from hiPSCs show similar responses as primary cells react to pro-fibrotic stimuli (Polonchuk et al., 2017). Disease modelling with stem cells is a popular and promising route to understanding and treating cardiac fibrosis. Stem cell therapy following MI and cardiac fibrosis has also shown insights into recovery capabilities, highlighting stem cells to be a multifunctional tool in cardiac research and therapy (Elnakish et al., 2013).

## 1.6. hiPSCs

### 1.6.1. Establishing Lines

Generation of hiPSC lines can be achieved through multiple methods. One such method involved the use of a Cre-Lox single cleaving cassette, releasing all four required Yamanaka factors inserted via lentiviral transfection. This method would guarantee production of all reprogramming factors in the successfully transfected cells, following Cre-mediated excision (Chang et al., 2009). Other non-integrating methods have been developed, including the use

of adenovirus, Sendia virus and protein upregulation, although all these methods have a very low level of reprogramming efficiency (Malik and Rao, 2013). Transfection of the reprogramming factors via mRNA induces a higher level of reprogramming efficiency in fibroblasts, further enhanced if media is supplemented with histone deacetylase inhibitor valproic acid (Warren et al., 2010).

hiPSC lines can be generated from patients with specific genetic mutations. These lines can generate each of the cell types of the body, while containing the same genotype of the patient they were generated from, ideal for investigating a specific disorder. Since 2006, following Yamanaka and colleagues reprograming mouse fibroblasts to iPSCs (Takahashi and Yamanaka, 2006), hiPSCs have been generated from multiple tissue sources. As well as actively dividing somatic cells shown the capability of reprogramming to hiPSCs, non-proliferative cells, including cardiomyocytes, have been reprogrammed to hiPSCs, suggesting most cell types can undergo reprogramming (Eminli et al., 2009; Grath and Dai, 2019; Watanabe et al., 2011). Due to hiPSC models fast becoming a promising system to study development and diseases, the need for validated hiPSC banks is increasing. International Stem Cell Banking Initiative has suggested specific criteria to be met for hiPSC lines generated. These include, embryonic morphology, transgene silencing, pluripotency markers, differentiation potential, karyotype analysis and guaranteed contamination free cultured conditions (Huang et al., 2019). Access to hiPSC banks allows future scientists the reliability of hiPSC lines generated from specific disorders to be used for a reliable model.

### 1.6.2. Genetic Manipulation

hiPSCs generated from patients with genetic abnormalities can be retargeted to revert specific mutations, thereby creating a healthy version of the patients hiPSCs. Genetic manipulation can also be performed to genetically tag specific proteins, insert inducible overexpression systems, or generate custom gene deletions or mutations. Of the methods to genetically manipulate hiPSCs the most popular and easy to use is CRISPR/Cas9 (Figure 1.11, A) (clustered regularly interspaced short palindromic repeats and CRISPR associated

protein 9). CRISPR/Cas9 was first discovered in the defence of prokaryote cells against foreign genetic elements, such as bacteriophage (Quiberoni et al., 2010). The process of CRISPR/Cas9 within the prokaryote acts as an adaptive immunity to the cell, whereby the protospacer-adjacent motif (PAM) sites direct the Cas9 protein to cleave invading viral DNA (Hsu et al., 2014). CRISPR/Cas9s function was manipulated to allow insertion of a custom guide RNA, allowing specific targeting and double strand cleavage of any target DNA (Jinek et al., 2012). The genetic manipulation of eukaryote cells via CRISPR/Cas9 became a household method, with easy access to specific targeting and cleavage of DNA, to allow insertion of selection cassettes via homologous recombination (Sander and Joung, 2014). The functions of CRISPR/Cas9 were expanded when groups demonstrated CRIPSR/Cas9 could upregulate specific genes, without cleaving DNA. The Cas9 protein was mutated to be unable to cleave, labelled CRISPRa or dCas9, but still target a specific region of DNA. CRISPRa was fused with transcriptional activators such as VP64 causing upregulation of downstream target genes (Figure 1.11, B) (Maeder et al., 2013; Perez-Pinera et al., 2013).

The ‘PiggyBac’ system has been developed to generate “footprint-free” genetic mutations in hiPSCs. This method involves a dual selection approach, after initial antibiotic purification the selection cassette is removed, resulting in a minimally altered, targeted genetic mutation (Kondrashov et al., 2018). Isogenic models can also be created using CRISPR/Cas9 to restore a healthy genotype to the generated lines. Smith and colleagues generated hiPSC lines from both healthy and E99K-ACTC1 mutation suffering family members, these lines were then restored to a healthy genotype or E99K mutation was induced. Cardiomyocytes could then be generated from these hiPSC lines, and investigated revealing differences found specifically from the use of isogenic pairs (Smith et al., 2018). Alternatively, Mosqueira and colleagues display use of isogenic pairs through insertion of indel mutations into the β-myosin heavy chain gene, inducing hypertrophic cardiomyopathy (Mosqueira et al., 2018). Overall highlighting the power of hiPSC isogenic pairs in disease modelling,

and further instilling confidence in the use of hiPSCs to investigate genetic disorders.

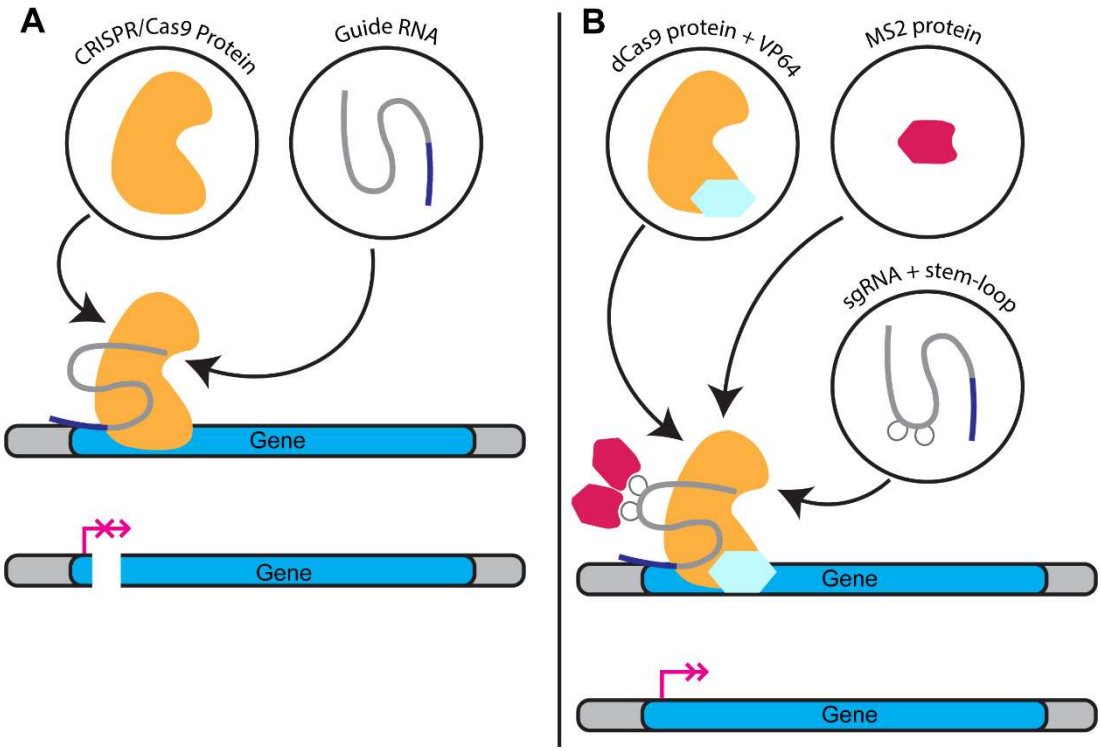


***Figure 1.11 – Methods of CRISPR genetic manipulation.*** *(A) The guide RNA directs the cas9 protein to target gene followed by proteolytic cleavage of the DNA. (B) Dead cas9 (dCas9) combined with guide RNA and MS2 proteins is guided to the target gene causing downstream upregulation via recruitment of transcriptional promotors.*

## 1.7. Differentiation of hiPSCs to Cardiomyocytes

### 1.7.1. hiPSCs to Cardiomyocyte differentiation progression

Methods for CM generation from hiPSCs have evolved from initial protocols relying on spontaneous differentiation of aggregated embryoid bodies (Kehat et al., 2001). Newer protocols started introducing growth factors FGF2, BMP4 and activin A improving differentiation in both monolayer and embryoid body techniques (Burridge et al., 2007; Laflamme et al., 2007). Small molecules were since introduced to simulate cross talk in the BMP4/activin A and WNT/B-catenin pathways to progress optimisation of CM differentiation protocols

(Paige et al., 2010). Burridge and colleagues were the first to generate a chemically defined protocol, the essential components of the B27 supplement, commonly used in CM differentiation, were identified (Burridge et al., 2014). These initial differentiation protocols lead to the generation of mostly ventricular cells simulating FHF development. Researchers investigated utilising retinoic acid (vitamin A) as part of CM differentiation protocols, simulating formation of the SHF, suppressing ventricular genes, and increasing the generation of atrial cells (Wiesinger et al., 2021). Liang and colleagues found modulation of WNT in the cardiac precursor phase would increase specification to nodal pacemaker cells (Liang et al., 2020).

### 1.7.2. Transdifferentiation to Cardiomyocytes

Instead of differentiation from hiPSCs to cardiomyocytes, scientists investigated the potential for transdifferentiation to cardiomyocytes from resident cell populations found in the heart (Klose et al., 2019). Utilising cardiac transcription factors *GATA4*, *MEF2C* and *TBX5* the generation of induced CMs (iCMs) from CFs was performed (Wang et al., 2015). When including cardiac transcription factor *HAND2*, CFs were able to be transdifferentiated to iCMs *in vivo* in mouse (Park et al., 2015). Using these cardiac transcription factors, human CFs are also able to be transdifferentiated to iCMs *in vitro* (Nam et al., 2013). The use of small molecules to induce these cardiac transcription factors and induce iCM transdifferentiation creates the possibility to restore lost CMs following myocardial infarction (Klose et al., 2019).

### 1.7.3. Immaturity of hiPSC-CMs and maturation strategies

The generation of hiPSC-CMs offer great potential in cardiotoxic drug screening, disease modelling, and even regenerative therapies applications. Unfortunately, despite advancements, the immature phenotype of hiPSC-CMs hinders their use (Ahmed et al., 2020). The hiPSC-CMs generated phenotypically and genotypically resemble a foetal CM over an adult CM, with the degree of maturation being considered via several parameters. Immature hiPSC-CMs are smaller in size with an aspect ratio of 1-3:1, less organised

sarcomeres, and no transverse-tubules (t-tubules). This compared to adult CMs, larger cells with an aspect ratio of 10:1, organised sarcomere apparatus and t-tubule formation (Ahmed et al., 2020; Guo and Pu, 2020; Lyra-Leite et al., 2022). Immature hiPSC-CMs spontaneously contract, compared to adult CMs that require external pacing. These cells have reduced calcium stores, less developed sarcoplasmic reticulum, lack of t-tubules and calcium handling proteins, leading to deficient calcium handling kinetics and underdeveloped excitation coupling (Koivumäki et al., 2018). As stated before, adult CM mitochondria are further developed and rely mainly on fatty acid OXPHOS for generation of ATP, compared to foetal glycolytic metabolism seen in immature hiPSC-CMs (Hu et al., 2018). Adult CMs also switch to express sarcomeric isoforms MYH7 and TNNI3 to a higher ratio over immature isoforms MYH6 and TNNI1, respectively, found in hiPSC-CMs (Guo and Pu, 2020).

To improve the maturation of hiPSC-CMs distinct methods have been implemented to enhance this process (Figure 1.12). Initially prolonged culture, up to one year, of hiPSC-CMs were performed showing structural changes, contractile performance and electrophysical properties were enhanced closer to an adult CM than a foetal CM (J. Li et al., 2020; Lundy et al., 2013). Although this strategy did promote some level of maturation, it is not a viable option for the uses of hiPSC-CMs previously stated.

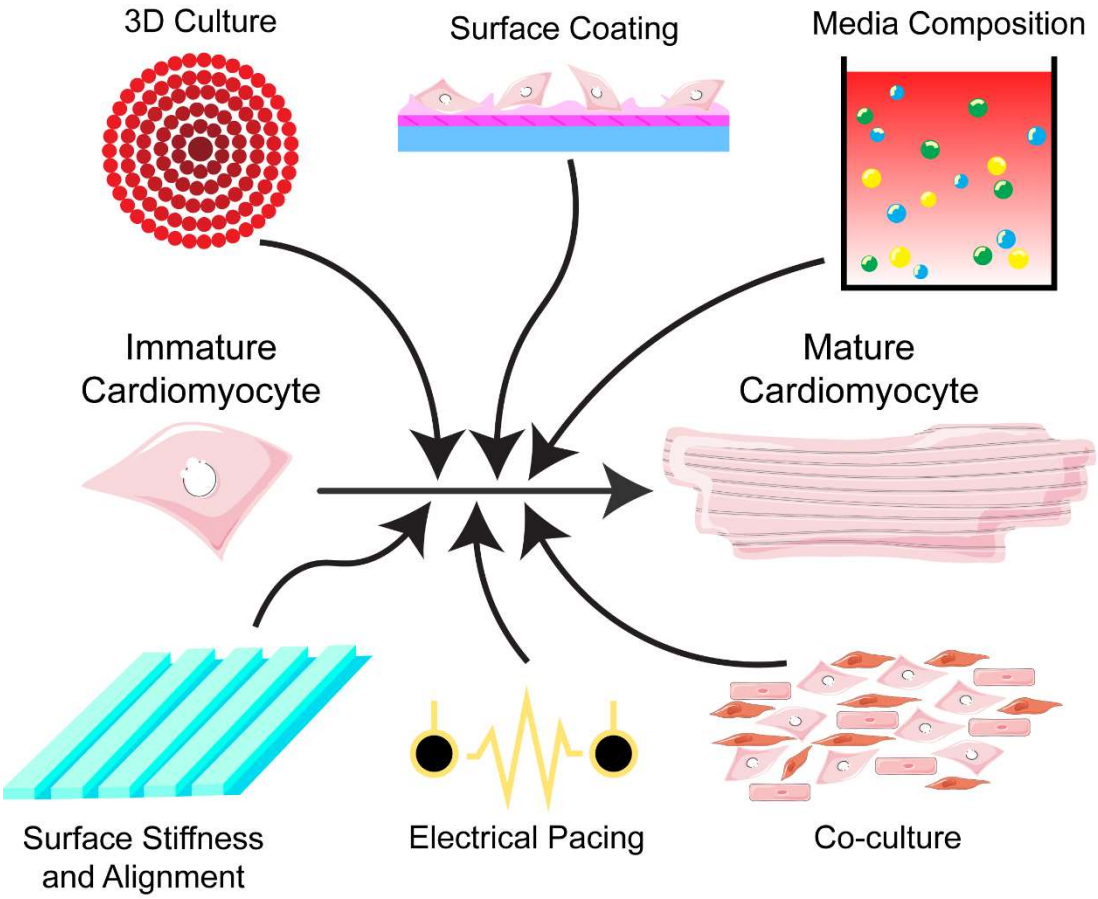


***Figure 1.12 – Approaches to maturation of CMs.*** *Multiple different approaches are being implemented in the aim of maturing hiPSC CMs. This includes techniques such as 3D culture, surface coatings, media compositions, surface stiffness and micropatterning, electrical pacing and co-culture.*

Manipulation of matrix rigidity is shown to enhance hiPSC-CM maturation. Research found the matrix stiffness in the myocardium (10kPa) to be much softer than tissue culture plastics (1GPa) currently being used (Engler et al., 2008). Generating a softer matrix through use of substrates such as hydrogels, enhanced hiPSC-CM maturation, whereby the CMs could generate more force than those cultured on stiffer substrates (Shkumatov et al., 2014). Use of micropatterning on substrates forced alignment of hiPSC-CMs into rectangular rod patterns. Researchers show how these aligned hiPSC-CMs had improved electrophysiology and contractile performance, with generation of t-tubles and more mature mitochondria (Ribeiro et al., 2015). Encapsulating hiPSC-CMs in ECM scaffolds and suspending this construct between silicone posts is an

alternative for creating a softer environment. These hiPSC-CM constructs generated are engineered heart tissues (EHTs), and due to the known resistance properties of the silicone rods, true force can be calculated from EHT contractions. The hiPSC-CMs encapsulated in EHTs undergo structural and contractile maturation, plus an increase in metabolic output and mitochondrial composition (Breckwoldt et al., 2017; Mannhardt et al., 2016). Interestingly, the addition of non-CMs enhanced ECM remodelling and compaction of EHTs, improving CM contractile performance, whereby an EHT compromising of 30% non-CMs and 70% CMs generated the highest contractile force (Tiburcy et al., 2020).

Compositions of media have also been interrogated to further progress the maturation of hiPSC-CMs. These include the addition of factors such as thyroid hormone triiodothyronine (T3), a factor essential for cardiac development that enhances the maturation of hiPSC-CMs. T3 increased the size of CMs in culture, increasing sarcomere length and contractile force (Yang et al., 2014). Media supplemented with T3 and other developmental factors such as glucocorticoid hormones, have been reported to initiate t-tubule formation and enhance contraction of hiPSC-CMs (Parikh et al., 2017). An alternative media composition shown to improve maturation of hiPSC-CMs in culture is one containing fatty acids. Culture conditions for hiPSC-CMs often contain glucose, maintaining the cells in a glycolytic state, while the replacement with fatty acids would recapitulate the switch seen at birth. hiPSC-CMs cultured in fatty acid media showed a maturation status with increased size and contractile force, improved sarcomere alignment and mitochondrial oxidative function (Lopez et al., 2021; Ulmer and Eschenhagen, 2020).

Finally, research has shown that combinations of co-culture methods lead to a more mature CM. Yoshida and colleagues show how hiPSC-CMs had enhanced structural, electrophysiological and metabolic maturation when co-cultured with mesenchymal stem cells (MSCs) (Yoshida et al., 2018). MSCs could increase hiPSC-CM maturation through transwell assays, implying the cytokines released by MSCs (VEGF, FGF, SDF-1, GM-CSF etc.) could improve hiPSC-CM maturity. Exosomes containing microRNAs, released by

MSCs, would also promote hiPSC-CM maturation (Leuning et al., 2018; Yoshida et al., 2018). Giacomelli and colleagues have shown encapsulation of three cardiac populations into a 3D organoid greatly improved the maturation of hiPSC-CMs (Giacomelli et al., 2020). The combination of CFs and ECs in a co-culture helped to mature the hiPSC-CMs through two pathways. The ECs are theorised to enhance CM maturation through release of endothelin-1, causing downstream upregulation of adrenergic receptors. ECs are also known to produce nitric oxide (NO), this can be used by CFs to enhance gap junction formation and connexins, further enhancing the maturation of hiPSC-CMs (Giacomelli et al., 2020; Song and Zou, 2014).

Maturation of hiPSCs through manipulation of ECM presents a highly feasible and simple alternative for mature hiPSC generation. Block and colleagues have shown how the use of an ECM laid down by perinatal stem cells induced the maturation of hiPSC-CMs (Block et al., 2020). Mass spectrometry characterization of the ECM found an increased percentage of composition consisted of perlecan, 19.7% compared to 7.4%. Highlighting perlecan as a potential component of the perinatal stem cell ECM causing the hiPSC-CM maturation recorded.

Implantation of hiPSC-CMs into neonatal rat hearts rapidly matured hiPSC-CMs over 2 months, highlighting CM maturation is enhanced *in vivo* (Ahmed et al., 2020). Immunostaining performed on 3D hiPSC-CM tissues before and after *in vivo* transplantation show perlecan is highly expressed after 12 weeks of transplantation (Yokoyama et al., 2021). This observation suggests perlecan ECM may play a role in CM maturation, although more investigation is required into its mechanism. Indeed, CMs are not the main source of ECM in the heart, this role belongs to the CF.

## 1.8. Differentiation of hiPSCs to Cardiac Fibroblasts

### 1.8.1. Methods for hiPSC to cardiac fibroblast differentiation

Protocols for developing hiPSC-CFs are more recently developed due to the relatively late discovery that a cardiac fibroblast is a specific cell type, different

to fibroblasts of other origin (Ivey and Tallquist, 2016). Of the protocols developed, further differentiation from epicardial cells to CFs has been pursued, these generate CFs representing those that populate the ventricular walls (Fang et al., 2016; Moore-Morris et al., 2016; Whitehead et al., 2022). While other protocols aim at differentiating cardiac progenitor cells to CFs, leading to the production of atrial fibroblasts (J. Zhang et al., 2019). Protocols by both J. Zhang and Giacomelli rely on differentiation methods generating cardiac progenitor cells, then further differentiation to epicardial cells followed by cardiac fibroblast induction with FGF (Giacomelli et al., 2020; J. Zhang et al., 2019). These methods demonstrate how all the major cell types of the heart can be differentiated following an initial differentiation to a cardiac progenitor cell. CFs generated in these protocols will be highly activated, indicative of a CF responding to damage. These CFs are highly proliferative and migratory, but do not fully represent the CFs that exist in a quiescent state in the healthy myocardium. Due to this, the protocol I utilised to differentiate hiPSCs to hiPSC-CFs was generated by H. Zhang and colleagues, whereby they display generation of quiescent hiPSC-CFs (H. Zhang et al., 2019a). This protocol also opts for an initial differentiation to a cardiac progenitor. H. Zhang also utilises a TGFβ inhibitor (SB-431542) to further inhibit differentiation of smooth muscle cells, and further suppress myofibroblast genes such as *ACTA2*. Using these newly developed protocols researchers could now incorporate hiPSC derived CFs into cardiac disease models.

### 1.8.2. Models of cardiac fibrosis

The CFs developed from H. Zhang protocol were utilised in an initial model of cardiac fibrosis. Through co-culturing hiPSC-CMs and CFs, crosstalk through the atrial/brain natriuretic peptide (ANP/BNP) receptor 1 pathways was identified in suppressing cardiac fibrosis (H. Zhang et al., 2019a). Indeed, inhibition of ANP/BNP degradation enzyme exhibited antifibrotic effects on the hiPSC-CFs, although this model of cardiac fibrosis was entirely reliant on MF induction using TGFβ. Lee and colleagues used a three-dimensional model including the use of MSCs, whereby MSCs generate myofibroblasts within the tissue following TGFβ stimulation (Lee et al., 2019). Iseoka and colleagues created a multicellular model utilising CMs and non-CM populations, seeded

at ratios to create a range of CM percentage tissues, following TGFβ treatment to induce a fibrotic response (Iseoka et al., 2021). Mastikhina and colleagues took the hiPSC models of cardiac fibrosis and further developed this using an engineered on-chip model for drug screening (Mastikhina et al., 2020). When analysing these hiPSC models of cardiac fibrosis it can be found that they all rely on induction of a pro fibrotic response by TGFβ. Indeed, TGFβ is one of the major instigators of fibrosis and one of the most studied pro-fibrotic compounds (Leask, 2007), these models only account for this factor to be the cause of activation. hiPSC cardiac fibrosis models should start to incorporate other methods of fibrotic induction. Future models should also aim to include other anti-inflammatory cells such as macrophages to recapitulate the process of cardiac fibrosis to a higher level of accuracy. Although these models are in early stages of development with promise towards identifying anti-fibrotic drugs, with the overall outcome encouraging more research in this fast-developing field.

### 1.9. Rationale

Cardiovascular disease remains one of the leading causes of death around the world and is a financial burden to health care providers, estimated to cost $3.7 trillion between 2011 and 2015 in low- and middle-income countries alone (Gheorghe et al., 2018). *HSPG2*, one of the most evolutionary conserved genes across species (Martinez et al., 2018), is known to be essential in the heart of developing mice and zebrafish where a KO is lethal (Castellanos et al., 2021; Sasse et al., 2008a) . It is known that perlecan is not found initially in the basement membrane of CMs, but expanded over development (Roediger et al., 2009a). The role *HSPG2* plays in the human heart is currently understudied, and if this role changes in each cardiac cellular population is unknown. *HSPG2* and *AGRN* share similar structures, whereby the critical role for *AGRN* in the heart is already defined (Bigotti et al., 2020; Sun et al., 2021). Indeed, an increase in perlecan ECM has been shown after cardiac injury (Nakahama et al., 2000) and hiPSC-CM *in vivo* transplantation (Yokoyama et al., 2021), although the downstream mechanisms of its presence have yet to be fully explored and only theorised. *HSPG2* has been shown to regulate

calcium signalling, fatty acid metabolism and mitochondrial biogenesis in other cell types, these functions are key to the healthy myocardium.

By using hiPSCs human cardiomyocytes can be generated; genetic manipulation can also be performed on hiPSCs to investigate these genetic changes in each cell population generated from the same line. hiPSCs allow the possibility of developing human cardiac disease models, although with some limitations (Giacomelli et al., 2020; Lippi et al., 2020). CMs that are generated from hiPSCs are less mature than adult CMs, representing a more foetal like CM in multiple parameters (Lyra-Leite et al., 2022). This remains a major obstacle for the use of hiPSC-CMs in drug screens and disease models. Despite being an area of high research interest, *in vitro* hiPSC-CM maturation is still not equivalent to adult CM maturity.

*HSPG2* has an essential role in the heart, perlecans presence is not detected in early CMs, but is expressed over development. Both agrin and perlecan competitively bind to the aDGC, agrin shown to be pro-proliferative, therefore perlecan is an ideal candidate for investigation of the phenotypic switch seen in maturation. *HSPG2* is also upregulated after cardiac assault and involved in ECM binding and growth factor sequestration, implying it may also have a role in cardiovascular fibrotic disease.

### 1.10. Hypothesis

Here I hypothesise perlecan is essential in the phenotypic switch in cardiac development and maturation. Perlecan competes with agrin, binding to the aDGC, enabling downstream sequestration of cytokines and ECM regulation to enhance cardiac maturation. Further to this, I hypothesise perlecan may have cell-specific roles within cardiac populations (CMs and CFs). And the development and maturation of CMs reliant on the secretion of perlecan ECM from non-CM populations. I also hypothesise perlecan to be a crucial regulator in cardiovascular fibrotic disease and recovery and therefore has a key role in CFs and wound healing responses. To address these hypothesises, I have set several aims (Figure 1.13).

## 1.11. Aims

1- Generation and characterisation of a *HSPG2* deficient hiPSC cell line, compared to isogenic WT control hiPSCs.
2- Differentiation and characterisation of *HSGP2* deficient CMs and CFs, with phenotypic analysis at multiple developmental stages.
3- Generation of a CM/CF fibrotic disease model in which to interrogate the role of *HSPG2* signalling.
4- Enhance *HSPG2* signalling, through CRISPRa or synthetic culture coating, as an alternative system to provide mechanistic insights.

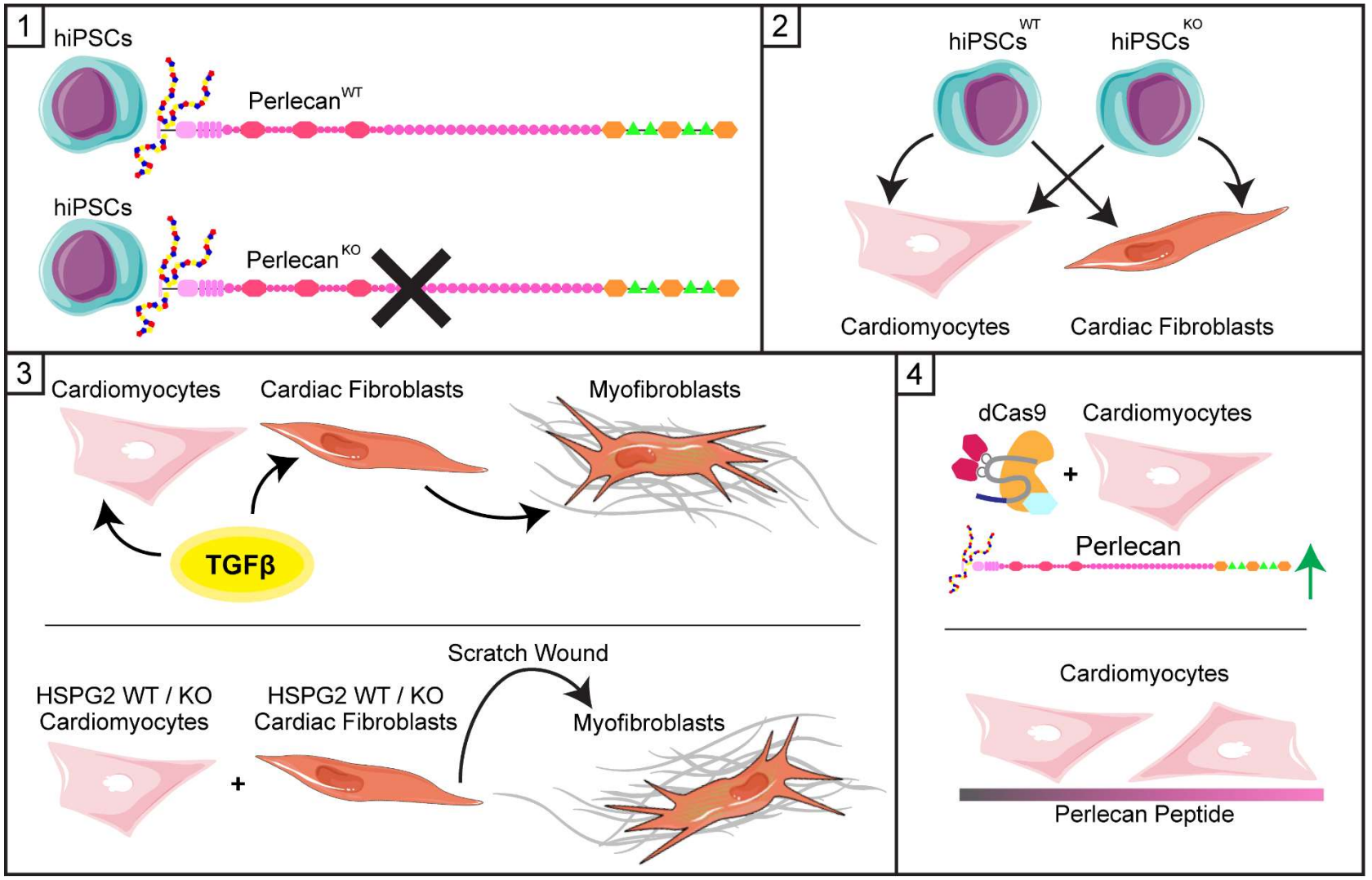
1
hiPSCs
Perlecan WT
hiPSCs
Perlecan KO
2
hiPSCs WT
hiPSCs KO
Cardiomyocytes
Cardiac Fibroblasts
3
Cardiomyocytes
Cardiac Fibroblasts
Myofibroblasts
TGFβ
Scratch Wound
HSPG2 WT / KO
Cardiomyocytes
+
HSPG2 WT / KO
Cardiac Fibroblasts
Myofibroblasts
4
dCas9
Cardiomyocytes
+
Perlecan
Cardiomyocytes
Perlecan Peptide

***Figure 1.13 – (Previous page) Summarised project aims.*** *(1) CRISPR/Cas9 editing of hiPSCs to KO HSPG2. (2) Differentiation of these lines to cardiomyocytes and cardiac fibroblasts. (3) Effects of TGFβ on cardiac cell populations and modelling cardiac fibrosis. (4) Upregulation of HSPG2 or use of HSPG2 coatings to investigate maturation of cardiomyocytes.*

# 2. Methods and Materials

## 2.1. Materials

All reagents and materials used in the study are shown in Table 2.1 and described in the Methods section below. The reagents were obtained from the manufacturers as detailed below.

***Table 2.1 – Reagents and Materials***

| PRODUCT | MANUFACTURER | CATALOGUE NUMBER |
|---|---|---|
| ACTIVIN A | R&D Systems | 338-AC-010 |
| ADVANCED DMEM | Gibco | 12634010 |
| AGAROSE | Fisher Scientific | BP1356-100 |
| AGN 193109 SODIUM SALT | Santa Cruz Biotechnology | sc-210768 |
| AMPICILLIN | Sigma-Aldrich | A9393-5G |
| ANTI-AGRIN PRIMARY ANTIBODY | Thermo Fisher Scientific | 103585 |
| ANTI-ALPHA-SMOOTH MUSCLE ACTIN PRIMARY ANTIBODY | Invitrogen | 14-9760-82 |
| ANTI-PERLECAN A74 PRIMARY ANTIBODY | Abcam | ab23418 |
| ANTI-PERLECAN A76 PRIMARY ANTIBODY | Abcam | ab26265 |
| ANTI-PERLECAN CCN1 PRIMARY ANTIBODY | - | - |
| ANTI-SARCOMERIC ALPHA ACTININ PRIMARY ANTIBODY | Abcam | ab9465 |
| APROTININ | Sigma-Aldrich | A1153 |
| B27™ SUPPLEMENT (50X) | Gibco | 17504044 |
| B27™ SUPPLEMENT, MINUS VITAMIN A 50X) | Gibco | 12587010 |
| B-27™ SUPPLEMENT, MINUS INSULIN (50X) | Gibco | A1895601 |
| BIOLOG MAS | BioLog | 72303 |
| BIOLOG MITOPLATE S-1 | BioLog | 14105 |
| BIOLOG REDOX DYE MIX MC | BioLog | 74353 |
| BLASTICIDIN | Tocris | 5502 |
| CELL DISSOCIATION BUFFER, ENZYME-FREE, PBS-BASED | Gibco | 13151041 |
| CELL STRAINER, 70 UM | Falcon | 352350 |
| CELLTITER-GLO 2.0 | Promega | G9242 |
| CHIR-99021 (CT99021) HCL | Selleck Chemicals | S2924 |
| CLONE-R™ | Stem Cell Technologies | 5888 |
| COLLAGENASE TYPE 2 | Worthington Biochem | LS004174 |
| DAPI | Thermo Fisher Scientific | 62248 |
| DIMETHYL SULFOXIDE (DMSO) | Fisher Scientific | 67685 |
| DMEM | Gibco | 11995040 |
| DONKEY ANTI-MOUSE IGG (H+L) HIGHLY CROSS-ADSORBED SECONDARY ANTIBODY, ALEXA FLUOR™ 647 | Invitrogen | A-31571 |
| DPBS | Gibco | 14190094 |
| ECL EXTRA | Expedeon | ECLA0250 |
| ECL EXTREME | Expedeon | ECLM0100 |
| ESSENTIAL 8™ BASAL MEDIUM | Gibco | A1516901 |
| ESSENTIAL 8™ SUPPLEMENT (50X) | Gibco | A1517101 |
| FETAL BOVINE SERUM (FBS), QUALIFIED, HEAT INACTIVATED | Gibco | 16140071 |
| HORSE SERUM | Gibco | 26050 |

| | | |
|---|---|---|
| FIBRINOGEN | Sigma-Aldrich | F4753 |
| FORMALDEHYDE SOLUTION 4%, BUFFERED, PH 6.9 | Sigma-Aldrich | P6148 |
| GEL LOADING DYE PURPLE (6X) | New England BioLabs | B7024S |
| GENERULER 1KB DNA LADDER | Thermo Fisher Scientific | SM0311 |
| GLUTAMAX™ (100X) | Gibco | 35050061 |
| GLYCEROL | Fisher Scientific | 56-81-5 |
| GOAT ANTI-MOUSE IGG (H+L) CROSS-ADSORBED SECONDARY ANTIBODY, ALEXA FLUOR™ 488 | Invitrogen | A-11001 |
| GOAT ANTI-MOUSE IGG H&L HRP | Abcam | ab6728 |
| GOAT ANTI-RABBIT IGG H&L SECONDARY ANTIBODY (ALEXA FLUOR® 594) | Abcam | ab150080 |
| GOAT ANTI-RABBIT IGG H&L HRP | Abcam | ab6721 |
| GOAT SERUM | Sigma-Aldrich | G9023 |
| HBSS, MINUS CALCIUM CHLORIDE, MINUS MAGNESIUM CHLORIDE, MINUS MAGNEISUM SULFATE (1X) | Gibco | 14175095 |
| IBIDI µ-DISH 35 MM QUAD | Ibidi | 80416 |
| INSULIN | Sigma-Aldrich | I9278 |
| IWR | Sigma-Aldrich | I0161-25MG |
| KANAMYCIN | Tocris | 5505 |
| L-ASCORBIC ACID 2-PHOSPHATE | Sigma-Aldrich | A8960-5G |
| LB AGAR | Invitrogen | 11518916 |
| LB BROTH BASE | Invitrogen | 12780052 |
| LIGHTCYCLERÂ 480 MULTIWELL PLATE, 384, WHITE | Roche Diagnostics | 4729749001 |
| LUMIBLUE ECL EXTREME | Expedeon | ECLM0100 |
| LURIA BROTH (LB) AGAR | Invitrogen | 22700025 |
| LURIA BROTH (LB) BASE | Invitrogen | 12795027 |
| MATRIGEL HESC-QUALIFIED | Corning Incorporated | 54277 |
| MILK POWDER | Thermo Scientific | 16694685 |
| MILLEXÂ SYRINGE-DRIVEN FILTER UNIT, 0.22µm PORE SIZE | Sigma-Aldrich | SLGVV255F |
| MTESR | STEMCELL Technologies | 85850 |
| MTESR PLUS | STEMCELL Technologies | 100-0276 |
| OPTIMEM Â | Gibco | 31985047 |
| P3 PRIMARY CELL 4D-NUCLEOFECTOR® X KIT L | Lonza | V4XP-3024 |
| PRIMARY HUMAN CARDIAC FIBROBLASTS | Promocell | C-12377 |
| PRIMARY HUMAN SKIN FIBROBLASTS | Promocell | C-12352 |
| PENICILLIN-STREPTOMYCIN | Gibco | 15140122 |
| PHOSPHATE BUFFERED SALINE (PBS) TABLETS | Gibco | 18912014 |
| PHUSION HIGH-FIDELITY DNA POLYMERASE | New England BioLabs | M0530L |
| PRECISION PLUS PROTEIN™ STANDARDS DUAL COLOUR PRESTAINED LADDER | Bio-Rad | 161-0374 |
| PROTEINASE K | Thermo Fisher Scientific | EO0491 |
| QPCRBIO CDNA SYNTHESIS KIT | PCR Biosystems | PB30.11-10 |
| QPCRBIO SYGREEN MIX LO-ROX | PCR Biosystems | PB20.11-05 |
| RECOMBINANT HUMAN BMP4 | R&D Systems | 314-BP-010 |
| RECOMBINANT HUMAN FGF BASIC (FGF2) | R&D Systems | 233-FB-025 |

| | | |
|---|---|---|
| RECOMBINANT HUMAN TGFB | R&D Systems | 7754-BH |
| RESTRICTION ENZYME – ASISI | New England Biolabs | R0630S |
| RESTRICTION ENZYME – BSAI | New England Biolabs | R0535S |
| RESTRICTION ENZYME – ECORI | New England Biolabs | R0101S |
| RESTRICTION ENZYME – NSII | New England Biolabs | |
| RESTRICTION ENZYME - SALI | New England Biolabs | R0138S |
| RETINOIC ACID | Alfa Aesar | 44540 |
| REVERT™ 700 TOTAL PROTEIN STAIN | LI-COR Biosciences | 926-11011 |
| RPMI 1640 | Gibco | 11875 |
| RPMI 1640 MEDIUM, NO GLUCOSE | Gibco | 11879020 |
| SAPONIN | Sigma-Aldrich | 47036-50G-F |
| SB 431542 | Tocris | 1614 |
| SDS SOLUTION, 10% SODIUM DODECYL SULFATE SOLUTION | Fisher Scientific | 151-21-3 |
| SEAHORSE XF BASE MEDIUM | Agilent | 1033335-100 |
| SEAHORSE XF CELL MITO STRESS TEST KIT | Agilent | 103015-100 |
| SODIUM DL-LACTATE | Sigma-Aldrich | 71720-5G |
| SYBR SAFE DNA GEL STAIN | Invitrogen | S33102 |
| T4 DNA LIGASE | New England BioLabs | M0202 |
| THROMBIN | Sigma-Aldrich | T7513 |
| TRANSBLOT TURBO™ MINI-SIZE NITROCELLULOSE | BioRad | 1704156 |
| TRANSBLOT TURBO™ MINI-SIZE TRANSFER STACKS | BioRad | 1704158 |
| TRANSFORMING GROWTH FACTOR-B1 HUMAN (TGFB) | Sigma-Aldrich | T7039-2UG |
| TRIFLUOROACETIC ACID | Sigma-Aldrich | 76-05-1 |
| TRIS-BASE | Sigma-Aldrich | 77-86-1 |
| TRITON™ X-100 SOLUTION | Sigma-Aldrich | 93443-100ML |
| TRYPLE EXPRESS, MINUS PHENOL RED | Gibco | 12604021 |
| TWEEN20 | Sigma-Aldrich | P1379-100ML |
| VIAFECT™ TRANSFECTION REAGENT | Promega | E4983 |
| VITRONECTIN (VTN-N) RECOMBINANT HUMAN PROTEIN, TRUNCATED | Gibco | A14700 |
| Y-27632 DIHYDROCHLORIDE (ROCK INHIBITOR) | MedChemExpress | HY-10583 |
| SEAHORSE XFP CELL MITO STRESS TEST KIT | Agilent | 103010-100 |

### 2.2. Cell Culture

Tissue culture and incubation was carried out under normal atmospheric pressure. Cells were incubated at 37°C, 5% $CO_2$ and 20% $O_2$ (unless stated otherwise) in the HERACELL 150i $CO_2$ incubator (Thermo Fisher Scientific). Tissue culture was carried out in the Scanlaf Mars Safety class 2 MBSC4C safety cabinet (Labogene) under sterile conditions.

### 2.2.1. Maintenance of hiPSCs in culture

Human induced pluripotent stem cells (hiPSCs) were maintained and grown in Essential 8 (E8) media (Gibco, Life Technologies) on Vitronectin (Gibco, Life Technologies) coated surfaces in a humidified atmosphere (5% $CO_2$) at 37 °C. The media was replaced every 24 hours. When hiPSCs reached 90% confluency they were dissociated using TrypLE Express (Gibco, Life Technologies) or Cell Dissociation Reagent (Gibco, Life Technologies) following the manufacturer's protocol. Cells were seeded at 20,000 cells/$cm^2$ with E8 supplemented with 10μM Y-27632 dihydrochloride (ROCK inhibitor) (MedChemExpress). ROCK inhibitor was made up into a 10mM stock solution in sterilised water and stored at -80$^oC$.

### 2.2.2. Long term storage of hiPSCs

For long-term storage and preservation, iPSCs were stored in 1.8mL cryogenic tubes as 1mL aliquots of 1 million cells per aliquot in a suspension composed of 50% (v/v) E8 media, 30% (v/v) Foetal Bovine Serum (FBS) (Gibco) and 20% (v/v) Dimethyl sulfoxide (DMSO) (Thermo Fisher Scientific).

To thaw iPSCs, frozen cryovials were placed in a Grant Sub 6 unstirred water bath (Grant Instruments Ltd) at 37$^OC$ for 60 seconds. The cell solution was transferred to 9 mL PBS solution and pelleted in an Eppendorf Centrifuge 5804 (Eppendorf) at 160 RCF for 4 minutes. The supernatant was aspirated, and the cells were resuspended in pre-warmed E8 media supplemented with 10μM ROCK inhibitor.

### 2.2.3. Maintenance of primary fibroblasts in culture

Primary fibroblasts were provided by James Smith. Cardiac (Promocell) and skin fibroblasts (Promocell) were maintained and grown in a Fibroblast Growth Media consisting of Advanced DMEM (Gibco, Life Technologies) supplemented with 5% (v/v) Foetal Bovine Serum (Gibco, Life Technologies), 1% (v/v) GlutaMax (Gibco, Life Technologies) and 1% (v/v) Pen/Strep (Gibco, Life Technologies) on Matrigel (Corning) coated surfaces in a humidified atmosphere (5% $CO_2$) at 37°C. The media were replaced every 2-3 days. At 70% confluency primary fibroblasts were dissociated using TrypLE Express

(Gibco, Life Technologies) and seeded at 10,000 cells/cm$^2$ in a Fibroblast Growth Media.

### 2.2.4. Differentiation of hiPSCs to Cardiac Fibroblasts

Human iPSC lines were maintained as described before for 2 passages after thawing before being seeded on Matrigel (Corning) coated surfaces. 48 hours after seeding hiPSCs on Matrigel coated surfaces the media was replaced with RPMI medium (Gibco, Life Technologies) with B27 supplement minus insulin (Gibco, Life Technologies) (RPMI/B27- insulin) and 2 μM CHIR99021 (Abcam) for 2 days. Media were replaced with fresh RPMI/B27- insulin supplemented with 5 μM IWR-1 (Tocris) for 2 days. On day 4 hiPSC-cardiac progenitor cells (hiPSC-CPCs) were dissociated using TrypLE Express (12604013, Gibco, Life Technologies) and seeded at 20,000 cells/cm$^2$ in Advanced DMEM medium (Gibco, Life Technologies) supplemented with 3 μM CHIR99021 (Abcam) and 2 μM Retinoic Acid (Tocris). Media and supplements were changed daily for 3 days followed by hiPSC-CPCs being recovered in Advanced DMEM (Gibco®, Life Technologies) for 4 days. hiPSC-epicardial cells (hiPSC-EPCs) were dissociated using TrypLE Express (Gibco, Life Technologies) and seeded at 10,000 cells/cm$^2$ in a Fibroblast Growth Media supplemented with 10 ng/ml FGF2 (Sigma-Aldrich) and 10 μM SB431542 (Tocris) for a further 6 days. All cultures were maintained in a humidified atmosphere (5% $CO_2$) at 37 °C.

### 2.2.5. Growth curves using CellTitre-GLO

To perform growth curves cells were seeded into 3 separate 96 well plates. On the first plate cells were seeded as a standard curve ranging from 0, 100, 500, 1000, 2500, 5000, 10000, 20000, 40000. Cells were then seeded in 3 wells per condition. For analysis of cell viability and growth cells were initially washed with 100 μL DMEM. Cells were then incubated in 50 μL DMEM for 30 minutes. Meanwhile CellTitre-Glo was incubated at room temperature for 30 minutes to acclimatise. Following incubation 50 μL CellTitre-Glo is added to cells, wrapped in foil and incubated at 37°C on a shaker for 2 minutes. Cell solution is then mixed and 90 μL is transferred to a white 96-well assay plate (Corning) and incubated for 5 minutes covered in foil. Luminescence is then

measured using the FLUOstar OPTIMA microplate reader (BMG Labtech). Using the standard curve cell count was generated for all following timepoints.

### 2.2.6. Differentiation of hiPSCs to Cardiomyocytes

hiPSCs were differentiated into cardiomyocytes using a protocol developed and kindly shared by Andreia Bernardo (Francis Crick Institute/ Imperial College London) (Dark et al. manuscript in preparation, patent submission WO2020245612). Human iPSC lines were maintained as described before for 2 passages after thawing before being seeded between 15,000 and 45,000 cells/cm$^2$ on Matrigel (Corning) coated 24 well plates. hiPSCs were maintained in E8 media (Gibco, Life Technologies) for 2 days before starting the differentiation on Day 0 with by switching media to HM1 (Table 2.2) supplemented with 3 µM CHIR99021 (Abcam), 3 ng/mL BMP4 (PeproTech), 5 ng/mL FGF2 (PeproTech) and 5 ng/mL Activin A (PeproTech). HM1 was replaced after on Day 1 with HM1 containing no additional supplements. On Day 2 media was replaced with HM1 supplemented with 65 µg/mL L-Ascorbic Acid (Tocris) and 1 µM IWR-1 (Tocris). Media was changed with fresh HM1 supplemented with 65 µg/mL L-Ascorbic Acid (Tocris) on differentiation days 4 and 6. On day 8 media is replaced with HM2. On day 10 media is replaced with HM3 supplemented with 4 mM L-lactic acid (Sigma-Aldrich). Media is replaced on day 12 and 14 with fresh HM3 supplemented with 4 mM L-lactic acid (Sigma-Aldrich) and 65 µg/mL L-Ascorbic Acid (Tocris) until purification was complete. Cardiomyocytes were dissociated using Collagenase (Worthington Biochem,), counted, and reseeded on Vitronectin (Gibco, Life Technologies) coated tissue culture plastics in RMPI (Gibco, Life Technologies) plus B27 (Gibco, Life Technologies) supplemented with 10% (v/v) Foetal Bovine Serum (Gibco, Life Technologies). Cardiomyocytes were maintained in RMPI (Gibco, Life Technologies) plus B27 (Gibco, Life Technologies) with media being replaced every 3 days.

***Table 2.2 – Media compositions for cardiomyocyte differentiation***

| HM1 | HM2 | HM3 |
|---|---|---|
| 49 mL RMPI (11875093, Gibco, Life Technologies) | 49 mL RMPI (11875093, Gibco, Life Technologies) | 49 mL RPMI – No Glucose (11879020, Gibco, Life Technologies) |

| | | |
|---|---|---|
| 1 mL B27 -Insulin (A1895601, Gibco, Life Technologies) | 1 mL B27 -Vitamin A (12587010, Gibco, Life Technologies) | 1 mL B27 -Vitamin A (12587010, Gibco, Life Technologies) |
| 10 nM AGN-193109 (5758, Tocris) | 10 nM AGN-193109 (5758, Tocris) | 10 nM AGN-193109 (5758, Tocris) |

### 2.2.7. Culture of hiPSC-CMs and hiPSC-CFs with TGFβ

To induce stress response with TGFβ in hiPSC-CFs and hiPSC-CMs, media was supplemented with 10 ng/mL TGFβ (R&D Biosystems). Media was changed every 24 hours for 4 days before RNA extraction and cDNA synthesis was performed.

### 2.2.8. Co-culture scratch wound assays

To perform co-culture scratch wound hiPSC-CMs and hiPSC-CFs were seeded at varying percentages (Table 2.3).

***Table 2.3 – Cells seeded in co-culture assays***

| Percentage | hiPSC-CF cells seeded | hiPSC-CMs cells seeded |
|---|---|---|
| 100% CMs | 0 | 200,000 |
| 90% CMs | 20,000 | 180,000 |
| 75% CMs | 50,000 | 150,000 |
| 50% CMs | 100,000 | 100,000 |
| 25% CMs | 150,000 | 50,000 |
| 0% CMs | 200,000 | 0 |

Co-cultures were recovered for 72 hours before scratch would with a p10 pipette tip was performed. Following manual scratch, the wells were gently washed with PBS 2 times before media replaced with RPMI/B27. Media was replaced every 48 hours, with images taken every 24 hours.

Using ImageJ 5 measurements were taken across each aligned image between the minimum distance between each side of the scratch wound. This was repeated for each image and each condition. Output measurements were exported to Microsoft Excel and GraphPad for graph generation and statistics.

Difference in action potential is calculated identifying the difference between each side of scratch wound contraction action potential. Overall videos of the scratch wound were cropped to highlight each side separately. MUSCLEMOTION trace outputs were then plotted in Microsoft Excel, change in action potential of the contraction was then identified followed by the time between each switch. Results were averaged from 2 video repeats and plotted using GraphPad Prism.

Media was changed every 48 hours for all scratch wound experiments. Media compositions generated for scratch wounds consisted of hypoxic and normoxic CM conditioned media and indole-3-carbanol. hiPSC-CMs were cultured in RPMI/B27 at 37°C, 5% $CO_2$ and 2% $O_2$ for 48 and 96 hours before media was removed. This method was repeated for normoxic CM conditioned media except hiPSC-CMs were maintained at 20% $O_2$. This media was mixed with fresh RPMI/B27 at a 1:1 ratio before use. Indol-3-carbanol was resuspended in DMSO and supplemented in media at 100 µM in RPMI/B27.

### 2.2.9. hiPSC-CM culture on synthetic perlecan peptide

hiPSC-CMs were dissociated as previously described and seeded onto perlecan synthetic peptide 24 well plates (DenovoMatrix). For RNA expression 200,000 hiPSC-CMs were seeded, while for nuclear quantification and imaging 100,000 hiPSC-CMs were seeded. Cultures were maintained in RPMI/B27 at standard conditions, with media changes every 48 hours for 14 days.

## 2.3. Generation of *HSPG2* deficient cell lines

### 2.3.1. Creation of initial *HSPG2* CRISPR/Cas9 plasmid

PCR was performed to generate both arms of homology using two primer pairs, “HSGP_LEFT1_FWD”, “HSGP_LEFT1_REV”, “HSGP_Right1_FWD” and “HSGP_Right1_REV” (Table 2.4).

***Table 2.4 – Primers for generation of arms of homology***

| PRIMER | SEQUENCE |
|---|---|
| HSGP_LEFT1_FWD | TCGCGAATGCATCCTCATGCCAGGCCATTGCC |

| | |
|---|---|
| HSGP_LEFT1_REV | TCGCGAGCGATCGCCTAGGTCACCTGTAAGCAAACGA |
| HSGP_RIGHT1_FWD | TCGCGAGAATTCCATGGGCTGAGGGCATACGA |
| HSGP_RIGHT1_REV | TCGCGAGTCGACACTATAAGTCCCCATCCCAG |

The PCR product generated was extracted using NucleoSpin Gel and PCR Clean-up Mini kit (Macherey-Nagel, 740609). The left homology arm was digested with NsiI (New England BioLabs) and AsiSI (New England BioLabs). While the right homology arm was digested with SalI (New England BioLabs) and EcoRI (New England BioLabs). The arms of homology are ligated into a pre-designed plasmid containing a puromycin resistance cassette using T4 DNA Ligase (New England BioLabs).

The ligation mixture was transformed into One Shot TOP10 Competent Cells (Invitrogen). 5 µl of ligation mixture was mixed with 25 µl thawed One Shot TOP10 Competent Cells and left on ice for 30 minutes, after which competent cells were heat-shocked at 42 °C for 30 seconds and returned to ice for 2 minutes. 125 µL of SOC medium (Invitrogen) was gently added to the competent cell mixture and incubated at 37 °C for 1 hour in a shaking incubator at 225 rpm. 200 µL of the transformation mix was spread onto pre-prepared LB agar plates supplemented with kanamycin (Tocris) and left at 37 °C overnight.

Colonies on kanamycin LB agar plates were picked using a pipette tip and incubated in 5ml broth supplemented with 5 µl of 50 µg/ml kanamycin. The broth was left overnight at 37 °C in a shaking incubator at 225 rpm. Broth mixtures were pelleted at 5000 rpm for 15 minutes at 4 °C and residual supernatant removed. Plasmids were extracted from pelleted competent cells using the Wizard Plus SV Minipreps DNA Purification System (Promega) following the manufacturers' protocol. Plasmids extracted were sent to Genewiz Sanger Sequencing service for confirmational sequencing.

### 2.3.2. Creation of *HSPG2* full deletion CRISPR/Cas9 plasmid

PCR was performed to generate the 5' prime arm of homology using "HSPG_Right5_FWD" and "HSPG_Right5_REV" primers (Table 2.5).

***Table 2.5 – Primers for generation of arms of homology full HSPG2 insert***

| PRIMER | SEQUENCE |
|---|---|
| HSPG_RIGHT5_FWD | TCGCGAGCGATCGCGGCAGCCTGCCACCTGACAGCCG |
| HSPG_RIGHT5_REV | CTATGAGTCGACGGGTGGGCACCACTGTGTAA |

The PCR product generated was extracted using NucleoSpin Gel and PCR Clean-up Mini kit (Macherey-Nagel). Both extracted PCR product and previously generated HSPG2 CRISPR/Cas9 insert plasmid was digested with EcoRI (New England BioLabs) and SalI (New England BioLabs). Enzymatic digestion was performed at 37 °C for 1 hour and 65 °C for 10 minutes in a PCR cycler. Following digestion, ligation was performed using T4 DNA ligase (New England BioLabs) at 16 °C overnight in a PCR cycler.

The ligation mixture was transformed into One Shot TOP10 Competent Cells (Invitrogen). 5 µL of ligation mixture was mixed with 25 µl thawed One Shot TOP10 Competent Cells and left on ice for 30 minutes, after which competent cells were heat-shocked at 42 °C for 30 seconds and returned to ice for 2 minutes. 125 µL of SOC medium (Invitrogen) was gently added to the competent cell mixture and incubated at 37 °C for 1 hour in a shaking incubator at 225 rpm. 200 µL of the transformation mix was spread onto pre-prepared LB agar plates supplemented with kanamycin (Tocris) and left at 37 °C overnight.

Colonies on kanamycin LB agar plates were picked using a pipette tip and incubated in 5ml broth supplemented with 5 µl of 50 µg/ml kanamycin. The broth was left overnight at 37 °C in a shaking incubator at 225 rpm. Broth mixtures were pelleted at 5000 rpm for 15 minutes at 4 °C and residual supernatant removed. Plasmids were extracted from pelleted competent cells using the Wizard Plus SV Minipreps DNA Purification System (Promega) following the manufacturers' protocol. Plasmids extracted were sent to Genewiz Sanger Sequencing service for confirmational sequencing.

### 2.3.3. Transfection of iPSCs with CRISPR/Cas9 and clone generation

Human iPSC lines media was switched from E8 (Gibco, Life Technologies) to mTeSR-1 (StemCell Technologies) 2 days prior to transfection. iPSC lines were dissociated using TrypLE Express (Gibco, Life Technologies), resuspended in mTeSR-1, and prepared for $1x10^6$ cells per transfection. Cells were centrifuged at 300 rpm for 5 minutes, resuspended in P3 Buffer and transfected following the manufacturers' guidelines using the Lonza 4D-Nucleofector Amaxa kit and program CA-137. Cells were transfected with 3 plasmids at 350ng each: pU6 guide RNA plasmid, pCas9 plasmid and HSPG2-targeting insert plasmid. Transfected cells were incubated within the cuvettes at 37 °C for 5 minutes before being seeded onto Matrigel (Corning) coated 6-well plates in mTeSR-1 Plus (StemCell Technologies) supplemented with Clone R (StemCell Technologies) following the manufacturers' guidelines. Cells were fed for another day before antibiotic selection using mTeSR-1 Plus (StemCell Technologies) supplemented with blasticidin (Tocris) at 2.5 µg/ml. Following 3-6 days of antibiotic selection clones were manually picked and transferred to 96-well plates and media replaced with E8. Following clonal expansion, individual clones were analysed for correct cassette insertion using PCR.

### 2.3.4. Clone Selection and quantification using PCR

Genomic DNA was extracted from clones resistant to blasticidin selection using the Macherey-Nagel DNA extraction kit (Qiagen). Extractions were preformed following the manufacturer's instructions. PCRs (Table 2.6, Table 2.7) were performed using 100 ng of gDNA, NEB Phusion Polymerase (New England Biolabs) and GC Buffer (New England Biolabs) following the manufacturers' recommendations for a 20 µl reaction.

***Table 2.6 – Clone quantification PCR set up***

**PCR SETUP**

| **TEMP** | Time | Cycles |
|---|---|---|
| **98°C** | 30 Seconds | x1 |
| **98°C** | 10 Seconds | x30 |
| **60°C** | 30 Seconds | |
| **72°C** | 1 minute 30 seconds | |

| | | |
|---|---|---|
| **72°C** | 5 minutes | x1 |
| **4°C** | - | - |

***Table 2.7 – Primers used in PCR for quantification of clones***

| PRIMER NAME | FORWARD PRIMER | PRIMER NAME | REVERSE PRIMER |
|---|---|---|---|
| **DI F1** | GGGCATTCCAGCAGAGGGCC | *HSPG2* Ex2 Rev (D1R1) | TCCAGCGCATTTGGCTTGCT |
| **BLAST FWD** | AGAACAGGGGCATCTTGAGC | EF-1α Rev | ACCCGTTGCGAAAAAGAACG |
| **DV F1** | TTGTTGGGGGACAGTGAGTG | | |
| **DV F2** | CCCTCGGTGCTCATCAACAT | | |

PCR reactions were mixed with 1x Gel Loading Dye, loaded on a 1% (w/v) agarose gel (Fisher Bioreagents) supplemented with 1x SYBR Safe DNA Gel Stain (Thermo Fisher Scientific) in 1x TAE buffer (242 g Tris base, 57.1 ml acetic acid, 100 ml of 500 mM EDTA, 850ml $H_2O$) and ran at 90 V for 1 hour. Selected bands were extracted using the NucleoSpin Gel and PCR Clean-up Kit (Macherey-Nagel) following the manufacturers' protocol and sent for sequencing using Genewiz Sanger Sequencing service.

## 2.4. Creation of guide RNA plasmids for CRISPRa

### 2.4.1. Design and annealing of oligonucleotide pairs

For each gene of interest, 3 different guide DNAs were created, with oligonucleotides designed using 'CRISPR-ERA: a comprehensive designer tool for CRISPR genome editing, (gene) repression, and activation', along with a 4-nucleotide sequence to match sticky ends, synthesised by Sigma-Aldrich. Oligonucleotides (*Table 2.8*) were annealed using 2.5 µg of forward and reverse oligo at 100 µM with 10 µL of 5x annealing buffer (NEB buffer 2: 100 µL 1M Tris pH 7.5-8, 100 µL 5M NaCl, 100 µL 0.1M EDTA, 700 µL $H_2O$) and 35 µL $H_2O$. The mixture was incubated at 98 °C for 5 minutes followed by removal from heat block and cooled at room temperature for 3 hours. Annealed oligos were then further diluted with 450 µl $H_2O$.

***Table 2.8 – Primer pairs annealed to create double stranded insert for guide RNA to target specific genes as part of CRISPRa***

| GUIDE NAME | FORWARD SEQUENCE | REVERSE SEQUENCE |
|---|---|---|
| HSPG2 G1 | ACCG-CAAAGGCCTAGTAGGCTGCG | AAAC-CGCAGCCTACTAGGCCTTTG |
| HSPG2 G2 | ACCG-TACTCCAGGCCGGGTTTGGC | AAAC-GCCAAACCCGGCCTGGAGTA |
| HSPG2 G3 | ACCG-AAAAGCTGCGCGAGTGGAGT | AAAC-ACTCCACTCGCGCAGCTTTT |
| AGRN G1 | ACCG-GCGTCCCGGGGCTTTGTTCG | AAAC-CGAACAAAGCCCCGGGACGC |
| AGRN G2 | ACCG-TCCCGGGGCTTTGTTCGCGG | AAAC-CCGCGAACAAAGCCCCGGGA |
| AGRN G3 | ACCG-GACAGGACGGGACGCAGCTC | AAAC-GAGCTGCGTCCCGTCCTGTC |
| AGRN G4 | ACCG-ACCCGAGTTAATGCCTAATC | AAAC-GATTAGGCATTAACTCGGGT |

### 2.4.2. CRISPRa gRNA plasmid digestion and extraction

Digestion of pU6 gRNA plasmid was performed using 3 µl BsaI (New England Biolabs®), 3 µl 10x CutSmart Buffer (New England Biolabs), 3 µg plasmid and $H_2O$ to a 30 µl total volume. Reaction mixtures were incubated at 37 °C for 1 hour followed by 70 °C for 10 minutes. The digest mix was run on a 1% (w/v) agarose gel (Fisher Bioreagents) supplemented with 1x SYBR Safe DNA Gel Stain (Thermo Fisher Scientific) in 1x TAE buffer (242 g Tris base, 57.1 ml acetic acid, 100 ml of 500 mM EDTA, 850ml $H_2O$) at 90 V for 1 hour. Digested plasmids were visualised using a CCD camera, excised using a scalpel and extracted using the NucleoSpin Gel and PCR Clean-up Kit (Macherey-Nagel) following the manufacturers' protocol.

### 2.4.3. Ligation of oligonucleotides and CRISPRa gRNA plasmid

Extracted digested plasmid was ligated with previously annealed oligonucleotide pairs, using 2 µl of 10x T4 DNA Ligase Reaction Buffer (New England Biolabs) mixed with 50 ng of digested plasmid, 2 µl annealed oligonucleotide pairs, 1 µl T4 DNA Ligase and additional $H_2O$ to a total volume

of 20 µl. The reaction mixture was left at 10 °C overnight followed by 65°C for 10 minutes.

### 2.4.4. Transformation of competent cells

The ligation mixture was transformed into One Shot TOP10 Competent Cells (Invitrogen). 5 µl of ligation mixture was mixed with 25 µl thawed One Shot TOP10 Competent Cells and left on ice for 30 minutes, after which competent cells were heat-shocked at 42 °C for 30 seconds and returned to ice for 2 minutes. 125 µL of SOC medium (Invitrogen) was gently added to the competent cell mixture and incubated at 37 °C for 1 hour in a shaking incubator at 225 rpm. 200 µL of the transformation mix was spread onto pre-prepared LB agar plates supplemented with kanamycin (Tocris) and left at 37 °C overnight.

### 2.4.5. Plasmid expansion and DNA minipreps

Colonies on kanamycin LB agar plates were picked using a pipette tip and incubated in 5ml broth supplemented with 5 µl of 50 µg/ml kanamycin. The broth was left overnight at 37 °C in a shaking incubator at 225 rpm. Broth mixtures were pelleted at 5000 rpm for 15 minutes at 4 °C and residual supernatant removed. Plasmids were extracted from pelleted competent cells using the Wizard Plus SV Minipreps DNA Purification System (Promega) following the manufacturers' protocol.

### 2.4.6. Transfection of iPSCs with CRISPRa

Human iPSC lines were transfected as previously described using the Amaxa nucleofector with a combination of 333 ng of U6 gRNA guide plasmid, 333 ng of MS2 plasmid and 333 ng of dCas9 plasmid (provided by James Smith). Transfected cells were seeded onto Matrigel (Corning) coated 6 well plates in E8 media (Gibco, Life Technologies) supplemented with Y-27632 (Abcam). hiPSCs were lysed 48 to 72 hours after transfection using supplied Macherey-Nagel NucleoSpin RNA Kit lysis buffer.

### 2.4.7. Transfection of hiPSC-CMs with CRISPRa

Transfection of hiPSC-CMs was adapted from Bodbin et al., 2020. 12 hours pre transfection media was switched to RPMI/B27 supplemented with 10%

(v/v) FBS. On the day of transfection, media is replaced with fresh RMPI/B27 +10% (v/v) FBS. Transfection solution consists of 300 ng of plasmid with ViaFect™ in a 6:1 ratio of volume (in µL) to plasmid mass (in µg) in Opti-MEM (Gibco) media. The solution is incubated at room temperature for 15 minutes after which transfection solution is added to the cells. Cells are incubated for 24 hours at 37°C in a humidified incubator before media is replaced with fresh RPMI/B27. Analysis was performed 72 hours and 10 days following transfections.

## 2.5. RNA extraction, cDNA synthesis and Quantitative real-time PCR

### 2.5.1. RNA Extraction

RNA was extracted from cells using the Macherey-Nagel NucleoSpin RNA Kit (Macherey-Nagel) or Qiagen RNeasy Mini Kit (Qiagen) following the manufacturers' provided protocols.

### 2.5.2. 1.5.2. cDNA synthesis

Reverse transcription was performed using the PCR Biosystems Ultrascript 2.0 cDNA Synthesis Kit (PCR Biosystems) following the manufacturers' protocol, excluding the final extension time that was altered from 30 minutes to 1 hour. Final cDNA was diluted to 100 µL with the initial cDNA template synthesised from 1 µg of mRNA.

### 2.5.3. 1.5.3. qRT-PCR using SYBR™ Green or TaqMan™

Real-time quantitative PCR was performed using 1 µL of the cDNA reaction with 2.5 µL SYBR Green PCR Master Mix (PCR Biosystems), 0.5 µL primer master mix and 1 µL $H_2O$ for SYBR-specific primers. For TAQMan 1 µL cDNA was mixed with 2.5 µL TAQMan Master Mix (PCR Biosystems), 0.25 µL TAQMan assay and 1.25 µL $H_2O$. Both SYBR and TAQ qRT-PCR reactions were performed on Roche LightCycler 480 Multiwell Plates (Roche) in a Roche LightCycler 480 II (Roche). All qRT-PCR reactions were performed in triplicate, normalised to housekeeper genes *18S* (for TaqMan) or *GAPDH* (for SYBR Green) and assessed using a comparative $C_t$ method.

***Table 2.9 – Primer pairs used for quantitative analysis of gene expression using the SYBR system.***

| GENE NAME | FORWARD PRIMER | REVERSE PRIMER |
|---|---|---|
| ***ACTA2*** | CCAGAGCCATTGTCACACAC | CAGCCAAGCACTGTCAGG |
| ***ACTC1*** | CCAGCCCTCCTTCATTGGT | GGTGCCTCCAGATAAGACATTGTT |
| ***ACYL*** | GCTCTGCCTATGACAGCACCAT | GTCCGATGATGGTCACTCCCTT |
| ***AGRN*** | CATGGCTGTGTTCTTCATGTGTT | GGTCATTCTGAGACAAGGACGACT |
| ***CASQ2*** | AGCTTGTGGAGTTTGTGAAG | GGATTGTCAGTGTTGTCCC |
| ***CCNB1*** | CCAAATCAGACAGATGGAAA T | GCCAAAGTATGTTGCTCGA |
| ***CD36*** | AGCTTTCCAATGATTAGACG | GTTTCTACAAGCTCTGGTTC |
| ***COL18*** | TCCAGAGAATGCCGCTTG | GGAACTTGTCAGGGTCCG |
| ***COL1A1*** | TCTGCGACAACGGCAAGGTG | GACGCCGGTGGTTTCTTGGT |
| ***COL3A1*** | AGGGGAGCTGGCTACCCTCC | ACGTTTCCCTGAAGGGACTT |
| ***COL4A2*** | AGGGTCGCAGGGAGAGCTGG | TGGGCCTCGTTCCCCTGGAG |
| ***DDR2*** | GGAGCCATCCAGGCTGATAC | GGCAGGCACTGAGTATGTGT |
| ***GAPDH*** | GTCTCCTCTGACTTCAACAGCG | ACCACCCTGTTGCTGTAGCCAA |
| ***GATA4*** | TCAAACCAGAAAACGGAAGC | GCATCTCTTCACTGCTGCTG |
| ***GPC3*** | CATTCTCAACAACGCCAATA | GATGTAGCCAGGCAAAGC |
| ***HK2*** | GTCCGATGATGGTCACTCCCTT | GTCCGATGATGGTCACTCCCTT |
| ***HSPG2*** **(D1)** | AGCATCTCAGGAGACGACCT | GAAATTCACCAGGGCTCGGA |
| ***HSPG2*** **(D5)** | CCCGACTTCATCTCCTTCGG | GGTCACCCACAATCAGGGAG |
| ***ITGB1BP2*** | GATGCACTTAAGGGTTGGTCCT | TGTAGCAGGGCCTTCAGGTT |
| ***ITGB6*** | GCAAGCTGCTGTGTGTAAGGAA | CTTGGGTTACAGCGAAGATCAA |
| ***KI67*** | TCCTTTGGTGGGCACCTAAAGACCTG | TGATGGTTGAGGTCGTTCCTTGATG |
| ***LDHA*** | GGATCTCCAACATGGCAGCCTT | AGACGGCTTTCTCCCTCTTGCT |
| ***MHH7*** | CACTGATAACGCTTTTGATGTGC | TAGGCAGACTTGTCAGCCTCT |
| ***MYH6*** | TCAGCTGGAGGCCAAAGTAAAGGA | TTCTTGAGCTCTGAGCACTCGTCT |
| ***NNAT*** | CGGCTGGTACATCTTCCGC | TGTCCCTGGAGGATTTCGAAA |
| ***RYR2*** | GTCCGATGATGGTCACTCCCTT | GTCCGATGATGGTCACTCCCTT |
| ***SDC4*** | TCGATCCGAGAGACTGAGGT | CCAGATCTCCAGAGCCAGAC |
| ***SLC2A1*** | CATCAACGCTGTCTTCTATTACTC | ATGCTCAGATAGGACATCCA |
| ***SLC2A4*** | CTTCGAGACAGCAGGGGTAC | ACAGTCATCAGGATGGCACA |
| ***TCF21*** | AGCTACATCGCCCACTTGAG | CGGTCACCACTTCTTTCAGG |
| ***TNNI1*** | AGTCACCAAGAACATCACGGAGAT | GCAGCGCCTGCATCATG |
| ***TNNI3*** | CGTGTGGACAAGGTGGATGA | TTCCTTCTCGGTGTCCTCCT |
| ***VCAN*** | CCCAGTGTGGAGGTGGTCTAC | CGCTCAAATCACTCATTCGACGTT |
| ***VIM*** | GGACCAGCTAACCAACGACA | AAGGTCAAGACGTGCCAGAG |
| ***WT1*** | TGCTTACCCAGGCTGCAATA | CTGAAGGGCTTTTCACCTGT |
| ***YAP*** | CGCTCTTCAACGCCGTCA | AGTACTGGCCTGTCGGGAGT |

***Table 2.10 – TaqMan™ probes quantitative analysis of gene expression***

| GENE TARGETED | ASSAY NAME | CATALOGUE NUMBER | EXONS TARGETED |
|---|---|---|---|
| *HSPG2* | Hs01078466_m1 | 4351372 | 25-26 |
| *HSPG2* | Hs01078536_m1 | 4331182 | 91-92 |
| *HSPG2* | Hs01078483_g1 | 4331182 | 4-5 |

## 2.6. RNA Sequencing

Cell lysate was collected from each timepoint through cardiac differentiation using QIAzole (QIAGEN) lysis buffer and extracted using RNeasy Mini Kit (QIAGEN) following the manufacturers protocol. RNA samples were quantified using a NanoDrop 2000 Spectrometer (Thermo Fisher Scientific) before being sent to the Francis Crick Institute whereby RNA sequencing was performed. Initial DeSeq2 normalisation of data, fold change comparisons and statistics were performed by Tegan Gilmore (Francis Crick). All further analysis, PCA plots, GO analysis and graphs were generated using RStudio Build 576. All RStudio library packages used highlighted in Table 2.11.

***Table 2.11 – RStudio packages used for RNA sequence analysis***

| RStudio Packages |
|---|
| pylr |
| dplyr |
| tidyverse |
| ggplot2 |
| devtools |
| ggbiplot |
| DESeq2 |
| gprofiler2 |
| goseq |
| EnhancedVolcano |
| clusterProfiler |
| enrichplot |
| DOSE |

To generate PCA plots DeSeq2 was performed on normalised counts. DeSeq2 package generated PCA plot data which was subsequently plotted using ggplot2. The graph generated was exported to Adobe Illustrator where clusters were highlighted, and colour coded.

EnhancedVolcano RStudio package was used to generate volcano plots with example script highlighted below.

```
EnhancedVolcano(d6v0,
                lab = NA,
                x = 'log2FoldChange',
                y = 'pvalue',
                title = "HSPG2 WT Day 6 vs Day 0",
                labSize = 4,
                legendPosition = 'right',
                legendLabSize = 10,
                pointSize = 2,
                colAlpha = 3/4,
                axisLabSize = 14,
                pCutoff = 0.05,
                ylim = c(0, max(300)),
                xlim = c(max(-15), max(15))) #-> EVD0
```

For cluster analysis DEGs were isolated via filtering of genes above or below log2fold change and were statistically changed (p value <0.05). Library package gprolfiler2 was used to perform DEG cluster analysis for Gene Ontology Molecular Functions, Gene Ontology Cellular Components, Gene Ontology Binding Proteins, Reactome and Wiki-pathways, followed by reformatting for output.

```
Day0 <- read.csv("CSVs/Crick_WTvsC6_d0_Flip.csv")

d0genes <- Day0 %>% filter(Day0$pvalue <0.05)
d0genesplus <- d0genes %>% filter(d0genes$log2FoldChange >1)
d0genesneg <- d0genes %>% filter(d0genes$log2FoldChange < -1)

gostresd0 <- gost(query = d0genesplus$x,
                  organism = "hsapiens", ordered_query = FALSE,
                  multi_query = FALSE, significant = TRUE, exclude_iea = FALSE,
                  measure_underrepresentation = FALSE, evcodes = T,
                  user_threshold = 0.05, correction_method = "gSCS",
                  domain_scope = "annotated", custom_bg = NULL,
                  numeric_ns = "",sources = c("GO:MF","GO:CC","GO:BP", "REAC","WP"), as_short_link = FALSE)

gp_upD0 = gostresd0$result[,c("query", "source", "term_id",
                              "term_name", "p_value", "query_size",
                               "intersection_size", "term_size",
                                "effective_domain_size", "intersection")]

gostplot(gostresd0, capped = F, interactive = T)
gostresd0_p <- gostplot(gostresd0, capped = F, interactive = F)
```

Data is then rearranged to arrange based on number of DEGs found in each cluster previously analysed.

```
C620v15total_ryan_down <- C620v15total_down %>%
  mutate(Description = str_to_sentence(Description)) %>%
  filter(str_detect(ID,"TF:",negate = T)) %>%
  filter(str_detect(`Description`,",",negate = T)) %>%
  dplyr::select(-ID) %>%
  mutate(`geneID` = sapply(strsplit(`geneID`, "/"), length)) %>%
  arrange(desc(`geneID`)) %>%
  filter(`p.adjust` < 0.05) %>%
  filter(str_detect(`Description`,"nadp",negate = T)) %>%
  arrange(desc(`geneID`))
```

Following rearrangement of data ggplot2 is used to plot the Family Cluster graphs.

```
GO_family_fig <- ggplot(data = C620v15total_ryan2, aes(x=
`Count`,y=reorder(`Description`,`geneID`),color=`Category`,size=`p.adjust`)) +
    geom_point(alpha=0.5) +
  xlab("# Genes") + ylab("Pathways / Ontological terms") + theme_classic() +
  theme(text = element_text(size=12),
        axis.text.y = element_text(size = 9),
        axis.text.x = element_text(size = 9),
        legend.position = "right",
        plot.title = element_text(hjust = 0.6, size=15)) +
  scale_y_discrete(labels = function(x) str_wrap(x, width = 27)) +
  ggtitle("Cluster changes due to Upregulated genes HSPG2 +/- D20 vs D15") +
scale_size(range = c(1,6), name="p-value", trans = "reverse")
```

## 2.7. Protein extraction, Slot Blots and Western Blots

### 2.7.1. Protein Extraction form Cells and Media

Protein was extracted from cells by scraping 100 µL of SDS-PAGE sample buffer supplemented with Proteinase inhibitor (at 10 µL/ml) over the surface of the cells. Cell protein lysate was boiled at 100 °C for 5-10 minutes before being frozen at -80 °C. Protein from media was concentrated by addition of Trichloroacetic Acid (Sigma-Aldrich) to 5% (v/v) and incubated at 4°C for 24 hours. Media were then centrifuged (21,000 g for 6 minutes), residual supernatant removed, and the pellet resuspended in 50 µL SDS-PAGE sample buffer and boiled at 100 °C for 5-10 minutes.

### 2.7.2. Slot Blot

PVDF membrane (Bio-Rad) was placed over a vacuum source with extra uncovered slots being blocked to maintain suction. 1 mL of media or 1 mL of 1:100 diluted cell protein lysate was passed through the PVDF membrane (Bio-Rad) via suction from a vacuum pump. PVDF membrane was then blocked in 5% (w/v) Milk in PBS for 3 hours, blocking solution was replaced with fresh 5% (w/v) Milk in PBS with primary antibodies at 1:10000 [A74 (Abcam), A76 (Abcam), or CCN1 (provided by John Whitelock)] incubated at 4°C on a rocker overnight. Membranes were then washed 3 times with 0.1% (v/v) Tween (Sigma-Aldrich) in PBS followed by incubation with secondary antibody at 1:5000 [Goat anti-mouse IgG H&L HRP (Abcam) or Goat anti-Rabbit IgG H&L HRP (Abcam)] in 5% (w/v) Milk in PBS for 2 hours at room temperature. Membranes were then washed 3 times with 0.1% (v/v) Tween (Sigma-Aldrich) in PBS, wash was removed, membranes transferred to a clean wash tray where they were incubated using LumiBlue ECL Extra

(Expedeon) (A74 or A76) or LumiBlue ECL Extreme substrate (Expedeon) (CCN1) for 5 minutes. ECL substrates were removed, and membranes were imaged for chemiluminescence using the GelDock (Syngene).

### 2.7.3. Western Blots

15 µL of SDS-cell lysate or SDS-media was loaded into the wells of a 4-15% gradient polyacrylamide gel (Bio-Rad). Gels were run at 180V for 50 minutes, transferred to a nitrocellulose membrane (Bio-Rad) using the Trans-Blot Turbo Transfer System (Bio-Rad). To quantify membrane total loaded protein, Revert Total Protein (LI-COR Biosciences) stain was used following manufacturers guidelines. Membranes are incubated in Revert Total Protein for 5 minutes, following 2 washes with water. Membranes are then imaged using Odyssey CLx Imaging System (LI-COR Biosciences) at 700 nm. Membranes were blocked in 5% (w/v) Milk in PBS for 3 hours, blocking solution was replaced with fresh 5% (w/v) Milk in PBS with primary antibodies at 1:1000 [Agrin (Thermo Fisher Scientific), A74 (Abcam), A76 (Abcam), or CCN1 (provided by John Whitelock)] incubated at 4°C on a rocker overnight. Membranes were then washed 3 times with 0.1% (v/v) Tween (P1379, Sigma-Aldrich) in PBS followed by incubation with secondary antibody at 1:5000 [Goat anti-mouse IgG H&L HRP (Abcam) or Goat anti-Rabbit IgG H&L HRP (Abcam)] in 5% (w/v) Milk in PBS for 2 hours at room temperature. Membranes were then washed 3 times with 0.1% (v/v) Tween (Sigma-Aldrich) in PBS, wash was removed, membranes transferred to a clean wash tray where they were incubated using LumiBlue ECL Extreme (Expedeon) (A74, A76 or Agrin) or LumiBlue ECL Extra substrate (Expedeon) (CCN1) for 5 minutes. ECL substrates were removed, and membranes were imaged for chemiluminescence using the G:BOX F3 GelDock (Syngene).

### 2.7.4. Total Protein Quantification

Images following Revert Total Protein stain and chemiluminescence antibody staining were imported into ImageJ. Total Protein intensity was calculated per column loaded and used to normalise against the intensity of individual bands on chemiluminescent western blots thereby calculating relative intensity.

### 2.8. Immunostaining

For immunostaining, primary and hiPSCs were plated on thin black bottom 96 well plates. Cells were washed using PBS followed by fixing using 4% (v/v) PFA (Sigma-Aldrich) for 15 minutes followed by 2 PBS washes. Fixed cells were then washed for 15 minutes in 0.1% (v/v) Triton X-100 (Sigma-Aldrich) in PBS on a plate rocker at RT followed by 3 further 5-minute washes in PBS. Fixed cells were then blocked in 4% (v/v) Goat Serum (Sigma-Aldrich) in PBS for 1 hour minimum, followed by a further 5-minute PBS wash. Primary antibody was added to the plates, diluted in 4% (v/v) Goat Serum (Sigma-Aldrich) in PBS [CCN1 (1:2000, provided by John Whitlock), αSMA (1:400, Abcam), A74 (1:200, Abcam), A76 (1:400, Abcam), α-Actinin (1:800, Abcam), Agrin (Thermo Fisher Scientific)] and left overnight at 4°C on a rocking plate. The following day fixed cells were washed with 0.1% (v/v) Tween (Sigma-Aldrich) in PBS 3 times for 10 minutes followed by secondary antibodies diluted in 4% (v/v) Goat Serum (Sigma-Aldrich) in PBS [Anti-Mouse Alexa Fluor® 488 (1:500, Abcam), Anti-Mouse Alexa Fluor® 568 (1:500, Abcam), Anti-Rabbit Alexa Fluor® 488 (1:500, Abcam), Anti-Rabbit Alexa Fluor® 568 (1:500, Abcam)] for 1 hour at room temperature. The fixed cells were then washed 3 times with 0.1% (v/v) Tween-PBS (Sigma-Aldrich) for 10 minutes followed by incubation in PBS supplemented with DAPI (Tocris) at 1:500 for 10 minutes and optional CellMask™ Orange Plasma Membrane Stain (Invitrogen) at 1:1000 for 10 minutes. A further wash was performed using filtered PBS after which the fixed cells were submerged in filtered PBS and the plate wrapped in foil. Images were taken using the EVOS™ M5000 Imaging System and Zeiss Confocal Microscope.

### 2.9. Seahorse assay

The OCR and ECAR of hiPSC-CMs and hiPSC-CFs were analysed using the XF Cell Mito Stress Kit (Agilent) on the Seahorse XF Analyser (Agilent Technologies). Operation of Seahorse XF Analyser was performed by Katherine Hampton and Jamie Clark. hiPSC-CMs and hiPSC-CFs were seeded at a density of 30,000 and 15,000 cells per well of a VTN-coated 96-well Seahorse XF Cell Culture Microplate, respectively. The cells were

analysed 72-hours post-transfection. In preparation for the assay, XF flux cartridges were hydrated with XF Calibrant overnight at 37°C. Flux cartridges were loaded with Oligomycin (2 µM), carbonyl cyanide-4-(trifluoromethoxy) phenylhydrazone (FCCP) (1 µM), and Rotenone (0.5 µM). The assay was performed in Seahorse XF Media, supplemented with 1 mM Sodium pyruvate, 2 mM l-Glutamine, and 10 mM Glucose. Following the seahorse assay, the Seahorse plate was washed with PBS and fixed at room temperature in 4% (v/v) formaldehyde solution (Sigma-Aldrich) for 10 min, then stained with 1 µg/mL DAPI (Thermo Fisher Scientific) for 15 min. Cell count was calculated using automated nuclei counting on the EVOS M5000 imaging system (Thermo Fisher Scientific). All results were normalised to output cell count.

### 2.10. BioLog Mitoplate substrate metabolism assay

hiPSC-CMs and hiPSC-CFs were seeding into VTN coated 96 well plates at 40,000 and 30,000 cells per well respectively. The wells of the MitoPlate S-1 plate (BioLog) were hydrated in 30 µL assay mix composed of sterile water supplemented with 2X BioLog MAS (BioLog), 6X Redox Dye MC (BioLog) and 1,200 µg/mL saponin, (Sigma-Aldrich). The plates were incubated for 1 hour at 37$^{o}$C. Incubated substrate suspension was mixed with a further 30 µL 2X BioLog MAS. Seeded cells were washed with PBS and media replaced with incubated substrate suspension. The MitoPlate was read for 6 h with 5 min intervals at OD590 using a OmniLog plate reader (BioLog). Results were calculated using the OmniLog Data Analysis 1.7 software before being exported to Microsoft Excel. substrate usage was analysed using the BioLog MitoPlate assay (BioLog)

### 2.11. Engineered heart tissue generation and force output

Engineered heart tissues (EHTs) were generated in the Francis Crick Institute with help from Lorenza Tsansizi and Andreia Burnardo. hiPSC-CMs were transported to the Francis Crick Institute the day before EHT generation and incubated to allow for acclimatisation. EHT casting moulds were generated using Teflon spaces in 24 well plates and 2% (w/v) agarose in PBP, following cooling Teflon spacers were removed and silicone posts places in place.

hiPSC-CMs were dissociated, 4.1x$10^6$ cells/mL were resuspended in 5 mg/mL fibrinogen (Sigma-Aldrich), 100 µL/mL Matrigel and DMEM 2x. 145 µL of cell suspension is briefly mixed with 4.5 µL thrombin (Sigma-Aldrich) before pipetting into agarose slots. Fibrinogen construct polymerisation was performed by placing seeded wells into a 37°C, 5% humidified incubator for 2 hours. 1 hour into incubation 300 µL cell culture medium is added on top of EHTs to reduce risk of dehydration. After incubation, silicone constructs were removed with EHTs attached and placed into new 24 well plate with EHT medium (DMEM, 10% (v/v) horse serum (Gibco), insulin (Sigma-Aldrich), aprotinin (Sigma-Aldrich) and 1% (v/v) penicillin/streptomycin). Media was changed every 48-72 hours with fresh EHT media.

Pacing and video recording was performed by Lorenza Tsansizi at the Francis Crick Institute. ImageJ MUSCLEMOTION was used to analyse contraction of both paced and un-paced EHTs. True force was calculated using Youngs modulus due to parameters of silicone rods known.

$$Force = 3EI\delta/L3 = 3\pi ER4\delta/4L3$$

Delta of contraction was recorded using ImageJ and true force calculated used Microsoft Excel.

## 2.12. ImageJ plugins

### 2.12.1. Migration Wound Healing Experimental Method

Culture well quarters (Ibidi) were coated with Vitronectin (Gibco, Life Technologies) 24 hours before use. Approximately 40,000 cells were seeded into each quarter, cells were allowed 1 week to recover in appropriate media before the silicone dam was removed. Photos were taken every day using the EVOS™ M5000 Imaging System between each migration gap until the end of the experiment. Images were compiled and aligned using Adobe Photoshop CC 2020 and used to create a tiff stack. Gap analysis was performed using the MRI Wound Healing Tool as run using an Image J script.

***Table 2.12 – List of parameters used for the MRI Wound Healing Tool***

| PARAMETER | VALUE |
|---|---|
| **METHOD** | Variance |

| | |
|---|---|
| **VARIANCE FILTER RADIUS** | 5 |
| **THRESHOLD** | 25 |
| **RADIUS OPEN** | 4 |
| **MIN. SIZE** | 2000 |

### 2.12.2. Analysis of ECM patterns using TWOMBLI pipeline

Immunostaining was performed followed the previously explained protocol, the ECM channel was isolated and used for ECM Analysis using TWOMBLI (The Workflow of Matrix Biology Informatics). ECM images were converted to black and white images and inverted using Adobe Photoshop CC 2020. Images were then taken into Image J where threshold was adjusted on all images to the same value. These images were then cropped to show the appropriate sections of the wound healing assay and ran through the TWOMBLI pipeline with the following prechosen parameters.

***Table 2.13 – List of parameters used for running ECM analysis using TWOMBLI pipeline***

| PARAMETER | VALUE |
|---|---|
| **CONTRAST SATURATION** | 0.35 |
| **MIN LINE WIDTH** | 2 |
| **MAX LINE WIDTH** | 23 |
| **MIN CURVATURE WINDOW** | 40 |
| **MAX CURVATURE WINDOW** | 40 |
| **MINIMUM BRANCH LENGTH** | 5 |
| **MAXIMUM DISPLAY HDM** | 150 |
| **MINIMUM GAP DIAMETER** | 20 |

### 2.12.3. Contraction analysis using MUSCLEMOTION

Videos of contracting cardiomyocytes were recorded using a 1080p screen capture device via the EVOS™ M5000 Imaging System. Videos were then cropped and cut to length using Adobe Photoshop CC 2020, following rendering to a Tiff stack. Images were run through Muscle Motion script using the batch analysis method with set parameters.

***Table 2.14 – List of parameters used for running MUSCLEMOTION ImageJ script***

| PARAMETER | VALUE |
|---|---|
| **A. BATCH OPTION** | Yes |
| **B. TIFF IMAGE SEQUENCE** | Yes |
| **C. GAUSSIAN BLUR** | No |
| **D. FRAME RATE OF RECORDINGS** | 30 |
| **E. SPEED/WINDOW TO USE** | 5 |
| **F. DECREASE NOISE** | Yes, but keep it simple |
| **G. DETECT REFERENCE FRAMES** | Yes, but keep it simple |
| **H. ANALYSE TRANSCRIPTS** | Yes, but keep it simple |

## 2.13. Statistical analysis, production of graphs and figures

GraphPad Prism software version 5.0 (GraphPad) and Microsoft Excel were used for data analysis and statistical analysis. Statistical comparison was performed using paired t-test unless otherwise stated. For comparison of more than two groups the Two-way ANOVA followed by Tukey multiple comparison test was used. Differences among groups were considered significant when the probability value, p, was less than 0.05 (*P < 0.05, **P < 0.01, ***P < 0.001, no* = not significant). Results are represented showing each sample value and the standard deviation or standard error of mean (SEM). Standard deviation was used on results where the N=3, while SEM was used for N=1 results. No statistical methods were used to pre-determine sample size. Generation of figures was performed using Adobe Illustrator CC 2020.

# 3. Generation of *HSPG2* deficient hiPSC lines and the further manipulation of *HSPG2* in hiPSCs

## 3.1. Introduction

Despite being evolutionarily conserved, species differences are found in the *HSPG2* genome (Zelenski et al., 2018). Current models of *HSPG2* role in cardiac populations rely on mice KO models. Sasse *et al* created *HSPG2* deficient mouse embryonic cells, capable of differentiation into mouse CMs. However, this 2008 study used early, inefficient differentiation protocols on the *HSPG2* deficient mouse lines. In this chapter I aimed to create a human *HSPG2* knockout iPSC line, to do this I will use CRIPSR/Cas9 (Clustered Regularly Interspaced Short Palindromic Repeats/Cas9) gene editing. I also aimed to upregulate the expression of *HSPG2* using CRISPRa. CRISPRa utilises a mutated form of the Cas9 protein that is unable to cleave (dCas9), but still target a specific region of DNA. CRISPRa has the capability of being fused with transcriptional activators such as VP64 causing upregulation of downstream target genes (Maeder et al., 2013; Perez-Pinera et al., 2013).

As the ECM is a major component of the stem cell niche that surrounds and maintains stem cells in a naïve state, the manipulation of its composition may alter cellular phenotype (Ullah et al., 2020; Yu et al., 2017). In the self-renewal of hiPSCs, FGF-2 and TGFβ1 are key growth factors required in the cell culture medium (Eiselleova et al., 2009). FGF-2 and TGFβ1 are both heparin-binding growth factors (Sarrazin et al., 2011), and as such, HSPGs play a role in the regulation of these growth factors for the maintenance of pluripotency. Perlecan (HSPG2) is an essential sequester of FGF-2 (Chang et al., 2015; Chuang et al., 2010; Kerever et al., 2014), and has been estimated to hold up to 123 molecules of FGF-2 per molecule of *HSPG2* (Smith et al., 2007a). It is therefore possible that the knockout of *HSPG2* would alter pluripotency through altering FGF-2 signalling capabilities.

In addition to growth factor signalling, metabolic pathways can also regulate the balance between self-renewal and differentiation (Ito et al., 2014). HSPGs

have been linked to regulating lipid metabolism via the LDL receptor found on many HSPGs (Wilsie and Orlando, 2003), including *HSPG2* (Alan D Murdoch et al., 1992). This occurs through HSPGs binding circulating lipids to the cell surface, processing via lipases and internalisation of the final products (Ji et al., 1994; Mulder et al., 1993; Wilsie and Orlando, 2003). Yamashita *et al* show how transgenic *HSPG2* knockout mice are resistant to obesity whereby white adipose tissue had reduced lipid accumulation combined with an increased and preferential metabolism of fatty acids (Yamashita et al., 2018b). As such, it is also possible that the knockout of *HSPG2* would alter pluripotency through modulating metabolic pathways.

The aim of this chapter is to create a human system to study *HSPG2*s role in cardiac cell populations. I aim to create a *HSPG2* deficient hiPSC line using CRISPR/Cas9 gene-editing. In this chapter I will analyse any differences seen between the healthy and perlecan deficient hiPSCs lines before these are used in future chapters investigating the role of *HSPG2* in the cardiac system. Additionally, I also aim to investigate the potential of a CRISPRa system to upregulate *HSPG2* as an opposing modulating technology.

### 3.2. Creating a *HSPG2* knockout in hiPSCs

With the aim of utilising CRISPR/Cas9 I designed a targeting strategy that would insert a designed section cassette into exon two of *HSPG2*. To do these two plasmids needed to be designed and created: 1) a targeting plasmid homologous to *HSPG2* and, 2) a guide RNA plasmid specific to *HSPG2*. The role of the guide RNA plasmid is to direct the Cas9 protein to a specific DNA region for cleavage (Figure 3.1, A). Following this break in DNA, the role of the targeting plasmid is to provide a homologous sequence capable of providing a template for homology directed repair (Figure 3.1, B).

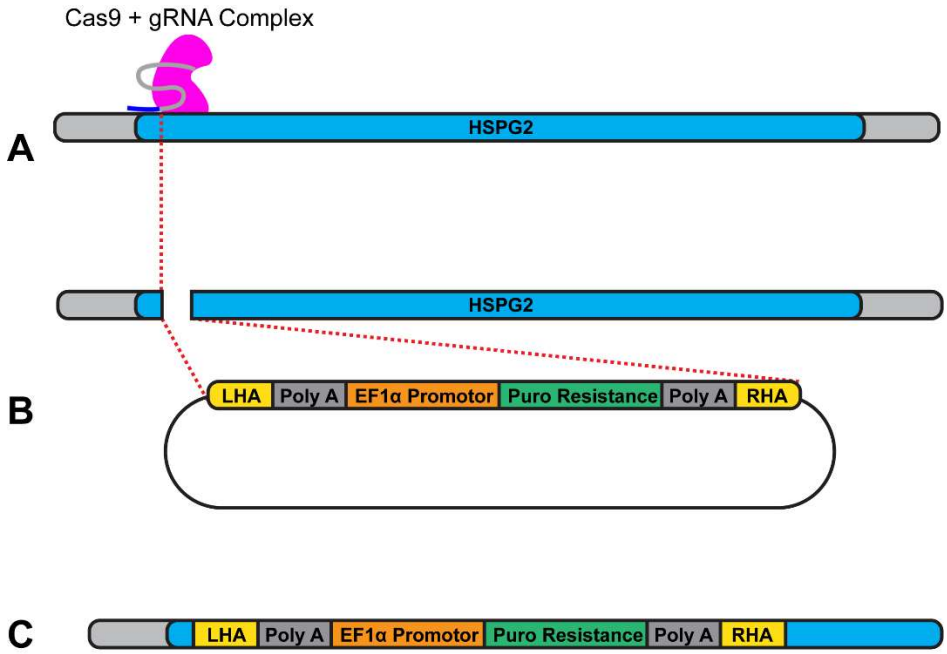


***Figure 3.1 –Schematic showing CRISPR/Cas9 targeting strategy for HSPG2 knockdown.*** *(A) The CRISPR/Cas9 and guide RNA create a complex that is guided to an cleaves exon two of HSPG2. (B) Through homology directed repair the selection cassette will be used as a template for repair. (C) If the genome uptakes the selection cassette translation of HSPG2 will be inhibited and create a knockout of HSPG2.*

The guide RNA sequence (possessing a PAM site) was designed complementary to exon two of HSPG2 (CAAAATACGTGACGTAGAAAG). The targeting plasmid was created containing flanking 1000bp arms of homology, complimentary to the *HSPG2* sequence either side of the DNA break. Within the arms of homology are polyA tails to stop translation and a EF1a promotor for the transcription of puromycin resistance. If the cell uptakes this plasmid using homology directed repair (Figure 3.1, C) the translation of *HSPG2* mRNA will be inhibited, thereby knocking out the transcription of *HSPG2*.

Following transfection in hiPSCs, Cas9 protein is synthesised and colocalizes with the gRNA to form the Cas9/gRNA complex. This complex translocates to the nucleus whereby the gRNA proceeds to bind to targeted PAM site and

proteolytic cleavage of the DNA follows (Figure 3.2, A). The targeting homology plasmid is transfected in parallel and provides the template for homologous recombination (Figure 3.2, B). Due to the uptake of a puromycin resistance gene by the cells that have undergone homologous recombination with the selection cassette the culture medium can be switched to one containing puromycin at a concentration capable of removing untargeted cells (Figure 3.2, C). Any colonies that have undergone targeting undergo proliferation in a media containing puromycin while untargeted cells will die. Once colonies have reached 1mm in size they were manually picked using a p20 pipette. The colonies were placed into individual wells of a 96 well plate, expanded to 24 well format then split to bank or for use in validation of correct genetic targeting.

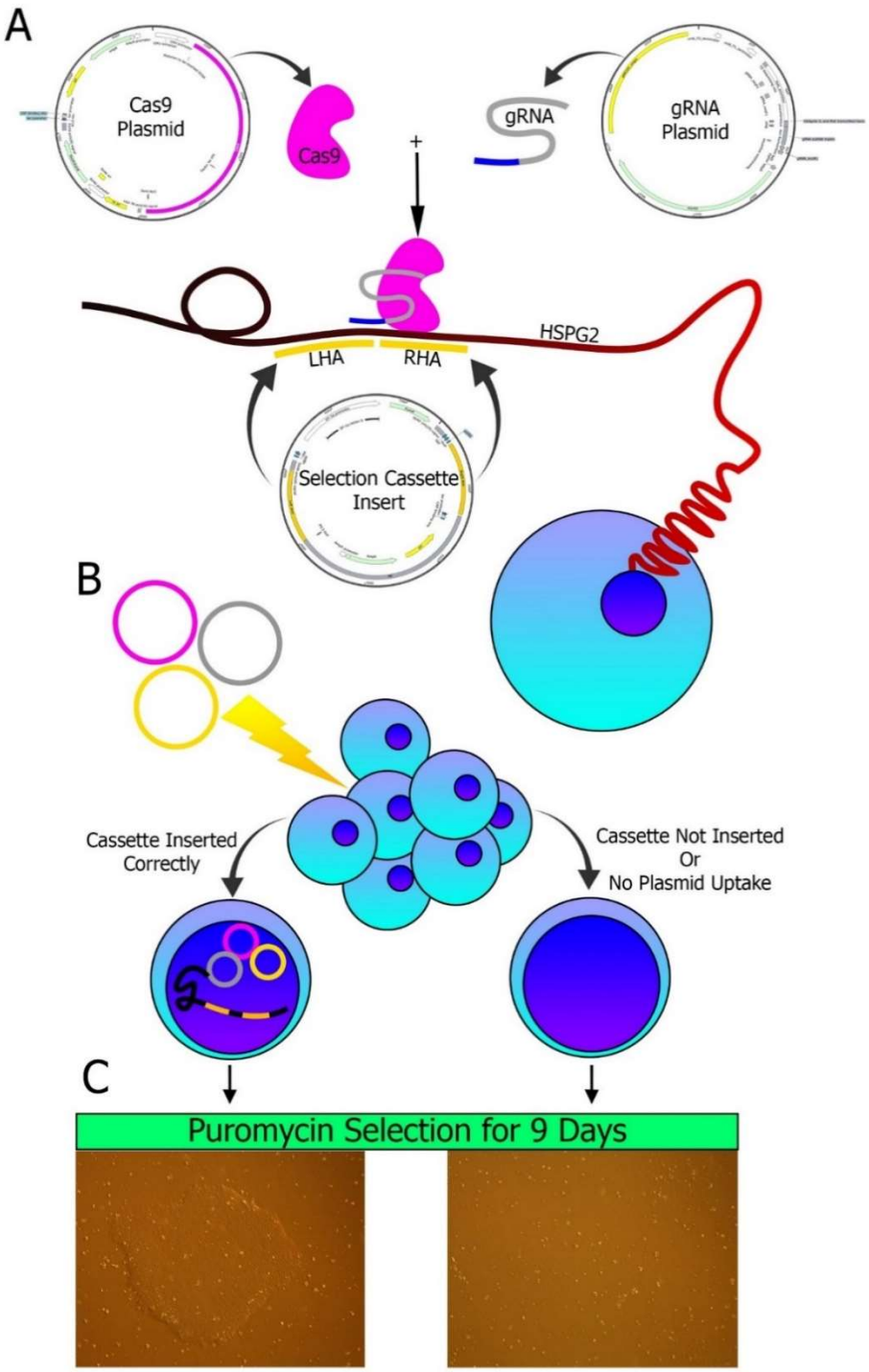


***Figure 3.2 – Selection of targeted clones following CRISPR/Cas9 cassette insertion.*** *(A) The Cas9 plasmid is combined with an appropriate gRNA guide plasmid and the insert plasmid containing a selection cassette. The Cas9 protein combined with the gRNA insert cleave the DNA at the desired cut site, homologous recombination occurs leading to the insert of the selection cassette. (B) The iPSCs are electroporated using a Amaxa Nucleofector to allow plasmid uptake. (C) Cells then undergo antibiotic selection to form clear colonies that will be later cultivated.*

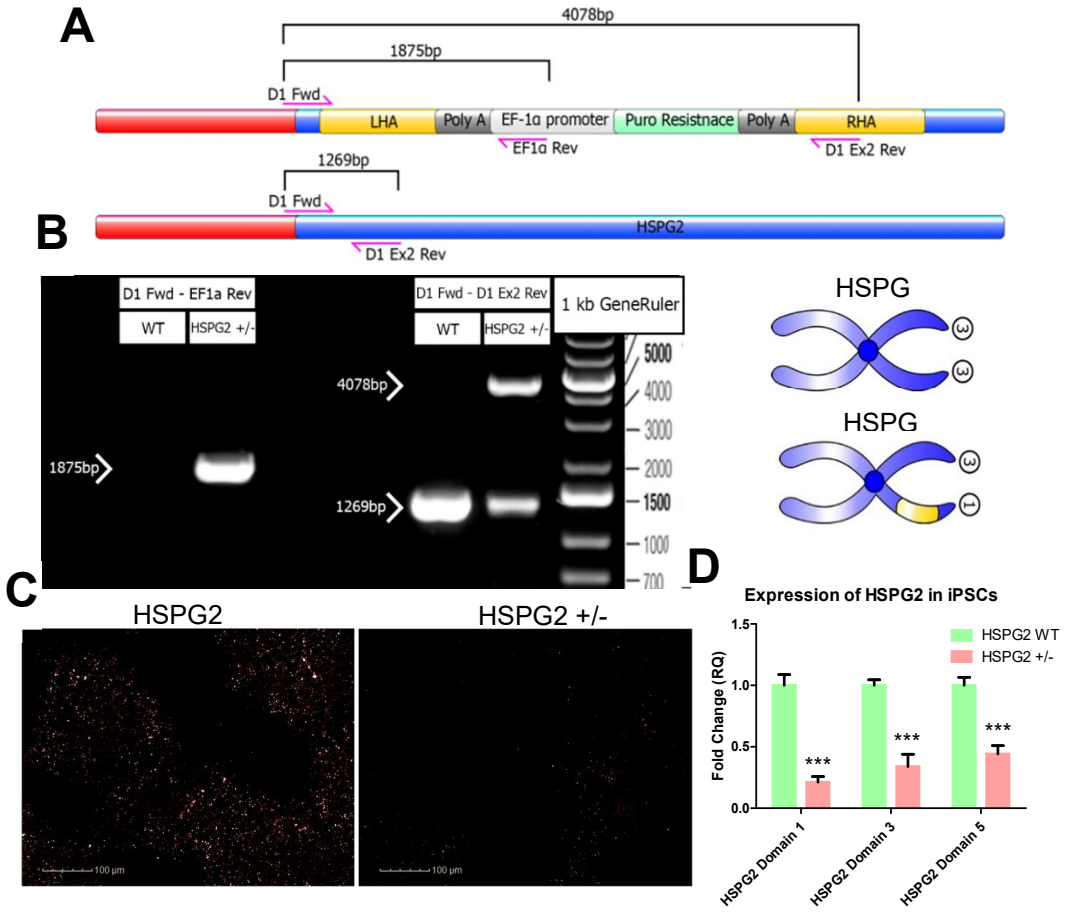


***Figure 3.3 – Confirmation of a HSPG2 heterozygous knockdown in iPSCs.*** *(A) Primer binding sites on targeted and untargeted DNA used to confirm selection cassette uptake. (B) PCR products produced from previously shown primers ran on 1% agarose gel confirming band sizes at predicted weights, overall confirming a healthy and targeted allele. (C) Immunostaining of WT vs +/- iPSCs using monoclonal A76 HSPG2 antibody. (D) Quantitative PCR performed of cDNA synthesised from HSPG2$^{+/-}$ iPSCs in 3 separate domains of HSPG2. . N=3, statistical test performed using t-tests. P-value <0.05 = *, <0.01 = **, <0.001 = ***.*

To confirm successful integration into *HSPG2* gDNA primers 'D1_Fwd' and 'EF1a_Rev' were designed so that a 1875bp band would form if the EF1a promotor was present in the gDNA (Figure 3.3, A & B). To identify homozygous and heterozygous clones a third primer was designed, 'D1_Exon2_Rev'. PCR on WT cells using 'D1_Fwd' and 'D1_Exon2_Rev' would create a small band (1269bp), while PCRs on targeted clones would create a larger band at 4078bp. Sanger sequencing of the healthy PCR fragments confirms no

insertions or deletions have occurred in the untargeted allele via sequence alignment of both $HSPG2^{WT}$ and $HSPG2^{+/-}$. Both iPSC lines were then expanded, fixed, and stained using monoclonal perlecan specific antibody A76 (Figure 3.3, C) with staining confirming the predicted reduction in perlecan secretion. Quantitative PCR was then performed to confirm the selection cassette inserted was inhibiting the transcription of *HSPG2*, results show over 50% reduction in *HSPG2* mRNA production in the $HSPG2^{+/-}$ iPSC line in 3 separate domains of HSPG2 (Domain 1 – 0.2 Fold, Domain 3 – 0.33 Fold, Domain 5 – 0.44 Fold) (Figure 3.3, D). Together, these data confirmed the CRISPR strategy designed was successful in producing hiPSC clonal lines with the heterozygous knockout of *HSPG2* expression. Since only heterozygous clones were produced from this targeting method, I attempted to repeat this with a new CRISPR approach in the aim of creating a full homozygous knockout of *HSPG2*.

### 3.3. Alternative *HSPG2* CRISPR/Cas9 KO approach

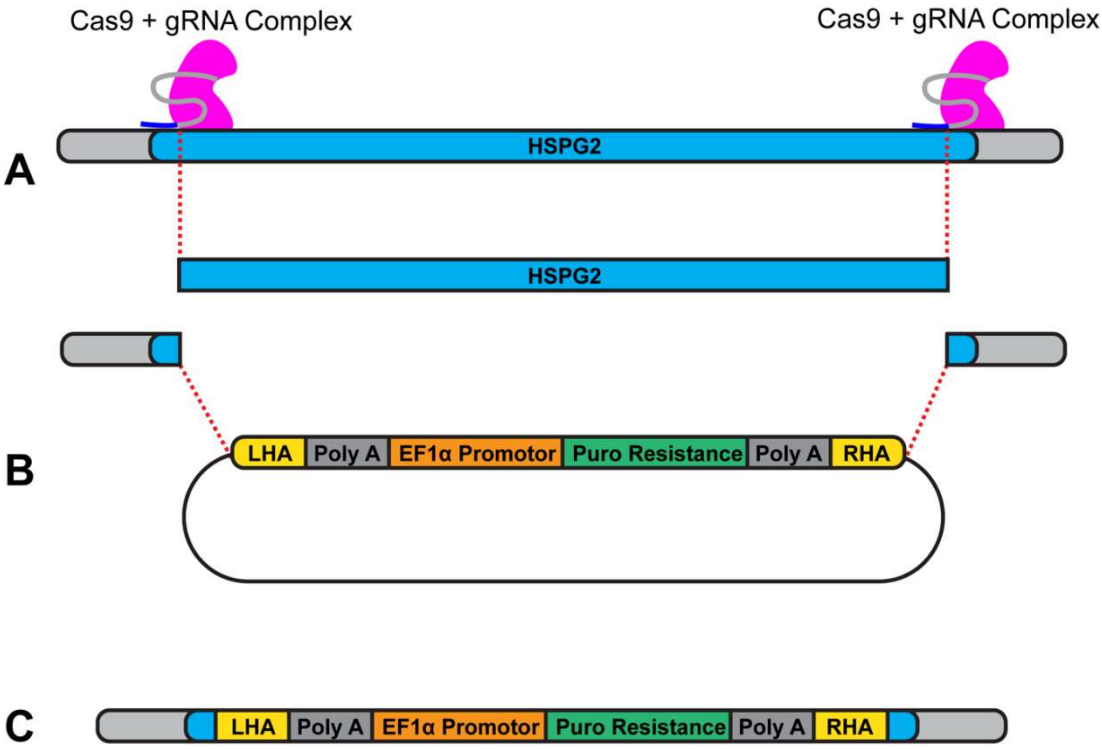


***Figure 3.4 - Schematic of newer method of creating a HSPG2 KO iPSC line.*** *(A) Two targeted PAM sites will be cleaved by the Cas9 enzyme. (B) The entire region of HSPG2 will then be removed and (C) replaced with the selection cassette designed to slot in place.*

Due to the creation of only a heterozygous KO of *HSPG2* the aim was to repeat this CRISPR targeting with a newer approach, to perform two separate cleavages of *HSPG2* genome and remove the entirety of the *HSPG2* gene (Figure 3.4). This strategy uses two cleavage sites within the genome to be performed instead of one, with the aim of removing the entire region of *HSPG2* would give rise to a cleaner *HSPG2* KO leaving no potential off transcripts to be synthesised in place.

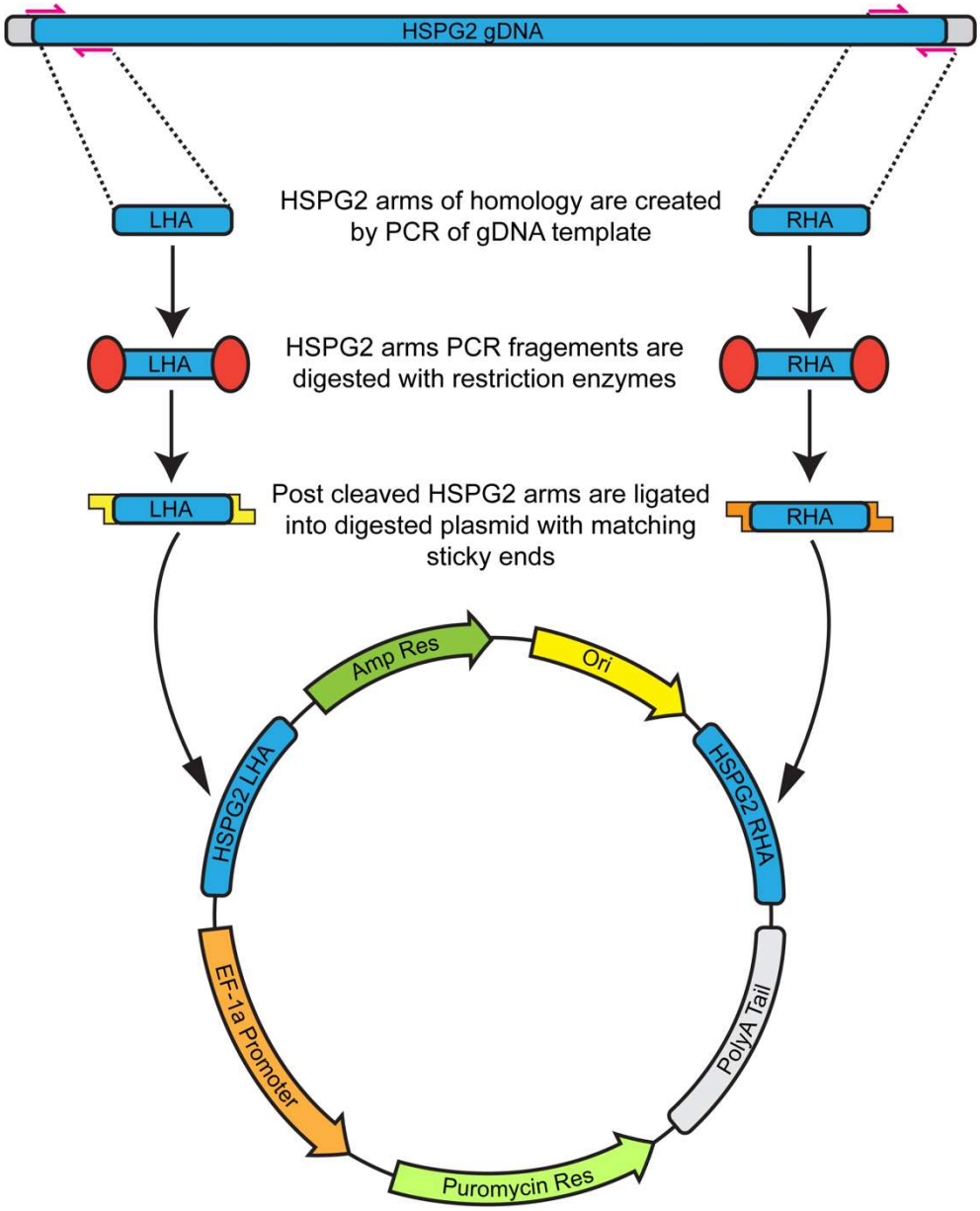


***Figure 3.5 – Creation of HSPG2 KO insert plasmid.*** *Arms of homology are created using PCR from WT gDNA. These are then digested alongside the plasmid backbone with restriction enzymes to create sticky ends. The digested PCR products and digested plasmid are then ligated together in separate reactions to create a complete plasmid containing correct arms of homology.*

The creation of the new plasmid was done utilising the previous plasmid as the main backbone for the new insert (Figure 3.5). Since the targeting plasmid from previous rounds of CRISPR/Cas9 targeting had the correct left arm of

homology this was not needed to be removed. The plasmid was digested with EcoRI and SalI restriction enzymes to create appropriate sticky ends that matched the sticky ends that would be created on the PCR product. After performing the PCR for the right arm of homology the fragment was extracted from and agarose gel, restriction enzyme digested and ran through PCR purification columns. Ligation was performed on both the digested plasmid and digested PCR product creating a complete plasmid able to target both ends of *HSPG2*, containing the selection cassette. Confirmation of correct arm insertion into the newly created plasmid was done by sanger sequencing (Figure 3.6) with schematic to show finalised plasmid creation. Sequences were compared against arm template in genomic DNA and confirmed to be correctly created and inserted.

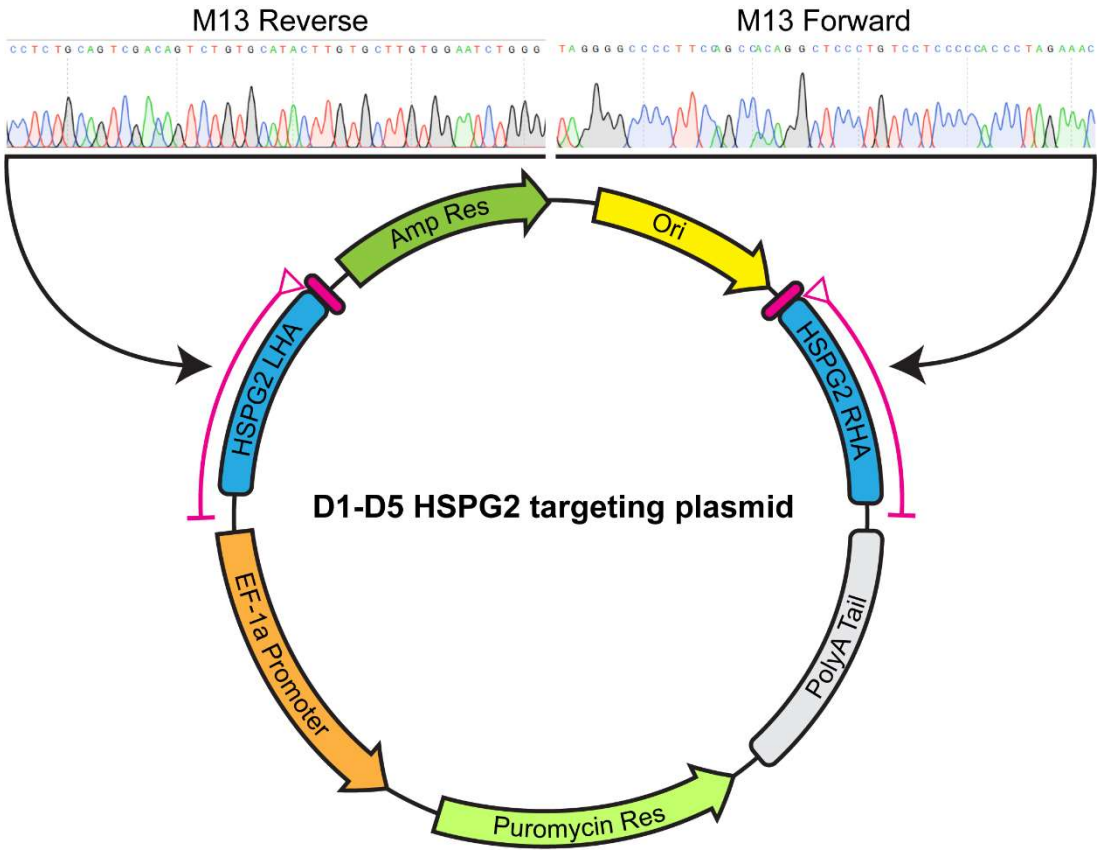


***Figure 3.6 – Confirmation of newly created targeting plasmid.*** *Sanger sequencing results confirming creation of new HSPG2 targeting plasmid by showing clean reads into each arm of homology inserted into the plasmid. Schematic shows regions where reads were taken to confirm correct HSPG2 arms were inserted into targeting plasmid.*

With the creation of a new CRIPSR/Cas9 targeting plasmid the process of transfection of iPSCs was repeated. Following growth of transfected cells in

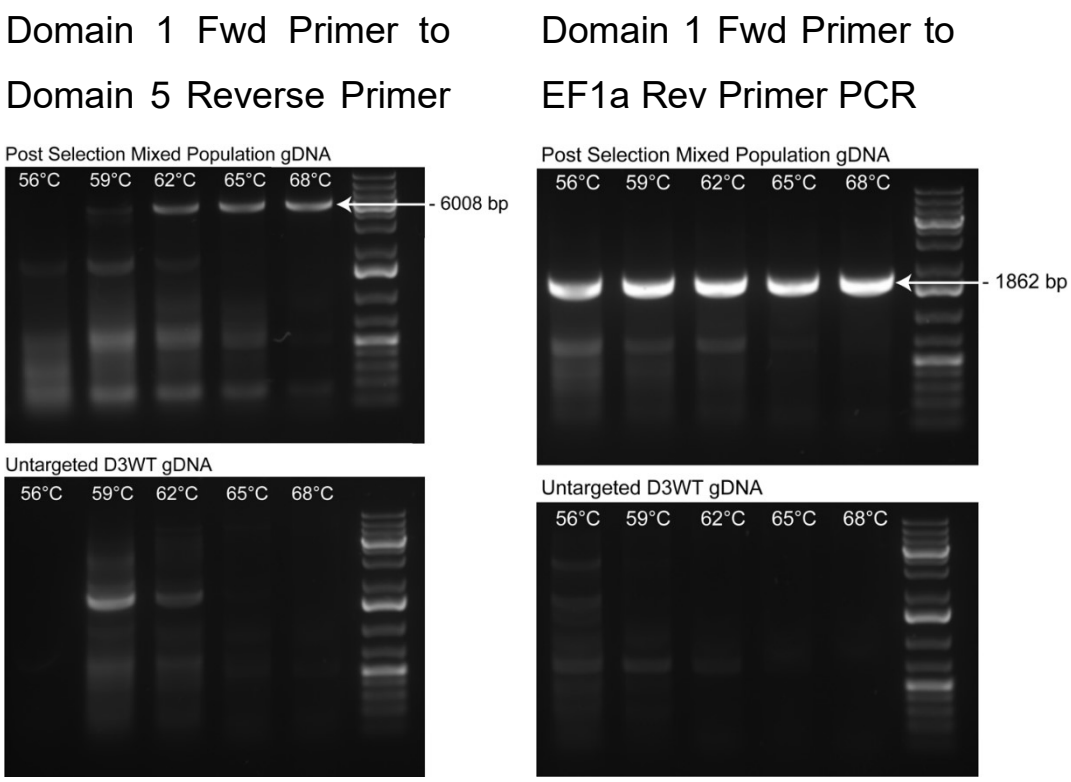


***Figure 3.7 – Gradient PCR to optimise screening primers.*** *Initial optimisation of quantification primers on mixed clone and WT gDNA using gradient PCRs ranging from 56°C to 68°C. PCR products were run on a 1% agarose gel next to 1Kb Gene ruler. Arrows point to approximate sized bands based off ladder markings.*

selection media colonies were picked for single cell expansion. During this time all remaining unpicked colonies were collected and lysed for gDNA to be compared against the WT untargeted gDNA, this is to create a gDNA pool that will contain both targeted and untargeted clones for primer optimisation. Gradient PCRs confirm the creation of a band around 6008bp in targeted gDNA implying the removal of HSPG2 from the genome and insert of the plasmid (Figure 3.7). This band is unable to be created in WT gDNA as would be expected since the final PCR product size would be too large therefore is only possible to form with the correct cleavage of both targeted PAM sites.

PCRs using EF1a_Rev primer confirm the existence of the selection cassette inside the gDNA of the targeted cells but not in the WT gDNA.

PCR primer optimisation was performed using gradient PCR at temperatures ranging from 56oC to 68oC to evaluate newly designed primers (Figure 3.7). The results show a faint band lowly produced at ~6008bp using 'D1_Fwd' to 'D5_Rev' in the post selection gDNA, indicating complete removal of HSPG2 gDNA and insertion of selection cassette. 'D1_Fwd' to 'EF1a_Rev' PCR confirms the insertion of the selection cassette, due to the EF1a promotor region in the plasmid, at all temperatures while no bands seen in the WT gDNA.

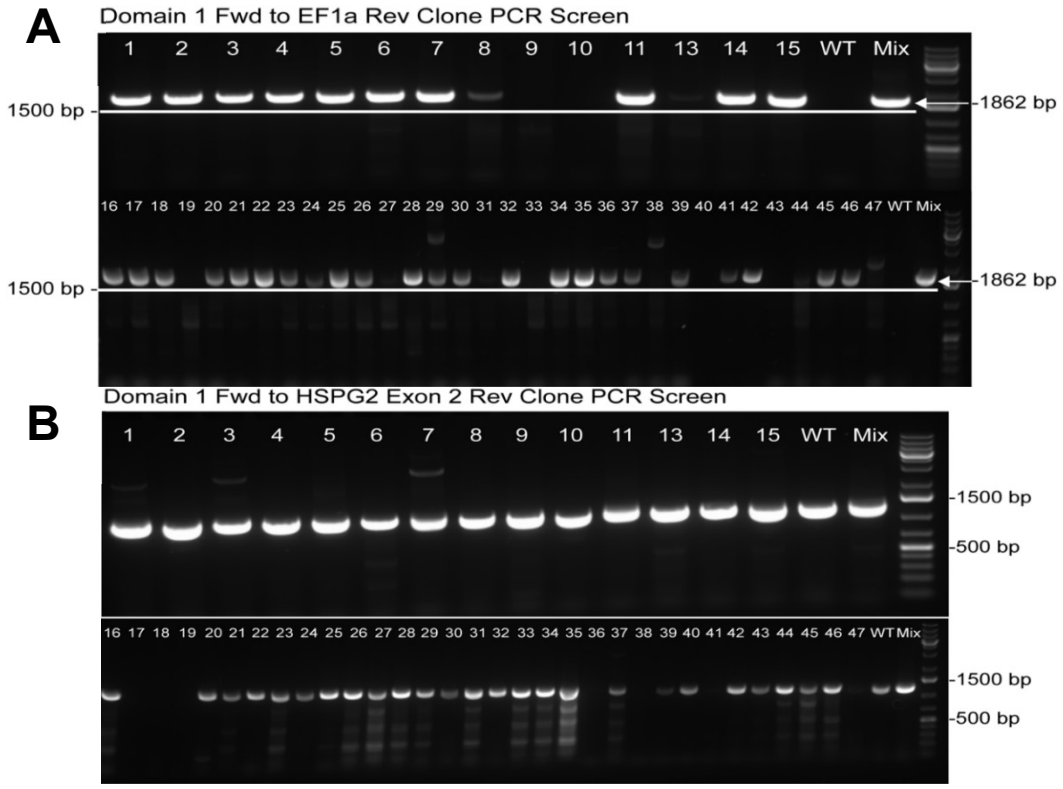


***Figure 3.8 – Initial PCR clone screening using optimised primers. (A)*** *PCR on initial batch of 47 picked clones using primers 'D1_Fwd' against 'EF1a_Rev', with a band at ~1862 bp would only be possible with insertion of the selection plasmid. (B) Followed by PCR using primer pairs 'D1Fwd' and 'Exon2_ Rev' showing and band at ~1269 bp if there is an untargeted WT region of DNA in the chromosome still. PCR annealing temperature was set to 68°C.*

PCRs were performed on all single clones that were expanded after selection to both confirm plasmid insertion and removal of WT *HSPG2* (Figure 3.8). Initial PCRs using primers targeting the EF1a promotor of the selection cassette reveal a band at 1862bp if correct insertion has occurred, showing most clones are correctly targeted while several do not have correct insertion (Figure 3.8, A). The second PCR targeting two WT regions of the *HSPG2* genome show most clones again have this band at 1400 bp (Figure 3.8, B). The loss of this band either confirms removal of *HSPG2* from the genome or impure gDNA that does not show any bands in either PCR. Several promising clones include, 17, 18, 36 and 41, where they confirm plasmid insertion with the ‘D1_Fwd’ to ‘EF1a_Rev’ PCR but show no banding for ‘D1_Fwd’ to ‘Exon2_Rev’ PCR. This pattern confirms at least a heterozygous knockout of *HSPG2* with the potential to be a homozygous KO.

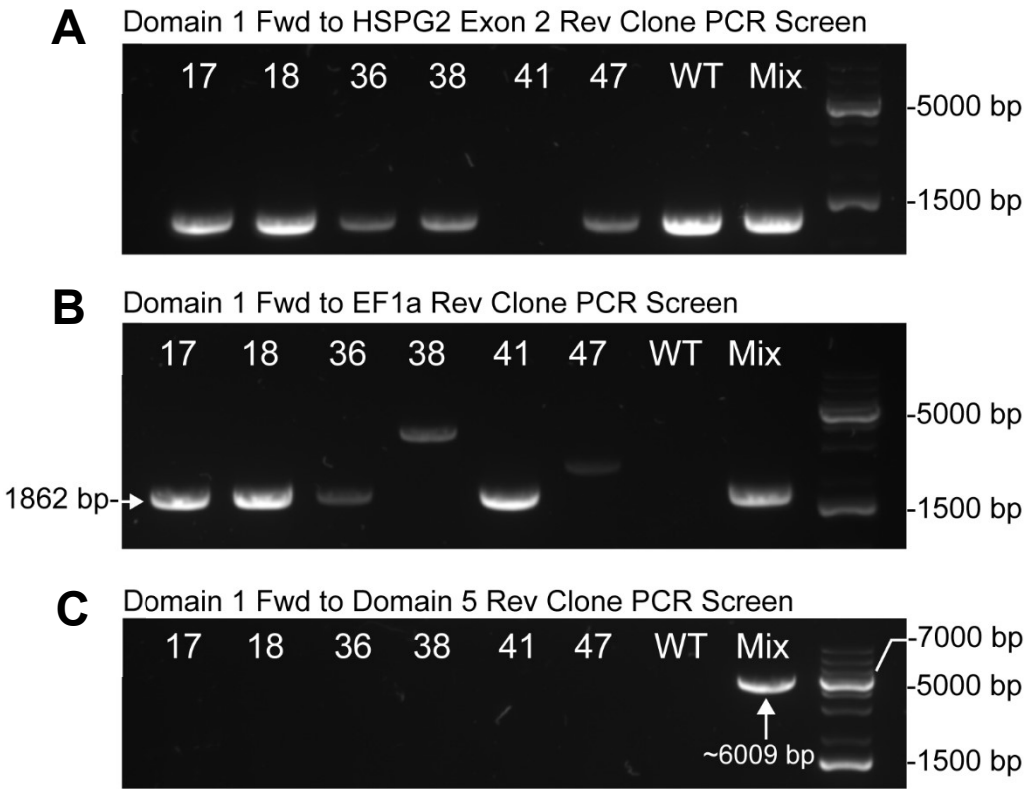


***Figure 3.9 – Selected clones taken forward for further screening include 17,18,36,38,41,47. (A)*** *PCR using 'D1_Fwd' and 'Exon_2' Rev primers was initially repeated looking for no clear band at ~1400bp. (B) PCR with 'D1_Fwd' and 'EF1a_Rev' primers also repeated aiming for a clear band at ~1862bp. (C) A further PCR was performed using 'D1_Fwd' to 'D5_Rev' PCR primers aiming for a band at ~6009bp, although only the mixed population was able to make this band.*

PCRs were repeated on the most promising clones with new gDNA to confirm the previous results were accurate (Figure 3.9). Of these PCRs we see that several from the previous PCRs show varying results. The only clone able to repeat what was seen before was clone 41, although this clone is still unable to create the 6009 bp band that would confirm removal of *HSPG2* and insertion of a selection cassette.

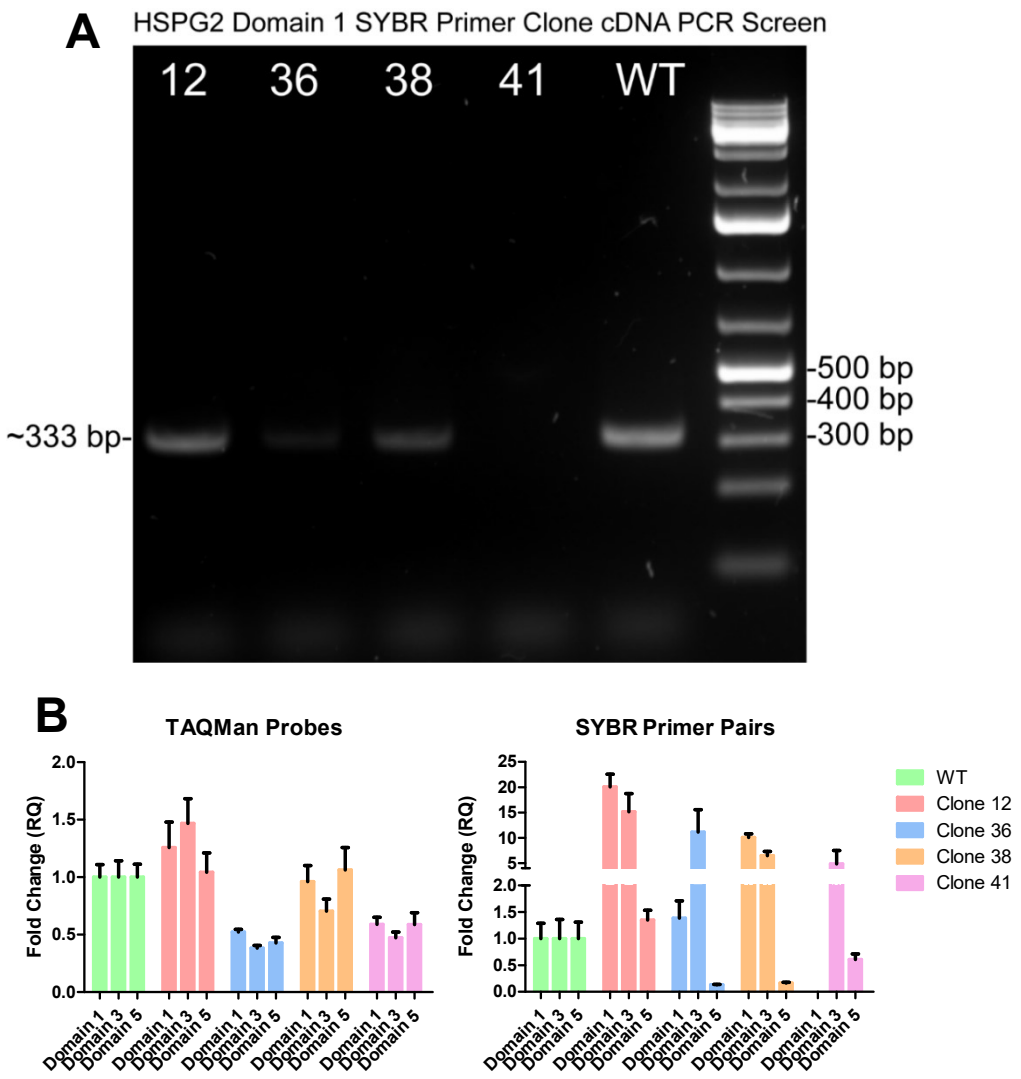


***Figure 3.10 – Further analysis of promising clones. (A)*** *Selected clone cDNA was created and ran on a PCR using HSPG2 D1 SYBR primer pairs looking for the differences between the clones. (B) Selected clones were further analysed using qRT-PCR with both TAQ and SYBR primers targeting 3 separate domains of HSPG2 to try to analyse why clone 41 appeared to have no HSPG2 domain 1 expression. N=1*

Selected clones were taken further by screening being performed on cDNA. The clone cDNA was used in a PCR reaction looking at the bands produced using HSPG2_D1_SYBR primers (Figure 3.10, A) showing how clone 41 had no visible banding, while the 3 other remaining clones (12, 36, 38) show some level of product creation. Running the cDNA in a qRT-PCR using both TAQ and SYBR *HSPG2* domain primers revealed varying results between the two

methods (Figure 3.10, B). Clone 36 has a ~50% reduction in *HSPG2* expression across 3 domains according to the TAQ qRT-PCR, although SYBR qRT-PCR results show reduced expression in domain 5, although 1.5-fold increased expression in domain 1. Importantly, *HSPG2* domain 1 show a 50% expression reduction in clone 41 when using TAQ, but no expression can be seen when using SYBR primers. Due to this observation the clones were ran with new PCR primers aiming at looking at changes in the untargeted allele of the clones (Figure 3.11).

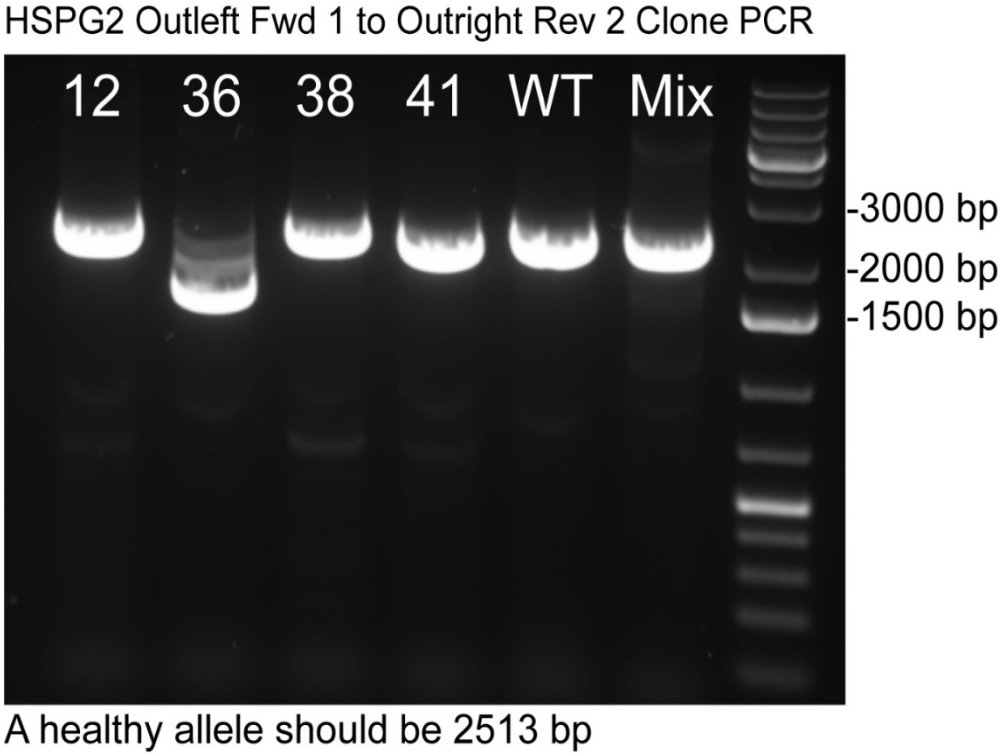


***Figure 3.11 – Further analysis of promising clones continued.*** *PCR reaction using 'HSPG2_Outleft_Fwd_1' and 'Outright_Rev_2' primers targeting the healthy allele of selected clones looking at differences in band size, a healthy allele is ~2514bp.*

Clone 36 shows the largest difference in size suggesting some level of deletion occurring, although when taken with the qRT-PCR results it can be presumed that deletions have occurred in both arms where *HSPG2* mRNA is still able to be produced. The multiple bands seen could also indicate that clone 36 is a mixed population and was not cleanly picked and expanded. The other band

that shows a small size change is clone 41. The band was extracted and sent for sanger sequencing to clarify results seen up to this point.

WT and Clone 41 Sequencing read into Exon 2 of HSPG2

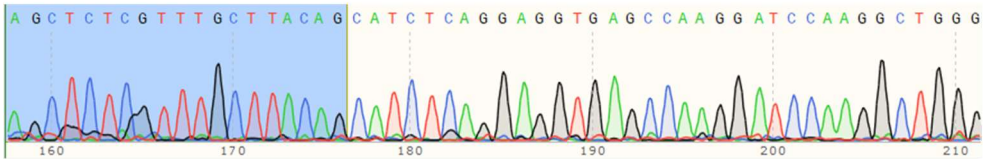


```
HSPG2Sequence          actcaatcagctctcgtttgcttacaggtgacccatgggctgagggcatacgatggcttg     1380
Clone41Sequencing      ACTCAATCAGCTCTCGTTTGCTTACAGCATCTCAGGAGGTGAGCCAAGGATCCAAGGCTG     180
                       **************************     *    **          *     *  **

HSPG2Sequence          tctctgcctgaggacatagagaccgtcacagcaagccaaatgcgctggacacattcgtac     1440
Clone41Sequencing      GGA-------------------------------------------------------     183

HSPG2Sequence          ctttctgatgatgaggacatgctggctgacagcatctcaggaggtgagccaaggatccaa     1500
Clone41Sequencing      -------------------------------------------------------------     183

HSPG2Sequence          ggctgggagcagaggggtgggggtgagactgtgcttcttcccactggcatgggggagga     1560
Clone41Sequencing      --------GCAGAGGGGTGGGGGGTGAGACTGTGCTTCTTCCCACTGGCATGGGGGAGGA     235
                               **************************************************
```

***Figure 3.12 – Sequencing and alignment of clone 41.*** *Sequencing showing clean peaks on the DNA sequence trace highlighted region before Exon 2 truncated section. Clustal Omega sequence alignment comparing WT to Clone41 sequence showing matching regions outside a missing section.*

Sequencing results confirmed that the presumed untargeted allele of clone 41 did have a deletion where most of exon 2 was removed but following on the remaining region of *HSPG2* was unaffected (Figure 3.12). This deletion caused a frame shift to occur in which the rest of *HSPG2* would still be fully transcribed, just missing a region of exon 2 (Figure 3.13, C).

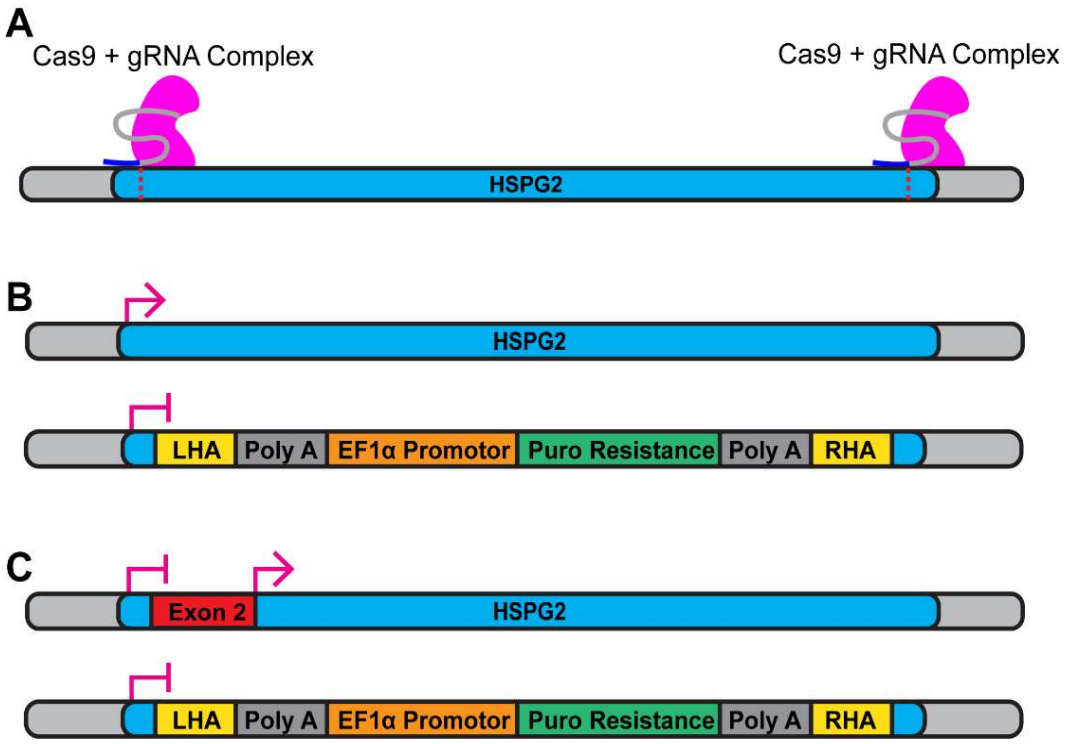


***Figure 3.13 – Outcome of clone 41 insertion.*** *(A) Schematic showing the initial targeting strategy using CRISPR/Cas9, (B) following correct insertion via homologous recombination a heterozygous insert was most seen. (C) It was possible to create a truncated form of HSPG2 due to a deletion of part of exon 2, although a downstream frame shift creates a new transcription start site that allows translation of the remaining HSPG2 gene.*

The process of excising the entire *HSPG2* genome and replacing with the selection cassette was repeated for a third time, with the aim of creating a full *HSPG2* KO iPSC line. In the following attempt the targeted iPSC cell line was replaced with mEGFP-ACTN2 tagged iPSC line (Allen Institute). mEGFP-ACTN2 iPSCs were transfected with the same plasmid cocktail as used previously, following puromycin selection, colony picking and expansion. Since this targeting was again able to only create a heterozygous knockout of *HSPG2* using a new strategy I aimed to repeat this targeting again.

### 3.4. Third attempt at full *HSPG2* knockout using mEGFP-ACTN2 tagged hiPSCs

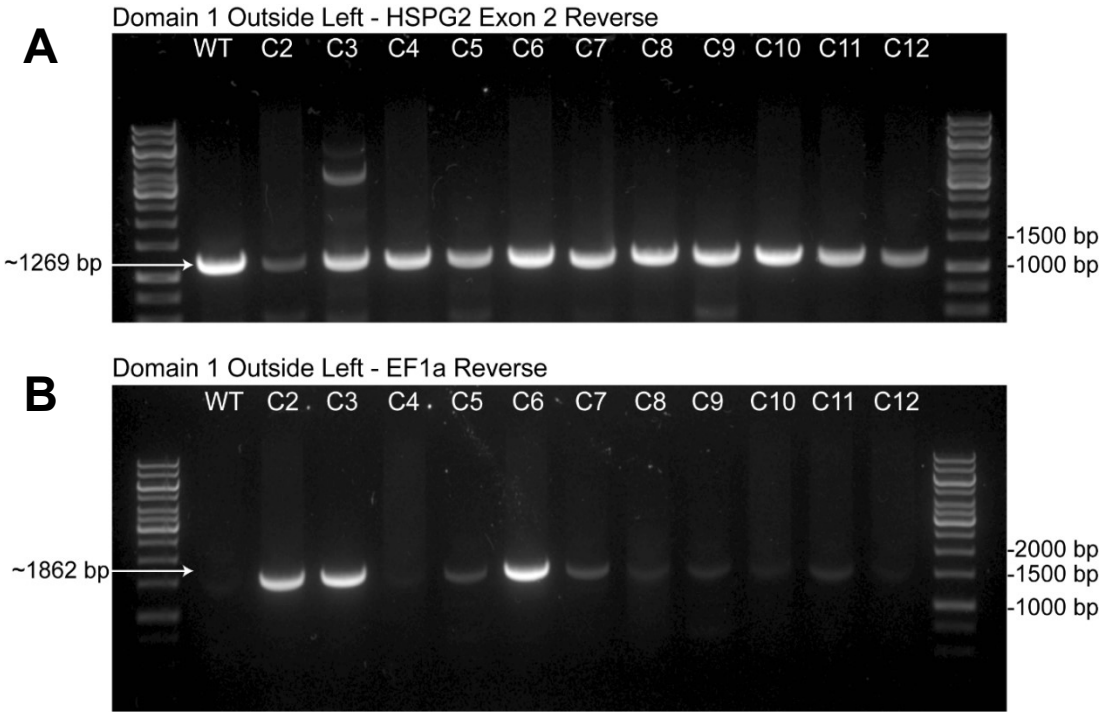


***Figure 3.14 – Selection of clones screened for a HSPG2 KO in third targeting attempt.*** *Screening PCR looking for deletion of HSPG2 from gDNA in newly targeted clones using primer pairs Domain 1 Outleft and HSPG2 Exon 2 Reverse aiming to remove the ~1268bp band (A). Following PCR targeting the selection cassette aiming for a band around ~1862 bp implying correct insertion of the selection cassette (B).*

Screening PCRs of the mEGFP-ACTN2 targeted iPSCs show that all clones show a band around 1269 bp suggesting all targeted clones would at least be heterozygous and potentially some untargeted (Figure 3.14, A). Although the screening PCR using 'Domain_1_outside_left' to 'EF1a_Rev' primers show that only 3 clones have a clear insertion of the selection cassette (C2, C3, C6 in Figure 3.14, B).

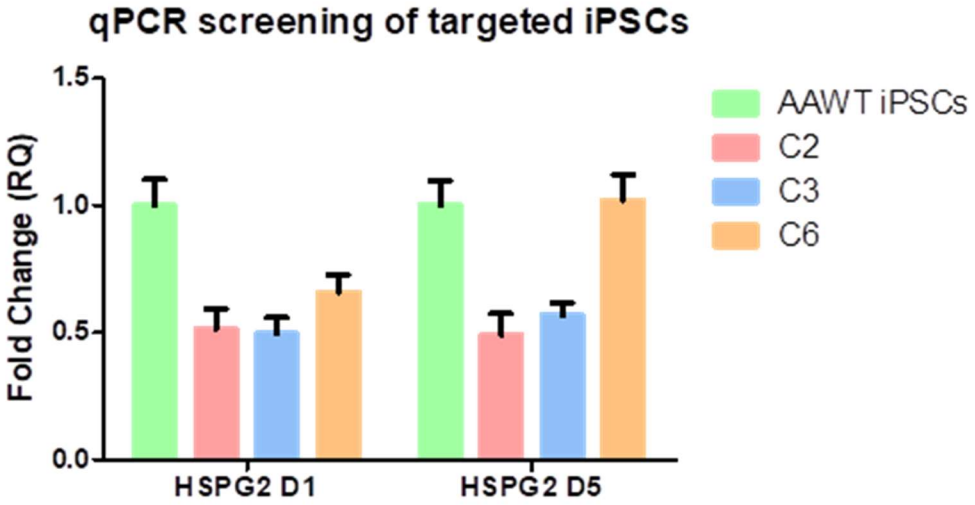


***Figure 3.15 – Confirmation of HSPG2 knockdown in newly created iPSC lines.*** *qRT-PCR results show only 50% reduction in HSPG2 in varying clones implying creation of heterozygous knockout iPSCs. All clones show a reduction in domain 1 of HSPG2 although only clone C2 and C3 show a similar reduction in HSPG2 domain 5.*

Selected clones were taken forward for further screening via qRT-PCR analysis of cDNA (Figure 3.15). Using *HSPG2* domain 1 SYBR primers we see a ~50% reduction of *HSPG2* (C2 – 0.51, C3 – 0.50, C6 – 0.66-fold reduction). While when using domain 5 SYBR primer we see both C2 and C3 have a reduction in *HSPG2* expression, 0.49 and 0.59, respectively. While C6 shows domain 5 expression at 1.02-fold change compared to mEGFP-ACTN2 WT iPSC *HSPG2* expression, implying no difference has occurred. Two different methods and three separate targeting events of hiPSCs were only able to create heterozygous knockouts and no homozygous knockouts, so for the future experiments a heterozygous was to be used.

### 3.5. Characterisation of HSPG2$^{+/-}$ hiPSCs

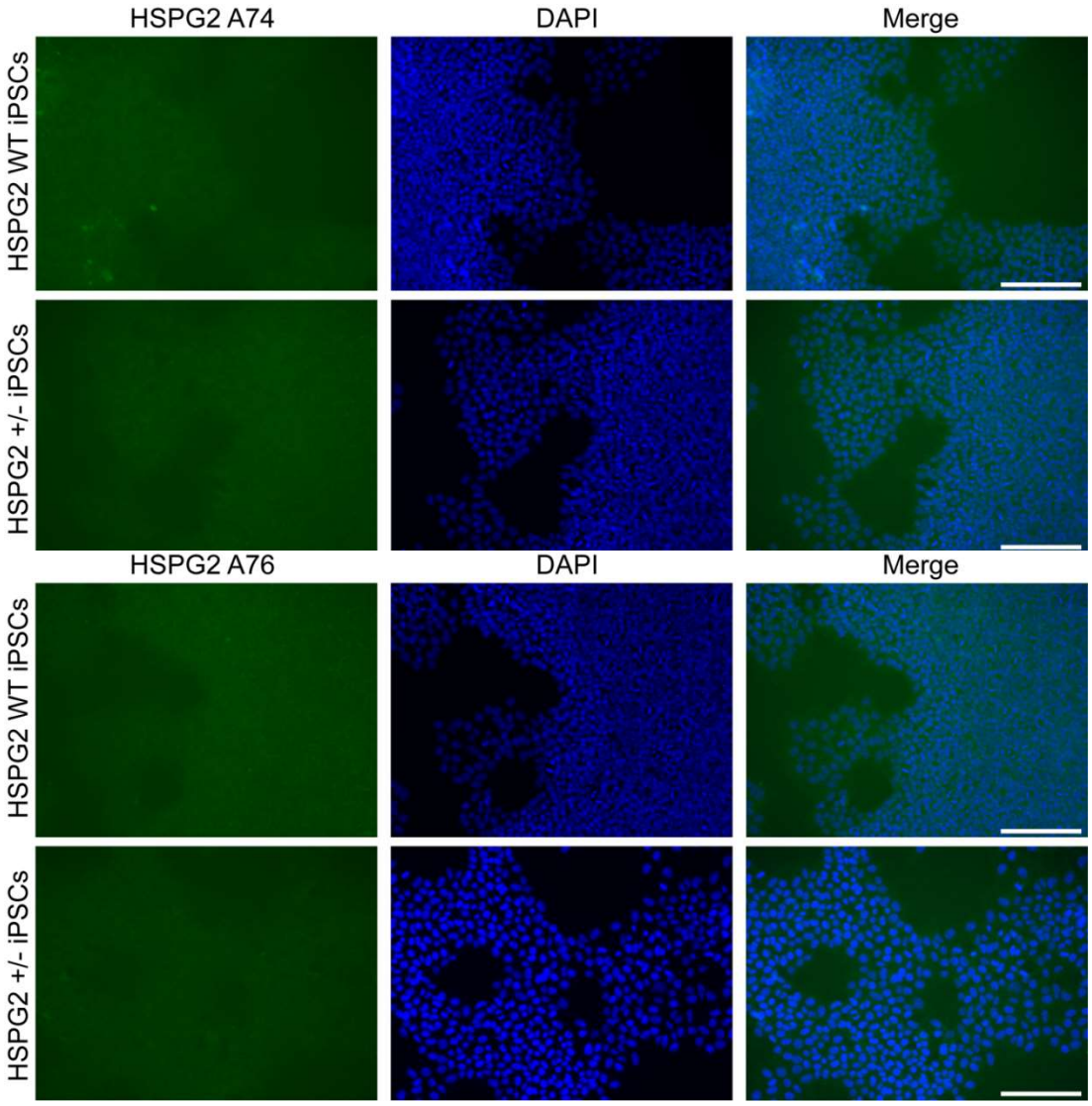


***Figure 3.16 – No visible change in HSPG2 protein secretion in iPSCs.*** *Immunostaining images of confluent iPSCs show similar levels of HSPG2 with two monoclonal antibodies, both A74 (Domain 5 targeting) and A76 (Domain 1 targeting). Channels split to show green channel for HSPG2 and DAPI in blue, plus combined to show HSPG2 is preferentially secreted around the cells. Scale bar = 600 µM.*

Immunostaining of WT and HSPG2$^{+/-}$ iPSC colonies revealed low levels of perlecan when stained using monoclonal antibodies A74 and A76 (Figure 3.16). Faint outlines of colonies can be seen but no difference is apparent between the two cell lines confirming the perlecan is very lowly secreted in iPSCs.

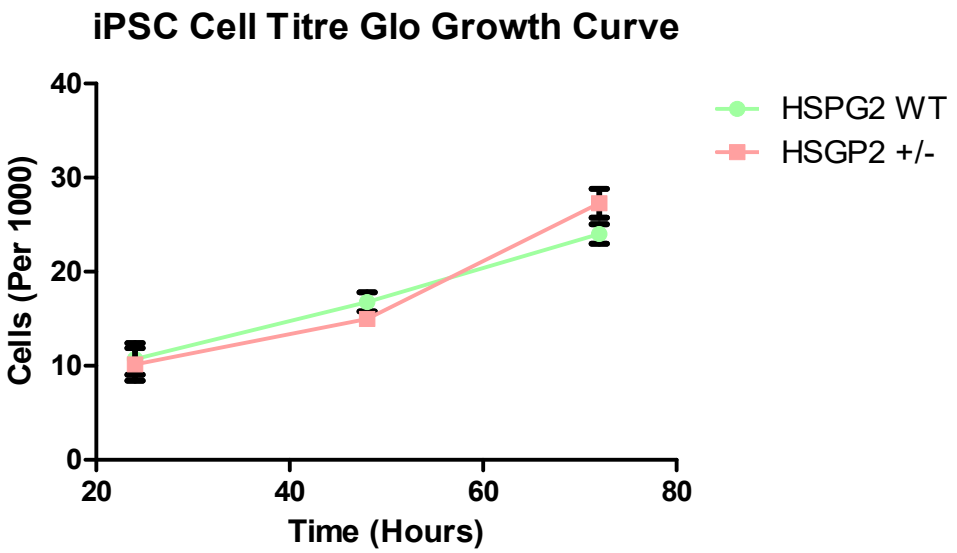


***Figure 3.17 – HSPG2 reduced iPSCs show no reduction in proliferation capabilities.*** *Cell titre GLO growth curve of iPSC lines in culture over 3 days, with time points taken at 24, 48 and 72 hours. Luminosity was measuring using OMEGA plate reader and compared to a seeded standard curve to allow accurate estimation of cell number at each time point. N=3.*

I wanted to further see how the heterozygous knockout of *HSPG2* in iPSCs affected their culture. To do this I performed a CellTitre-Glo assay on each iPSC line at different timepoint throughout their culture. Cells were seeded into 96 well plates and taken for analysis at 24, 48 or 72 hours. At the first timepoint (24 hours) a standard curve was also analysed using cells seeded in a range from 1000 to 40,000. Cells were lysed at each timepoint using CellTitre-Glo reagent and read on an OMEGA plate reader measuring luminescence. Using this method, we can see the reduction of *HSPG2* mRNA in our HSPG2$^{+/-}$ iPSC lines had no effect on proliferative capabilities of the iPSCs over 3 days in culture (Figure 3.17).

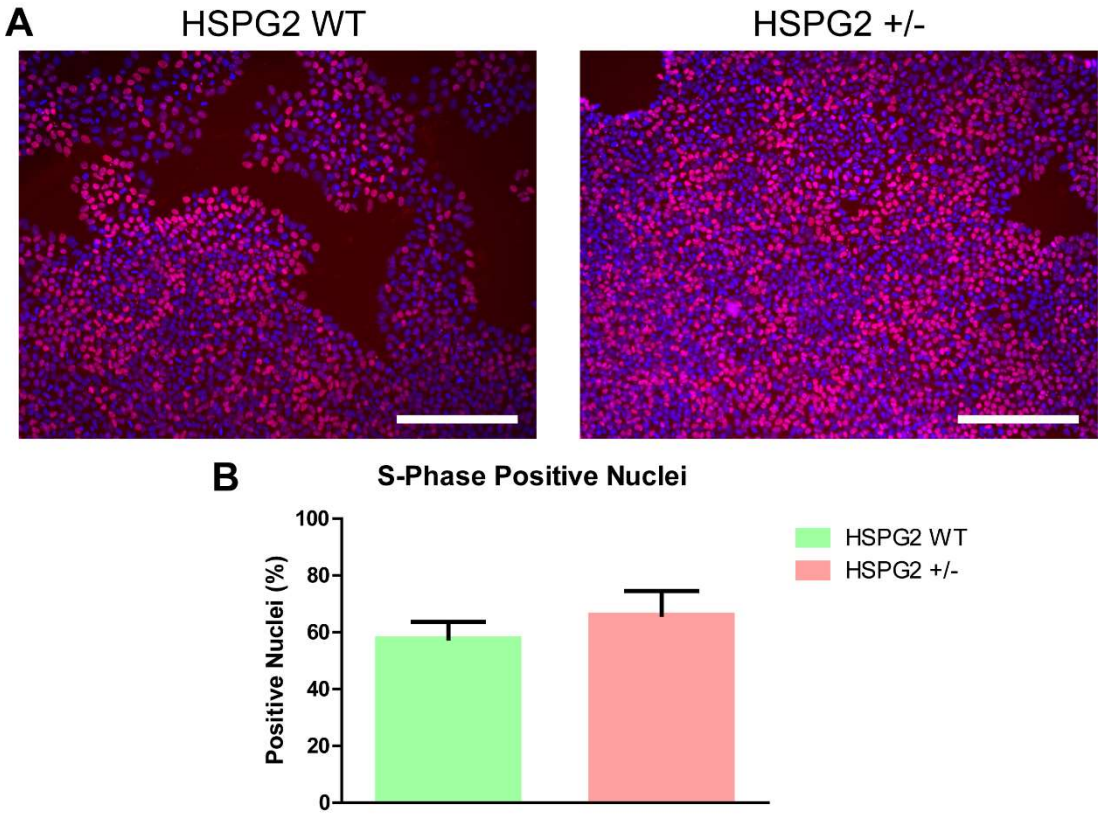


***Figure 3.18 – S-phase staining of hiPSC cell lines.*** *hiPSCs stained with CLICK IT S-phase kit (red) and DAPI (blue), scale bar at 600 µm. Quantification of positive red nuclei performed using Cell Profiler pipeline and plotted as percentage positive red nuclei against total. N=3*

To further confirm no changes occurred in hiPSC proliferation both cell lines were stained using an S-phase kit (CLICK IT) to identify Edu positive cells. Nuclei that fluoresce red after excitation were fixed with in S-phase of the cell cycle (Figure 3.18, A). Further staining with DAPI was used to quantify total nuclei count. Using a Cell Profiler pipeline the intensity of red fluorescence in each nucleus was calculated and total number counted, data was plotted to represent the number of red positive nuclei against total nuclei count (Figure 3.18, B). No statistical significance is seen between the WT (57.9% ±16.5) and HSPG2$^{+/-}$ (66.2% ±23.6) S-phase positive nuclei. I also wanted to see if the pluripotency of hiPSCs had changed due to lack of *HSPG2* expression.

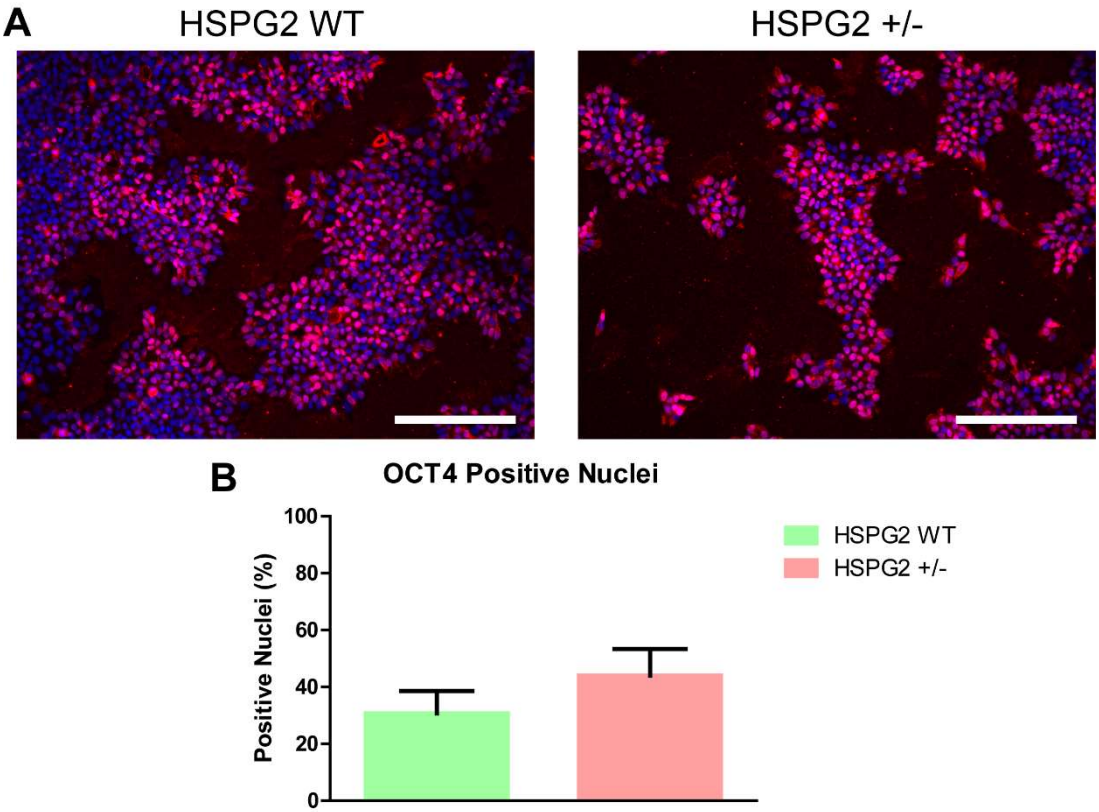


***Figure 3.19 – OCT4 staining of hiPSC cell lines.*** *hiPSCs stained with OCT4 pluripotency marker (red) and DAPI (blue), scale bar at 600 µm. Quantification of positive red nuclei performed using Cell Profiler pipeline and plotted as percentage positive red nuclei against total. N=3*

To identify changes in pluripotency between the cell lines hiPSCs were grown for several days before fixation and staining with nuclear pluripotency marker OCT4 (Figure 3.19, A). To further quantify any differences seen between the two cell lines the total nuclear count was calculated using DAPI and previously described Cell Profiler pipeline was used (Figure 3.19, B). The quantification of total red nuclei shows no statistical differences between the two lines implying the level of nuclear OCT4, and therefore pluripotency, was not affected by a *HSPG2* heterozygous KO. To further look for differences between our hiPSC lines the cells were ran on a mitochondrial BioLog assay to study any differences in specific substrate metabolism.

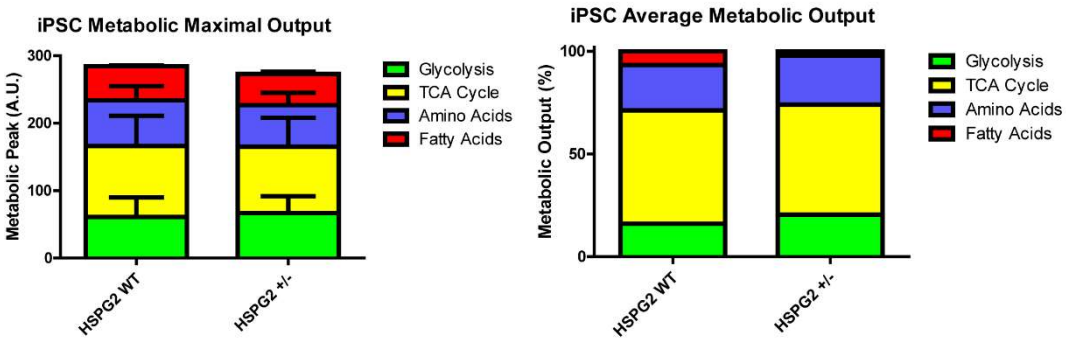


***Figure 3.20 – iPSC grouped metabolism.*** *iPSC overall metabolic maximal output is averaged for each designated metabolic category showing no difference between the two cell lines. Upon removing baseline metabolism from samples, the percentage of preferential metabolism can be shown to be TCA cycle. N=3*

After running the Mitoplates assay on the BioLog, specific substrates are categorised into metabolic pathways, glycolysis, TCA cycle, amino acids, and fatty acids. The average of the groups shows how similar the HSPG2$^{+/-}$ iPSC line is to the control (Figure 3.20). The highest metabolically active group is the TCA cycle, with the WT iPSCs averaging 104.9 A.U. compared to HSPG2$^{+/-}$ iPSCs 98.1 A.U. By removing the no substrate background levels and converting each group to a percentage we can see how the TCA cycle makes up more than 50% of the metabolic output in iPSCs (WT:55.1%, HSPG2$^{+/-}$:53.4%). Following on the next preferential category of metabolism is amino acids (WT: 22.1%, HSPG2$^{+/-}$: 23.9%), glycolysis (WT: 16.1%, HSPG2$^{+/-}$: 20.6%) and finally fatty acids (WT: 6.7%, HSPG2$^{+/-}$: 2.2%). These results show how little iPSCs can metabolise fatty acids and the reliance on TCA cycle metabolism. They also point to the HSPG2$^{+/-}$ iPSC having a slight increased reliance in glycolysis and a reduction in fatty acid metabolism.

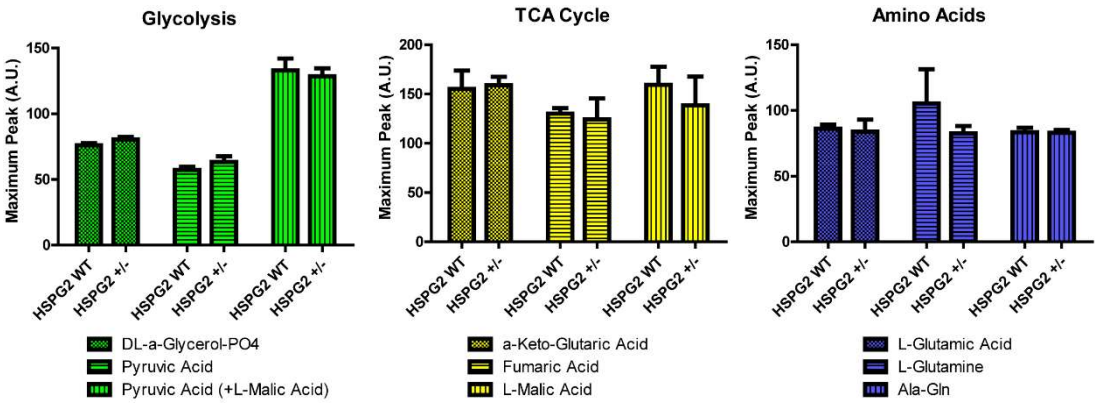


***Figure 3.21 – Specific substrate maximal metabolism in iPSCs.*** *The highest metabolised substrates from glycolysis, TCA cycle and amino acids are plotted to show no significant difference between HSPG2 WT and HSPG2$^{+/-}$ iPSCs. N=3*

Looking more closely at the individual substrates, three of the most metabolised substrates were selected from each significant group (Figure 3.21). Both iPSC lines metabolise these substrates with no significant difference between the lines. But again, the highest metabolised substrates are in the TCA cycle with a-Keto-Glutaric Acid (WT: 155.3 A.U., HSPG2$^{+/-}$: 159.0 A.U.), Fumaric acid (WT: 130.1 A.U., HSPG2$^{+/-}$: 123.4 A.U.) and L-Malic Acid (WT: 159.5 A.U., HSPG2$^{+/-}$: 138.5 A.U). The highest peak in glycolysis was pyruvic acid combined with sparking L-malic acid (WT: 133.0 A.U., HSPG2$^{+/-}$: 128.6 A.U) compared to pyruvic acid without L-malic acid (WT: 57.2 A.U., HSPG2$^{+/-}$: 63.3 A.U) implying the necessity of sparking L-malic acid. Out of the 3 amino acids L-Glutamine is the most metabolised substrate in the HSPG2$^{WT}$ iPSCs (WT: 105.3 A.U., HSPG2$^{+/-}$: 82.6 A.U) with both L-Glutamic Acid and Ala-Gln being metabolised at similar levels ( WT: 86.2 A.U., HSPG2$^{+/-}$ : 84.0 A.U, WT: 83.4 A.U., HSPG2$^{+/-}$: 83.1 A.U, respectively)

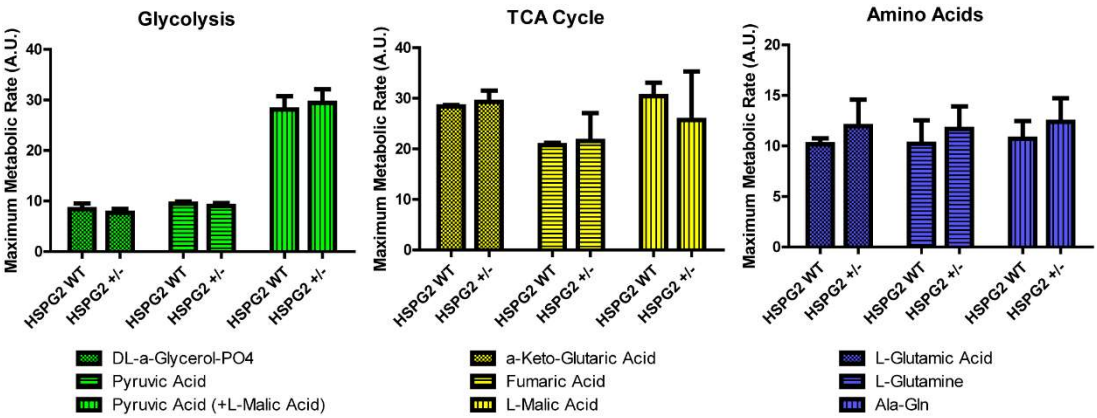


***Figure 3.22 – Maximal rate of specific substrate metabolism in iPSCs.*** *Output values from Data Profiler 1.17 calculating maximum rate of metabolism reached in specific substrates over 6 hours. N=3*

Since this assay records real time substrate metabolism, the rate of each substrate can also be calculated (Figure 3.22). The data suggests pyruvic acid plus sparking L-Malic acid is one of the fastest metabolised substrates in iPSCs (WT: 28.1 A.U., HSPG2$^{+/-}$: 29.3 A.U.). The 3 specified TCA substrates are metabolised to a similar rate, a-Keto-Glutaric Acid (WT: 28.4 A.U., HSPG2$^{+/-}$: 29.3 A.U.), Fumaric Acid (WT: 20.8 A.U., HSPG2$^{+/-}$: 21.5 A.U.) and L-Malic Acid (WT: 30.4 A.U., HSPG2$^{+/-}$: 25.7 A.U). There is no significant difference in any of the rates of substrate metabolism between HSPG2$^{WT}$ and HSPG2$^{+/-}$ iPSC lines. Implying the heterozygous knockdown of *HSPG2* in iPSCs has no effect on the iPSC to metabolise specific substrates. The combined data showing no change in growth rate or metabolism suggests HSPG2$^{+/-}$ iPSCs are comparable to the HSPG2$^{WT}$. RNA sequencing was performed on both WT and HSPG2$^{+/-}$ deficient hiPSCs as part of a larger experiment.

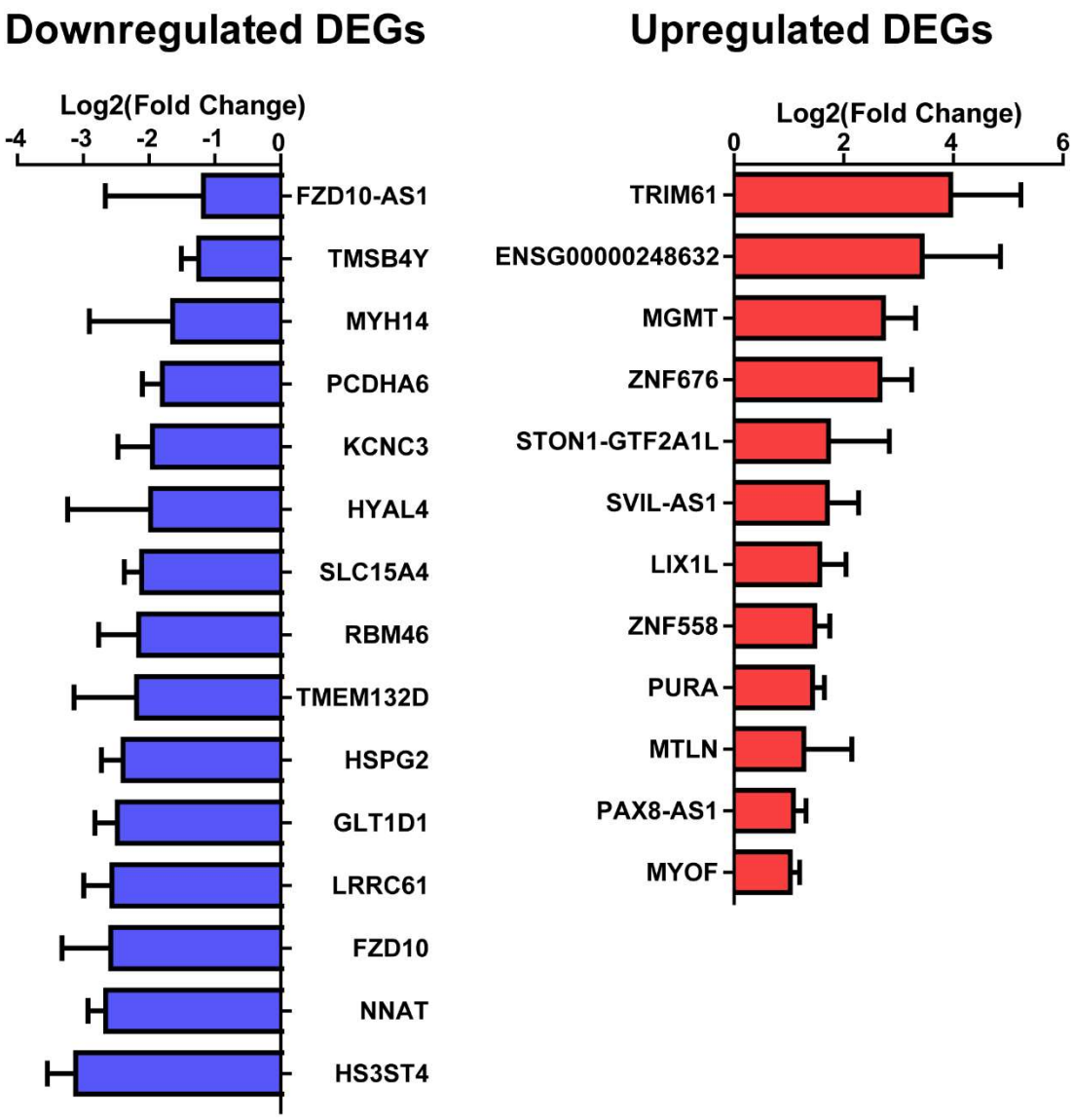


***Figure 3.23 – Fold change of DEGs found between WT and HSPG2+/- hiPSCs.*** *Log2 fold change calculated after DESeq2 normalisation for statistically significant DEGs between hiPSC cell lines. N=3*

DESeq2 gene analysis identified 27 differentially expressed genes (DEGs) between WT and HSPG2$^{+/-}$ hiPSCs. Of the 27 DEGs 15 are downregulated in the HSPG2$^{+/-}$ hiPSC line, while 12 were upregulated (Figure 3.23). The downregulated genes include *HS3ST4, NNAT, FZD10, LRRC61, GLT1D1, HSPG2, TMEM132D, RBM46, SCL15A4, HYAL4, KCNC3, PCDHA6, TMSB4Y* and *FZD10-AS1*. Interestingly *HSPG2* is only the sixth most downregulated gene at -2.4 Log2 fold change implying other genes are more drastically reduced due to the reduction of *HSPG2* in the hiPSC. 12 DEGs were upregulated in the HSPG2$^{+/-}$ hiPSC line compared to WT including

*TRIM61, ENSG00000248632, MGMT, ZNF676, STON1-GTF2A1L, SVIL-AS1, LIX1L, ZNF588, PURA, MTLN, PAX8-AS1* and *MYOF*. *TRIM61* shows the highest upregulation in HSPG2$^{+/-}$ hiPSCs at 3.9 Log2 fold expression, while *HS3ST4* shows the largest downregulation at -3.1 Log2 fold expression.

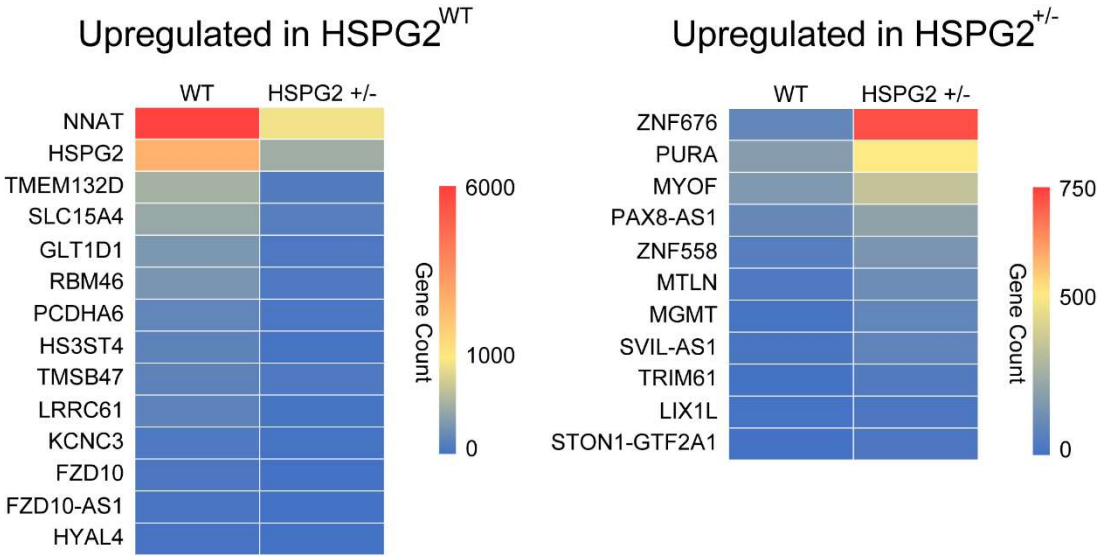


***Figure 3.24 – Gene counts of 27 DEGs.*** *Heatmaps plotting gene counts of the DEGs upregulated in HSPG2$^{WT}$ and upregulated in HSPG2$^{+/-}$ hiPSC cell lines. N=3*

When investigating the gene counts of each DEG found between the hiPSC lines, several genes are highlighted showing a substantial expression in hiPSCs (Figure 3.24). The majorly expressed genes in HSPG2$^{WT}$ hiPSCs include *NNAT, HSPG2, TMEM132D* and *SLC15A4*, while highly expressed genes in HSPG2$^{+/-}$ hiPSCs include *ZNF676*, *PURA* and *MYOF*. These results show *NNAT* and *HSPG2* are amongst the highest expressed genes that undergo dysregulation due to the perlecan deficiency in hiPSCs.

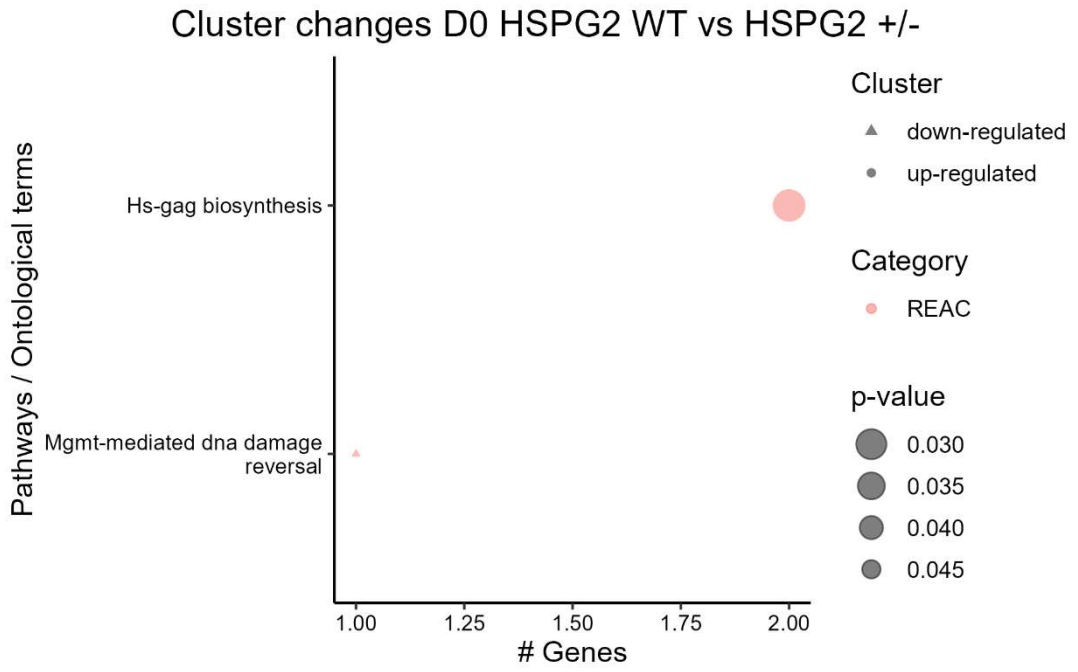


***Figure 3.25 – GO Term analysis of 27 DEGs found between WT and HSPG2$^{+/-}$ hiPSCs.*** *Clustered terms plotted against gene count per term found using GO and REAC pathway analysis.*

Running gene ontology (GO) and Reactome (REAC) term analysis on the 27 DEGs found between the two lines identified only two terms (Figure 3.25). Both terms, HS-GAG biosynthesis, and MGMT-mediated DNA damage reversal, were found using REAC pathway analysis.

Overall, the WT and HSPG2$^{+/-}$ hiPSCs show trivial difference in proliferation, metabolism, and protein secretion. RNA sequencing shows 27 DEGs between the two lines, when further analysed two terms were highlighted. I next wanted to attempt upregulating *HSPG2* in hiPSC lines using CRISPRa, this is to determine if the upregulation of *HSPG2* would cause the opposite effect seen in HSPG2$^{+/-}$ hiPSCs.

### 3.6. Upregulation of *HSPG2* in hiPSCs using CRISPRa

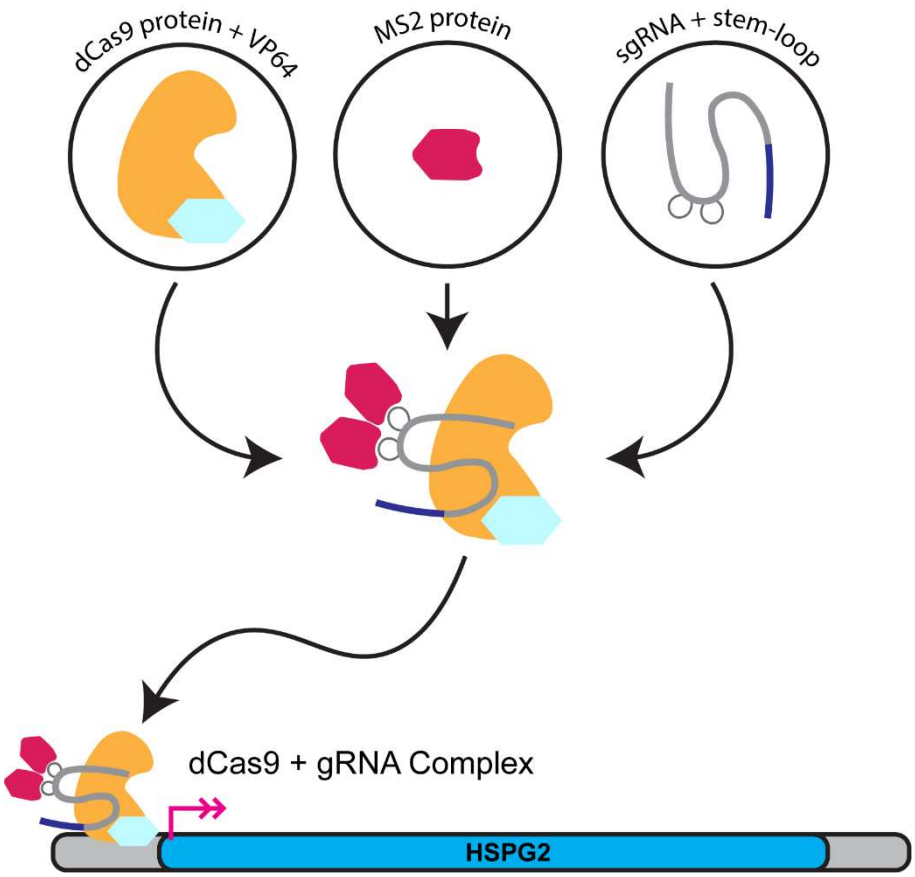


***Figure 3.26 – Schematic of gene upregulation via dCas9.*** *Three plasmids are inserted into the target cell. A dCas9 protein with attached VP64 site, MS2 creation plasmid and the sgRNA + stem loop plasmid. The created products form a complex and bind to a transcription start site causing downstream upregulation of target gene.*

To further manipulate the production of *HSPG2* in cells I looked to upregulate it rather than downregulate. To do this the CRISPRa system was used, this involves the use of dCas9 (dead Cas9) that will not cleave but bind to the targeted PAM site. Inserting all three plasmids into a cell creates a complex that when bound to a transcriptional start site recruits' promotors that cause downstream upregulation (Figure 3.26). Initially I had to create the sgRNA plasmids with a sequence that would guide the dCas9 complex to a promotor of *HSPG2*. To do this, two sequences were chosen using the CRISPR-ERA sgRNA search for upregulation (Liu et al., 2015).

| Guide Name | sgRNA Sequence | Distance to TSS | E Score | S Score |
|---|---|---|---|---|
| HSPG2 Guide 1 | CAAAGGCCTAGTAGGCTGCG | -160 | 20 | 0 |
| HSPG2 Guide 2 | TACTCCAGGCCGGGTTTGGC | -230 | 20 | 0 |

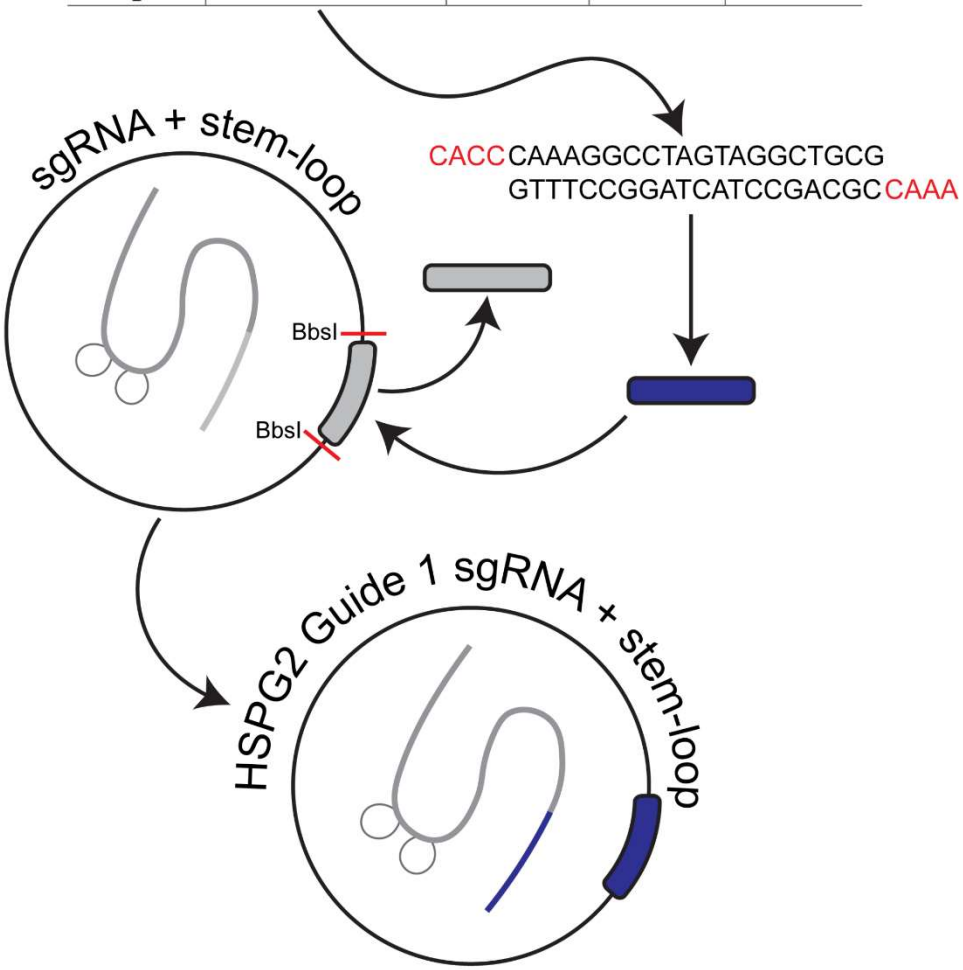


***Figure 3.27 – Schematic for creation of sgRNA for CRISPRa upregulation of HSPG2.*** *Initial guide sequences are found using CRIPSR-ERA search engine. Complimentary strands are created leaving sticky ends for insertion into BbsI cut sites. Oligonucleotides are annealed together and ligated into enzymatically digested sgRNA plasmids.*

Oligonucleotides are designed and chosen based on their relative distance to the transcriptional start site as well as their efficacy and specificity score (Figure 3.27). Complimentary strands are also designed to bind with the chosen guideRNA leaving a sticky end after creations. After annealing the pair

of oligonucleotides together they are ligated into a BbsI digested sgRNA plasmid, transformed into Top10 *E.coli* and expanded. The next step was to transfect iPSCs with the created plasmids and complimentary dCas9 and MS2 plasmids.

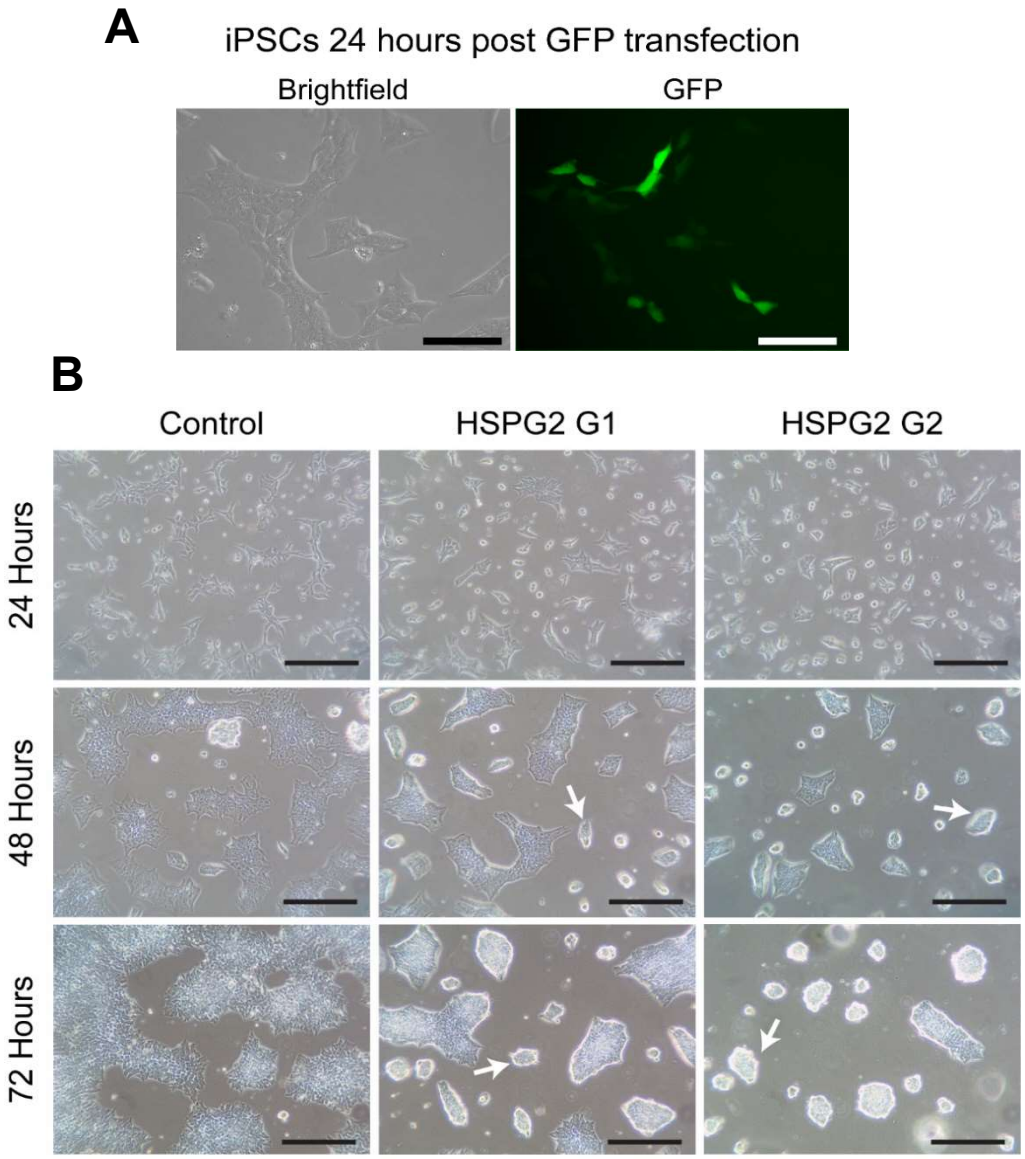


***Figure 3.28 – Images post transfection of iPSCs with GFP or dCas9 with HSPG2 guides.*** *(A) Cells transfected with a GFP plasmid express GFP after 24 hours indicating successful transfection. (B) Brightfield images taken at 24-hour intervals post transfection of dCas9 show cells clumping and lifting (arrows) as early as 48 hours post transfection. N=1*

Cells were initially transfected with a GFP plasmid to confirm transfection efficiencies and that plasmid uptake and expression in an iPSC had occurred 24 hours following on from transfection (Figure 3.28, A). Following this iPSCs that had been transfected with either the scrambled control plasmid, HSPG2-G1 or HSPG2-G2. Photos of these populations over the time course show how cells that have been transfected with a HSPG2 guide sequence cause clumping of the iPSCs (Figure 3.28, B). These iPSC clumps eventually detach leaving behind no cells, the difference is apparent when compared to the confluency of the scrambled control sample.

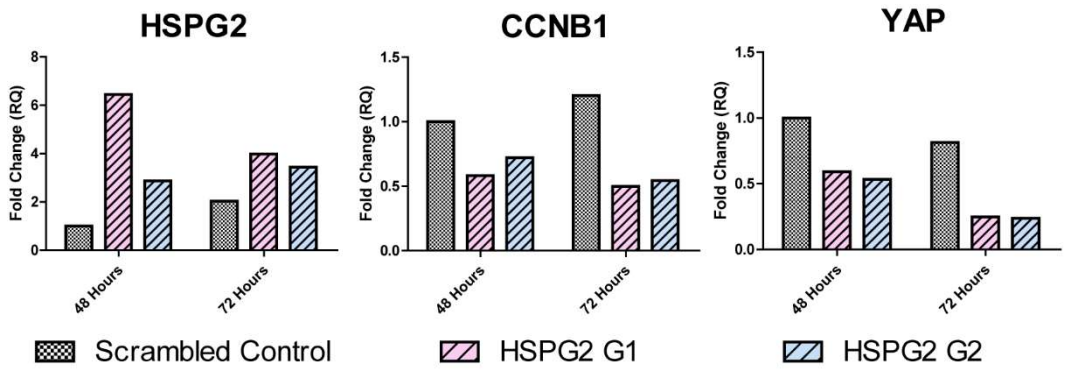


***Figure 3.29 – qRT-PCR Expression of iPSCs after HSPG2 upregulation with dCas9.*** *SYBR Green qRT-PCR expression shows upwards trend of HSPG2 expression when transfected with HSPG2 G1 and G2. Transfection of guides 1 and 2 also show a reduction in CyclinB1 and YAP expression. N=1*

To further quantify the efficiency of the upregulation system qRT-PCR was performed on the iPSCs at 48- and 72-hour timepoints (Figure 3.29). Results show how using HSPG2-G1 cause upregulation of *HSPG2* expression to 6-fold which reduced to 4-fold after 72 hours. This expression was higher than HSPG2-G2 which only increased *HSPG2* expression to 2.5-fold and saw a slight increase to 3-fold after 72 hours. The upregulation of *HSPG2* seemed to reduce the expression of proliferation gene *CyclinB1* by around 0.5-fold in both guides at each timepoint. *YAP*, a gene involved in mechanotransduction, has expression attenuated in the samples targeted with HSPG2 guide sequences (0.5-fold after 48 hours followed by 0.3-fold after 72 hours). Overall, I show I

can upregulate *HSPG2*s expression, this over expression hindered the viability of the hiPSCs and caused detachment of hiPSC colonies.

### 3.7. Summary

In this chapter I have attempted to make a full knockout of *HSPG2* in hiPSCs. I show through multiple rounds of CRISPR targeting that only heterozygous knockouts were able to be created, with no homozygous clones. Although it is possible this is a technical issue, the multiple rounds and attempts suggest fully *HSPG2* knockout to be lethal in our current culture conditions. The current culture conditions used in our hiPSC culture are highly defined and may be too strict for an hiPSC to be maintained in an environment lacking *HSPG2*. These conditions utilise E8 media containing no serum and eight chemically defined components. The cells are also cultured on vitronectin peptide which contains no perlecan, unlike other coatings such as Matrigel or feeder layers. The final results of the CRISPR targeting lead to multiple different cell lines only containing a heterozygous knockout of *HSPG2*.

The ~50% reduction of *HSPG2* mRNA does not seem to have a major effect on perlecan secretion into the matrix, although the baseline for this is extremely low. From the literature I theorised *HSPG2* would play a crucial role in both hiPSC proliferation and maintenance of pluripotency. The $HSPG2^{+/-}$ hiPSC line shows a matched rate of proliferation and no difference between number of cells found in S-phase. There was also no difference between the number of nuclei containing OCT4 implying the *HSPG2* reduction had no effect on hiPSCs pluripotency. These results could be the outcome of a reduction of *HSPG2*, compared to a full KO which may show the essential properties of *HSPG2* in the maintenance of hiPSCs.

Both cell lines also metabolise substrates at a similar level and rate. *HSPG2* KO mice show metabolic differences in adipocytes (Yamashita et al., 2018), while the hiPSC het KO created here shows no changes in metabolism. The lack of metabolic alteration could be due to *HSPG2* having little to no effect on hiPSC metabolism, or more likely that a full KO would reveal these differences

not seen in the heterozygous KO. The only difference is a slight shift in increased glycolysis at the detriment to a reduced fatty acid metabolism percentage. Using CRISPRa I also show the capabilities of upregulating *HSPG2* mRNA. The upregulation of *HSPG2* appeared to be detrimental to the cells causing clumping and detachment of colonies. From this we can assume not only a full KO, but also over-expression of *HSPG2* is lethal to hiPSCs, and *HSPG2* is required to be maintained in equilibrium for hiPSC survival.

Transcriptomic analysis between the two lines showed only minimal differences (27 DEGs) caused by perlecan haploinsufficiency. Of these, two genes (*HSPG2* and *NNAT*) had notable higher baseline expression levels in hiPSCs. The reduction in *HSPG2* was the direct consequence of the CRISPR-Cas9 gene editing. The second gene (*NNAT*, encoding Neurontin) could be considered as a candidate functional gene effected by perlecan deficiency in hiPSCs worthy of further investigation.

# 4. Perlecan and the formation of the cardiovascular system

## 4.1. Introduction

Perlecan (*HSPG2*) is found to be present in the basement membrane of cardiac endocardium and pericardium in gestational week 6/7 of the early developing heart, but not in the cardiomyocytes (CMs) (Roediger et al., 2009a). Following further development, CM expression of perlecan begins during gestational week 8/9, suggesting CM perlecan expression is not required at the earliest stage of CM development (Roediger et al., 2009b).

In *HSPG2* KO mice Sasse and colleagues found embryonic lethality had occurred in >80% of the mice. When examining the cause of embryonic lethality, the authors found cardiac basement membrane remodelling had occurred leading to the creation of a 'leaky' heart (Sasse et al., 2008b). This showed perlecan to be an essential cardiac ECM component, and although CM perlecan expression occurs later in cardiac development, its global KO causes embryonic lethality due to cardiac defects.

As well as structure, perlecan has a role in signalling and metabolism, with this role appearing to change in a cell specific manner. When investigating perlecan role in adipocytes Tran-Lundmark found a knockout in mice caused a higher level of lipid metabolism and oxygen conception (Tran-Lundmark et al., 2008). When investigating osteocytes Pei and colleagues found a *HSPG2* KO led to an attenuation of calcium channel colocalization and calcium signalling (Pei et al., 2020b). A *HSPG2* mice KO has also been shown to cause an increase in smooth muscle cell (SMC) mitochondria production (Tran-Lundmark et al., 2008). The ability of perlecan to act in a cell specific manner could be linked to changes in *HSPG2* transcript variants. Data has shown the expression of cell-specific forms of perlecan, suggesting these forms may vary in their functions (MoonSun Jung et al., 2013; Melrose et al., 2006; Whitelock et al., 2008).

Following the creation of a *HSPG2* deficient iPSC line (chapter 3), I attempted to differentiate these to cardiac populations in this chapter. Optimisation of CM

differentiation methods have evolved from spontaneous differentiation of aggregated embryoid bodies, to chemically defined media compositions (Burridge et al., 2014; Kehat et al., 2001). The CMs generated from these differentiation protocols produce immature CMs closer representing foetal CMs. With the aim of maturing hiPSC-CMs methods were developed involving 3D encapsulation of cells between silicone rods generating engineered heart tissue (EHTs) (Mannhardt et al., 2016). Combining hiPSCs and non CMs such as cardiac fibroblasts (CFs) in EHTs showed enhanced contractile performance (Tiburcy et al., 2020).

### 4.2. Generation of hiPSC-CMs

To investigate the role of perlecan in a cardiac environment, I first optimised the differentiation of hiPSCs to CMs. Three main culture medias were used to achieve this. These were heart media 1, 2 and 3 (HM1, HM2 & HM3) (Figure 4.1, A). Differentiation was initiated using HM1 supplemented with the factors activin A, FGF-2, BMP4 and CHIR99021 to direct differentiation towards the mesoderm lineage. On day two, the media was switched to HM1 supplemented with WNT inhibitor IWR. Spontaneous contraction becomes evident by day 6. Ventricular specification is directed on day eight by using HM2, containing insulin, but lacking vitamin A. Purification is performed to increase cardiomyocyte purity differentiations, by the removal of glucose and replacement with L-lactic acid, which non-cardiomyocytes are unable to metabolise. Finally, cells are maintained in HM2 and undergo some level of maturation following purification.

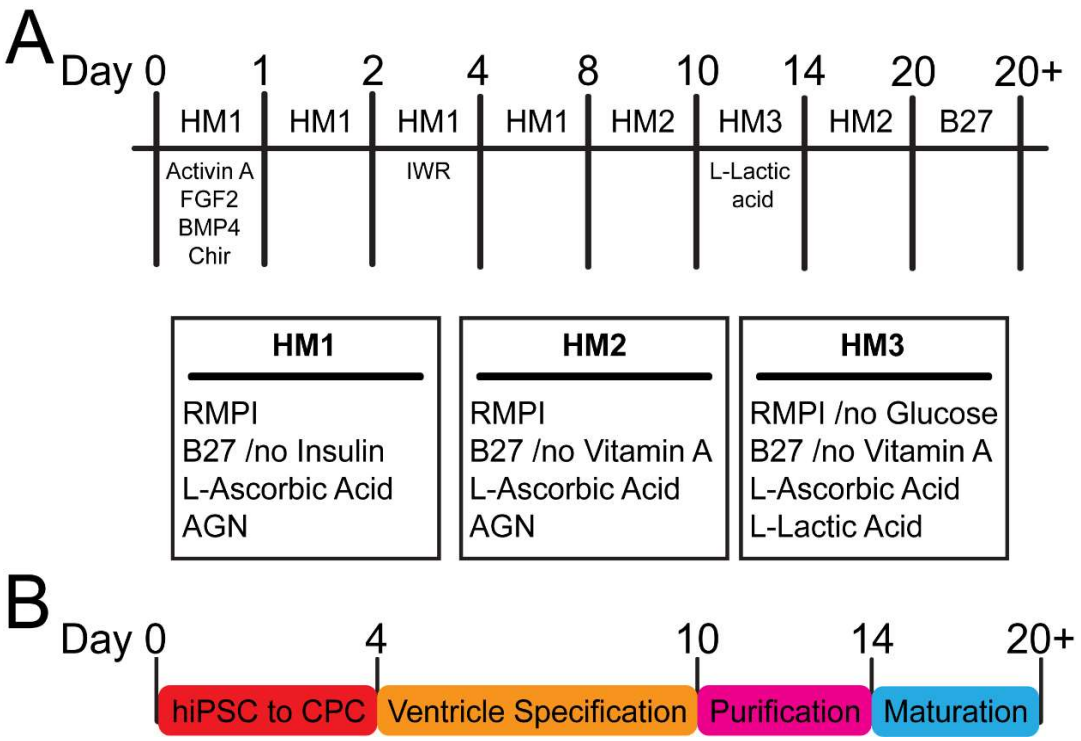


***Figure 4.1 - Method for differentiating iPSCs to cardiomyocytes.*** *(A) Outline of media added at each timepoint throughout the cardiomyocyte differentiation. (B) Overview of cellular processes occurring between key media changes.*

When differentiating the hiPSCs to CMs we see morphological changes over the days (Figure 4.2, A). Epithelial to mesenchymal transition begins on D2 shown by spiked borders of colonies followed by mass expansion filling empty spaces shown on D4. Cluster of spontaneous contraction are visible on D6 however this becomes more apparent on D15 by the contraction of all cells in a wave and the formation of a more 3D tissue. After dissociation the CMs can be reseeded into a monolayer format, stained with a-Actinin sarcomeric protein clear sarcomere banding can be seen in all CMs within the culture (Figure 4.2, B). We performed RNA sequencing at key timepoints throughout the differentiation to confirm characteristic gene expression changes.

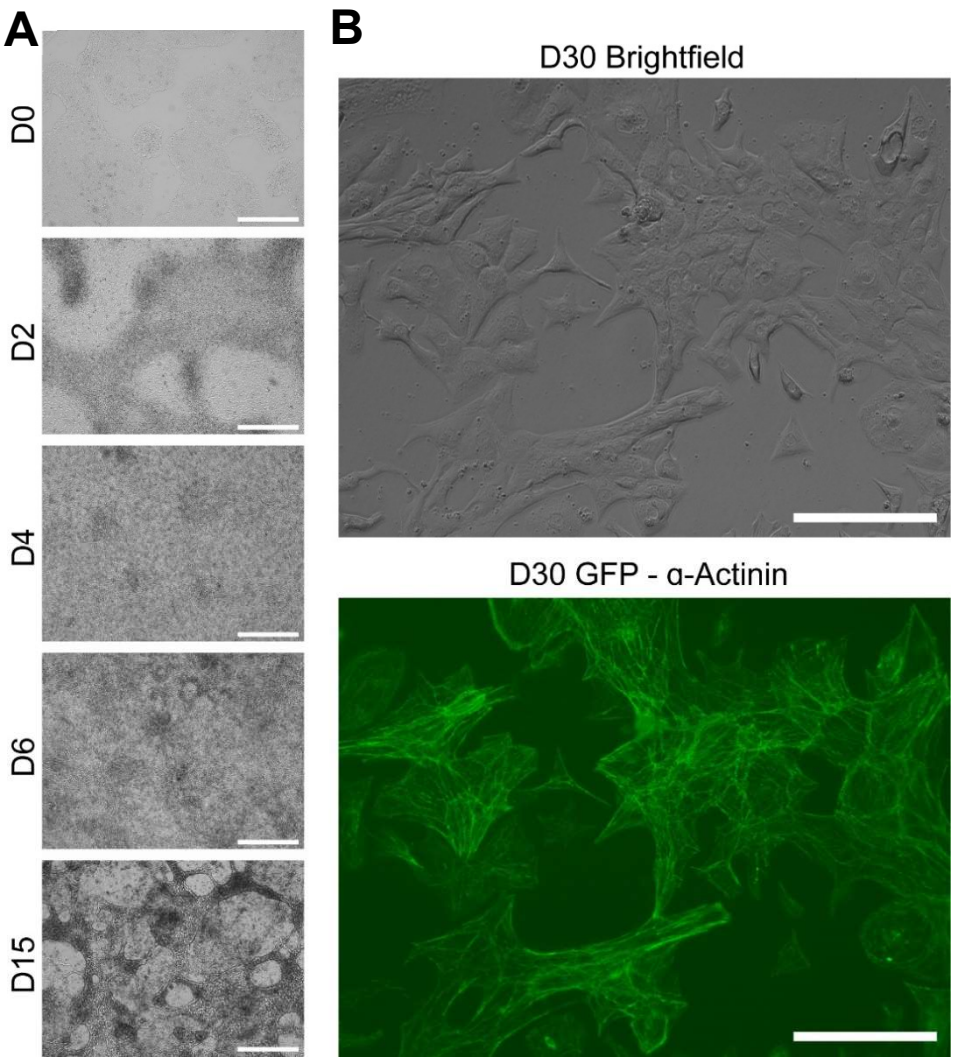


***Figure 4.2 – Generation of hiPSC-derived cardiomyocytes. (A)*** *Initial brightfield images show morphological changes of cells in culture becoming more 3D by D15. D0 to D15 scale bar: 600um. (B) Brightfield and GFP images of D30 cardiomyocytes of high purity α-Actinin+ cells., D30 Brightfield and GFP scale bar: 150um.*

To confirm the statistical cluster changes that occurred over the differentiation I generated a PCA plot created in R studio (Figure 4.3). The plot shows how during differentiation, each timepoint contains a cluster of replicates of similar PCA variance, with the only exception being around day 20 and 30 where clusters are grouped closely. We can then take the confidence in our data forward to look at markers expected to increase during cardiomyocyte development. Subsequent DeSeq2 normalisation of data and fold change comparisons was performed by Tegan Gilmore, bioinformation at the Francis Crick Institute.

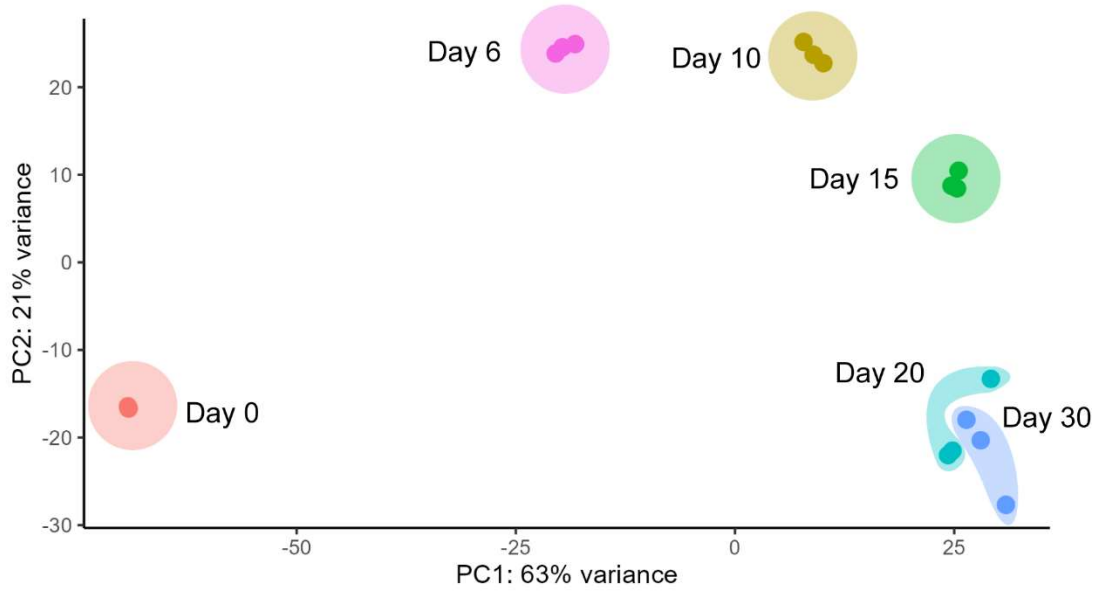


***Figure 4.3 – PCA plot from RNA sequencing.*** *PCA plot of HSPG2$^{WT}$ cardiomyocyte differentiation from RNA sequencing outputs at each timepoint. Timepoint clusters are colour coded, day 0 – red, day 6 – pink, day 10 – yellow, day 15 – green, day 20 – cyan and day 30 – blue.*

To confirm differentiation of hiPSCs I looked at pluripotency markers *NANOG* and *SOX2* through the differentiation (Figure 4.4). *NANOG* gene counts at day 0 (9923.7) drops to only 5.3 at day 6 and then to 0 for the remaining timepoints. *SOX2* follows a similar trend where the gene count at day 0 (6082.0) is drastically reduced to 17 on day 6 and is maintained around this level for the remainder of the differentiation. The results suggest that the differentiation protocol has caused the hiPSCs to rapidly lose pluripotency as would be expected.

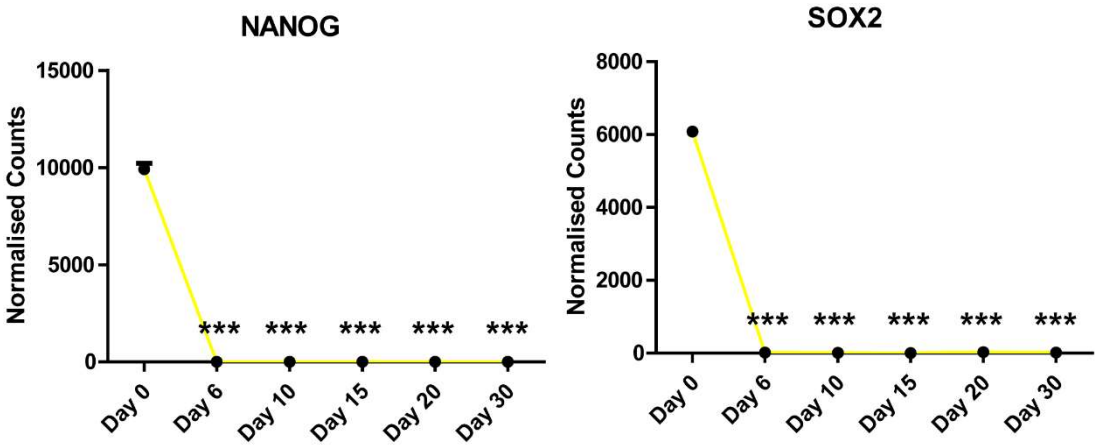

***Figure 4.4 – Panel of pluripotency markers through cardiomyocyte differentiation.*** *DeSeq2 normalisation of RNA sequencing at each timepoint of cardiomyocyte differentiation showing gene counts of pluripotency genes NANOG and SOX2. N=3, statistical test performed on SD using Tukey Test. P-value <0.05 = *, <0.01 = **, <0.001 = ***.*

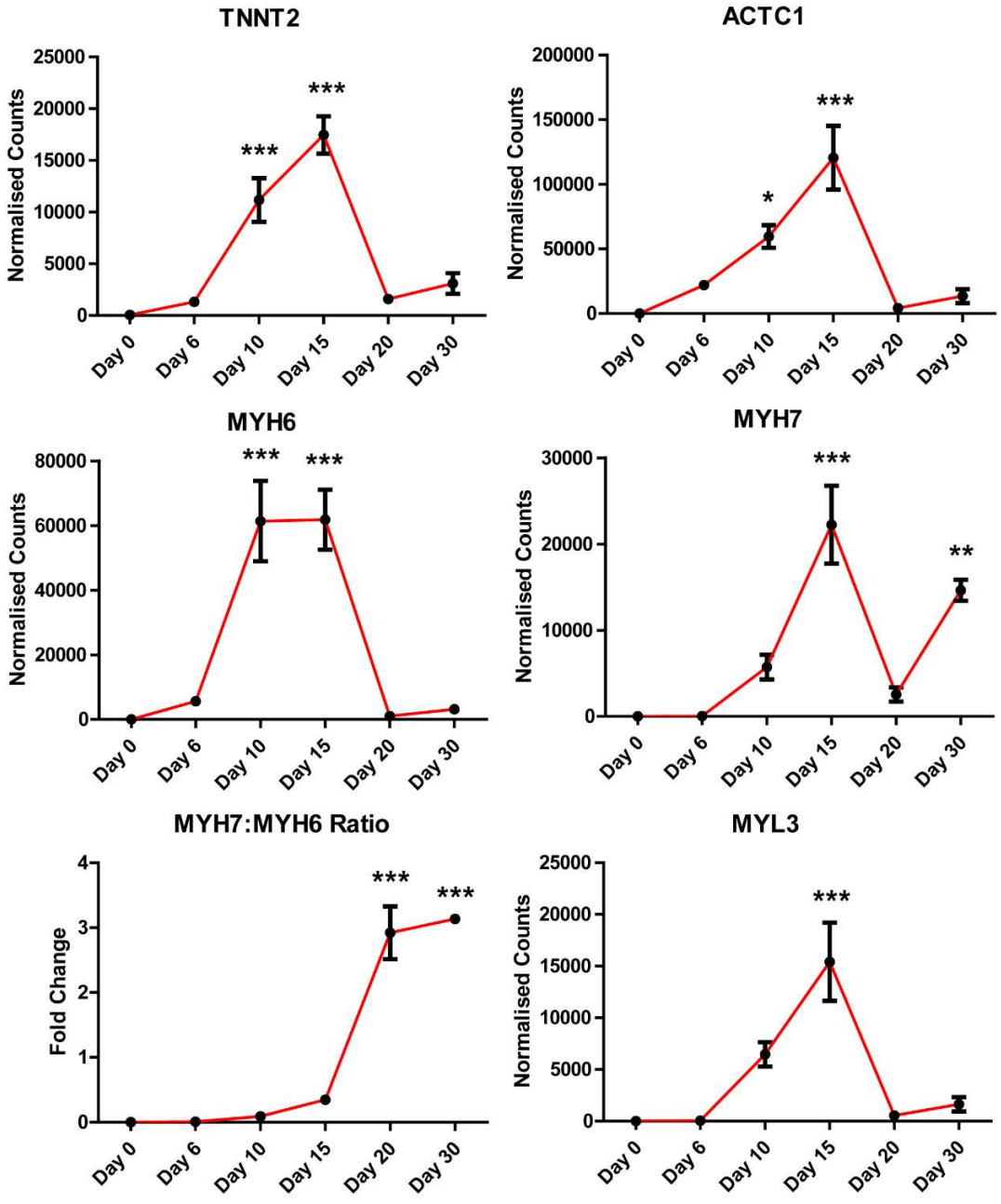


***Figure 4.5 - Structural Cardiomyocyte gene expression changes during hiPSC-CM differentiation.*** *RNA sequencing at each of the timepoint provides gene counts for each targeted gene. Several structural cardiac development genes displayed for normalised count at each timepoint. TTNT2-Cardiac*

*Troponin 2, ACTC1-Cardiac Actin, MYH6-Myosin Heavy Chain 6, MYH7-Myosin Heavy Chain 7 and MYL3-Myosin Light Chain. N=3, statistical test performed on SD using Tukey Test. P-value <0.05 = *, <0.01 = **, <0.001 = ***.*

Following on from pluripotency markers I investigated the expression of cardiac structural markers (Figure 4.5). The results show how hiPSCs and early-stage cardiac differentiation (day 6) don't express structural cardiac markers compared to the later stage CMs. Several structural cardiac genes that change over differentiation show the highest gene count at day 15. This includes *TNNT2* (17460.3), *ACTC1* (120564.3), *MYH6* (61835.3), *MYH7* (22244.3) and *MYL3* (15415), implying at this timepoint development of a structural cardiomyocyte was at its highest priority. All structural cardiac genes appear to be reduced at day 20 and 30 implying some switch has occurred whereby the cell is no longer preferentially expressing these genes to the same extent seen at day 15. Plotting the ratio of *MYH7* over *MYH6* shows a higher expression of *MYH6* compared to *MYH7* at timepoints from day 0 to day 15 (*MYH7*:*MYH6* fold change - day 0: 0, day6: 0.09, day 10: 0.09, day 15: 0.35). Although this pattern alternates to *MYH7* having an overall higher expression than *MYH6* in day 20 (2.92) and day 30 (3.13) of cardiac differentiation.

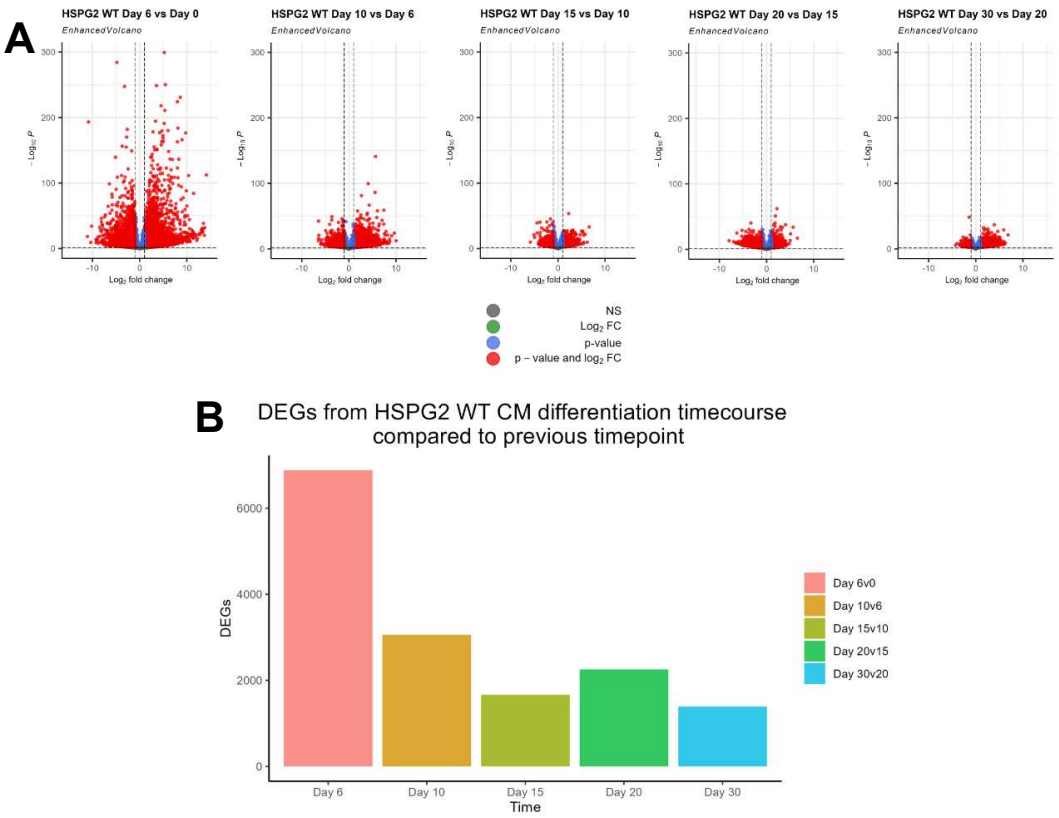


***Figure 4.6 – Enhanced volcano plots of changes seen in WT cells over cardiomyocyte differentiation.*** *(A) R studio script Enhanced volcano plot was used to produce plots highlighting differentially expressed genes in red. Genes that had a less that Log2(1) fold change but were significantly changed (p<0.05) are in blue, while those that expressed higher than Log2(1) but were not significantly (p>0.05) changed are in green. Genes that fit none of the above parameters were designated grey and not significant (NS). (B) Differentially expressed genes (DEGs) were arranged in a bar chart to show changes during cardiomyocyte differentiation.*

To look further in the data, I highlighted the differentially expressed genes (DEGs) found throughout the differentiation (Figure 4.6). To do this I took the data from the CSVs it was provided in and imported into R studio into a data frame. The data was split to only include gene name, p-adjusted value and Log2 fold change. I then performed -Log10 on the p-adjusted columns before rearranging data to be ran through the Enhanced volcano package (Figure 4.6, A). Parameters were designated that for a statistically different change genes must have at least -Log10 p-adjusted value of -1.3, and Log2 fold

change higher than 1 or below -1. Using these same parameters, the total number of DEGs found in each timepoint when compared to the previous was arranged in a bar graph (Figure 4.6, B) highlighting the differences that occurred as cells underwent cardiac differentiation. The DEGs found between day 6 and day 0 were the largest number of genes changes that occurred throughout the cardiomyocyte differentiation (6881 DEGs). This reduced to 3060 DEGs between day 10 and 6, 1666 between day 10 and 15, and 2256 between day 20 and 15. The lowest number of DEGs registered occurred in the final stages of the differentiation between day 20 and 30 (1391). To delve further into the differences seen in cardiac differentiation R package gProfiler2 was used to perform GO Cluster analysis on the DEGs found at each timepoint. The selected clustering profilers chosen were Gene Ontology: Molecular Functions (GO:MF), Gene Ontology: Biological processes (GO:BP), Gene Ontology: Cellular Components (GO:CC), Kyoto Encyclopaedia of Genes and Genomes (KEGG), Reactome (REAC) and WikiPathways (WP). I highlight the pathways found using GO:BP and then further combine all data to produce cluster graphs based on highest number of genes changed inside each pathway term.

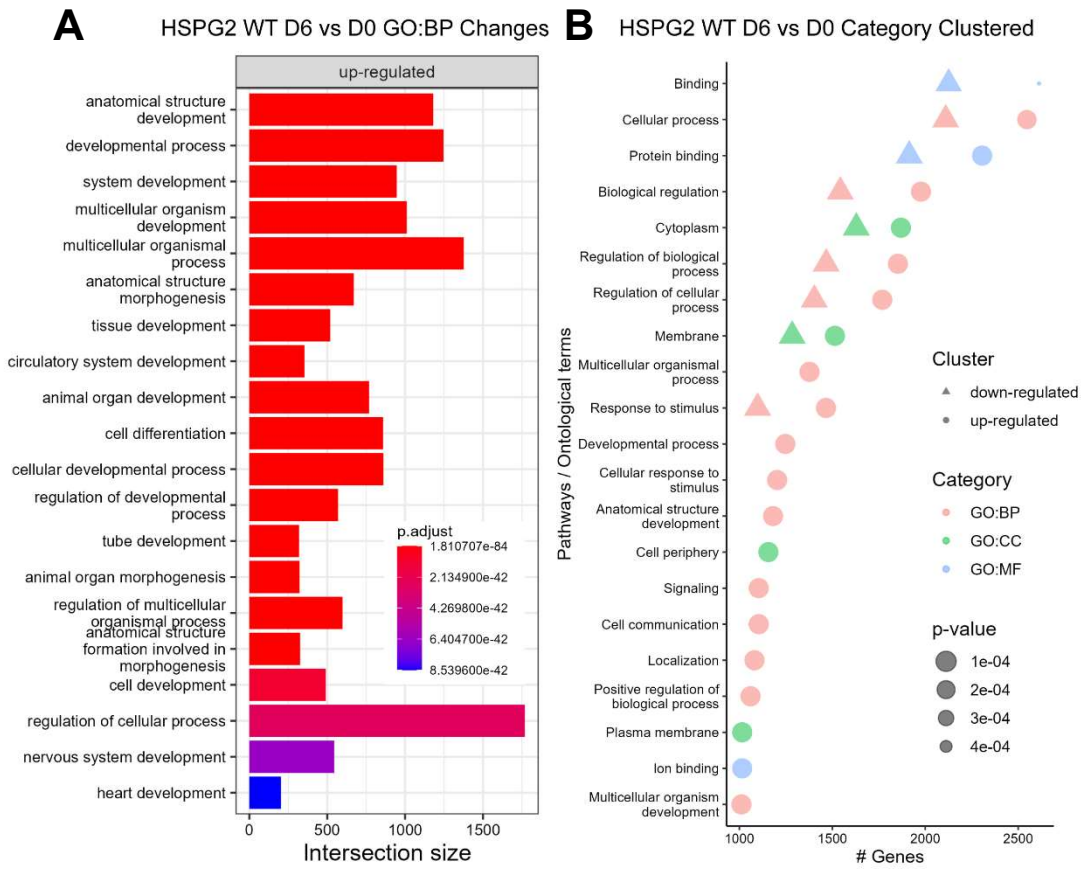


***Figure 4.7 - Day 6 vs Day 0 DEG gene ontology term outputs.*** *(A) The top 25 GO:BP pathways identified based on p-adjusted value were output into a ggPlot2 bar graph. (B) All cluster pathways examined were grouped and ordered based on number of genes changed in each and the highest 30 selected. These were then plotted onto a ggPlot2 dot plot separating out clusters of downregulated (triangle) and upregulated (circle) genes.*

From the 6881 DEGs found between day 6 and 0 GO:BP analysis found that most terms were linked to genes that were upregulated (Figure 4.7, A). The most significant terms found all include some description linking them to development or differentiation. In the more specific development terms GO:BP flagged upregulation of gene involved in heart development, tube development and circulatory system development. These terms align with the process of hiPSC differentiation towards cardiac linages. The only other terms highlighted that aren't linked to development or differentiation are towards morphogenesis. The cluster graph shows there are both upregulated and downregulated genes fitting into the same term implying a shift in cell state

(Figure 4.7, B). Here we don't see any cardiac specific terms, but a large majority of the gene changes are linked to binding, regulation of the cell and signalling or communication.

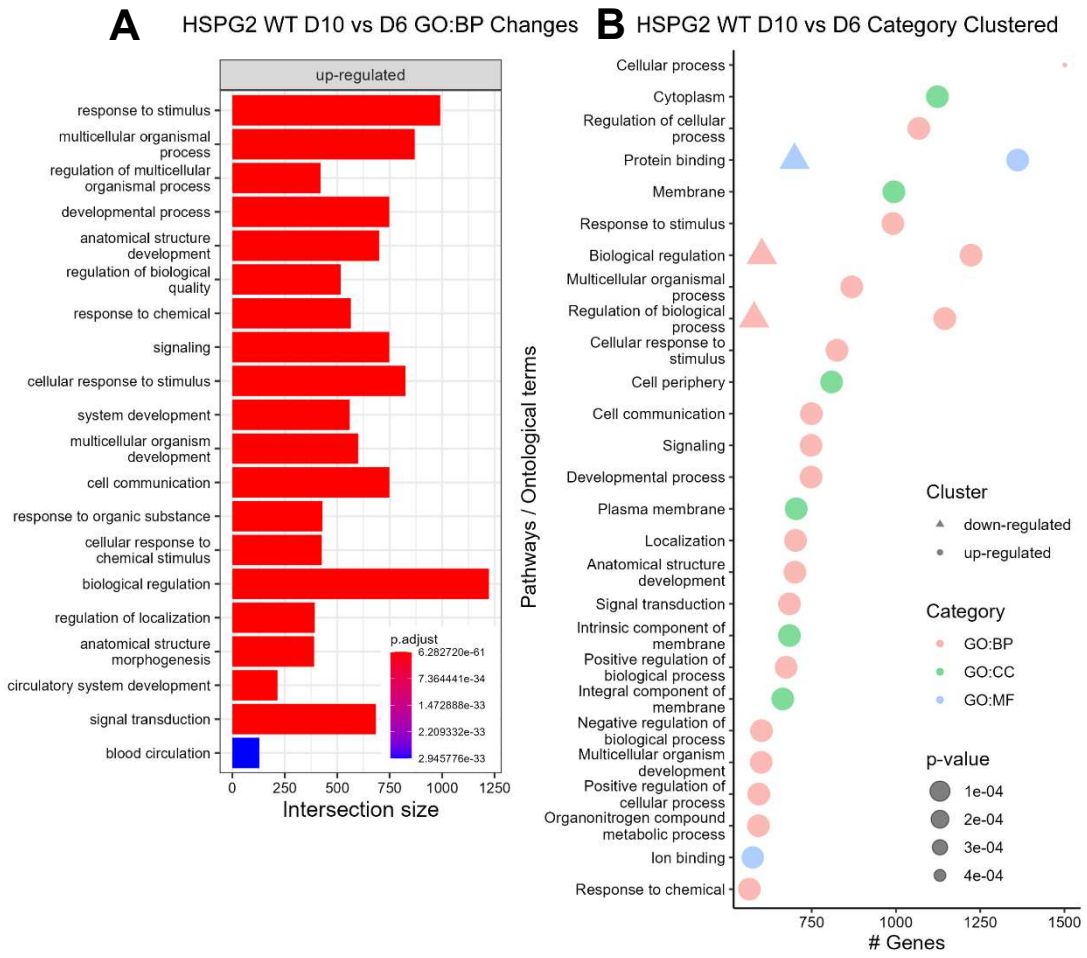


***Figure 4.8 - Day 10 vs Day 6 DEG gene ontology term outputs.*** *(A) The top 25 GO:BP pathways identified based on p-adjusted value were output into a ggPlot2 bar graph. (B) All cluster pathways examined were grouped and ordered based on number of genes changed in each and the highest 30 selected. These were then plotted onto a ggPlot2 dot plot separating out clusters of downregulated (triangle) and upregulated (circle) genes.*

Of the 3060 DEGs found between day 10 and 6 we can see using GO:BP how the majority of terms have shifted to a response to a stimulus and developmental focus (Figure 4.8, A). The developmental terms (circulatory system development, blood circulation, system development) flagged up

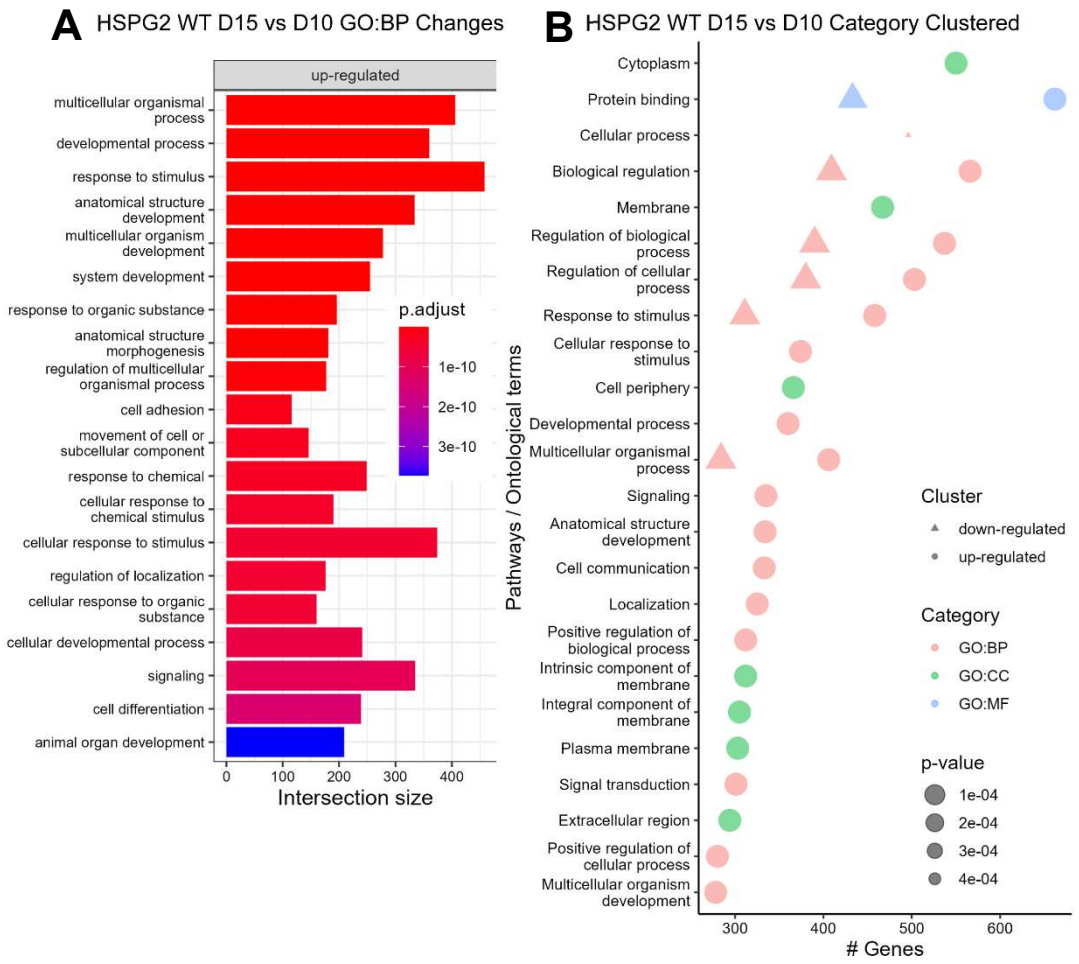


***Figure 4.9 - Day 15 vs Day 10 DEG gene ontology term outputs.*** *(A) The top 25 GO:BP pathways identified based on p-adjusted value were output into a ggPlot2 bar graph. (B) All cluster pathways examined were grouped and ordered based on number of genes changed in each and the highest 30 selected. These were then plotted onto a ggPlot2 dot plot separating out clusters of downregulated (triangle) and upregulated (circle) genes.*

confirm the ongoing differentiation of the cells as they are still under stimulus that would push the cells further down the cardiac lineage. Many of the terms highlighted suggest a shift in signalling genes in response to a stimulus or chemical. When looking at the cluster gene graphs the data suggest an increase of cellular processes and genes affecting cytoplasm are amongst the highest changes during day 10 to day 6 differentiation (Figure 4.8, B). Here we can also see further changes in protein binding genes and further genes involved in regulation of biological processes as there are both clusters of up and down regulated DEGs.

There were only 1666 DEGs found between day 15 and day 10, one of the lowest values. This is during the stage the cardiac differentiation would undergo a change in media to initiate purification of cardiomyocytes. This is confirmed by the increased GO:BP terms linked to development of all umbrella terms (Figure 4.9, A). Some of the highest terms highlighted are due to multicellular processes and development as cells are forming more 3D tissue in the differentiation. The other popular terms are linked to responses to stimulus or organic substances, this could be linked to the response of Lactic Acid used in the purification media. The clustering graph shows similar grouped changes as seen in day 6 to 10, the only major change seen is a large reduction in cellular processes (Figure 4.9, B). In day 6 to 10 there were ~1500 upregulated genes linked to this term, but in day 10 to 15 this shifted to ~500 genes downregulated between these time points.

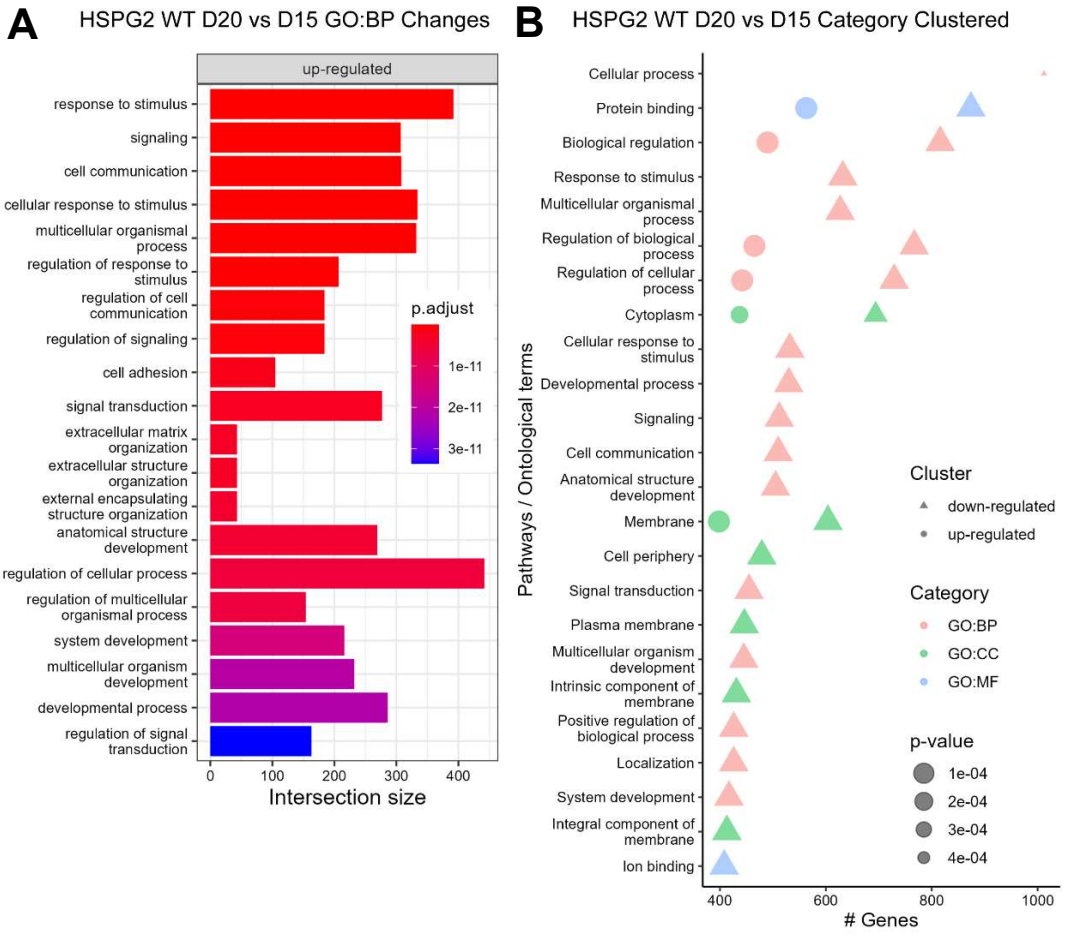

***Figure 4.10 - Day 20 vs Day 15 DEG gene ontology term outputs.*** *(A) The top 25 GO:BP pathways identified based on p-adjusted value were output into a ggPlot2 bar graph. (B) All cluster pathways examined were grouped and ordered based on number of genes changed in each and the highest 30 selected. These were then plotted onto a ggPlot2 dot plot separating out clusters of downregulated (triangle) and upregulated (circle) genes.*

The changes found in day 20 to day 15 interestingly show a difference compared to the other timepoints whereby the majority of the genes were downregulated. The major terms identified using GO:BP here suggested responses and regulation of the cell due to external stresses (Figure 4.10, A). There are still developmental terms highlighted, but the major terms appear to be linked to responses of stimulation and signalling, with a further focus on ECM remodelling. These changes highlighted in the cluster plot (Figure 4.10, B) suggest a halting of many processes that were undergoing in the day 15 cells. This could be linked to the stresses the cells were under post purification, dissociation and disruption of the cells, or a slowing down of the differentiation process.

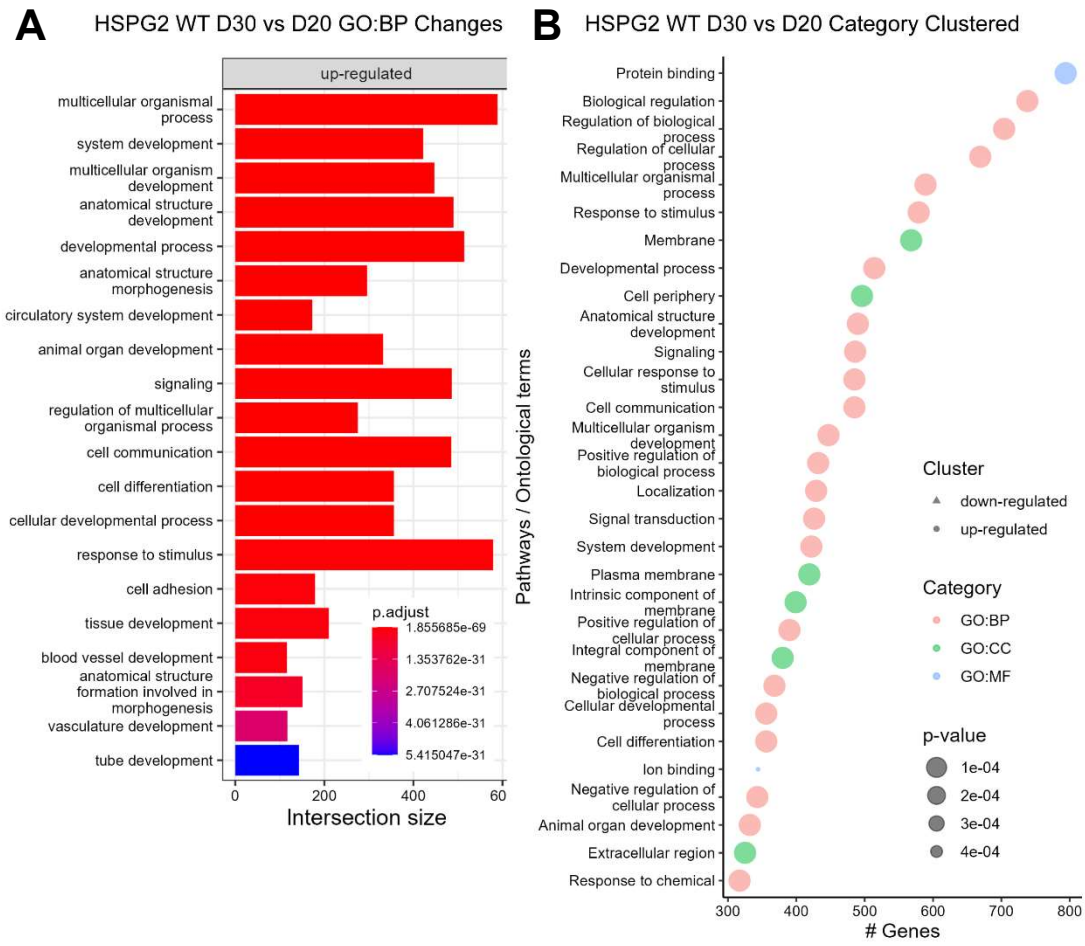


***Figure 4.11 - Day 30 vs Day 20 DEG gene ontology term outputs.*** *(A) The top 25 GO:BP pathways identified based on p-adjusted value were output into a ggPlot2 bar graph. (B) All cluster pathways examined were grouped and ordered based on number of genes changed in each and the highest 30 selected. These were then plotted onto a ggPlot2 dot plot separating out clusters of downregulated (triangle) and upregulated (circle) genes.*

The DEGs highlighted in day 20 to 30 show the opposite effect than seen in the day 15 to 20 genes, the majority are upregulated during this timepoint. Again, the main terms found using GO:BP appear to be developmental processes including tube development, circulatory system development and tissue development (Figure 4.11, A). The cluster graph shows how all the top 30 terms found in all cluster terms analysed were all due to upregulated genes (Figure 4.11, B). These upregulated terms refer to binding of protein, signals, and ions, along with further increases in membranes and developmental

processes. Since GO:BP, GO:CC and GO:MF contained large umbrella terms that would encompass thousands of genes this pathway software would always have terms in the top 30 of cluster graphs. Therefore, to utilise a different pathway analysis software I focused on the top 10 terms highlighted using the REAC output data.

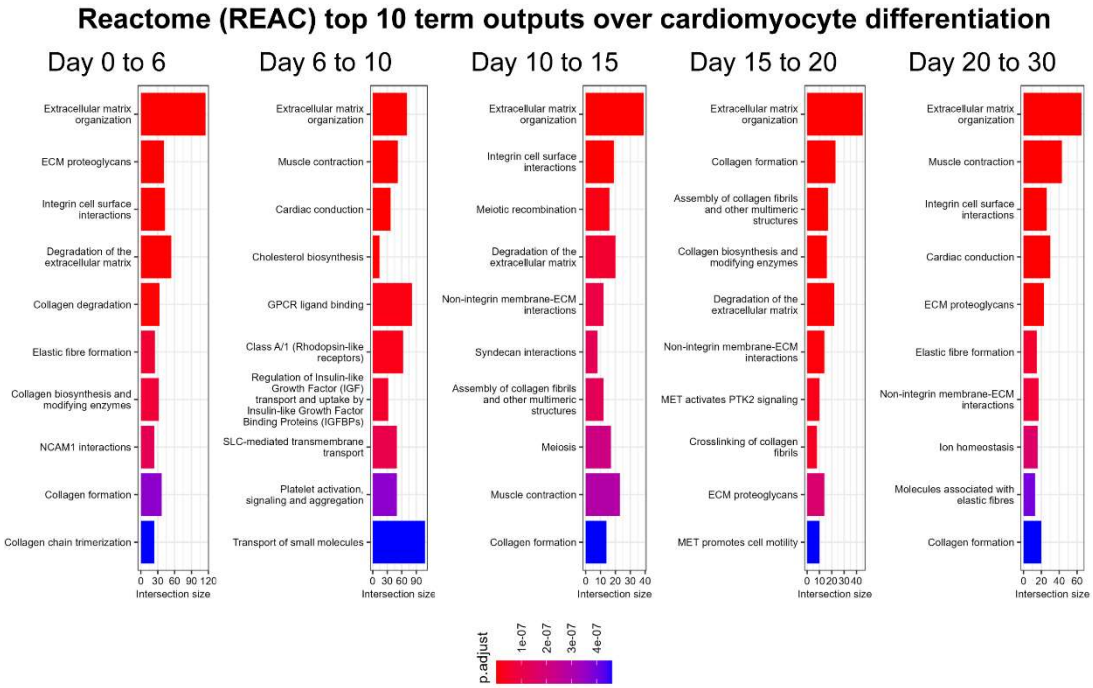


***Figure 4.12 – REAC pathway top 10 terms linked to cardiomyocyte differentiation.*** *The top 10 terms based on p-adjusted value from REAC analysis of each timepoints extracted and plotted into a ggPlot2 bar graph.*

Throughout the differentiation the most significantly affected term at each timepoint discovered by REAC analysis is ECM organisation (Figure 4.12). Other ECM terms highlighted include ECM proteoglycans, degradation of ECM and collagens, formation of Elastic fibres, implying the cells are undergoing ECM remodelling as differentiation occurs. Muscle contraction and cardiac conduction are the 2$^{nd}$ and 3$^{rd}$ term flagged between day 6 and 10 confirming cardiac differentiation was underway, cholesterol biosynthesis and regulation of IGF also suggest cardiac genes. The term muscle contraction reduced over the next timepoints until day 30 where it was returned to 2$^{nd}$. Between day 10 and 15 REAC highlighted terms linking to cell surface integrin, ECM non-integrin and syndecan interactions not seen before this point.

Overall, I show the creation of genotypic CMs, confirmed with characteristic cardiac gene changes throughout the differentiation. Fluorescent imaging of the CMs shows sarcomere banding which are α-actinin positive. RNA sequencing and PCA analysis was performed to determine timepoint accuracy and clustering, each timepoint shows similar clustering and follows a curved trend throughout the differentiation. RNA sequencing confirms the attenuation of pluripotency *NANOG* and *SOX2* markers while cardiac structural markers increase over the differentiation to day 15. Plotting the ratio of MYH7 over MYH6 shows a shift in preferential production of MYH7 over MYH6 over the 30-day protocol. Highlighting of DEGs, showed most of the gene changes occur between day 0 and day 6, with a reduction in DEG number as differentiation continues. Preforming GO and REAC analysis on DEGs found at each timepoint confirms induction of pathways linked to cardiac and muscle contraction. Further to this REAC pathway analysis shows changes in ECM matrix organisation over differentiation implying ECM remodelling is an essential part of CM differentiation.

### 4.3. Expression of *HSPG2* over the course of cardiomyocyte differentiation

I next wanted to analyse the levels of *HSPG2* and other basement membrane HSPGs throughout the course of CM differentiation. To do this I initially looked

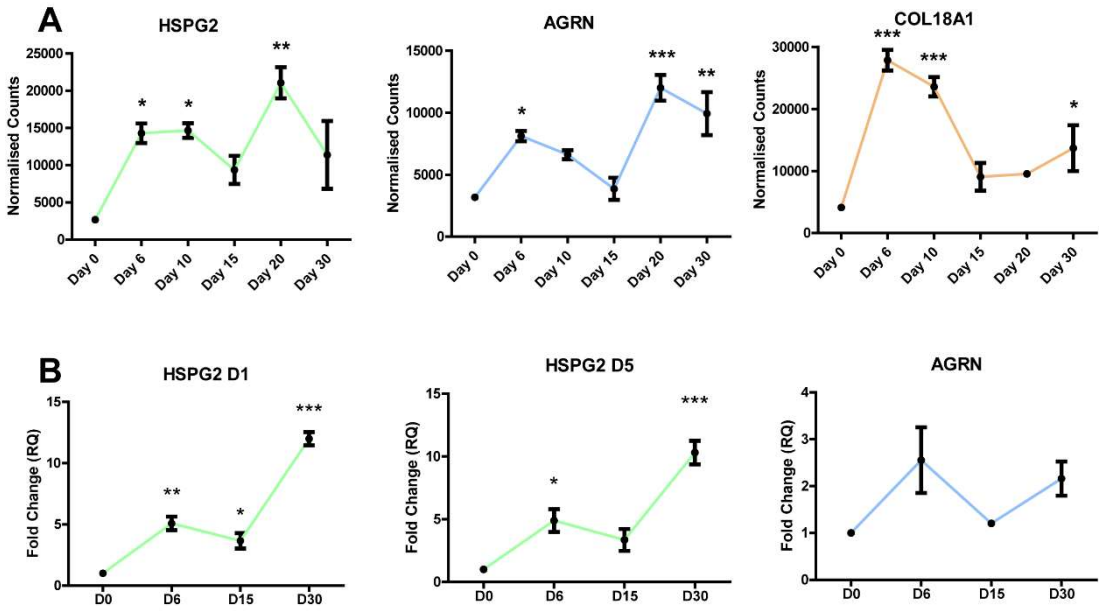

***Figure 4.13 - Basement membrane heparin sulfate proteoglycan gene expression through cardiomyocyte differentiation.*** *(A) HSPG2-Perlecan, AGRN-Agrin and COL18A1-Colagen 18 are displayed as gene counts following deSeq2 normalisation of RNA sequencing analysis. (B) SYBR Green qRT-PCR performed on separate n=3 CM differentiation with primers targeting HSPG2 domain 1 (D1) and 5 (D5), and AGRN. N=3, statistical test performed on SD using Tukey Test. P-value <0.05 = *, <0.01 = **, <0.001 = ***.*

at the RNA sequencing data and confirmed changes using qRT-PCR with custom SYBR green primers.

RNA sequencing confirms of the three-basement membrane HSPGs, *COL18A1* has the highest gene count in hiPSCs (4120.3) followed by *AGRN* (3185.0) and then *HSPG2* (2671.0) (Figure 4.13, A). There is a statistical increase in all three HSPGs (*HSPG2, AGRN* and *COL18A1) gene* counts as hiPSCs differentiation to CMs at day 6 (*HSPG2*: 14295.0, *AGRN*: 8117.3, *COL18A1*: 27873.7). *HSPG2* shows further statistical increased gene counts at day 10 and day 20 of CM differentiation (day 10: 14666.7, day 20: 21079.0) although due to variation in samples day 30 is not statistically increased. To confirm the RNA sequencing results qRT-PCR was performed on a separate CM differentiation timeline. Contrary to the RNA sequencing, a statistical increase in *HSPG2* expression is recorded at day 30 of CM differentiation (Figure 4.13, B). *AGRN* follows a similar trend of expression compared to *HSPG2,* with an increase around day 6 and 10, followed by a reduction at day 15 then an increase at day 20 and 30. qRT-PCR performed investigating *AGRN* expression shows the same trend as RNA sequencing, although the fold change shows no statistically significant difference at any timepoint compared to day 0 expression. *COL18A1* appears to only be highly expressed in the early timepoints over the course of CM differentiation (day 6: 27873.7, day 10: 23587.0), showing no statical changes at day 15 and day 20 and a slight increase at day 30 (13689). This steady increase in gene expression of *HSPG2* and *AGRN* further suggests their importance in the developing cardiomyocyte. I next wanted to investigate how the changes seen in *HSPG2*

and *AGRN* gene expression over the course of CM differentiation translate to protein changes.

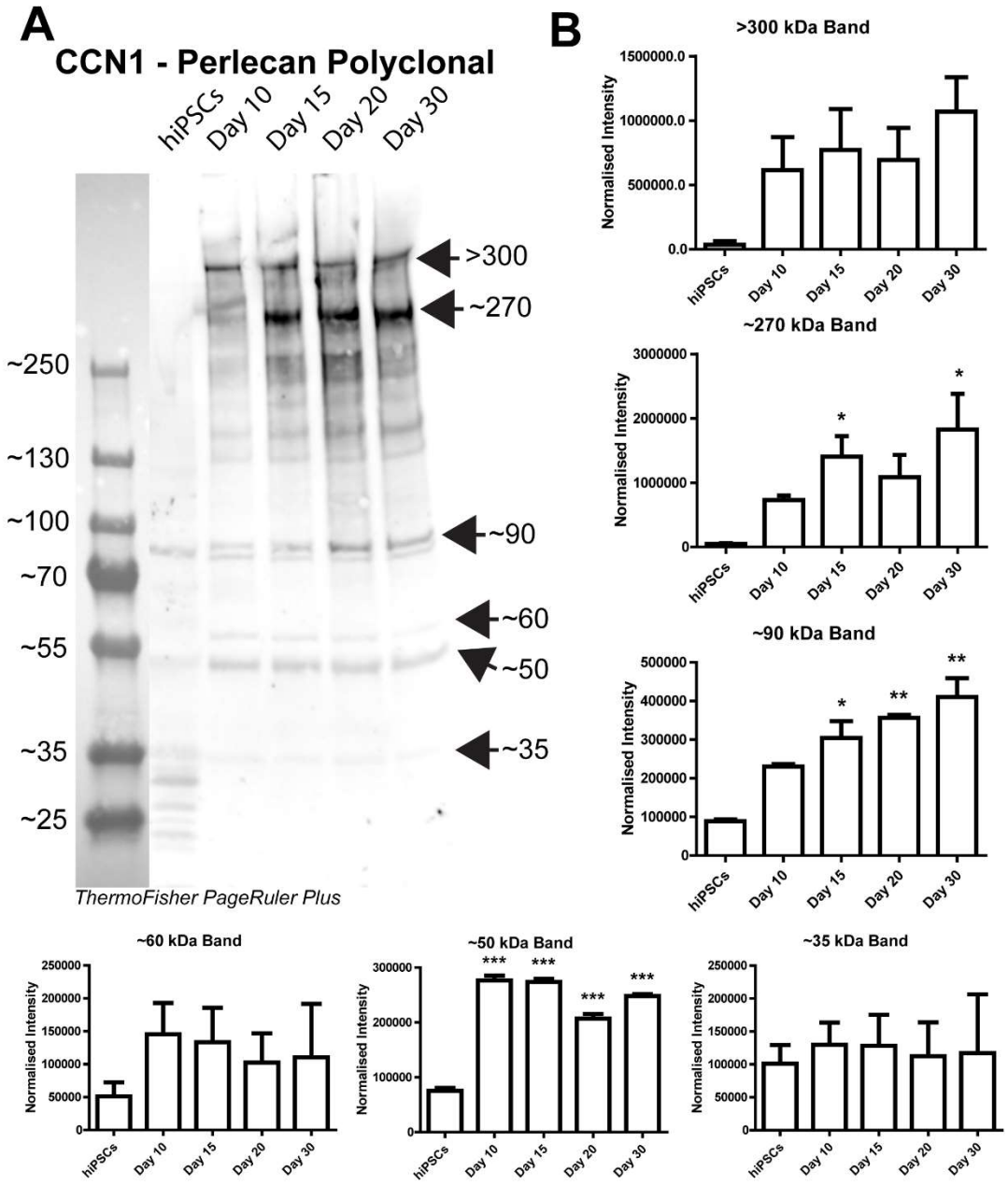


***Figure 4.14 - CCN1 western of cardiomyocyte differentiation.*** *(A) Western blot using a perlecan polyclonal antibody (CCN1) of cell lysate at D0, 10, 15, 20 and 30 of CM differentiation. (B) Band quantification at approximate sizes quantified against total protein stain (See methods 2.7.4). N=2, statistical test performed on SD using Tukey Test. P-value <0.05 = *, <0.01 = **, <0.001 = ***.*

A custom polyclonal antibody for perlecan (CCN1) was obtained from collaborators at UNSW (MoonSun Jung et al., 2013).Initially performing a western blot on differentiation cell lysate show a steady increase of perlecan expression from hiPSCs to day 30 cardiomyocytes (Figure 4.14, A). Six bands were selected for quantification based off their clarity and compared against total protein stain for quantification (Figure 4.14, B). The largest change in perlecan expression seen was in the ~300 kDa band where it isn't expressed in hiPSCs but is expressed in day 10 cells showing slow increase from day 10 to day 30. Similar to the ~300 kDa band, the ~270 kDa band is not found in hiPSCs but shows a steady increase through the differentiation. The band at ~90 kDa appears as a single band in hiPSCs but shows two separate bands through the differentiation, these also show a steady increase throughout the differentiation. Interestingly the ~60 kDa band shows an increase in day 10 cells compared to hiPSCs followed by a reduction over the remaining differentiation. The band seen at ~50 kDa follows a similar trend as seen in the >300 band, showing a sharp increase from hiPSCs to day 10 followed by a plateau. Although, due to this western blot only being an N of 2 only the trends can be hypothesised. To further validate some of the changes seen in this polyclonal western I aimed to repeat the westerns using commercially available monoclonal perlecan antibodies, specific to the domain 5 (A74) and domain 1 (A76) of perlecan.

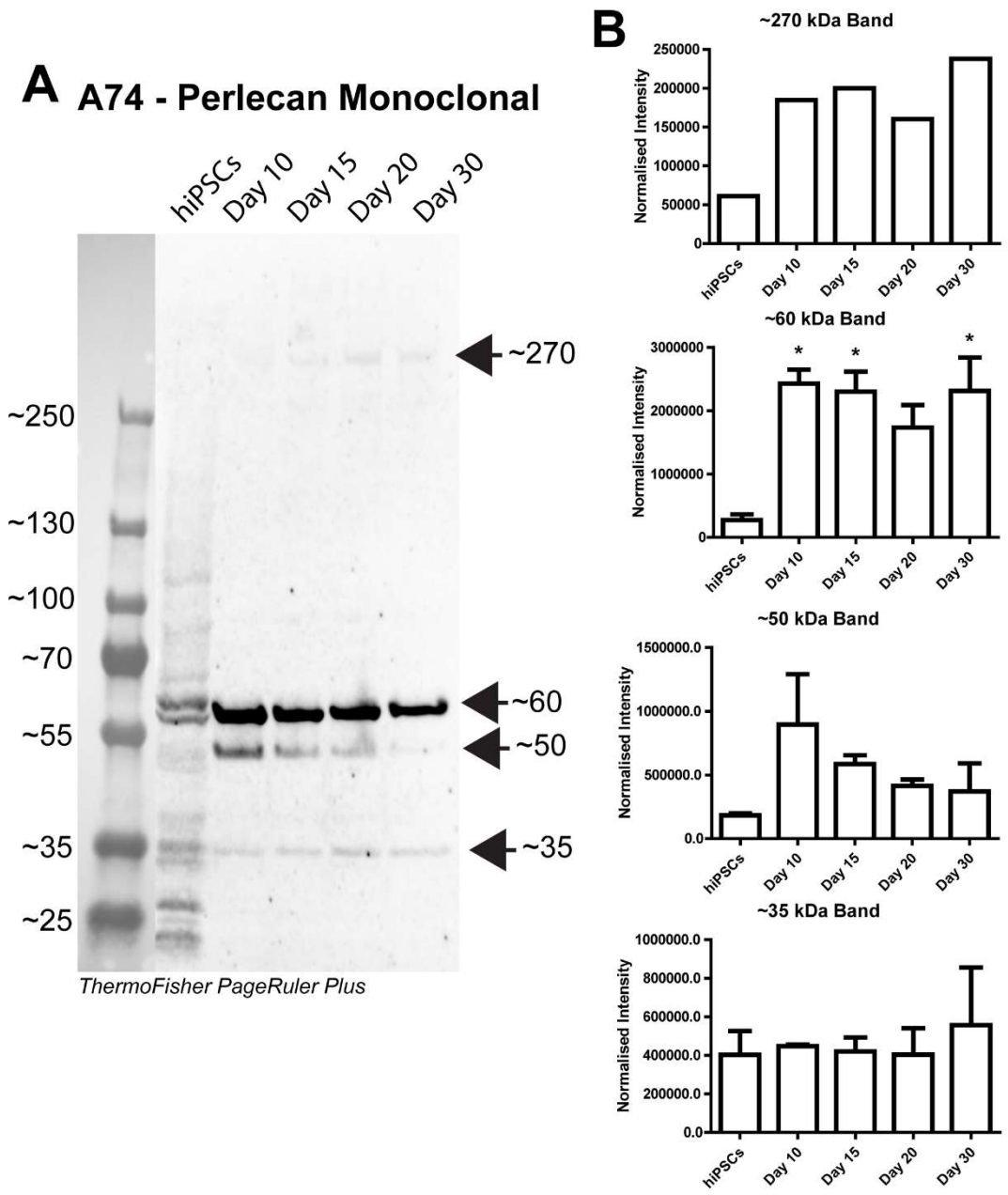


***Figure 4.15 - A74 western of cardiomyocyte differentiation.*** *(A) Western blot using a perlecan monoclonal antibody (A74) of cell lysate at D0, 10, 15, 20 and 30 of CM differentiation. (B) Band quantification at approximate sizes quantified against total protein stain (See methods 2.7.4). N=2, statistical test performed on SD using Tukey Test. P-value <0.05 = *, <0.01 = **, <0.001 = ***.*

Using the monoclonal antibody A74 several bands found using CCN1 can also be seen here (Figure 4.15, A). The A74 western shows a faint band around 270 kDa and several clean bands at 60, 50 and 35 kDa in differentiating cells. Although this antibody seems to be unable to show the bands around 300 and

bands between 270 to 90 kDa shown in CCN1 western blot. The western blot using A74 also shows no smearing compared to the CCN1 western. Analysing the 270 and 60 kDa bands found during cardiomyocyte differentiation show how there is an increase in perlecan expression from hiPSCs (Figure 4.15, B). Interestingly the band at ~50 kDa shows a sharp increase between hiPSCs and day 10 cardiomyocytes, this then shows a steady reduction during the remaining differentiation. These results are the opposite to what was seen with most other perlecan bands and opposite to the CCN1 band quantification. The band around 35 kDa shows no major changes throughout the differentiation similar to the ~35 kDa band found in the CCN1 western blot. This western blot only being an N of 2 implied the trends can be hypothesised but not taken for granted. The increase of the ~60 kDa band over the differentiation is the only statically significant change identified. The band at ~270 kDa was only identified in one of the two western blots therefore, there is an element of either technical error or sample difference between the two western blots performed.

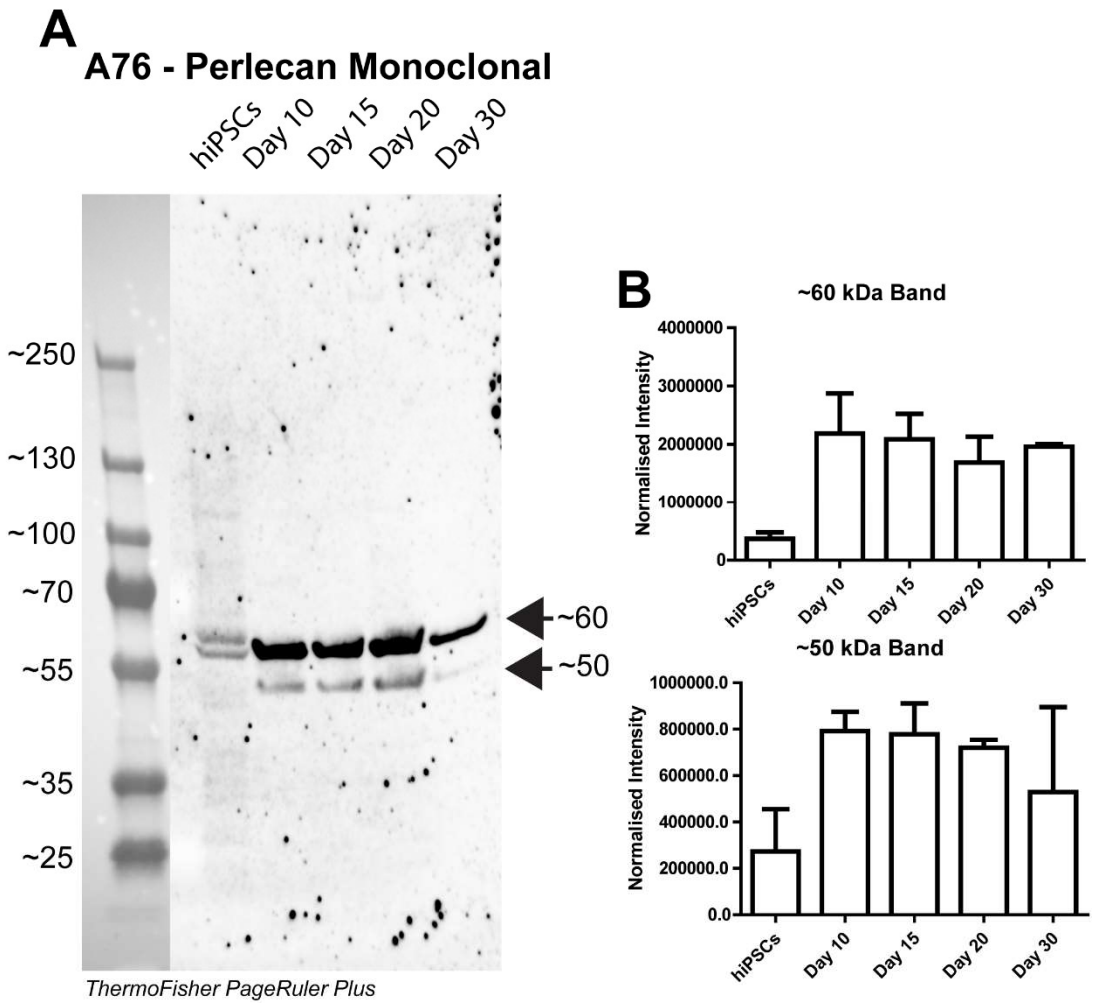


***Figure 4.16 - A76 western of cardiomyocyte differentiation.*** *(A) Western blot using a perlecan monoclonal antibody (A76) of cell lysate at D0, 10, 15, 20 and 30 of CM differentiation. (B) Band quantification at approximate sizes quantified against total protein stain (See methods 2.7.4). N=2, statistical test performed on SD using Tukey Test. P-value <0.05 = *, <0.01 = **, <0.001 = ****

Using monoclonal antibody A76 for at timepoints during the CM differentiation, western blots show only two bands are clearly found in the cardiac cells, ~60 and ~50 kDa (Figure 4.16, A). These represent the same pair of bands seen in both the CCN1 and A74 antibody. The only main difference is the lack of a band that was seen around 270 kDa and 35 kDa, although this could be due to the intensity of the 60/50 kDa band pair. Analysing the ~60 and 50 kDa bands show a similar expression level is seen compared to the A74 western (Figure 4.16, B). The ~60 kDa band in hiPSCs is initially lowly expressed followed by a 5-fold increase in day 10 cells, the early differentiation shows a

slow decrease over differentiation following this spike. The ~50 kDa band appears to only be present between days 10 and 20 of the differentiation before expression is reduced in day 30, although these increases are not statistically significant since this is only a N of 2. Both A74 and A76 show a double band around ~60 kDa in hiPSCs which is not seen in the differentiated cells, although this is not repeated in CCN1.

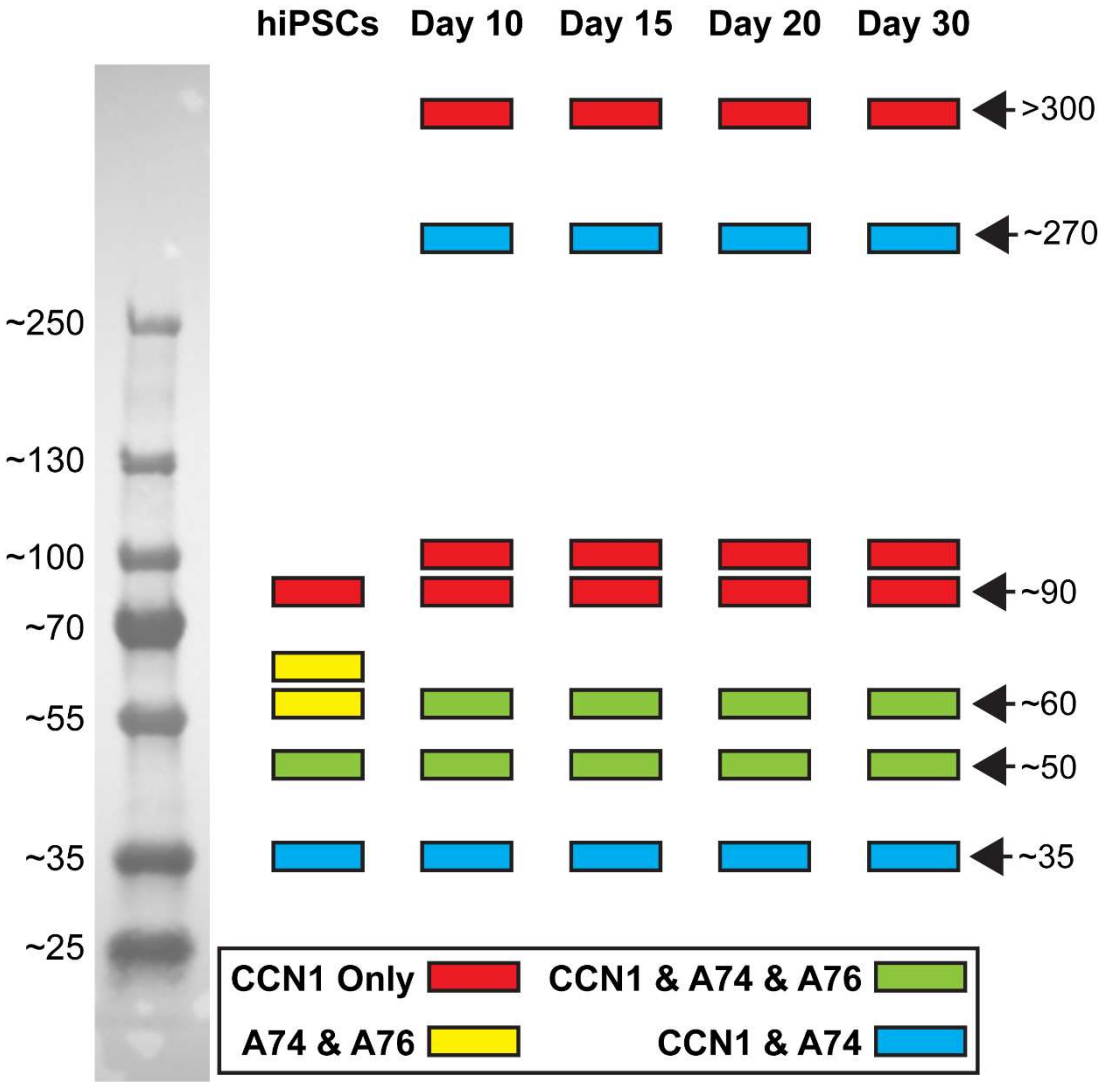


***Figure 4.17 – Summary of bands found in perlecan western blots.*** *Highlighted bands of CCN1, A74 and A76 western blots plotted as a colour coded summary. CCN1 only (red), A74 & A76 (yellow), CCN1 & A74 (blue) and all antibodies (green).*

A summary figure of bands found in perlecan westerns was created to further analyse differences in antibody binding (Figure 4.17). CCN1 the perlecan

polyclonal antibody, in the only antibody to show bands at >300 and ~90 kDa. Although interestingly the only bands this polyclonal antibody doesn't pick up are the pair found in hiPSCs ~60 kDa, while A74 and A76 do. A74 and CCN1 are able to highlight a band around ~270 and 35 kDa while A76 doesn't, either due to low intensity or perhaps the binding site for A76 is not present in these fragments. As previously discussed, another HSPG that is known to be involved in cardiac development is agrin. I next performed western blot analysis to see how agrin protein expression changed over cardiac differentiation.

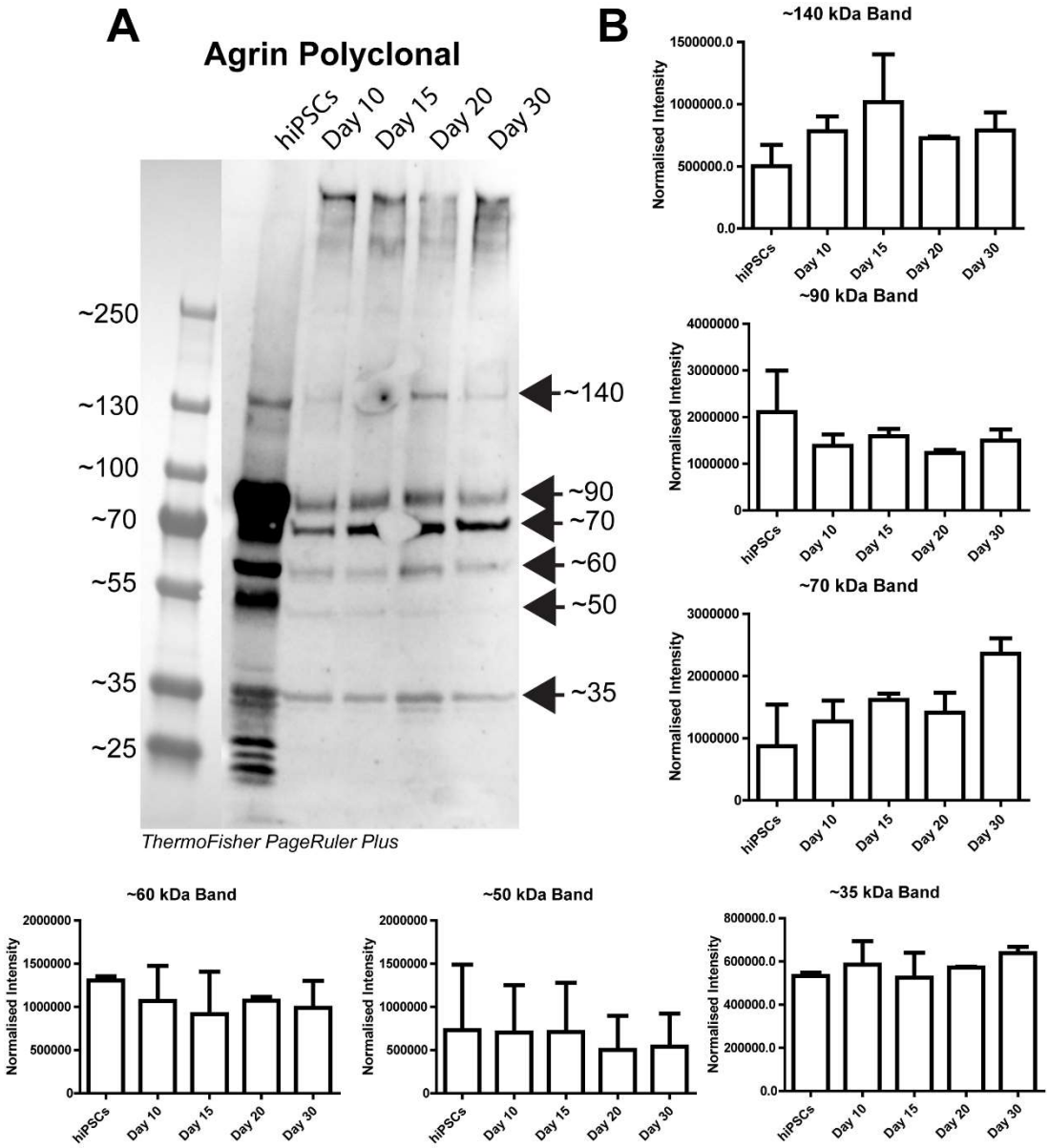


***Figure 4.18 - Agrin western of cardiomyocyte differentiation.*** *(A) Western blot using an agrin monoclonal antibody of cell lysate at D0, 10, 15, 20 and 30 of CM differentiation. (B) Band quantification at approximate sizes quantified against total protein stain (See methods 2.7.4). N=2, statistical test performed on SD using Tukey Test. P-value <0.05 = *, <0.01 = **, <0.001 = ***.*

The western blot for agrin over differentiation shows multiple sized bands in hiPSCs similar to perlecan and only a few clear bands during cardiac differentiation (Figure 4.18, A). Quantifying the larger bands seen around 140, 90 and 70 kDa show how agrin expression is already at a relatively high level in hiPSCs (Figure 4.18, B). In the 140 kDa band expressions shows a slight

increase to day 15 followed by a reduction, although this spike could be due to the spot of higher exposure seen on the blot. Both bands around 90 and 70 kDa show similar protein levels throughout the cardiomyocyte differentiation after normalisation to total protein stain, confirming the levels of agrin do not follow those seen in perlecan. Several bands are seen to be similar sizes as bands found in the perlecan westers, these include ~60, 50 and 35 kDa bands. Quantifying these bands, the same trend in agrin protein levels is recorded throughout the differentiation. The protein levels of agrin ~60 and 50 kDa bands are different to the expression seen in the perlecan ~60 and 50 kDa bands. But the plateau of expression seen in the ~35 kDa band is repeated in the perlecan A74 antibody potentially indicating some cross reactivity. Indeed, this western blot was only an N of 2, no statistical difference was recorded between any of the bands over the differentiation. These results further confirm the presence of agrin is consistent over cardiac differentiation.

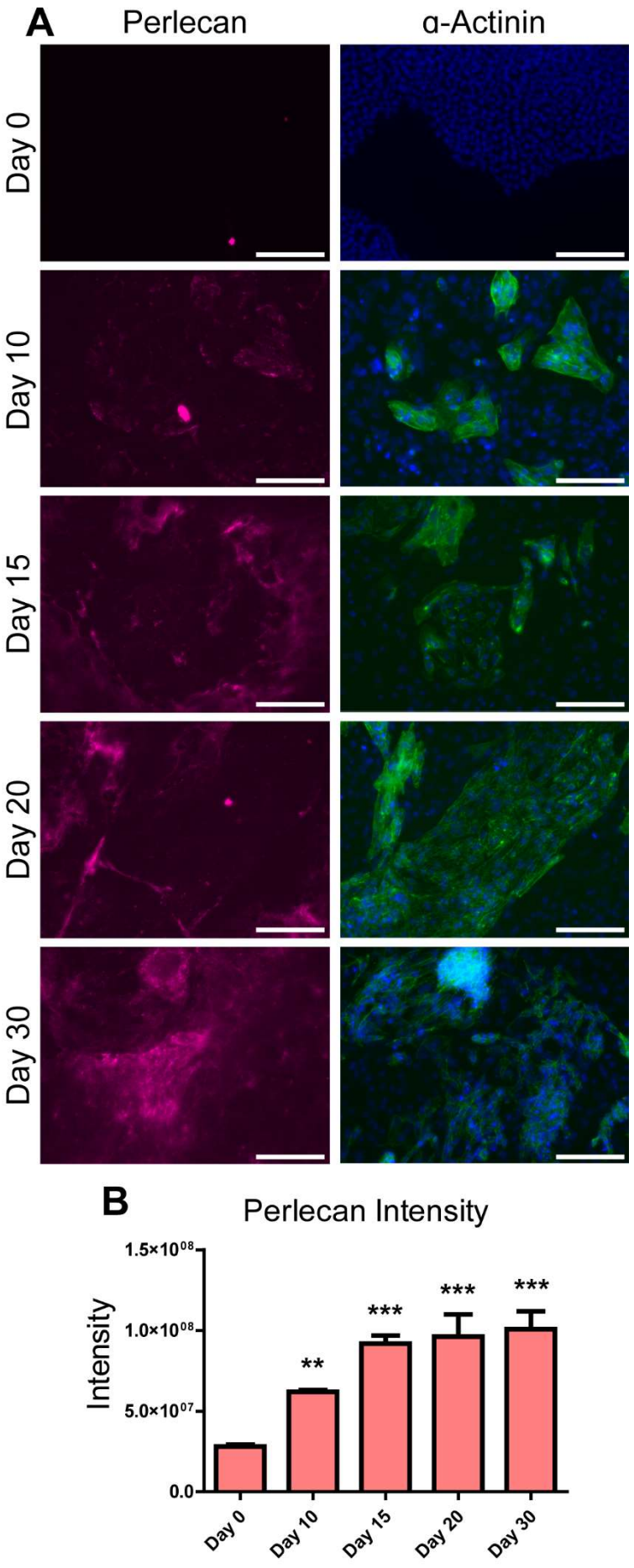
A
Perlecan
α-Actinin
Day 0
Day 10
Day 15
Day 20
Day 30
B
Perlecan Intensity
Intensity
1.5×10^08
1.0×10^08
5.0×10^07
0.0
**
***
***
***
Day 0
Day 10
Day 15
Day 20
Day 30

***Figure 4.19 – Immunostaining of perlecan over CM differentiation.*** *(A) Representative fluorescent images of perlecan monoclonal antibodies A74 and A76 at each timepoints of CM differentiation pseudo-coloured purple. GFP and DAPI channels showing cardiac a-Actinin (green) and nuclei (blue). (B) Perlecan intensity based on fluorescent intensity at each timepoint. Scale bar: 150 µm. N=3, statistical test performed on SD using Tukey Test. P-value <0.05 = *, <0.01 = **, <0.001 = ***.*

To further quantify the increase of perlecan through CM differentiation seen in westerns I performed immunostaining using a combination of A74 and A76 monoclonal antibodies at each timepoint (Figure 4.19, A). Perlecan secretion cannot be seen in hiPSCs, and only fainty visible at day 10, this secretion gains fluorescent intensity as the differentiation is continued quantified using intensity against background (Figure 4.19, B). At day 10 there is a significant increase of perlecan intensity compared to hiPSC, followed by a further increase of perlecan over the differentiation. GFP tagged α-Actinin sarcomeres are not seen in hiPSCs but are found at day 10 implying cardiac induction has occurred. Over the following days clusters of α-Actinin positive CMs are seen to increase in size and confluency as the differentiation progresses.

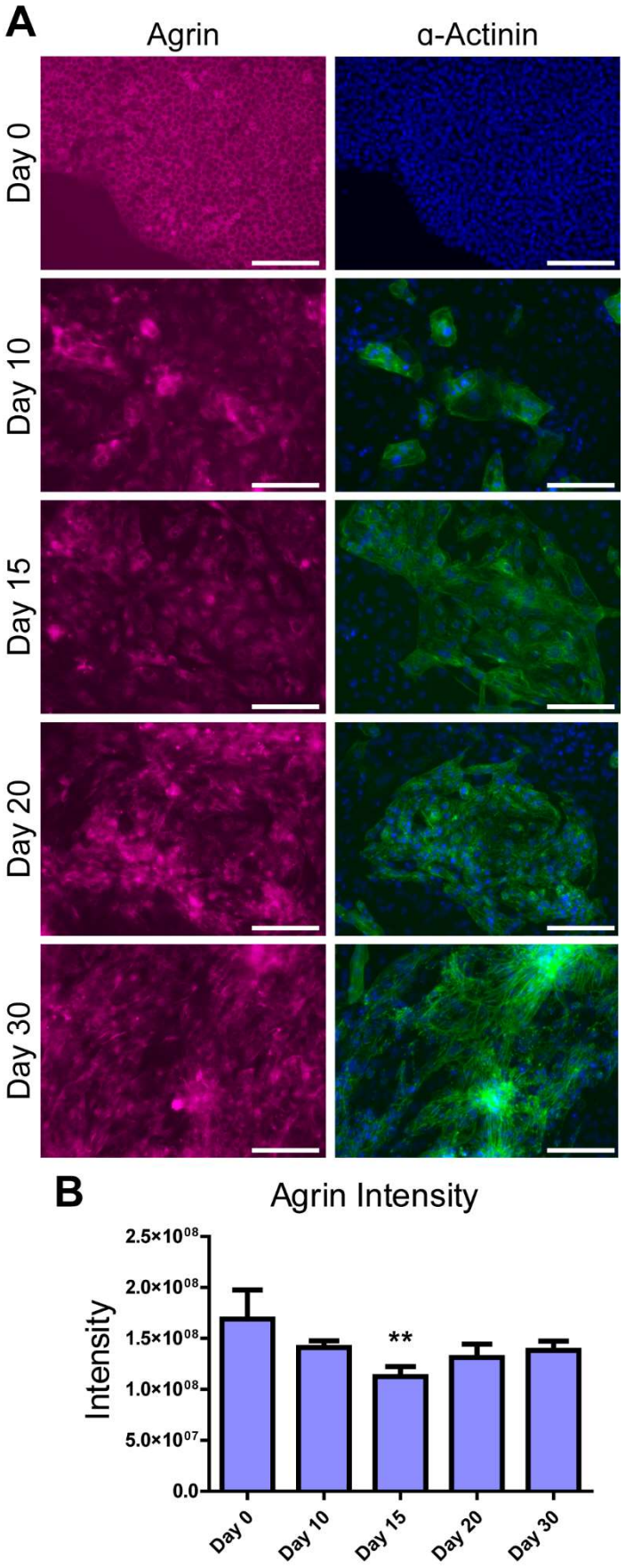
A
Agrin
α-Actinin
Day 0
Day 10
Day 15
Day 20
Day 30
B
Agrin Intensity
Intensity
2.5×10^08
2.0×10^08
1.5×10^08
1.0×10^08
5.0×10^07
0.0
**
Day 0
Day 10
Day 15
Day 20
Day 30

***Figure 4.20 – Immunostaining of agrin over CM differentiation.*** *(A) Representative fluorescent images of agrin polyclonal antibody at each timepoints of CM differentiation pseudo-coloured purple. GFP and DAPI channels showing cardiac a-Actinin (green) and nuclei (blue). (B) Agrin intensity based on fluorescent intensity at each timepoint. Scale bar: 150 µm. N=3, statistical test performed on SD using Tukey Test. P-value <0.05 = *, <0.01 = **, <0.001 = ***.*

Immunostaining over the course of CM differentiation timepoints was also performed using agrin polyclonal antibody (Figure 4.20, A). Agrin appears around all cells from hiPSCs throughout the CM differentiation, quantifying this intensity over the time course shows only a slight reduction at day 15, similar to what was recorded in RNA sequencing and qRT-PCR (Figure 4.20, B). Overall, the expression of agrin is maintained throughout the CM differentiation in both mRNA and protein quantified by both western blots and immunostaining.

As perlecan western blots had showed banding of multiple sizes, I next used RNA sequencing outputs to investigate differences in *HSPG2* transcripts. According to the ensemble database there are 15 different transcripts of *HSPG2* (Table 4.15) and these were investigated in our RNA sequencing data set.

***Table 4.15 – List of all HSPG2 transcripts based off ensembl.org database.***

| Transcript ID | Name | Bp | Protein | Biotype |
|---|---|---|---|---|
| ENST00000374695.8 | HSPG2-203 | 14341 | 4391aa | Protein coding |
| ENST00000635682.1 | HSPG2-214 | 921 | 307aa | Protein coding |
| ENST00000374673.4 | HSPG2-201 | 865 | 288aa | Protein coding |
| ENST00000644714.1 | HSPG2-215 | 708 | 236aa | Protein coding |
| ENST00000374676.4 | HSPG2-202 | 411 | 109aa | Protein coding |
| ENST00000427897.1 | HSPG2-205 | 589 | 197aa | Non-stop decay |

| | | | | |
|---|---|---|---|---|
| ENST00000412328.5 | HSPG2-204 | 828 | No protein | Protein coding CDS not defined |
| ENST00000486901.1 | HSPG2-211 | 3586 | No protein | Retained intron |
| ENST00000471322.2 | HSPG2-208 | 1602 | No protein | Retained intron |
| ENST00000481644.1 | HSPG2-210 | 839 | No protein | Retained intron |
| ENST00000439717.2 | HSPG2-206 | 637 | No protein | Retained intron |
| ENST00000453796.1 | HSPG2-207 | 621 | No protein | Retained intron |
| ENST00000493940.2 | HSPG2-212 | 584 | No protein | Retained intron |
| ENST00000480900.1 | HSPG2-209 | 500 | No protein | Retained intron |
| ENST00000498495.1 | HSPG2-213 | 488 | No protein | Retained intron |

The count of each transcript was calculated at each timepoint of the CM differentiation. Any transcripts that reached above double digit (10+) counts at any timepoint along the differentiation were included for further analysis, other transcripts were considered background. The +10 transcripts were created in Snapgene to calculate their protein coding regions and estimated protein structure based on the perlecan protein (Figure 4.21).

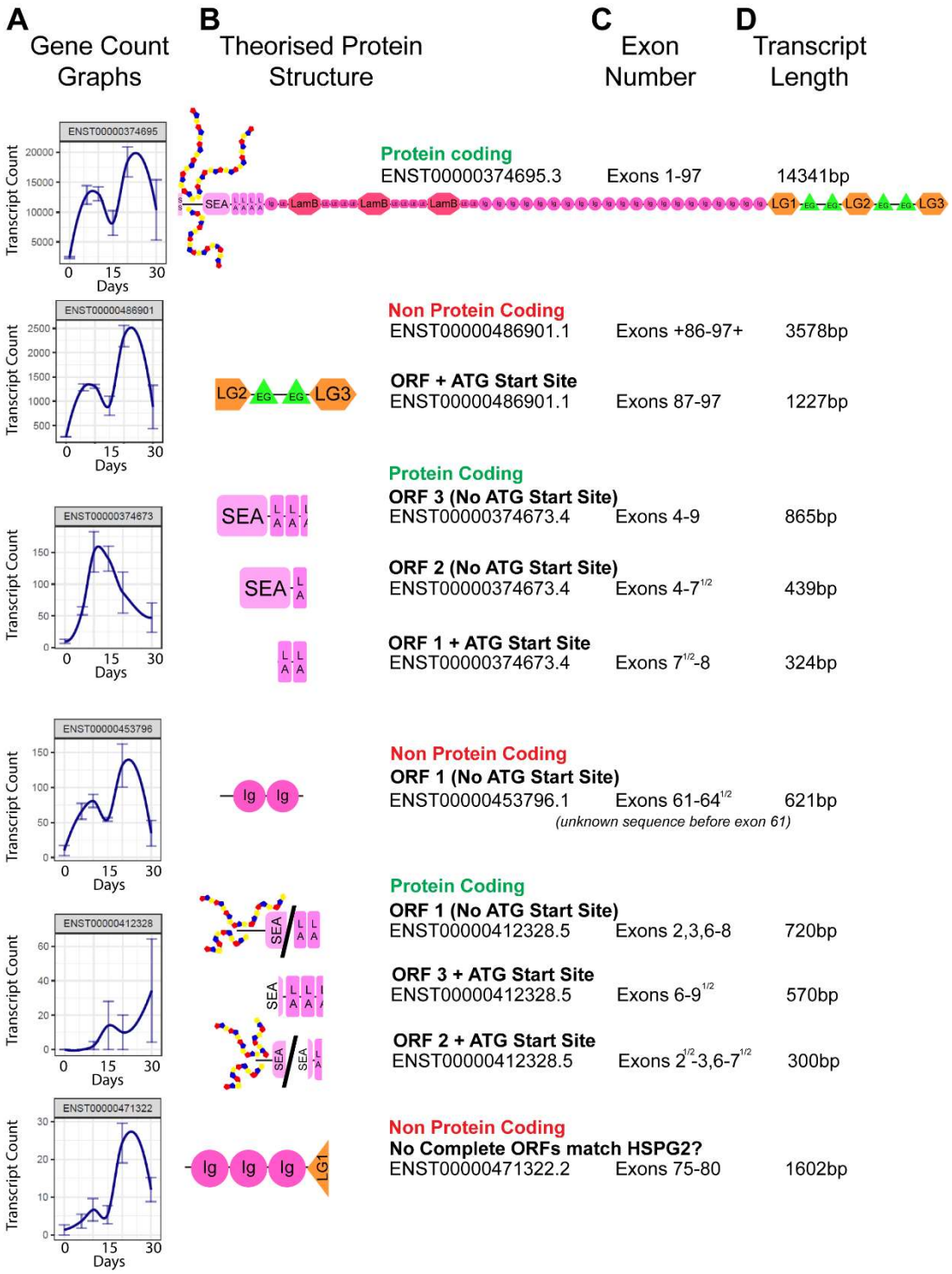


***Figure 4.21 – Transcripts of HSPG2 expressed through CM differentiation.*** *(A) Transcript counts over cardiomyocyte differentiation. (B) Theorised perlecan protein structures are displayed assuming ORF transcription, separated if containing different ORFs. Transcript number, exons of HSPG2 in the transcript (C), transcript length (D) also displayed.*

I used Snapgene software to generate the exons sequences of HSPG2 that are found in each transcript. These exons align to parts of perlecans protein structure. Assuming the open reading frames (ORFs) found in these files are used to create protein fragments I generated the predicted protein structure based off these transcripts. The highest expressed transcript found throughout the differentiation is full length HSPG2 containing all 97 exons. This is followed by a transcript containing two laminin G domains (LG2 and LG3) found in domain 5 of *HSPG2*, this transcript also follows the same trend as full *HSPG2* through differentiation at a ~10-fold reduction. Interestingly according to ensemble this transcript is not protein coding although within there is an ATG start site and ORF. The next transcript (ENST000000374673.4) shows a different trend with its highest expression at day 10 and is found within domain 1 of *HSPG2*. This transcript contains 3 different reading frames although only one with a ATG start site. The transcript ENST000000453796.1 again follows a similar trend to the full length *HSPG2* transcript, although at a ~100-fold reduction in count and is classed as non-protein coding. The transcript ENST000000412328.5 shows a steady increase over the course of CM differentiation although variation between samples may have caused this trend. This transcript is found in domain 1 and appears to skip *HSPG2* exons 4 and 5. Finally the transcript ENST000000471322.2 also shows a trend similar to full length *HSPG2* transcript at a ~1000-fold reduction. This transcript is considered non protein coding and looking at the Snapgene file no ORFs appear to match sequences found in *HSPG2*.

Overall, *HSPG2*s expression is increased over cardiomyocyte differentiation. *AGRN*s level remain similar and *COL18A1* mRNA increases between day 0 and 6 before decreasing over the following timepoints. Immunostaining confirms an increase in perlecan while agrin remains constant throughout. Western blots also show changes in band sizes between hiPSCs and cardiac progenitor cells in both perlecan and agrin. Further analysis of the different splice variants of *HSPG2* over cardiac differentiation show how cardiac differentiation causes a shift in specific *HSPG2* transcripts. With further analysis into these transcripts produced we can speculate which transcripts are beneficial to either a hiPSC or cardiac environment, and which protein

structures these would transcribe. These experiments that display how *HSPG2* is increased over the cardiac differentiation confirm its presence is correlated the formation of cardiac tissues, while the expression of agrin remains constant implying a different role. To further investigate this role of *HSPG2* in cardiac differentiation I aim to utilise the HSPG2$^{+/-}$ hiPSCs created previously and differentiate them to CMs.

### 4.4. Gene expression changing during HSPG2$^{+/-}$ cardiomyocyte differentiation

Before I analysed the RNA sequencing of both cell lines, I wanted to compare the PCA plot to determine if HSPG2$^{+/-}$ followed a similar trend over differentiation recorded in the previous HSPG2$^{WT}$ PCA plot.

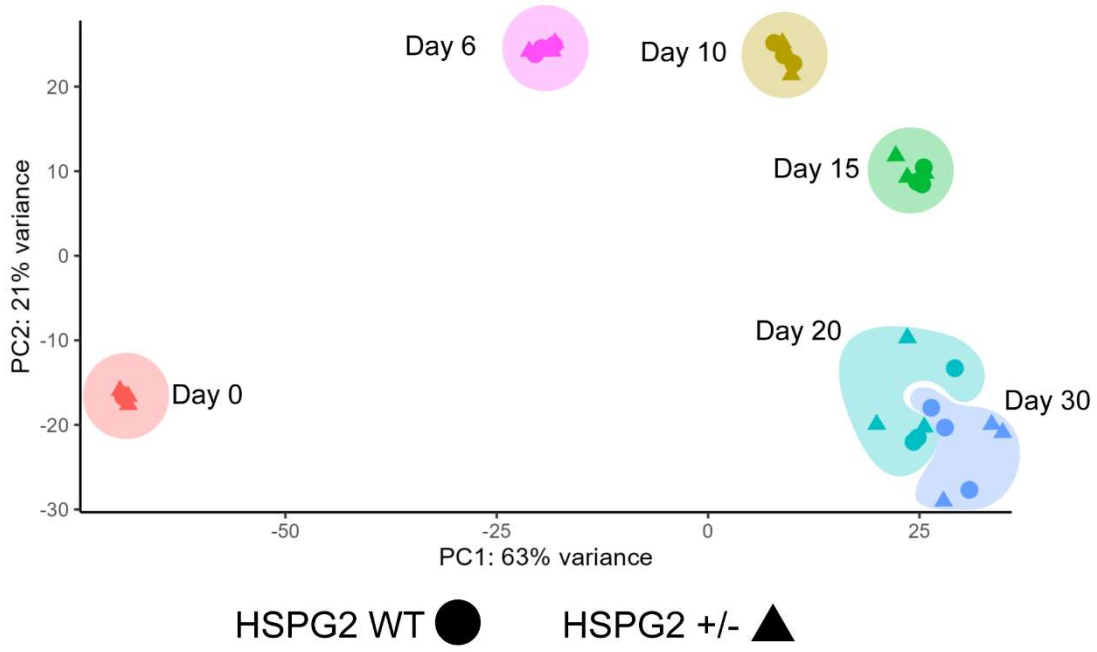


***Figure 4.22 - PCA plot from RNA sequencing of both cell lines.*** *PCA plot of HSPG2WT and HSPG2+/- cardiomyocyte differentiation from RNA sequencing outputs at each timepoint. Timepoint clusters are colour coded, day 0 – red, day 6 – pink, day 10 – yellow, day 15 – green, day 20 – cyan and day 30 – blue.*

Comparing PCA plot analysis of HSPG2$^{WT}$ and HSPG2$^{+/-}$ timepoints show how both cell lines have similar clustering, implying both cell differentiations follow

the same trend (Figure 4.22). These results suggest the reduction of *HSPG2* did not cause a major change in the differentiation capabilities of the HSPG2$^{+/-}$ cell line.

Following PCA plot analysis showing HSPG2$^{+/-}$ cells follow the same differentiation trend as the WT I investigated if the markers previously investigated in the HSPG2$^{WT}$ differentiation.

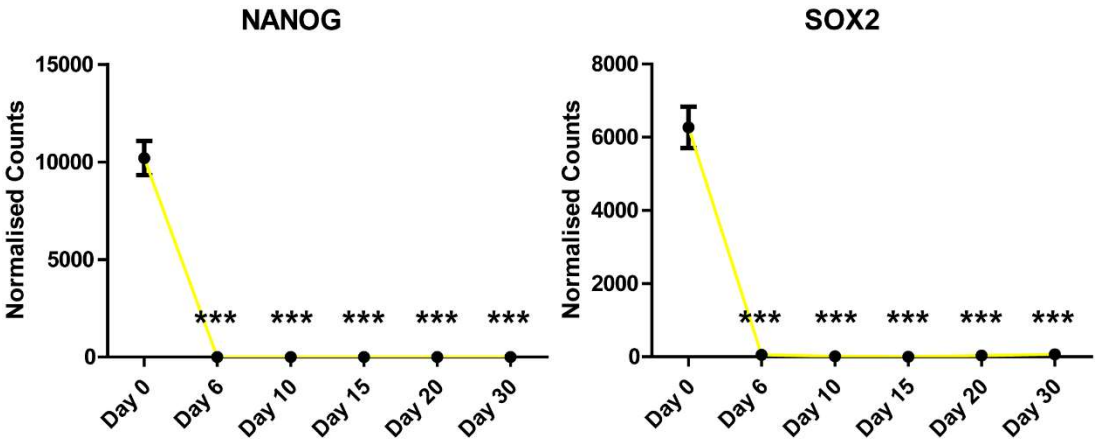


***Figure 4.23 - Panel of pluripotency markers through HSPG2+/- cardiomyocyte differentiation.*** *DeSeq2 normalisation of RNA sequencing at each timepoint of cardiomyocyte differentiation showing gene counts of pluripotency genes NANOG and SOX2. N=3, statistical test performed on SD using Tukey Test. P-value <0.05 = *, <0.01 = **, <0.001 = ***.*

Pluripotency markers *NANOG* and *SOX2* were again used to confirm a shift from a pluripotent to a defined cell had occurred though differentiation in the HSPG2$^{+/-}$ cell line (Figure 4.23). Both *NANOG* (10198.7) and *SOX2* (6270.7) gene counts at hiPSCs were statistically attenuated to negligible expression for the remaining timepoints of differentiation.

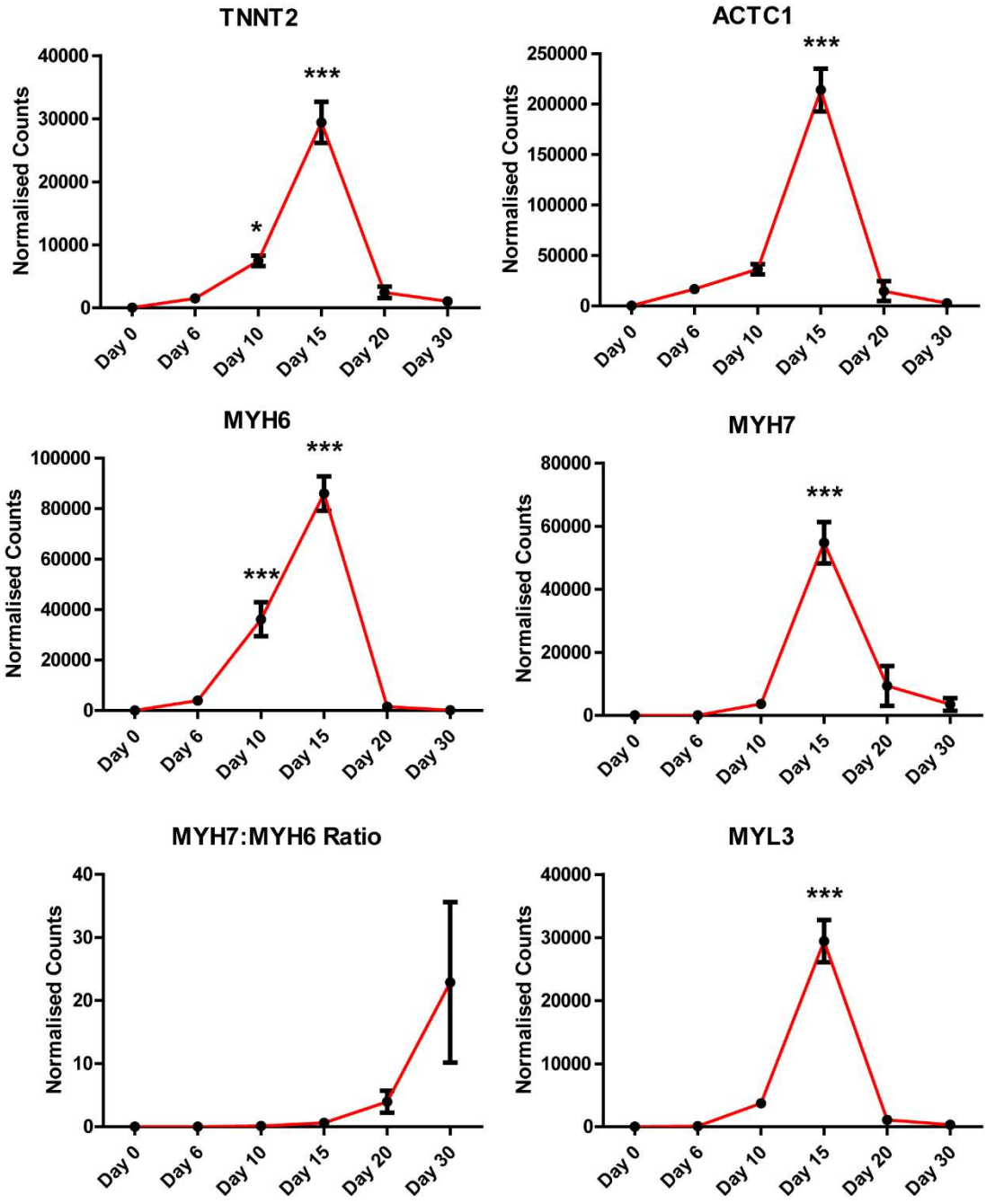


***Figure 4.24 - Structural Cardiomyocyte gene expression changes during hiPSC-CM differentiation.*** *RNA sequencing at each of the timepoint provides gene counts for each targeted gene. Several structural cardiac development genes displayed for normalised count at each timepoint. TTNT2-Cardiac Troponin 2, ACTC1-Cardiac Actin, MYH6-Myosin Heavy Chain 6, MYH7-Myosin Heavy Chain 7 and MYL3-Myosin Light Chain. N=3, statistical test performed on SD using Tukey Test. P-value <0.05 = *, <0.01 = **, <0.001 = ***.*

Looking at structural markers of cardiomyocytes the HSGP2$^{+/-}$ cell line produced a similar trend as seen in the WT cells where most markers show a statistical increase at day 15, with several increasing at day 10 (*TNNT2* & *MYH6*) (Figure 4.24). The ratio of *MYH7* over *MYH6* shows an upwards trend as differentiation continues but due to variation in day 20 and 30 samples this increase is not statistically significant compared to the ratio in hiPSCs.

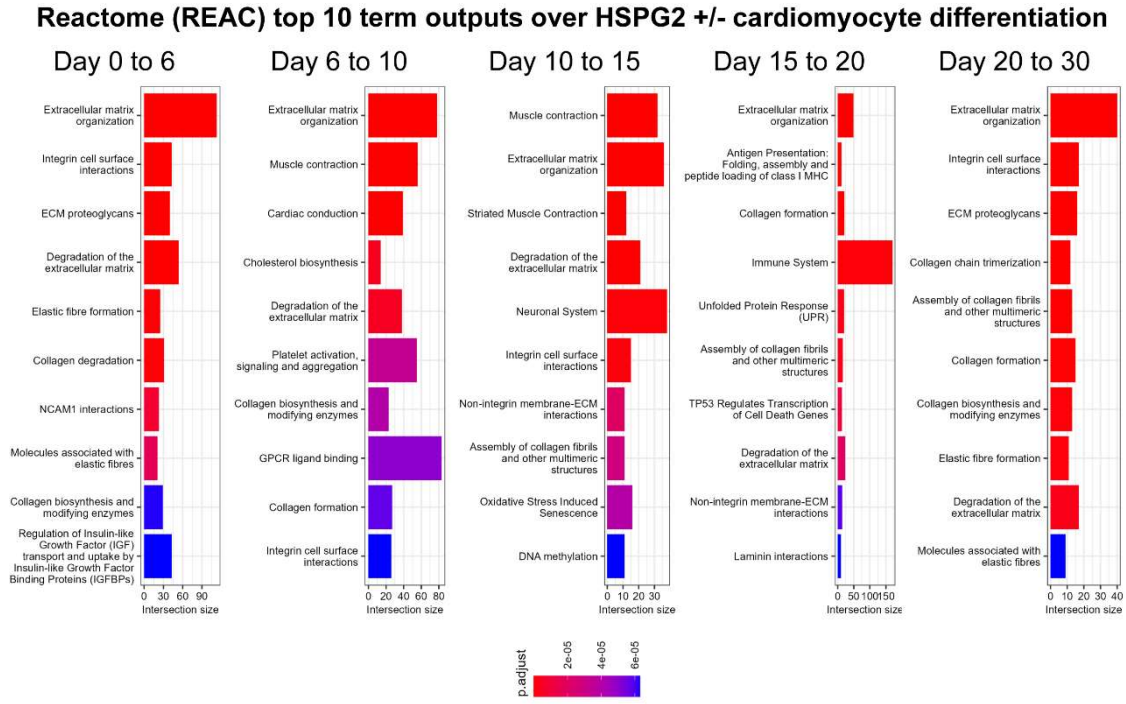


***Figure 4.25 - REAC pathway top 10 terms linked to HSPG2+/- cardiomyocyte differentiation.*** *The top 10 terms based on p-adjusted value from REAC analysis of each timepoints extracted and plotted into a ggPlot2 bar graph.*

For further confirmation of HSPG2$^{+/-}$ iPSC to CM differentiation REAC analysis was used at each timepoint (Figure 4.25). Muscle contraction and cardiac conduction are top terms highlighted during the differentiation implying correct differentiation was underway. ECM organisation also remains as one of the top terms throughout the differentiation similar to the WT differentiation. I next wanted to look at what the differences were between the WT and HSPG2$^{+/-}$ cells throughout the differentiation.

I initially looked at the counts of HSPGs throughout the differentiation compared to WT to confirm levels of *HSPG2* were lower throughout differentiation and if there was a compensatory effect due to the reduction of *HSPG2* (Figure 4.26).

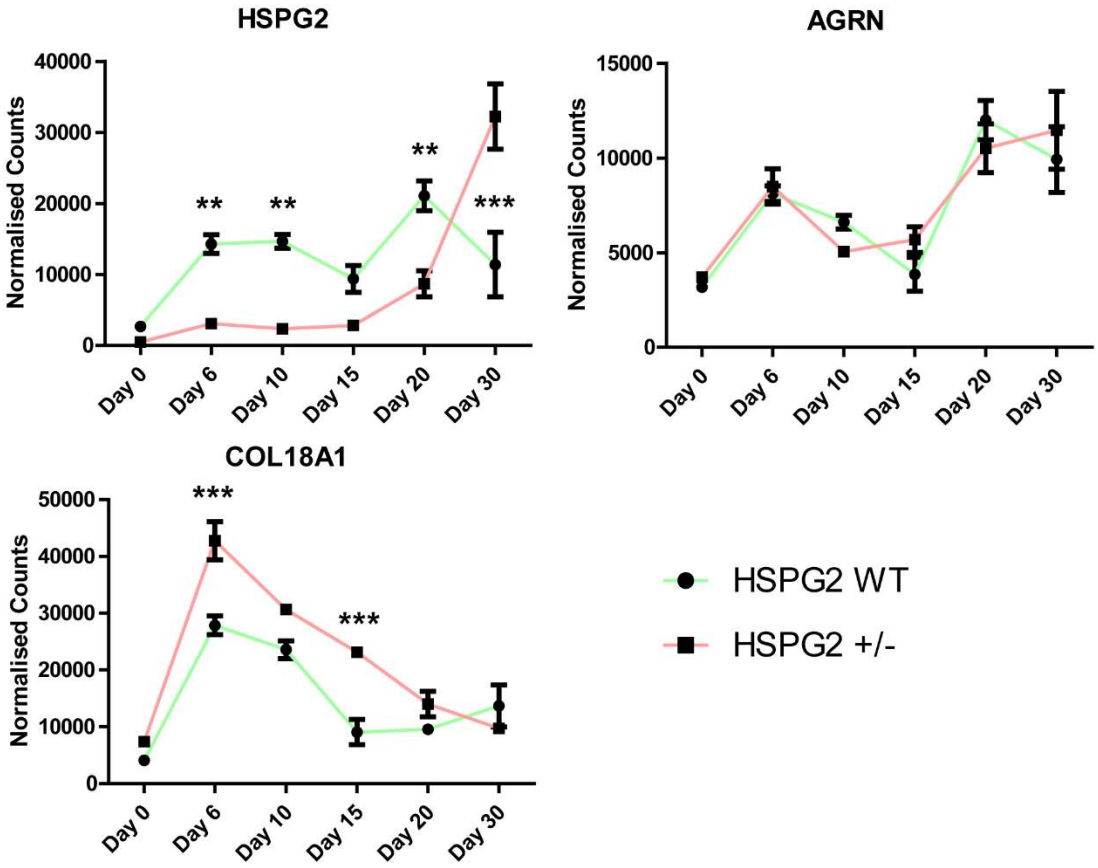


***Figure 4.26 – WT vs +/- HSPG gene counts through cardiomyocyte differentiation.*** *HSPG2-Perlecan, AGRN-Agrin and COL18A1-Colagen 18 are displayed as gene counts following deSeq2 normalisation of RNA sequencing analysis with lines for both HSPG2$^{WT}$ (green) and HSPG2$^{+/-}$ (red). N=3, statistical test performed via multiple t-tests. P-value <0.05 = *, <0.01 = **, <0.001 = ***.*

The *HSPG2* deficient line shows a statistical reduction in *HSPG2* at day 6, 10 and 20, interestingly there is a switch at day 30 whereby the deficient line produces a higher level of *HSPG2* than the WT cell line (HSPG2$^{WT}$: 11395.0, HSPG2$^{+/-}$: 32254.7). Looking at levels of *AGRN* there is no difference between either line throughout the differentiation. *COL18A1* shows a trend of higher

expression at all timepoints till day 30, although this increase is only statistically significant at day 6 and day 15.

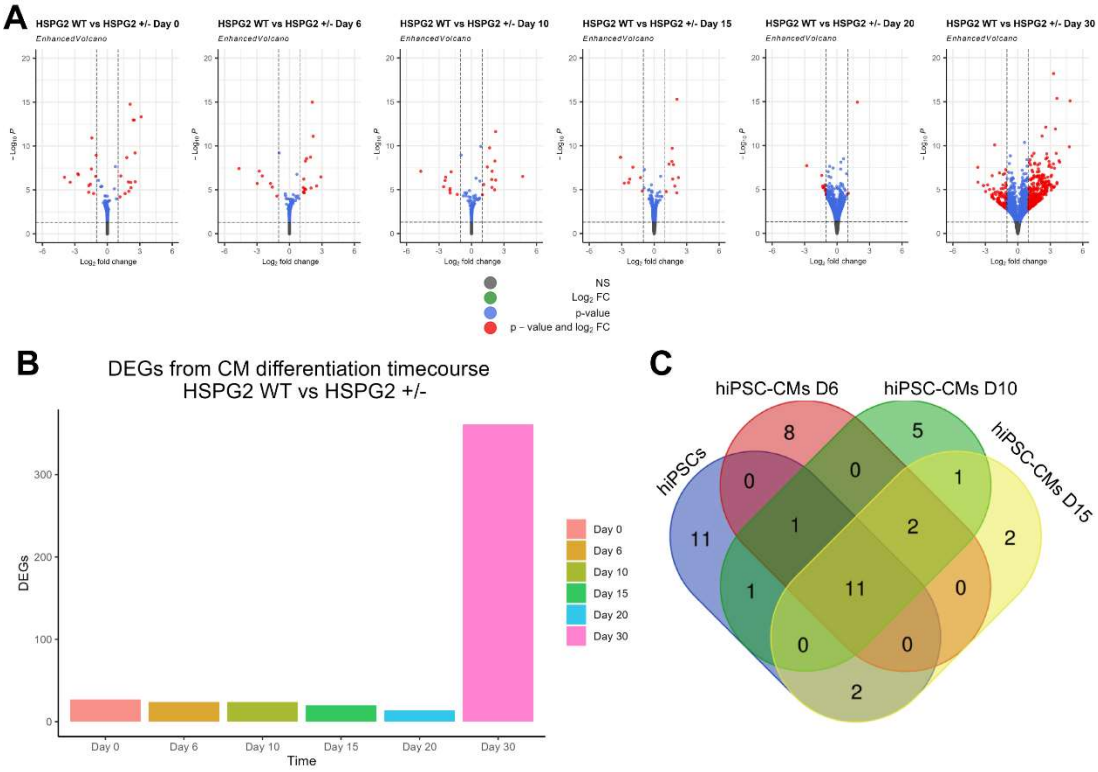


***Figure 4.27 - Enhanced volcano plots of changes seen between WT and HSPG2+/- cells over differentiation.*** *(A) Volcano plots highlighting differentially expressed genes (DEGs) in red. Genes that had a less that Log2(1) fold change but were significantly changed (p<0.05) are in blue, while those that expressed higher than Log2(1) but were not significantly (p>0.05) changed are in green. Genes that fit none of the above parameters were designated grey and not significant (NS). (B) DEG count was arranged in a bar chart to show changes during cardiomyocyte differentiation. (C) Venn diagram of similar DEGs between timepoints ranging from day 0 to day 15.*

The volcano plots show how there are few DEGs between the two cell lines through differentiation until day 30 (Figure 4.27, A). Plotting these DEGs as a bar graph the lack of difference between each early timepoint becomes more clear (Day 0: 27, Day 6: 24, Day 10: 24, Day 15: 20, Day 20: 14)), it is only at the day 30 timepoint where there are a large number of DEGs identified (Day 30: 361) (Figure 4.27, B). Looking into the early timepoints (day 0 to day 15)

of each cell line over the differentiation 11 genes are flagged up as consistently differentially expressed between the two cell lines (Figure 4.27, C).

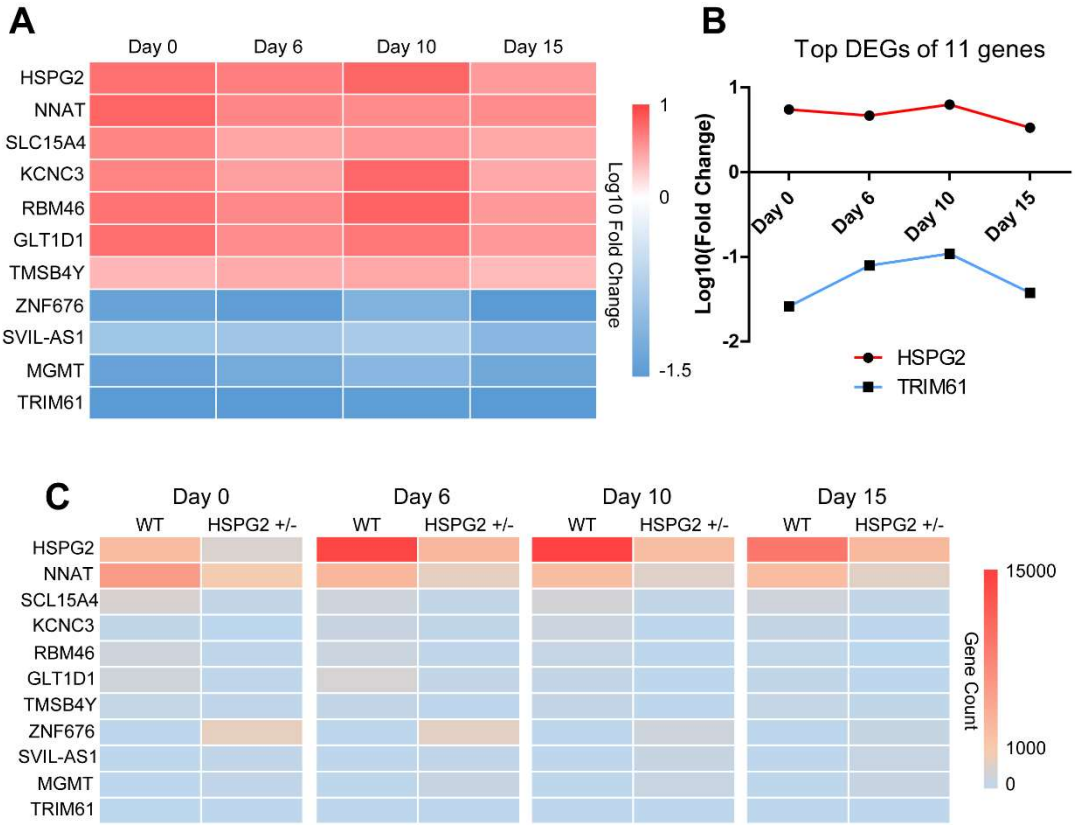


***Figure 4.28 - Heatmap of consistently changed genes over early cardiac differentiation.*** *(A) 11 genes are found to be statistically dysregulated between HSPG2$^{WT}$ and HSPG2$^{+/-}$ cell lines between day 0 and day 15 differentiation. (B) Both highest and lowest DEGs plotted as line graph from day 0 to day 15 showing Log10 fold change. (C) Gene counts plotted as heat map for each cell line from day 0 to day 15.*

Of the 11 genes found seven are upregulated in HSPG2$^{WT}$ line when compared to HSPG2$^{+/-}$ (Figure 4.28, A). The genes found to be consistently upregulated throughout the early differentiation timepoints include *HSPG2*, *NNAT, SCL15A4, KCNC3, RBM46, GLT1D1, TMSB4Y*. While four of the genes were found to be constantly downregulated including *ZNF676, SVIL-AS1, MGMT* and *TRIM61*. Plotting the highest and lowest of these 11 DEGs show *HSPG2* to be overall highest expressed gene in the HSPG2$^{WT}$ cells, while *TRIM61* is the lowest (Figure 4.28, B). Interestingly, when investigating

gene counts *HSPG2* and *NNAT* remain the highest count DEGs expressed throughout the differentiation (Figure 4.28, C).

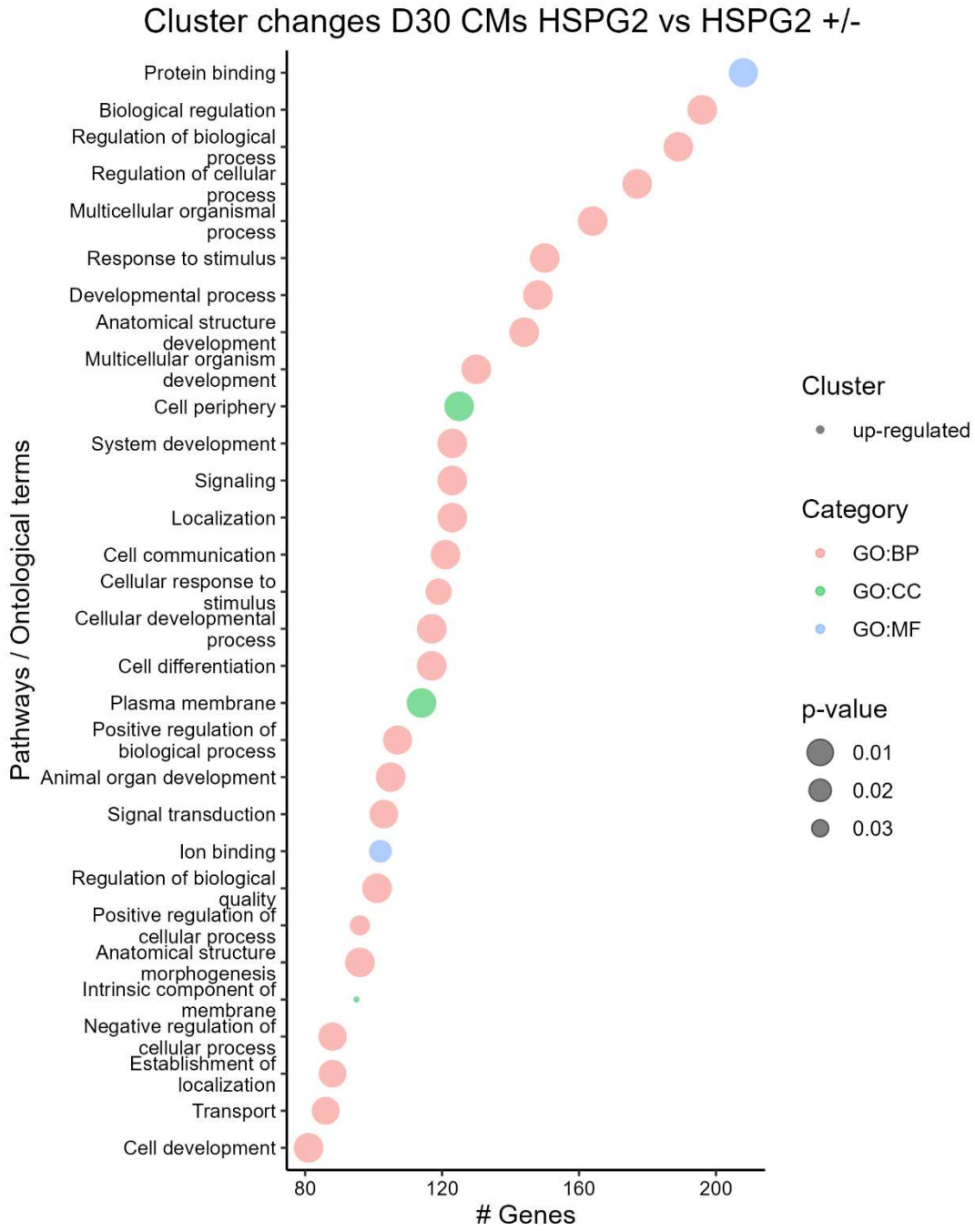


***Figure 4.29 – Day 30 cluster differences between HSPG2 WT and HSPG +/- CMs.*** *Cluster analysis of 361 DEGs found between HSPG2 WT and HSPG2 +/- cardiomyocytes run through gene ontology cluster analysis.*

These results from pathway analysis suggest there are very little differences between WT and HSPG2$^{+/-}$ hiPSCs as previously shown by hiPSC analysis done in the previous chapter (chapter 3). Therefore, I was interested in using

GO analysis to investigate terms found from the 361 DEGs at day 30. Using cluster analysis on the 361 DEGs between $HSPG2^{WT}$ and $HSPG2^{+/-}$ shows how all the top 30 terms were linked to upregulated terms (Figure 4.29). Many of the terms found are linked to cell development and differentiation while other top term clusters were linked to signalling, communication, and ion binding. This overall shows the HSPG2 WT CMs are operating at a higher function than the HSPG2 +/- CMs.

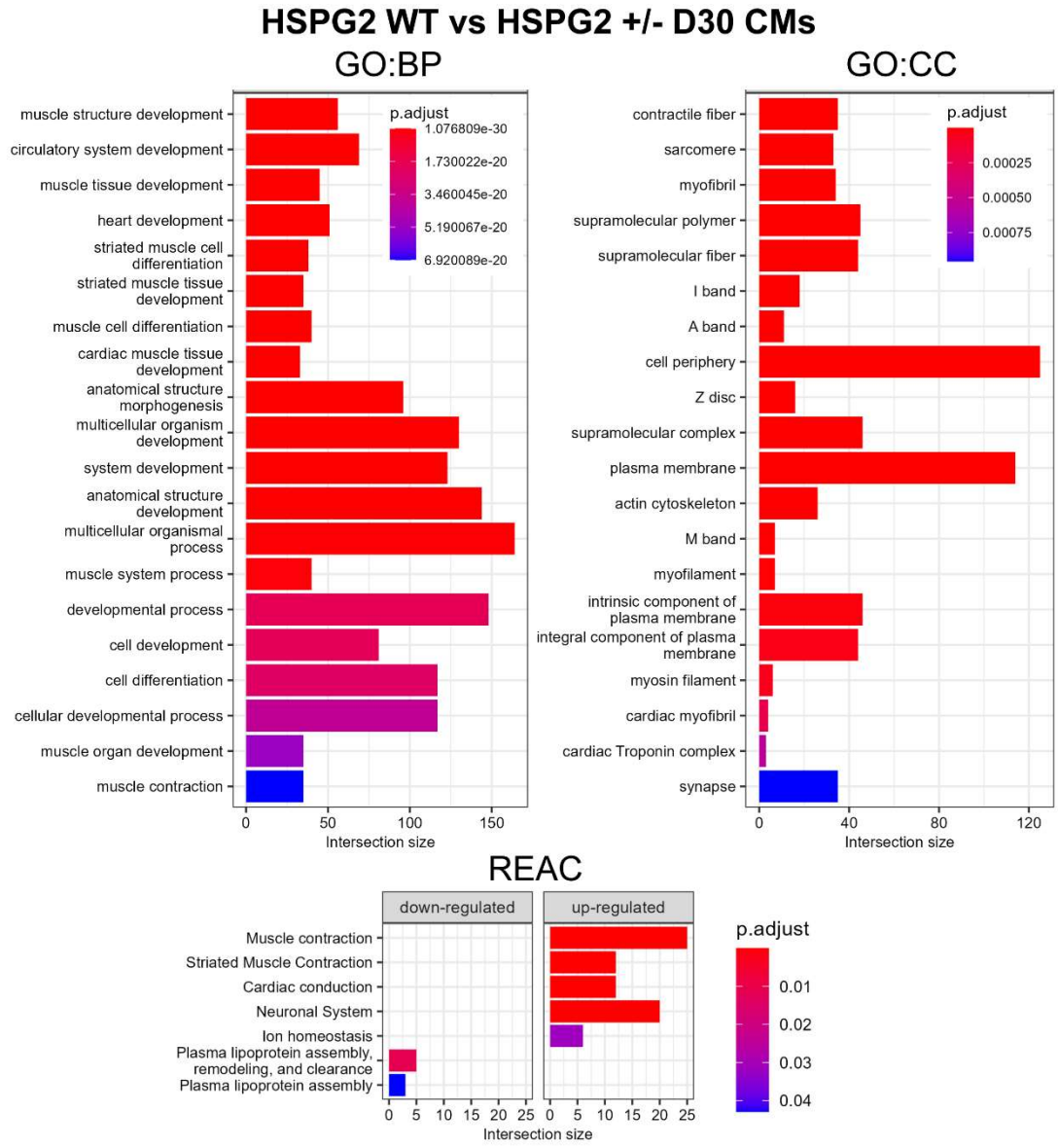


***Figure 4.30 – Day 30 focused terms with GO:BP, GO:CC and REAC pathways.*** *Differences in HSPG2 WT and HSPG2 +/- day 30 DEG gene cluster analysis for GO: Biology Processes, GO: Cellular components and Reactome. Top 20 terms were highlighted and ordered based on most significant.*

Looking at the specific terms based on statistical value of the GO searches and REAC shows increased cardiac terms in the HSPG2$^{WT}$ CMs compared to the HSPG2$^{+/-}$ (Figure 4.30). GO:BP terms are linked to heart and muscle development and differentiation and combined with GO:CC terms link to an increased level of structural cardiac genes. The increased level of structural terms found upregulated in the WT CMs leads towards the idea of a more mature and functional CMs than the HSPG2$^{+/-}$ CMs. REAC analysis terms that are upregulated in HSPG2$^{WT}$ CMs are all linked to conduction and the handling of ions, essential to the contraction and maturation of CMs. The two downregulated terms in the HSPG2$^{WT}$ CMs are both linked to lipoprotein assembly and clearance.

The final stages of the cardiac differentiation would be linked to maturing of the CMs. The increased DEGs found between the two cell lines indicate the lack of *HSPG2* is having the largest effect during this stage. Further analysis of these DEGs show how HSPG2$^{WT}$ CMs have an expression profile characteristic of more structurally mature cardiomyocytes, with increased expression of genes involved in cardiac contraction than HSPG2$^{+/-}$ CMs. GO analysis terms in HSPG2$^{WT}$ day 30 CMs upregulated DEGs highlighted cardiac muscle cell differentiation, muscle contraction, and calcium signalling as several pro-cardiac maturation terms (Figure 4.31). While downregulated DEGs highlighted terms such as phospholipid efflux, carboxylic acid metabolic process and membrane. These terms suggest the HSPG2$^{+/-}$ day 30 CMs have upregulated genes linked to metabolic function. Interestingly, both upregulated and downregulated DEGs emphasized GO terms linking to extracellular matrix and space. Downregulation of ECM DEGs, but upregulation of extracellular space in HSPG2$^{+/-}$ day 30 CMs suggests preferential matrix remodelling.

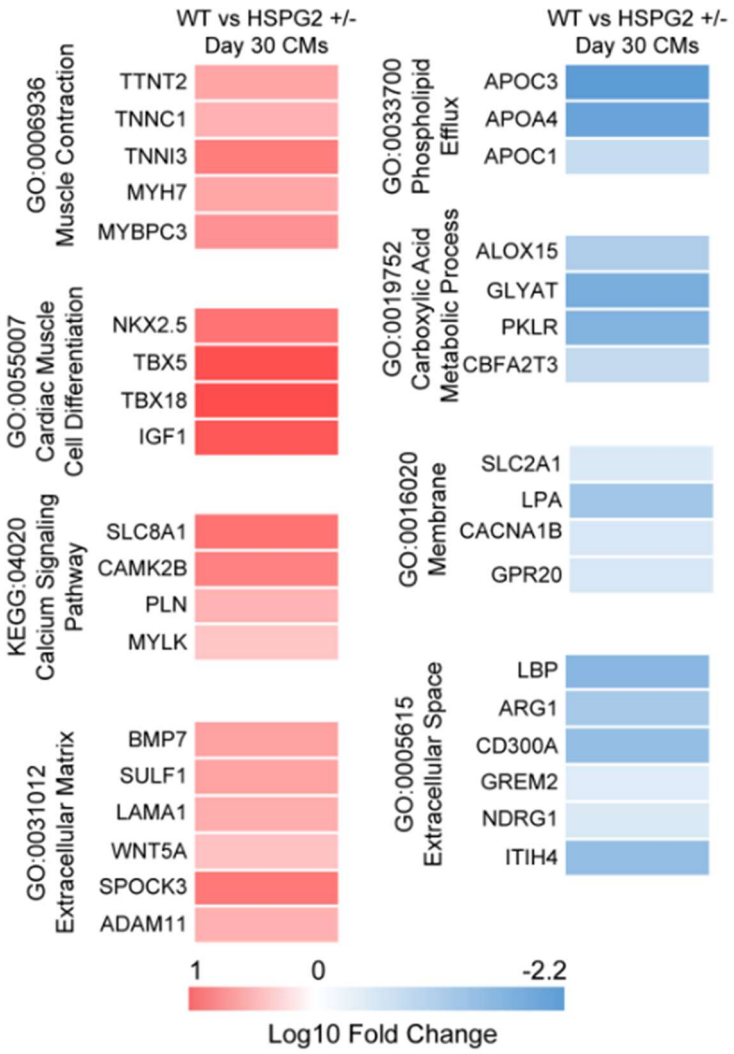


***Figure 4.31 – Highlighted DEGs from GO pathway analysis.*** *Heatmap showing Log10 fold change of selected DEGs found though GO cluster analysis terms of HSPG2WT vs HSPG2+/- day 30 CMs.*

RNA sequencing revealed DEGs associated with metabolic changes in HSPG2$^{+/-}$ day 30 CMs. Attenuation of HSPG2 in mice has previously shown to encourage fatty acid metabolism in white adipocytes. Indeed, my results highlight abnormal metabolic gene expression in HSPG2$^{+/-}$ CMs, and therefore I next want to investigate metabolic changes between the cell lines.

### 4.5. Metabolism of HSPG2$^{WT}$ and HSPG2$^{+/-}$ CMs

A metabolic shift is essential for cardiac maturation and *HSPG2* is known to have a role in metabolism, to further investigate this I performed the CM differentiation in the aim of looking at *HSPG2*s role in cardiac metabolism. In Johnson et al, 2022, I describe a novel assay for assessing metabolic changes that occur during hiPSC-CM differentiation (Johnson et al., 2022). Here I exploit this assay to monitor metabolic changes in WT and HSPG2$^{+/-}$ cell lines.

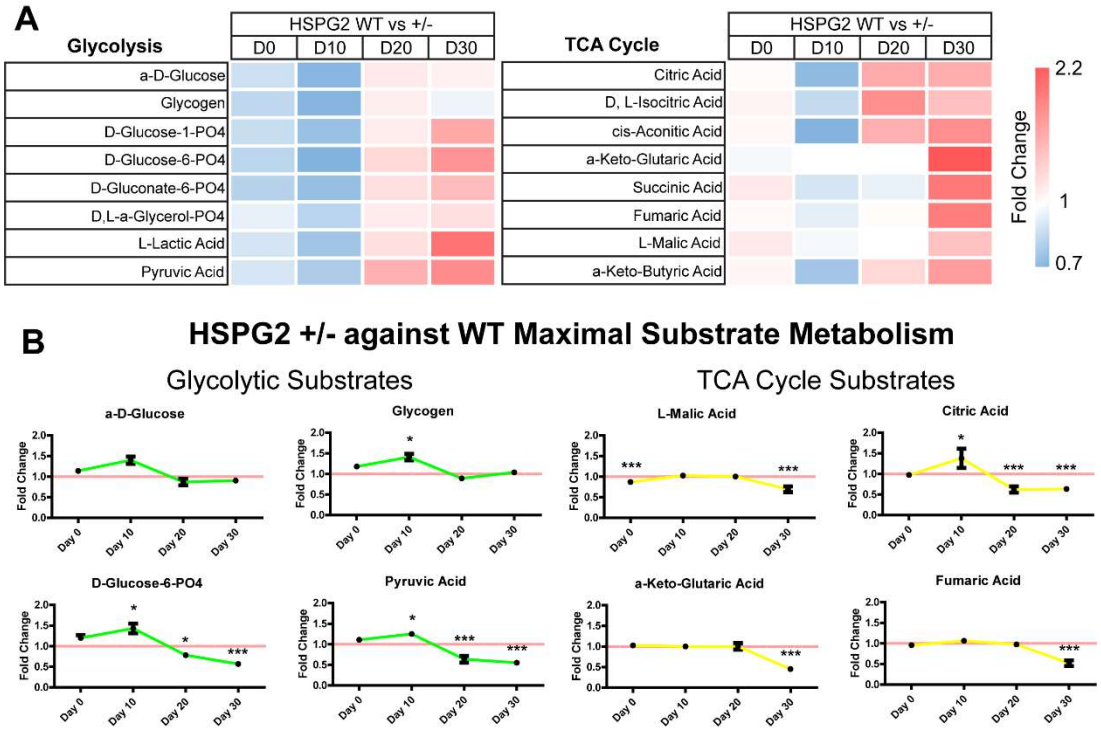


***Figure 4.32 – Mitoplate analysis of glycolysis and TCA cycle over cardiac differentiation.*** *(A) Fold change of maximal substrate metabolism between HSPG2 WT and HSPG2 +/- cells of each glycolysis and TCA cycle substrate over the cardiac differentiation. (B) Fold change line graphs of selected lowly and highly changes substrates over differentiation. N=3, statistical test performed via multiple t-tests. P-value <0.05 = *, <0.01 = **, <0.001 = ***.*

Glycolysis and TCA cycle substrates were plotted as a fold change of HSPG2$^{WT}$ vs HSPG2$^{+/-}$. HSPG2$^{WT}$ hiPSCs appear to have a slightly lower ability to metabolise glycolytic substrates than the HSPG2$^{+/-}$ hiPSCs (Figure 4.32, A). This difference between the lines is further exacerbated at day 10 cardiac cells. This trend is switched in day 20 and 30 timepoints whereby WT cells become more metabolically active and can metabolise glycolytic and TCA

cycle substrates at a higher level. Comparing several of the maximal fold changes, no statistical difference was found in a-D-Glucose metabolism over the differentiation. Glycogen metabolism is statistical increase at day 10 with no other difference at the other timepoints (Figure 4.32, B). While both D-glucose-6-PO4 and pyruvic acid show a statistical attenuation in HSPG2$^{+/-}$ cells at day 20 and 30. All of the TCA cycle metabolites highlighted here have a statistical reduction in maximal metabolism in HSPG2$^{+/-}$ day 30 CMs. Interestingly, L-malic acid is significantly attenuated in HSPG2$^{+/-}$ hiPSCs compared to the HSPG2$^{WT}$ control.

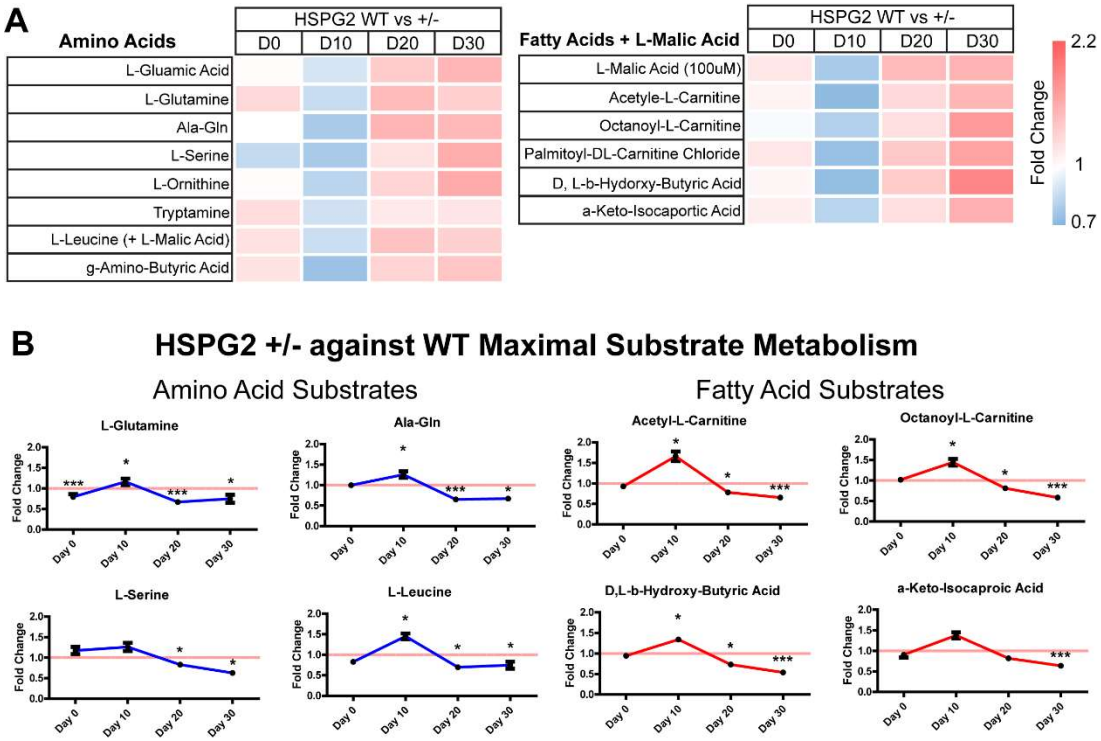


***Figure 4.33 – Mitoplate analysis of amino acid and fatty acid metabolism over cardiac differentiation.*** *(A) Fold change of maximal substrate metabolism between HSPG2 WT and HSPG2 +/- cells of each amino acids and fatty acid substrate over the cardiac differentiation. (B) Fold change line graphs of selected lowly and highly changes substrates over differentiation. N=3, statistical test performed via multiple t-tests. P-value <0.05 = *, <0.01 = **, <0.001 = ***.*

Investigating amino acids and fatty acid metabolite metabolism highlights a similar trend as the glycolytic and TCA cycle substrates, with an increase in HSPG2$^{+/-}$ day 10 metabolism, followed by further reductions (Figure 4.33, A).

Of the highlighted amino acid substrates, L-glutamine is statistically reduced in HSPG2$^{+/-}$ hiPSCs compared to the WT (Figure 4.33, B). All highlighted amino acids barring L-serine are metabolised to a higher level than the WT at day 10, although at day 20 and 30 all the amino acids substrates are statistically attenuated in the HSPG2$^{+/-}$ CMs. A similar trend is identified in fatty acid substrates, whereby the HSPG2$^{+/-}$ cell have a higher metabolism of substrates at day 10, but attenuated at day 20 and 30 compared to the WT. These results suggest the major difference between the cell lines is identified in day 30 CMs, like results found using RNA sequencing. Due to this finding I wanted to highlight the difference between cell lines after mitoplate analysis of day 30 CMs in a clean summary figure.

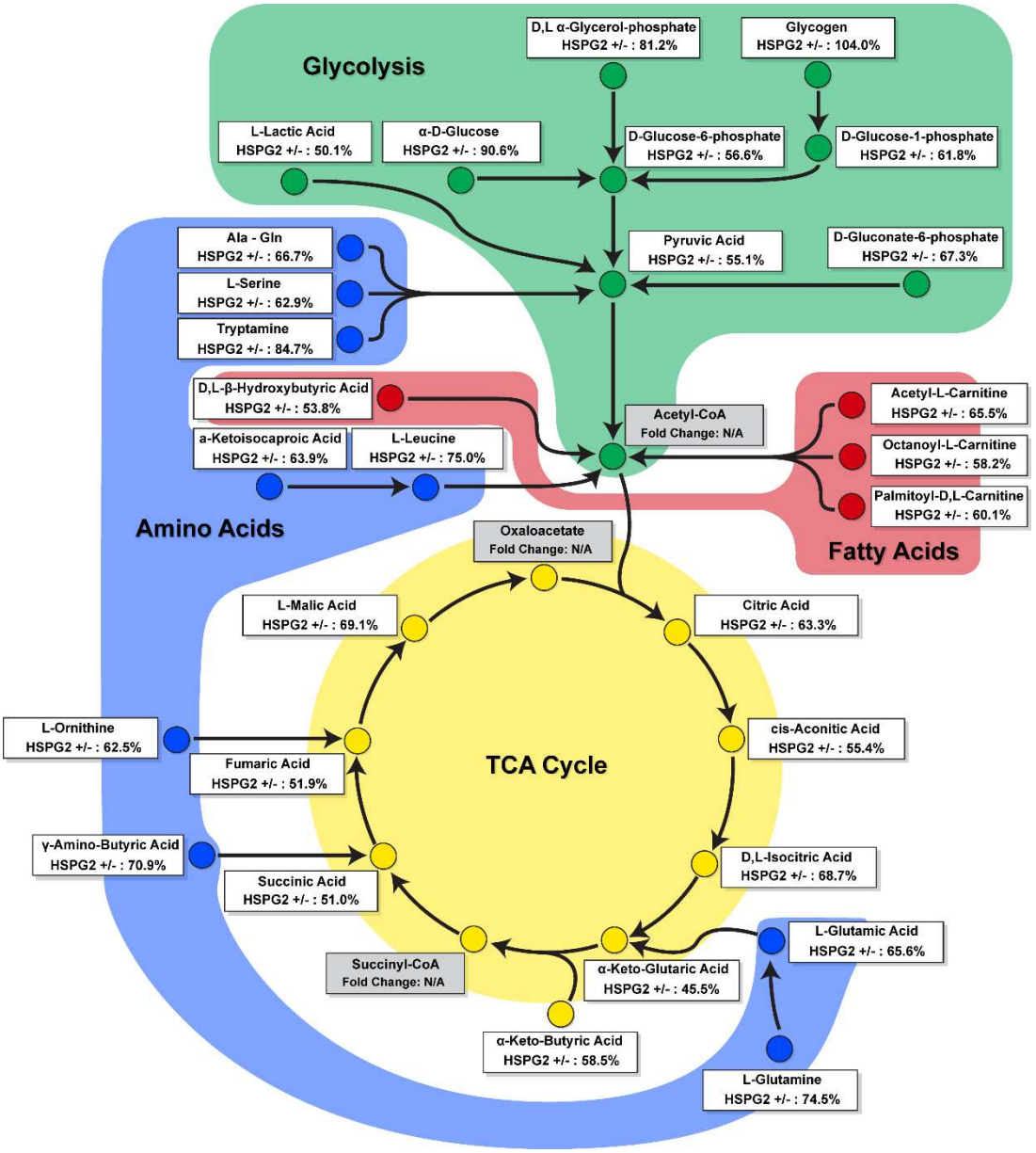


***Figure 4.34 – Metabolic map showing reduction in HSPG2$^{+/-}$ specific substrate metabolism in day 30 CMs.*** *Percentage of substrate metabolism is calculated against the maximal substrate metabolism vs HSPG2$^{WT}$ day 30 CMs. Each metabolic clustered group is highlighted and coloured, Green: Glycolysis, Red: Fatty Acids, Blue: Amino Acids and Yellow: TCA Cycle.*

Summarising differences seen between day 30 HSPG2 WT and HSPG2 +/- day 30 cardiomyocytes on a metabolic map shows an across-the-board reduction of HSPG2 +/- CMs metabolic function (Figure 4.34).

To further analyse the metabolic function of these day 30 CMs I utilised a seahorse assay to investigate differences between oxidative phosphorylation (OXPHOS) and extracellular acidification rate (ECAR).

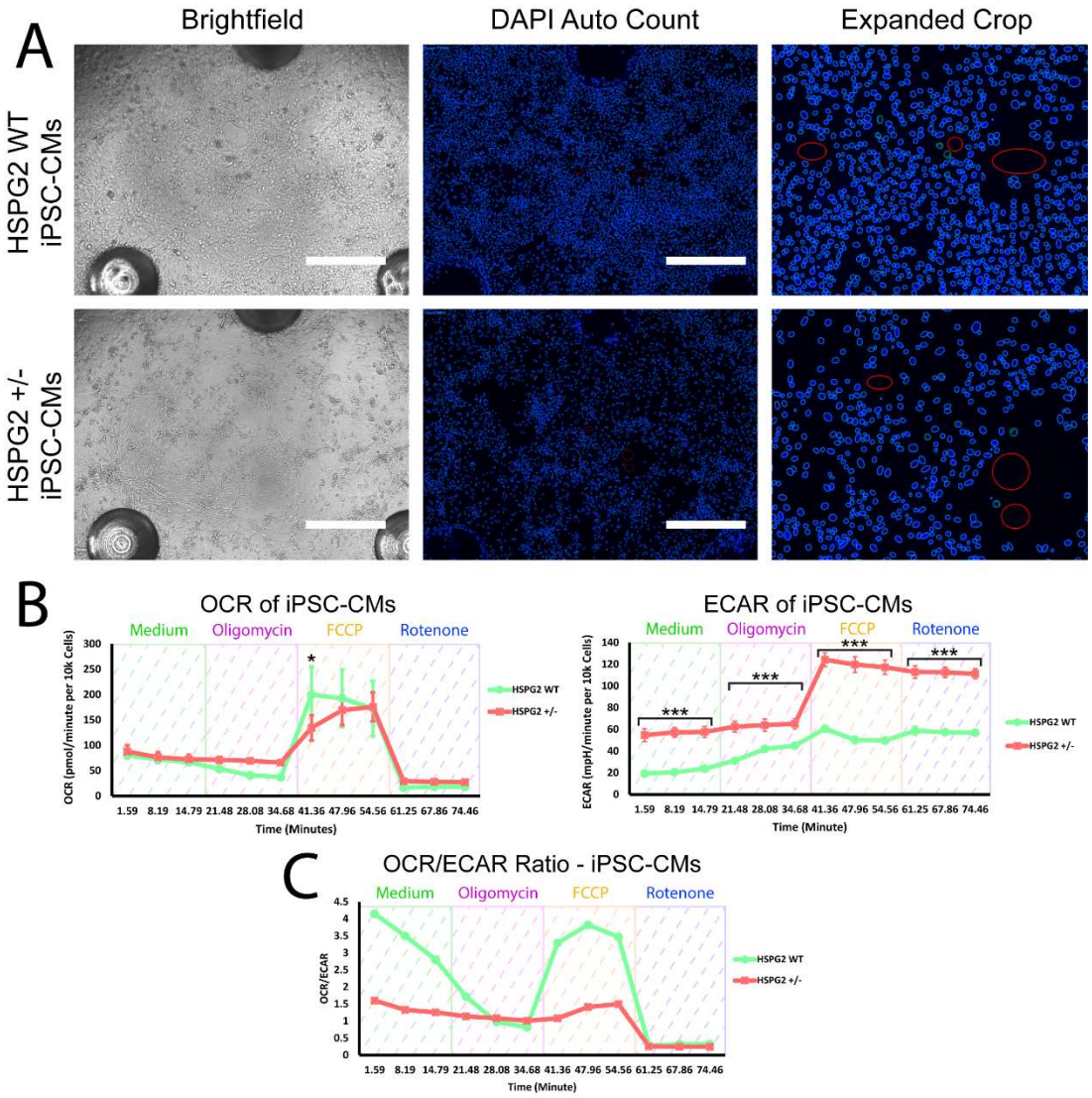


***Figure 4.35 – Seahorse assay of WT and HSPG2$^{+/-}$ cardiomyocytes.*** *(A) Images of cardiomyocytes seeded onto seahorse plates, stained with DAPI and EVOS 3000 automated cell count performed. Blue circles represent automatic recognised nuclei, red circles identify background. (B) Seahorse output graphs plotted and normalised against 10,000 cells based of DAPI auto counts. (C) Ratio of OCR vs ECAR plotted showing differences between HSPG2$^{WT}$ and HSPG2$^{+/-}$ CMs. N=3, statistical test performed via multiple t-tests. P-value <0.05 = *. <0.01 = **. <0.001 = ***.*

Following seahorse assay plates were taken and stained with DAPI to count average nuclei of each well for each line (WT: 22883 ±303.7, HSPG2 +/-: 10478 ±1266.5) (Figure 4.35, A). Results from seahorse OCR and ECAR are plotted against 10,000 cells showing both cell lines follow a similar trend in OCR (Figure 4.35, B). With only the first point recorded after FCCP administration showing a statistical increase in WT CMs vs $HSPG2^{+/-}$ CMs. ECAR on the other hand shows how throughout varying mitochondrial stresses the $HSPG2^{+/-}$ CMs maintain a statistically higher ECAR than WT CMs. Plotting the results from OCR over ECAR show how in both the control and FCCP WT CMs have a higher reliance on OXPHOS than ECAR (Figure 4.35, C). These changes show the higher reliance on glycolytic metabolism over OXPHOS in $HSPG2^{+/-}$ CMs, like the changes seen by use of mitoplates.
In this chapter I investigated differences in metabolism found between WT and perlecan deficient cells during CM differentiation. Interestingly, $HSPG2^{+/-}$ early CMs at day 10 have higher specific substrate metabolism of most metabolites compared to the WT counterpart. This trend is reversed during later stages of differentiation whereby day 30 the $HSPG2^{WT}$ CMs are capable of metabolising specific substrates to an increased level compared to the $HSPG2^{+/-}$. Utilising a seahorse assay was performed for further investigation into cell glycolysis and OXPHOS levels. Results shown suggest $HSPG2^{+/-}$ CMs have a higher reliance on glycolysis over the $HSPG2^{WT}$ preferential OXPHOS. Overall suggesting the day 30 $HSPG2^{+/-}$ CMs are less metabolically active and represent a more immature CM.

### 4.6. Generation of HSPG2$^{+/-}$ EHTs

The previous sections of this chapter have highlighted the differences found between HSPG2$^{WT}$ and HSPG2$^{+/-}$ CMs. Results suggest the HSPG2$^{+/-}$ CMs are less structurally mature, and show reduced metabolic capabilities combined with a higher reliance on glycolysis, overall suggesting a more immature CM. To further enhance the hiPSC-CMs maturation I aimed at generating engineered heart tissues (EHTs) from both cell lines to investigate if the maturation differences between the lines are exacerbated.

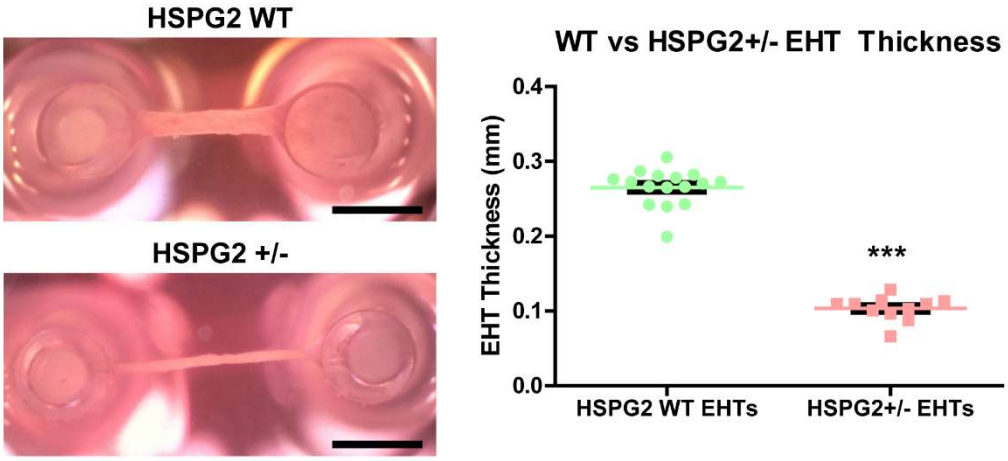


***Figure 4.36 – HSPG2$^{WT}$ and HSPG2$^{+/-}$ EHT images and sizes.*** *Brightfield images of EHTs showing morphological changes after 14 days in culture (Scale bar: 1 cm). Measurements of EHT thickness were performed by triple measurements along each EHT and averaged (WT n=16, HSPG2 +/- n=11). Statistical test performed using t-test. P-value <0.05 = *, <0.01 = **, <0.001 = ***.*

A striking difference in EHT tissue morphology was observable between the two cell lines. Quantitative image analysis showed a thinning of HSPG2$^{+/-}$ EHTs compared to the WT (Figure 4.36). The average thickness of the WT EHT was 0.265 cm (±0.0238) compared to the HSPG2$^{+/-}$ EHTs (0.103 cm ±0.0155). These changes occurred over the culture of EHTs imply the HSPG2$^{+/-}$ EHTs underwent some form of cardiac remodelling, where the EHTs become thinner and elongated.

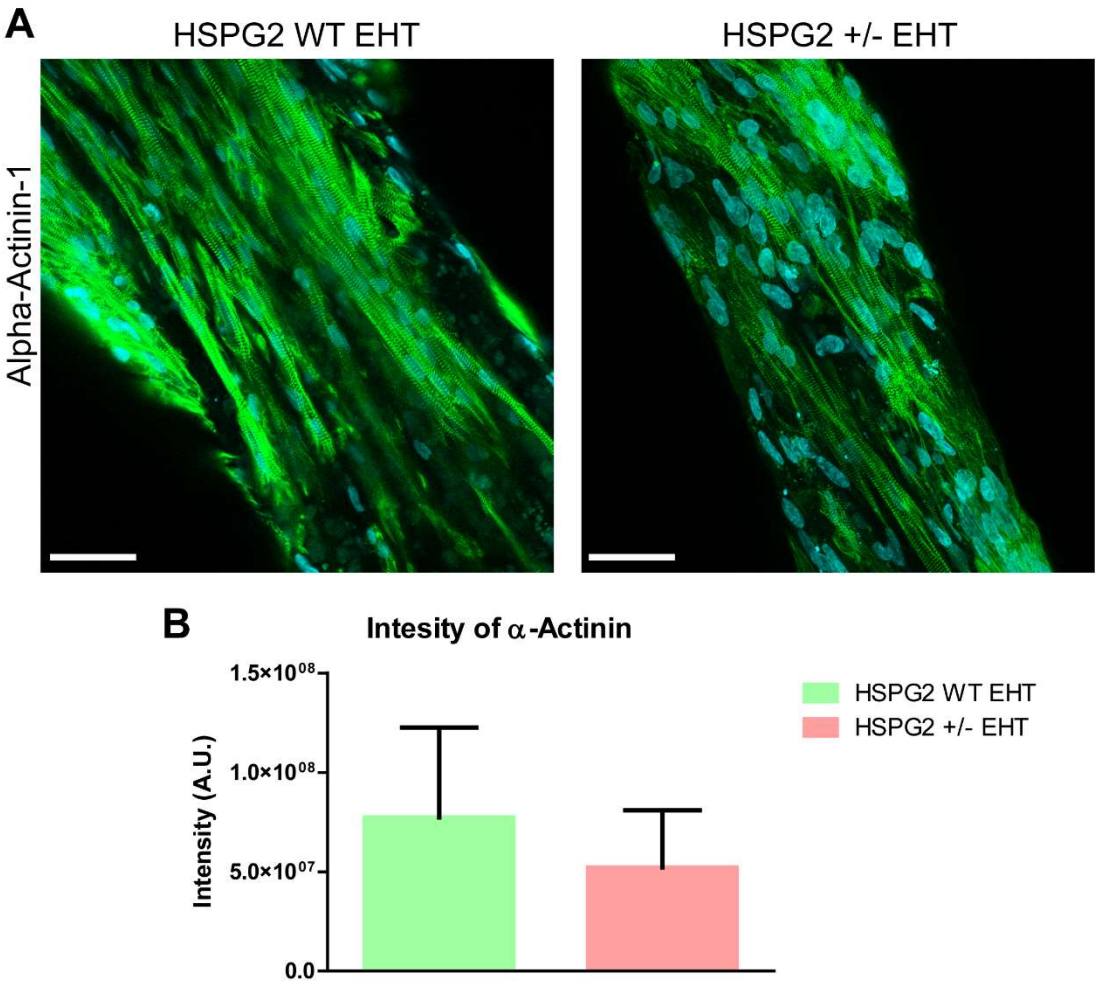


***Figure 4.37 – Confocal stacked slices of stained EHTs. (A)*** *Z-stack confocal slices were compressed creating composite images of immunostained EHTs. Blue: DAPI (nuclei) and Green: α-Actinin GFP tag. Scale bar = 50 μm (B) Quantification of α-Actinin staining intensity using ImageJ. N=3, statistical test performed using t-test. P-value <0.05 = *, <0.01 = **, <0.001 = ***.*

Immunostaining confirmed high purity cardiomyocytes throughout both WT and HSPG2$^{+/-}$ EHTs (Figure 4.37, A) and when quantified shows no significant difference in intensity of α-Actinin. Both EHTs show densely pack α-actinin positive cardiomyocytes suggesting remodelling that occurred in HSPG2 +/- EHTs is not due to cardiomyocyte number.

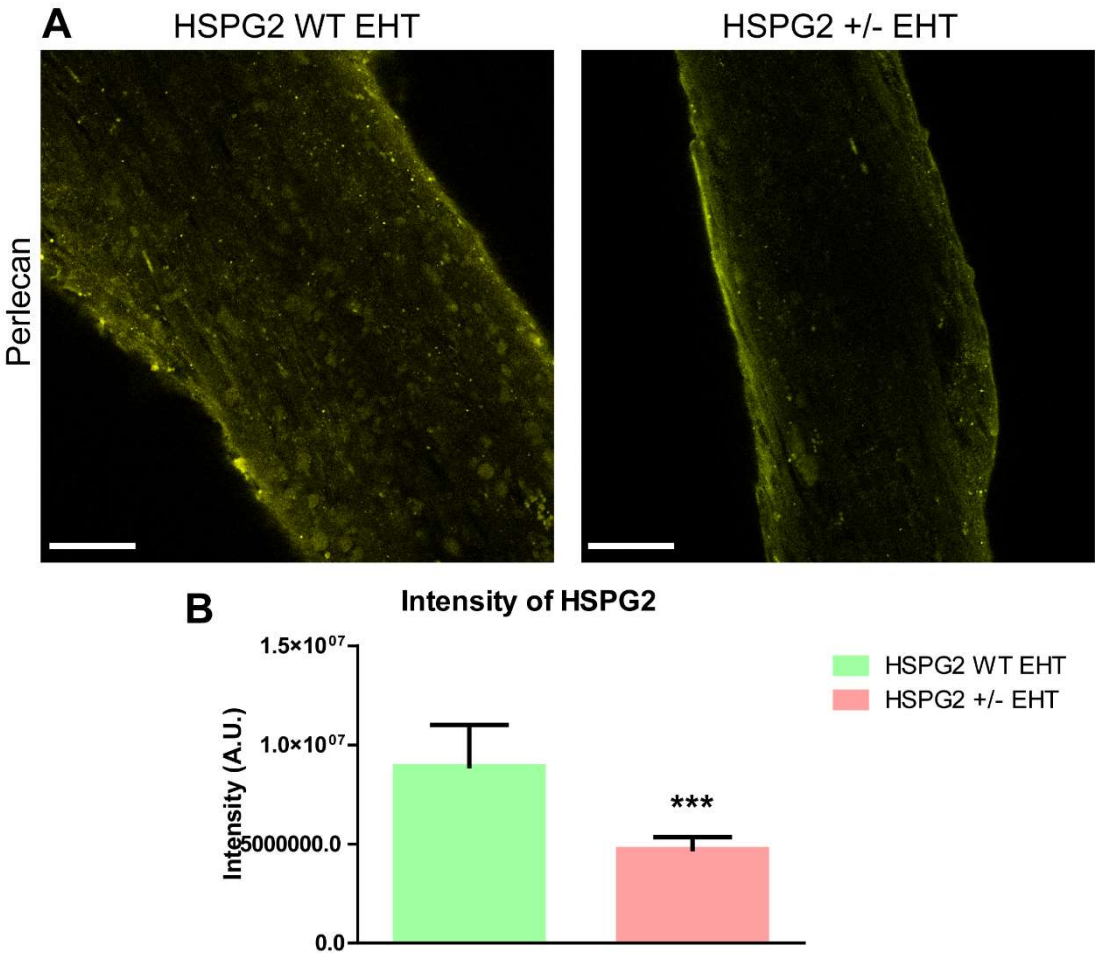


***Figure 4.38 - Confocal immunostaining images of HSPG2 stained EHTs.*** *(A) Compressed z-stack of EHTs stained with A74 HSPG2 monoclonal antibody. Scale bar = 50 µm (B) HSPG2 intensity quantification was performed on ImageJ and corrected against total cell fluorescence. N=3, statistical test performed using t-test. P-value <0.05 = *, <0.01 = **, <0.001 = ***.*

EHTs were stained with perlecan monoclonal antibody A74 to determine perlecan levels secreted throughout EHTs (Figure 4.38). Quantification confirmed increased perlecan levels two-fold higher in the WT EHTs than the HSPG2$^{+/-}$ EHTs. Despite the remodelling the HSPG2$^{+/-}$ EHTs underwent, there does not appear to be an increase in perlecan protein levels.

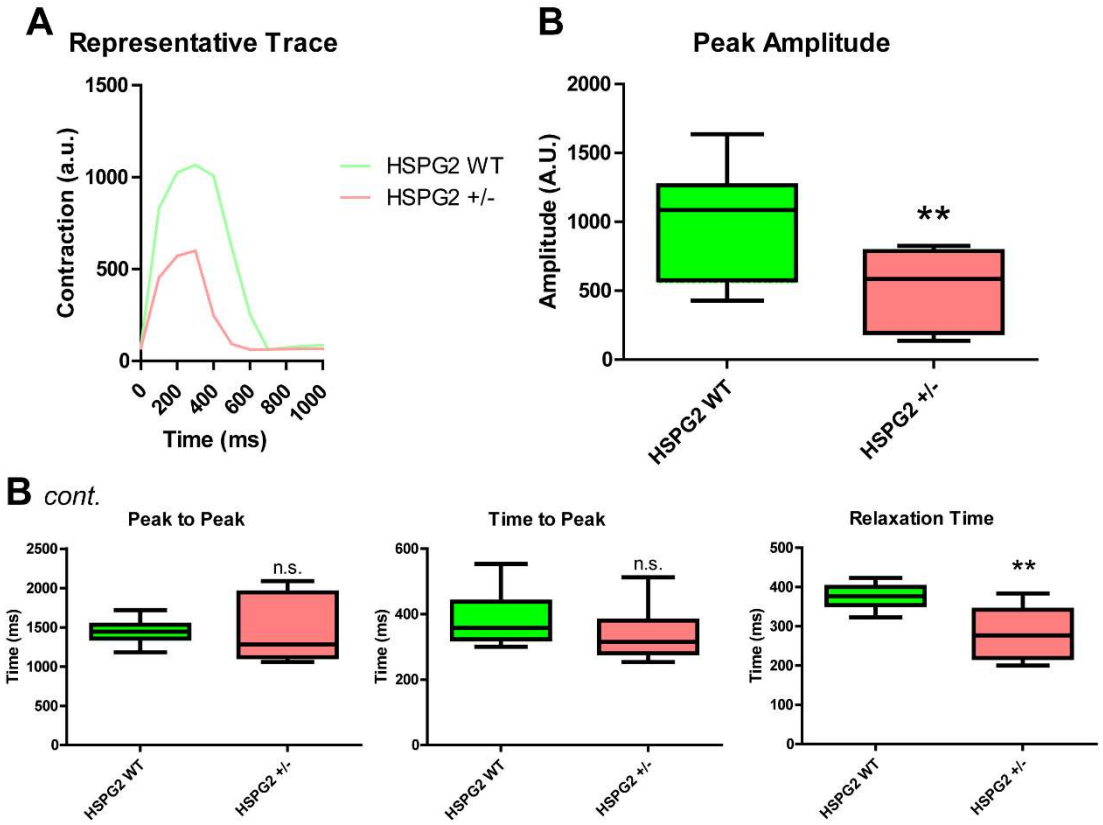


***Figure 4.39 – Contraction analysis of EHTs.*** *(A) Representative trace of contracting EHTs showing contraction force (a.u.) over time. MUSCLE MOTION outputs from contraction analysis showing peak amplitude, peak to peak, time to peak and relaxation time of both WT and HSPG2+/- EHTs. WT n=16, HSPG2 +/- n=11, statistical test performed using t-test. P-value <0.05 = *, <0.01 = **, <0.001 = ***.*

Using the ImageJ plugin MUSLCEMOTION (Sala et al., 2018) analysis of EHT contraction can be performed. $HSPG2^{+/-}$ EHTs show an overall reduced contraction amplitude and shorter contraction shown by a representative trace (Figure 4.39, A). Calculating the peak amplitude of each EHT show $HSPG2^{+/-}$ EHTs have an attenuated peak amplitude compared to the $HSPG2^{WT}$ (Figure 4.39, B). No difference is seen between the time-to-peak, and peak-to-peak time, mostly due to the variation in peak-to-peak time seen in $HSPG2^{+/-}$ EHTs. The relaxation time of each contraction show $HSPG2^{+/-}$ EHTs to have a faster relaxation that the WT EHTs, implying an overall sharper and weaker contraction.

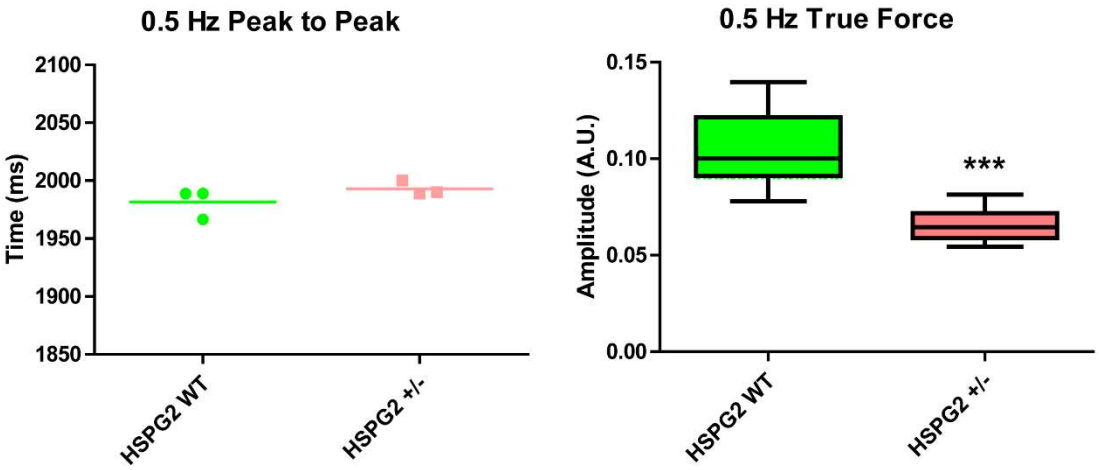


***Figure 4.40 – EHTs paced at 0.5 Hz.*** *EHTs were paced at 0.5Hz, MUSCLE MOTION was used to calculate frequency as peak-to-peak time and true force calculated for each contraction through ImageJ. N=3, true force technical readings per sample = 11, statistical test performed using t-test. P-value <0.05 = *, <0.01 = **, <0.001 = ***.*

To calculate the contraction force of the WT and HSPG2 deficient EHTs pacing at 0.5 Hz was performed at the Francis Crick Institute by Lorenza Tsansizi. MUSCLEMOTION was initially performed to analyse contraction videos and show both EHTs contracted at the same pace (Figure 4.40). Following this analysis true force contraction was calculated based on deflection distance of silicone posts during relaxed and contracted states of each EHT. The WT EHTs again output a higher contraction force than HSPG2$^{+/-}$ EHTs, similar to what was seen in the non-paced EHTs.

The above experiments lead the findings that a reduction in *HSPG2* creates a less functional cardiomyocyte. RNA sequencing suggested *HSPG2* limited the cardiomyocyte maturation with many of the DEGs highlighted linked to cardiac structural genes. Metabolomic analysis of the two cell lines show how HSPG2$^{+/-}$ cells have a higher reliance on glycolysis and less capability to metabolise fatty acids. When HSPG2$^{+/-}$ CMs are put into EHTs they undergo cardiac remodelling and show a reduced contraction force. Since the activation of cardiac fibroblasts has been shown to induce cardiac remodelling (Thomas et al., 2022) I also wanted to investigate the role of HSPG2 in cardiac fibroblasts.

### 4.7. Differentiation of WT and HSGP2$^{+/-}$ cardiac fibroblasts

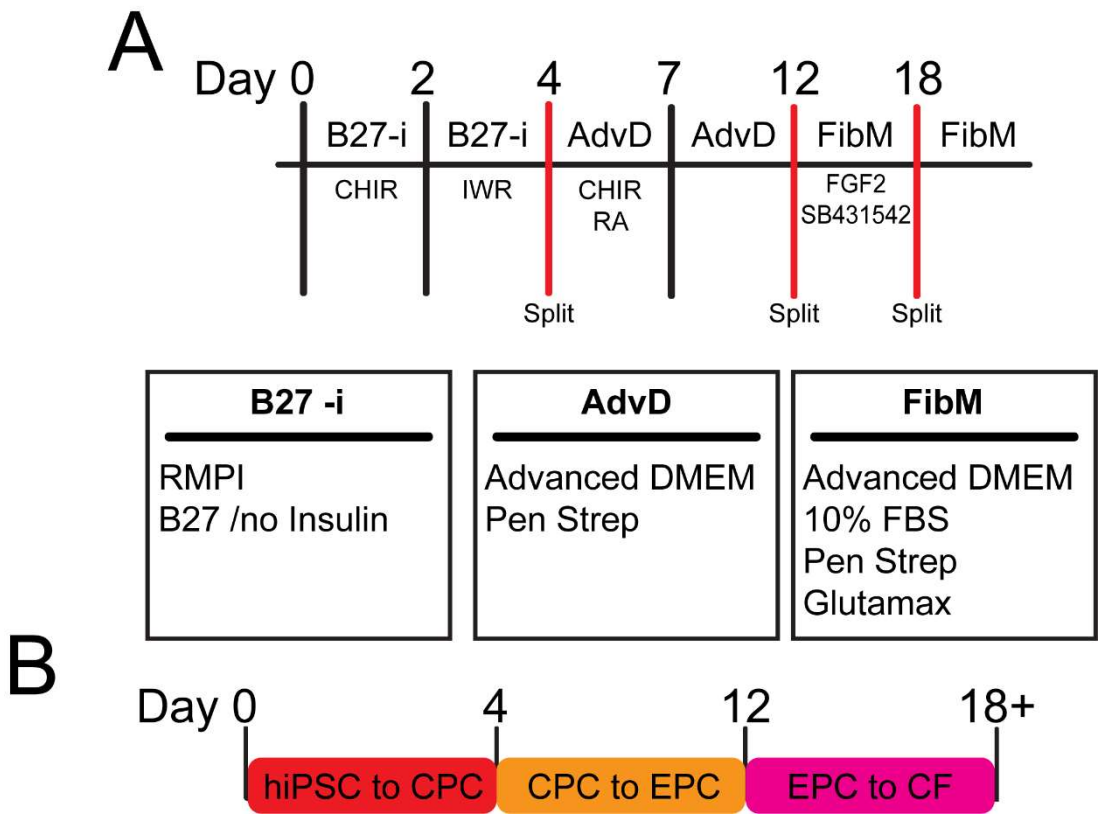


***Figure 4.41 – Cardiac fibroblast differentiation protocol.*** *(A) Outline of media added at each timepoint throughout the cardiac fibroblast (CF) differentiation. (B) Overview of cellular processes occurring between key stages of differentiation.*

Utilizing a cardiac fibroblast differentiation protocol from Zhang et al 2019 hiPSCs were differentiated into cardiac fibroblasts (Figure 4.41) (H. Zhang et al., 2019). hiPSCs are initially differentiated to cardiac progenitor cells (CPCs) before being split and reseeded. The CPCs then differentiate to epicardial progenitor cells (EPCs) using CHIR and RA, these cells are then reseeded before final differentiation to CFs using FGF-2 and TGFβ inhibitor SB431542 (Figure 4.41, B).

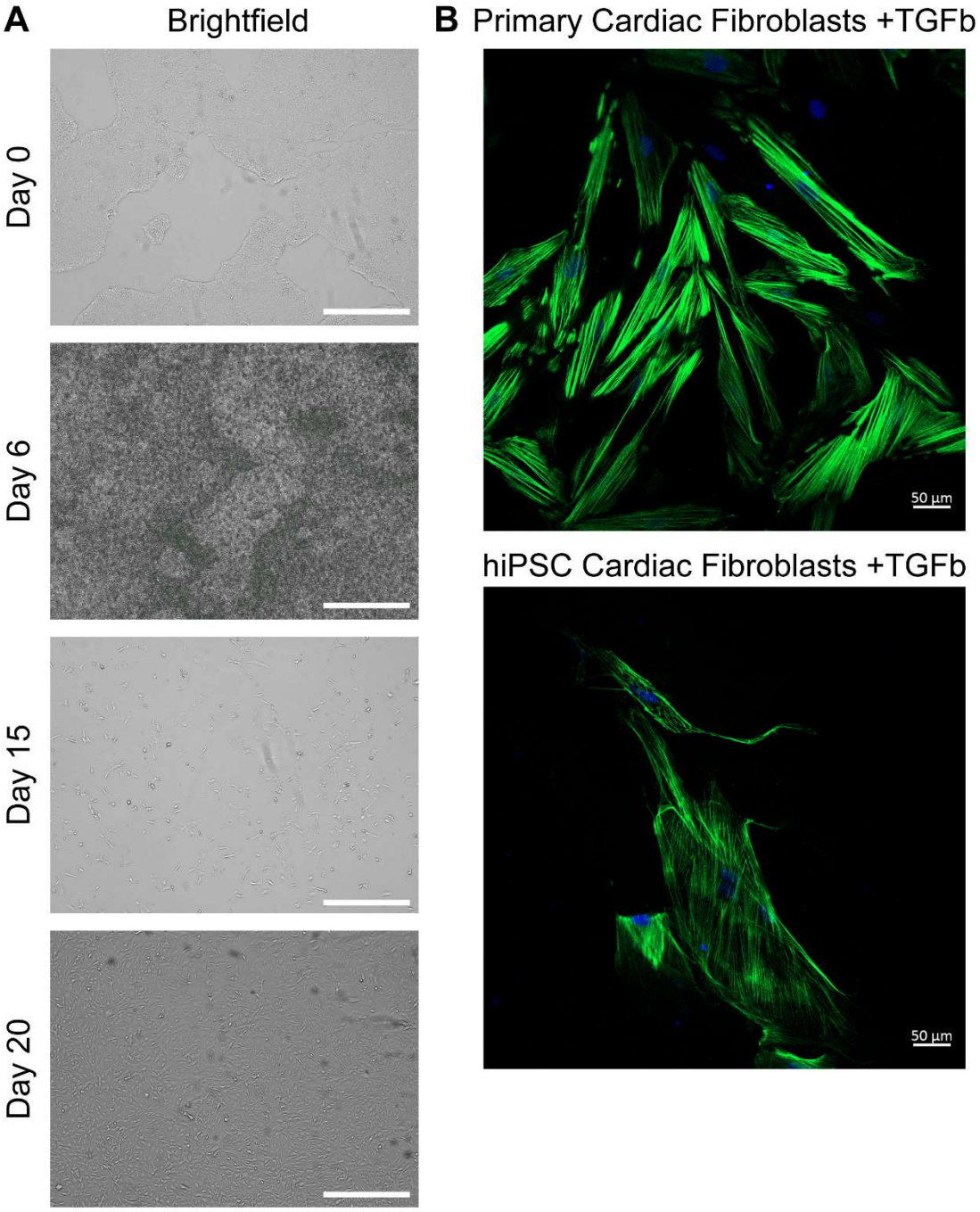


***Figure 4.42 – CF differentiation images and activation to MFs with TGFβ.*** *(A) Brightfield images of timepoints throughout CF differentiation. Scale bar 600 µm. (B) Confocal immunostaining of αSMA positive MFs after TGFβ activation in primary and hiPSC-CFs. αSMA (Green), DAPI (blue) and scale bar at 50 µm.*

Photos were taken throughout the cardiac fibroblast's differentiation, and by day 15 the fibroblast morphology becomes evident (Figure 4.42, A). Cells were then activated to myofibroblasts (MFs) via use of TGFβ and stained with αSMA to confirm the presence of stress fibres (Figure 4.42, B). Both primary and hiPSC-CFs form αSMA positive stress fibres indicative of CF activation to a MF, further confirming the generation of characteristic CF and MF from hiPSCs. I next performed qRT-PCR on a panel of genes to confirm the levels of the markers were genotypically closer to primary cardiac fibroblasts than to skin fibroblasts or cardiomyocytes.

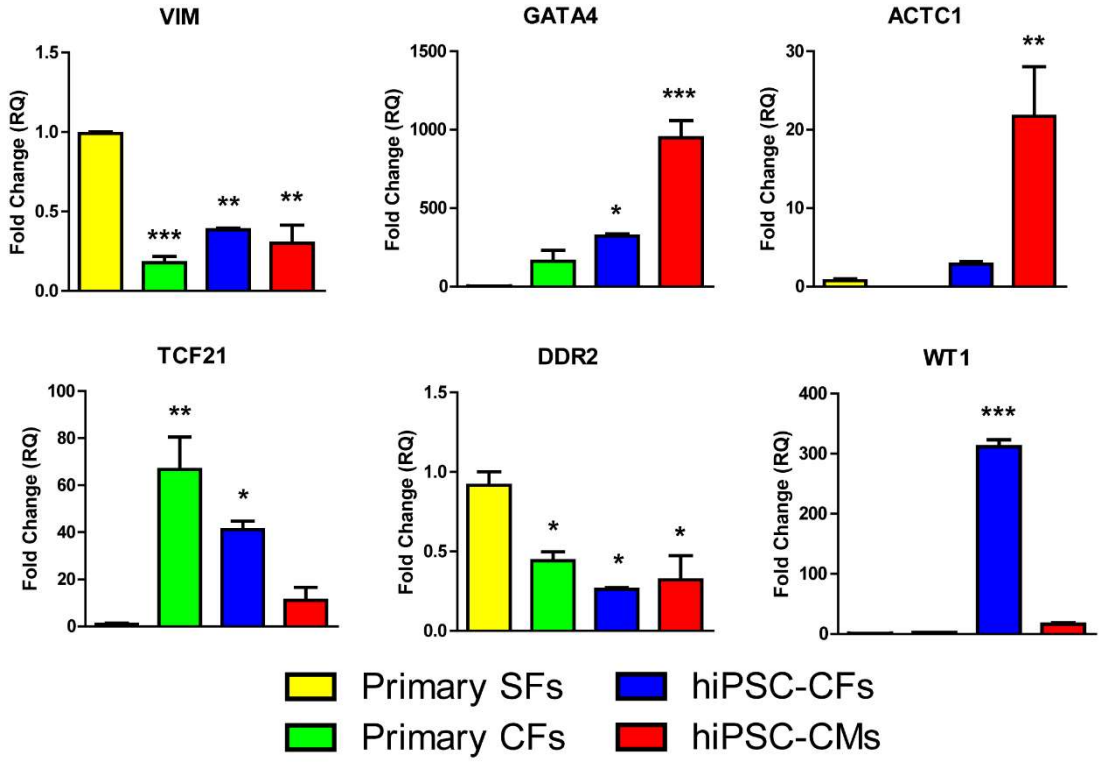


***Figure 4.43 – Gene panel of markers looking at expression levels between differentiated cell types.*** *qRT-PCR was performed on primary skin and cardiac fibroblasts and iPSC derived cardiac fibroblasts and cardiomyocytes. Expression was compared against primary skin fibroblasts. N=3, statistical test performed using Tukey test. P-value <0.05 = *, <0.01 = **, <0.001 = ***.*

The genes selected would identify differences between each of the cell types confirming the generation of characteristic CFs instead of generic SFs. The

panel of genes selected include *VIM, GATA4, ACTC1, TCF21, DDR2* and *WT1* (Figure 4.43). Primary SFs show the highest level of *VIM* expression over primary CFs and hiPSC-CFs implying a difference between the cell types, both primary CFs and hiPSC-CFs express similar levels of *VIM*. *GATA4*, a cardiac marker, is expressed in all cardiac cell types but shows no expression in primary SFs. *ACTC1* is a cardiomyocyte marker and shows the highest expression in cardiomyocytes, interestingly its expression is also found lowly in hiPSC-CFs but not in primary CFs. *TCF21* is a cardiac fibroblast marker where its expression is highest in both primary CFs and hiPSC-CFs, cardiomyocytes have the lowest level of *TCF21* expression out of the four cell types. *DDR2* is a marker found in SFs, its expression is found highest primary SFs while no expression was found in any of the cardiac cells. *WT1* is suggested to be a cardiac fibroblast specific marker (Fu et al., 2020), here we show its highest expression is found in the hiPSC-CFs while both primary CFs and hiPSC-CMs express similar levels.

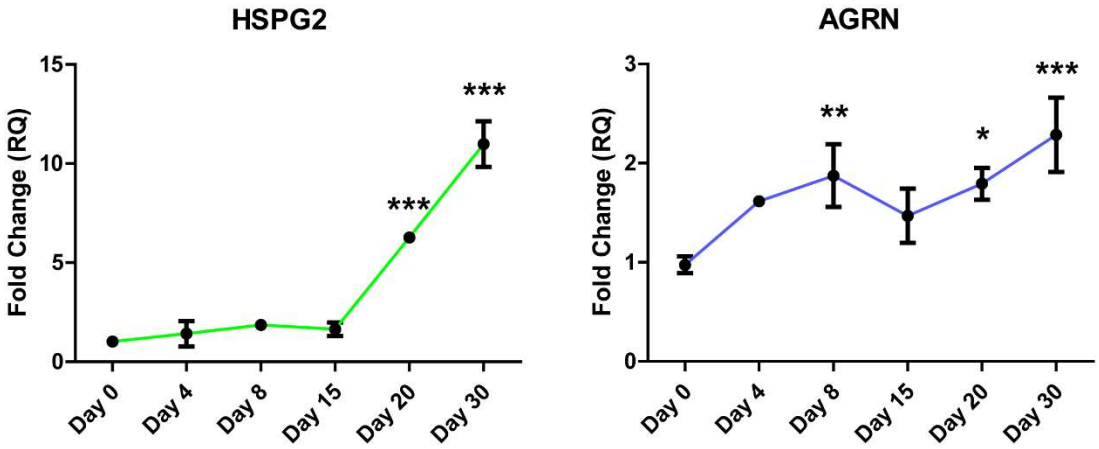


***Figure 4.44 - Gene expression of HSPGs over cardiac fibroblast differentiation.*** *qRT-PCR performed on cDNA samples collected of cardiac fibroblast differentiation timeline for HSGP2 and AGRN. N=3, statistical test performed using t-test. P-value <0.05 = *, <0.01 = **, <0.001 = ***.*

I next wanted to analysis the expression of key HSPGs *HSPG2* and *AGRN* over the CF differentiation. Timepoints at day 0, 4, 8, 15, 20 and 30 were taken and qRT-PCR performed on these samples showing the expression of *HSPG2*

only increase after the differentiation is finished (Figure 4.44). At day 20 expression of *HSPG2* is statistically increased to 6.28-fold change compared to hiPSCs, this is then further increased over the next 10 days to 10.98-fold change. The expression of *AGRN* follows an upwards trend over the differentiation showing statistical increases at day 8, 20 and 30 showing *AGRN* may be more important for differentiation and proliferation while *HSPG2* is prioritised in fully differentiated CFs.

After confirmation of generating hiPSC specific CFs and results confirming the hiPSC-CF expressed *HSPG2* mRNA in a similar trend to hiPSC-CMs, I wanted to investigate differences between $HSPG2^{WT}$ and $HSPG2^{+/-}$ CFs. I aimed at investigating proliferative capabilities, activation, ECM secretion and any metabolic changes between CF lines.

## 4.8. Differences between WT and HSPG2$^{+/-}$ hiPSC-CFs

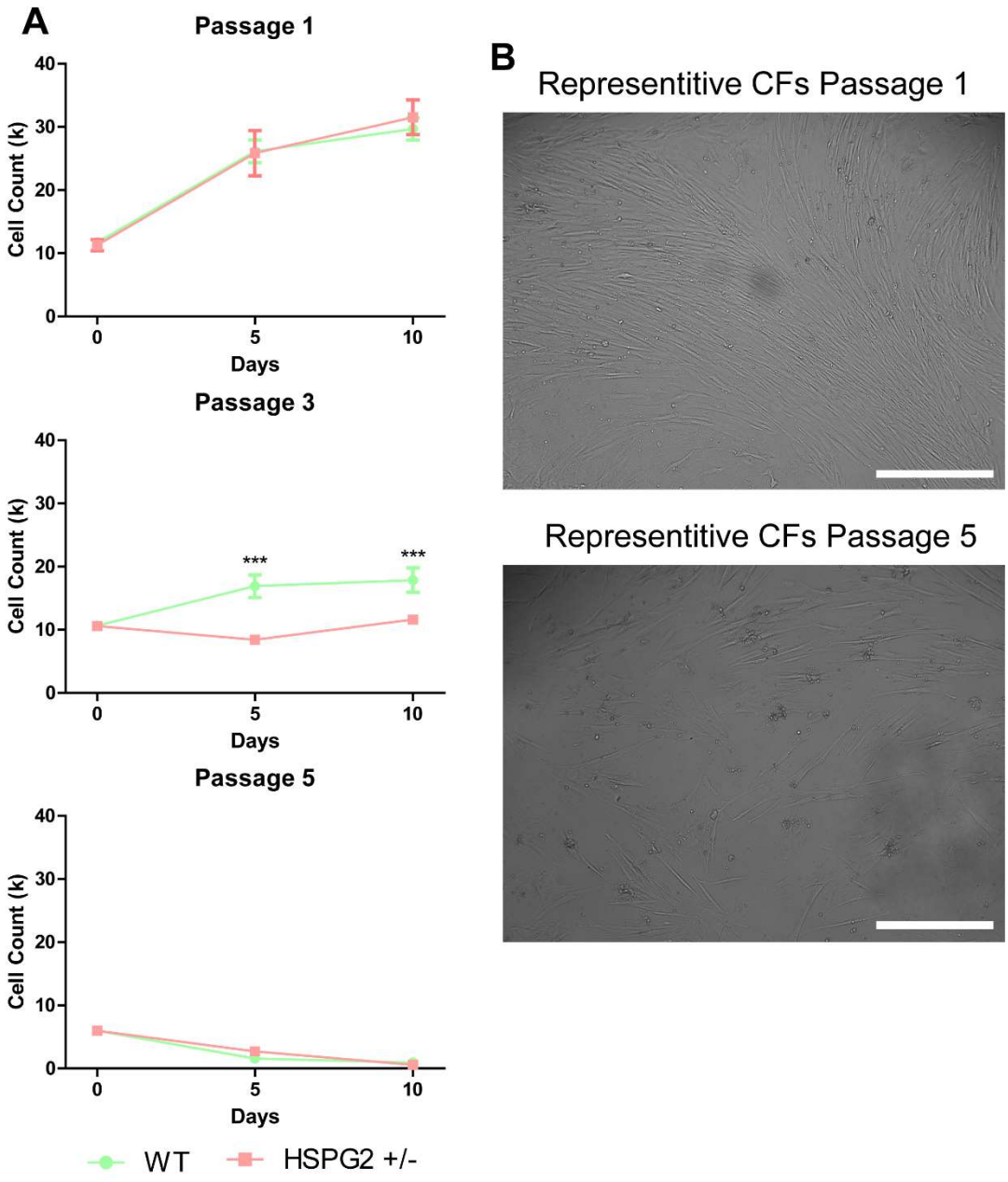


***Figure 4.45 – Growth curves of WT and HSPG2$^{+/-}$ hiPSC-CFs over passages.*** *(A) Cell titre quantified cell count of hiPSC-CFs over 10 days at each passage number. (B) Representative brightfield image of hiPSC-CFs at P1 compared to P5. Scale bar at 600 µm. N=1, Technical N=3, statistical test performed using multiple t-test. P-value <0.05 = *, <0.01 = **, <0.001 = ***.*

Upon differentiating both cell lines to hiPSC-CFs growth curves were performed every 5 days for 10 days at passage 1, 3 and 5 (Figure 4.45, A). No

difference was seen between the two cell lines in passage 1 hiPSC-CFs proliferative capability. This shifts in passage 3 hiPSC-CFs as WT hiPSC-CFs show increased proliferation over the 10 days while HSPG2$^{+/-}$ hiPSC-CFs become quiescent and show no changes in cell number. By passage 5 both cell lines have become unable to proliferate in culture and show a reduction in cell number over the 10 days. Representative brightfield images of hiPSC-CFs show passage 1 hiPSC-CFs in confluency while only sparsely present hiPSC-CFs remain by passage 5 (Figure 4.45, B).

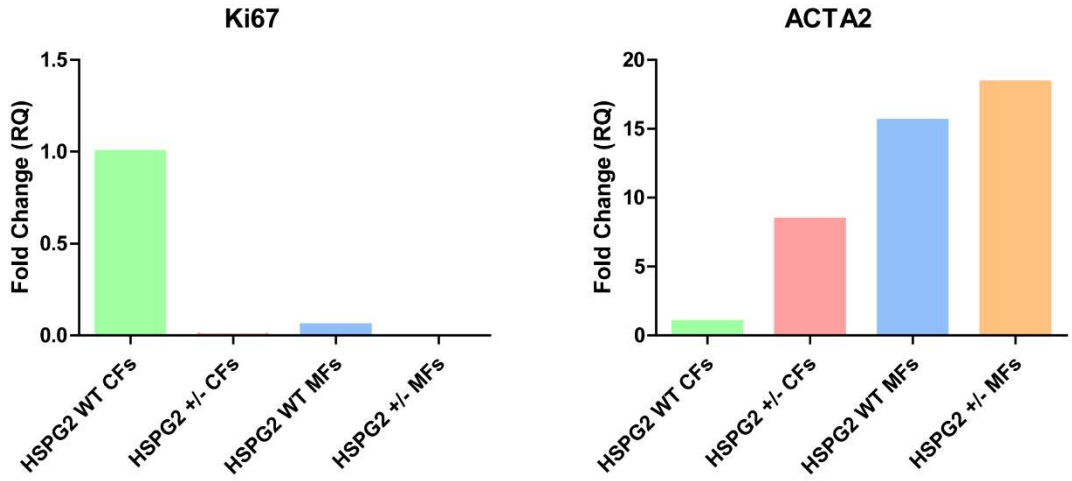


***Figure 4.46 – Markers of hiPSC-CF to MF activation.*** *Ki67 and ACTC2 qRT-PCR was performed on samples from both cell lines as either inactivated hiPSC-CFs or following TGFβ activation to MFs. N=1*

Early passage hiPSC-CFs from both cell lines were cultures with or without TGFβ to cause MF activation and compared between each other. WT hiPSC-CFs show to have the highest level of *Ki67* and the lowest of *ACTA2* implying an inactivated hiPSC-CF compared to HSPG2$^{+/-}$ CFs which follow a similar expression level to that seen in activated MFs (Figure 4.46).

One of the main functions of the hiPSC-CF is to secrete ECM and support neighbouring cells. I wanted to analyse any changes in perlecan ECM secretion between the cell lines using ImageJ plugin TWOMBLI (Wershof et al., 2021).

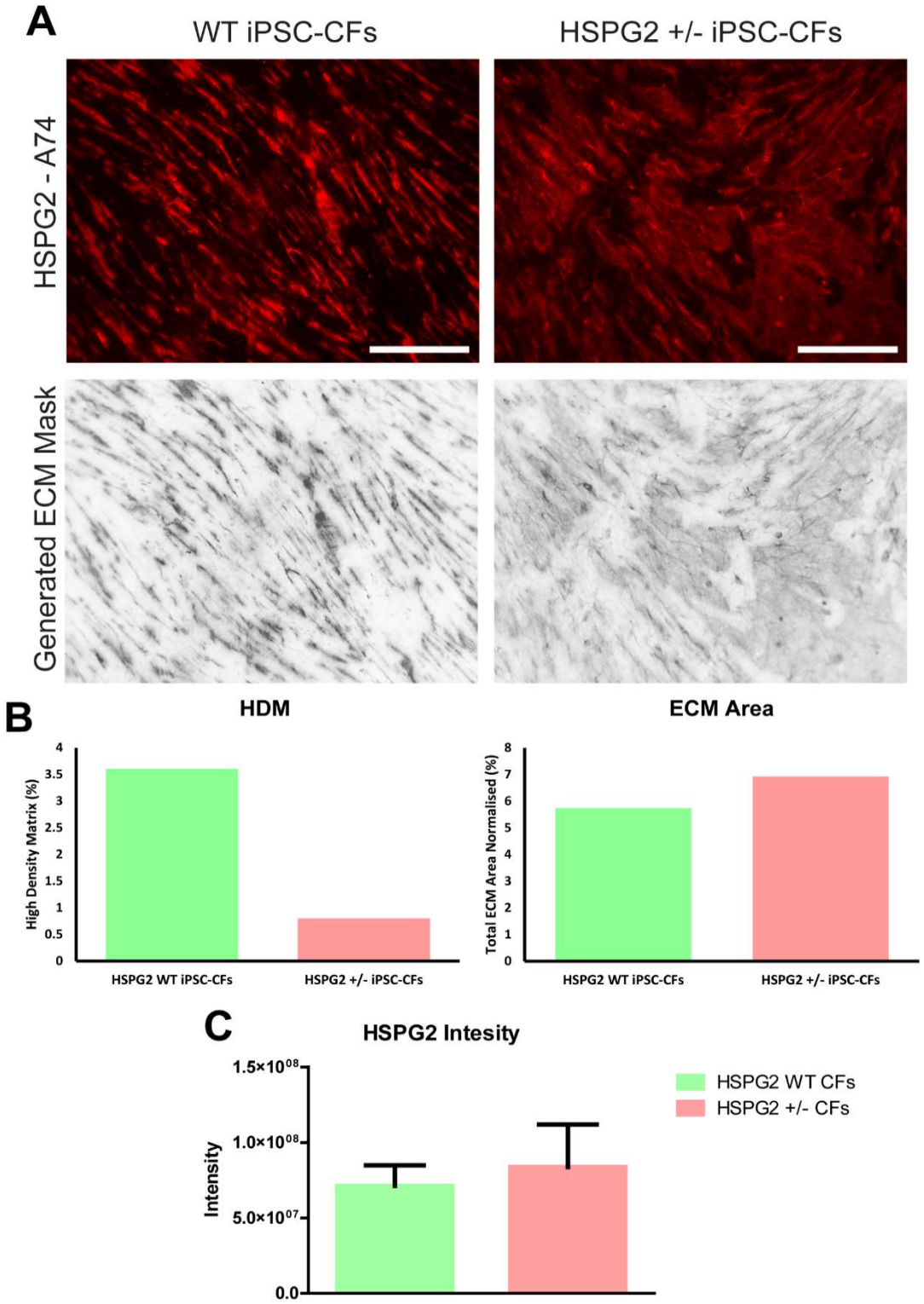


***Figure 4.47 – Analysis of perlecan ECM from hiPSC-CFs.*** *Immunostaining of perlecan secreted by WT and HSPG2+/- hiPSC-CFs including TWOMBLI ECM generated mask. (B) TWOMBLI outputs of ECM analysis. (C) Intensity of hiPSC-CF secretion of perlecan ECM, scale bar at 250 µm. N=1, intensity technical n=3, statistical test performed using t-test.*

Immunostaining was performed on WT and HSPG2$^{+/-}$ hiPSC-CFs targeting perlecan ECM, the immunostaining images were then used in the TWOMBLI pipeline to generate ECM masks (Figure 4.47, A). Outputs from TWOMBLI pipeline include high density matrix (HDM) and ECM area. The WT hiPSC-CFs are shown to have a higher density matrix than the HSPG2$^{+/-}$ CFs although both cell lines show similar values of ECM area (Figure 4.47, B). Measuring the intensity of perlecan from the immunostaining show no statistical difference between the cell lines, potentially due to the HSPG2$^{+/-}$ hiPSC-CFs still able to cover a similar area in perlecan ECM as the WT hiPSC-CFs.

Metabolic analysis was then performed on the hiPSC-CF cell lines to determine if the reduction of *HSPG2* caused a similar shift in metabolism as was seen in the hiPSC-CMs.

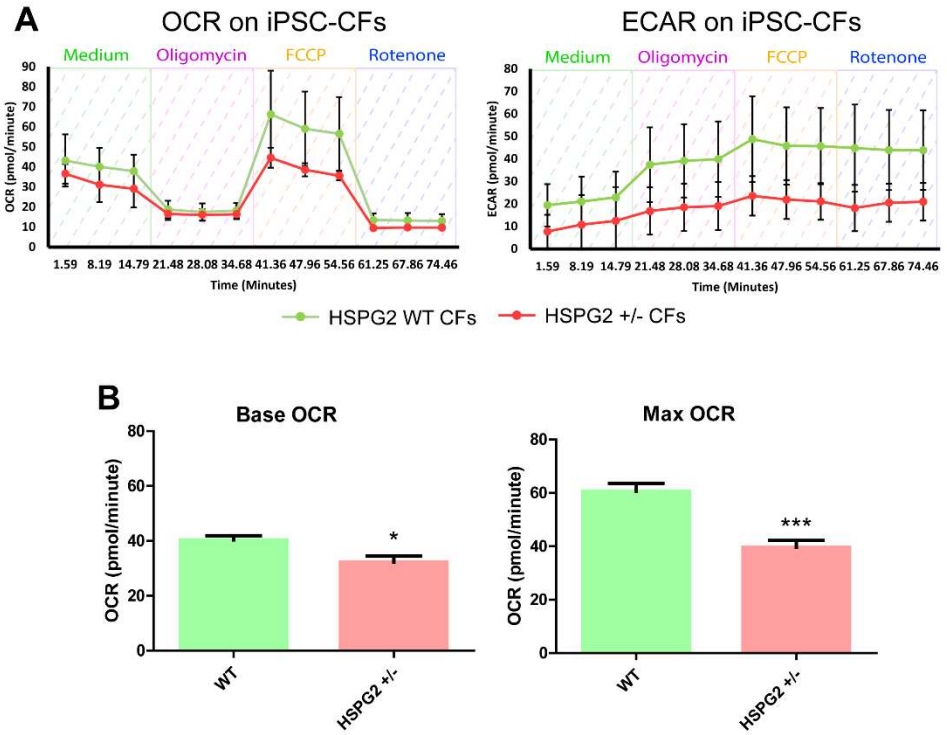


***Figure 4.48 – Seahorse OCR and ECAR of WT and HSPG2$^{+/-}$ hiPSC-CFs.*** *(A) OCR and ECAR outputs from seahorse assay of each cell line including each seahorse stage. (B) Base and maximal OCR outputs of both cell lines grouped. N=3, statistical test performed using multiple t-tests, p-value <0.05 = *, <0.01 = **, <0.001 = ***.*

Seahorse assay was performed on WT and HSPG2$^{+/-}$ hiPSC-CFs analysing changes in OCR and ECAR (Figure 4.48, A). WT CFs have a slightly higher OCR over HSPG2$^{+/-}$ hiPSC-CFs, with this difference being exacerbated when the mitochondria are stressed due to administration of FCCP (Figure 4.48, B). WT hiPSC-CFs have a higher ECAR over the seahorse assay, although due to the variation between the samples a statistical increase isn't recorded.

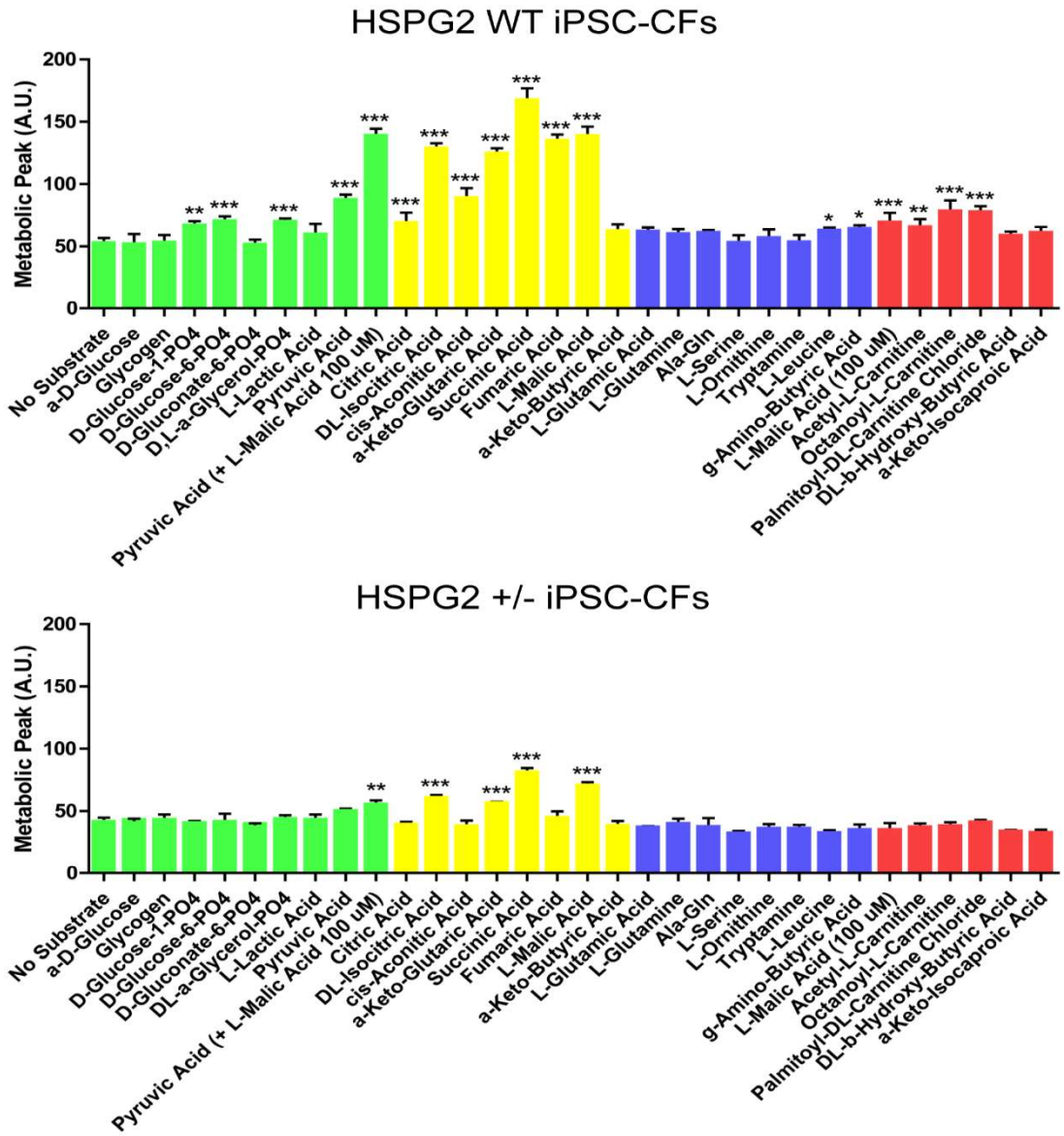


***Figure 4.49 – Mitoplate analysis of specific substrate metabolism in WT and HSPG2$^{+/-}$ CFs.*** *Individual substrate metabolism mitoplate outputs clustered into allocated metabolic pathway; glycolysis (green), TCA cycle (yellow), amino acids (blue) and fatty acids (red). N=3, statistical test performed using multiple t-tests, p-value <0.05 = *, <0.01 = **, <0.001 = ***.*

Utilising the mitoplate assay the hiPSC-CF metabolism of specific substrates can be isolated and analysed against each cell line. WT hiPSC-CFs have a statistically higher metabolism of all TCA cycle substrates and several glycolytic substrates (Figure 4.49). WT hiPSC-CFs also metabolise amino acids L-leucine and g-amino-butyric acid to a low level compared to the no substrate control. These hiPSC-CFs also show capable substrate metabolism of the three carnitines, acetyl-L, octanoyl-L, and palmitoyl-DL. When analysing the HSPG2$^{+/-}$ hiPSC-CF substrate metabolism the cells only seem to be able to metabolise several TCA cycle substrates and pyruvic acid (combined with sparking l-malic acid).

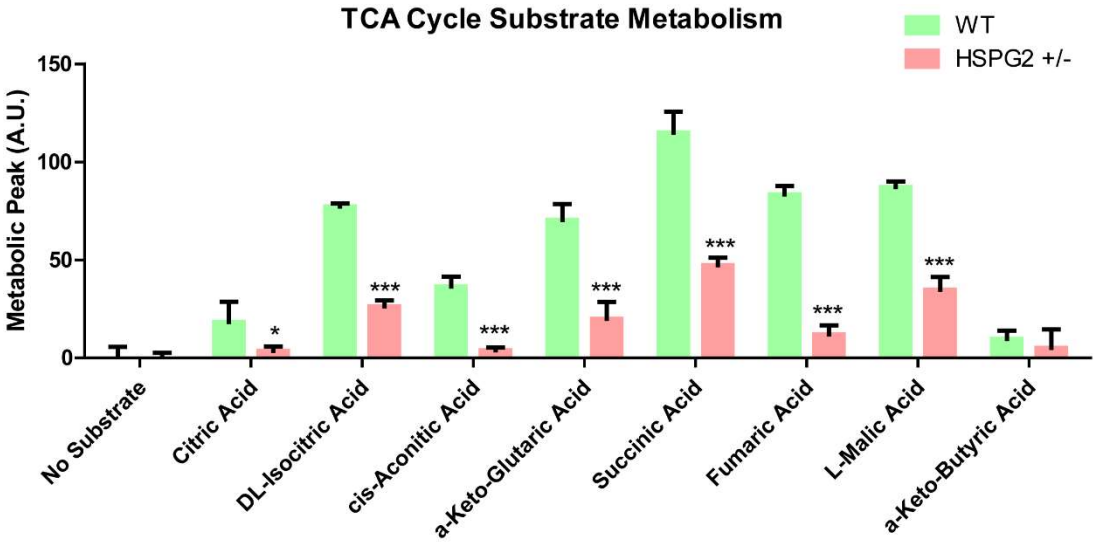


***Figure 4.50 – hiPSC-CF metabolism of TCA substrates.*** *HSPG2$^{WT}$ and HSPG2$^{+/-}$ CF peak metabolism of TCA cycle substrates after removal of no substrate control. N=3, statistical test performed using multiple t-tests, p-value <0.05 = *, <0.01 = **, <0.001 = ***.*

To investigate the differences further the TCA cycle substrates had the no substrate negated from the metabolic peak and the two cell lines were compared against each other. Results show an across the board reduction of HSPG2$^{+/-}$ hiPSC-CFs capability to metabolise TCA cycle substrates to the same extent as the WT (Figure 4.50). The substrate a-Keto-Butyric Acid is the only TCA cycle substrate whereby there is no difference found between the lines.

### 4.9. Conclusion

In this chapter I differentiated hiPSCs to both CMs and hiPSC-CFs, through qRT-PCR marker expression was investigated confirming specific CFs were generated compared to primary SFs and CMs (Figure 4.51).

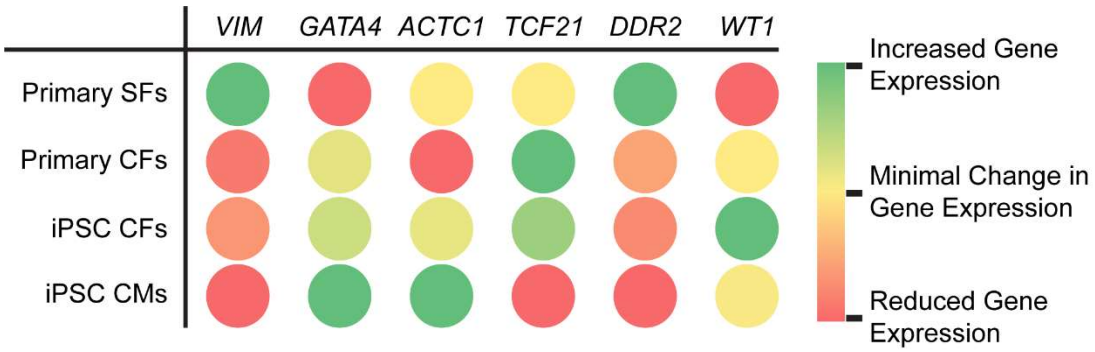


***Figure 4.51 – Summary marker panel between cell types.*** *qRT-PCR was performed on primary skin and cardiac fibroblasts and iPSC derived cardiac fibroblasts and cardiomyocytes. Expression was compared against primary skin fibroblasts and fold change used to plot heat map.*

Of the markers chosen, both hiPSC-CFs and primary CFs expressed comparable levels to each other, except *ACTC1* and *WT1*. *ACTC1* is a marker indicative of CM populations and was used to clearly separate CMs from the fibroblast populations. Interestingly, primary CFs expressed little to no *ACTC1*, unable to generate any CT values from qRT-PCR, compared to the hiPSC-CFs. This result may be due to primary CFs in prolonged storage losing cardiac specificity, or an impure differentiation of hiPSC-CFs. Despite transcription factor *WT1* being suggested as a cardiac fibroblast marker, *WT1* is also a known marker of endothelial cells and epicardial CFs (Fu et al., 2020; McGregor et al., 2018). Therefore, the hiPSC-CFs generated could be of closer origin to epicardial CFs than the primary CFs. Or the final stages of differentiation were unable to fully differentiate the epicardial progenitor cells to cardiac fibroblasts, whereby the expression of *WT1* may be attenuated to a similar level as primary CFs.

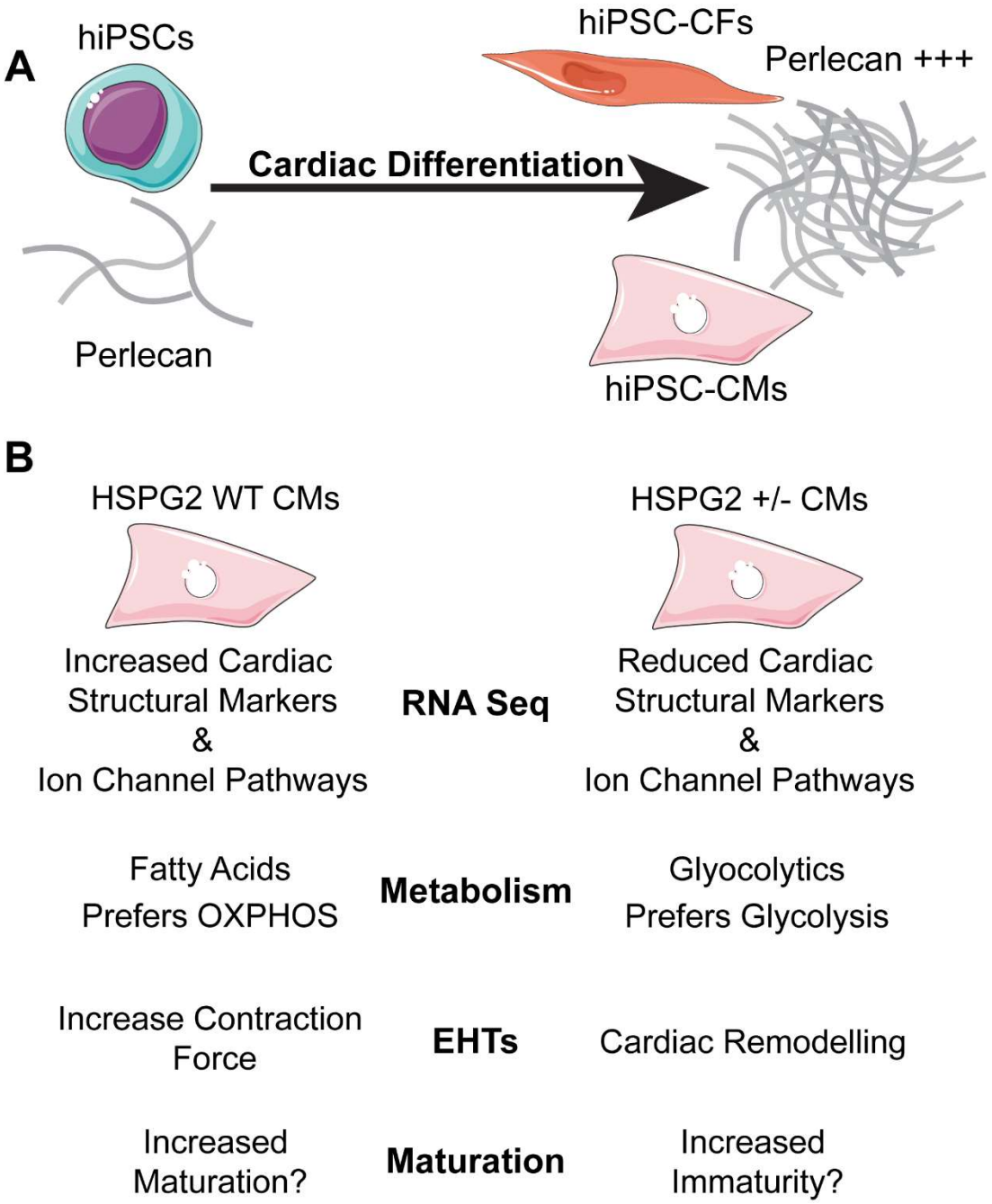


***Figure 4.52 – Summary of differences between CM cell lines.***

*HSPG2* accumulates during the differentiation of CMs, with RNA expression increasing between day 0 and day 20, and protein levels highest at day 30 CMs (Figure 4.52, A). Agrin levels are seen to be high in hiPSCs and remain at a constant level throughout, implying an initial need for agrin presence early on while perlecan expression is required later in the cardiac differentiation.

Multiple sized protein bands and variations of *HSPG2* splice variants imply different *HSPG2* transcripts may have a role in different stages of cardiac

differentiation. The full-length transcript is the most prominent variation of *HSPG2* transcripts found throughout the differentiation, the next most expressed transcript is a domain 5 containing transcript. This transcript follows the same trend as full length *HSPG2* just at a lower level. The same pattern is seen with all other transcripts, excluding one, at lower levels than the full-length transcript. Following this trend could link these transcripts together by one master regulator linked to changes in the cells over CM differentiation, or the generation of these transcripts is reliant on full length *HSPG2* mRNA being present and a fraction being cleaved to form the other transcripts. One transcript follows a different trend to the rest showing a rapid increase in transcript count to day 10 before a reduction over the following timepoints. This transcript is a domain 1/2 variation theorised to contain the SEA domain and parts of the LDL receptor but lacking any GAG attachment sites.

When differentiating HSPG2$^{+/-}$ hiPSCs to CMs there are only small differences between the perlecan deficient and WT cells until the maturation stages of differentiation (Figure 4.52, B). The sensitive and slow secretion of *HSPG2* requires prolonged culture to see the build-up of *HSPG2* in the ECM, this could explain why the effect of *HSPG2* is only seen in later stages of differentiation. Due to a *HSPG2* knock out there are 11 DEGs found consistently changed over early cardiac differentiation. Looking closer at each of these genes we can theorise their link to *HSPG2*. *NNAT* and *KCNC3* are linked to regulation of ion channels (Braun et al., 2020a; Khare et al., 2018). *SLC15A4* involved in peptide transmembrane transporter activity and mitochondrial integrity (Katewa et al., 2021; Kobayashi et al., 2021). *RBM46* is involved in mRNA stabilisation and binding activity (Qian et al., 2022). *GLT1D1* is involved in glycosyltransferase activity (X. Liu et al., 2020), this gene appears at a higher level in HSPG2$^{WT}$ cells but over the differentiation expression becomes more similar to HSPG2$^{+/-}$ cells. *TMSB4Y* has links to ERK signalling pathways and interestingly roles in actin monomer sequestering and binding (Öner et al., 2020; Xiong et al., 2022). Four of the genes consistently changed were downregulated in HSPG2$^{WT}$ cells compared to HSPG2$^{+/-}$ cells, these include *ZNF676*, *SVIL-AS1*, *MGMT* and *TRIM61*. Both *ZNF676* and *MGMT* are linked to regulation of DNA binding transcription factor activity and DNA repair (Han

and Kamdar, 2018; Mangino et al., 2012).*SVIL-AS1* is a long noncoding RNA found to suppress lung adenocarcinoma cell proliferation (Acha-Sagredo et al., 2020). Finally, *TRIM61* is predicted to be involved in protein ubiquitination and the innate immune response (Versteeg et al., 2013).

The main differences found between the two cell lines as day 30 CMs are cardiac structural and ion channel pathways, essential for CM maturation. To further analyse metabolic differences between the two lines I employed the use of mitoplates. Mitoplates show the HSPG2$^{+/-}$ cells have a higher reliance on glycolysis and struggle to metabolise fatty acids to the same extent the HSPG2$^{WT}$ cell can. The final day 30 CMs show how HSPG2$^{+/-}$ CMs are overall less metabolically active compared to the HSPG2$^{WT}$ CMs, more indicative of an immature CM. To reconfirm metabolic differences between the cell lines day 30 CMs were analysed using the seahorse assay. Results from the seahorse further suggested a higher reliance on glycolytic metabolism in the HSPG2$^{+/-}$ CMs than the WT CMs, this reliance is a sign of immaturity in the CMs.

When putting CMs into EHTs the HSPG2$^{+/-}$ EHTs underwent cardiac remodelling, they became elongated and thinner than the WT counterparts. This remodelling could be the same as what was seen in *HSPG2* deficient mice where cardiac remodelling causes a weakened basement membrane. Both EHTs were densely packed with CMs but the HSPG2$^{+/-}$ show a lower perlecan intensity through immunostaining. Pacing the EHTs and calculating true force show the HSPG2$^{WT}$ EHTs can produce a higher force than the HSPG2$^{+/-}$ EHTs at both 0.5 and 1 Hz.

Both cell lines can be differentiated to hiPSC-CFs, become quiescent and lose proliferative capabilities over prolonged culture, while the HSPG2$^{+/-}$ hiPSC-CFs appear to do this at a faster rate and suggest a more MF genotype based on upregulated MF markers (*ACTA2*). Analysing the perlecan ECM secretion in both cell lines revealed the HSPG2$^{WT}$ hiPSC-CFs are able to produce a perlecan high density matrix. This differs from the HSPG2$^{+/-}$ hiPSC-CFs which can produce a similar perlecan matrix area, but they are unable to produce the

same high-density matrix as the WT. Although performing perlecan immunostaining intensity quantification shows no difference in the levels of perlecan in either cell types of hiPSC-CF ECM.

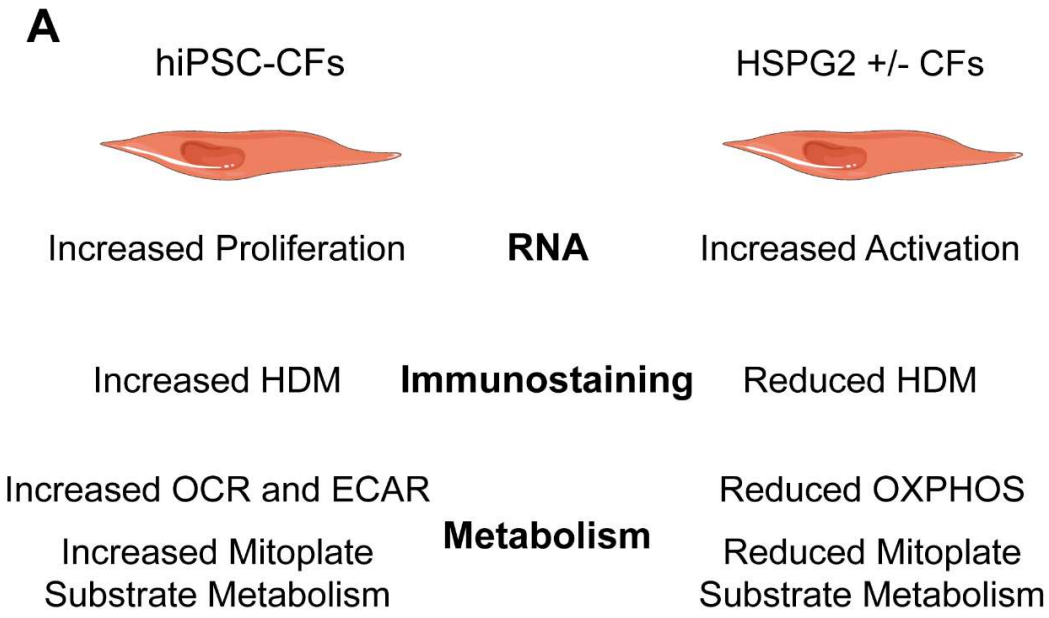


***Figure 4.53 - Summary of differences between CF cell lines.***

Analysing the hiPSC-CF metabolism in both cell lines a similar trend is seen as was in the hiPSC-CMs, the HSPG2$^{+/-}$ CFs are unable to maintain the same level of metabolic function as the HSPG2$^{WT}$ CFs, this is displayed in both mitoplate data and seahorse assays (Figure 4.53). Seahorse assay confirms a slight reduction in the HSGP2$^{+/-}$ CFs mitochondrial OCR, but when stressed using FCCP the discrepancy between the two cell lines is exacerbated, showing the HSPG2$^{+/-}$ hiPSC-CFs mitochondria are unable to appropriately respond. Variation between the two lines ECAR doesn't allow us to draw statistical differences although the WT hiPSC-CFs show a higher level throughout compared to the HSPG2$^{+/-}$. Analysing TCA cycle substrate metabolism of both WT and HSPG2$^{+/-}$ hiPSC-CFs show how HSPG2 deficient hiPSC-CFs are unable to metabolise any TCA cycle substrates to the same level as WT, except a-Keto-Butyric acid which neither cell type appears to metabolise.

This chapter reiterated the importance of HSPG2 in the cardiac environment, with HSPG2 having a major role in CM maturation and remodelling, while also affecting metabolism in both hiPSC-CMs and hiPSC-CFs.

# 5. Perlecan in inflammatory response and wound healing response

## 5.1. Introduction

After cardiac injury, apoptotic and necrotic cardiomyocytes release chemokines, initiating an inflammatory response cascade. This cascade proceeds, activating quiescent cardiac fibroblasts (CFs) to a pro migratory cell type (Fang et al., 2015; Frangogiannis, 2015). Activated CFs migrate to the wound site to undergo initial stages of cardiac ECM remodelling (W. Zhao et al., 2020). Perlecan has been identified to be a promigratory ECM component. Nakamura shows how perlecan is essential for the migration of vascular endothelial cells and mesenchymal stem cells but hinders smooth muscle cell (SMC) migratory capabilities (Nakamura et al., 2014). Lin et al shows fibroblasts isolated from Schwartz-Jampel syndrome patients have an impaired migratory capability, although a normal rate of proliferation (Lin et al., 2021b). These investigations into the migratory role of *HSPG2* confirms a cell specific function, with further investigation required into its role in the migration of cardiac cell populations.

During the initial remodelling process, macrophages secrete pro-inflammatory cytokines while removing necrotic cells (Fang et al., 2015). Under the prolonged presence of pro-inflammatory mediators and mechanical stresses, the activated CFs can transdifferentiate to a myofibroblast (MF). The leading role of the MF is ECM secretion, remodelling, and wound closure. One of the main inflammatory cytokines involved in MF transdifferentiation is TGFβ (Ivey and Tallquist, 2016b; Travers et al., 2016). A consistent presence of inflammatory factors, such as TGFβ, maintains MFs in the wound site leading to an overproduction of ECM build-up and eventually, cardiac fibrosis (Thomas and Grisanti, 2020). As well as activating MFs, TGFβ has been shown to interact and increase *HSPG2* expression. TGFβ causes the upregulation of

*HSPG2* via transcriptional activation of an upstream *HSPG2* promotor containing NF-1 transcription factors (Iozzo et al., 1997; Warren et al., 2014). Activated MFs secrete an increased range of ECM components, including collagens and perlecan into the wound site (Travers et al., 2016). TGFβ is bound to the ECM in the wound site and the presence of this maintains the presence of pro-fibrotic MFs (Hinz, 2015). As such, it is anticipated that *HSPG2* is increased in activated MFs, due to the increased presence of TGFβ, along with a higher secretion of perlecan in the matrix after TGFβ treatment.
In this chapter I aim to use perlecan deficient stem cells in a disease model of cardiac fibrosis and wound healing. Cardiac fibrosis is the result of increased ECM production and deficient matrix degradation. The perpetual build-up of ECM leads to cardiac defects including arrhythmias, electrophysiology interference and contractile dysfunction (Berk et al., 2007; Travers et al., 2016). Most models of cardiac fibrosis involve the use of in vivo mouse models, simulating a pro-fibrotic response through either myocardial infarction or chemical induction with treatments such as aldosterone, angiotensin II, or isoproterenol (Sun and Weber, 2005). Due to cost and time, drug screening on mouse models of cardiac fibrosis is inefficient, compared to the cost of in vitro cell models (Lee et al., 2019). Currently hiPSC models of cardiac fibrosis are being developed for rapid drug screening along with further investigation into fibrotic responses and mechanical properties of fibrotic scar tissue (Iseoka et al., 2021; Mastikhina et al., 2020).

Before generating an hiPSC model of cardiac fibrosis in which the role of *HSPG2* can be studied, I first wanted to investigate the response of hiPSC cardiac cell populations to the inflammatory cytokine, TGFβ. Specifically I wanted to investigate the response in *HSPG2* expression. Following this, I would utilise hiPSC cardiac co-cultures and aim to induce a fibrotic response using both physical and chemical insults, a model in which the role of *HSPG2* could be interrogated.

## 5.2. Effect of TGFβ on hiPSC CFs and CMs

I initially aimed to induce a stress response in both hiPSC CMs and CFs through TGFβ stimulation to determine if the *HSPG2* response was similar to that shown in the literature.

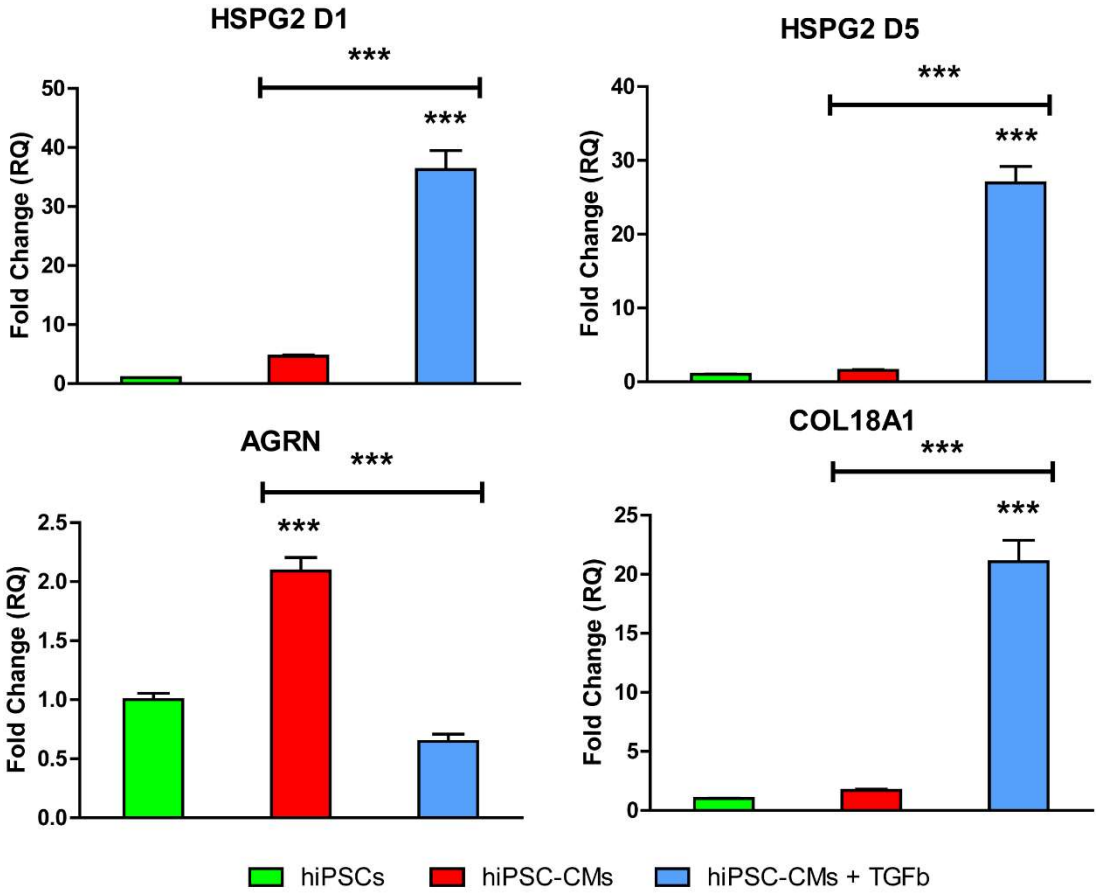


***Figure 5.1 – qRT-PCR expression of HSPGs on hiPSC-CMs after TGFβ.*** *Relative fold changes of HSPGs in cDNA from hiPSC-CMs (red) and hiPSC-CM after TGFβ treatment (blue) compared against hiPSCs (green). N=1, Technical N = 3. Statistical test performed on SD using Tukey Test. P-value <0.05 = *, <0.01 = **, <0.001 = ***.*

CMs were treated with 10mM TGFβ for 4 days before RNA extraction and cDNA synthesis was performed. I initially looked at the expression of HSPGs of CMs and CMs after TGFβ treatment compared to hiPSCs (Figure 5.1). The untreated CMs show an increase in *HSPG2* domain 1 (D1) expression (4.6-fold change) compared to hiPSCs while after the addition of TGFβ this is statistically amplified to 36.3-fold change. Expression of *HSPG2* domain 5 (D5)

and *COL18A1* follow the same expression profile, with CMs expressing slightly more *HSPG2* D5 (1.6-fold change) and *COL18A1* (1.7-fold change) than hiPSCs. Both *HSPG2* D5 and *COL18A1* are statistically increased after the addition of TGFβ (*HSPG2* D5-26.9 and *COL18A1*-21.1-fold change) compared to both hiPSCs and CMs. The expression of *AGRN* is statistically increased to 2.1-fold in CMs compared to hiPSCs, although following TGFβ treatment expression is attenuated to 0.65 -fold.

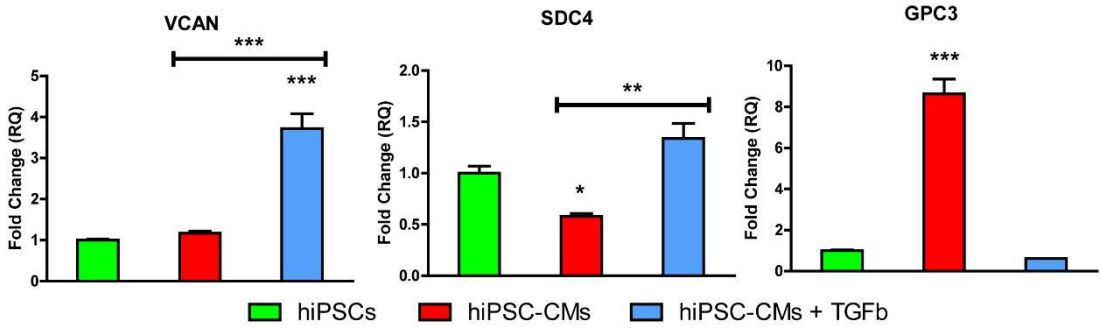


***Figure 5.2 – qRT-PCR expression of other PGs on hiPSC-CMs after TGFβ.*** *Relative fold changes of VCAN, SDC4 and GPC3 in cDNA from hiPSC-CMs (red) and hiPSC-CM after TGFβ treatment (blue) compared against hiPSCs (green). N=1, Technical N = 3. Statistical test performed on SD using Tukey Test. P-value <0.05 = *, <0.01 = **, <0.001 = ***.*

I also wanted to further investigate other proteoglycans (PGs), *VCAN* (Versican), *SDC4* (Syndecan 4), *GPC3* (Glypican 3) to demine their role in a cardiac inflammatory response (Figure 5.2). *VCAN* follows similar expression trends as *HSPG2* and *COL18A1* with the addition of TGFβ creating a statistical increase in expression (3.7-fold change) compared to each other condition. *SDC4* expression is reduced from hiPSCs to CMs (0.58-fold change) although this is increased after TGFβ treatment to 1.3-fold change. *GPC3* expression is increased in CMs to 8.6-fold change, interestingly here the expression is attenuated to 0.68-fold following TGFβ treatment, although due to technical errors no statistics could be performed on this sample.

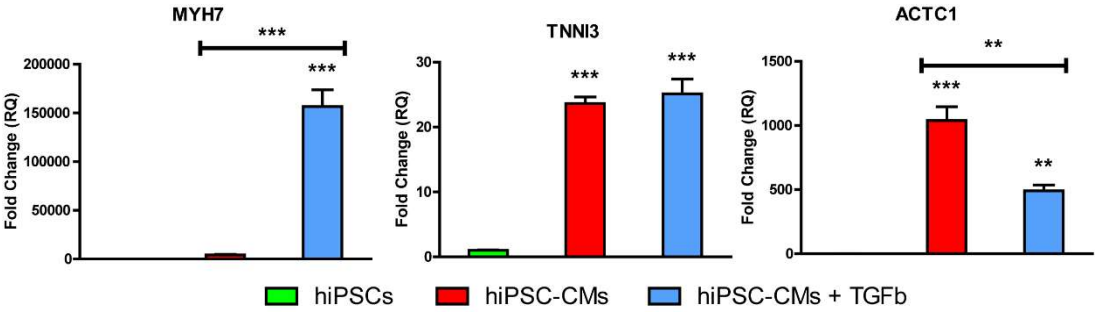


***Figure 5.3 – qRT-PCR expression of structural cardiac gene on hiPSC-CMs after TGFβ.*** *Relative fold changes of structural cardiac markers in cDNA from hiPSC-CMs (red) and hiPSC-CM after TGFβ treatment (blue) compared against hiPSCs (green). N=1, Technical N = 3. Statistical test performed on SD using Tukey Test. P-value <0.05 = *, <0.01 = **, <0.001 = ***.*

To analyse structural changes in the CMs I performed qRT-PCR investigating the expression changes of *MYH7*, *TNNI3* and *ACTC1* (Figure 5.3). *MHY7* increases expression to 4699.6-fold change in CMs compared to hiPSCs, this is further elevated to 156593.7-fold change after TGFβ treatment. The expression of *TNNI3* is increased in CMs compared to hiPSCs as expected (23.6-fold), although this is not further statistically increased in CMs treated with TGFβ (25.8). Expression of *ACTC1* is statistically increased in both CMs (1038.3-fold) and CMs treated with TGFβ (491.6) compared to hiPSCs. A statistical attenuation in *ACTC1* expression is noted in CMs treated with TGFβ compared to CMs.

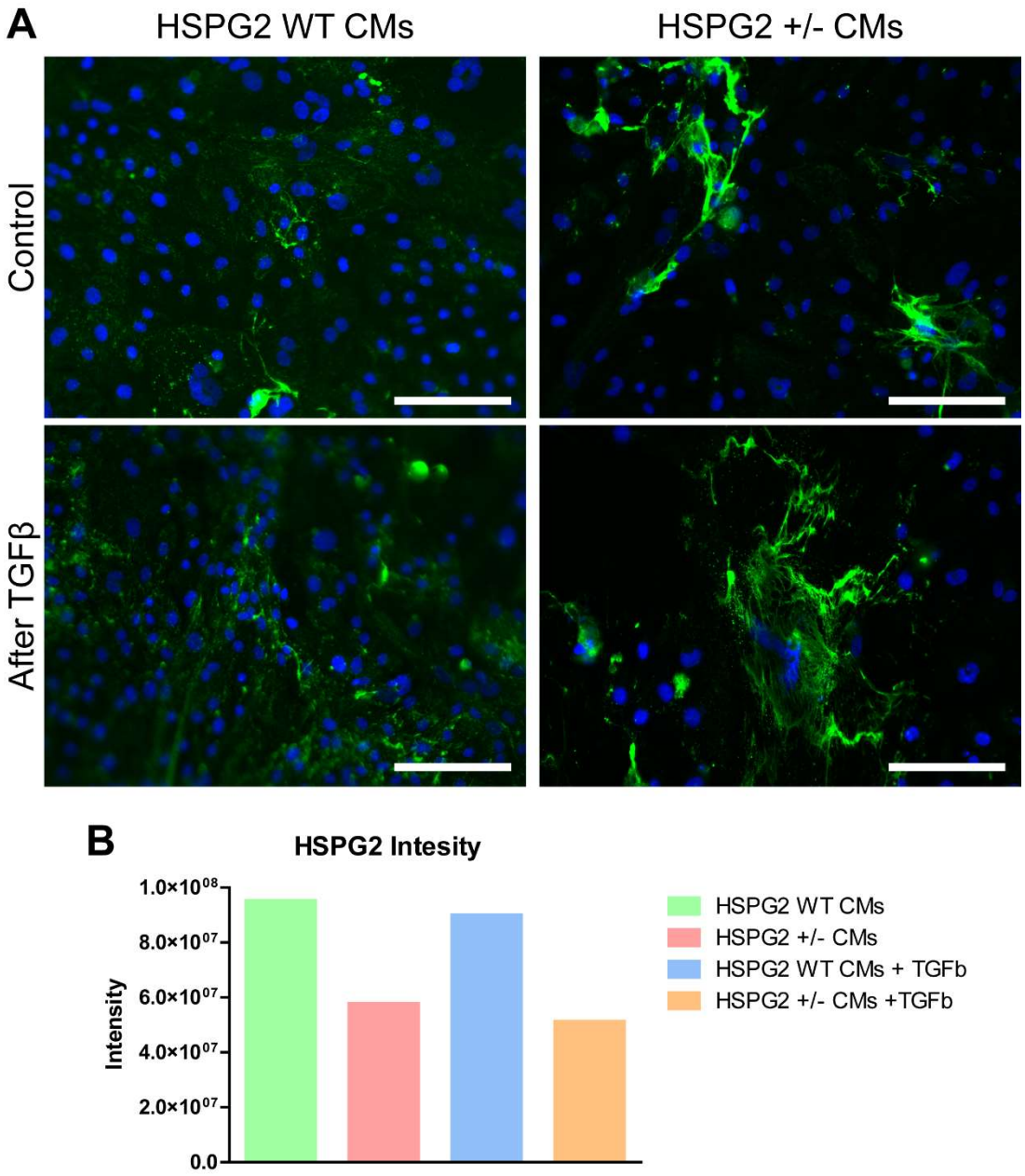


***Figure 5.4 – Immunostaining of HSPG2$^{WT}$ and HSPG2$^{+/-}$ CMs after TGFβ treatment.*** *(A) Staining of perlecan (A74 – green) and DAPI (blue) of hiPSC WT and +/- CMs after TGFβ, scale bar at 150 µm. (B) Quantification of perlecan immunostaining total intensity. N=1*

Immunohistochemistry was performed on HSPG2$^{WT}$ and HSPG2$^{+/-}$ CMs, with and without TGFβ, using perlecan monoclonal antibody A74 (Figure 5.4, A). The images show how HSPG2$^{WT}$ CMs secrete more lower intensity perlecan but over the entire cell with and without TGFβ. HSPG2$^{+/-}$ CMs show patches of high intensity perlecan ECM but not the same overall presence surrounding

the cells. Quantifying perlecan immunostaining reveals a reduction of perlecan intensity in both HSPG2$^{+/-}$ conditions compared to HSPG2$^{WT}$ CMs (Figure 5.4, B). Meanwhile the addition of TGFβ shows no increase in perlecan staining, despite an increase in mRNA expression. I next wanted to look at how CFs would respond to inflammatory stimulant TGFβ.

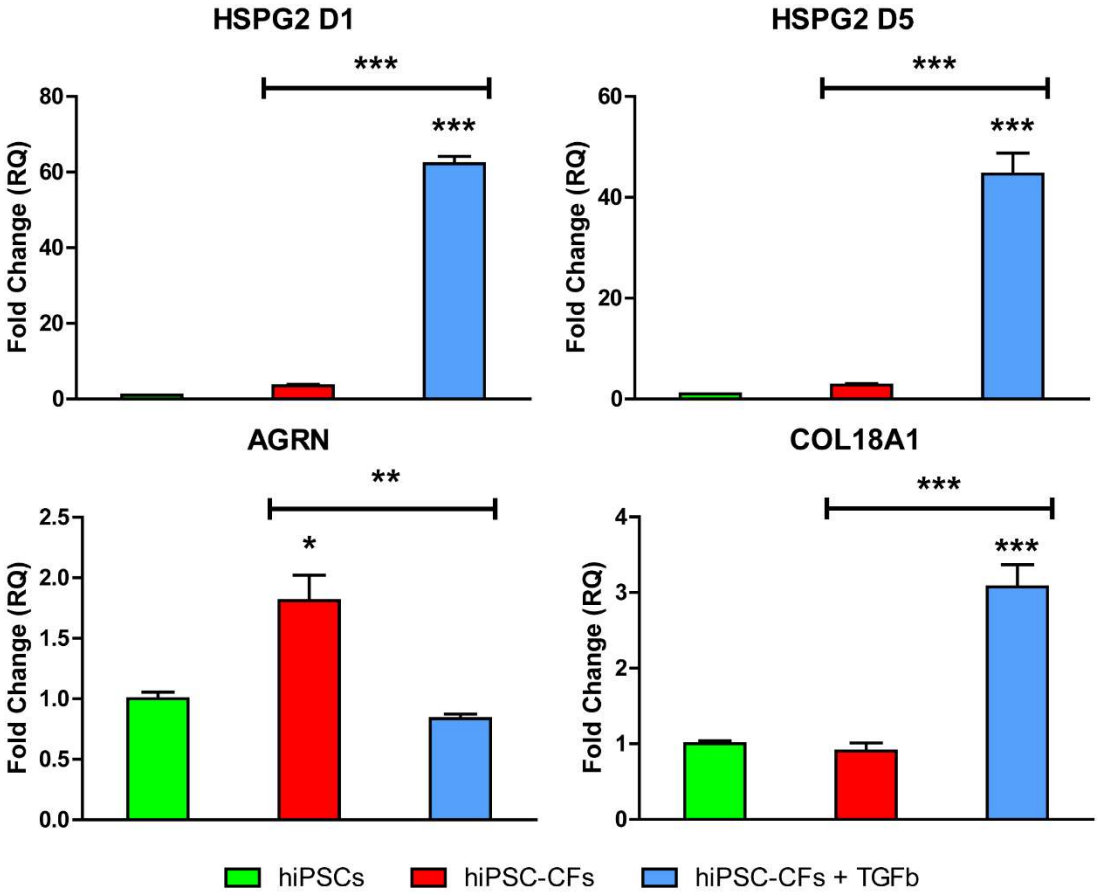


***Figure 5.5 – qRT-PCR expression of HSPGs on hiPSC-CFs after TGFβ.*** *Relative fold changes of HSPGs in cDNA from hiPSC-CFs (red) and hiPSC-CF after TGFβ treatment (blue) compared against hiPSCs (green). Biological N=1, Technical N = 3. Statistical test performed on SD using Tukey Test. P-value <0.05 = *, <0.01 = **, <0.001 = ***.*

CFs were treated with 10ng/mL TGFβ for 4 days before undergoing qRT-PCR analysis for expression of HSPGs (Figure 5.5). Expression of both domains of *HSPG2* are increased between hiPSCs to CFs, this expression is statistically increased following TGFβ treatment of CFs (*HSPG2* D1 – 3.5 to 62.2-fold, *HSPG2* D5 – 2.8 to 44.6-fold change). The expression of *AGRN* follows a

similar trend seen in the CMs, a statistical increase in CF (1.8-fold change) from hiPSCs. The expression of *AGRN* is then attenuated in CFs after TGFβ treatment to 0.84-fold change. *COL18A1* expression shows no change

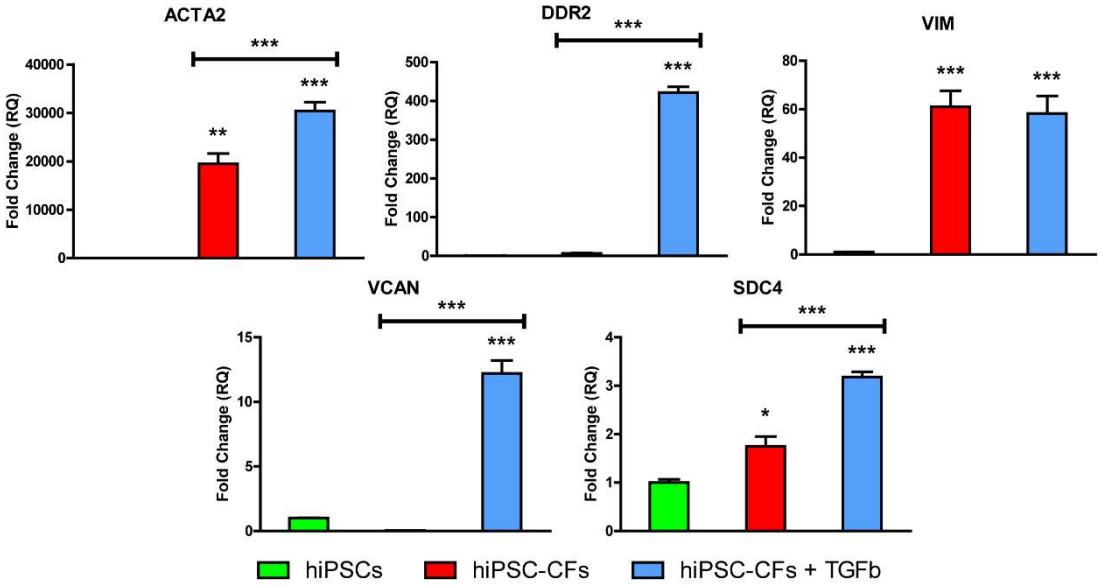


***Figure 5.6 – qRT-PCR expression of activated CF markers on hiPSC-CFs after TGFβ.*** *Relative fold changes of MF markers in cDNA from hiPSC-CFs (red) and hiPSC-CF after TGFβ treatment (blue) compared against hiPSCs (green). N=1, Technical N = 3. Statistical test performed on SD using Tukey Test. P-value <0.05 = *, <0.01 = **, <0.001 = ***.*

between hiPSCs and CFs, although when treated with TGFβ this is statistically increased to 3.1-fold change.

Examining other CF and MF markers shows how expression of hiPSC-CFs shifts to a hiPSC-MF phenotype. The expression of stress fibre marker *ACTA2* is increased in CFs (19484.0-fold change) compared to hiPSCs, this expression is further increased to 30432.7-fold change following TGFβ treatment. *DDR2* expression is increased 6.2-fold from hiPSCs to CFs, this is drastically increased to 421.7-fold change in activated MFs. *VIM* expression is increased by a 61-fold change from hiPSCs to CFs but shows no further expression shift following TGFβ treatment. *VCAN* expression is reduced from hiPSCs to CFs (0.03-fold change), this is increased following TGFβ treatment to 12.2-fold change. The expression of *SDC4* is increased in CFs compared to hiPSCs (1.8-fold change), this is further increased to 3.2-fold change after 4 days of TGFβ treatment.

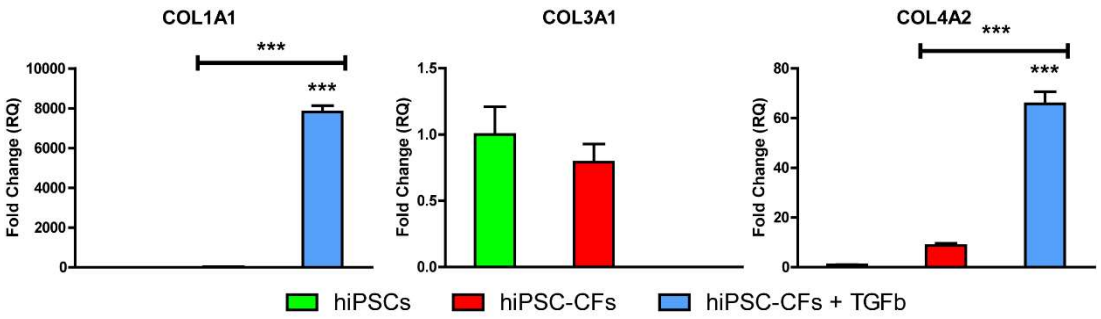


***Figure 5.7 – qRT-PCR expression of collagens on hiPSC-CFs after TGFβ.*** *Relative fold changes of collagens in cDNA from hiPSC-CFs (red) and hiPSC-CF after TGFβ treatment (blue) compared against hiPSCs (green). N=1, Technical N = 3. Statistical test performed on SD using Tukey Test. P-value <0.05 = *, <0.01 = **, <0.001 = ***.*

I also wanted to investigate the levels of collagens in CFs and activated MFs compared to hiPSCs (Figure 5.7). *COL1A1* expression shows no change from hiPSCs to CFs, following TGFβ treatment of CFs this expression is increased to 7822.1-fold change. *COL3A1* expression shows no change between hiPSCs and CFs, all CT values of *COL3A1* in CF + TGFβ samples expression were above the cycle limit and therefore were not used. Expression of *COL4A2* is increased in CFs (8.7-fold change) compared to hiPSCs. This is further increased in activated MFs to 65.8-fold change after TGFβ treatment.

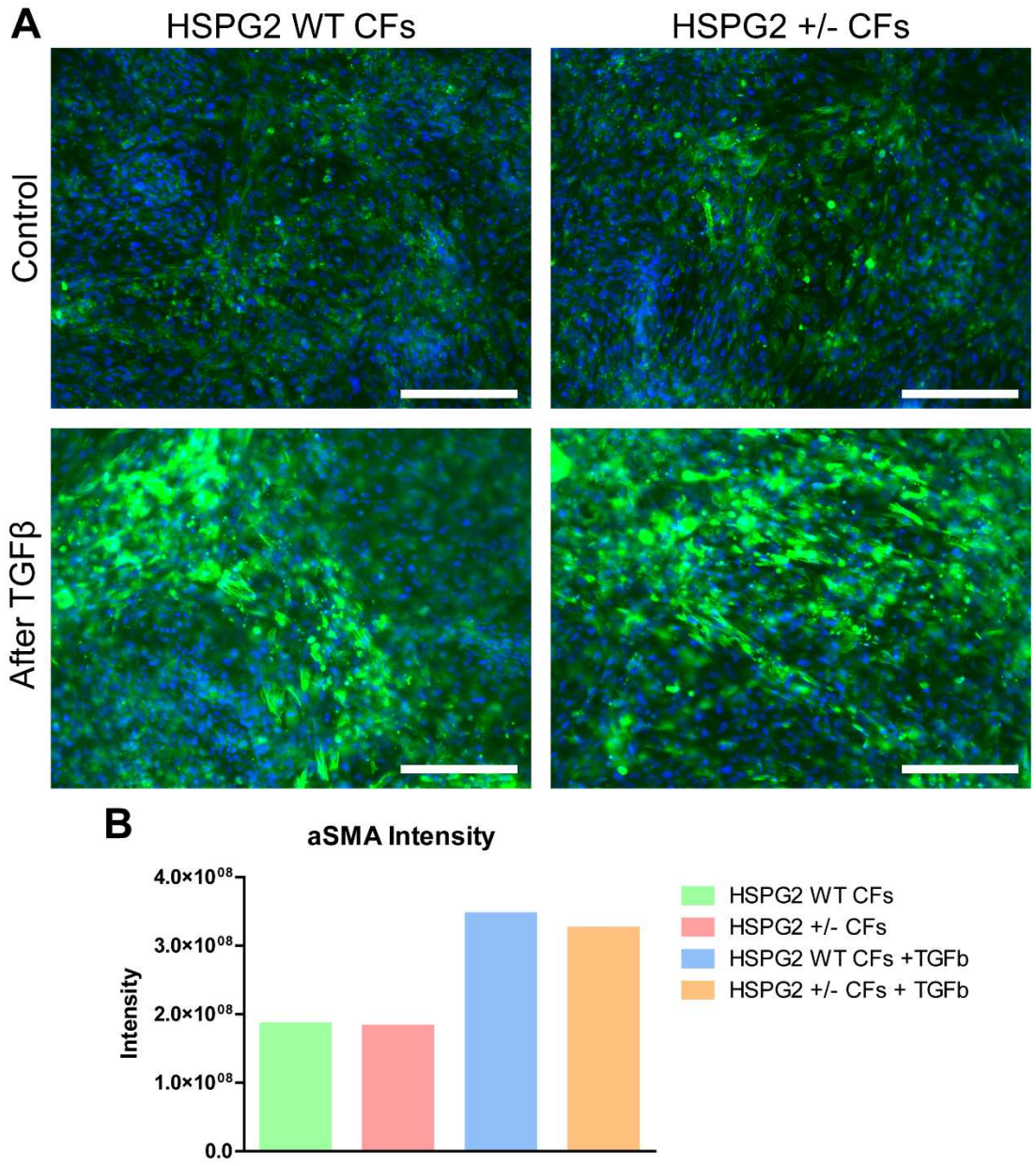


***Figure 5.8 – αSMA immunostaining of HSPG2$^{WT}$ and HSPG2$^{+/-}$ CFs after TGFβ treatment.*** *(A) Staining of αSMA (green) and DAPI (blue) of hiPSC WT and +/- CFs after TGFβ, scale bar at 150 μm. (B) Quantification of αSMA immunostaining total intensity. N=1*

Immunostaining of HSPG2$^{WT}$ and HSPG2$^{+/-}$ CFs under both normal conditions and TGFβ treatment using αSMA monoclonal antibody (Figure 5.8, A). Quantifying the intensity of αSMA shows no difference between the two lines, with both lines showing a similar increase in αSMA expression after TGFβ treatment (Figure 5.8, B).

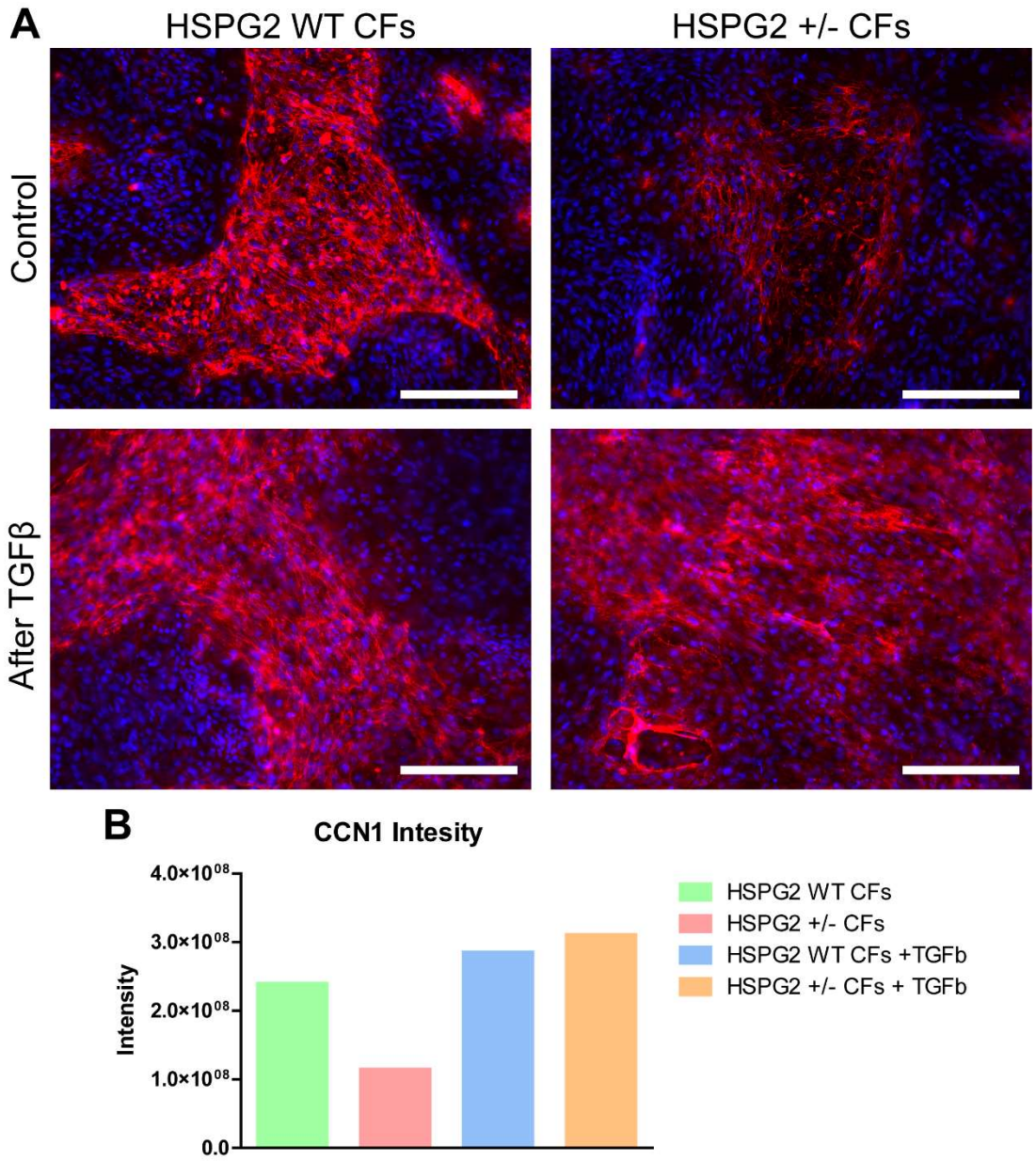


***Figure 5.9 – Perlecan immunostaining of HSPG2$^{WT}$ and HSPG2$^{+/-}$ CFs after TGFβ treatment.*** *(A) Staining of perlecan (CCN1 - red) and DAPI (blue) of hiPSC WT and +/- CFs after TGFβ, scale bar at 150 µm. (B) Quantification of perlecan immunostaining total intensity. N=1*

Immunostaining was also performed on both HSPG2$^{WT}$ and HSPG2$^{+/-}$ CFs under both normal conditions and TGFβ treatment using polyclonal perlecan antibody CCN1 (Figure 5.9, A). Both conditions show dense regions of CFs with rich perlecan ECM within clusters of cells. Quantification shows HSPG2$^{WT}$ CFs have twice the intensity of perlecan compared to HSPG2$^{+/-}$ CFs (Figure 5.9, B). After treatment with TGFβ the intensity of perlecan is slightly increased

in the HSPG2$^{WT}$ CFs while drastically increased in HSPG2$^{+/-}$ CFs. This could be due to location of the images taken whereby perlecan ECM is clustered in certain areas although overall intensity is the same.

In summary, here I investigated the response of both CMs and CFs following TGFβ stimulation. Interestingly, I showed that *HSPG2* mRNA is increased in both cell types, whilst *AGRN* mRNA decreases in both cell types. However, despite this mRNA increase, no increase in perlecan ECM secretion was observed. I next aimed to combine the two cell types in co-culture to investigate *HSPG2*s role in a wound healing response.

### 5.3. Combining hiPSC CMs and CFs into a disease model scratch wound

One of my aims was to create a model of cardiac injury and investigate the role of *HSPG2* in the healing response. My plan to investigate this was to perform a scratch wound assay, allow for wound closure and monitor *HSPG2*s role in this process. I initially wanted to optimise the scratch wound process, to do this I performed a scratch wound on confluent hiPSCs using a variation of pipette tip sizes.

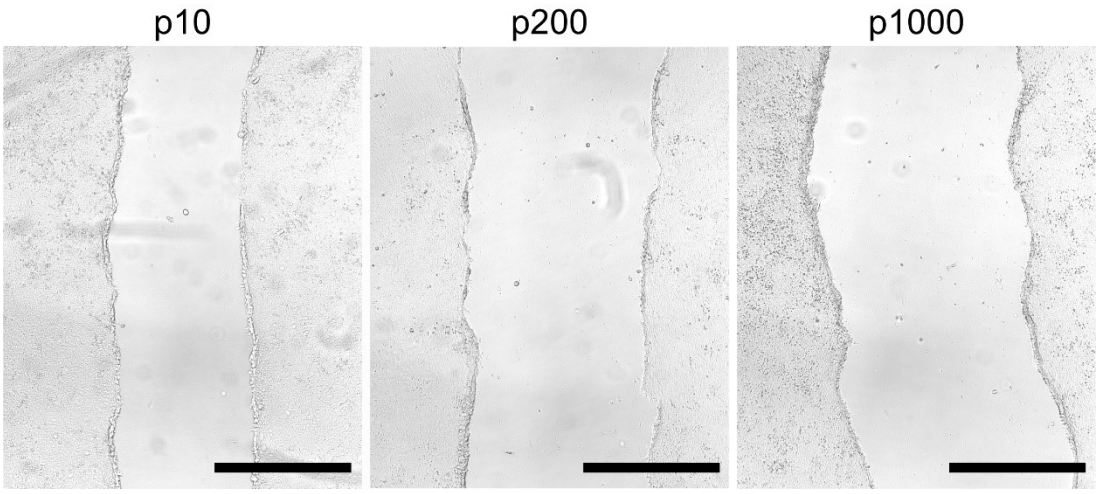


***Figure 5.10 – Scratch wound optimisation on hiPSCs.*** *Three different pipette tip sizes (p10, p200 and p1000) used to scratch confluent hiPSC wells, scale bar = 250μm. N=1*

From the scratches performed on hiPSCs the p10 produced the cleanest scratch (Figure 5.10). While both the p200 and p1000 tip produced an overly

large scratch and produced more tearing of the cells, thus a p10 was to be taken forward to perform future scratch wounds. I then created co-cultures containing a range of $HSPG2^{WT}$ and $HSPG2^{+/-}$ CMs combined with a total percentage of CFs.

Before performing the scratch wound assay, each co-culture condition was recorded, and videos underwent contraction analysis (Figure 5.11) to investigate how contraction of the CMs was altered by the presence of CFs (Figure 5.12). Contraction duration of the $HSPG2^{WT}$ CMs shows no difference in the 90 and 75% co-cultures, this is statistically reduced as the presence of CFs is increased in the 50%. Interestingly $HSPG2^{+/-}$ CMs show a slight increase in contraction duration with the presence of 10% CFs although the duration is reduced as CF presence is increased in 50 and 25% CM conditions. There is a statistical increase in the contraction time-to-peak of the 25% $HSPG2^{WT}$ CMs co-culture condition, with no other conditions showing a change in time-to-peak.

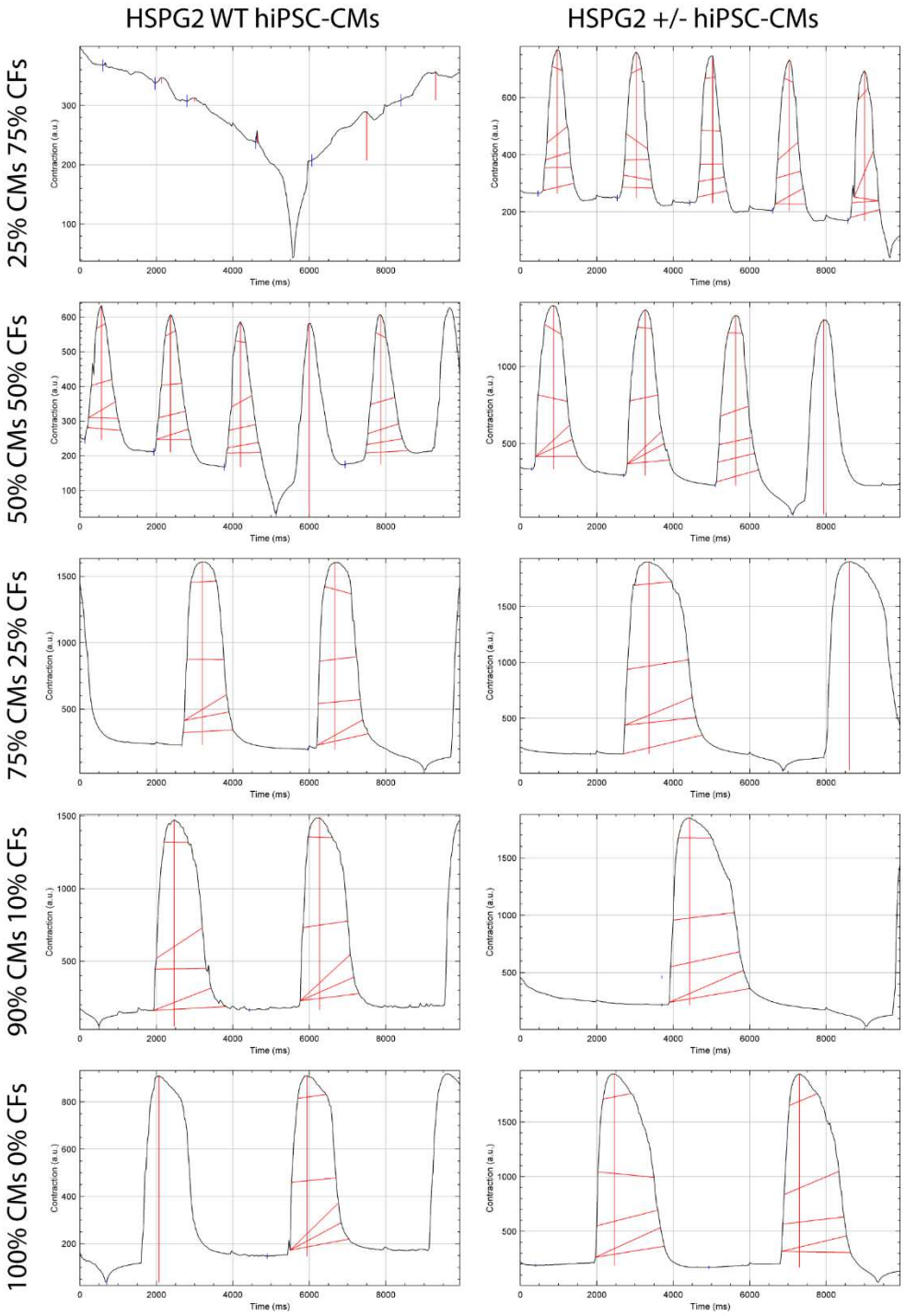


***Figure 5.11 – Representative MUSCLEMOTION outputs.*** *Contraction traces output through ImageJ macro MUSCLEMOTION for each co-culture condition for both HSPG2WT and HSPG2+/- CMs.*

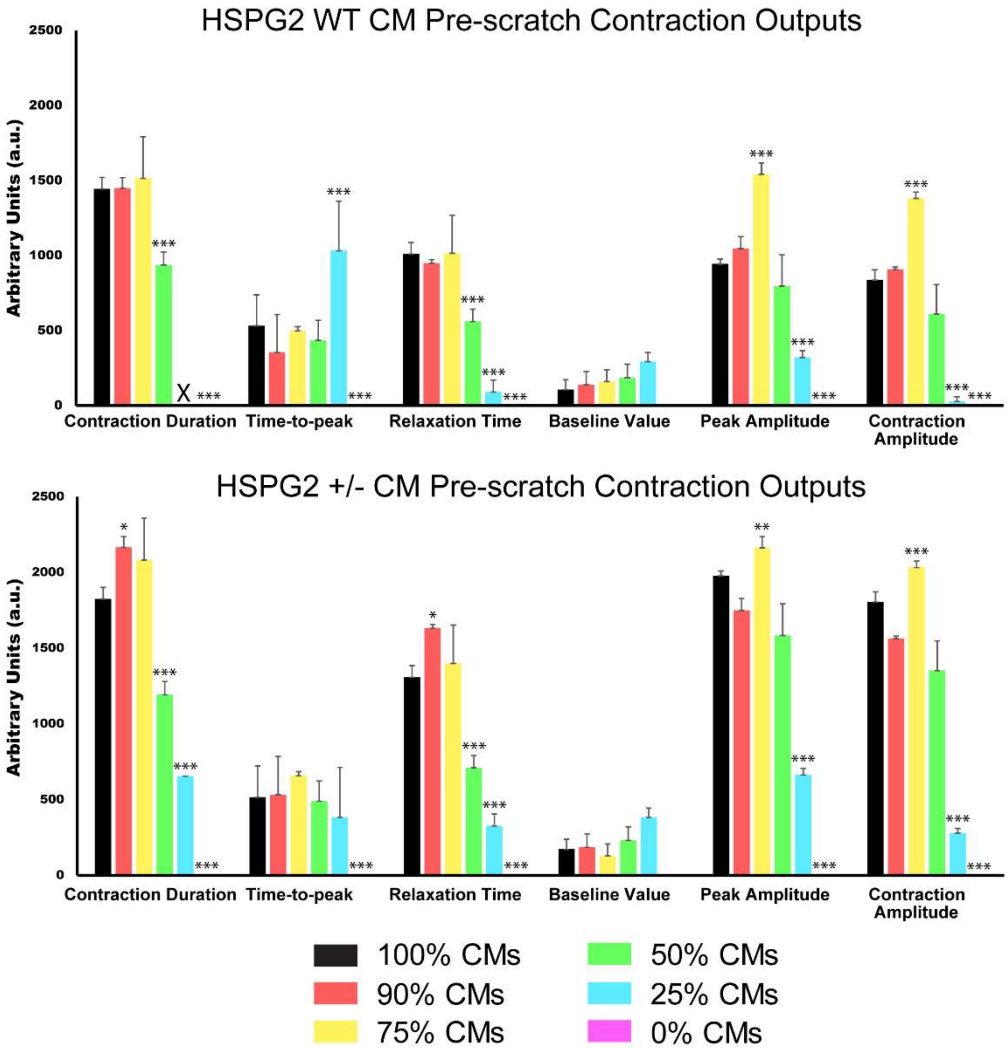


***Figure 5.12 – Contraction analysis of HSPG2 WT and +/- hiPSC-CMs co cultured with hiPSC-CFs.*** *MUSCLEMOTION contraction analysis (contraction duration, time-to-peak, relaxation time, baseline value, peak amplitude, and contraction amplitude) of HSPG2 WT and +/- hiPSC CMs co-cultured with hiPSC-CFs at different percentages (100% - black, 90% - red, 75% - yellow, 50% - green, 25% - blue, 0% - pink). N=1, Technical N=3, significance determined through Tukey-test, P-value <0.05 = *, <0.01 = **, <0.001 = ***.*

Contraction relaxation time follows a similar trend as seen in the contraction duration with a statistical reduction in conditions containing 50 and 25% CMs. Both peak and contraction amplitude of CMs show a statistical increase in the condition containing 75% CMs and 25% CFs compared to a 100% pure population of CMs. The amplitude is then statistically attenuated in both CM

cell lines when the population is reduced to 25% and co-cultured with 75% CFs. The scratch wound was then performed on each co-culture condition and allowed to recover over 15 days.

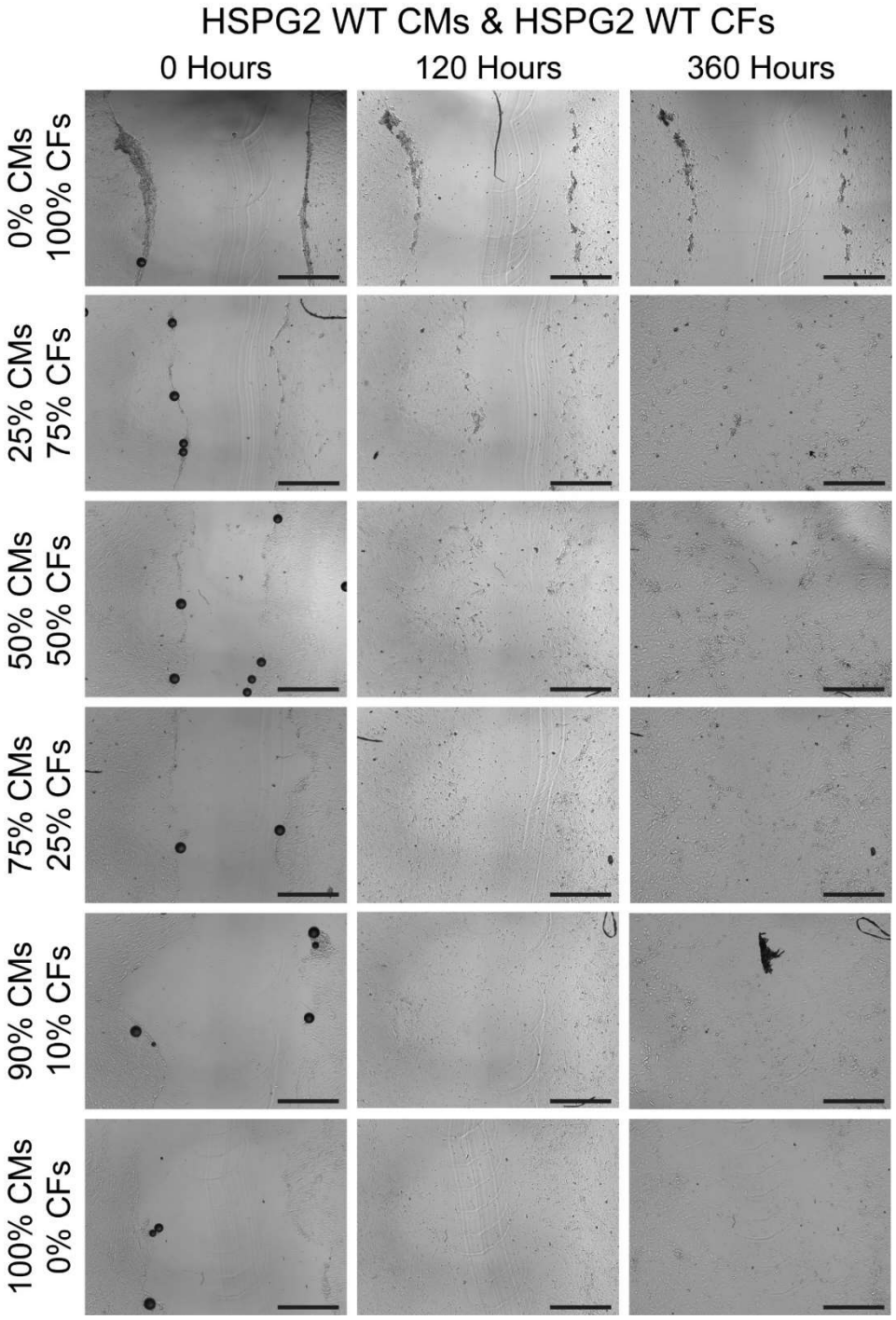


***Figure 5.13 – Wound closure of HSPG2$^{WT}$ CMs and CFs co-culture scratch wound.*** *Representative brightfield images of scratch wound closure after 0 hours, 120 hours and 360 hours at each co-culture condition. Scale bar at 600 µm. N=1*

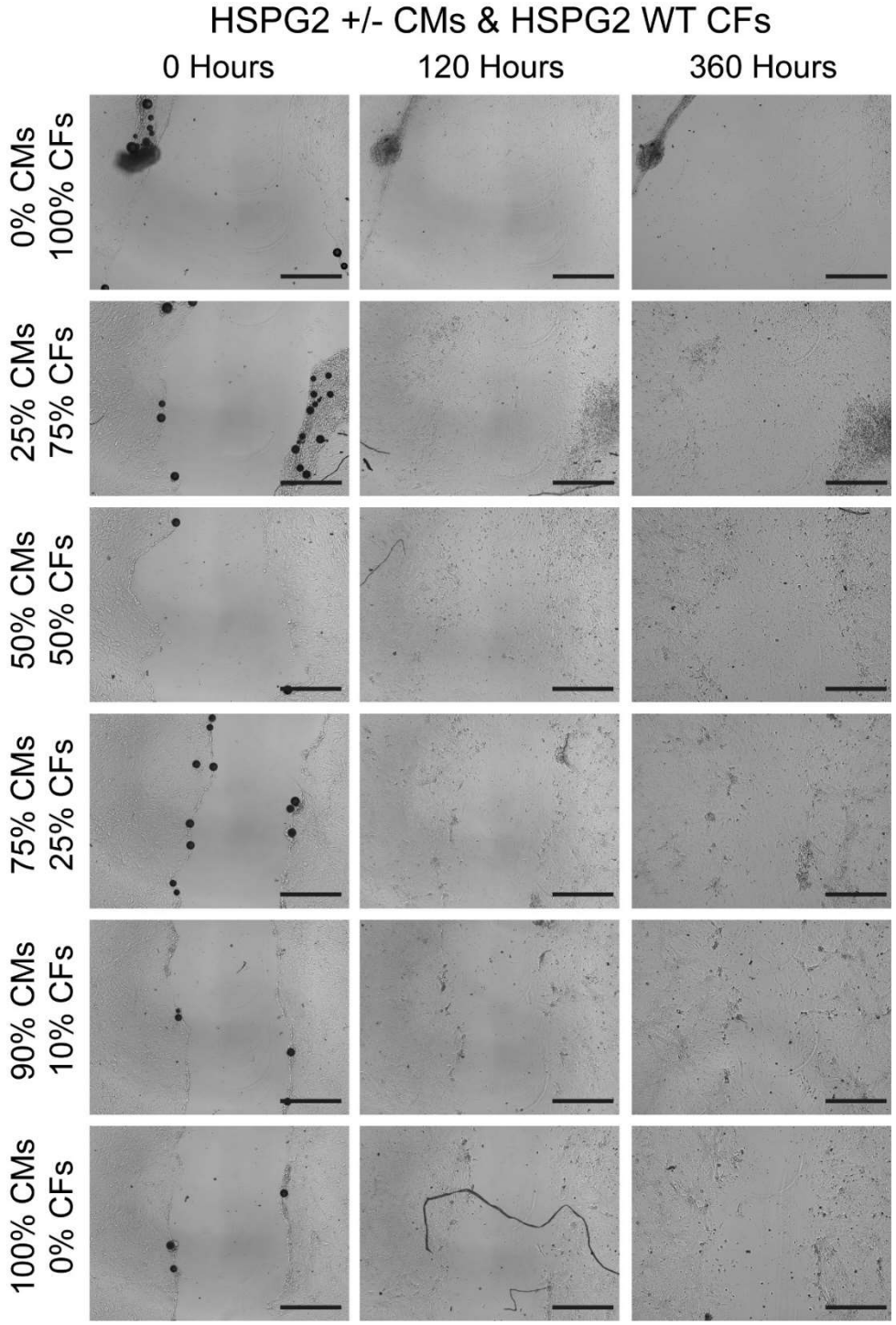


***Figure 5.14 - Wound closure of HSPG2$^{WT}$ CMs and HSPG2$^{+/-}$ CFs co-culture scratch wound.*** *Representative brightfield images of scratch wound closure after 0 hours, 120 hours and 360 hours at each co-culture condition. Scale bar at 600 µm. N=1*

Brightfield images were taken in the same location of each scratch every 24 hours for 15 days. Representative images for scratch wounds at 0, 120 and 360 hours for both $HSPG2^{WT}$ CMs (Figure 5.13) and $HSPG2^{+/-}$ CMs (Figure 5.14) show the wound closure in conditions containing CFs compared to those that don't. Each image was taken into ImageJ where five measurements were taken at the same plane calculating the minimal distance between each side.

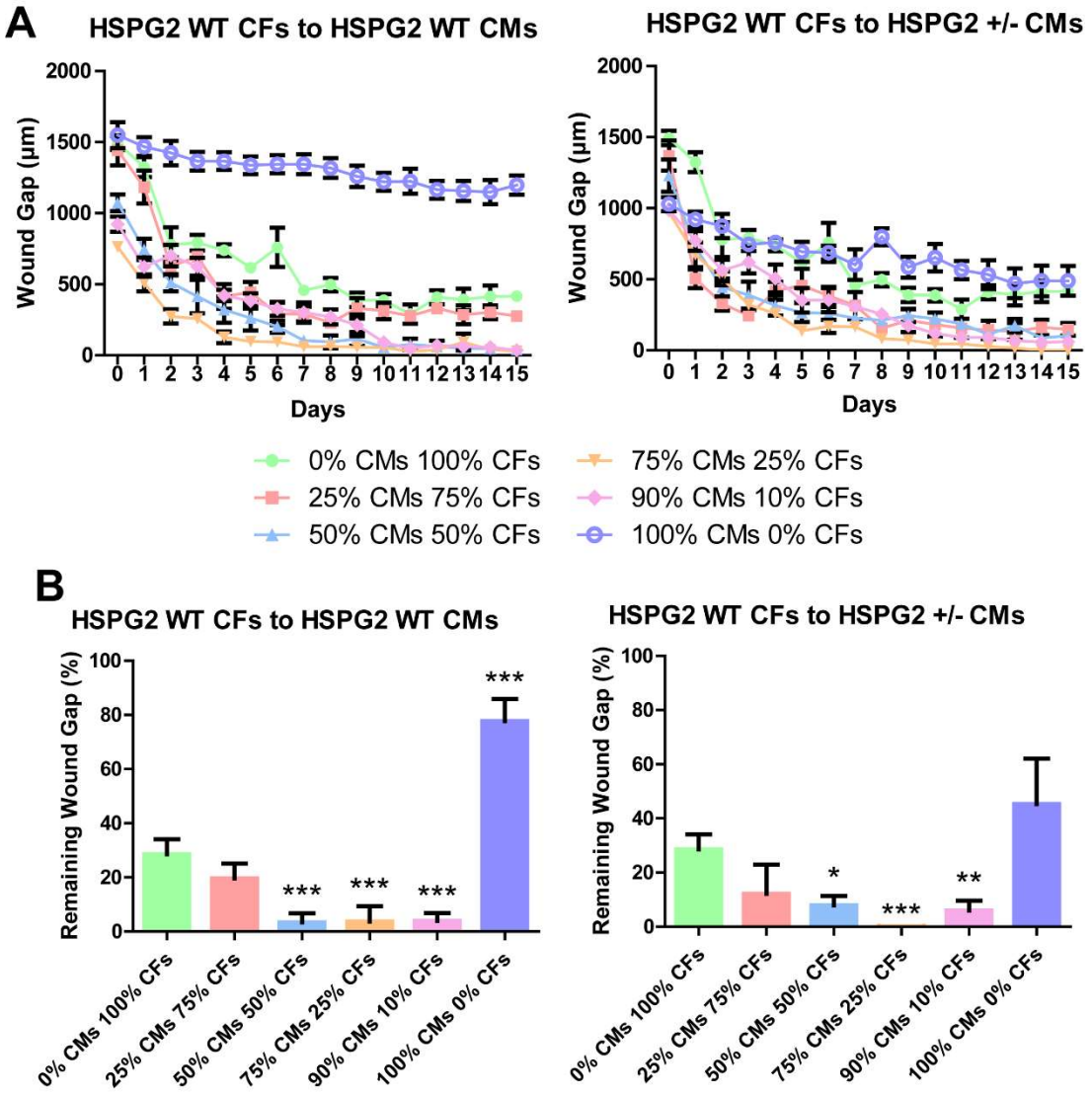


***Figure 5.15 – Co-culture scratch wound closure measurements.*** *(A) Measurements of remaining wound gap calculated over each day of wound closure for each condition. (B) Remaining unclosed wound gap 15 days after initial scratch for each co-culture condition calculated as a percentage. N=1, technical N=5, significance determined through Tukey-test, P-value <0.05 = *, <0.01 = **, <0.001 = ***.*

Measurements between each condition the HSPG2$^{WT}$ CMs show no migration as would be expected, while there is a rapid wound closure in the first few days in all conditions containing CFs, this closure rate then slows over the remaining days (Figure 5.15, A). The difference between the CM lines is the HSPG2$^{+/-}$ CMs show more capability to migrate than HSPG2$^{WT}$ CMs. Quantifying the final wound closure as a percentage show that when CFs are co-cultured with CMs the remaining wound gap after 15 days is smaller than a pure population of CFs (Figure 5.15, B). There is a statistical reduction in final wound gap in the co-cultures containing 90, 75 and 50% CMs of either HSPG2$^{WT}$ or HSPG2$^{+/-}$ cell line. The 100% population of HSPG2$^{WT}$ CMs shows a statistical increase in remaining wound gap compared to the 100% CFs, although interestingly this is not seen in the remaining wound gap of the HSPG2$^{+/-}$ CMs.

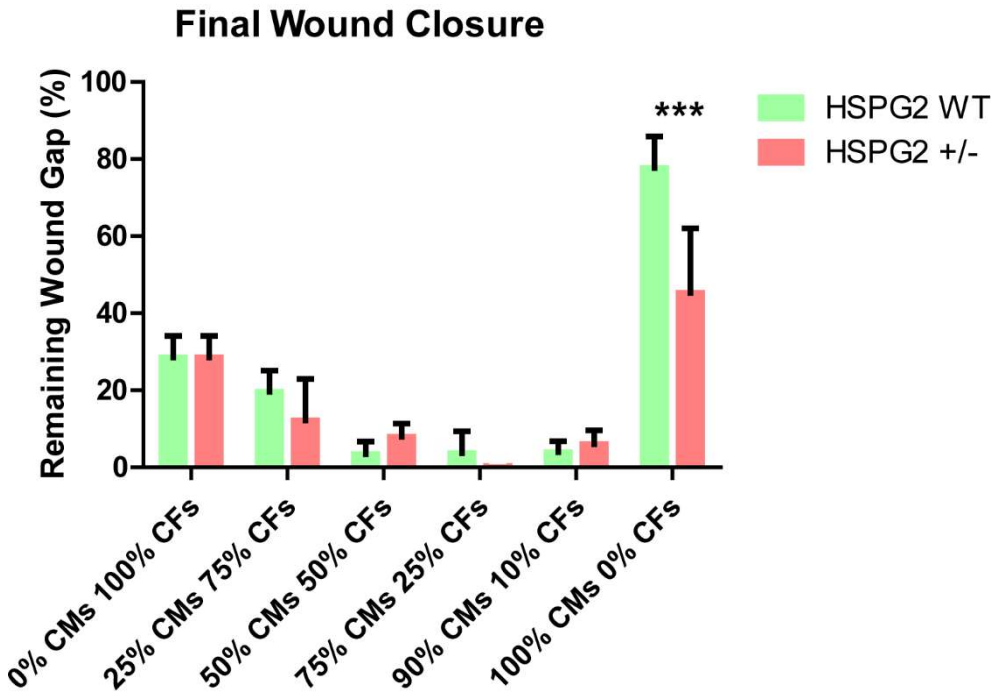


***Figure 5.16 – Comparison of wound closure between HSPG2$^{WT}$ and HSPG2$^{+/-}$ co-culture.*** *Wound closure measurements on day 15 after initial scratch for each co-culture condition comparing between HSPG2WT and HSPG2+/-- CMs. N=1, technical N=5, significance determined through Tukey-test, P-value <0.05 = *, <0.01 = **, <0.001 = ***.*

When comparing the two cell lines final wound closure the only difference is seen between the 100% population of CM migration where the WT shows no

wound closure but the HSPG2$^{+/-}$ CMs 50% remaining wound gap (Figure 5.16). This difference could be due to the HSPG2$^{+/-}$ CMs remaining on the edge of the scratch becoming hypertrophic compared to the HSPG2$^{WT}$ leading to a perceived level of migration. After the scratch wound was complete both sides of the scratch were recorded for MUSCLEMOTION contraction analysis. This was performed to determine if both sides of the of the scratch became electro coupled due to the migrating cells.

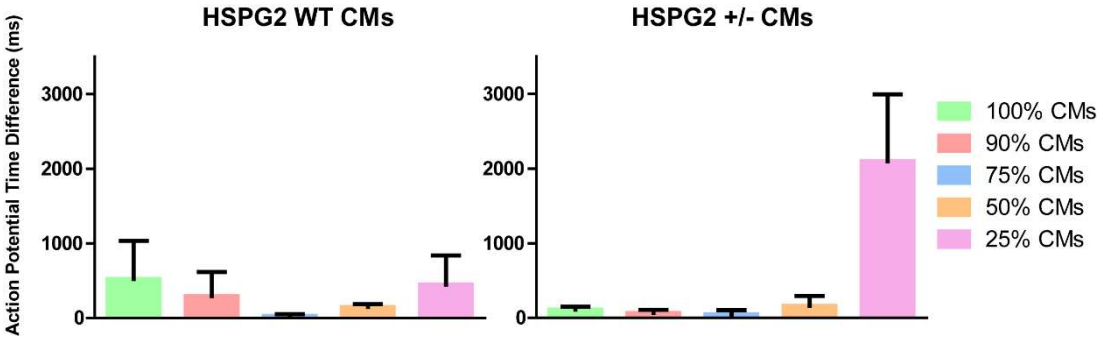


***Figure 5.17 – Difference in action potential between left and right sides of co-culture scratch.*** *MUSCLEMOTION contraction analysis was performed on each side of the co-culture scratch wound, the difference between each peak was calculated and plotted displaying difference in action potential. N=2*

The action potential was calculated for each side of the scratch, these were then overlaid and the difference in action potential between each contraction trace (Figure 5.17). Results show how the HSPG2$^{WT}$ CMs show no action potential difference in the 75% CM co-culture recovered scratch implying both sides are contracting is synchronicity. The difference in action potential between the two sides increases in the 90 and 50% HSPG2$^{WT}$ CM co-culture conditions, showing the largest difference in the 100 and 25% CM healed wound. Minor difference in action potential is seen in 100, 90, 75 HSPG2$^{+/-}$ CM scratch wounds. This is increased in the 50% CM condition and further increased in the 25% CM condition which shows the greatest difference between action potential differences. After the scratch wound assay was complete cells were fixed and stained to determine changes in perlecan secreted ECM in all conditions.

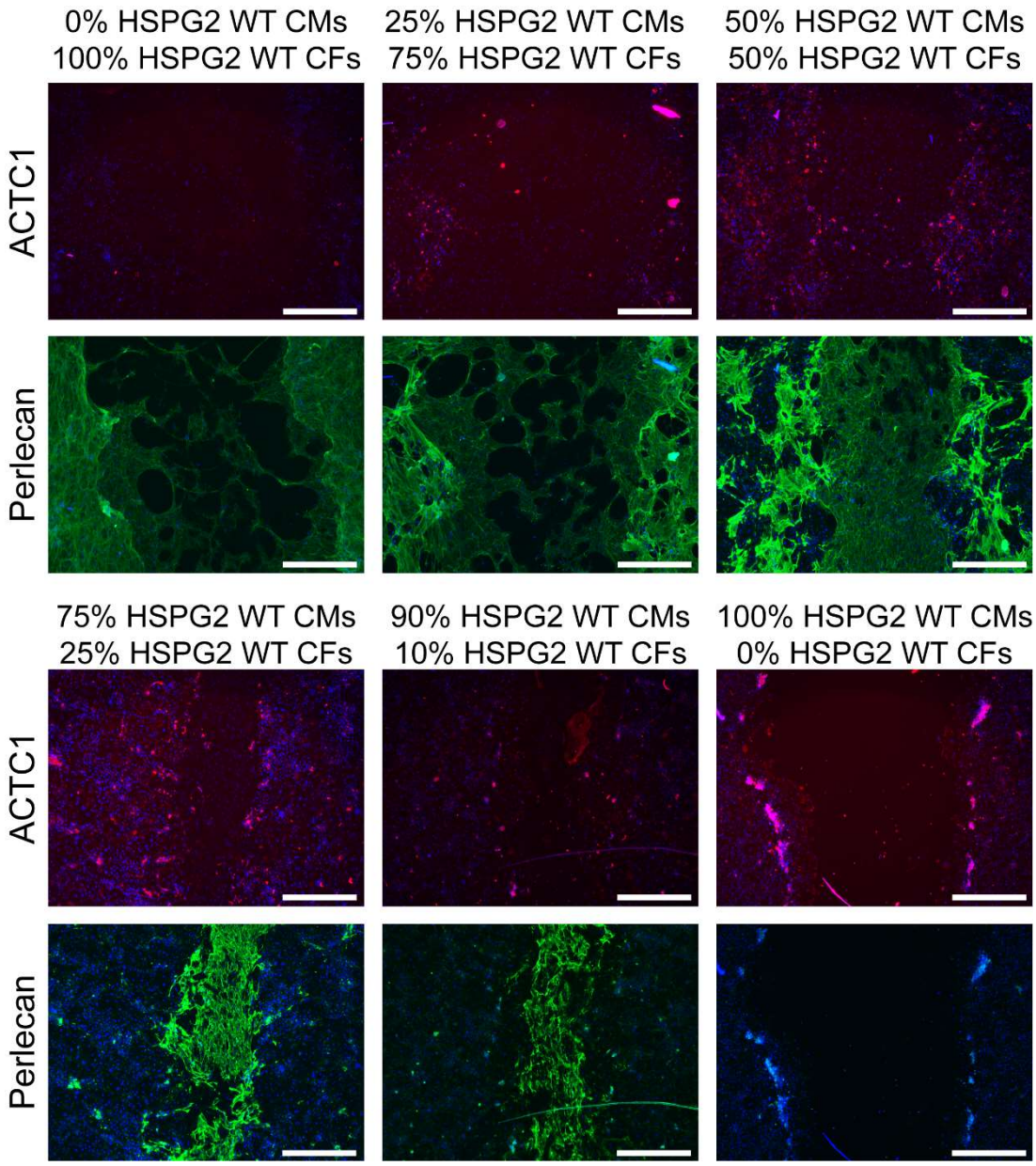


***Figure 5.18 – Immunostaining of day 15 HSPG2$^{WT}$ CMs and CF co-culture scratch wound.*** *Staining of cardiac marker ACTC1 (red) and perlecan (CCN1 – green) on day 15 following co-culture scratch for each condition. Scale bar at 600 µm. N=1*

Conditions were stained with CM marker ACTC1 and perlecan polyclonal antibody CCN1 on each condition revealing a perlecan rich ECM that is secreted in the wound gap (Figure 5.18). Staining with ACTC1 (red) reveals an increased presence of CMs as the seeded percentage was increased, this also reveals that CMs do not migrate into the scratch wound. Perlecan staining (green) reveals a preferential secretion in the scratch wound by the migrating

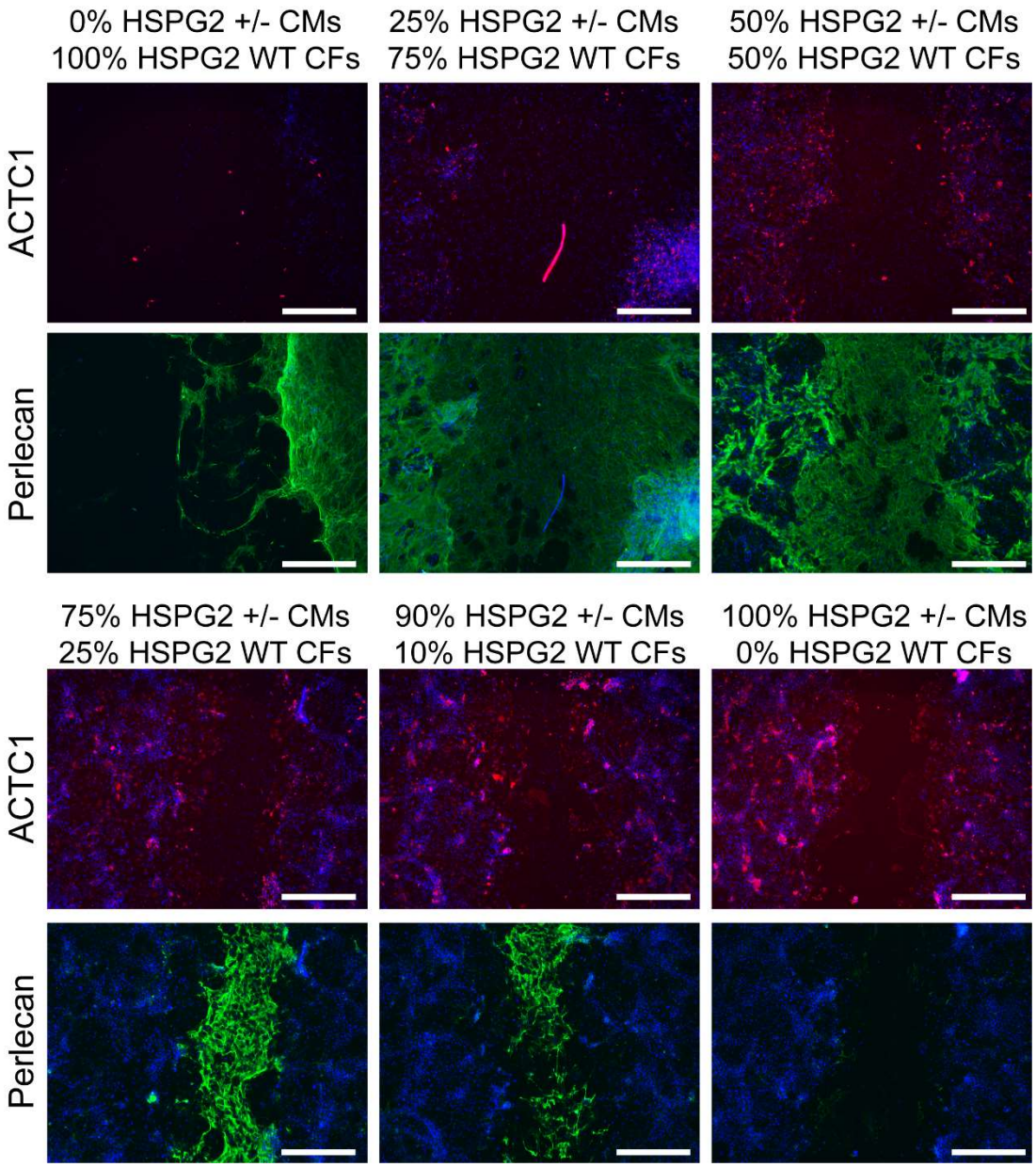


***Figure 5.19 – Immunostaining of day 15 HSPG2$^{+/-}$ CMs and HSPG2$^{WT}$ CF co-culture scratch wound.*** *Staining of cardiac marker ACTC1 (red) and perlecan (CCN1 – green) on day 15 following co-culture scratch for each condition. Scale bar at 600 µm. N=1*

cells when a low percentage of CFs are seeded alongside a high percentage of CMs (90/75% CMs). This trend is changed in the 50% CMs and 50% CFs where perlecan ECM can be seen secreted in both the scratch wound and regions of undamaged cells. As the percentage of CFs is increased above the percentage of CMs the perlecan ECM secretion becomes preferentially found within the undamaged regions of the scratch. One clear difference can be seen within the HSPG2$^{+/-}$ CMs co-culture immunostaining (Figure 5.19) compared

to the HSPG2$^{WT}$ CM co-cultures. The scratch wound performed on the 100% CFs tore the left side of the scratch leading to no clear staining of either side of the scratch wound, for this reason the measurement values from the scratch wound performed on 100% CFs, 0% HSPG2$^{WT}$ CMs were used. Taking the perlecan immunostaining images ECM analysis could be performed using ImageJ plugin TWOMBLI.

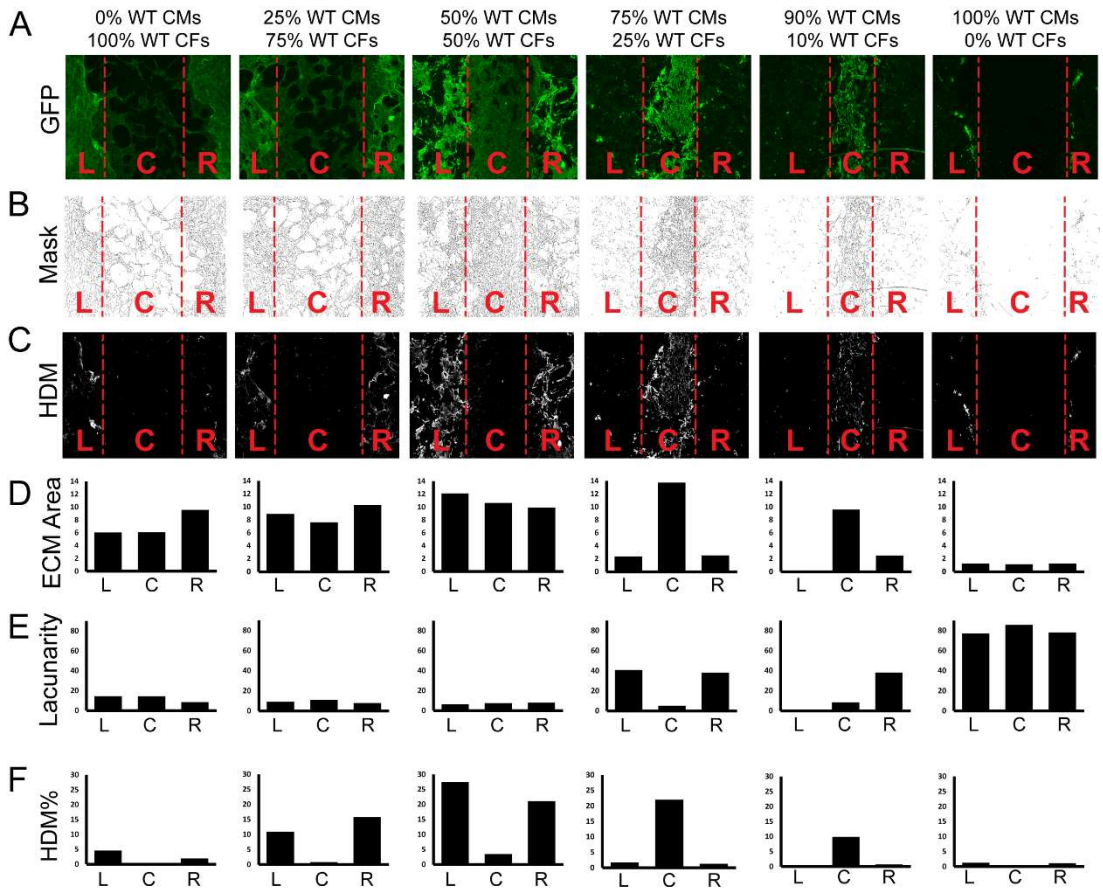


***Figure 5.20 – TWOMBI ECM analysis of perlecan immunostaining of HSPG2$^{WT}$ CM and CF co-culture scratch wound.*** *(A) CCN1 (green) immunostaining of scratch wound split into left, centre and right (L, C, R) segments. (B) ECM mask and (C) High density matrix (HDM) generated by TWOMBLI ECM analysis of perlecan immunostaining images. (D-F) TWOMBLI ECM analysis measurements calculated from mask and HDM images generated from perlecan immunostaining. N=1*

Each image was split into the left, centre, and right sections of the scratch wound before being processed using TWOBLI ECM analysis (Figure 5.20, A). TWOMBLI output creates a line mask of the ECM based of predetermined parameters of maximal and minimal branch lengths (Figure 5.20, B). The high-density matrix (HDM) images are created by a threshold value to determine which regions contained the regions of HDM perlecan ECM (Figure 5.20, C). TWOMBLI outputs results for the total ECM area showing how no differences are seen between each region in the 0, 25, 50 and 100% HSPG2$^{WT}$ CM co-cultures (Figure 5.20, D). This changes in the 75 and 90% CM co-cultures where the centre region of the scratch has a higher perlecan ECM area than

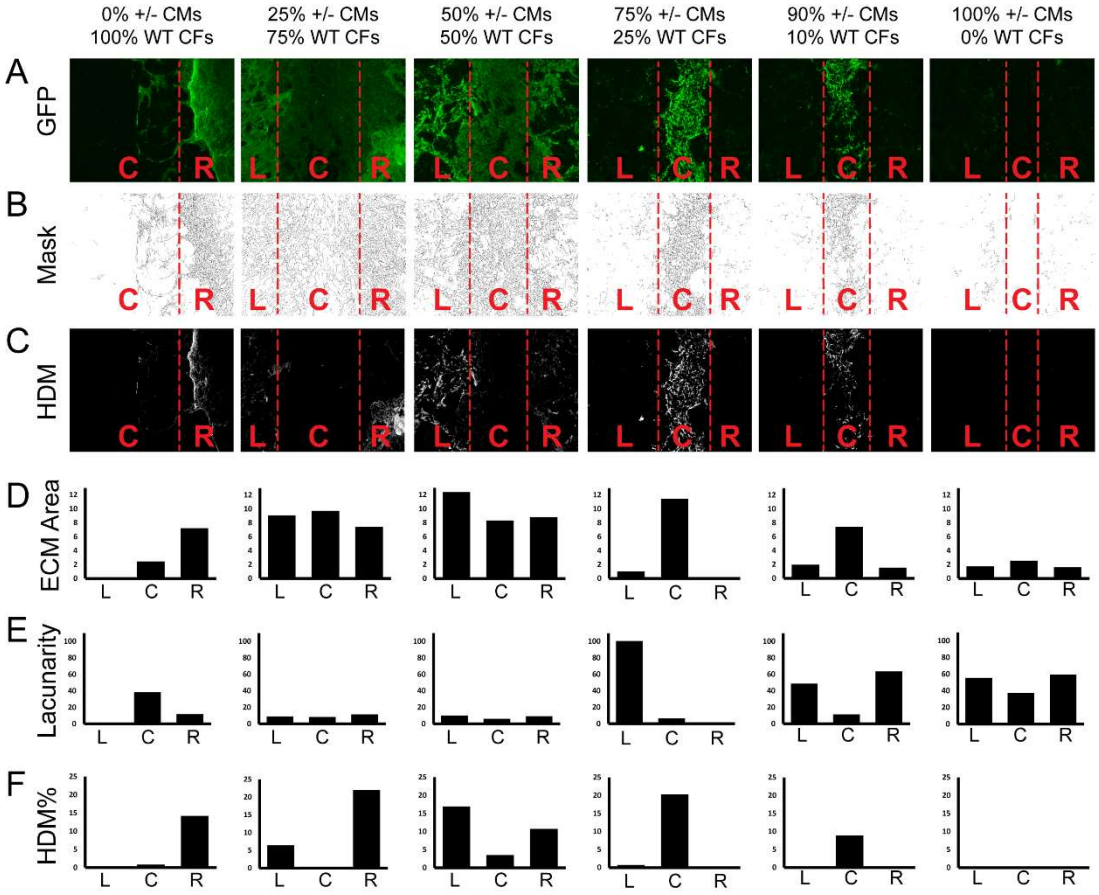


***Figure 5.21 - TWOMBI ECM analysis of perlecan immunostaining of HSPG2$^{+/-}$ CM and HSPG2$^{WT}$ CF co-culture scratch wound.*** *(A) CCN1 (green) immunostaining of scratch wound split into left, centre and right (L, C, R) segments. (B) ECM mask and (C) High density matrix (HDM) generated by TWOMBLI ECM analysis of perlecan immunostaining images. (D-F) TWOMBLI ECM analysis measurements calculated from mask and HDM images generated from perlecan immunostaining. N=1*

either the left or right regions. The lacunarity reflects the size of gaps found within the ECM mask, this shows again no difference in the low percentage CM co-cultures, where a high percentage of CFs creates a tight, low lacunarity perlecan ECM (Figure 5.20, E). The highest levels of lacunarity are shown in the 100% CM ECM whereby the ECM is sparse and less structured than that laid down by CFs. Lacunarity is also slightly increased in the left and right regions of the 75 and 90% CM co-cultures compared to the centre scratch. Quantifying the HDM reveals the results comparable to what is seen in the immunostaining images, the presence of both CFs and CMs in a culture increases the presence of perlecan ECM secretion (Figure 5.20, F). HDM analysis reveals a preferential secretion of perlecan HDM in the left and right regions of the scratch wound in 25 and 50% CM co-cultures, while this is switched to perlecan HDM in the centre of both 75 and 90% CM co-cultures. Analysing the $HSPG2^{+/-}$ co-culture scratch wound perlecan ECM reveals comparable results as seen in the $HSPG2^{WT}$ scratch wounds (Figure 5.21, A-C). TWOMBLI analysis reveals results showing very little difference in ECM area (Figure 5.21, D) lacunarity (Figure 5.21, E) and HDM (Figure 5.21, F) compared to the $HSPG2^{WT}$ scratch wounds.

These results displayed increased contractile force of CMs when co-cultured with a low level of CFs. A CF overpopulated culture led to a reduction in CM contractile capabilities. The migration of CFs after a cardiac scratch was also seen to be altered by co-culture composition, whereby a presence of damaged CMs enhances wound closure. Perlecan ECM immunostaining reveals HDM is preferentially secreted in the wound site of high CM populated co-cultures compared to the high CF populated conditions. After performing this scratch wound, I next wanted to investigate if the migration and wound closure was affected by the presence of different cytokines in the media.

### 5.4. Scratch wound testing anti fibrotic drugs against wound closure

To further investigate the changes seen in migration and wound closure of CFs I performed a repeated scratch wound with two conditions, 100% CFs and 25% CFs co-cultured with 75% CMs. To each of these conditions I aim at

utilising different medias to effect migration, these include media that are conditioned by both normoxic and hypoxic CMs, and media supplemented with potential antifibrotic drug indole-3-carbanol (Chen et al., 2019).

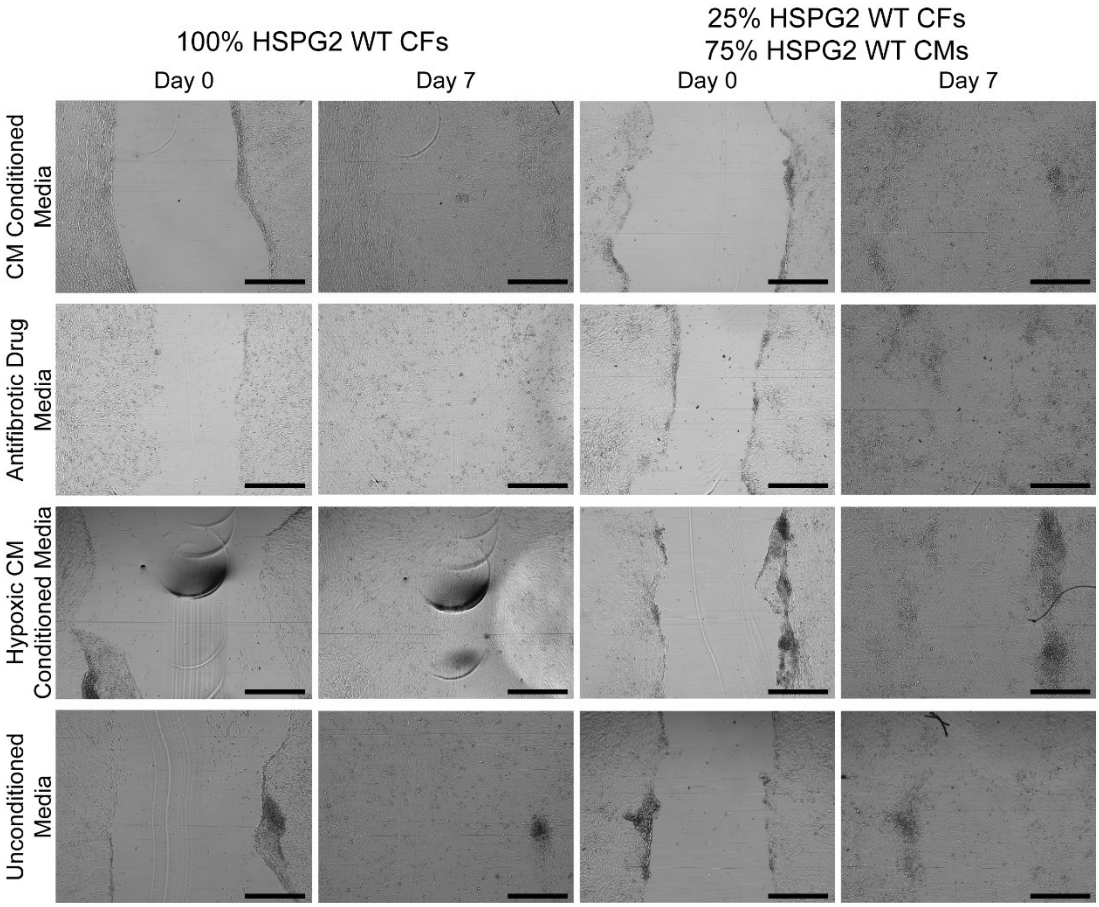


***Figure 5.22 – Comparing effects on media causing scratch wound closure.*** *Brightfield images taken at day 0 and 7 of scratch wound closure under the effects of different media compositions and with and without the presence of CMs. Scale bar is at 600 µm. N=1*

The scratch wound was performed on all cultures with brightfield images taken in the same location every 24 hours for 7 days (Figure 5.22). Scratch wounds performed on the 100% CF population wells underwent more tearing than the mixed populations containing 25% CFs and 75% CMs. 7 days was enough time for almost complete wound closure in all conditions. Using the brightfield images measurements were taken in five planes for each of the 24-hour timepoints to determine wound gap closure.

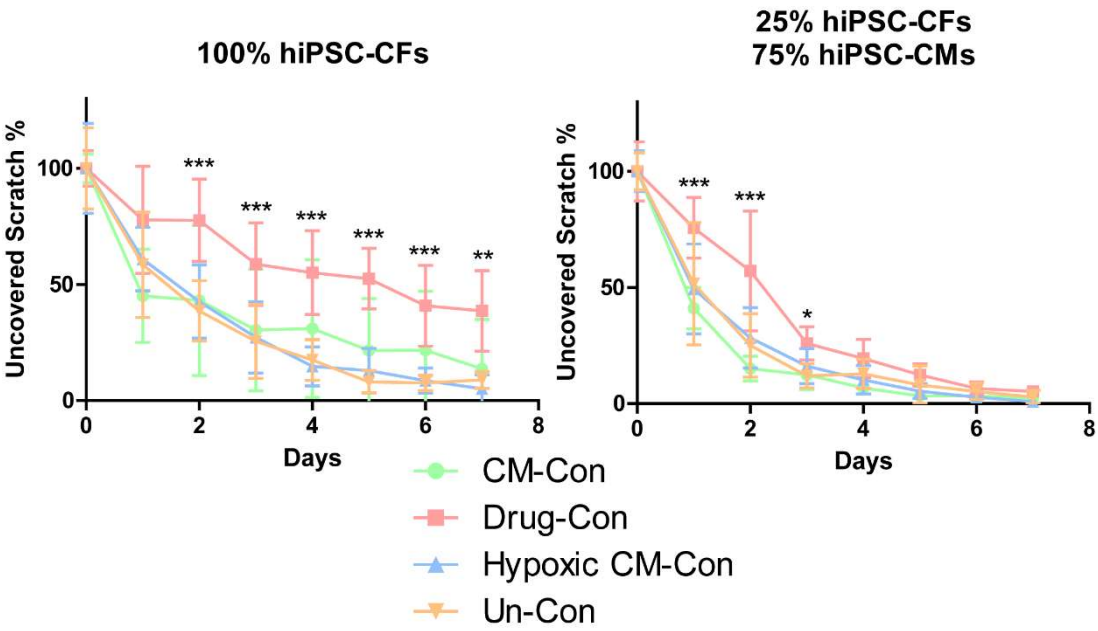


***Figure 5.23 – Wound closure comparing conditioned medias over 7 days.*** *Scratch distance remaining calculated each day in multiple points for each conditioned media used and plotted against unconditioned (Un-con) media. N=1, Technical N=3, significance determined through Tukey test, P-value <0.05 = *, <0.01 = **, <0.001 = ***.*

Measurements from the images show how all medias closed the 100% CF wound gap over the 7 days at a similar rate (Figure 5.23). The only difference in wound gap closure was found in media supplemented indole-3-carbanol. This wound is still closing over the 7 days although at a slower rate compared to the other conditions. A similar trend is seen in the mixed CF CM population, with rapid wound closure in all media conditions except the indole-3-carbanol media. Wound closure is initially stunted for the first 3 days due to indole-3-carbanol; the wound gap is then closed to a similar level as the other three conditions over the remaining days showing no differences between the medias. The wounds were then fixed and stained to investigate changes in CF activation to MFs and perlecan secretion.

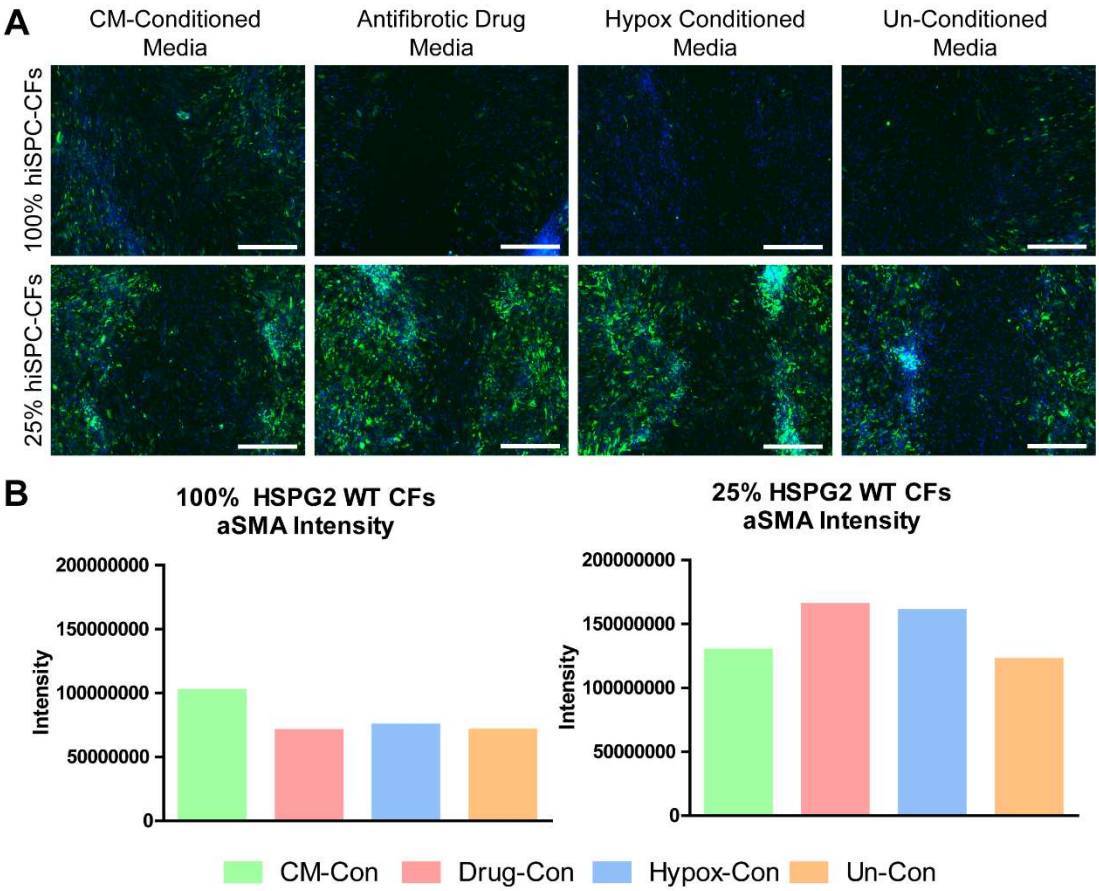


***Figure 5.24 – αSMA immunostaining of scratch wound comparing conditioned media.*** *(A) Staining of MF marker αSMA (green) and DAPI (blue) on 100% and 25% CF scratch wound healed under conditioned medias. Scale bar at 600 μM. (B) Intensity of αSMA immunostaining.*

Scratch wounds were immunostained for αSMA stress fibres found in activated MFs (Figure 5.24, A). Images reveal a higher presence of MFs in the borders of the scratch rather than the centre where migratory cells would be found. Interestingly when quantifying the intensity of αSMA immunostaining a higher intensity can be found in all media conditions of the mixed population scratch wounds compared to the 100% CFs (Figure 5.24, B). These results imply there is a higher level of CF activation to MFs occurring in cultures containing CMs compared to those that don't.

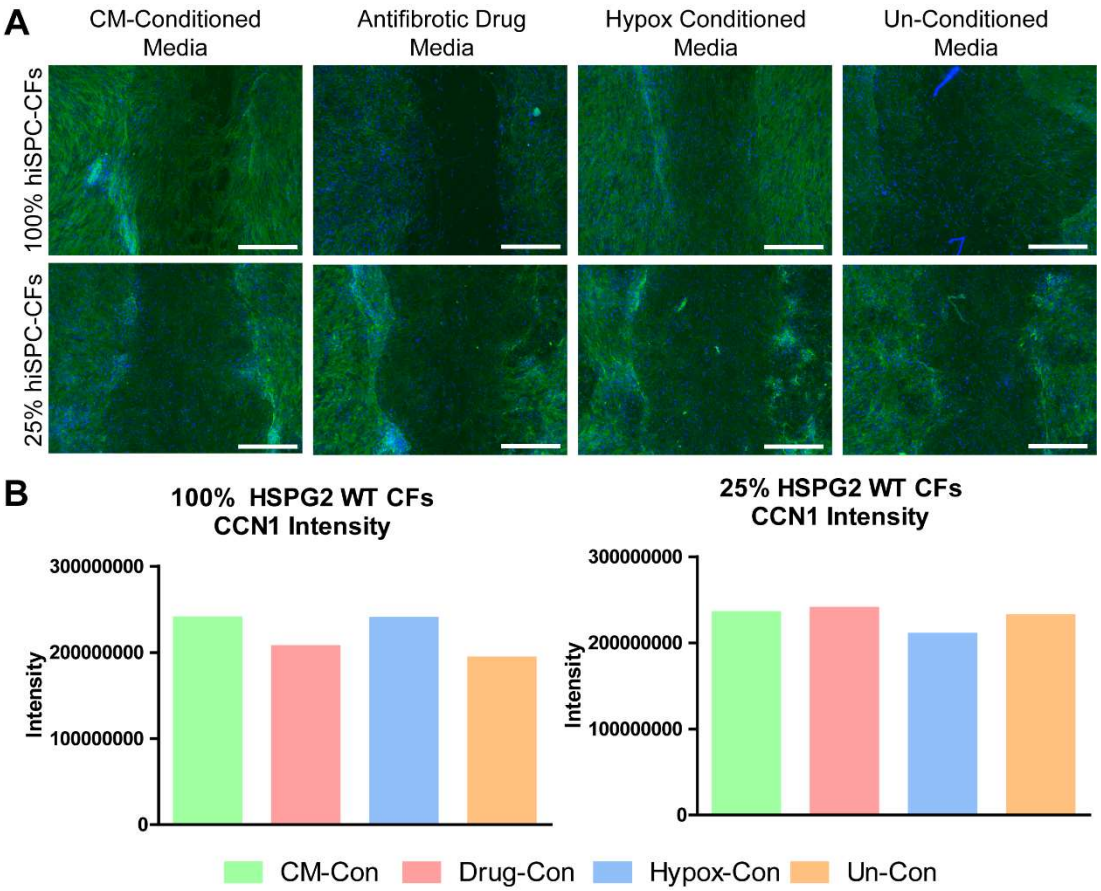


***Figure 5.25 – CCN1 immunostaining of scratch wound comparing conditioned media.*** *(A) Staining using perlecan polyclonal antibody (CCN1 – green) and DAPI (blue) on 100% and 25% CF scratch wound healed under conditioned medias. Scale bar at 600 µm. (B) Intensity of CCN1 immunostaining.*

Immunostaining using perlecan polyclonal antibody was performed to determine any changes in perlecan ECM due to media compositions during scratch wound healing (Figure 5.25, A). The same level of perlecan ECM appears throughout the unscratched and healed areas of the scratch wound. Quantification of perlecan ECM intensity reveals no difference in all the conditions, showing over the 7 days of wound healing perlecan ECM isn't affected by changes in media or culture conditions (Figure 5.25, B).

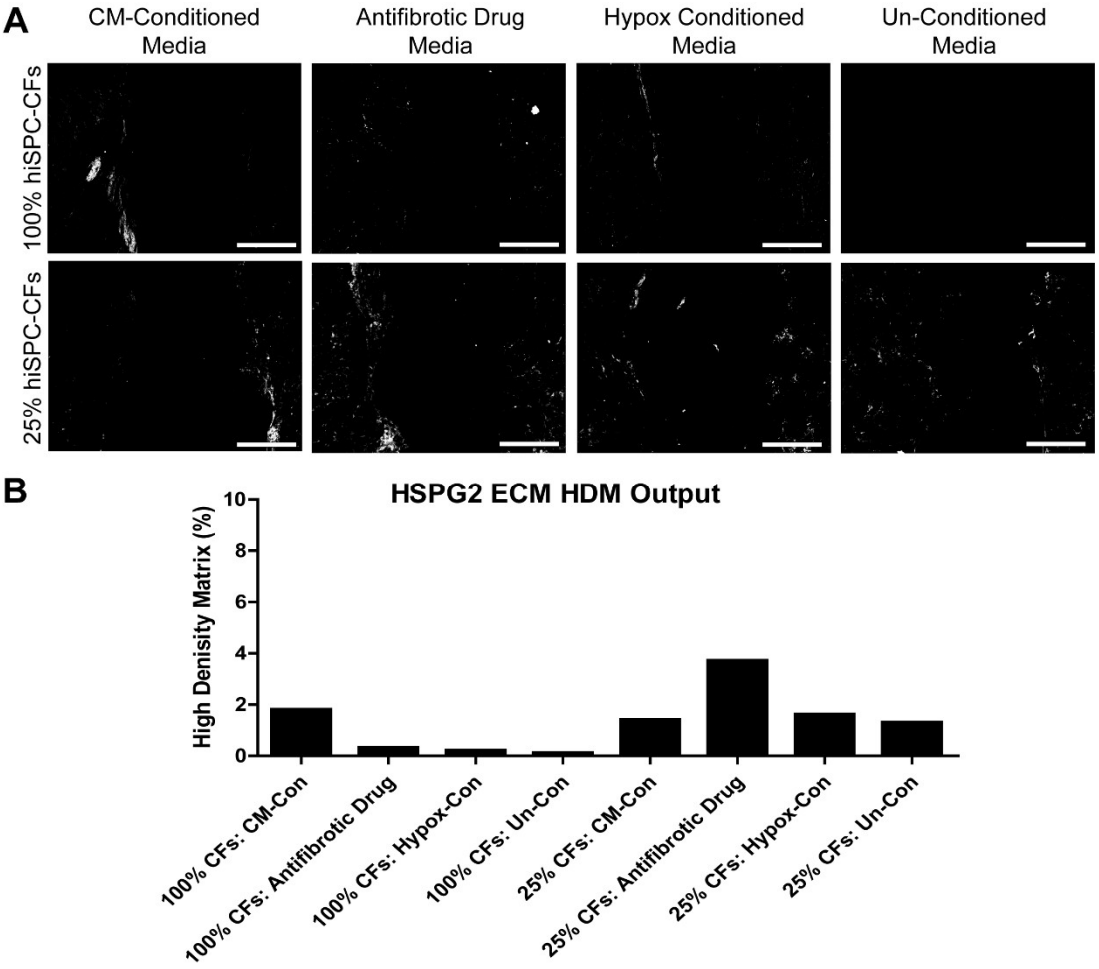


***Figure 5.26 – TWOMBLI ECM analysis of final scratch wound closure after conditioned medias.*** *(A) Highlighted perlecan high density matrix (HDM) and (B) TWOMBLI HDM output measurements compared to conditioned medias. Scale bar at 600 µm.*

Using these perlecan ECM immunostaining images TWOMBLI ECM analysis can be performed revealing any changes between the conditions. ECM analysis reveals similar levels of HDM found along the edges of the scratched wound (Figure 5.26, A). Output results from HDM analysis reveal very low levels of HDM in each condition, further to this no major difference between each condition can be seen (Figure 5.26, B). The creation of HDM seen in the first scratch wound could be due to the prolonged culture the assay was maintained for. This would imply the creation of a perlecan rich HDM is part of a later stage in the wound healing process, and this can't be produced after 7 days of wound healing but is seen after 15 days.

The results from this experiment show the use of an indole-3-carbanol drug was able to inhibit the initial wound closure of both population conditions after a scratch wound. Although these results show no difference in transdifferentiation of CFs to MFs or perlecan ECM secretion. Results also show there is a higher level of CF activation in the culture containing CMs compared to the 100% CF population. Since the culture was only maintained for 7 days there was no signs of perlecan HDM implying this ECM is secreted over a longer period. I next aimed at using the results gained from the two previous scratch wounds to create a more replicable model and to investigate if the response of *HSPG2* deficient CFs differed from the WT.

### 5.5. Co-culture migration of HSPG2$^{WT}$ and HSPG2$^{+/-}$ CFs towards CMs

Following the encouraging results from these manual scratch wound assays, I switched to commercially available Ibidi quadrant migration chambered wells (Ibidi, µ-Dish 35 mm Quad, 80416) to reduce variability. These migration wells would create a clean gap between, each seeded cell quadrant with the same distance. I aimed at investigating how HSPG2$^{+/-}$ CFs would respond to the migration assays compared to HSPG2$^{WT}$ CFs. I seeded HSPG2$^{WT}$ CMs into two separate quadrants in the migration wells, in the remaining quadrants HSPG2$^{WT}$ and HSPG2$^{+/-}$ CFs were seeded. I allowed the cells to recover following seeding and walls between the quadrants were removed. To recreate the stress caused by creating a scratch on CMs in the migration assays I aimed at using both normoxic and hypoxic CM conditioned medias.

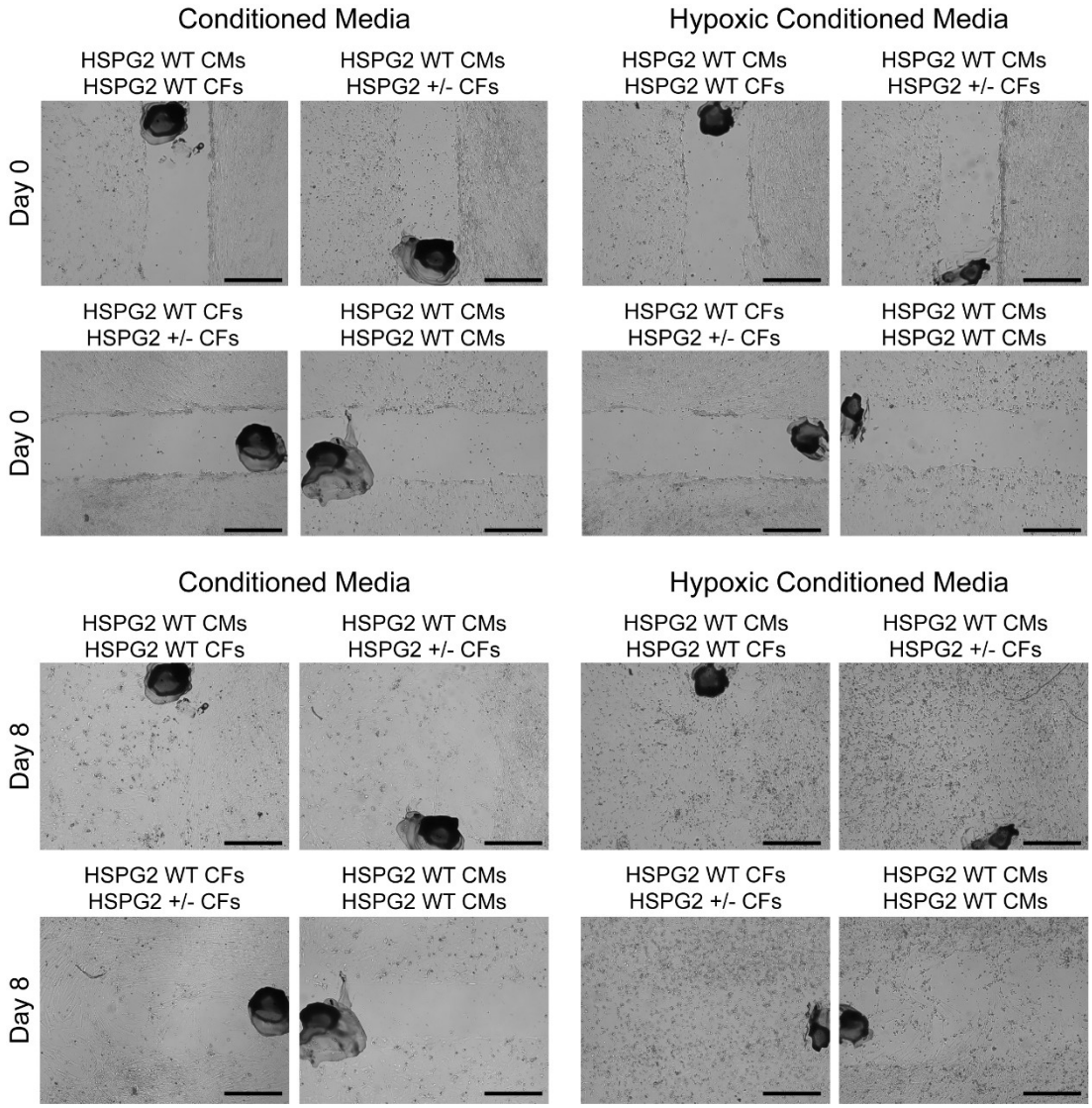


***Figure 5.27 – Brightfield images of migration wells at day 0 and 8.*** *Brightfield images taken at same location after removal of wall between cell quadrants at day 0 and day 8. Scale bar at 600 µm.*

Following removal of the quadrant walls each gap left between the cell populations was imaged in the same location over 8 days (Figure 5.27). The use of hypoxic media within the migration assay shows a level of death on the cell surface which is not seen in the control conditioned media. The overall assay was continued for 14 days in the aim of creating a perlecan HDM matrix within the wound gap. Although, migration was only quantified for 8 days since the wound gap was covered by this point.

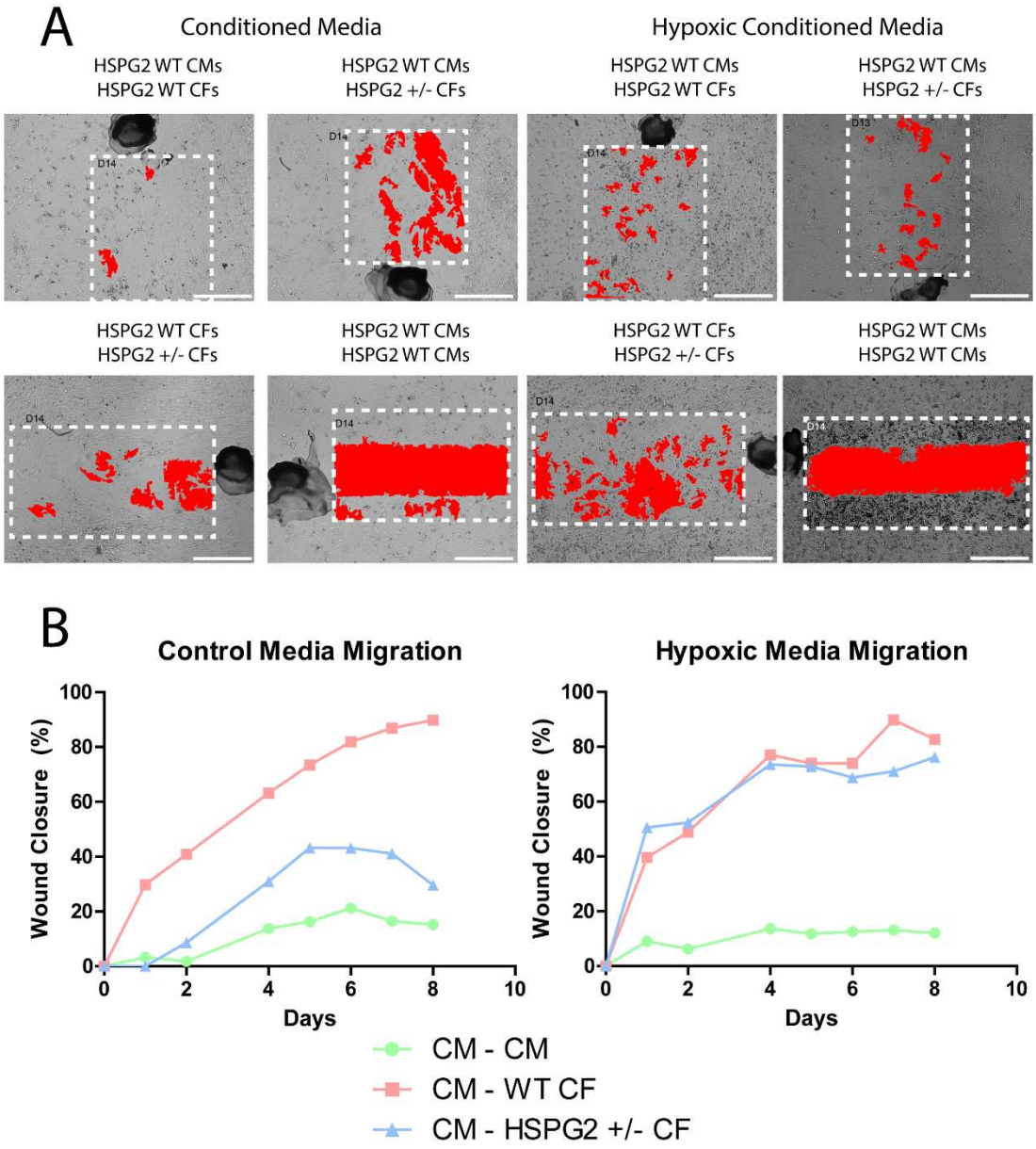


***Figure 5.28 – Wound closure measurements of migration well assay.*** *(A) ImageJ wound healing plugin output highlighting unclosed regions of each migration well section (red) and cropped regions used for scratch analysis (white). Scale bar at 600 µm (B) Wound healing measurements between each quadrant at each timepoint during the migration well assay. N=1*

Brightfield images taken for each section were analysed using ImageJ Wound Healing plugin. The remaining area of each gap is calculated for each day over the assay and highlighted in red (Figure 5.28, A). Images reveal how no migration occurred between the CMs in both the conditioned medias compared to the other cell populations. Analysing the wound closure

measurements shows how the fastest gap closure occurs between $HSPG2^{WT}$ CFs and CMs (Figure 5.28, B). The gap closure between $HSPG2^{+/-}$ CFs and CMs is reduced compared to the $HSPG2^{WT}$ CFs, reaching a maximal closure of 40% after 5 days, this wound closure rate then reduces over the following days. Wound closure results of cells under hypoxic CM conditioned media show no difference in $HSPG2^{WT}$ CF to CM closure, interestingly the $HSPG2^{+/-}$ CFs show the same wound gap closure rate as $HSPG2^{WT}$ CFs. This shows the $HSPG2^{+/-}$ CFs exist in a more quiescent state than the $HSPG2^{WT}$ CFs under the presence of control conditioned media. When the $HSPG2^{+/-}$ CFs are cultured in hypoxic CM conditioned media they become activated to the same extent as the $HSPG2^{WT}$ CFs implying a switch has occurred in the $HSPG2^{+/-}$ CFs.

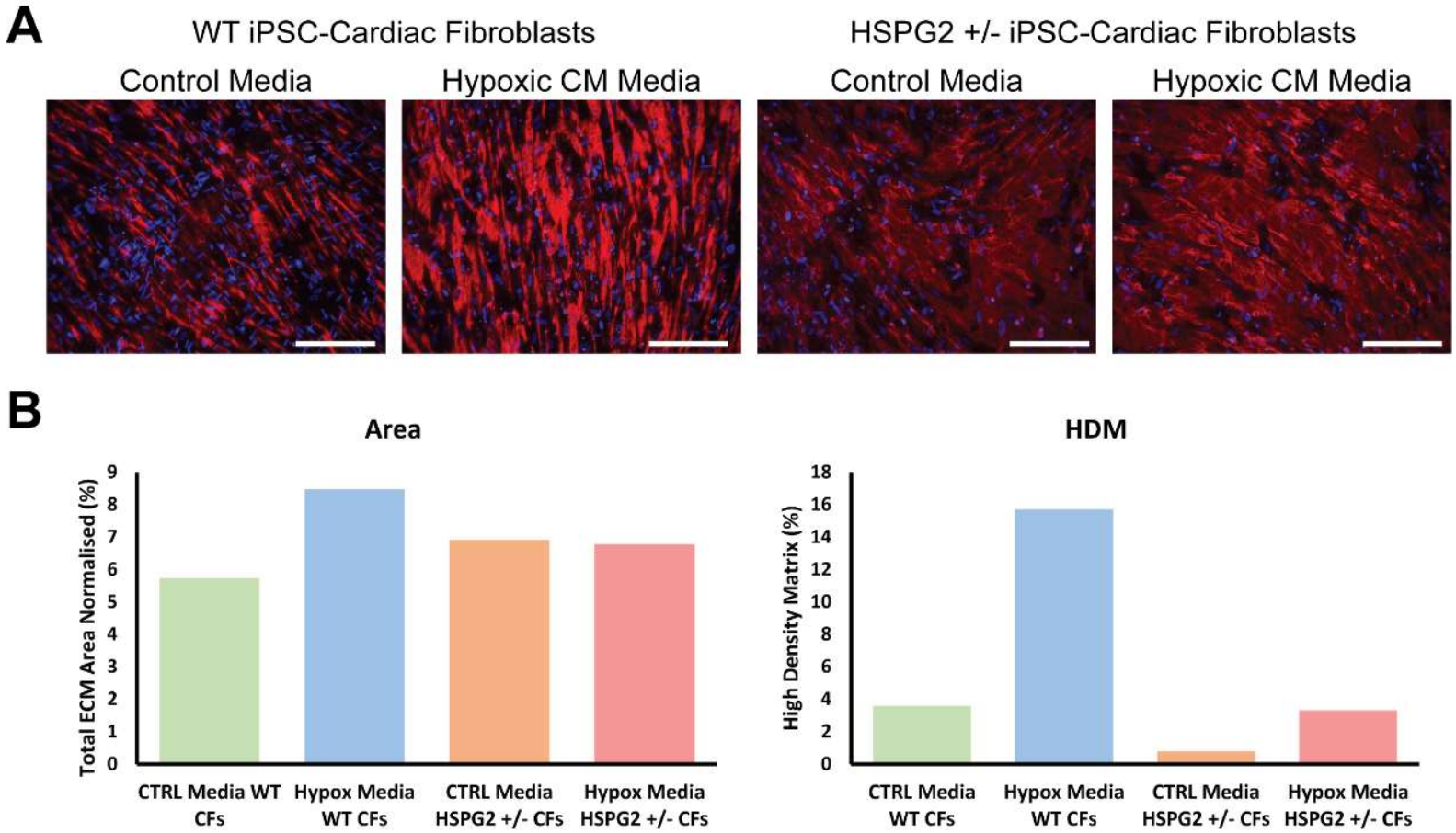


***Figure 5.29 – Perlecan immunostaining of CFs in migration wells and ECM analysis.*** *(A) Perlecan polyclonal antibody staining (CCN1 – red) and DAPI (blue) of WT and +/- CFs in migration wells under each media condition. Scale bar at 250 µm. (B) TWOMBLI ECM analysis of perlecan immunostaining images. N=1*

Immunostaining was then performed on both HSPG2$^{WT}$ and HSPG2$^{+/-}$ CFs under both control and hypoxic CM conditioned media after the migration assay had finished (Figure 5.29, A). Images show how CFs in this assay produced a perlecan rich ECM, the ECM laid down by the HSPG2$^{+/-}$ CFs is fainter but covers a similar area as calculated by ECM analysis (Figure 5.29, B). When the HSPG2$^{WT}$ CFs are cultured under hypoxic CM conditioned media the intensity of perlecan ECM secreted is increased and with this the level of HDM is also increased. Calculating the HDM for HSPG2$^{+/-}$ CFs shows they respond in an equivalent way to the presence of hypoxic CM media increasing the level of perlecan HDM, although this level is the same as found in the control HSPG2$^{WT}$ CFs. Interestingly the HSPG2$^{WT}$ CFs show directionality to the ECM secretion, while the HSPG2$^{+/-}$ CFs don't. This is potentially due to the location of the photo taken or the confluency of CFs involved HSPG2$^{WT}$ CFs to form a unidirectionality.

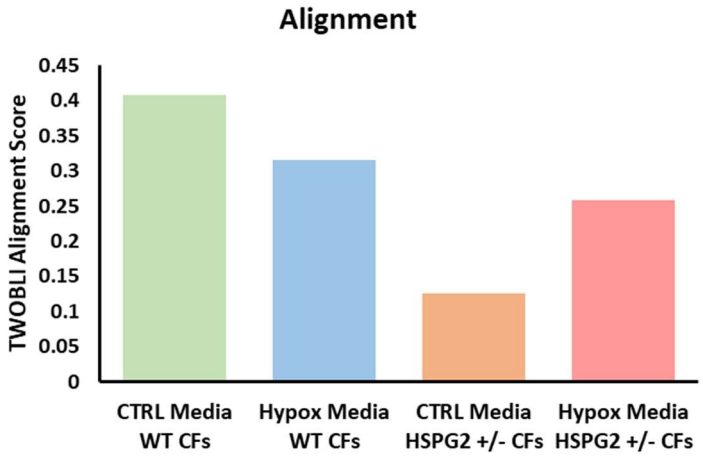


***Figure 5.30 – TWOMBLI ECM analysis on HSPG2 WT and +/- CFs in control and hypoxic conditioned medias.*** *ECM alignment score is output following TWOMBLI ECM analysis of perlecan immunostaining images. N = 1*

Using TWOMBLI ECM analysis to investigate ECM alignment a clear trend is seen showing HSPG2$^{WT}$ CFs in control media having the most aligned ECM (Figure 5.30). Even after culturing in hypoxic CM conditioned media the HSPG2$^{WT}$ CFs show a higher level of alignment than HSPG2$^{+/-}$ CF conditions. Interestingly the alignment is increased in HSPG2$^{+/-}$ CFs when cultured in hypoxic CM conditioned media over control media.

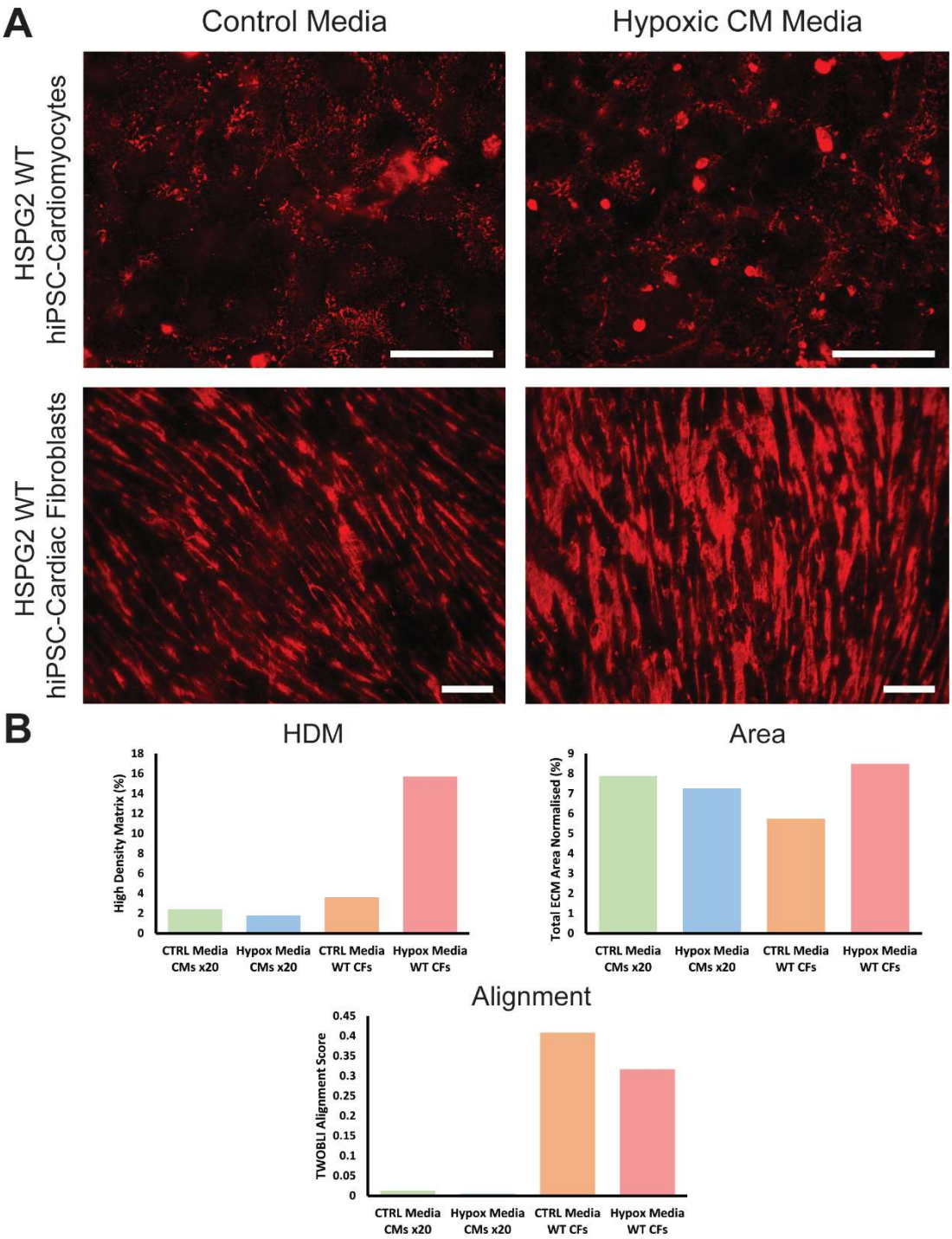


***Figure 5.31 – Perlecan immunostaining of CMs and CFs under control or hypoxic conditioned medias.*** *(A) Perlecan polyclonal antibody staining (CCN1 – red) of WT CMs and CFs in migration wells under each media composition. Scale bar at 125 µm. (B) TWOMBLI ECM analysis of perlecan immunostaining. N=1*

I then wanted to compare differences in perlecan ECM between CMs and CFs, plus how the addition of hypoxic CM conditioned media enhanced these differences. Immunostaining reveals perlecan on CMs appears punctate, disorganised fashion localised on the cells, while CFs secrete a perlecan ECM throughout the culture and between cells (Figure 5.31, A). CFs cultured in hypoxic media show changes in perlecan ECM secretion while the CMs don't show a similar response. Using TWOMBLI ECM analysis shows the CFs respond to hypoxic CM conditioned media by increasing the production of perlecan rich HDM, this is not reciprocated in the CMs (Figure 5.31, B). Interestingly the area of perlecan ECM is similar between both cell types, this could be due to the CM images being taken at a higher intensity or magnification due to the low levels of perlecan secreted by CM compared to CFs. Perlecan ECM alignment analysis shows the largest discrepancy between each cell type, the CMs show almost no alignment in ECM compared to the CFs cultured under either media.

## 5.6. Conclusion

In this chapter I aimed at investigating how CMs and CFs responded to inflammatory TGFβ stimulation, and how this altered *HSPG2* expression. To investigate *HSPG2*s role further in cardiac disease, I aimed to create co-cultures of both cell types. These co-cultures underwent a scratch wound assay to investigate wound closure and if *HSPG2* played a role in this.

### TGFβ treatment on cardiac populations

The use of TGFβ on CMs confirmed its role as an up regulator of *HSPG2* via the SMAD pathway (Iozzo et al., 1997). Both domain 1 and domain 5 of *HSPG2* were upregulated in hiPSC-CMs after TGFβ treatment, along with *COL18A1*. Interestingly, the third basement membrane HSPG (*AGRN*), showed the opposing expression pattern, reducing in both cell type. *COL18A1* and *HSPG2* expression follows the same trend under inflammatory assault implying these HSPGs may play a role in inflammatory response and therefore wound healing. *AGRN*s attenuated expression under the presence of TGFβ implies this HSPG may play an opposite role in the inflammatory process. The

expression of structural cardiac markers is altered slightly after TGFβ treatment. *MYH7* expression increased, although *MYH6* expression wasn't quantified so the ratio of the two genes wasn't able to be performed. Although one CM structural gene was increased (*MYH7*), another, *TNNI3*, showed no change and *ACTC1* expression was attenuated. If the ratio of *MYH6* and *MYH7* was calculated, the increase in expression seen in *MYH7* could link to an increased structural CM maturity, at the reduction of *ACTC1* expression.

Interestingly the immunostaining revealed no changes in perlecan ECM secretion after TGFβ treatment in both cell lines. The fibrous strands of perlecan ECM seen in the $HSPG2^{+/-}$ CMs could be created by an impure CM differentiation leading to creation of multiple cell types, as the fibrous ECM wasn't seen in $HSPG2^{WT}$ CM cultures. TGFβ treatment of CFs shows an increase in MF marker *ACTA2* and collagens *COL1A1* and *COL4A2* confirming transition from an inactivated CF to an activated MF. Interestingly *COL3A1* shows no difference in expression between hiPSCs and hiPSC-CFs, although CT values for hiPSC-MFs were above 40 cycles and therefore voided. This is most likely due to only n of 1 sample used and a technical error. The change in HSPG expression follows the same trend in CFs as seen in CMs. Both perlecan domains are increased in the activated MFs to a higher extent than the CMs treated with TGFβ showing a higher response to TGFβ stimulation. Interestingly the expression of *COL18A1* is only increased 3-fold in activated MFs compared to the 20-fold expression increase seen in CMs treated with TGFβ. This shows an increase in *HSPG2* in CFs is the most preferential HSPG expression response to inflammatory stimulant TGFβ, compared to CM response showing an increase in both *HSPG2* and *COL18A1*.

Both CMs and CFs show a similar reduction in *AGRN* expression, showing how as *HSPG2* and *COL18A1* expression increases *AGRN*s expression counters this response. Immunostaining targeting αSMA shows no difference in activation between the *HSPG2* lines. Staining shows how there is a level of αSMA MF activation found in the CF populations without TGFβ treatment, this appears mostly in the compact regions of the CF culture. When treated with

TGFβ the expression of αSMA becomes more apparent throughout both cultures. Staining with perlecan monoclonal antibody CCN1 shows perlecan ECM secretion is localised around the clusters of CFs that were αSMA positive. Due to this, the level of confluency of these wells could play a role in extent of perlecan secreted ECM. TGFβ treatment caused an increase in MF presence in the cultures, this increased the perlecan ECM throughout the conditions, although the most intense regions were still localised around αSMA positive MF clusters. Following analysis of both cell types responding to TGFβ I then aimed at combining the two cell types as analysed their response to damage.

**Cardiac co-cultures and models of cardiac fibrosis**

The initial co-culture was created to analyse how a presence of CFs within a CM population would affect the contraction of CMs. Contraction analysis on these co-cultures shows a low presence of CFs increased the contraction force generated by CMs compared to a pure population of CMs. As the level of CFs in the population are further increased, the ability for CMs to contract is attenuated. The same trend was seen in $HSPG2^{+/-}$ CMs co-cultured with $HSPG2^{WT}$ CFs, where a low presence increased contractile function, but an over population would hinder contraction. After performing a scratch wound on these co-cultures, the migration was monitored, and wound closure calculated. Results show how the scratch wound is closed to a higher extent in cultures containing both CMs and CFs compared to those that contain a 100% population of either. The population containing 25% CMs and 75% CFs closed the wound to a similar extent as the 100% CF scratch, while those containing a higher percentage of CMs with CFs fully close the wound. These results suggest CFs are the cell type that will migrate into a wound site after damage, reducing the number of CFs had no effect in limiting wound closure suggesting the death of CMs caused an increased migratory response.

Comparing the wound closure of cultures containing $HSPG2^{WT}$ and $HSPG2^{+/-}$ CMs show $HSPG2^{+/-}$ CMs reduced the wound gap more than $HSPG2^{WT}$ CMs. The $HSPG2^{+/-}$ CMs on the edge of the wound gap did migrate to a small extent, but most of the wound gap closure was the result of CMs becoming

hypertrophic, taking up the empty space left behind from the scratch wound. Analysing contraction on both sides of the scratch wound was performed to determine if electrocoupling had occurred from the migratory cells over the scratch. Results show the scratch wounds that had healed the most also show the least difference between either sides action potential delta.

In $HSPG2^{WT}$ action potential differences the 100% and 25% CMs show the largest variation. The 100% was fully uncoupled due to no connection to either side, while the 25% CM population wound gap was not fully formed and potentially had reduced electrocoupling. The trend is similar with $HSPG2^{+/-}$ CMs, large variation in either sides contraction recorded in the 25% CM population scratch wound, although here the 100% CM scratch wound appears to be electro coupled to the same extent as the other scratch wounds. On further examination the scratch performed on the 100% $HSPG2^{+/-}$ CM culture was not complete, leaving a small subsection of CMs connecting in the top corner of the well. This small bridge of CMs would allow both sides to remain electro coupled and therefore explain the lack of change in action potential difference seen in the $HSPG2^{WT}$ CM culture.

Perlecan immunostaining reveals the migratory cells secreted a perlecan rich ECM preferentially into the healed scratch wound over the undamaged regions. These results suggest perlecan ECM is a crucial part of the healing process in cardiac damage. The level of perlecan HDM laid down follows the same trend as final wound closure, implying the more migration that occurred the more perlecan HDM is secreted in the wound. The low level of CFs co-cultured with the CMs show preferential perlecan secretion in the wound gap over the undamaged regions. These results suggest when a population containing mostly CMs is damaged, CFs will secrete perlecan as a reparative ECM. As the population of CFs are increased in the co-culture, the perlecan ECM secretion is less focused within the healed wound and becomes secreted throughout the whole culture.

One of the aims of this assay was to determine if $HSPG2^{WT}$ CFs would respond in a different manner depending on if they are co-cultured with

HSPG2$^{WT}$ or HSPG2$^{+/-}$ CMs. From the results the HSPG2$^{WT}$ CFs respond similarly to either CM showing the reduction of *HSPG2* in CMs was not enough to cause a change on CF behaviour. CMs are not the main perlecan producing cell type and so would not show a significant difference in ECM secretion, but I theorised a lack of *HSPG2* in CMs could have signalled a stress response from the CFs, although this was not seen.

Following this scratch wound I aimed at investigating the role of media compositions and how these would affect migration, MF activation and perlecan ECM secretion. To simulate a response that would be found after cardiac injury I used conditioned media created from hypoxic CMs. I also wanted to investigate if this assay could be used as an initial drug screen for antifibrotic drugs. With collaboration with Andrew Chantry, UEA I used prototype antifibrotic drug indole-3-carbanol (Chen et al., 2019) on my scratch wound assay. The results show how indole-3-carbanol had a significant effect on reducing the wound closure of both culture conditions. Interestingly analysis of αSMA intensity showed no difference between the cultures suggesting the antifibrotic drug did not reduce activation of CFs, or the hypoxic CM media increase it. These results suggest the antifibrotic drug influences the migratory capability of CFs rather than the activation and ECM secretion of MFs. The assay was not performed for a long enough period to see the same extent of perlecan ECM as was seen in first scratch wound. Another complication with this assay was the seeded CFs quickly became over confluent. The scratch performed tore the confluent CFs, these left overhangs of clumped CFs that would proceed to rapidly close the wound and could explain the rapid gap reduction and the standard deviation seen between results.

In the final migration assay I aimed at investigating HSPG2$^{+/-}$ CFs compared to the WT, if there was a difference in migration and perlecan ECM secretion. The HSPG2$^{+/-}$ CFs were unable to migrate into the wound gap and close the wound compared to the HSPG2$^{WT}$ CFs when under normoxic CM conditioned media. Although under hypoxic CM conditioned media the HSPG2$^{+/-}$ CFs migrated and closed the gap at the same rate as the HSPG2$^{WT}$ CFs. During

this assay I was also able to monitor the migration between both CF cell lines, these don't fully close the wound. This highlights a preferential migration direction of CFs towards CMs, over other CFs. Although, this assay is not able to fully differentiate a difference between migration or proliferation. Due to this, the increased speed in wound gap closure by $HSPG2^{+/-}$ CFs under hypoxic media cannot be determined an improved migration or proliferation.

Active migration and proliferation are indicative of an activated CF compared to a quiescent CF or MF; these results suggest the $HSPG2^{+/-}$ CFs exist in the quiescent state until activated by hypoxic CM conditioned media. ECM analysis of the two cell lines shows $HSPG2^{WT}$ CFs lay an aligned perlecan ECM, when the $HSPG2^{+/-}$ CFs became activated under hypoxic media they also proceeded to lay a more aligned matrix. The alignment of the ECM laid down appears to be higher in activated CFs compared to quiescent CFs, implying directionality may play a role in activated CF migration or proliferation. ECM analysis confirms an increase in perlecan HDM after growth in hypoxic CM conditioned media. This increase was not seen in the previous scratch wound, implying prolonged exposure to hypoxic stress signals are required to increase perlecan HDM production.

I also wanted to compare the difference between CM and CF perlecan ECM secretion. ECM analysis shows how the CM perlecan ECM is punctate and pericellular showing no alignment, CMs also don't increase HDM perlecan ECM when cultured in hypertrophic stressed media. These results suggest different forms of perlecan ECM are preferentially secreted depending on the cell type, the ECM from CFs would be structural and forms a large ECM mesh throughout the culture. The CM perlecan ECM appears focused around the cells suggesting its role may be growth factor sequestration and binding over a structural ECM.

# 6. Response of hiPSC-CMs to enhanced perlecan expression

## 6.1. Introduction

Enhancing maturation of hiPSC-cardiomyocytes (CMs) is desirable for progressing hiPSC-CM disease models, drug screens and therapies. As such, many different hiPSC-CM maturation strategies have been explored. The culturing of hiPSC-CM as 3D tissues *in vivo* induces maturation (Ahmed et al., 2020). Interestingly, ECM composition of implanted hiPSC-CM tissue significantly alters, with perlecan expression greatly increased after 12 weeks *in vivo* culture (Yokoyama et al., 2021). Furthermore, hiPSC-CMs seeded onto perinatal stem cell-derived ECM (enriched with perlecan), was also capable of enhancing CM maturation (Block et al., 2020). Although it is known that perlecan is essential in the developing heart, these studies highlight a potential role in CM maturation. The phenotyping of my perlecan deficient hiPSC-CMs presented (Chapter 4), were suggestive of reduced maturity, further supporting this hypothesis. In this chapter I will explore this hypothesis, investigating whether increasing perlecan signalling was indeed capable of enhancing hiPSC-CM maturation.

Previously, I demonstrated the successful use of CRISPRi to upregulate expression of *HSPG2* in hiPSCs (Chapter 3). Here I will attempt this same strategy in hiPSC-CMs, although due to CM sensitivity to electroporation, an alternate lipofection transfection method will be used (Bodbin et al., 2020). Furthermore, I will investigate the effect of switching the substrate used for the 10-day maturation period from the routinely used vitronectin peptide to a synthetic perlecan peptide (PER-P).

## 6.2. hiPSC-CM and CRISPRi upregulation of HSPG2

Upregulation of HSPG2 was previously achieved in hiPSCs using CRISPRi (dCas9) and electroporation (chapter 3). To transfect hiPSC-CMs with dCas9

plasmids I opted for lipofection (Viafect) transfection method, previously optimised for hiPSC-CMs (Bodbin et al., 2020).

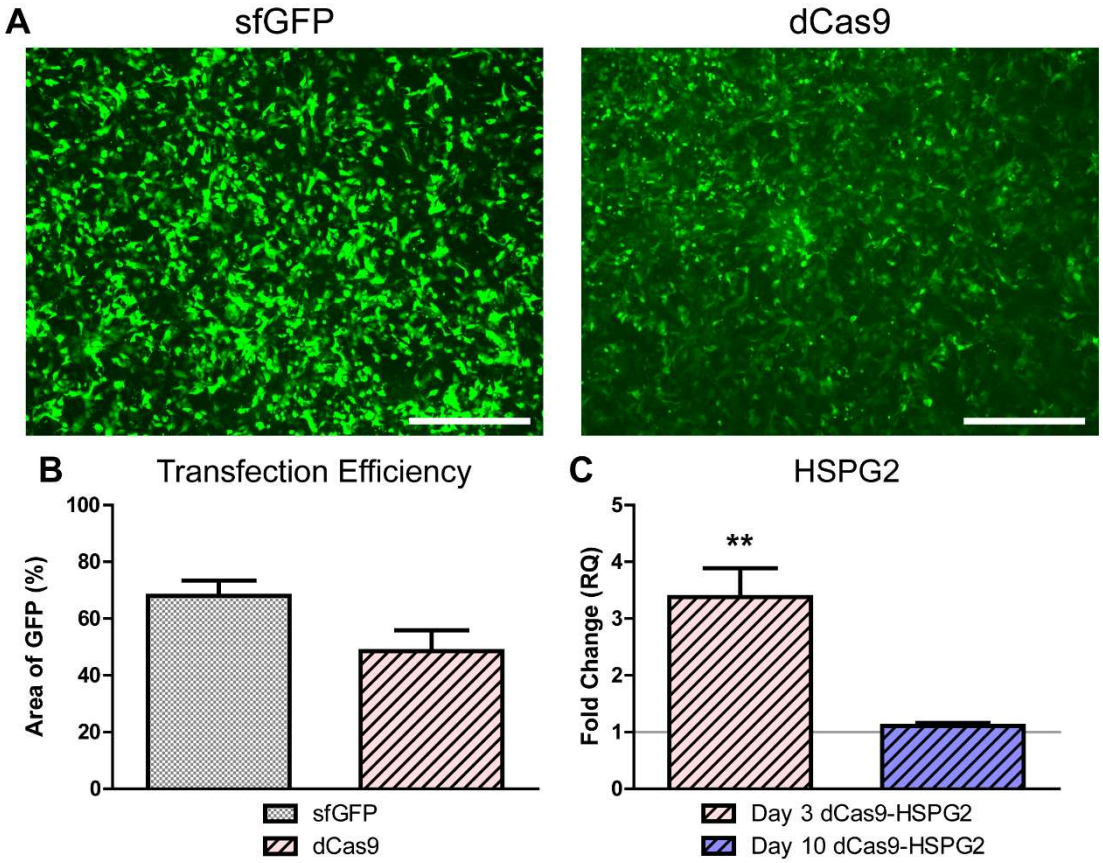


***Figure 6.1 – Transfection of hiPSC-CMs with CRISPRi.*** *(A) Fluorescent imaging of transfected hiPSC-CMs with sfGFP or dCas9 plasmids. Scale bar at 600 µm. (B) Quantified transfection efficiency with ImageJ analysis of GFP area. (C) qRT-PCR fold change of HSPG2 expression in transfected dCas9 hiPSC-CMs at day 3 and day 10 normalised to sfGFP hiPSC-CMs on representative timepoints. n=3, significance determined through t-test, P-value <0.05 = *, <0.01 = **, <0.001 = ***.*

To confirm transfection efficiency, I opted to transfect super fold GFP (sfGFP) into hiPSC-CMs. Indeed, dCas9 plasmids contained a GFP sequence, although for quantifying transfection efficiency through GFP intensity, sfGFP provides a brighter signal (Pédelacq et al., 2005) (Figure 6.1, A). ImageJ quantification confirms 68.1 ±4.40% of hiPSC-CMs are expressing GFP after sfGFP transfection, and 48.6 ±5.97% after dCa9 plasmid transfection (Figure 6.1, B). Following confirmation of successful transfection of hiPSC-CMs I performed qRT-PCR to analyse expression of *HSPG2* and if this was

maintained over prolonged culture. Indeed, transfection of dCas9 plasmids into hiPSC-CMs upregulated *HSPG2* expression post 3 days transfection by 3.38 ±0.72-fold change (Figure 6.1, C). Although, over prolonged culture the overexpression deteriorated whereby expression of *HSPG2* was equivalent to the sfGFP transfection control (1.11 ±0.077-fold change).

Due to hiPSC-CMs being non-proliferative the CRISPRi system has been shown to maintain overexpression for prolonged periods of culture (Bodbin et al., 2020). Unfortunately, here HSPG2 upregulation was only seen early after transfection, where ideally a stable *HSPG2* upregulation would be maintained throughout culture. Since this system did not maintain overexpression in culture, I opted to focus on a synthetic perlecan surface for the maturation period of hiPSC-CM culture.

### 6.3. hiPSC-CMs on PER-P

To investigate if hiPSC-CMs showed increased maturation on a perlecan rich surface, PER-P plates were used. After 14 days of culture on PER-P hiPSC-CMs displayed abnormal morphology compared to hiPSC-CMs cultured on vitronectin (VTN). Fluorescent imaging of hiPSC-CMs revealed less defined borders between cells cultured on PER-P compared to VTN (Figure 6.2, A). PER-P cultured hiPSC-CMs also displayed excessive multinucleation, an indication of hypertrophic growth (Figure 6.2, B). A high content imaging algorithm was used to calculate nuclear quantity on both substrates, previously validated for hiPSC-CMs (Mosqueira et al., 2019). hiPSC-CMs seeded on VTN show 90.1% ±2.8 mononucleated CMs, compared to 75.1% ±1.5 on PER-P. Binucleated and multinucleated CMs were more present on PER-P, (9.0% ±2.3 to 18.8% ±1.2 respectively) compared to VTN (0.9% ±0.5 to 5.7% ±0.5 respectively) (Figure 6.2, C).

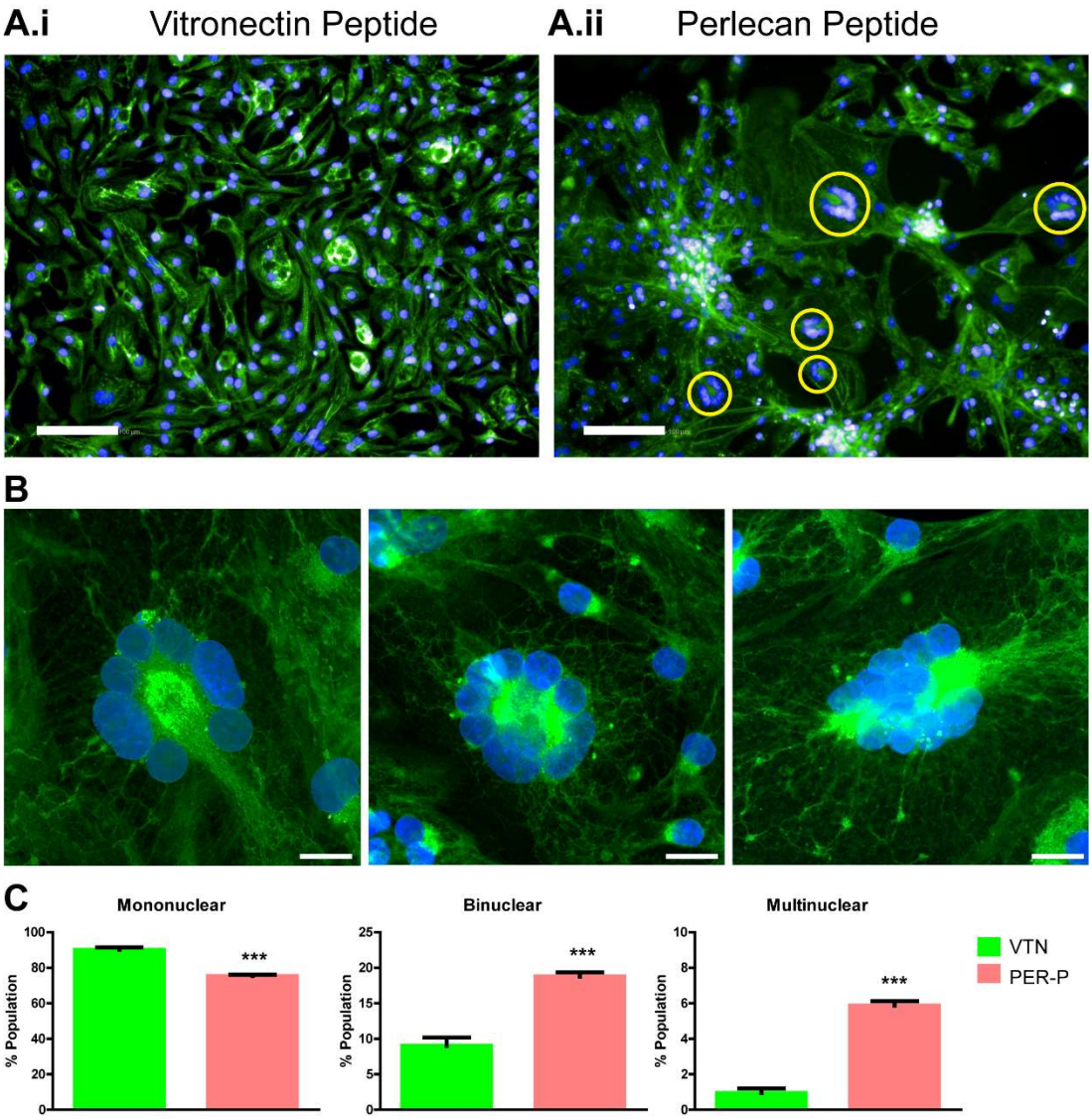


***Figure 6.2 – hiPSCs seeded on vitronectin and perlecan peptide.*** *(A) hiPSC-CMs seeded on vitronectin (VTN) and perlecan peptide (PER-P). Fluorescent images highlighting α-Actinin (green) sarcomere banding and nuclear stain DAPI (blue). Multinucleation identified in several hiPSC-CMs on PER-P (circles). Scale bar 100 µm. (B) Magnified zoom of multinucleated hiPSC-CMs identifying clusters of 8+ nuclei. Scale bar 20 µm. (C) Image analysis quantifying nuclear count per cell is split between mononuclear, binuclear, and multinuclear. n=3, significance determined through multiple t-tests, P-value <0.05 = *, <0.01 = **, <0.001 = ***.*

Following morphological changes observed, I investigated the expression of cardiac structural markers between hiPSC-CMs on both substrates using qRT-PCR (Figure 6.3).

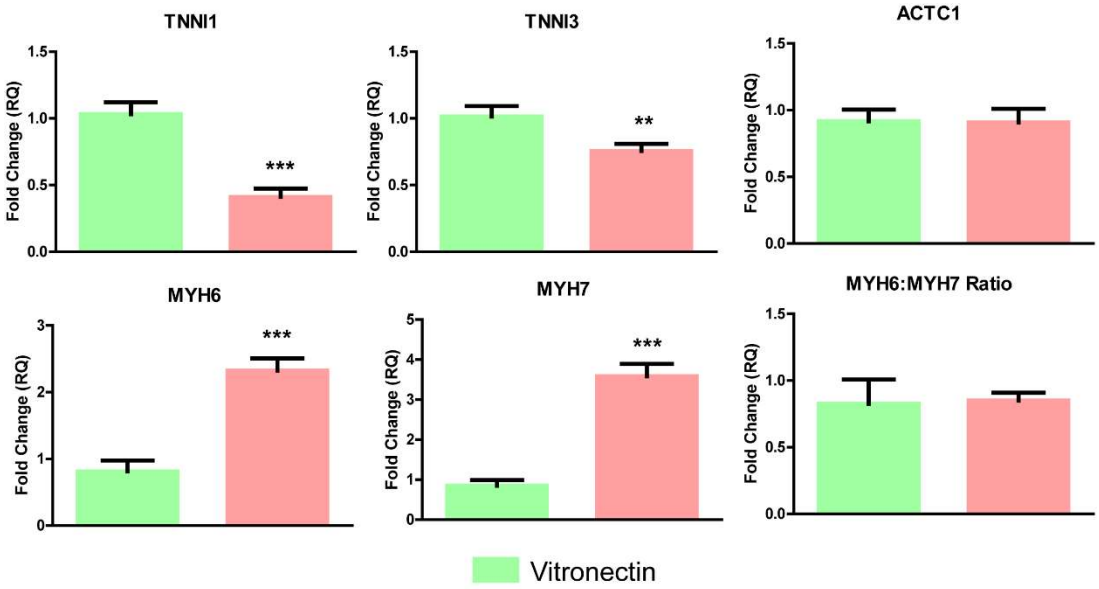


***Figure 6.3 – qRT-PCR of structural cardiac genes.*** *Fold change expression of hiPSC-CMs after 14 days of culture on PER-P compared to VTN. n=3, statistical test performed using t-test. P-value <0.05 = *, <0.01 = **, <0.001 = ***.*

Both *TNNI1* and *TNNI3* are downregulated in hiPSC-CMs cultured on PER-P, 0.41 ±0.052 and 0.76 ±0.044-fold change respectively. Interestingly, both α and β isoforms of cardiac myosin heavy chain (MYH6 and MYH7) are upregulated in hiPSC-CMs cultured on PER-P (2.32 ±0.115 and 3.59 ±0.25 respectively). To determine if *MYH7* was expressed to a higher magnitude than *MYH6* the ratio was plotted between the genes showing no significant difference. qRT-PCR of sarcomeric cardiac actin marker *ACTC1* found no significant difference between hiPSC-CMs cultured on VTN and PER-P. I next wanted to investigate HSPG expression in hiPSC-CMs following maturation on PER-P substrates (Figure 6.4).

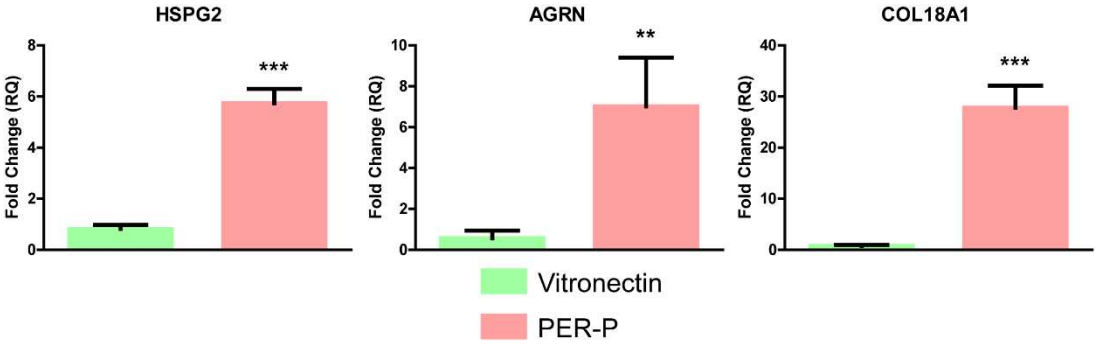


***Figure 6.4 – qRT-PCR of key HSPGs.*** *Fold change expression of hiPSC-CMs after 14 days of culture on PER-P compared to VTN. n=3, statistical test performed using t-test. P-value <0.05 = *, <0.01 = **, <0.001 = ***.*

After culture of hiPSC-CMs on PER-P expression of all three HSPGs (*HSPG2*, *AGRN*, *COL18A1*) were increased. Of the 3 HSPGs, *COL18A1* expression was enhanced the greatest compared to VTN (27.8 ±3.51). Expression of both *HSPG2* and *AGRN* was statistically increased in hiPSC-CMs after culturing on PER-P (5.74 ±0.46 and 7.01 ±1.94-fold change respectively). hiPSC-CMs cultured on PER-P have increased expression of *HSPG2*, I next wanted to investigate if metabolic genes had abnormal expression.

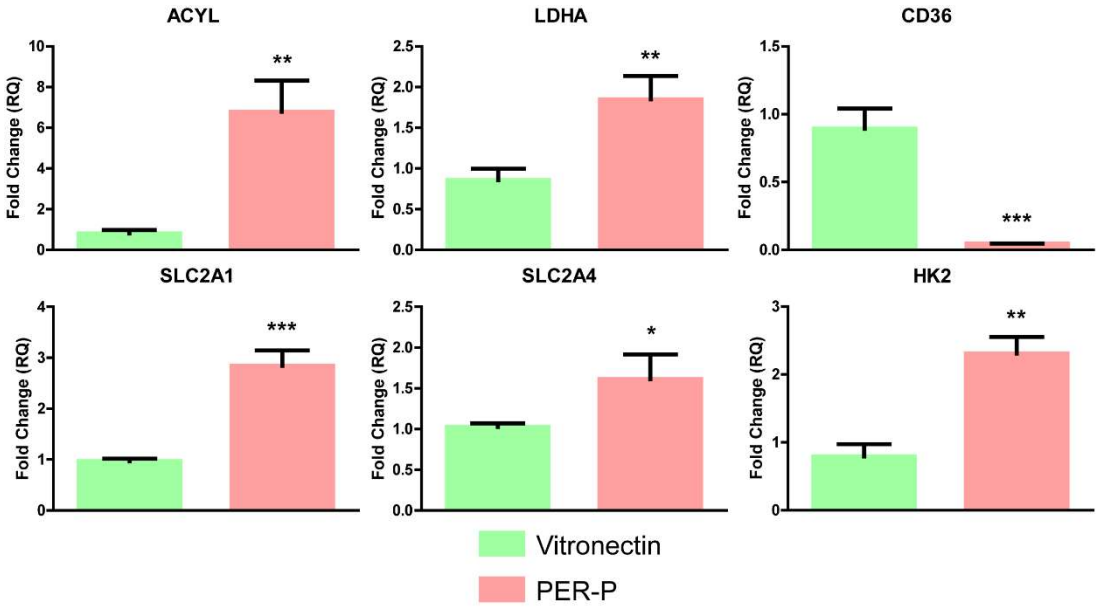


***Figure 6.5 – qRT-PCR of metabolic genes.*** *Fold change expression of hiPSC-CMs after 14 days of culture on PER-P compared to VTN. n=3, statistical test performed using t-test. P-value <0.05 = *, <0.01 = **, <0.001 = ***.*

Expression of fatty acid metabolic gene ATP citrate lysate (*ACYL*) is expressed at 6.79 ±1.25-fold change in hiPSC-CMs cultured on PER-P compared to VTN (Figure 6.5). Interestingly, expression of surface marker *CD36*, involved in fatty acid binding and transportation, was attenuated in hiPSC-CMs cultures on PER-P (0.048 ±0.00073). Glycolytic genes (*LDHA*, *HK2*, *SLC2A1*, *SLC2A4*) investigated all show statistical upregulated expression in hiPSC-CMs on PER-P (*LHDA* 1.85 ±0.23, *HK2* 2.31 ±0.20, *SLC2A1* 2.84 ±0.25, *SLC2A4* 1.61 ±0.25-fold change). The increased expression of glycolytic genes combines with attenuation of *CD36* would suggest the hiPSC-CMs cultured on PER-P are less mature than those on VTN (Poon et al., 2020). Although, upregulation *ACYL* would suggest increased fatty acid metabolism and therefore more mature hiPSC-CMs.

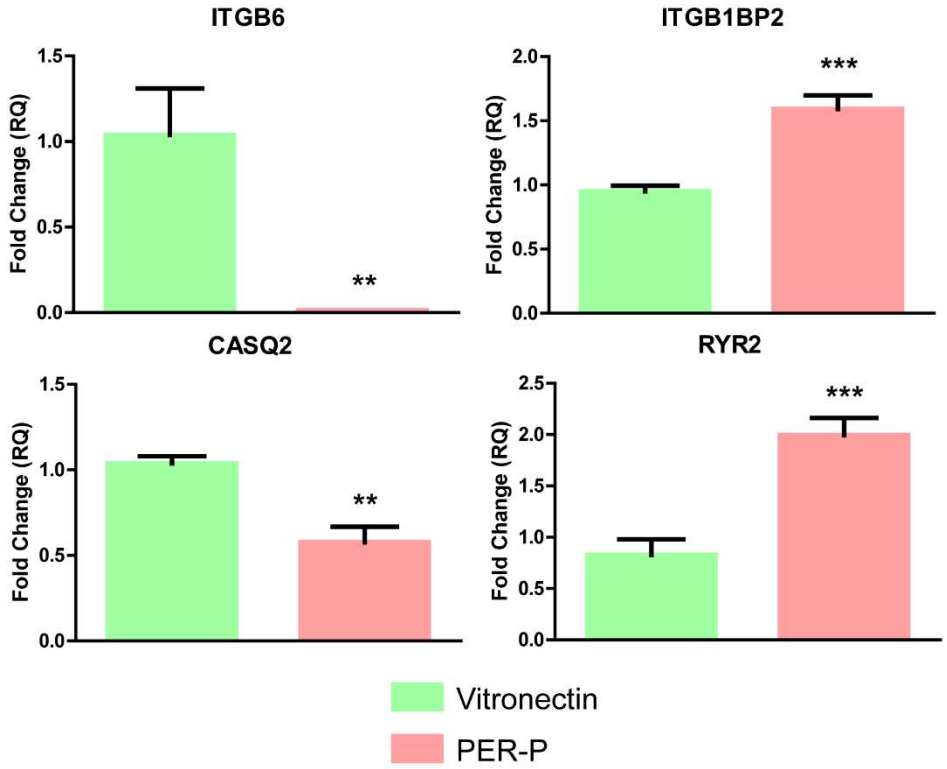


***Figure 6.6 – qRT-PCR of integrin and calcium genes.*** *Fold change expression of hiPSC-CMs after 14 days of culture on PER-P compared to VTN. n=3, statistical test performed using t-test. P-value <0.05 = *, <0.01 = **, <0.001 = ***.*

Due to hiPSC-CMs cultured on PER-P showing hypertrophic morphological changes I opted to investigate potential integrins and biomarkers in cardiomyopathy (Zhuang et al., 2017) (Figure 6.6). *ITGB6* expression is significantly attenuated in hiPSC-CMs cultured on PER-P (0.014 ±0.00023-fold change), while *ITGB1BP2* expression is increased to 1.59 ±0.086-fold change. *CASQ2* and *RYR2* are both involved in calcium handling in CMs, here hiPSC-CMs cultured on PER-P have adverse expression of these genes (0.58 ±0.07 and 1.99 ±0.14-fold change respectively).

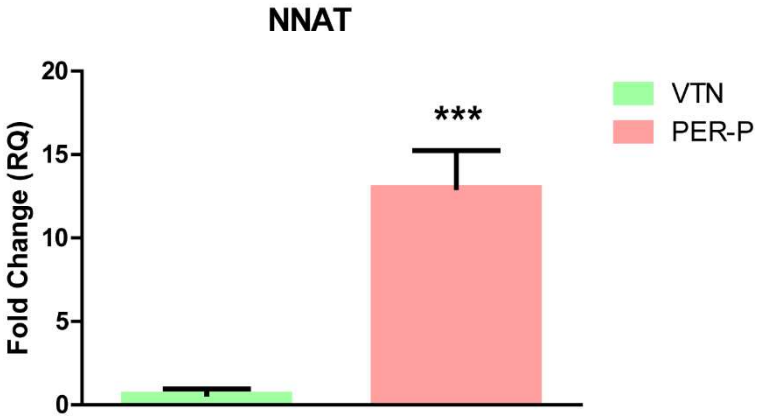


***Figure 6.7 – qRT-PCR of NNAT.*** *Fold change expression of hiPSC-CMs after 14 days of culture on PER-P compared to VTN. n=3, statistical test performed using t-test. P-value <0.05 = *, <0.01 = **, <0.001 = ***.*

Since *NNAT* expression was attenuated in HSPG2$^{+/-}$ cell lines throughout cardiac differentiation I investigated expression after hiPSC-CM culture on PER-P. Expression of *NNAT* was increased by 13.01 ±1.81-fold change in hiPSC-CMs on PER-P. These results suggest *NNAT* expression could be regulated by *HSPG2*.

### 6.4. Conclusion

CRISPRi has previously shown to enhance the expression of *HSPG2* in hiPSCs, although this led to cell clumping and detachment. hiPSC-CMs were successfully transfected with dCas9 plasmids, upregulating *HSPG2* up to 3 days post transfection. The overexpression system deteriorated over the remaining culture leading to no change between control and CRISPRi hiPSC-CMs, therefore an alternate solution was sought.

Use of a synthetic perlecan peptide created an artificial perlecan rich surface in which to culture hiPSC-CMs. Indeed, the perlecan synthetic surface would not represent a physiological ECM but provides a controlled method of investigating cellular response to increased perlecan binding. Following 14 days of culture on PER-P, hiPSC-CMs displayed morphological characteristics of hypertrophic growth. The hiPSC-CMs on PER-P had increased multinucleation compared to hiPSC-CMs cultured on VTN.

Following birth, CMs cease cell division (hyperplastic growth) and switch to hypertrophic growth to continue developmental heart expansion. Thereby the process of hypertrophic growth can be considered part of physiological maturation. Multinucleation also occurs following birth, remaining cell cycle activation and inhibition of cell division results in polyploid cells, this process is also a characteristic of CM maturation (Denning et al., 2016; Yuan and Braun, 2017). Increased multinucleation and hypertrophic growth of hiPSC-CMs on PER-P therefore suggests phenotypic maturation.

Despite morphological changes, qRT-PCR analysis of hiPSC-CMs on PER-P does not indicate increased maturation of the CMs. The expression of both myosin heavy chains (*MYH6* and *MYH7*) increased while troponin genes (*TNNI1* and *TNNI3*) were statistically reduced. Overall glycolytic (*LDHA*, *HK2*, *SCL2A1* and *SLC2A4*) and fatty acid (*ACYL*) metabolic genes were increased suggesting PER-P hiPSC-CMs had a total increase in metabolism. Although, reduction of *CD36* suggested these hiPSC-CMs were less mature of PER-P than VTN. Both perlecans LDL receptor and *CD36* bind and import fatty acids, therefore the reduction of *CD36* expression could be linked to the synthetic perlecan rich culture surface. Indeed, metabolic analysis using BioLog Mitoplates would be a more useful measurement to determine enhanced or reduced metabolic maturity.

Interestingly, the three ECM HSPGs were statistically upregulated in hiPSC-CMs cultured on PER-P. In a model of hiPSC-CM hypertrophy perlecan was one of 23 proteins found to be differentially expressed (Johansson et al., 2022). The increased expression of *HSPG2* in hypertrophic hiPSC-CMs on

PER-P corelate with this data. *COL18A1* expression has also been reportedly increased in fibronectin induced cardiomyocyte hypertrophy (Chen et al., 2004), again reconfirming expression of hypertrophic hiPSC-CMs on PER-P. Post myocardial damage induced cardiac hypertrophy in pig hearts was reduced after treatment with recombinant human agrin (Baehr et al., 2020). This result suggests increased agrin reduces hypertrophy, unlike *HSPG2* and *COL18A1*. Overall, the literature here supports increased HSPG gene expression seen in hypertrophic hiPSC-CMs on PER-P with models of induced CM hypertrophy.

Investigating integrin and calcium genes associated with cardiomyopathies revealed contradictory results to the literature. *ITGB6* is upregulated in both hypertrophic and dilated cardiomyopathy KEGG pathways but is drastically attenuated in hiPSC-CMs cultured on PER-P. Interestingly *ITGB1BP2*, also known as Melusin, overexpression protects the heart from dilated cardiomyopathy (de Acetis et al., 2005) with ablation impairing hypertrophy (Palumbo et al., 2009). *ITGB1BP2* expression is increased in PER-P hiPSC-CMs, this response is expected in left ventricular hypertrophy and therefore reconfirming hypertrophic growth in PER-P hiPSC-CMs. *RYR2* is a major part of calcium release from the sarcoplasmic reticulum, mutations in this channel are known to cause hypertrophic cardiomyopathy (Tang et al., 2012). hiPSC-CMs on PER-P have increased expression of *RYR2*, therefore not coinciding with hypertrophic cardiomyopathy in the literature (Zhuang et al., 2017). Increased *RYR2* expression is linked to cardiomyocyte maturation and therefore the increased expression in PER-P hiPSC-CMs could suggest increased maturation (Guo et al., 2022). *CASQ2* associates with *RYR2* (Knollmann et al., 2006), although interestingly, hiPSC-CMs on PER-P have reduced expression of *CASQ2*, thereby suggesting overall calcium handling wasn’t improved in the CMs.

# 7. Discussion

## 7.1. General discussion

As the impact of cardiovascular disease worsens, the need for improved treatment and prevention strategies are becoming of increased importance (Gheorghe et al., 2018). The development of hiPSC technology allows for generation of adult tissue types, giving rise to more relevant models of human development and disease investigation (Giacomelli et al., 2020; Lippi et al., 2020). The combination of hiPSC plasticity, with improved genetic manipulation methods (such as CRISPR/Cas9), provides researchers with a powerful tool to investigate the role of genes in specific tissue types.

Indeed, one of the major findings of this thesis was the role of HSPG2 in altering metabolic function of cardiac populations. All RT-qPCRs were performed against the housekeeper gene GAPDH, an enzyme involved in glucose metabolism. Although, analysing the RNA sequencing dataset found no statistical difference between the expression of GAPDH at any of the timepoints taken over the CM differentiation.

Unfortunately, a major limitation of hiPSCs in the investigation of cardiovascular disease is the immaturity of hiPSC-CMs (Lyra-Leite et al., 2022). Countless studies are performed with the aim of creating a mature hiPSC-CM, although these fall short of achieving the same characteristics of an adult CM (Guo and Pu, 2020). Immature CMs provide unsatisfactory outputs for drug screening and disease models, and due to insufficient electro handing and increased risk of arrhythmias, cannot be used to repopulate post infarcted hearts (Karbassi et al., 2020).

Despite confirmation as an essential ECM component of the heart, the role of perlecan remains understudied. *HSPG2* KO cause embryonic lethality due to weakened basement membranes (Sasse et al., 2008a). Perlecan is also shown to increase in the heart during maturation stages of cardiomyocyte development (Roediger et al., 2009a), suggesting a crucial role during this

process. Since CMs are not the main ECM secretory cell of the heart I also aimed at investigating the cardiac fibroblast (CF), known for ECM turnover and a crucial cell type in the response to heart disease (Travers et al., 2016). Perlecan ECM is also known to increase in the infarct following myocardial damage, showing *HSPG2* is a preferential component of cardiac development and healing (Nakahama et al., 2000).

The aim of my research is to expand the current knowledge of *HSPG2* and its role in the cardiac environment in both development and disease. The literature confirms its presence is essential in the developing heart and appears in response to cardiac damage showing *HSPG2* as an overall crucial component of the cardiac environment.

## 7.2. Key findings

### 7.2.1. *HSPG2* regulation is essential for hiPSC survival

The generation of a full *HSPG2* KO hiPSC cell line was not able to be performed during my PhD. Despite attempting multiple different CRISPR/Cas9 targeting strategies, on different hiPSC lines, no full HSPG2 KOs were created. Over one hundred heterozygous *HSPG2* clones were created and identified, giving me confidence that the inability to generate a homozygous clone was not due to a lack of technical ability, but most likely hindered by biological factors. Perlecan is known to sequester growth factors to the cell surface, of the growth factors, FGF signalling relies on co-operation with perlecan (Chang et al., 2015; Chuang et al., 2010). FGF2 is one of the essential factors used in hiPSC culture to maintain cell pluripotency (Mossahebi-Mohammadi et al., 2020). In the culture conditions we use, FGF2 is one of the main components of E8 supplement. The E8 supplement consist only of the essential components required to maintain hiPSCs in culture, these compounds include L-ascorbic acid, selenium, FGF2, insulin, transferrin, TGF$\beta$1, $NaHCO_3$ in DMEM/F12.

Indeed, perlecan also has roles in ECM binding, essential to the basement membrane of the heart (Sasse et al., 2008), and potentially essential to the adherence of hiPSCs. My culture conditions rely on hiPSC adherence to

vitronectin peptide coated surfaces. Vitronectin is one of the many components found in an alternate surface coating, Matrigel. The main components found in Matrigel consist of laminins, collagens, entactin and perlecan. Due to the presence of perlecan in Matrigel, it was not used as part of my culture system. In hindsight, the use of Matrigel would have been an effective way to determine if the lack of full *HSPG2* KO clones was due to surface coatings vs media composition. Furthermore, use of hiPSC HSPG2$^{KO}$ culture on PER-P could be implemented to replace the lack of *HSPG2,* although if hiPSCs can survive on PER-P is unknown. The combination of using a minimal defined supplement media, E8, and a single peptide, vitronectin, for cell attachment may provide an answer as to why no full *HSPG2* KO hiPSCs were generated.

*HSPG2* upregulated in hiPSCs using CRISPRi hindered survival via cell compaction. The clumping and detachment seen following upregulation is a clear sign of an overproduced, restrictive EMC, whereby the cells were proliferating in an enclosed capsule of ECM. The cell count and RNA content was shown to be like control transfected hiPSCs, showing proliferation was unchanged, just the capability of the hiPSCs to remain attached to the surface. Interestingly, if the hiPSCs with upregulated *HSPG2* were dissociated using TrypLE and reseeded, they returned to the same phenotype as control hiPSCs. This shows once the ECM that was constricting and causing detachment is removed the hiPSCs were able to resort back to a phenotypically normal morphology. This also highlighted the short half-life of HSPG2 upregulation in hiPSCs using CRISPRi, although no qRT-PCR was performed to confirm an expression profile change.

WT and HSPG2$^{+/-}$ hiPSCs appeared morphologically comparable. Markers of proliferation and pluripotency were unchanged, with investigation into the metabolism of these hiPSC lines identifying slight differences between the two lines. One noticeable difference was a reduction in fatty acid metabolism, possibly due to the lack of perlecan LDL receptors, reducing fatty acid uptake (Kallunki and Tryggvason, 1992; Zhang et al., 2016). By utilising RNA sequencing in-depth analysis of genetic differences can be highlighted

between the lines. 27 DEGs were identified between the two cell lines, 12 genes were upregulated, while 15 were downregulated in the HSPG2$^{+/-}$ hiPSC line. Gene ontology (GO) cluster analysis of the 27 DEGs highlighted two terms, whereby HS-GAG biosynthesis was downregulated, and MGMT-mediated DNA damage reversal upregulated in the HSPG2$^{+/-}$ hiPSC. These terms were only highlighted due to a small number of altered genes, and therefore, not as reliable as terms containing a larger pool of altered genes. Indeed, RNA sequencing shows *HS6ST3* to be amongst the most downregulated DEGs in HSPG2$^{+/-}$ hiPSCs. Although, gene counts reveal the highest expressed DEGs altered by *HSPG2* gene-editing to be *NNAT* (Neuronatin), and *HSPG2* as expected.

Overall, these results suggest a full reduction of *HSPG2* is detrimental to hiPSCs, either reducing viability, or adherence to vitronectin peptide coated surfaces. The upregulation of *HSPG2* was also detrimental to hiPSC culture, causing clumping and detachment of colonies. Very few differences were seen between WT and HSPG2$^{+/-}$ hiPSCs, with RNA sequencing highlighting only 27 DEGs and metabolic analysis revealing a minor decrease in fatty acid metabolic potential. The relationship between *HSPG2* and the regulation of *NNAT* expression is an interesting finding that warrants further investigation.

### 7.2.2. *HSPG2* increases through the differentiation of hiPSCs to both cardiomyocytes and cardiac fibroblasts

Using hiPSCs we can recapitulate human cardiac specific development *in vitro*. Immunostaining and western blotting performed on cell populations over the cardiac differentiation show variable outcomes. Perlecan immunostaining was performed using two monoclonal antibodies to cover both the C and N terminus of perlecan. Quantification of staining shows a steady increase from hiPSCs to day 15, whereby over the following days expression plateaus. While western blotting using the monoclonal antibodies shows a substantial increase in intensity between hiPSCs and day 10, although no further increase is seen following this timepoint. Intensity of western blotting bands shows a comparable trend, with perlecan intensity increasing as hiPSCs are

differentiated to CMs. Although, most bands increase between hiPSCs and day 10 followed by a plateau, compared to the day 15 plateau recorded through immunostaining. Western blotting using polyclonal CCN1 shows perlecan intensity levels increasing at comparable timepoints to monoclonal immunostaining, a gradual increase over the differentiation. Since these westerns were only an N of 2 trends could be identified and theorised, although no statistical data can be concluded as such.

Through both qRT-PCR and RNA sequencing the expression of *HSPG2* mRNA increases during the differentiation. Interestingly, in both qRT-PCR and RNA sequencing, *HSPG2* mRNA is attenuated at day 15 compared to the previous timepoint. This is due to the CMs going through the final stages of lactate purification, where-by the harsh environment appears to attenuate expression of all HSPGs. RNA sequencing shows the counts of *HSPG2* decrease in day 30 CMs, compared to the qRT-PCR suggesting this timepoint is the highest level of *HSPG2* expression. One theory for this, is the differentiations could be in distinct stages of development, potentially the CMs used for qRT-PCR samples were at a lower level of maturation. Another possibility is due to the level of CM purity, changes in the total percentage population could account for the differences seen here.

A comparable trend was seen performing qRT-PCR on hiPSC-CF timeline samples, whereby *HSPG2* increases in expression in the later timepoints. Interestingly, in these samples *HSPG2* expression does not increase between hiPSCs and day 15 cells showing epicardial progenitor cells do not express high levels of *HSPG2*. Only during the finial differentiation to a CF does *HSPG2* expression increase, highlighting the CFs role in ECM generation, and specifically and ECM containing perlecan.

Previous literature has shown perlecan increases as *in vivo* CMs undergo developmental maturation (Roediger et al., 2009). Here, I differentiate hiPSCs to both CMs and CFs, highlighting as these cells develop, perlecan expression increases. Not only does this result highlight the hiPSC model recapitulated human cardiac developmental gene expression instilling confidence in future

experiments. But also, confirms both cardiac populations express perlecan in later stages of development, insinuating *HSPG2* has a role in later stage cardiac maturation.

### 7.2.3. *HSPG2* has different splice variants and forms between hiPSCs and cardiomyocytes

Previous analysis highlighted transcript and protein size expression changes over cardiac differentiation. By combining both transcripts count identified from RNA sequencing and western blotting I aimed to investigate the forms of perlecan expressed is cardiac populations and how these changed from hiPSCs.

Following RNA sequencing, the splice variant transcripts of *HSPG2* were calculated at each of the timepoints. Of the transcripts that had any expression above 10 counts, no transcript was higher in hiPSCs than CMs. Most the transcripts followed a similar trend as seen in full length *HSPG2*, showing peaks of expression at day 10 and day 20. Only one transcript shows its highest count at day 30, suggesting this may be a form of *HSPG2* involved in the later stages of CM maturation. Interestingly, one of the other transcripts spikes at day 10 and 15, followed by attenuation over the remaining differentiation. These results suggest this transcript may be crucial in early cardiac development but are not required in later stage development. The transcripts found only code for small sections of *HSPG2*, not accounting for the banding sizes found in the western blots performed.

Western blotting using monoclonal antibodies found multiple different bands formed throughout the differentiation. hiPSCs highlight five different perlecan bands, between ~90 kDa and ~35 kDa, compared to the seven bands found in CMs. Only one perlecan band is unique to hiPSCs, found around ~65 kDa, this band was only highlighted using monoclonal perlecan antibodies, and not shown in western blots using polyclonal CCN1. No perlecan bands are above ~55 kDa using monoclonal antibody A76, suggesting none of the larger bands found contain the region of domain 1 that A76 binds to. Most of the larger bands are only found using polyclonal CCN1 (~90, 100, >300) suggesting

either these bands don't contain the fragments of domain 1 or domain 5 that A76 and A74 would identify. The exception to this, is a band at ~270 kDa identified by both A74 and CCN1, but not A76, implying this fragment would contain domain 5 of perlecan, but lack domain 1.

Combining the transcript results from RNA sequencing, and the banding patterns found from western blots, it can be presumed mRNA splice transcripts combine, generating the lengths and sizes of perlecan bands reported. Thereby, explaining the several fragments of perlecan identified through western blotting that lack specific domains. Indeed, these sized fragments can be created due to post translation protein cleavage, although the western blotting should still identify the uncleaved protein too. Therefore, mRNA splicing is a potential source of generating the perlecan banding patterns recorded in this thesis. Different band patterning of hiPSCs vs cardiac cells hypothesises the role of perlecan changes between cell types, and this is due to changes in spliced forms generated. Jung *et al* has shown different banding of perlecan in mast cells whereby forms are produced that lack domain III, although this has yet to be investigated in cardiac tissue until now (Jung et al., 2013). Perlecan is suggested to be ~500 kDa at full length, depending on GAG attachment, although the western did not highlight any bands at this length. Indeed, the ladder used for western blotting here was not appropriate, due to the maximum weight marker of 250 kDa.

These results highlight several splice variants of *HSPG2* that are expressed at different timepoints of the CM differentiation process. Western blotting shows banding patterns of perlecan in hiPSCs differs from CMs, therefore suggesting an alternate function. Over the course of CM differentiation perlecan splice variant length and protein banding sizes do not align, therefore suggesting a more complex system may be regulating *HSPG2*. I theorise this involves enhanced post transcriptional *HSPG2* mRNA manipulation, combining both splicing and stitching before translation to perlecan fragments of varied sizes. More in-depth analysis is needed to investigate these forms of perlecan found in both the mRNA and protein banding to determine the role each plays, and how they are generated. Three bands were found in hiPSC-

CMs that were not in hiPSCs, these could be cardiac specific bands and crucial in cardiac development, therefore worthy of further investigation.

### 7.2.4. *HSPG2* alters the metabolic capacity of cardiac cell populations

In both CMs and CFs, *HSPG2* deficiency significantly altered cellular metabolism. Using mitoplate metabolite and seahorse metabolic flux assays I was able to assess the metabolic function of both CMs and CFs. During early CM differentiation the $HSPG2^{+/-}$ cells had a higher level of substrate metabolism over the $HSPG2^{WT}$ line, although in later stage day 30 CMs this was reversed.

RNA sequencing over early CM differentiation identified *NNAT* expression to be greatly reduced in $HSPG2^{+/-}$ cell lines. Indeed, during brain development *NNAT* generates $Ca^{2+}$ signals for differentiation and synaptic development. *NNAT* also has a role in regulating calcium pump SERCA and promoting insulin secretion, thereby highlighting *NNATs* role in maintaining glucose homeostasis (Braun et al., 2020b). Pei and colleagues show *HSPG2* deficient osteoblasts cannot co-localise with calcium sensitive channels (Pei et al., 2020). A recent pre-print showed perlecan binding to α2δ1 subunit of voltage-sensitive calcium channels to be involved in bone mechanotransduction (Reyes Fernandez et al., 2022). Attenuation of *NNAT* is an initial indicator of metabolic dysfunction of early *HSPG2* deficient differentiating CMs, although the prevalent difference in metabolism was identified in fully differentiated cell populations.

*SLC2A1* (GLUT-1) was identified as one of the 361 DEGs found between WT and *HSPG2* deficient day 30 CMs. Interestingly, *NNAT* has also been implicated in regulation of *SLC2A1* through activation of PI3K-Akt2 signalling pathways (Gao et al., 2016). These results suggest the loss of *HSPG2* attenuated expression of *NNAT*, and thereby altered downstream glucose handling genes, further deforming metabolic output. Indeed, both seahorse and mitoplate assays performed on day 30 $HSPG2^{+/-}$ CMs highlighted an increased reliance on glycolysis, implying the reduction of *HSPG2* also inhibited other metabolic pathways.

The LDL-receptor of perlecan has been implicated in sequestering and regulation of lipoproteins, thereby assuming a downregulation of *HSPG2* would attenuate lipid handling. *HSPG2* deficient CMs and CFs both shows attenuated fatty acid substrate metabolism through mitoplate assays compared to the WT. Controversially, *HSPG2* KOs in mice show increased lipid metabolism in adipose tissue, showing the inverse trend to that found in CMs and CFs. Indeed, these results highlight perlecan has tissue-specific roles, whereby perlecan may hinder lipid metabolism in adipose tissue, but enhance this in cardiac tissues.

However, culture of hiPSC-CMs on synthetic perlecan peptide (PER-P) drastically attenuated expression of fatty acid transporter *CD36*, although upregulated expression of fatty acid metabolic gene *ACYL*. The presence of PER-P would simulate a perlecan rich ECM, therefore, sequestering fatty acids could be controlled by the LDL-receptor and the requirement for *CD36* reduced. Increased expression of *ACYL* suggests the hiPSC-CMs would have a higher fatty acid metabolism, reinforcing the trend of perlecan altering fatty acid metabolism. Indeed, mitoplate assays revealed day 30 HSPG2$^{+/-}$ hiPSC-CMs had an overall reduced metabolism, while hiPSC-CMs cultured on PER-P have increased metabolic gene expression (*SLC2A1, SCL2A4, HK2, LDHA, ACYL*). Expression of *NNAT* in PER-P hiPSC-CMs was increased, thereby confirming the increased level of *NNAT* correlated with enhanced glycolytic *SLC2A1* expression.

Overall, these results confirm *HSPG2*s involvement in metabolism of hiPSC-CMs. The expression of *NNAT*, correlating with *HSPG2* regulation, alters glycolytic gene *SLC2A1*. *HSPG2* is an essential co-localiser of calcium channels in other cell types, and through regulation of *NNAT*, a SERCA regulator, demonstrates calcium signalling control in a cardiac environment. Use of synthetic PER-P surfaces increases fatty acid gene *ACYL*, potentially due to enhanced fatty acid surface sequestering from synthetic perlecan, replacing the role of *CD36*. Indeed, metabolic dysfunction is a hallmark of cardiovascular disease whereby a metabolic switch from mature to foetal

occurs (Bae et al., 2021). The findings showing perlecan could regulate a developmental switch from glycolytic to fatty acid metabolism during maturation. Thus, may provide therapeutic avenues for further investigation into metabolic dysfunction in heart disease.

### 7.2.5. *HSPG2* and cardiomyocyte maturation

As described in previous chapters alterations of matrix can enhance maturation of hiPSC-CMs. One such matrix from perinatal stem cells has increased levels of perlecan and can enhance hiPSC-CM maturation (Block et

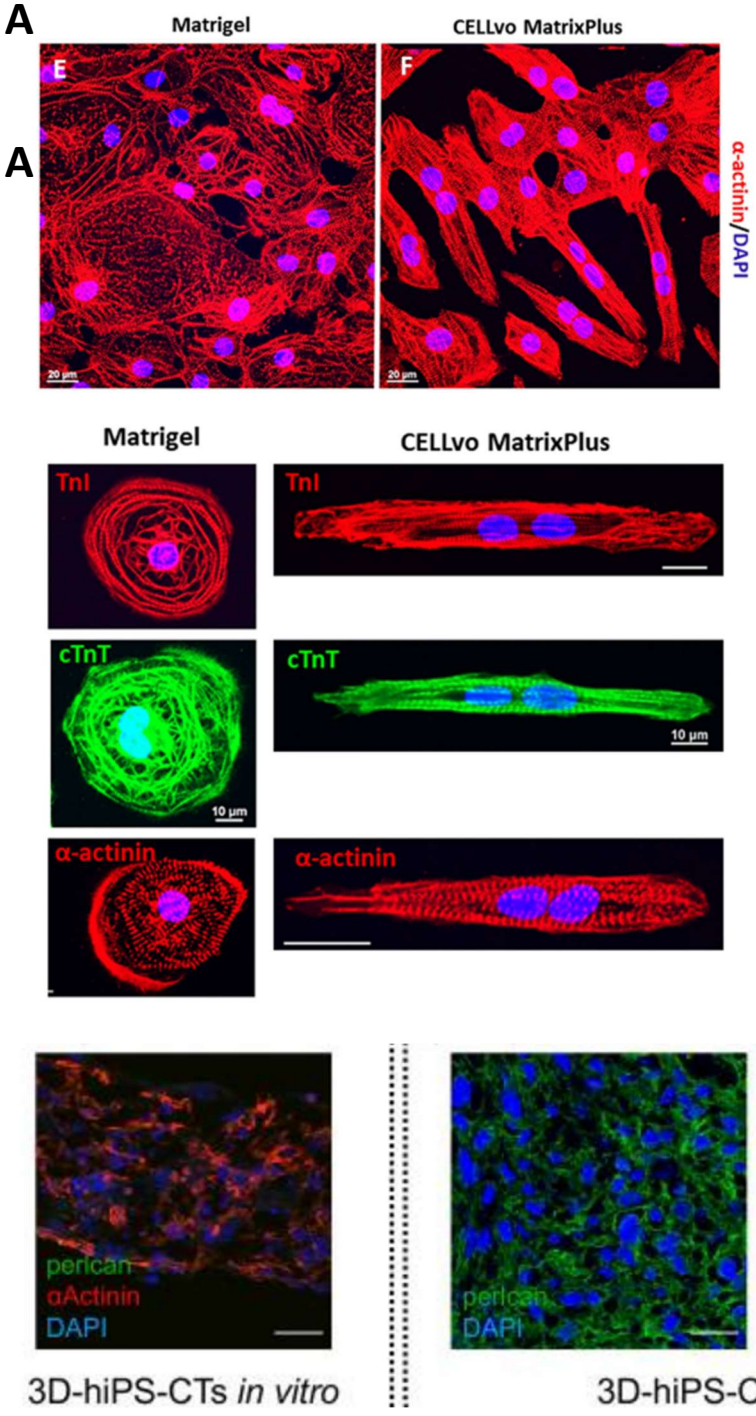


| Entrez Gene Symbol | MatrixPlus Relative Abudance (% Total Spectra) | CELLvo Matrix Relative Abudance (% Total Spectra) |
|---|---|---|
| | LAMININS | |
| LAMC1 | - | 0.1% |
| LAMA5 | 0.1% | - |
| LAMB1 | 0.1% | - |
| | COLLAGENS | |
| COL6A3 | - | 13.5% |
| COL1A2 | - | 8.9% |
| COL6A1 | - | 3.2% |
| COL6A2 | - | 2.1% |
| COL1A1 | 1.8% | 1.9% |
| COL5A1 | - | 7.6% |
| COL4A2 | 2.2% | 0.6% |
| COL4A1 | 0.8% | 0.6% |
| COL16A1 | - | 0.3% |
| COL3A1 | - | 0.2% |
| COL8A1 | 1.1% | 0.1% |
| COL18A1 | 3.8% | - |
| COL12A1 | 1.2% | - |
| COL5A2 | 0.2% | - |
| COL4A5 | 0.2% | - |
| COL2A1 | 0.1% | - |
| | PROTEOGLYCANS | |
| HSPG2 | 19.7% | 7.4% |
| BGN | - | 1.1% |
| VCAN | 1.5% | 0.7% |
| HAPLN1 | - | 0.5% |
| CSPG4 | - | 0.3% |
| DCN | - | 0.1% |
| | GLYCOPROTEINS | |
| FN1 | 52.4% | 36.3% |
| TNC | 3.2% | 5.6% |
| TGFBI | 3.2% | 3.9% |
| THBS1 | - | 3.4% |
| POSTN | - | 2.4% |
| FBN1 | - | 2.2% |
| FBLN1 | - | 1.4% |
| EMILIN1 | - | 1.1% |
| CYR61 | 1.2% | 0.2% |
| FBN2 | - | 0.1% |
| AGRN | 2.5% | - |
| | ECM-Associated Components | |
| ANXA2 | - | 1.10% |
| SEMA7A | - | 0.22% |
| LTBP2 | - | 0.17% |
| EFEMP2 | - | 0.17% |
| ADAMTSL1 | - | 0.10% |
| NID2 | - | 0.10% |
| PXDN | 0.05% | 0.05% |
| IGFBP7 | - | 0.05% |
| CTHRC1 | - | 0.05% |
| GREM1 | - | 0.05% |
| TIMP3 | | 0.04% |
| TINAGL1 | 2.80% | - |
| MUC16 | 0.70% | - |
| CALR | 0.05% | - |
| GDF15 | 0.04% | - |
| LRRC17 | 0.03% | - |

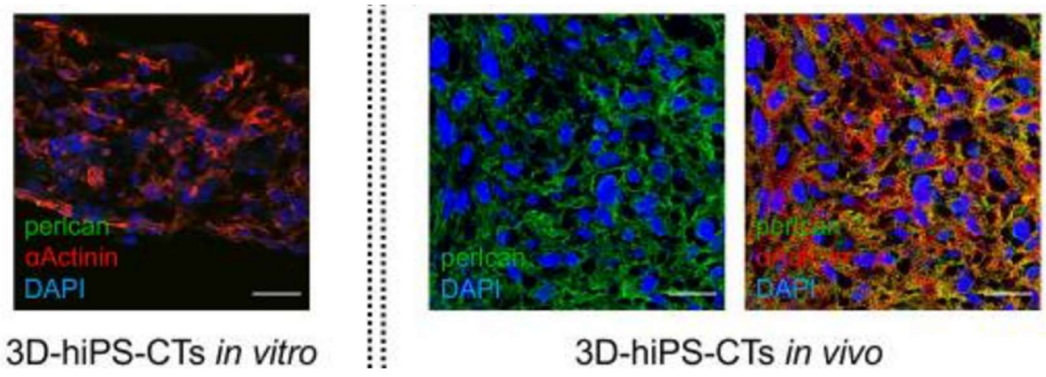


***Figure 7.1 – Perlecan in hiPSC-CM maturation.*** *(A) From Block et al, 2020. (B) From Yokoyama et al, 2021.*

al., 2020) (Figure 7.1, A). Furthermore, hiPSC-CMs undergo *in vivo* maturation following implantation into rat hearts, including an upregulated perlecan ECM (Yokoyama et al., 2021) (Figure 7.1, B).

The overall results following RNA sequencing and metabolic analysis of day 30 hiPSC-CMs suggested HSPG2$^{+/-}$ CMs are less mature than HSPG2$^{WT}$. The DEGs found between each cell line highlight the largest difference is recorded during hiPSC-CM maturation stages, between day 20 and 30. Upregulated DEGs in WT hiPSC-CMs are categorised into cardiac structural and developmental pathways suggesting a more mature CM.

RNA sequencing of HSPG2$^{+/-}$ day 30 CMs highlighted several upregulated lipoprotein genes, *APOC1, APOC3* and *APOA4*. The lack of *HSPG2* in early cardiac differentiation created dysfunction in metabolic handling potentially through *NNAT* signalling. Abnormal metabolic function of the developing CMs could hinder maturation and development, creating a negative feedback loop whereby lipoprotein genes are upregulated during later stages of maturation. Encapsulating hiPSC-CMs into engineered heart tissues (EHTs) was performed to enhance maturation and exacerbate differences between lines. Interestingly, all HSPG2$^{+/-}$ EHTs underwent cardiac remodelling, becoming thinner and stretched. These remodelled EHTs produced less force than the WT per contraction. Although, due to remodelling, the reduction of force recorded cannot be attributed entirely to just *HSPG2* reduction. Indeed, the lack of *HSPG2* appears to induce cardiac remodelling in EHTs, comparable to cardiac basement membrane remodelling reported in *HSPG2* deficient mice (Sasse et al., 2008). Reduction of force can also initiate cardiac remodelling (Davis et al., 2016), therefore the HSPG2$^{+/-}$ hiPSC-CMs may produce less force, and remodelling is a response and not the cause. Furthermore, distinction between hypertrophic and dilated cardiomyopathy induced by R312-ACTC variants has been linked to contractile abnormalities (Jones et al., 2022).

Overall, the results suggest HSPG2$^{+/-}$ CMs are less mature than the WT, although the mechanism behind this is yet to be concluded. Reduced

metabolic function through *NNAT* attenuation during development could generate a more immature CM, although how *HSPG2* is regulating NNAT is unclear. Glycolysis is the major metabolic output during neonatal CM development, although *HSPG2* reduction did not seem to effect early CM differentiation. HSPG2$^{+/-}$ cells during day 10 of cardiac differentiation had higher overall metabolism than the HSPG2$^{WT}$. Suggesting the *HSPG2* deficient hiPSCs accelerate differentiation to CMs over the WT, but due to lack of perlecan development, later stage maturation is inhibited while WT progress normally.

Perlecan is not found in the basement membrane of gestational week 6/7 CMs (Roediger et al., 2009a), suggesting it is not required for early development, reconfirming my results. The difference between the hiPSC-CM lines is exacerbated during the last stages of differentiation, suggesting the *HSPG2* reduction hinders the final maturation process. Combined with evidence from previous studies suggesting a role for perlecan in hiPSC-CM maturation (Block et al., 2020; Yokoyama et al., 2021). My data provides further evidence to support this hypothesis. Methods of enhancing hiPSC-CM maturation are critical for disease modelling and drug screening (Guo and Pu, 2020), therefore targeting perlecan may be worthy of further investigation.

### 7.2.6. *HSPG2* in cardiomyocyte multinucleation and hypertrophic growth

Multinucleation and hypertrophic growth are hallmarks of postnatal cardiomyocyte maturation and development. These phenotypic changes in hiPSC-CMs would suggest development of a more mature CM in culture. Indeed, RNA sequencing results and metabolic analysis suggest the HSPG2$^{+/-}$ hiPSC-CMs are less mature than the WT. Although, culture on PER-P substrate did not show expression changes expected in mature hiPSC-CMs. Instead, a hypertrophic growth phenotype was identified with PER-P hiPSC-CMs having enlarged morphology and enhanced multinucleation. Indeed, although enhanced *HSPG2* expression is correlated with hypertrophic hiPSC-CMs (Johansson et al., 2022), the opposite output is recorded in mice

chondrocytes and smooth muscle cells. *HSPG2* deficient mice have enhanced hypertrophy in smooth muscle cells (Xu et al., 2010) and chondrocytes (Ocken et al., 2020), reconfirming *HSPG2'*s role is tissue specific.

Expression of *NNAT* is increased in PER-P hiPSC-CMs, and indeed *NNAT* regulates *SLC2A1* expression, but is also a mediator of NF-κβ signalling (Yang et al., 2019). NF-κβ signalling pathway upregulates inflammatory cytokines and is hypothesised to regulate CM hypertrophy (Yamamoto et al., 2001). Therefore, the increased *NNAT* expression generated from hiPSC-CM culture on synthetic PER-P surfaces could enhance expression of pro-inflammatory and hypertrophic cytokines through *NNAT* mediated NF-κβ signalling. This theory would account for the hypertrophic growth observed and lack of enhanced CM maturation. As discussed previously, *NNAT* is implicated in regulation of calcium signalling. An indicative phenotype of hypertrophic cardiomyocytes is abnormal calcium signalling, and enhanced expression of *CASQ2* (Bhagwan et al., 2020). Although hiPSC-CMs cultured on PER-P have attenuated expression of *CASQ2*, further suggesting the response seen is not hypertrophic cardiomyopathy.

Indeed, hypertrophic growth is an essential switch during cardiac development, but also a response to myocardial damage. Therefore, the question remains if hiPSC-CMs on PER-P were undergoing hypertrophic growth towards development, or an injury response. And, if *in vitro* hypertrophic growth is an essential step towards CM maturation, further recapitulating the developmental phenotype. PER-P is a synthetic fragment of perlecan with customisable GAG attachment, therefore with optimisation, the fragment, concentration, and bound GAG could be manipulated to enhance maturation over hypertrophy.

### 7.2.7. The switch between perlecan and agrin

A proposed mechanism for the role of perlecan in maturation of CMs is through the binding to the aDGC (Figure 7.2). Agrin-aDGC binding in CMs reduces maturation of CMs and enhances their proliferative capabilities (Bassat et al,

2017). Binding of ECM components to the aDGC is regulated by binding affinity, whereby higher affinity proteins are preferentially bound over others. Perlecan has a higher binding affinity to the aDGC over agrin (Dempsey et al., 2019), therefore as perlecan ECM is enhanced, so too is the formation of a perlecan-aDGC complex (Figure 7.3).

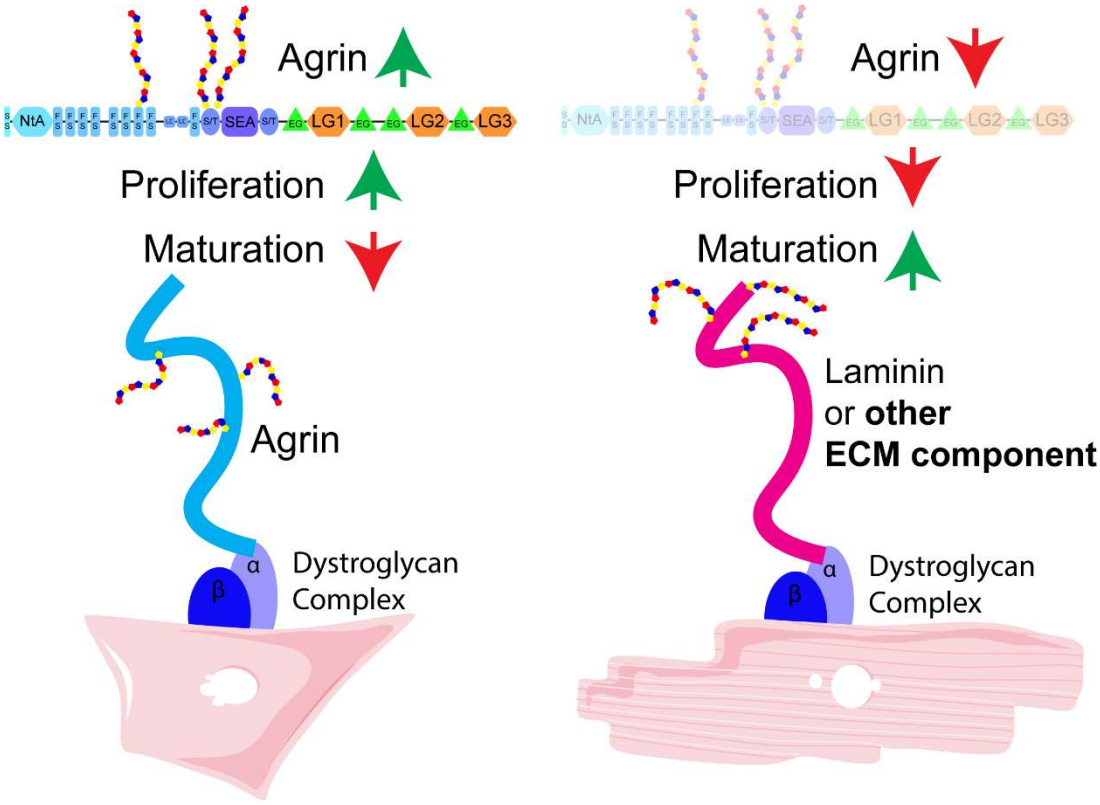


***Figure 7.2 – Agrin-aDGC induced proliferation in CMs.*** *An increase of agrin bound to the aDGC complex on CMs show an increased proliferative capability to the detriment of maturation. This response is reversed when another ECM component is bound to the aDGC over agrin. Adapted from Bassat et al, 2017*

Indeed, perlecan is lowly expressed during early hiPSC cardiac development, but increases over differentiation, compared to the stable expression of agrin. Suggesting as differentiation occurs, higher binding affinity perlecan replaces agrin in the aDGC complex, reducing proliferative capabilities of CMs and therefore increasing maturation. Perlecan is a multifunctional HSPG, binding to the aDGC complex would not only hinder the agrin-aDGC complex formation, but also enhance downstream perlecan specific functions.

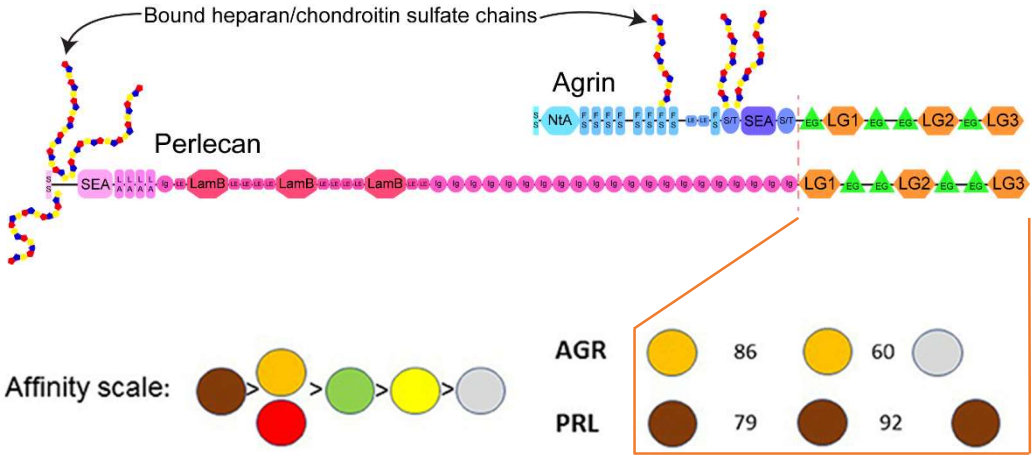


***Figure 7.3 – Perlecan and agrin binding affinity to aDGC.*** *Affinity scale showing how LG1, LG2 and LG3 have the highest binding affinity to the aDGC compared to agrin. Adapted from Dempsey et al, 2019.*

### 7.2.8. *HSPG2* deficient cardiac fibroblasts are quiescent compared to the WT

Generation of *HSPG2* deficient CFs had comparable proliferation capabilities compared to the WT, although following culture passages, revealed an increased sensitivity to activation in HSPG2$^{+/-}$ CFs. Indeed, prolonged culture of hiPSC-CFs did enhance activation to a myofibroblast in both cell lines, the HSPG2$^{+/-}$ CFs show accelerated activation. These results suggest HSPG2$^{+/-}$ hiPSC-CFs have a higher sensitivity to culture conditions, leading to accelerated activation and quiescence.

Metabolic analysis of hiPSC-CF lines identified HSPG2$^{+/-}$ CF, like HSPG2$^{+/-}$ CMs, have overall attenuated substrate metabolism compared to the WT. The reduced metabolic function of the HSPG2$^{+/-}$ hiPSC-CFs could account for increased activation of hiPSC-CFs in culture. Indeed, metabolic shift increasing glycolytic reliance encourages transdifferentiation of CFs to MFs (Bernard et al., 2015; Xie et al., 2015). Therefore, the *HSPG2* deficiency induced metabolic changes that may encourage myofibroblast activation over sensitivity to culture conditions.

Through quadrant migration wells I investigated CF migration of both cell lines. The initial results highlight hiPSC-CFs preferentially migrate towards hiPSC-

CMs, suggesting a role of endocrine signalling between the two cell types encouraging migration. Interestingly, HSPG2$^{+/-}$ hiPSC-CFs did not migrate to the same extent as the WT hiPSC-CFs, indicative of a more quiescent CF. Indeed, the difference in migration could also be accounted by a loss of proliferative capability in HSPG2$^{+/-}$ hiPSC-CFs. Following culture in hypoxic CM media the HSPG2$^{+/-}$ CFs migrated across the wound gap at the same rate as WT. This further suggests the HSPG2$^{+/-}$ CFs were in a quiescent state, and exposure to stress cytokines induced an activated response. Although, these results were only N of 1 and therefore should be treated as such.

Both cell lines in culture lose proliferative capabilities and undergo transdifferentiation towards a myofibroblast, HSPG2$^{+/-}$ CFs respond at a faster rate, potentially due to mechanical sensitivity or attenuated metabolism. In hiPSC-CMs my findings suggest perlecan is in involved in a phenotypic switch in cardiomyocyte maturation. These results suggest *HSPG2* may be involved in the phenotypic switch between activated and non-activated CFs and therefore worthy of further investigation as a potential mechanism in fibrotic heart disease.

### 7.2.9. Perlecan is preferentially secreted following cardiac damage

Following myocardial damage perlecan ECM is secreted by fibroblasts in the wound site around 7 days following injury, with full coverage of the infarct zone by day 14-28 (Nakahama et al., 2000). During matrix breakdown perlecan is one of the most sensitive ECM components, with a decrease occurring up to 1 hour post damage (Kang and Yao, 2020). Reduction of perlecan ECM is rapid, 37% to 61% within 2 hours of damage, compared to agrin which shows a gradual decline over 24 hours (Baumann et al., 2009). Since agrin is rapidly turned over in a healthy environment and perlecan is rapidly lost after damage, generation of perlecan over would healing would be essential to replenish damaged ECM.

Combining hiPSC-CMs and CFs in a scratch wound model I revealed preferential perlecan secretion in the wound site following migration from CFs.

This confirmed function use of my model for recapitulating cardiac damage and early stages of recovery. The initial model was maintained for 14 days in culture allowing the generation of a perlecan rich ECM in the wound site, while the repeated scratch was only performed for 7 days. In this assay only low levels of perlecan were reported, reconfirming results from the literature. Interestingly, the migration and pro perlecan ECM secretion into the scratch wound was not mediated by macrophages, therefore suggesting death of CMs was enough to initiate the response.

Indeed, perlecan ECM secretion into a wound site following myocardial damage has been reported in animal models. Here I confirm a comparable response in a hiPSC cardiac models utilising scratch wounds and migration assays. Although, each model was only repeated once, so trends can be theorised, but not guaranteed. Since perlecan ECM is rapidly degraded in damage, preferential replenishment is logical, although perlecan's role in this process requires more investigation.

### 7.3. Limitations

hiPSC are a promising strategy in replacement of animal models and creating *in vitro* models, although they have their limitations. The ideal model would utilise both hiPSCs and mice models to instil confidence in the hiPSC models generated. Further to this, *in vitro* models cannot recapitulate *in vivo* responses, therefore inclusion of *in vivo* experiments is also required to further investigate the role of *HSPG2* in a cardiac environment. Due to this, any findings of the role of *HSPG2* in this thesis should be reconfirmed with *in vivo* animal models.

Before generation of cardiac populations from hiPSCs I aimed at creating a *HSPG2* deficient hiPSC line. Despite multiple retargeting attempts and generation of over 100 heterozygous clones, no homozygous knockouts were produced. Generation of a full *HSPG2* KO may show additional or enhanced differences to the $HSPG2^{+/-}$ providing further confidence in *HSPG2s* role. Indeed, upregulation of *HSPG2* in hiPSCs would provide further insight into

the role of *HSPG2*, although this overexpression instigated cellular clumping and detachment. Therefore, both stable overexpression and, complete reduction of *HSPG2* was not achieved, leaving crucial areas to be researched still.

As previously mentioned, hiPSC-CMs generated represent a less mature, foetal like CM, compared to an adult CM. CM immaturity due to a *HSPG2* reduction is one of the key findings of this thesis, therefore generation of immature hiPSC-CMs in both cell lines only highlights small differences in maturity. Ideally, hiPSC-CMs could be matured to adult CMs, whereby the maturation deficit caused by HSPG2 deficiency would be exacerbated. Indeed, I attempted to enhance maturation of the hiPSC-CMs by encapsulation into EHTs. Indeed, the *HSPG2* deficiency instigating EHT remodelling is an interesting finding. Remodelling altered gene expression and contractility outputs, thereby adding more variables to the system and reducing confidence in maturation differences. As such, alternate maturation methods should have been employed for further quantification of *HSPG2* deficiency inducing hiPSC-CM immaturity.

The hiPSC-CMs cultured on PER-P had initial morphological changes comparable to those seen in hypertrophic CMs. This claim from immunostaining, although visually confirming, was yet to be statistically quantified through actual area and size measurements (Mosqueira et al., 2019). Therefore, without quantifying hypertrophic measurements the PER-P hiPSC-CMs cannot be termed as hypertrophic CMs. Indeed, I suggest hypertrophic growth occurred, which again should be quantified with size measurements that were not yet performed.

In the progression of maturation, hiPSC-CMs loose proliferative capabilities, therefore less mature hiPSC-CMs should have enhanced proliferative capabilities. In both attenuated and overexpressed *HSPG2* I did not investigate the proliferative capabilities of hiPSC-CMs, instead focusing more on maturity status. In the hypertrophic like hiPSC-CMs, the transition between

proliferative and hypertrophic growth could have been investigated had I performed cardiomyocyte proliferation assays, such as S-phase staining.
One of the most consistent and interesting findings throughout *HSPG2* downregulation and PER-P culture was regulation of *NNAT*. The data suggests a clear link between *HSPG2* regulation of *NNAT*, although the mechanism behind this regulation was yet to be discovered. Both *NNAT* and *HSPG2* have multifaceted roles, suggesting many of the changes recorded in altered *HSPG2* cells could coincide with *NNAT* regulation. Investigation into how *HSPG2* regulates *NNAT* would provide further insight into ECM regulation of cardiac intracellular metabolic and calcium functions.

During CM differentiation I investigated novel forms of perlecan through both western blotting and RNA sequencing transcript analysis. These results revealed a potential switch in forms of perlecan found in hiPSCs and cardiac cell populations. Although due to limitations in technical capabilities and time, further investigation into quantifying the perlecan fragments was not performed. Identification and quantification of novel forms of perlecan could provide insight into the protein's specific role in each cell type, and when this shift occurs over differentiation.

Despite perlecan ECM being mainly secreted and maintained by CFs in the heart, the generation and investigation of *HSPG2* deficient CFs was lacking the same intensity as CMs. Generation of CFs from hiPSCs was initially a challenging task compared to optimisation of CM differentiation. CFs generated also quickly lost proliferative capabilities in culture and underwent apoptosis, having a limited total culture length. Quantification of CF markers revealed high expression of *WT1* in hiPSC-CFs compared to primary CFs. *WT1* expression is linked to both endothelial cells and CFs, it could be presumed hiPSC-CFs generated were still in an endothelial stage, suggesting more work was required in optimising CF differentiation. Indeed, I show *HSPG2* deficient CFs have abnormal metabolism, migration, proliferation, and activation. Although the work here needs to be both repeated and investigated further to determine how *HSPG2* deficiency is instigating these alterations.

### 7.4. Future Work

Through collaboration with Andreia Bernardo at the Francis Crick institute I gained access to techniques including RNA sequencing and EHT generation. Future plans aimed to build on this collaboration and combine our hiPSC-CMs with in vivo mouse models. To investigate the transition from agrin to perlecan rich ECM, and further binding to the aDGC, mouse heart histology slices from the Francis Crick institute are planned. Immunostaining will be performed on these slices to determine both co-localisation of ECM components to the aDGC, but also the transition from agrin-aDGC to perlecan-aDGC theorised to occur over development. For further quantification ECM-aDGC complexes, immunoprecipitation will be used to isolate agrin and perlecan-aDGC complexes for in-depth sequencing and analysis. Not only will this be performed on mice hearts through development, but also on hiPSC cardiac differentiation samples, to confirm limited species differences in *HSPG2*.

Generation of a homozygous *HSPG2* knockout is essential to fully investigate *HSPG2*s role in human cardiac populations. One of the theories to why I was unable to generate *HSPG2* null hiPSCs was due to stringent culture conditions inhibiting hiPSC survival without perlecan. The culture conditions could be altered to accommodate for the *HSPG2* deficiency in the hiPSC state, through use of Matrigel culture substrate, which contains perlecan, or more complex media such as mTeSR compared to E8. These culture conditions could be maintained while clone quantification was performed to identify full knockouts, then removed to confirm culture conditions are not sustainable without *HSPG2*. If perlecan altered pluripotency through FGF signalling, the culture conditions would be essential to ensure maintenance of HSPG2$^{-/-}$ hiPSCs. Following differentiation these conditions would not need to be maintained and when removed, the difference between cell lines could be examined. Instead of altering culture conditions for hiPSC survival, a conditional knockout method could be utilised. Here *HSPG2* could be removed following differentiation, thereby alleviating issues with *HSPG2* null hiPSC survival.

Through western blotting I revealed distinct banding patterns of perlecan in different antibodies, with both hiPSCs and hiPSC-CMs. Ideally, complete

proteomics could be performed for in depth perlecan analysis. Alternatively, the different perlecan fragments identified through western blotting could be isolated and extracted for proteomic analysis. Through sequencing of perlecan fragments, mRNA splice variants could be aligned, and further investigation would identify how and why perlecan fragments were generated.

To determine if hiPSC-CMs cultured on PER-P were hypertrophic, more investigation is required (Mosqueira et al., 2019). To quantify size of hiPSC-CMs flow cytometry would be performed, calculating cell volume. Further qRT-PCR analysis of hypertrophic markers is required due to previous variable results not confirming either state. Using ImageJ plugins, sarcomere alignment can be analysed, thereby confirming hypertrophic sarcomeric disarray (Cao et al., 2022; Neininger-Castro et al., 2023). Further analysis using seahorse assays would confirm mitochondrial changes comparable to hypertrophic CMs, and indeed would be interesting in investigating if the opposite response is seen to HSPG2$^{+/-}$ hiPSC-CMs.

Since alterations to *NNAT* expression appear to correlate with perlecan expression I want to investigate the mechanism of this regulation. *HSPG2* can regulate cell surface calcium channels in osteoblasts, inhibited through gabapentin (Reyes Fernandez et al., 2022.). Therefore, use of gabapentin in a cardiac cell population should inhibit perlecan binding to voltage-sensitive calcium channels, potentially regulating *NNAT*. *NNAT* expression is associated with calcium induced responses in β-cells and medulloblastomas (Li et al., 2010), therefore a comparable response in cardiac populations is feasible. Indeed, *NNAT* has been studied in brain development, adipocytes, and osteoblasts, although further investigation is required for how *NNAT* functions in the cardiac environment.

### 7.5. Final Remarks

In this thesis I show regulation of *HSPG2* is crucial for maintenance and survival of hiPSCs. Overexpression caused detachment due to constricted growth and clumping, while the mechanism behind *HSPG2* null hiPSC demise

is yet to be investigated. *HSPG2* reduction in both CM and CF attenuated total metabolic output and increased reliance on glycolysis in HSPG2$^{+/-}$ cardiac cells.

*HSPG2* deficient CMs are less mature than the WT, showing reduced cardiac structural and metabolic function. RNA sequencing confirmed 11 DEGs consistently altered throughout early cardiac differentiation due to *HSPG2* deficiency. Of the 11 DEGs besides *HSPG2*, *NNAT* had the highest transcript count, and expression was altered throughout differentiation, representative to *HSPG2* expression. After culturing CMs on PER-P surfaces *NNAT* expression was increased further confirming *HSPG2* is a regulator of *NNAT*. PER-P CMs had enhanced multinucleation and signs of hypertrophic growth. These results suggest regulation of *NNAT* during cardiac development could assist in later stage maturation of CMs, and that *HSPG2* is a major regulator.

Perlecan ECM is slowly developed over the course of cardiac differentiation compared to agrin. A possible mechanism of perlecan influencing development could occur through binding to the aDGC, whereby higher affinity perlecan replaces bound agrin. Agrin binding to the aDGC induces proliferation in CM, therefore replacement by perlecan would reduce proliferation and enhance maturation. Utilising a co-culture scratch wound assay, I show preferential perlecan ECM secretion in the recovering wound gap, comparable to the literature, and furthermore confirming perlecans involvement in wound healing. Overall, I theorise perlecan is required for CM maturation, potentially linked through metabolic regulation and hypertrophic growth (Figure 7.4) *HSPG2* expression correlates to *NNAT* expression, initiating regulation of both metabolic channels and NF-κβ signalling pathways, thereby regulating key maturation factors.

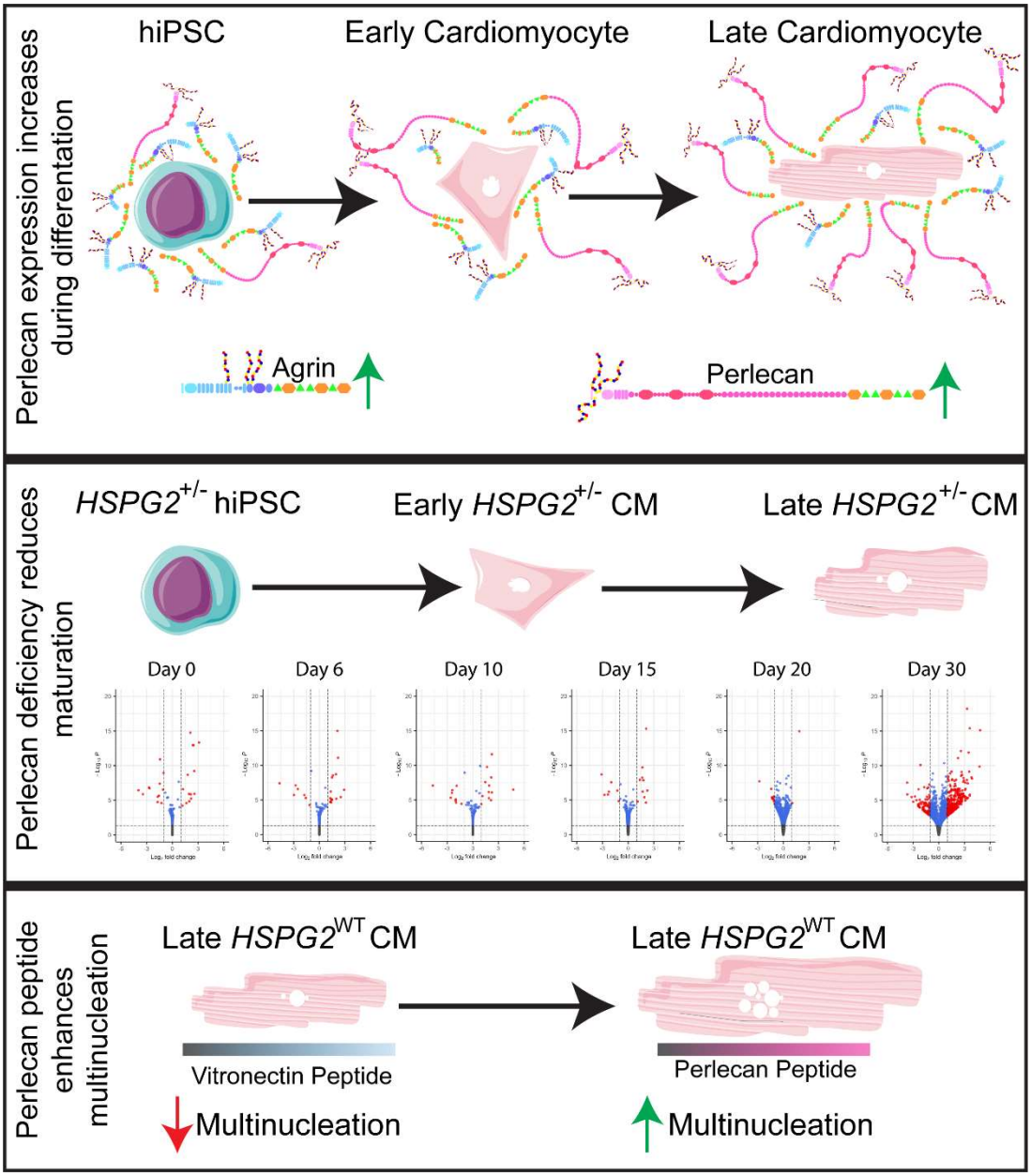


***Figure 7.4 – Graphical summary.*** *Early CM differentiation found increased agrin expression shifting to increased perlecan expression. RNA sequencing comparing between lines over the course of CM differentiation show most differences occur at day 30. Culture of CMs on a perlecan peptide enhanced multinucleation compared to those cultured on a vitronectin surface.*

## 8. References


Acharya, A., Baek, S.T., Huang, G., Eskiocak, B., Goetsch, S., Sung, C.Y., Banfi, S., Sauer, M.F., Olsen, G.S., Duffield, J.S., Olson, E.N., Tallquist, M.D., 2012. The bHLH transcription factor Tcf21 is required for lineagespecific EMT of cardiac fibroblast progenitors. Development (Cambridge) 139, 2139–2149. https://doi.org/10.1242/DEV.079970/-/DC1

Acha-Sagredo, A., Uko, B., Pantazi, P., Bediaga, N.G., Moschandrea, C., Rainbow, L., Marcus, M.W., Davies, M.P.A., Field, J.K., Liloglou, T., 2020. Long non-coding RNA dysregulation is a frequent event in non-small cell lung carcinoma pathogenesis. British Journal of Cancer 2020 122:7 122, 1050–1058. https://doi.org/10.1038/s41416-020-0742-9

Ahmed, R.E., Anzai, T., Chanthra, N., Uosaki, H., 2020. A Brief Review of Current Maturation Methods for Human Induced Pluripotent Stem Cells-Derived Cardiomyocytes. Front Cell Dev Biol 8. https://doi.org/10.3389/FCELL.2020.00178

Arikawa-Hirasawa, E., Le, A.H., Nishino, I., Nonaka, I., Ho, N.C., Francomano, C.A., Govindraj, P., Hassell, J.R., Devaney, J.M., Spranger, J., Stevenson, R.E., Iannaccone, S., Dalakas, M.C., Yamada, Y., 2002. Structural and Functional Mutations of the Perlecan Gene Cause Schwartz-Jampel Syndrome, with Myotonic Myopathy and Chondrodysplasia. Am J Hum Genet 70, 1368. https://doi.org/10.1086/340390

Artham, S.M., Lavie, C.J., Milani, R. v., Ventura, H.O., 2009. Obesity and Hypertension, Heart Failure, and Coronary Heart Disease—Risk Factor, Paradox, and Recommendations for Weight Loss. Ochsner J 9, 124.

Asundi, V.K., Keister, B.F., Stahl, R.C., Carey, D.J., 1997. Developmental and Cell-Type-Specific Expression of Cell Surface Heparan Sulfate Proteoglycans in the Rat Heart. Exp Cell Res 230, 145–153. https://doi.org/10.1006/EXCR.1996.3400

Aviezer, D., Hecht, D., Safran, M., Eisinger, M., David, G., Yayon, A., 1994. Perlecan, basal lamina proteoglycan, promotes basic fibroblast growth

factor-receptor binding, mitogenesis, and angiogenesis. Cell 79, 1005–1013. https://doi.org/10.1016/0092-8674(94)90031-0

Bae, J., Paltzer, W.G., Mahmoud, A.I., 2021. The Role of Metabolism in Heart Failure and Regeneration. Front Cardiovasc Med 8, 763. https://doi.org/10.3389/FCVM.2021.702920

Baehr, A., Umansky, K.B., Bassat, E., Jurisch, V., Klett, K., Bozoglu, T., Hornaschewitz, N., Solyanik, O., Kain, D., Ferraro, B., Cohen-Rabi, R., Krane, M., Cyran, C., Soehnlein, O., Laugwitz, K.L., Hinkel, R., Kupatt, C., Tzahor, E., 2020. Agrin Promotes Coordinated Therapeutic Processes Leading to Improved Cardiac Repair in Pigs. Circulation 142, 868–881. https://doi.org/10.1161/CIRCULATIONAHA.119.045116

Baker, A.B., Ettenson, D.S., Jonas, M., Nugent, M.A., Iozzo, R. V., Edelman, E.R., 2008. Endothelial Cells Provide Feedback Control for Vascular Remodeling Through a Mechanosensitive Autocrine TGF-β Signaling Pathway. Circ Res 103, 289–297. https://doi.org/10.1161/CIRCRESAHA.108.179465

Balakumar, P., Maung-U, K., Jagadeesh, G., 2016. Prevalence and prevention of cardiovascular disease and diabetes mellitus. Pharmacol Res 113, 600–609. https://doi.org/10.1016/J.PHRS.2016.09.040

Barcelona-Estaje, E., Dalby, M.J., Cantini, M., Salmeron-Sanchez, M., 2021. You Talking to Me? Cadherin and Integrin Crosstalk in Biomaterial Design. Adv Healthc Mater 10, 2002048. https://doi.org/10.1002/ADHM.202002048

Bassat, E., Mutlak, Y.E., Genzelinakh, A., Shadrin, I.Y., Baruch Umansky, K., Yifa, O., Kain, D., Rajchman, D., Leach, J., Riabov Bassat, D., Udi, Y., Sarig, R., Sagi, I., Martin, J.F., Bursac, N., Cohen, S., Tzahor, E., 2017. The extracellular matrix protein agrin promotes heart regeneration in mice. Nature 547, 179–184. https://doi.org/10.1038/NATURE22978

Baum, J., Duffy, H.S., 2011. Fibroblasts and myofibroblasts: what are we talking about? J Cardiovasc Pharmacol 57, 376–379. https://doi.org/10.1097/FJC.0B013E3182116E39

Baumann, E., Preston, E., Slinn, J., Stanimirovic, D., 2009. Post-ischemic hypothermia attenuates loss of the vascular basement membrane proteins, agrin and SPARC, and the blood-brain barrier disruption after

global cerebral ischemia. Brain Res 1269, 185–197. https://doi.org/10.1016/J.BRAINRES.2009.02.062

Beetz, N., Rommel, C., Schnick, T., Neumann, E., Lother, A., Monroy-Ordonez, E.B., Zeeb, M., Preissl, S., Gilsbach, R., Melchior-Becker, A., Rylski, B., Stoll, M., Schaefer, L., Beyersdorf, F., Stiller, B., Hein, L., 2016. Ablation of biglycan attenuates cardiac hypertrophy and fibrosis after left ventricular pressure overload. J Mol Cell Cardiol 101, 145–155. https://doi.org/10.1016/J.YJMCC.2016.10.011

Bergmann, O., Zdunek, S., Felker, A., Salehpour, M., Alkass, K., Bernard, S., Sjostrom, S.L., Szewczykowska, M., Jackowska, T., dos Remedios, C., Malm, T., Andrä, M., Jashari, R., Nyengaard, J.R., Possnert, G., Jovinge, S., Druid, H., Frisén, J., 2015. Dynamics of Cell Generation and Turnover in the Human Heart. Cell 161, 1566–1575. https://doi.org/10.1016/J.CELL.2015.05.026

Berhrsin, J., Gibson, A., 2011. Cardiovascular system adaptation at birth. Paediatr Child Health 21, 1–6. https://doi.org/10.1016/J.PAED.2010.08.016

Berk, B.C., Fujiwara, K., Lehoux, S., 2007. ECM remodeling in hypertensive heart disease. J Clin Invest 117, 568–575. https://doi.org/10.1172/JCI31044

Bernard, K., Logsdon, N.J., Ravi, S., Xie, N., Persons, B.P., Rangarajan, S., Zmijewski, J.W., Mitra, K., Liu, G., Darley-Usmar, V.M., Thannickal, V.J., 2015. Metabolic Reprogramming Is Required for Myofibroblast Contractility and Differentiation. J Biol Chem 290, 25427. https://doi.org/10.1074/JBC.M115.646984

Bhagwan, J.R., Mosqueira, D., Chairez-Cantu, K., Mannhardt, I., Bodbin, S.E., Bakar, M., Smith, J.G.W., Denning, C., 2020. Isogenic models of hypertrophic cardiomyopathy unveil differential phenotypes and mechanism-driven therapeutics. J Mol Cell Cardiol 145, 43–53. https://doi.org/10.1016/j.yjmcc.2020.06.003

Bigotti, M.G., Skeffington, K.L., Jones, F.P., Caputo, M., Brancaccio, A., 2020. Agrin-Mediated Cardiac Regeneration: Some Open Questions. Front Bioeng Biotechnol 8, 594. https://doi.org/10.3389/FBIOE.2020.00594/BIBTEX

Black, B.L., n.d. Transcriptional pathways in second heart field development.

Block, T., Creech, J., da Rocha, A.M., Marinkovic, M., Ponce-Balbuena, D., Jiménez-Vázquez, E.N., Griffey, S., Herron, T.J., 2020. Human perinatal stem cell derived extracellular matrix enables rapid maturation of hiPSC-CM structural and functional phenotypes. Sci Rep 10. https://doi.org/10.1038/S41598-020-76052-Y

Bodbin, S.E., Denning, C., Mosqueira, D., 2020. Transfection of hPSC-Cardiomyocytes Using Viafect™ Transfection Reagent. Methods and Protocols 2020, Vol. 3, Page 57 3, 57. https://doi.org/10.3390/MPS3030057

Borgdorff, M.A.J., Koop, A.M.C., Bloks, V.W., Dickinson, M.G., Steendijk, P., Sillje, H.H.W., van Wiechen, M.P.H., Berger, R.M.F., Bartelds, B., 2015. Clinical symptoms of right ventricular failure in experimental chronic pressure load are associated with progressive diastolic dysfunction. J Mol Cell Cardiol 79, 244–253. https://doi.org/10.1016/J.YJMCC.2014.11.024

Bork, P., Patthy, L., 1995. The SEA module: a new extracellular domain associated with O-glycosylation. Protein Sci 4, 1421–1425. https://doi.org/10.1002/PRO.5560040716

Brade, T., Pane, L.S., Moretti, A., Chien, K.R., Laugwitz, K.L., 2013. Embryonic Heart Progenitors and Cardiogenesis. Cold Spring Harb Perspect Med 3. https://doi.org/10.1101/CSHPERSPECT.A013847

Braun, J.L., Geromella, M.S., Hamstra, S.I., Fajardo, V.A., 2020a. Neuronatin regulates whole-body metabolism: is thermogenesis involved? FASEB Bioadv 2, 579–586. https://doi.org/10.1096/FBA.2020-00052

Braun, J.L., Geromella, M.S., Hamstra, S.I., Fajardo, V.A., 2020b. Neuronatin regulates whole-body metabolism: is thermogenesis involved? FASEB Bioadv 2, 579–586. https://doi.org/10.1096/FBA.2020-00052

Bray, M.S., Shaw, C.A., Moore, M.W.S., Garcia, R.A.P., Zanquetta, M.M., Durgan, D.J., Jeong, W.J., Tsai, J.Y., Bugger, H., Zhang, D., Rohrwasser, A., Rennison, J.H., Dyck, J.R.B., Litwin, S.E., Hardin, P.E., Chow, C.W., Chandler, M.P., Abel, E.D., Young, M.E., 2008. Disruption of the circadian clock within the cardiomyocyte influences myocardial contractile function, metabolism, and gene expression. Am J Physiol Heart Circ Physiol 294. https://doi.org/10.1152/AJPHEART.01291.2007/SUPPL_FILE/TABLE

Breckwoldt, K., Letuffe-Brenière, D., Mannhardt, I., Schulze, T., Ulmer, B., Werner, T., Benzin, A., Klampe, B., Reinsch, M.C., Laufer, S., Shibamiya, A., Prondzynski, M., Mearini, G., Schade, D., Fuchs, S., Neuber, C., Krämer, E., Saleem, U., Schulze, M.L., Rodriguez, M.L., Eschenhagen, T., Hansen, A., 2017. Differentiation of cardiomyocytes and generation of human engineered heart tissue. Nat Protoc 12, 1177–1197. https://doi.org/10.1038/NPROT.2017.033

Buckingham, M., Meilhac, S., Zaffran, S., 2005. Building the mammalian heart from two sources of myocardial cells. Nature Reviews Genetics 2005 6:11 6, 826–835. https://doi.org/10.1038/nrg1710

Bujak, M., Frangogiannis, N.G., 2007. The role of TGF-β signaling in myocardial infarction and cardiac remodeling. Cardiovasc Res 74, 184–195. https://doi.org/10.1016/J.CARDIORES.2006.10.002/2/74-2-184-FIG4.GIF

Burridge, P.W., Anderson, D., Priddle, H., Barbadillo Muñoz, M.D., Chamberlain, S., Allegrucci, C., Young, L.E., Denning, C., Barbadillo Mun˜oz, M.D., Mun˜oz, M., 2007. Improved Human Embryonic Stem Cell Embryoid Body Homogeneity and Cardiomyocyte Differentiation from a Novel V-96 Plate Aggregation System Highlights Interline Variability. Stem Cells 25, 929–938. https://doi.org/10.1634/STEMCELLS.2006-0598

Burridge, P.W., Keller, G., Gold, J.D., Wu, J.C., 2012. Production of de novo cardiomyocytes: human pluripotent stem cell differentiation and direct reprogramming. Cell Stem Cell 10, 16–28. https://doi.org/10.1016/J.STEM.2011.12.013

Burridge, P.W., Matsa, E., Shukla, P., Lin, Z.C., Churko, J.M., Ebert, A.D., Lan, F., Diecke, S., Huber, B., Mordwinkin, N.M., Plews, J.R., Abilez, O.J., Cui, B., Gold, J.D., Wu, J.C., 2014. Chemically defined generation of human cardiomyocytes. Nature Methods 2014 11:8 11, 855–860. https://doi.org/10.1038/nmeth.2999

Cai, X., Wang, K.C., Meng, Z., 2021. Mechanoregulation of YAP and TAZ in Cellular Homeostasis and Disease Progression. Front Cell Dev Biol 9, 1333. https://doi.org/10.3389/FCELL.2021.673599/BIBTEX

Camelliti, P., Borg, T.K., Kohl, P., 2005. Structural and functional characterisation of cardiac fibroblasts. Cardiovasc Res 65, 40–51. https://doi.org/10.1016/J.CARDIORES.2004.08.020/2/65-1-40-FIG8.GIF

Camelliti, P., Devlin, G.P., Matthews, K.G., Kohl, P., Green, C.R., 2004. Spatially and temporally distinct expression of fibroblast connexins after sheep ventricular infarction. Cardiovasc Res 62, 415–425. https://doi.org/10.1016/J.CARDIORES.2004.01.027

Cao, L., Schoenmaker, L., ten Den, S.A., Passier, R., Schwach, V., Verbeek, F.J., 2022. Automated Sarcomere Structure Analysis for Studying Cardiotoxicity in Human Pluripotent Stem Cell-Derived Cardiomyocytes. Microscopy and Microanalysis. https://doi.org/10.1093/MICMIC/OZAC016

Castellanos, B.S., Reyes-Nava, N.G., Quintana, A.M., 2021. Knockdown of hspg2 is associated with abnormal mandibular joint formation and neural crest cell dysfunction in zebrafish. BMC Dev Biol 21, 1–14. https://doi.org/10.1186/S12861-021-00238-4/FIGURES/7

Chang, C.W., Lai, Y.S., Pawlik, K.M., Liu, K., Sun, C.W., Li, C., Schoeb, T.R., Townes, T.M., 2009. Polycistronic lentiviral vector for “hit and run” reprogramming of adult skin fibroblasts to induced pluripotent stem cells. Stem Cells 27, 1042–1049. https://doi.org/10.1002/STEM.39

Chang, Y.T., Tseng, C.N., Tannenberg, P., Eriksson, L., Yuan, K., de Jesus Perez, V.A., Lundberg, J., Lengquist, M., Botusan, I.R., Catrina, S.B., Tran, P.K., Hedin, U., Tran-Lundmark, K., 2015. Perlecan heparan sulfate deficiency impairs pulmonary vascular development and attenuates hypoxic pulmonary hypertension. Cardiovasc Res 107, 20–31. https://doi.org/10.1093/CVR/CVV143

Chen, C., Li, D., Deng, L., 2016. Letter by Chen et al Regarding Article, “left Ventricular Ejection Fraction and Risk of Stroke and Cardiac Events in Heart Failure: Data from the Warfarin Versus Aspirin in Reduced Ejection Fraction Trial.” Stroke 47, e272. https://doi.org/10.1161/STROKEAHA.116.015175

Chen, C.X.Q., Abdian, N., Maussion, G., Thomas, R.A., Demirova, I., Cai, E., Tabatabaei, M., Beitel, L.K., Karamchandani, J., Fon, E.A., Durcan, T.M., 2021. A Multistep Workflow to Evaluate Newly Generated iPSCs and

Their Ability to Generate Different Cell Types. Methods Protoc 4. https://doi.org/10.3390/MPS4030050

Chen, H., Huang, X.N., R Stewart, A.F., Sepulveda, Jorge L, Sepulveda Gene, J.L., Sepulveda, J L, 2004. Gene expression changes associated with fibronectin-induced cardiac myocyte hypertrophy. Physiol Genomics 18, 273–283. https://doi.org/10.1152/physiolgenomics.00104.2004.-Fibro

Chen, H., Moreno-Moral, A., Pesce, F., Devapragash, N., Mancini, M., Heng, E.L., Rotival, M., Srivastava, P.K., Harmston, N., Shkura, K., Rackham, O.J.L., Yu, W.P., Sun, X.M., Tee, N.G.Z., Tan, E.L.S., Barton, P.J.R., Felkin, L.E., Lara-Pezzi, E., Angelini, G., Beltrami, C., Pravenec, M., Schafer, S., Bottolo, L., Hubner, N., Emanueli, C., Cook, S.A., Petretto, E., 2019. WWP2 regulates pathological cardiac fibrosis by modulating SMAD2 signaling. Nat Commun 10, 3616–3616. https://doi.org/10.1038/S41467-019-11551-9

Christensen, G., Herum, K.M., Lunde, I.G., 2019. Sweet, yet underappreciated: Proteoglycans and extracellular matrix remodeling in heart disease. Matrix Biol 75–76, 286–299. https://doi.org/10.1016/J.MATBIO.2018.01.001

Chuang, C.Y., Lord, M.S., Melrose, J., Rees, M.D., Knox, S.M., Freeman, C., Iozzo, R. v., Whitelock, J.M., 2010. Heparan sulfate-dependent signaling of fibroblast growth factor 18 by chondrocyte-derived perlecan. Biochemistry 49, 5524–5532. https://doi.org/10.1021/BI1005199/ASSET/IMAGES/MEDIUM/BI-2010-005199_0007.GIF

Combs, M.D., Yutzey, K.E., 2009. Heart Valve Development: Regulatory networks in development and disease. Circ Res 105, 408. https://doi.org/10.1161/CIRCRESAHA.109.201566

Cornelison, D.D.W., Wilcox-Adelman, S.A., Goetinck, P.F., Rauvala, H., Rapraeger, A.C., Olwin, B.B., 2004. Essential and separable roles for Syndecan-3 and Syndecan-4 in skeletal muscle development and regeneration. Genes Dev 18, 2231–2236. https://doi.org/10.1101/GAD.1214204

Costell, M., Sasaki, T., Mann, K., Yamada, Y., Timpl, R., 1996. Structural characterization of recombinant domain II of the basement membrane

proteoglycan perlecan. FEBS Lett 396, 127–131. https://doi.org/10.1016/0014-5793(96)01082-4

Couchman, J.R., Pataki, C.A., 2012. An Introduction to Proteoglycans and Their Localization. Journal of Histochemistry and Cytochemistry 60, 885. https://doi.org/10.1369/0022155412464638

Daniels, M.P., 2012. The Role of Agrin in Synaptic Development, Plasticity and Signaling in the Central Nervous System. Neurochem Int 61, 848. https://doi.org/10.1016/J.NEUINT.2012.02.028

Davis, J., Davis, L.C., Correll, R.N., Makarewich, C.A., Schwanekamp, J.A., Moussavi-Harami, F., Wang, D., York, A.J., Wu, H., Houser, S.R., Seidman, C.E., Seidman, J.G., Regnier, M., Metzger, J.M., Wu, J.C., Molkentin, J.D., 2016. A Tension-Based Model Distinguishes Hypertrophic versus Dilated Cardiomyopathy. Cell 165, 1147–1159. https://doi.org/10.1016/j.cell.2016.04.002

de Acetis, M., Notte, A., Accornero, F., Selvetella, G., Brancaccio, M., Vecchione, C., Sbroggiò, M., Collino, F., Pacchioni, B., Lanfranchi, G., Aretini, A., Ferretti, R., Maffei, A., Altruda, F., Silengo, L., Tarone, G., Lembo, G., 2005. Cardiac overexpression of melusin protects from dilated cardiomyopathy due to long-standing pressure overload. Circ Res 96, 1087–1094. https://doi.org/10.1161/01.RES.0000168028.36081.E0

de Boer, B.A., van den Berg, G., de Boer, P.A.J., Moorman, A.F.M., Ruijter, J.M., 2012. Growth of the developing mouse heart: An interactive qualitative and quantitative 3D atlas. Dev Biol 368, 203–213. https://doi.org/10.1016/J.YDBIO.2012.05.001

De Paolis, V., Maiullari, F., Chirivì, M., Milan, M., Cordiglieri, C., Pagano, F., La Manna, A.R., De Falco, E., Bearzi, C., Rizzi, R., Parisi, C., 2022. Unusual Association of NF-κB Components in Tumor-Associated Macrophages (TAMs) Promotes HSPG2-Mediated Immune-Escaping Mechanism in Breast Cancer. Int J Mol Sci 23, 7902. https://doi.org/10.3390/IJMS23147902/S1

de Sousa Lopes, S.M.C., Hassink, R.J., Feijen, A., van Rooijen, M.A., Doevendans, P.A., Tertoolen, L., de La Rivière, A.B., Mummery, C.L., 2006. Patterning the heart, a template for human cardiomyocyte

development. Developmental Dynamics 235, 1994–2002. https://doi.org/10.1002/DVDY.20830

Deb, A., Ubil, E., 2014. Cardiac fibroblast in development and wound healing. J Mol Cell Cardiol 70, 47–55. https://doi.org/10.1016/J.YJMCC.2014.02.017

Dempsey, C.E., Bigotti, M.G., Adams, J.C., Brancaccio, A., 2019. Analysis of α-dystroglycan/LG domain binding modes: Investigating protein motifs that regulate the affinity of isolated LG domains. Front Mol Biosci 6, 18. https://doi.org/10.3389/FMOLB.2019.00018/BIBTEX

Denning, C., Borgdorff, V., Crutchley, J., Firth, K.S.A., George, V., Kalra, S., Kondrashov, A., Hoang, M.D., Mosqueira, D., Patel, A., Prodanov, L., Rajamohan, D., Skarnes, W.C., Smith, J.G.W., Young, L.E., 2016. Cardiomyocytes from human pluripotent stem cells: From laboratory curiosity to industrial biomedical platform. Biochim Biophys Acta 1863, 1728–1748. https://doi.org/10.1016/J.BBAMCR.2015.10.014

Doppler, S.A., Carvalho, C., Lahm, H., Deutsch, M.A., Dreßen, M., Puluca, N., Lange, R., Krane, M., 2017. Cardiac fibroblasts: more than mechanical support. J Thorac Dis 9, S36. https://doi.org/10.21037/JTD.2017.03.122

Eiselleova, L., Matulka, K., Kriz, V., Kunova, M., Schmidtova, Z., Neradil, J., Tichy, B., Dvorakova, D., Pospisilova, S., Hampl, A., Dvorak, P., 2009. A Complex Role for FGF-2 in Self-Renewal, Survival, and Adhesion of Human Embryonic Stem Cells. Stem Cells 27, 1847. https://doi.org/10.1002/STEM.128

Eisner, D.A., Caldwell, J.L., Kistamás, K., Trafford, A.W., 2017. Calcium and Excitation-Contraction Coupling in the Heart. Circ Res 121, 181–195. https://doi.org/10.1161/CIRCRESAHA.117.310230

Eklund, L., Piuhola, J., Komulainen, J., Sormunen, R., Ongvarrasopone, C., Fässler, R., Muona, A., Ilves, M., Ruskoaho, H., Takala, T.E.S., Pihlajaniemi, T., 2001. Lack of type XV collagen causes a skeletal myopathy and cardiovascular defects in mice. Proc Natl Acad Sci U S A 98, 1194. https://doi.org/10.1073/PNAS.031444798

Elnakish, M.T., Kuppusamy, P., Khan, M., 2013. Stem cell transplantation as a therapy for cardiac fibrosis. J Pathol 229, 347–354. https://doi.org/10.1002/PATH.4111

Eminli, S., Foudi, A., Stadtfeld, M., Maherali, N., Ahfeldt, T., Mostoslavsky, G., Hock, H., Hochedlinger, K., 2009. Differentiation stage determines potential of hematopoietic cells for reprogramming into induced pluripotent stem cells. Nature Genetics 2009 41:9 41, 968–976. https://doi.org/10.1038/ng.428

Engebretsen, K.V.T., Lunde, I.G., Strand, M.E., Waehre, A., Sjaastad, I., Marstein, H.S., Skrbic, B., Dahl, C.P., Askevold, E.T., Christensen, G., Bjørnstad, J.L., Tønnessen, T., 2013. Lumican is increased in experimental and clinical heart failure, and its production by cardiac fibroblasts is induced by mechanical and proinflammatory stimuli. FEBS J 280, 2382–2398. https://doi.org/10.1111/FEBS.12235

Engler, A.J., Carag-Krieger, C., Johnson, C.P., Raab, M., Tang, H.Y., Speicher, D.W., Sanger, J.W., Sanger, J.M., Discher, D.E., 2008. Embryonic cardiomyocytes beat best on a matrix with heart-like elasticity: scar-like rigidity inhibits beating. J Cell Sci 121, 3794. https://doi.org/10.1242/JCS.029678

Fan, D., Takawale, A., Lee, J., Kassiri, Z., 2012. Cardiac fibroblasts, fibrosis and extracellular matrix remodeling in heart disease. Fibrogenesis Tissue Repair 5, 15. https://doi.org/10.1186/1755-1536-5-15

Fan, Y., Ho, B.X., Pang, J.K.S., Pek, N.M.Q., Hor, J.H., Ng, S.Y., Soh, B.S., 2018. Wnt/β-catenin-mediated signaling re-activates proliferation of matured cardiomyocytes. Stem Cell Res Ther 9. https://doi.org/10.1186/S13287-018-1086-8

Fang, L., Moore, X.L., Dart, A.M., Wang, L.M., 2015. Systemic inflammatory response following acute myocardial infarction. J Geriatr Cardiol 12, 305. https://doi.org/10.11909/J.ISSN.1671-5411.2015.03.020

Fang, M., Xiang, F.L., Braitsch, C.M., Yutzey, K.E., 2016. Epicardium-derived fibroblasts in heart development and disease. J Mol Cell Cardiol 91, 23. https://doi.org/10.1016/J.YJMCC.2015.12.019

Frangogiannis, N.G., 2015. Inflammation in cardiac injury, repair and regeneration. Curr Opin Cardiol 30, 240. https://doi.org/10.1097/HCO.0000000000000158

Frantz, C., Stewart, K.M., Weaver, V.M., 2010. The extracellular matrix at a glance. J Cell Sci 123, 4195. https://doi.org/10.1242/JCS.023820

Fu, R., Zhu, Y., Jiang, X., Li, Y., Zhu, M., Dong, M., Huang, Z., Wang, C., Labouesse, M., Zhang, H., 2018. CCAR-1 affects hemidesmosome biogenesis by regulating unc-52 /Perlecan alternative splicing in the C. elegans epidermis . J Cell Sci 131. https://doi.org/10.1242/JCS.214379/265601/AM/CCAR-1-AFFECTS-HEMIDESMOSOME-BIOGENESIS-BY

Fu, X., Liu, Q., Li, C., Li, Y., Wang, L., 2020. Cardiac Fibrosis and Cardiac Fibroblast Lineage-Tracing: Recent Advances. Front Physiol 11, 416. https://doi.org/10.3389/FPHYS.2020.00416/BIBTEX

Fukuda, R., Aharonov, A., Ong, Y.T., Stone, O.A., El-Brolosy, M.A., Maischein, H.M., Potente, M., Tzahor, E., Stainier, D.Y.R., 2019. Metabolic modulation regulates cardiac wall morphogenesis in zebrafish. Elife 8. https://doi.org/10.7554/ELIFE.50161

Galdos, F.X., Wu, S.M., 2019. Single-cell delineation of who's on first and second heart fields during development. Circ Res 125, 411–413. https://doi.org/10.1161/CIRCRESAHA.119.315576

Gao, Y.Y., Chen, L., Wang, T., Nie, Z.W., Zhang, X., Miao, Y.L., 2016. Oocyte aging-induced Neuronatin (NNAT) hypermethylation affects oocyte quality by impairing glucose transport in porcine. Scientific Reports 2016 6:1 6, 1–9. https://doi.org/10.1038/srep36008

Gheorghe, A., Griffiths, U., Murphy, A., Legido-Quigley, H., Lamptey, P., Perel, P., 2018. The economic burden of cardiovascular disease and hypertension in low- and middle-income countries: A systematic review. BMC Public Health 18, 1–11. https://doi.org/10.1186/S12889-018-5806-X/TABLES/4

Giacomelli, E., Meraviglia, V., Campostrini, G., Cochrane, A., Cao, X., van Helden, R.W.J., Krotenberg Garcia, A., Mircea, M., Kostidis, S., Davis, R.P., van Meer, B.J., Jost, C.R., Koster, A.J., Mei, H., Míguez, D.G., Mulder, A.A., Ledesma-Terrón, M., Pompilio, G., Sala, L., Salvatori, D.C.F., Slieker, R.C., Sommariva, E., de Vries, A.A.F., Giera, M., Semrau, S., Tertoolen, L.G.J., Orlova, V. v., Bellin, M., Mummery, C.L., 2020. Human-iPSC-Derived Cardiac Stromal Cells Enhance Maturation in 3D Cardiac Microtissues and Reveal Non-cardiomyocyte Contributions to

Heart Disease. Cell Stem Cell 26, 862. https://doi.org/10.1016/J.STEM.2020.05.004

Goda, N., Kanai, M., 2012. Hypoxia-inducible factors and their roles in energy metabolism. Int J Hematol 95, 457–463. https://doi.org/10.1007/S12185-012-1069-Y/FIGURES/2

Grath, A., Dai, G., 2019. Direct cell reprogramming for tissue engineering and regenerative medicine. J Biol Eng 13, 1–15. https://doi.org/10.1186/S13036-019-0144-9/FIGURES/7

Gubbiotti, M.A., Neill, T., Iozzo, R. v., 2017. A current view of perlecan in physiology and pathology: A mosaic of functions. Matrix Biol 57–58, 285. https://doi.org/10.1016/J.MATBIO.2016.09.003

Günthel, M., Barnett, P., Christoffels, V.M., 2018a. Development, Proliferation, and Growth of the Mammalian Heart. Molecular Therapy 26, 1599–1609. https://doi.org/10.1016/J.YMTHE.2018.05.022

Günthel, M., Barnett, P., Christoffels, V.M., 2018b. Development, Proliferation, and Growth of the Mammalian Heart. Molecular Therapy 26, 1599. https://doi.org/10.1016/J.YMTHE.2018.05.022

Guo, Y., Cao, Y., Jardin, B.D., Zhang, X., Zhou, P., Guatimosim, S., Lin, J., Chen, Z., Zhang, Y., Mazumdar, N., Lu, F., Ma, Q., Lu, Y.-W., Zhao, M., Wang, D.-Z., Dong, E., Pu, W.T., 2022. Ryanodine receptor 2 (RYR2) dysfunction activates the unfolded protein response and perturbs cardiomyocyte maturation. Cardiovasc Res. https://doi.org/10.1093/CVR/CVAC077

Guo, Y., Pu, W.T., 2020. Cardiomyocyte Maturation: New Phase in Development. Circ Res 126, 1086. https://doi.org/10.1161/CIRCRESAHA.119.315862

Gurtner, G.C., Werner, S., Barrandon, Y., Longaker, M.T., 2008. Wound repair and regeneration. Nature 453, 314–321. https://doi.org/10.1038/NATURE07039

Hall, C., Gehmlich, K., Denning, C., Pavlovic, D., 2021. Complex Relationship Between Cardiac Fibroblasts and Cardiomyocytes in Health and Disease. J Am Heart Assoc 10, 1–15. https://doi.org/10.1161/JAHA.120.019338

Han, L., Kamdar, M.R., 2018. MRI to MGMT: Predicting methylation status in glioblastoma patients using convolutional recurrent neural networks.

Pacific Symposium on Biocomputing 0, 331–342. https://doi.org/10.1142/9789813235533_0031

Handler, M., Yurchenco, P., Iozzo, R., 1997. Developmental expression of perlecan during murine embryogenesis. Developmental Dynamics. https://doi.org/10.1002/(SICI)1097-0177(199710)210:2

Harris, I.S., Black, B.L., 2010. Development of the Endocardium. Pediatr Cardiol 31, 391. https://doi.org/10.1007/S00246-010-9642-8

Herum, K.M., Lunde, I.G., McCulloch, A.D., Christensen, G., 2017. The Soft- and Hard-Heartedness of Cardiac Fibroblasts: Mechanotransduction Signaling Pathways in Fibrosis of the Heart. J Clin Med 6. https://doi.org/10.3390/JCM6050053

Hinderer, S., Schenke-Layland, K., 2019. Cardiac fibrosis - A short review of causes and therapeutic strategies. Adv Drug Deliv Rev 146, 77–82. https://doi.org/10.1016/J.ADDR.2019.05.011

Hinz, B., 2015. The extracellular matrix and transforming growth factor-β1: Tale of a strained relationship. Matrix Biology 47, 54–65. https://doi.org/10.1016/J.MATBIO.2015.05.006

Hinz, B., Gabbiani, G., 2003. Mechanisms of force generation and transmission by myofibroblasts. Curr Opin Biotechnol 14, 538–546. https://doi.org/10.1016/j.copbio.2003.08.006

Hirata, M., Ousaka, D., Arai, S., Okuyama, M., Tarui, S., Kobayashi, J., Kasahara, S., Sano, S., 2015. Novel Model of Pulmonary Artery Banding Leading to Right Heart Failure in Rats. Biomed Res Int 2015. https://doi.org/10.1155/2015/753210

Hopf, M., Göhring, W., Mann, K., Timpl, R., 2001. Mapping of binding sites for nidogens, fibulin-2, fibronectin and heparin to different IG modules of perlecan. J Mol Biol 311, 529–541. https://doi.org/10.1006/JMBI.2001.4878

Hsu, P.D., Lander, E.S., Zhang, F., 2014. Development and applications of CRISPR-Cas9 for genome engineering. Cell 157, 1262–1278. https://doi.org/10.1016/J.CELL.2014.05.010

Hu, D., Linders, A., Yamak, A., Correia, C., Kijlstra, J.D., Garakani, A., Xiao, L., Milan, D.J., van der Meer, P., Serra, M., Alves, P.M., Domian, I.J., 2018. Metabolic Maturation of Human Pluripotent Stem Cell Derived

Cardiomyocytes by Inhibition of HIF1α and LDHA. Circ Res 123, 1066. https://doi.org/10.1161/CIRCRESAHA.118.313249

Huang, C.Y., Liu, C.L., Ting, C.Y., Chiu, Y.T., Cheng, Y.C., Nicholson, M.W., Hsieh, P.C.H., 2019. Human iPSC banking: barriers and opportunities. J Biomed Sci 26. https://doi.org/10.1186/S12929-019-0578-X

Huang, Y., Harrison, M.R., Osorio, A., Kim, J., Baugh, A., Duan, C., Sucov, H.M., Lien, C.L., 2013. Igf Signaling is Required for Cardiomyocyte Proliferation during Zebrafish Heart Development and Regeneration. PLoS One 8, e67266. https://doi.org/10.1371/JOURNAL.PONE.0067266

Iozzo, R. v., Cohen, I.R., Grassel, S., Murdoch, A.D., 1994. The biology of perlecan: the multifaceted heparan sulphate proteoglycan of basement membranes and pericellular matrices. Biochem J 302 ( Pt 3), 625–639. https://doi.org/10.1042/BJ3020625

Iozzo, R. v., Pillarisetti, J., Sharma, B., Murdoch, A.D., Danielson, K.G., Uitto, J., Mauviel, A., 1997. Structural and Functional Characterization of the Human Perlecan Gene Promoter. Journal of Biological Chemistry 272, 5219–5228. https://doi.org/10.1074/jbc.272.8.5219

Iseoka, H., Miyagawa, S., Sakai, Y., Sawa, Y., 2021. Cardiac fibrosis models using human induced pluripotent stem cell-derived cardiac tissues allow anti-fibrotic drug screening in vitro. Stem Cell Res 54, 102420. https://doi.org/10.1016/J.SCR.2021.102420

Ishii, Y., Langberg, J., Rosborough, K., Mikawa, T., 2009. Endothelial cell lineages of the heart. Cell Tissue Res 335, 67. https://doi.org/10.1007/S00441-008-0663-Z

Ito, Kyoko, Ito, Keisuke, Gottesman, D.S., n.d. Metabolism and the Control of Cell Fate Decisions and Stem Cell Renewal. https://doi.org/10.1146/annurev-cellbio-111315-125134

Ivey, M.J., Tallquist, M.D., 2016a. Defining the Cardiac Fibroblast: A New Hope. Circ J 80, 2269. https://doi.org/10.1253/CIRCJ.CJ-16-1003

Ivey, M.J., Tallquist, M.D., 2016b. Defining the Cardiac Fibroblast: A New Hope. Circ J 80, 2269. https://doi.org/10.1253/CIRCJ.CJ-16-1003

Iwamoto, R., Mine, N., Kawaguchi, T., Minami, S., Saeki, K., Mekada, E., 2010. HB-EGF function in cardiac valve development requires interaction

with heparan sulfate proteoglycans. Development 137, 2205–2214. https://doi.org/10.1242/DEV.048926

J. Patterson, A., Zhang, L., 2010. Hypoxia and Fetal Heart Development. Curr Mol Med 10, 653–666. https://doi.org/10.2174/156652410792630643

Ji, Z.S., Lauer, S.J., Fazio, S., Bensadoun, A., Taylor, J.M., Mahley, R.W., 1994. Enhanced binding and uptake of remnant lipoproteins by hepatic lipase-secreting hepatoma cells in culture. Journal of Biological Chemistry 269, 13429–13436. https://doi.org/10.1016/S0021-9258(17)36850-3

JIANG, L., LI, J., ZHANG, C., SHANG, Y., LIN, J., 2020. YAP-mediated crosstalk between the Wnt and Hippo signaling pathways (Review). Mol Med Rep 22, 4101–4106. https://doi.org/10.3892/MMR.2020.11529/HTML

Jinek, M., Chylinski, K., Fonfara, I., Hauer, M., Doudna, J.A., Charpentier, E., 2012. A programmable dual-RNA-guided DNA endonuclease in adaptive bacterial immunity. Science (1979) 337, 816–821. https://doi.org/10.1126/SCIENCE.1225829/SUPPL_FILE/JINEK.SM.PDF

Johansson, M., Ulfenborg, B., Andersson, C.X., Heydarkhan-Hagvall, S., Jeppsson, A., Sartipy, P., Synnergren, J., 2022. Multi-Omics Characterization of a Human Stem Cell-Based Model of Cardiac Hypertrophy. Life 12, 293. https://doi.org/10.3390/LIFE12020293/S1

Johnson, B.B., Reinhold, J., Holmes, T.L., Moore, J.A., Cowell, V., Bernardo, A.S., Rushworth, S.A., Vassiliou, V., Smith, J.G.W., 2022. Modelling metabolic shifts during cardiomyocyte differentiation, iron deficiency and transferrin rescue using human pluripotent stem cells. Metabolites 12. https://doi.org/10.3390/METABO12010009/S1

Jones, M.R., Tran, C., Singh, J., Dawson, J.F., 2022. A gradient of force generation at rest differentiates cardiomyopathy outcomes with variants of actin located at the same residue. Journal of Molecular and Cellular Cardiology Plus 2, 100023. https://doi.org/10.1016/J.JMCCPL.2022.100023

Jung, MoonSun, Lord, M.S., Cheng, B., Lyons, J.G., Alkhouri, H., Hughes, J.M., McCarthy, S.J., Iozzo, R. v., Whitelock, J.M., 2013. Mast Cells Produce Novel Shorter Forms of Perlecan That Contain Functional

Endorepellin. Journal of Biological Chemistry 288, 3289–3304. https://doi.org/10.1074/jbc.m112.387811

Jung, Moonsun, Lord, M.S., Cheng, B., Lyons, J.G., Alkhouri, H., Hughes, J.M., McCarthy, S.J., Iozzo, R. V., Whitelock, J.M., 2013. Mast Cells Produce Novel Shorter Forms of Perlecan That Contain Functional Endorepellin: A ROLE IN ANGIOGENESIS AND WOUND HEALING*. J Biol Chem 288, 3289. https://doi.org/10.1074/JBC.M112.387811

Kabat, J.L., Barberan-Soler, S., Zahler, A.M., 2009. HRP-2, the Caenorhabditis elegans homolog of mammalian heterogeneous nuclear ribonucleoproteins Q and R, is an alternative splicing factor that binds to UCUAUC splicing regulatory elements. Journal of Biological Chemistry 284, 28490–28497. https://doi.org/10.1074/JBC.M109.023101

Kallunki, P., Tryggvason, K., 1992. Human basement membrane heparan sulfate proteoglycan core protein: A 467-kD protein containing multiple domains resembling elements of the low density lipoprotein receptor, laminin, neural cell adhesion molecules, and epidermal growth factor. Journal of Cell Biology 116, 559–571. https://doi.org/10.1083/jcb.116.2.559

Kamimura, K., Ueno, K., Nakagawa, J., Hamada, R., Saitoe, M., Maeda, N., 2013. Perlecan regulates bidirectional Wnt signaling at the Drosophila neuromuscular junction. J Cell Biol 200, 219–233. https://doi.org/10.1083/JCB.201207036

Kang, M., Yao, Y., 2020. Basement Membrane Changes in Ischemic Stroke. Stroke 1344–1352. https://doi.org/10.1161/STROKEAHA.120.028928

Kanisicak, O., Khalil, H., Ivey, M.J., Karch, J., Maliken, B.D., Correll, R.N., Brody, M.J., Lin, S.C.J., Aronow, B.J., Tallquist, M.D., Molkentin, J.D., 2016. Genetic lineage tracing defines myofibroblast origin and function in the injured heart. Nat Commun 7. https://doi.org/10.1038/NCOMMS12260

Karbassi, E., Fenix, A., Marchiano, S., Muraoka, N., Nakamura, K., Yang, X., Murry, C.E., 2020. Cardiomyocyte maturation: advances in knowledge and implications for regenerative medicine. Nature Reviews Cardiology 2020 17:6 17, 341–359. https://doi.org/10.1038/s41569-019-0331-x

Katewa, A., Suto, E., Hui, J., Heredia, J., Liang, J., Hackney, J., Anderson, K., Alcantar, T.M., Bacarro, N., Dunlap, D., Eastham, J., Paler-Martinez, A., Rairdan, X.Y., Modrusan, Z., Lee, W.P., Austin, C.D., Lafkas, D., Ghilardi, N., 2021. The peptide symporter SLC15a4 is essential for the development of systemic lupus erythematosus in murine models. PLoS One 16, e0244439. https://doi.org/10.1371/JOURNAL.PONE.0244439

Kehat, I., Kenyagin-Karsenti, D., Snir, M., Segev, H., Amit, M., Gepstein, A., Livne, E., Binah, O., Itskovitz-Eldor, J., Gepstein, L., 2001. Human embryonic stem cells can differentiate into myocytes with structural and functional properties of cardiomyocytes. J Clin Invest 108, 407–414. https://doi.org/10.1172/JCI12131

Kemmler, C.L., Riemslagh, F.W., Moran, H.R., Mosimann, C., 2021. From Stripes to a Beating Heart: Early Cardiac Development in Zebrafish. J Cardiovasc Dev Dis 8, 1–21. https://doi.org/10.3390/JCDD8020017

Kerever, A., Mercier, F., Nonaka, R., de Vega, S., Oda, Y., Zalc, B., Okada, Y., Hattori, N., Yamada, Y., Arikawa-Hirasawa, E., 2014. Perlecan is required for FGF-2 signaling in the neural stem cell niche. Stem Cell Res 12, 492. https://doi.org/10.1016/J.SCR.2013.12.009

Kern, C.B., Twal, W.O., Mjaatvedt, C.H., Fairey, S.E., Toole, B.P., Iruela-Arispe, M.L., Argraves, W.S., 2006. Proteolytic Cleavage of Versican During Cardiac Cushion Morphogenesis. Dev Dyn 235, 2238. https://doi.org/10.1002/DVDY.20838

Khare, S., Galeano, K., Zhang, Y., Nick, J.A., Nick, H.S., Subramony, S.H., Sampson, J., Kaczmarek, L.K., Waters, M.F., 2018. C-terminal proline deletions in KCNC3 cause delayed channel inactivation and an adult-onset progressive SCA13 with spasticity. Cerebellum 17, 692. https://doi.org/10.1007/S12311-018-0950-5

Kierans, S.J., Taylor, C.T., 2021. Regulation of glycolysis by the hypoxia-inducible factor (HIF): implications for cellular physiology. J Physiol 599, 23–37. https://doi.org/10.1113/JP280572

Klewer, S.E., Krob, S.L., Kolker, S.J., Kitten, G.T., n.d. Expression of Type VI Collagen in the Developing Mouse Heart. https://doi.org/10.1002/(SICI)1097-0177(199803)211:3

Kloesel, B., Dinardo, J.A., Body, S.C., 2016. Cardiac Embryology and Molecular Mechanisms of Congenital Heart Disease – A Primer for Anesthesiologists. Anesth Analg 123, 551. https://doi.org/10.1213/ANE.0000000000001451

Klose, K., Gossen, M., Stamm, C., 2019. Turning fibroblasts into cardiomyocytes: Technological review of cardiac transdifferentiation strategies. FASEB Journal 33, 49–70. https://doi.org/10.1096/FJ.201800712R

Knollmann, B.C., Chopra, N., Hlaing, T., Akin, B., Yang, T., Ettensohn, K., Knollmann, B.E.C., Horton, K.D., Weissman, N.J., Holinstat, I., Zhang, W., Roden, D.M., Jones, L.R., Franzini-Armstrong, C., Pfeifer, K., 2006. Casq2 deletion causes sarcoplasmic reticulum volume increase, premature Ca2+ release, and catecholaminergic polymorphic ventricular tachycardia. J Clin Invest 116, 2510–2520. https://doi.org/10.1172/JCI29128

Kobayashi, T., Nguyen-Tien, D., Ohshima, D., Karyu, H., Shimabukuro-Demoto, S., Yoshida-Sugitani, R., Toyama-Sorimachi, N., 2021. Human SLC15A4 is crucial for TLR-mediated type I interferon production and mitochondrial integrity. Int Immunol 33, 399–406. https://doi.org/10.1093/INTIMM/DXAB006

Koivumäki, J.T., Naumenko, N., Tuomainen, T., Takalo, J., Oksanen, M., Puttonen, K.A., Lehtonen, Š., Kuusisto, J., Laakso, M., Koistinaho, J., Tavi, P., 2018. Structural immaturity of human iPSC-derived cardiomyocytes: In silico investigation of effects on function and disease modeling. Front Physiol 9, 80. https://doi.org/10.3389/FPHYS.2018.00080/BIBTEX

Kondrashov, A., Hoang, M.D., Smith, J.G.W., Bhagwan, J.R., Duncan, G., Mosqueira, D., Munoz, M.B., Vo, N.T.N., Denning, C., 2018. Simplified Footprint-Free Cas9/CRISPR Editing of Cardiac-Associated Genes in Human Pluripotent Stem Cells. Stem Cells Dev 27, 391. https://doi.org/10.1089/SCD.2017.0268

Kong, P., Christia, P., Frangogiannis, N.G., 2013. The pathogenesis of cardiac fibrosis. Cellular and Molecular Life Sciences 2013 71:4 71, 549–574. https://doi.org/10.1007/S00018-013-1349-6

Krzyszczyk, P., Schloss, R., Palmer, A., Berthiaume, F., 2018. The Role of Macrophages in Acute and Chronic Wound Healing and Interventions to Promote Pro-wound Healing Phenotypes. Front Physiol 9, 419. https://doi.org/10.3389/FPHYS.2018.00419

Laflamme, M.A., Chen, K.Y., Naumova, A. v., Muskheli, V., Fugate, J.A., Dupras, S.K., Reinecke, H., Xu, C., Hassanipour, M., Police, S., O'Sullivan, C., Collins, L., Chen, Y., Minami, E., Gill, E.A., Ueno, S., Yuan, C., Gold, J., Murry, C.E., 2007. Cardiomyocytes derived from human embryonic stem cells in pro-survival factors enhance function of infarcted rat hearts. Nature Biotechnology 2007 25:9 25, 1015–1024. https://doi.org/10.1038/nbt1327

Leask, A., 2007. TGFβ, cardiac fibroblasts, and the fibrotic response. Cardiovasc Res 74, 207–212. https://doi.org/10.1016/J.CARDIORES.2006.07.012/2/74-2-207-FIG2.GIF

Lee, M.-O., Bo Jung, K., Jo, S.-J., Hyun, S.-A., Moon, K.-S., Seo, J.-W., Kim, S.-H., Son, M.-Y., 2019. Modelling cardiac fibrosis using three-dimensional cardiac microtissues derived from human embryonic stem cells. https://doi.org/10.1186/s13036-019-0139-6

Leung, S.W.S., Shi, Y., 2022. The glycolytic process in endothelial cells and its implications. Acta Pharmacol Sin 43, 251. https://doi.org/10.1038/S41401-021-00647-Y

Leuning, D.G., Beijer, N.R.M., du Fossé, N.A., Vermeulen, S., Lievers, E., van Kooten, C., Rabelink, T.J., de Boer, J., 2018. The cytokine secretion profile of mesenchymal stromal cells is determined by surface structure of the microenvironment. Sci Rep 8. https://doi.org/10.1038/S41598-018-25700-5

Li, A., Gao, M., Jiang, W., Qin, Y., Gong, G., 2020. Mitochondrial Dynamics in Adult Cardiomyocytes and Heart Diseases. Front Cell Dev Biol 8, 584800. https://doi.org/10.3389/FCELL.2020.584800

Li, J., Hua, Y., Miyagawa, S., Zhang, J., Li, L., Liu, L., Sawa, Y., 2020. hiPSC-Derived Cardiac Tissue for Disease Modeling and Drug Discovery. Int J Mol Sci 21, 1–32. https://doi.org/10.3390/IJMS21238893

Li, P., Cavallero, S., Gu, Y., Chen, T.H.P., Hughes, J., Hassan, A.B., Brüning, J.C., Pashmforoush, M., Sucov, H.M., 2011. IGF signaling directs ventricular cardiomyocyte proliferation during embryonic heart development. Development 138, 1795–1805. https://doi.org/10.1242/DEV.054338

Li, X., Thomason, P.A., Withers, D.J., Scott, J., 2010. Bio-informatics analysis of a gene co-expression module in adipose tissue containing the diet-responsive gene Nnat. BMC Syst Biol 4, 1–11. https://doi.org/10.1186/1752-0509-4-175/FIGURES/2

Lian, X., Hsiao, C., Wilson, G., Zhu, K., Hazeltine, L.B., Azarin, S.M., Raval, K.K., Zhang, J., Kamp, T.J., Palecek, S.P., 2012. Robust cardiomyocyte differentiation from human pluripotent stem cells via temporal modulation of canonical Wnt signaling. Proc Natl Acad Sci U S A 109. https://doi.org/10.1073/PNAS.1200250109

Liang, W., Han, P., Kim, E.H., Mak, J., Zhang, R., Torrente, A.G., Goldhaber, J.I., Marbán, E., Cho, H.C., 2020. Canonical Wnt signaling promotes pacemaker cell specification of cardiac mesodermal cells derived from mouse and human embryonic stem cells. Stem Cells 38, 352. https://doi.org/10.1002/STEM.3106

Lin, M.C., Rockman, H.A., Chien, K.R., 1995. Heart and lung disease in engineered mice. Nat Med 1, 749–751. https://doi.org/10.1038/NM0895-749

Lin, P.Y., Hung, J.H., Hsu, C.K., Chang, Y.T., Sun, Y.T., 2021a. A Novel Pathogenic HSPG2 Mutation in Schwartz–Jampel Syndrome. Front Neurol 12, 206. https://doi.org/10.3389/FNEUR.2021.632336/BIBTEX

Lin, P.Y., Hung, J.H., Hsu, C.K., Chang, Y.T., Sun, Y.T., 2021b. A Novel Pathogenic HSPG2 Mutation in Schwartz–Jampel Syndrome. Front Neurol 12, 632336. https://doi.org/10.3389/FNEUR.2021.632336

Lin, X., Perrimon, N., 2002. Developmental roles of heparan sulfate proteoglycans in Drosophila. Glycoconj J 19, 363–368. https://doi.org/10.1023/A:1025329323438

Lincoln, J., Florer, J.B., Deutsch, G.H., Wenstrup, R.J., Yutzey, K.E., 2006. ColVa1 and ColXIa1 are required for myocardial morphogenesis and

heart valve development. Dev Dyn 235, 3295–3305. https://doi.org/10.1002/DVDY.20980

Lindsey, S.E., Butcher, J.T., Yalcin, H.C., 2014. Mechanical regulation of cardiac development. Front Physiol 5. https://doi.org/10.3389/FPHYS.2014.00318

Lippi, M., Stadiotti, I., Pompilio, G., Sommariva, E., 2020. Human Cell Modeling for Cardiovascular Diseases. Int J Mol Sci 21, 1–27. https://doi.org/10.3390/IJMS21176388

Lister, R., Pelizzola, M., Kida, Y.S., Hawkins, R.D., Nery, J.R., Hon, G., Antosiewicz-Bourget, J., Ogmalley, R., Castanon, R., Klugman, S., Downes, M., Yu, R., Stewart, R., Ren, B., Thomson, J.A., Evans, R.M., Ecker, J.R., 2011. Hotspots of aberrant epigenomic reprogramming in human induced pluripotent stem cells. Nature 471, 68. https://doi.org/10.1038/NATURE09798

Liu, H., Wei, Z., Dominguez, A., Li, Y., Wang, X., Qi, L.S., 2015. CRISPR-ERA: a comprehensive design tool for CRISPR-mediated gene editing, repression and activation. Bioinformatics 31, 3676. https://doi.org/10.1093/BIOINFORMATICS/BTV423

Liu, W., Cui, Y., Wei, J., Sun, J., Zheng, L., Xie, J., 2020. Gap junction-mediated cell-to-cell communication in oral development and oral diseases: a concise review of research progress. Int J Oral Sci 12. https://doi.org/10.1038/S41368-020-0086-6

Liu, X., Wu, H., Byrne, M., Krane, S., Jaenisch, R., 1997. Type III collagen is crucial for collagen I fibrillogenesis and for normal cardiovascular development. Proc Natl Acad Sci U S A 94, 1852–1856. https://doi.org/10.1073/PNAS.94.5.1852

Liu, X., Zhang, Y., Han, Y., Lu, W., Yang, J., Tian, J., Sun, P., Yu, T., Hu, Y., Zhang, H., Huang, P., Liu, P., 2020. Overexpression of GLT1D1 induces immunosuppression through glycosylation of PD-L1 and predicts poor prognosis in B-cell lymphoma. Mol Oncol 14, 1028–1044. https://doi.org/10.1002/1878-0261.12664

Lockhart, M., Wirrig, E., Phelps, A., Wessels, A., 2011. Extracellular matrix and heart development. Birth Defects Res A Clin Mol Teratol 91, 535–550. https://doi.org/10.1002/BDRA.20810

Lopez, C.A., Al-Siddiqi, H.H.A.A., Purnama, U., Iftekhar, S., Bruyneel, A.A.N., Kerr, M., Nazir, R., da Luz Sousa Fialho, M., Malandraki-Miller, S., Alonaizan, R., Kermani, F., Heather, L.C., Czernuszka, J., Carr, C.A., 2021. Physiological and pharmacological stimulation for in vitro maturation of substrate metabolism in human induced pluripotent stem cell-derived cardiomyocytes. Sci Rep 11. https://doi.org/10.1038/S41598-021-87186-Y

Lord, M.S., Chuang, C.Y., Melrose, J., Davies, M.J., Iozzo, R. v., Whitelock, J.M., 2014a. The role of vascular-derived perlecan in modulating cell adhesion, proliferation and growth factor signaling. Matrix Biol 35, 112–122. https://doi.org/10.1016/J.MATBIO.2014.01.016

Lord, M.S., Jung, M.S., Cheng, B., Whitelock, J.M., 2014b. Transcriptional complexity of the HSPG2 gene in the human mast cell line, HMC-1. Matrix Biology 35, 123–131. https://doi.org/10.1016/J.MATBIO.2013.12.005

Lord, M.S., Tang, F., Rnjak-Kovacina, J., Smith, J.G.W., Melrose, J., Whitelock, J.M., 2018. The multifaceted roles of perlecan in fibrosis. Matrix Biol 68–69, 150–166. https://doi.org/10.1016/J.MATBIO.2018.02.013

Lother, A., Bergemann, S., Deng, L., Moser, M., Bode, C., Hein, L., 2018. Cardiac endothelial cell transcriptome. Arterioscler Thromb Vasc Biol 38, 566–574. https://doi.org/10.1161/ATVBAHA.117.310549

Louault, C., Benamer, N., Faivre, J.F., Potreau, D., Bescond, J., 2008. Implication of connexins 40 and 43 in functional coupling between mouse cardiac fibroblasts in primary culture. Biochimica et Biophysica Acta (BBA) - Biomembranes 1778, 2097–2104. https://doi.org/10.1016/J.BBAMEM.2008.04.005

Lukyanenko, V., Chikando, A., Lederer, W.J., 2009. Mitochondria in cardiomyocyte Ca2+ signaling. Int J Biochem Cell Biol 41, 1957–1971. https://doi.org/10.1016/J.BIOCEL.2009.03.011

Lunde, I.G., Herum, K.M., Carlson, C.C., Christensen, G., 2016. Syndecans in heart fibrosis. Cell Tissue Res 365, 539–552. https://doi.org/10.1007/S00441-016-2454-2

Lundy, S.D., Zhu, W.Z., Regnier, M., Laflamme, M.A., 2013. Structural and Functional Maturation of Cardiomyocytes Derived from Human

Pluripotent Stem Cells. Stem Cells Dev 22, 1991. https://doi.org/10.1089/SCD.2012.0490

Lyra-Leite, D.M., Gutiérrez-Gutiérrez, Ó., Wang, M., Zhou, Y., Cyganek, L., Burridge, P.W., 2022. A review of protocols for human iPSC culture, cardiac differentiation, subtype-specification, maturation, and direct reprogramming. STAR Protoc 3. https://doi.org/10.1016/J.XPRO.2022.101560

MacKenna, D., Summerour, S.R., Villarreal, F.J., 2000. Role of mechanical factors in modulating cardiac fibroblast function and extracellular matrix synthesis. Cardiovasc Res 46, 257–263. https://doi.org/10.1016/S0008-6363(00)00030-4/2/46-2-257-FIG2.GIF

Maeder, M.L., Linder, S.J., Cascio, V.M., Fu, Y., Ho, Q.H., Joung, J.K., 2013. CRISPR RNA–guided activation of endogenous human genes. Nature Methods 2013 10:10 10, 977–979. https://doi.org/10.1038/nmeth.2598

Mahmoud, A.I., Kocabas, F., Muralidhar, S.A., Kimura, W., Koura, A.S., Thet, S., Porrello, E.R., Sadek, H.A., 2013. Meis1 regulates postnatal cardiomyocyte cell cycle arrest. Nature 2013 497:7448 497, 249–253. https://doi.org/10.1038/nature12054

Malik, N., Rao, M.S., 2013. A Review of the Methods for Human iPSC Derivation. Methods Mol Biol 997, 23. https://doi.org/10.1007/978-1-62703-348-0_3

Mangino, M., Hwang, S.J., Spector, T.D., Hunt, S.C., Kimura, M., Fitzpatrick, A.L., Christiansen, L., Petersen, I., Elbers, C.C., Harris, T., Chen, W., Srinivasan, S.R., Kark, J.D., Benetos, A., el shamieh, S., Visvikis-Siest, S., Christensen, K., Berenson, G.S., Valdes, A.M., Vinuela, A., Garcia, M., Arnett, D.K., Broeckel, U., Province, M.A., Pankow, J.S., Kammerer, C., Liu, Y., Nalls, M., Tishkoff, S., Thomas, F., Ziv, E., Psaty, B.M., Bis, J.C., Rotter, J.I., Taylor, K.D., Smith, E., Schork, N.J., Levy, D., Aviv, A., 2012. Genome-wide meta-analysis points to CTC1 and ZNF676 as genes regulating telomere homeostasis in humans. Hum Mol Genet 21, 5385–5394. https://doi.org/10.1093/HMG/DDS382

Männer, J., Pérez-Pomares, J.M., Macías, D., Muñoz-Chápuli, R., 2001. The Origin, Formation and Developmental Significance of the Epicardium: A

Review. Cells Tissues Organs 169, 89–103. https://doi.org/10.1159/000047867

Männer, J., Yelbuz, T.M., 2019. Functional Morphology of the Cardiac Jelly in the Tubular Heart of Vertebrate Embryos. J Cardiovasc Dev Dis 6. https://doi.org/10.3390/JCDD6010012

Mannhardt, I., Breckwoldt, K., Letuffe-Brenière, D., Schaaf, S., Schulz, H., Neuber, C., Benzin, A., Werner, T., Eder, A., Schulze, T., Klampe, B., Christ, T., Hirt, M.N., Huebner, N., Moretti, A., Eschenhagen, T., Hansen, A., 2016. Human Engineered Heart Tissue: Analysis of Contractile Force. Stem Cell Reports 7, 29. https://doi.org/10.1016/J.STEMCR.2016.04.011

Martinez, J.R., Dhawan, A., Farach-Carson, M.C., 2018. Modular Proteoglycan Perlecan/ HSPG2: Mutations, Phenotypes, and Functions. Genes (Basel) 9. https://doi.org/10.3390/GENES9110556

Mastikhina, O., Moon, B.U., Williams, K., Hatkar, R., Gustafson, D., Mourad, O., Sun, X., Koo, M., Lam, A.Y.L., Sun, Y., Fish, J.E., Young, E.W.K., Nunes, S.S., 2020. Human cardiac fibrosis-on-a-chip model recapitulates disease hallmarks and can serve as a platform for drug testing. Biomaterials 233, 119741. https://doi.org/10.1016/J.BIOMATERIALS.2019.119741

McGregor, R.J., Chau, Y.Y., Kendall, T.J., Artibani, M., Hastie, N., Hadoke, P.W.F., 2018. WT1 expression in vessels varies with histopathological grade in tumour-bearing and control tissue from patients with breast cancer. Br J Cancer 119, 1508. https://doi.org/10.1038/S41416-018-0317-1

Mei, C., Tan, J., Lewandowski, Adam James, Lewandowski, Adam J, 2020. The Transitional Heart: From Early Embryonic and Fetal Development to Neonatal Life. Fetal Diagn Ther 47, 373–386. https://doi.org/10.1159/000501906

Melleby, A.O., Strand, M.E., Romaine, A., Herum, K.M., Skrbic, B., Dahl, C.P., Sjaastad, I., Fiane, A.E., Filmus, J., Christensen, G., Lunde, I.G., 2016. The Heparan Sulfate Proteoglycan Glypican-6 Is Upregulated in the Failing Heart, and Regulates Cardiomyocyte Growth through ERK1/2 Signaling. PLoS One 11. https://doi.org/10.1371/JOURNAL.PONE.0165079

Melrose, J., Roughley, P., Knox, S., Smith, S., Lord, M., Whitelock, J., 2006. The structure, location, and function of perlecan, a prominent pericellular proteoglycan of fetal, postnatal, and mature hyaline cartilages. J Biol Chem 281, 36905–36914. https://doi.org/10.1074/JBC.M608462200

Mikawa, T., Gourdie, R.G., 1996. Pericardial Mesoderm Generates a Population of Coronary Smooth Muscle Cells Migrating into the Heart along with Ingrowth of the Epicardial Organ. Dev Biol 174, 221–232. https://doi.org/10.1006/DBIO.1996.0068

Monaghan, M.G., Linneweh, M., Liebscher, S., van Handel, B., Layland, S.L., Schenke-Layland, K., 2016. Endocardial-to-mesenchymal transformation and mesenchymal cell colonization at the onset of human cardiac valve development. Development (Cambridge) 143, 473–482. https://doi.org/10.1242/DEV.133843/-/DC1

Mongiat, M., Fu, J., Oldershaw, R., Greenhalgh, R., Gown, A.M., Iozzo, R. v., 2003. Perlecan protein core interacts with extracellular matrix protein 1 (ECM1), a glycoprotein involved in bone formation and angiogenesis. J Biol Chem 278, 17491–17499. https://doi.org/10.1074/JBC.M210529200

Montanaro, F., Lindenbaum, M., Carbonetto, S., 1999. α-Dystroglycan Is a Laminin Receptor Involved in Extracellular Matrix Assembly on Myotubes and Muscle Cell Viability. J Cell Biol 145, 1325. https://doi.org/10.1083/JCB.145.6.1325

Montecucco, F., Marzo, V. di, 2012. At the heart of the matter: the endocannabinoid system in cardiovascular function and dysfunction. Trends Pharmacol Sci 33, 331–340. https://doi.org/10.1016/j.tips.2012.03.002

Moore-Morris, T., Cattaneo, P., Puceat, M., Evans, S.M., 2016. Origins of Cardiac Fibroblasts. J Mol Cell Cardiol 91, 1. https://doi.org/10.1016/J.YJMCC.2015.12.031

Morikawa, Y., Heallen, T., Leach, J., Xiao, Y., Martin, J.F., 2017. Dystrophin–glycoprotein complex sequesters Yap to inhibit cardiomyocyte proliferation. Nature 2017 547:7662 547, 227–231. https://doi.org/10.1038/nature22979

Mosqueira, D., Lis-Slimak, K., Denning, C., 2019. High-Throughput Phenotyping Toolkit for Characterizing Cellular Models of Hypertrophic

Cardiomyopathy In Vitro. Methods Protoc 2. https://doi.org/10.3390/MPS2040083

Mosqueira, D., Mannhardt, I., Bhagwan, J.R., Lis-Slimak, K., Katili, P., Scott, E., Hassan, M., Prondzynski, M., Harmer, S.C., Tinker, A., Smith, J.G.W., Carrier, L., Williams, P.M., Gaffney, D., Eschenhagen, T., Hansen, A., Denning, C., 2018. CRISPR/Cas9 editing in human pluripotent stem cell-cardiomyocytes highlights arrhythmias, hypocontractility, and energy depletion as potential therapeutic targets for hypertrophic cardiomyopathy. Eur Heart J 39, 3879. https://doi.org/10.1093/EURHEARTJ/EHY249

Mossahebi-Mohammadi, M., Quan, M., Zhang, J.S., Li, X., 2020. FGF Signaling Pathway: A Key Regulator of Stem Cell Pluripotency. Front Cell Dev Biol 8, 79. https://doi.org/10.3389/FCELL.2020.00079/BIBTEX

Mulder, M., Lombardi, P., Jansen, H., van Berkel, T.J.C., Frants, R.R., Havekes, L.M., 1993. Low density lipoprotein receptor internalizes low density and very low density lipoproteins that are bound to heparan sulfate proteoglycans via lipoprotein lipase. Journal of Biological Chemistry 268, 9369–9375. https://doi.org/10.1016/S0021-9258(18)98359-6

Murdoch, A. D., Dodge, G.R., Cohen, I., Tuan, R.S., Iozzo, R. v., 1992. Primary structure of the human heparan sulfate proteoglycan from basement membrane (HSPG2/perlecan). A chimeric molecule with multiple domains homologous to the low density lipoprotein receptor, laminin, neural cell adhesion molecules, and epidermal growth factor. Journal of Biological Chemistry 267, 8544–8557. https://doi.org/10.1016/s0021-9258(18)42478-7

Murdoch, Alan D, Dodge, G.R., Cohen, I., Tuans, R.S., Iozzo#, R. v, 1992. Primary Structure of the Human Heparan Sulfate Proteoglycan from Basement Membrane (HSPGB/Perlecan). J Biol Chem 267, 8544–8557. https://doi.org/10.1016/S0021-9258(18)42478-7

Murphy, S.P., Ibrahim, N.E., Januzzi, J.L., 2020. Heart Failure With Reduced Ejection Fraction: A Review. JAMA 324, 488–504. https://doi.org/10.1001/JAMA.2020.10262

Musunuru, K., Domian, I.J., Chien, K.R., 2010. Stem Cell Models of Cardiac Development and Disease. https://doi.org/10.1146/annurev-cellbio-

100109-103948 26, 667–687. https://doi.org/10.1146/ANNUREV-CELLBIO-100109-103948

Nakahama, M., Murakami, T., Kusachi, S., Naito, I., Takeda, K., Ohnishi, H., Komatsubara, I., Oka, T., Ninomiya, Y., Tsuji, T., 2000. Expression of Perlecan Proteoglycan in the Infarct Zone of Mouse Myocardial Infarction. J Mol Cell Cardiol 32, 1087–1100. https://doi.org/10.1006/JMCC.2000.1146

Nakamura, R., Nakamura, F., Fukunaga, S., 2014. Perlecan Diversely Regulates the Migration and Proliferation of Distinct Cell Types in vitro. Cells Tissues Organs 200, 374–393. https://doi.org/10.1159/000440950

Nam, Y.J., Song, K., Luo, X., Daniel, E., Lambeth, K., West, K., Hill, J.A., di Maio, J.M., Baker, L.A., Bassel-Duby, R., Olson, E.N., 2013. Reprogramming of human fibroblasts toward a cardiac fate. Proc Natl Acad Sci U S A 110, 5588–5593. https://doi.org/10.1073/PNAS.1301019110

Naqvi, N., Li, M., Calvert, J.W., Tejada, T., Lambert, J.P., Wu, J., Kesteven, S.H., Holman, S.R., Matsuda, T., Lovelock, J.D., Howard, W.W., Iismaa, S.E., Chan, A.Y., Crawford, B.H., Wagner, M.B., Martin, D.I.K., Lefer, D.J., Graham, R.M., Husain, A., 2014. A Proliferative Burst During Preadolescence Establishes the Final Cardiomyocyte Number. Cell 157, 795. https://doi.org/10.1016/J.CELL.2014.03.035

Neininger-Castro, A.C., Hayes, J.B., Sanchez, Z.C., Taneja, N., Fenix, A.M., Moparthi, S., Vassilopoulos, S., Burnette, D.T., 2023. Independent regulation of Z-lines and M-lines during sarcomere assembly in cardiac myocytes revealed by the automatic image analysis software sarcApp. bioRxiv 2023.01.11.523681. https://doi.org/10.1101/2023.01.11.523681

Ng, A., Wong, M., Viviano, B., Erlich, J.M., Alba, G., Pflederer, C., Jay, P.Y., Saunders, S., 2009. Loss of glypican-3 function causes growth factor-dependent defects in cardiac and coronary vascular development. Dev Biol 335, 208–215. https://doi.org/10.1016/J.YDBIO.2009.08.029

Noseda, M., Peterkin, T., Simões, F.C., Patient, R., Schneider, M.D., 2011. Cardiopoietic Factors. Circ Res 108, 129–152. https://doi.org/10.1161/CIRCRESAHA.110.223792

Ocken, A.R., Ku, M.M., Kinzer-Ursem, T.L., Calve, S., 2020. Perlecan Knockdown Significantly Alters Extracellular Matrix Composition and Organization During Cartilage Development. Mol Cell Proteomics 19, 1220. https://doi.org/10.1074/MCP.RA120.001998

Öner, D., Ghosh, M., Coorens, R., Bové, H., Moisse, M., Lambrechts, D., Ameloot, M., Godderis, L., Hoet, P.H.M., 2020. Induction and recovery of CpG site specific methylation changes in human bronchial cells after long-term exposure to carbon nanotubes and asbestos. Environ Int 137, 105530. https://doi.org/10.1016/J.ENVINT.2020.105530

Orlandini, M., Oliviero, S., 2001. In fibroblasts Vegf-D expression is induced by cell-cell contact mediated by cadherin-11. J Biol Chem 276, 6576–6581. https://doi.org/10.1074/JBC.M009573200

Padala, S.K., Cabrera, J.A., Ellenbogen, K.A., 2021. Anatomy of the cardiac conduction system. Pacing Clin Electrophysiol 44, 15–25. https://doi.org/10.1111/PACE.14107

Paige, S.L., Osugi, T., Afanasiev, O.K., Pabon, L., Reinecke, H., Murry, C.E., 2010. Endogenous Wnt/β-Catenin Signaling Is Required for Cardiac Differentiation in Human Embryonic Stem Cells. PLoS One 5, e11134. https://doi.org/10.1371/JOURNAL.PONE.0011134

Palumbo, V., Segat, L., Padovan, L., Amoroso, A., Trimarco, B., Izzo, R., Lembo, G., Zagrosek, V.R., Knoll, R., Brancaccio, M., Tarone, G., Crovella, S., 2009. Melusin gene (ITGB1BP2) nucleotide variations study in hypertensive and cardiopathic patients. BMC Med Genet 10, 140. https://doi.org/10.1186/1471-2350-10-140

Parikh, S.S., Blackwell, D.J., Gomez-Hurtado, N., Frisk, M., Wang, L., Kim, K., Dahl, C.P., Fiane, A., Tønnessen, T., Kryshtal, D.O., Louch, W.E., Knollmann, B.C., 2017. Thyroid and Glucocorticoid Hormones Promote Functional T-tubule Development in Human-Induced Pluripotent Stem Cell Derived Cardiomyocytes. Circ Res 121, 1323. https://doi.org/10.1161/CIRCRESAHA.117.311920

Park, G., Yoon, B.S., Kim, Y.S., Choi, S.C., Moon, J.H., Kwon, S., Hwang, J., Yun, W., Kim, J.H., Park, C.Y., Lim, D.S., Kim, Y.I., Oh, C.H., You, S., 2015. Conversion of mouse fibroblasts into cardiomyocyte-like cells using

small molecule treatments. Biomaterials 54, 201–212. https://doi.org/10.1016/J.BIOMATERIALS.2015.02.029

Payan, S.M., Hubert, F., Rochais, F., 2020a. Cardiomyocyte proliferation, a target for cardiac regeneration. Biochim Biophys Acta Mol Cell Res 1867. https://doi.org/10.1016/J.BBAMCR.2019.03.008

Payan, S.M., Hubert, F., Rochais, F., 2020b. Cardiomyocyte proliferation, a target for cardiac regeneration. Biochimica et Biophysica Acta (BBA) - Molecular Cell Research 1867, 118461. https://doi.org/10.1016/J.BBAMCR.2019.03.008

Pédelacq, J.D., Cabantous, S., Tran, T., Terwilliger, T.C., Waldo, G.S., 2005. Engineering and characterization of a superfolder green fluorescent protein. Nature Biotechnology 2005 24:1 24, 79–88. https://doi.org/10.1038/nbt1172

Pei, S., Parthasarathy, S., Parajuli, A., Martinez, J., Lv, M., Jiang, S., Wu, D., Wei, S., Lu, X.L., Farach-Carson, M.C., Kirn-Safran, C.B., Wang, L., 2020a. Perlecan/Hspg2 deficiency impairs bone's calcium signaling and associated transcriptome in response to mechanical loading. Bone 131, 115078. https://doi.org/10.1016/J.BONE.2019.115078

Pei, S., Parthasarathy, S., Parajuli, A., Martinez, J., Lv, M., Jiang, S., Wu, D., Wei, S., Lu, X.L., Farach-Carson, M.C., Kirn-Safran, C.B., Wang, L., 2020b. Perlecan/Hspg2 deficiency impairs bone's calcium signaling and associated transcriptome in response to mechanical loading. Bone 131, 115078. https://doi.org/10.1016/J.BONE.2019.115078

Pellman, J., Zhang, J., Sheikh, F., 2016. Myocyte-Fibroblast Communication in Cardiac Fibrosis and Arrhythmias: Mechanisms and Model Systems. J Mol Cell Cardiol 94, 22. https://doi.org/10.1016/J.YJMCC.2016.03.005

Perez-Pinera, P., Kocak, D.D., Vockley, C.M., Adler, A.F., Kabadi, A.M., Polstein, L.R., Thakore, P.I., Glass, K.A., Ousterout, D.G., Leong, K.W., Guilak, F., Crawford, G.E., Reddy, T.E., Gersbach, C.A., 2013. RNA-guided gene activation by CRISPR-Cas9–based transcription factors. Nature Methods 2013 10:10 10, 973–976. https://doi.org/10.1038/nmeth.2600

Pezhouman, A., Nguyen, N.B., Sercel, A.J., Nguyen, T.L., Daraei, A., Sabri, S., Chapski, D.J., Zheng, M., Patananan, A.N., Ernst, J., Plath, K.,

Vondriska, T.M., Teitell, M.A., Ardehali, R., 2021. Transcriptional, Electrophysiological, and Metabolic Characterizations of hESC-Derived First and Second Heart Fields Demonstrate a Potential Role of TBX5 in Cardiomyocyte Maturation. Front Cell Dev Biol 9. https://doi.org/10.3389/FCELL.2021.787684

Piquereau, J., Caffin, F., Novotova, M., Lemaire, C., Veksler, V., Garnier, A., Ventura-Clapier, R., Joubert, F., 2013. Mitochondrial dynamics in the adult cardiomyocytes: which roles for a highly specialized cell? Front Physiol 4. https://doi.org/10.3389/FPHYS.2013.00102

Piquereau, J., Ventura-Clapier, R., 2018. Maturation of Cardiac Energy Metabolism During Perinatal Development. Front Physiol 9, 959. https://doi.org/10.3389/FPHYS.2018.00959

Polonchuk, L., Chabria, M., Badi, L., Hoflack, J.C., Figtree, G., Davies, M.J., Gentile, C., 2017. Cardiac spheroids as promising in vitro models to study the human heart microenvironment. Scientific Reports 2017 7:1 7, 1–12. https://doi.org/10.1038/s41598-017-06385-8

Poon, E.N.Y., Luo, X. ling, Webb, S.E., Yan, B., Zhao, R., Wu, S.C.M., Yang, Y., Zhang, P., Bai, H., Shao, J., Chan, C.M., Chan, G.C.F., Tsang, S.Y., Gundry, R.L., Yang, H.T., Boheler, K.R., 2020. The cell surface marker CD36 selectively identifies matured, mitochondria-rich hPSC-cardiomyocytes. Cell Research 2020 30:7 30, 626–629. https://doi.org/10.1038/s41422-020-0292-y

Porter, K.E., Turner, N.A., 2009. Cardiac fibroblasts: at the heart of myocardial remodeling. Pharmacol Ther 123, 255–278. https://doi.org/10.1016/J.PHARMTHERA.2009.05.002

Qi, L., Kong, W., Fu, Y., 2021. Vascular Smooth Muscle Cell Development and Cardiovascular Malformations. Cardiology Discovery 1, 259–268. https://doi.org/10.1097/CD9.0000000000000035

Qian, B., Li, Y., Yan, R., Han, S., Bu, Z., Gong, J., Zheng, B., Yuan, Z., Ren, S., He, Q., Zhang, J., Xu, C., Wang, R., Sun, Z., Lin, M., Zhou, J., Ye, L., 2022. RNA binding protein RBM46 regulates mitotic-to-meiotic transition in spermatogenesis. Sci Adv 8, 2945. https://doi.org/10.1126/SCIADV.ABQ2945/SUPPL_FILE/SCIADV.ABQ2945_SM.PDF

Quiberoni, A., Moineau, S., Rousseau, G.M., Reinheimer, J., Ackermann, H.W., 2010. Streptococcus thermophilus bacteriophages. Int Dairy J 20, 657–664. https://doi.org/10.1016/J.IDAIRYJ.2010.03.012

Rahkonen, O., Su, M., Hakovirta, H., Koskivirta, I., Hormuzdi, S.G., Vuorio, E., Bornstein, P., Penttinen, R., 2004. Mice with a deletion in the first intron of the Col1a1 gene develop age-dependent aortic dissection and rupture. Circ Res 94, 83–90. https://doi.org/10.1161/01.RES.0000108263.74520.15

Rai, V., Sharma, P., Agrawal, S., Agrawal, D.K., 2017. Relevance of mouse models of cardiac fibrosis and hypertrophy in cardiac research. Mol Cell Biochem 424, 123. https://doi.org/10.1007/S11010-016-2849-0

Reyes Fernandez, P.C., Wright, C.S., Masterson, A.N., Yi, X., Tellman, T. v, Bonteanu, A., Rust, K., Noonan, M.L., Lewis, K.J., Sankar, U., Hum, J.M., Bix, G., Wu, D., Robling, A.G., Sardar, R., Farach-Carson, M.C., n.d. Gabapentin Disrupts Binding of Perlecan to the α2δ1 Voltage Sensitive Calcium 1 Channel Subunit and Impairs Skeletal Mechanosensation 2 3. https://doi.org/10.1101/2022.07.20.500827

Ribeiro, A.J.S., Ang, Y.S., Fu, J.D., Rivas, R.N., Mohamed, T.M.A., Higgs, G.C., Srivastava, D., Pruitt, B.L., 2015. Contractility of Single cardiomyocytes differentiated from pluripotent stem cells depends on physiological shape and substrate stiffness. Proc Natl Acad Sci U S A 112, 12705–12710. https://doi.org/10.1073/PNAS.1508073112/-/DCSUPPLEMENTAL

Rider, C.C., 2006. Heparin/heparan sulphate binding in the TGF-beta cytokine superfamily. Biochem Soc Trans 34, 458–460. https://doi.org/10.1042/BST0340458

Roediger, M., Kruegel, J., Miosge, N., Gersdorff, N., 2009a. Tissue distribution of perlecan domains III and V during embryonic and fetal human development. Histol Histopathol 24, 859–868. https://doi.org/10.14670/HH-24.859

Roediger, M., Kruegel, J., Miosge, N., Gersdorff, N., 2009b. Tissue distribution of perlecan domains III and V during embryonic and fetal human development. Histol Histopathol 24, 859–868. https://doi.org/10.14670/HH-24.859

Ruiz-Villalba, A., Hoppler, S., van den Hoff, M.J.B., 2016. Wnt signaling in the heart fields: Variations on a common theme. Developmental Dynamics 245, 294–306. https://doi.org/10.1002/DVDY.24372

Sala, L., van Meer, B.J., Tertoolen, L.G.J., Bakkers, J., Bellin, M., Davis, R.P., Denning, C., Dieben, M.A.E., Eschenhagen, T., Giacomelli, E., Grandela, C., Hansen, A., Holman, E.R., Jongbloed, M.R.M., Kamel, S.M., Koopman, C.D., Lachaud, Q., Mannhardt, I., Mol, M.P.H., Mosqueira, D., Orlova, V. v., Passier, R., Ribeiro, M.C., Saleem, U., Smith, G.L., Burton, F.L., Mummery, C.L., 2018. Musclemotion: A versatile open software tool to quantify cardiomyocyte and cardiac muscle contraction in vitro and in vivo. Circ Res 122, e5–e16. https://doi.org/10.1161/CIRCRESAHA.117.312067/-/DC1

Sander, J.D., Joung, J.K., 2014. CRISPR-Cas systems for editing, regulating and targeting genomes. Nature Biotechnology 2014 32:4 32, 347–355. https://doi.org/10.1038/nbt.2842

Sarrazin, S., Lamanna, W.C., Esko, J.D., 2011. Heparan Sulfate Proteoglycans. Cold Spring Harb Perspect Biol 3, a004952. https://doi.org/10.1101/CSHPERSPECT.A004952

Sasse, P., Malan, D., Fleischmann, M., Roell, W., Gustafsson, E., Bostani, T., Fan, Y., Kolbe, T., Breitbach, M., Addicks, K., Welz, A., Brem, G., Hescheler, J., Aszodi, A., Costell, M., Bloch, W., Fleischmann, B.K., 2008a. Perlecan is critical for heart stability. Cardiovasc Res 80, 435–444. https://doi.org/10.1093/CVR/CVN225

Sasse, P., Malan, D., Fleischmann, M., Roell, W., Gustafsson, E., Bostani, T., Fan, Y., Kolbe, T., Breitbach, M., Addicks, K., Welz, A., Brem, G., Hescheler, J., Aszodi, A., Costell, M., Bloch, W., Fleischmann, B.K., 2008b. Perlecan is critical for heart stability. Cardiovasc Res 80, 435–444. https://doi.org/10.1093/CVR/CVN225

Schellings, M.W.M., Vanhoutte, D., van Almen, G.C., Swinnen, M., Leenders, J.J.G., Kubben, N., van Leeuwen, R.E.W., Hofstra, L., Heymans, S., Pinto, Y.M., 2010. Syndecan-1 amplifies angiotensin II-induced cardiac fibrosis. Hypertension 55, 249–256. https://doi.org/10.1161/HYPERTENSIONAHA.109.137885

Shkumatov, A., Baek, K., Kong, H., 2014. Matrix Rigidity-Modulated Cardiovascular Organoid Formation from Embryoid Bodies. PLoS One 9. https://doi.org/10.1371/JOURNAL.PONE.0094764

Smith, C.L., Baek, S.T., Sung, C.Y., Tallquist, M.D., 2011. Epicardial-derived cell epithelial-to-mesenchymal transition and fate specification require PDGF receptor signaling. Circ Res 108. https://doi.org/10.1161/CIRCRESAHA.110.235531

Smith, J.G.W., Owen, T., Bhagwan, J.R., Mosqueira, D., Scott, E., Mannhardt, I., Patel, A., Barriales-Villa, R., Monserrat, L., Hansen, A., Eschenhagen, T., Harding, S.E., Marston, S., Denning, C., 2018. Isogenic Pairs of hiPSC-CMs with Hypertrophic Cardiomyopathy/LVNC-Associated ACTC1 E99K Mutation Unveil Differential Functional Deficits. Stem Cell Reports 11, 1226–1243. https://doi.org/10.1016/J.STEMCR.2018.10.006

Smith, S.M.L., West, L.A., Govindraj, P., Zhang, X., Ornitz, D.M., Hassell, J.R., 2007a. Heparan and chondroitin sulfate on growth plate perlecan mediate binding and delivery of FGF-2 to FGF receptors. Matrix Biology 26, 175–184. https://doi.org/10.1016/J.MATBIO.2006.10.012

Smith, S.M.L., West, L.A., Hassell, J.R., 2007b. The core protein of growth plate perlecan binds FGF-18 and alters its mitogenic effect on chondrocytes. Arch Biochem Biophys 468, 244–251. https://doi.org/10.1016/J.ABB.2007.10.006

Snider, P., Standley, K.N., Wang, J., Azhar, M., Doetschman, T., Conway, S.J., 2009. Origin of Cardiac Fibroblasts and the Role of Periostin. Circ Res 105, 934–947. https://doi.org/10.1161/CIRCRESAHA.109.201400

Song, P., Zou, M.H., 2014. Redox Regulation of Endothelial Cell Fate. Cell Mol Life Sci 71, 3219. https://doi.org/10.1007/S00018-014-1598-Z

Souders, C.A., Bowers, S.L.K., Baudino, T.A., 2009. Cardiac fibroblast: the renaissance cell. Circ Res 105, 1164–1176. https://doi.org/10.1161/CIRCRESAHA.109.209809

Später, D., Hansson, E.M., Zangi, L., Chien, K.R., 2014. How to make a cardiomyocyte. Development 141, 4418–4431. https://doi.org/10.1242/DEV.091538

Spike, C., Davies, A., Shaw, J., Herman, R.K., 2002. MEC-8 regulates alternative splicing of unc-52 transcripts in C. elegans hypodermal cells. Development.

Spike, C.A., Davies, A.A., Shaw, J.E., Herman, R.K., 2002. MEC-8 regulates alternative splicing of unc-52 transcripts inC. elegans hypodermal cells. Development 129, 4999–5008. https://doi.org/10.1242/DEV.129.21.4999

Spinale, F.G., 2002. Matrix Metalloproteinases: regulation and dysregulation in the failing heart. Circ Res 315–332. https://doi.org/10.1161/01.RES.0000013290.12884.A3

Strate, I., Tessadori, F., Bakkers, J., 2015. Glypican4 promotes cardiac specification and differentiation by attenuating canonical Wnt and Bmp signaling. Development 142, 1767–1776. https://doi.org/10.1242/DEV.113894

Sun, X., Malandraki-Miller, S., Kennedy, T., Bassat, E., Klaourakis, K., Zhao, J., Gamen, E., Vieira, J.M., Tzahor, E., Riley, P.R., 2021. The extracellular matrix protein agrin is essential for epicardial epithelial-to-mesenchymal transition during heart development. Development (Cambridge) 148. https://doi.org/10.1242/DEV.197525/261801

Sun, Y., Weber, K.T., 2005. Animal models of cardiac fibrosis. Methods Mol Med 117, 273–290. https://doi.org/10.1385/1-59259-940-0:273/FIGURES/3

Takahashi, K., Tanabe, K., Ohnuki, M., Narita, M., Ichisaka, T., Tomoda, K., Yamanaka, S., 2007. Induction of pluripotent stem cells from adult human fibroblasts by defined factors. Cell 131, 861–872. https://doi.org/10.1016/J.CELL.2007.11.019

Takahashi, K., Yamanaka, S., 2006. Induction of pluripotent stem cells from mouse embryonic and adult fibroblast cultures by defined factors. Cell 126, 663–676. https://doi.org/10.1016/J.CELL.2006.07.024

Tampakakis, E., Miyamoto, M., Kwon, C., 2019. In Vitro Generation of Heart Field-specific Cardiac Progenitor Cells. J Vis Exp 2019. https://doi.org/10.3791/59826

Tang, Y., Tian, X., Wang, R., Fill, M., Chen, S.R.W., 2012. Abnormal termination of Ca 2+ release is a common defect of RyR2 mutations

associated with cardiomyopathies. Circ Res 110, 968–977. https://doi.org/10.1161/CIRCRESAHA.111.256560/-/DC1

Tezuka, T., Inoue, A., Hoshi, T., Weatherbee, S.D., Burgess, R.W., Ueta, R., Yamanashi, Y., 2014. The MuSK activator agrin has a separate role essential for postnatal maintenance of neuromuscular synapses. Proc Natl Acad Sci U S A 111, 16556–16561. https://doi.org/10.1073/PNAS.1408409111/-/DCSUPPLEMENTAL

Thomas, D., Choi, S., Alamana, C., Parker, K.K., Wu, J.C., 2022. Cellular and Engineered Organoids for Cardiovascular Models. Circ Res 130, 1780–1802. https://doi.org/10.1161/CIRCRESAHA.122.320305

Thomas, T.P., Grisanti, L.A., 2020. The Dynamic Interplay Between Cardiac Inflammation and Fibrosis. Front Physiol 11. https://doi.org/10.3389/FPHYS.2020.529075

Tiburcy, M., Meyer, T., Liaw, N.Y., Zimmermann, W.H., 2020. Generation of Engineered Human Myocardium in a Multi-well Format. STAR Protoc 1, 100032. https://doi.org/10.1016/J.XPRO.2020.100032

Tkachenko, E., Rhodes, J.M., Simons, M., 2005. Syndecans: new kids on the signaling block. Circ Res 96, 488–500. https://doi.org/10.1161/01.RES.0000159708.71142.C8

Toivonen, S., Ojala, M., Hyysalo, A., Ilmarinen, T., Rajala, K., Pekkanen-Mattila, M., Äänismaa, R., Lundin, K., Palgi, J., Weltner, J., Trokovic, R., Silvennoinen, O., Skottman, H., Narkilahti, S., Aalto-Setälä, K., Otonkoski, T., 2013. Comparative Analysis of Targeted Differentiation of Human Induced Pluripotent Stem Cells (hiPSCs) and Human Embryonic Stem Cells Reveals Variability Associated With Incomplete Transgene Silencing in Retrovirally Derived hiPSC Lines. Stem Cells Transl Med 2, 83. https://doi.org/10.5966/SCTM.2012-0047

Tomanek, R.J., 2016. Developmental Progression of the Coronary Vasculature in Human Embryos and Fetuses. Anat Rec 299, 25–41. https://doi.org/10.1002/ar.23283

Tomasek, J.J., Gabbiani, G., Hinz, B., Chaponnier, C., Brown, R.A., 2002. Myofibroblasts and mechano-regulation of connective tissue remodelling. Nat Rev Mol Cell Biol 3, 349–363. https://doi.org/10.1038/NRM809

Tran-Lundmark, K., Tran, P.K., Paulsson-Berne, G., Fridén, V., Soininen, R., Tryggvason, K., Wight, T.N., Kinsella, M.G., Borén, J., Hedin, U., 2008. Heparan sulfate in perlecan promotes mouse atherosclerosis: roles in lipid permeability, lipid retention, and smooth muscle cell proliferation. Circ Res 103, 43–52. https://doi.org/10.1161/CIRCRESAHA.108.172833

Travers, J.G., Kamal, F.A., Robbins, J., Yutzey, K.E., Blaxall, B.C., 2016. Cardiac Fibrosis: The Fibroblast Awakens. Circ Res 118, 1021. https://doi.org/10.1161/CIRCRESAHA.115.306565

Tyser, R.C.V., Srinivas, S., 2020. The First Heartbeat—Origin of Cardiac Contractile Activity. Cold Spring Harb Perspect Biol 12, a037135. https://doi.org/10.1101/CSHPERSPECT.A037135

Ucar, A., Gupta, S.K., Fiedler, J., Erikci, E., Kardasinski, M., Batkai, S., Dangwal, S., Kumarswamy, R., Bang, C., Holzmann, A., Remke, J., Caprio, M., Jentzsch, C., Engelhardt, S., Geisendorf, S., Glas, C., Hofmann, T.G., Nessling, M., Richter, K., Schiffer, M., Carrier, L., Napp, L.C., Bauersachs, J., Chowdhury, K., Thum, T., 2012. The miRNA-212/132 family regulates both cardiac hypertrophy and cardiomyocyte autophagy. Nature Communications 2012 3:1 3, 1–11. https://doi.org/10.1038/ncomms2090

Uchimura, K., Morimoto-Tomita, M., Bistrup, A., Li, J., Lyon, M., Gallagher, J., Werb, Z., Rosen, S.D., 2006. HSulf-2, an extracellular endoglucosamine-6-sulfatase, selectively mobilizes heparin-bound growth factors and chemokines: Effects on VEGF, FGF-1, and SDF-1. BMC Biochem 7, 1–13. https://doi.org/10.1186/1471-2091-7-2/FIGURES/5

Ullah, I., Busch, J.F., Rabien, A., Ergün, B., Stamm, C., Knosalla, C., Hippenstiel, S., Reinke, P., Kurtz, A., 2020. Adult Tissue Extracellular Matrix Determines Tissue Specification of Human iPSC-Derived Embryonic Stage Mesodermal Precursor Cells. Advanced Science 7, 1901198. https://doi.org/10.1002/ADVS.201901198

Ulmer, B.M., Eschenhagen, T., 2020. Human pluripotent stem cell-derived cardiomyocytes for studying energy metabolism. Biochim Biophys Acta Mol Cell Res 1867. https://doi.org/10.1016/J.BBAMCR.2019.04.001

Utriainen, A., Sormunen, R., Kettunen, M., Carvalhaes, L.S., Sajanti, E., Eklund, L., Kauppinen, R., Kitten, G.T., Pihlajaniemi, T., 2004. Structurally

altered basement membranes and hydrocephalus in a type XVIII collagen deficient mouse line. Hum Mol Genet 13, 2089–2099. https://doi.org/10.1093/HMG/DDH213

Vadukkut, A.S., Meenu, •, Parasuram, B., Bijoy, •, Balakrishnan, K., Ganesan, P., Gopinathan, • K K, 2021. Dyssegmental Dysplasia-Silverman Handmaker Type: a Rare Case Report. Journal of Fetal Medicine 2021 8:4 8, 303–306. https://doi.org/10.1007/S40556-021-00323-5

Valiente-Alandi, I., Schafer, A.E., Blaxall, B.C., 2016. Extracellular matrix-mediated cellular communication in the heart. J Mol Cell Cardiol 91, 228–237. https://doi.org/10.1016/J.YJMCC.2016.01.011

van Aelst, L.N.L., Voss, S., Carai, P., van Leeuwen, R., Vanhoutte, D., Sanders-Van Wijk, S., Eurlings, L., Swinnen, M., Verheyen, F.K., Verbeken, E., Nef, H., Troidl, C., Cook, S.A., Brunner-La Rocca, H.P., Möllmann, H., Papageorgiou, A.P., Heymans, S., 2015. Osteoglycin prevents cardiac dilatation and dysfunction after myocardial infarction through infarct collagen strengthening. Circ Res 116, 425–436. https://doi.org/10.1161/CIRCRESAHA.116.304599

van den Borne, S.W.M., Diez, J., Blankesteijn, W.M., Verjans, J., Hofstra, L., Narula, J., 2010. Myocardial remodeling after infarction: the role of myofibroblasts. Nat Rev Cardiol 7, 30–37. https://doi.org/10.1038/NRCARDIO.2009.199

Vancheri, C., Failla, M., Crimi, N., Raghu, G., 2010. Idiopathic pulmonary fibrosis: a disease with similarities and links to cancer biology. Eur Respir J 35, 496–504. https://doi.org/10.1183/09031936.00077309

Vatta, M., Ackerman, M.J., Ye, B., Makielski, J.C., Ughanze, E.E., Taylor, E.W., Tester, D.J., Balijepalli, R.C., Foell, J.D., Li, Z., Kamp, T.J., Towbin, J.A., 2006. Mutant Caveolin-3 Induces Persistent Late Sodium Current and Is Associated With Long-QT Syndrome. Circulation 114, 2104–2112. https://doi.org/10.1161/CIRCULATIONAHA.106.635268

Velayutham, N., Alfieri, C.M., Agnew, E.J., Riggs, K.W., Baker, R.S., Ponny, S.R., Zafar, F., Yutzey, K.E., 2020. Cardiomyocyte cell cycling, maturation, and growth by multinucleation in postnatal swine. J Mol Cell Cardiol 146, 95–108. https://doi.org/10.1016/j.yjmcc.2020.07.004

Vennin, C., Mélénec, P., Rouet, R., Nobis, M., Cazet, A.S., Murphy, K.J., Herrmann, D., Reed, D.A., Lucas, M.C., Warren, S.C., Elgundi, Z., Pinese, M., Kalna, G., Roden, D., Samuel, M., Zaratzian, A., Grey, S.T., Da Silva, A., Leung, W., Johns, A.L., Chantrill, L.A., Chou, A., Steinmann, A., Arshi, M., Dwarte, T., Froio, D., Pereira, B., Ritchie, S., Chambers, C.R., Metcalf, X., Waddell, N., Pearson, J. V., Patch, A.M., Nones, K., Newell, F., Mukhopadhyay, P., Addala, V., Kazakoff, S., Holmes, O., Leonard, C., Wood, S., Grimmond, S.M., Hofmann, O., Christ, A., Bruxner, T., Samra, J.S., Pavlakis, N., High, H.A., Asghari, R., Merrett, N.D., Pavey, D., Das, A., Cosman, P.H., Ismail, K., O'Connnor, C., Stoita, A., Williams, D., Spigellman, A., Lam, V.W., McLeod, D., Kirk, J., Kench, J.G., Grimison, P., Cooper, C.L., Sandroussi, C., Goodwin, A., Mead, R.S., Tucker, K., Andrews, L., Texler, M., Forest, C., Epari, K.P., Ballal, M., Fletcher, D.R., Mukhedkar, S., Zeps, N., Beilin, M., Feeney, K., Nguyen, N.Q., Ruszkiewicz, A.R., Worthley, C., Chen, J., Brooke-Smith, M.E., Papangelis, V., Clouston, A.D., Barbour, A.P., O'Rourke, T.J., Fawcett, J.W., Slater, K., Hatzifotis, M., Hodgkinson, P., Nikfarjam, M., Eshleman, J.R., Hruban, R.H., Wolfgang, C.L., Lawlor, R.T., Beghelli, S., Corbo, V., Scardoni, M., Bassi, C., Biankin, A. V., Dixon, J., Jamieson, N.B., Chang, D.K., Mathivanan, S., Wang, Y., Braithwaite, A.W., Christ, D., Benda, A., Parkin, A., Phillips, P.A., Whitelock, J.M., Gill, A.J., Sansom, O.J., Croucher, D.R., Parker, B.L., Pajic, M., Morton, J.P., Cox, T.R., Timpson, P., 2019. CAF hierarchy driven by pancreatic cancer cell p53-status creates a pro-metastatic and chemoresistant environment via perlecan. Nature Communications 2019 10:1 10, 1–22. https://doi.org/10.1038/s41467-019-10968-6

Verrecchia, F., Chu, M.L., Mauviel, A., 2001. Identification of Novel TGF-β/Smad Gene Targets in Dermal Fibroblasts using a Combined cDNA Microarray/Promoter Transactivation Approach. Journal of Biological Chemistry 276, 17058–17062. https://doi.org/10.1074/jbc.M100754200

Versteeg, G.A., Rajsbaum, R., Sánchez-Aparicio, M.T., Maestre, A.M., Valdiviezo, J., Shi, M., Inn, K.S., Fernandez-Sesma, A., Jung, J., García-Sastre, A., 2013. The E3-Ligase TRIM Family of Proteins Regulates Signaling Pathways Triggered by Innate Immune Pattern-Recognition

Receptors. Immunity 38, 384–398. https://doi.org/10.1016/J.IMMUNI.2012.11.013

Vlodavsky, I., Miao, H.Q., Medalion, B., Danagher, P., Ron, D., 1996. Involvement of heparan sulfate and related molecules in sequestration and growth promoting activity of fibroblast growth factor. Cancer and Metastasis Reviews 15, 177–186. https://doi.org/10.1007/BF00437470/METRICS

Wang, L., Liu, Z., Yin, C., Asfour, H., Chen, O., Li, Y., Bursac, N., Liu, J., Qian, L., 2015. Stoichiometry of Gata4, Mef2c, and Tbx5 Influences the Efficiency and Quality of Induced Cardiac Myocyte Reprogramming. Circ Res 116, 237. https://doi.org/10.1161/CIRCRESAHA.116.305547

Warren, C.R., Grindel, B.J., Francis, L., Carson, D.D., Farach-Carson, M.C., 2014. Transcriptional Activation by NFκB Increases Perlecan/HSPG2 Expression in the Desmoplastic Prostate Tumor Microenvironment. J Cell Biochem 115, 1322–1333. https://doi.org/10.1002/JCB.24788

Warren, L., Manos, P.D., Ahfeldt, T., Loh, Y.H., Li, H., Lau, F., Ebina, W., Mandal, P.K., Smith, Z.D., Meissner, A., Daley, G.Q., Brack, A.S., Collins, J.J., Cowan, C., Schlaeger, T.M., Rossi, D.J., 2010. Highly efficient reprogramming to pluripotency and directed differentiation of human cells using synthetic modified mRNA. Cell Stem Cell 7, 618. https://doi.org/10.1016/J.STEM.2010.08.012

Watanabe, S., Hirai, H., Asakura, Y., Tastad, C., Verma, M., Keller, C., Dutton, J.R., Asakura, A., 2011. MyoD Gene Suppression by Oct4 Is Required for Reprogramming in Myoblasts to Produce Induced Pluripotent Stem Cells. Stem Cells 29, 505–516. https://doi.org/10.1002/STEM.598

Wenstrup, R.J., Florer, J.B., Brunskill, E.W., Bell, S.M., Chervoneva, I., Birk, D.E., 2004. Type V collagen controls the initiation of collagen fibril assembly. J Biol Chem 279, 53331–53337. https://doi.org/10.1074/JBC.M409622200

Werner, S., Krieg, T., Smola, H., 2007. Keratinocyte-fibroblast interactions in wound healing. J Invest Dermatol 127, 998–1008. https://doi.org/10.1038/SJ.JID.5700786

Wershof, E., Park, D., Barry, D.J., Jenkins, R.P., Rullan, A., Wilkins, A., Schlegelmilch, K., Roxanis, I., Anderson, K.I., Bates, P.A., Sahai, E.,

2021. A FIJI macro for quantifying pattern in extracellular matrix. Life Sci Alliance 4. https://doi.org/10.26508/LSA.202000880

Westermann, D., Schultheiss, H.P., Tschöpe, C., 2008. New perspective on the tissue kallikrein–kinin system in myocardial infarction: Role of angiogenesis and cardiac regeneration. Int Immunopharmacol 8, 148–154. https://doi.org/10.1016/J.INTIMP.2007.07.022

Weston, C., Yee, B., Hod, E., Prives, J., 2000. Agrin-induced acetylcholine receptor clustering is mediated by the small guanosine triphosphatases Rac and Cdc42. J Cell Biol 150, 205–212. https://doi.org/10.1083/JCB.150.1.205

Whitehead, A.J., Hocker, J.D., Ren, B., Engler, A.J., 2022. Improved epicardial cardiac fibroblast generation from iPSCs. J Mol Cell Cardiol 164, 58–68. https://doi.org/10.1016/j.yjmcc.2021.11.011

Whitelock, J.M., Melrose, J., Iozzo, R. v., 2008. Diverse cell signaling events modulated by Perlecan. Biochemistry 47, 11174–11183. https://doi.org/10.1021/BI8013938/ASSET/IMAGES/MEDIUM/BI-2008-013938_0003.GIF

Wiesinger, A., Boink, G.J.J., Christoffels, V.M., Devalla, H.D., 2021. Retinoic acid signaling in heart development: Application in the differentiation of cardiovascular lineages from human pluripotent stem cells. Stem Cell Reports 16, 2589. https://doi.org/10.1016/J.STEMCR.2021.09.010

Wijeratne, S.S., Martinez, J.R., Grindel, B.J., Frey, E.W., Li, J., Wang, L., Farach-Carson, M.C., Kiang, C.H., 2016. Single molecule force measurements of perlecan/HSPG2: A key component of the osteocyte pericellular matrix. Matrix Biology 50, 27–38. https://doi.org/10.1016/J.MATBIO.2015.11.001

Wilsie, L.C., Orlando, R.A., 2003. The Low Density Lipoprotein Receptor-related Protein Complexes with Cell Surface Heparan Sulfate Proteoglycans to Regulate Proteoglycan-mediated Lipoprotein Catabolism. Journal of Biological Chemistry 278, 15758–15764. https://doi.org/10.1074/JBC.M208786200

Wittig, J.G., Münsterberg, A., 2020. The Chicken as a Model Organism to Study Heart Development. Cold Spring Harb Perspect Biol 12, 1–17. https://doi.org/10.1101/CSHPERSPECT.A037218

Wu, D., Pan, W., 2010. GSK3: a multifaceted kinase in Wnt signaling. Trends Biochem Sci 35, 161. https://doi.org/10.1016/J.TIBS.2009.10.002

Wu, M., Singh, S.B., Wang, J., Chung, C.C., Salituro, G., Karanam, B. v., Lee, S.H., Powles, M., Ellsworth, K.P., Lassman, M.E., Miller, C., Myers, R.W., Tota, M.R., Zhang, B.B., Li, C., 2011. Antidiabetic and antisteatotic effects of the selective fatty acid synthase (FAS) inhibitor platensimycin in mouse models of diabetes. Proc Natl Acad Sci U S A 108, 5378–5383. https://doi.org/10.1073/PNAS.1002588108/SUPPL_FILE/PNAS.201002588SI.PDF

Wynn, T.A., 2007. Common and unique mechanisms regulate fibrosis in various fibroproliferative diseases. J Clin Invest 117, 524–529. https://doi.org/10.1172/JCI31487

Wynn, T.A., Barron, L., 2010. Macrophages: Master Regulators of Inflammation and Fibrosis. Semin Liver Dis 30, 245. https://doi.org/10.1055/S-0030-1255354

Wynn, T.A., Vannella, K.M., 2016. Macrophages in Tissue Repair, Regeneration, and Fibrosis. Immunity 44, 450–462. https://doi.org/10.1016/J.IMMUNI.2016.02.015

Xia, J., Meng, Z., Ruan, H., Yin, W., Xu, Y., Zhang, T., 2020. Heart Development and Regeneration in Non-mammalian Model Organisms. Front Cell Dev Biol 8. https://doi.org/10.3389/FCELL.2020.595488

Xia, Z., Li, H., Irwin, M.G., 2016. Myocardial ischaemia reperfusion injury: the challenge of translating ischaemic and anaesthetic protection from animal models to humans. BJA: British Journal of Anaesthesia 117, ii44–ii62. https://doi.org/10.1093/BJA/AEW267

Xie, N., Tan, Z., Banerjee, S., Cui, H., Ge, J., Liu, R.M., Bernard, K., Thannickal, V.J., Liu, G., 2015. Glycolytic reprogramming in myofibroblast differentiation and lung fibrosis. Am J Respir Crit Care Med 192, 1462–1474. https://doi.org/10.1164/RCCM.201504-0780OC/SUPPL_FILE/DISCLOSURES.PDF

Xie, Y., Garfinkel, A., Camelliti, P., Kohl, P., Weiss, J.N., Qu, Z., 2009. Effects of fibroblast-myocyte coupling on cardiac conduction and vulnerability to reentry: A computational study. Heart Rhythm 6, 1641–1649. https://doi.org/10.1016/J.HRTHM.2009.08.003

Xiong, Y., Qi, Y., Pan, Z., Wang, S., Li, B., Feng, B., Xue, H., Zhao, R., Li, G., 2022. Pancancer landscape analysis of the thymosin family identified TMSB10 as a potential prognostic biomarker and immunotherapy target in glioma. Cancer Cell Int 22, 1–22. https://doi.org/10.1186/S12935-022-02698-5/FIGURES/8

Xu, H.J., 2009. Role of Lactate in Lipid Metabolism, Just Always Inhibiting Lipolysis? J Biol Chem 284, le5. https://doi.org/10.1074/JBC.L806409200

Xu, Z., Ichikawa, N., Kosaki, K., Yamada, Y., Sasaki, T., Sakai, L.Y., Kurosawa, H., Hattori, N., Arikawa-Hirasawa, E., 2010. Perlecan deficiency causes muscle hypertrophy, a decrease in myostatin expression, and changes in muscle fiber composition. Matrix Biol 29, 461–470. https://doi.org/10.1016/J.MATBIO.2010.06.001

Yamamoto, K., Ohki, R., Lee, R.T., Ikeda, U., Shimada, K., 2001. Peroxisome Proliferator-Activated Receptor γ Activators Inhibit Cardiac Hypertrophy in Cardiac Myocytes. Circulation 104, 1670–1675. https://doi.org/10.1161/HC4001.097186

Yamamura, H., Zhang, M., Markwald, R.R., Mjaatvedt, C.H., 1997. A heart segmental defect in the anterior-posterior axis of a transgenic mutant mouse. Dev Biol 186, 58–72. https://doi.org/10.1006/DBIO.1997.8559

Yamashita, Y., Nakada, S., Yoshihara, T., Nara, T., Furuya, N., Miida, T., Hattori, N., Arikawa-Hirasawa, E., 2018a. Perlecan, a heparan sulfate proteoglycan, regulates systemic metabolism with dynamic changes in adipose tissue and skeletal muscle. Scientific Reports 2018 8:1 8, 1–14. https://doi.org/10.1038/s41598-018-25635-x

Yamashita, Y., Nakada, S., Yoshihara, T., Nara, T., Furuya, N., Miida, T., Hattori, N., Arikawa-Hirasawa, E., 2018b. Perlecan, a heparan sulfate proteoglycan, regulates systemic metabolism with dynamic changes in adipose tissue and skeletal muscle. Scientific Reports 2018 8:1 8, 1–14. https://doi.org/10.1038/s41598-018-25635-x

Yan, W., Wang, P., Zhao, C.X., Tang, J., Xiao, X., Wang, D.W., 2009. Decorin Gene Delivery Inhibits Cardiac Fibrosis in Spontaneously Hypertensive Rats by Modulation of Transforming Growth Factor-β/Smad and p38 Mitogen-Activated Protein Kinase Signaling Pathways.

https://home.liebertpub.com/hum 20, 1190–1200. https://doi.org/10.1089/HUM.2008.204

Yang, W., Yuan, W., Peng, X., Wang, M., Xiao, J., Wu, C., Luo, L., 2019. PPAR γ/Nnat/NF-κ B Axis Involved in Promoting Effects of Adiponectin on Preadipocyte Differentiation. Mediators Inflamm 2019. https://doi.org/10.1155/2019/5618023

Yang, X., Rodriguez, M., Pabon, L., Fischer, K.A., Reinecke, H., Regnier, M., Sniadecki, N.J., Ruohola-Baker, H., Murry, C.E., 2014. Tri-iodo-L-thyronine Promotes the Maturation of Human Cardiomyocytes-Derived from Induced Pluripotent Stem Cells. J Mol Cell Cardiol 72, 296. https://doi.org/10.1016/J.YJMCC.2014.04.005

Yokoyama, J., Miyagawa, S., Akagi, T., Akashi, M., Sawa, Y., 2021. Human induced pluripotent stem cell-derived three-dimensional cardiomyocyte tissues ameliorate the rat ischemic myocardium by remodeling the extracellular matrix and cardiac protein phenotype. PLoS One 16. https://doi.org/10.1371/JOURNAL.PONE.0245571

Yoshida, S., Miyagawa, S., Fukushima, S., Kawamura, T., Kashiyama, N., Ohashi, F., Toyofuku, T., Toda, K., Sawa, Y., 2018. Maturation of Human Induced Pluripotent Stem Cell-Derived Cardiomyocytes by Soluble Factors from Human Mesenchymal Stem Cells. Mol Ther 26, 2681–2695. https://doi.org/10.1016/J.YMTHE.2018.08.012

Yoshida, Y., Yamanaka, S., 2010. Recent stem cell advances: induced pluripotent stem cells for disease modeling and stem cell-based regeneration. Circulation 122, 80–87. https://doi.org/10.1161/CIRCULATIONAHA.109.881433

Yu, C., Griffiths, L.R., Haupt, L.M., 2017. Exploiting heparan sulfate proteoglycans in human neurogenesis—controlling lineage specification and fate. Front Integr Neurosci 11, 28. https://doi.org/10.3389/FNINT.2017.00028/BIBTEX

Yuan, X., Braun, T., 2017. Multimodal Regulation of Cardiac Myocyte Proliferation. Circ Res 121, 293–309. https://doi.org/10.1161/CIRCRESAHA.117.308428

Zaruba, M.M., Field, L.J., 2008. The mouse as a model system to study cardiac regeneration. Drug Discov Today Dis Models 5, 165. https://doi.org/10.1016/J.DDMOD.2009.03.002

Zelenski, N.A., Leddy, H.A., Sanchez-Adams, J., Zhang, J., Bonaldo, P., Liedtke, W., Guilak, F., 2018. Modular Proteoglycan Perlecan/HSPG2: Mutations, Phenotypes, and Functions. Genes 2018, Vol. 9, Page 556 9, 556. https://doi.org/10.3390/GENES9110556

Zhang, H., Tian, L., Shen, M., Tu, C., Wu, H., Gu, M., Paik, D.T., Wu, J.C., 2019a. Generation of Quiescent Cardiac Fibroblasts From Human Induced Pluripotent Stem Cells for In Vitro Modeling of Cardiac Fibrosis. Circ Res 125, 552–566. https://doi.org/10.1161/CIRCRESAHA.119.315491

Zhang, H., Tian, L., Shen, M., Tu, C., Wu, H., Gu, M., Paik, D.T., Wu, J.C., 2019b. Generation of Quiescent Cardiac Fibroblasts From Human Induced Pluripotent Stem Cells for In Vitro Modeling of Cardiac Fibrosis. Circ Res 125, 552–566. https://doi.org/10.1161/CIRCRESAHA.119.315491

Zhang, J., Tao, R., Campbell, K.F., Carvalho, J.L., Ruiz, E.C., Kim, G.C., Schmuck, E.G., Raval, A.N., da Rocha, A.M., Herron, T.J., Jalife, J., Thomson, J.A., Kamp, T.J., 2019. Functional cardiac fibroblasts derived from human pluripotent stem cells via second heart field progenitors. Nat Commun 10. https://doi.org/10.1038/S41467-019-09831-5

Zhang, P., Su, J., Mende, U., 2012. Cross talk between cardiac myocytes and fibroblasts: From multiscale investigative approaches to mechanisms and functional consequences. Am J Physiol Heart Circ Physiol 303, 1385–1396. https://doi.org/10.1152/AJPHEART.01167.2011/ASSET/IMAGES/LARGE/ZH40241205950002.JPEG

Zhang, Q., Raoof, M., Chen, Y., Sumi, Y., Sursal, T., Junger, W., Brohi, K., Itagaki, K., Hauser, C.J., 2010. Circulating mitochondrial DAMPs cause inflammatory responses to injury. Nature 2010 464:7285 464, 104–107. https://doi.org/10.1038/nature08780

Zhang, Y., Conrad, A.H., Conrad, G.W., 2011. Effects of ultraviolet-A and riboflavin on the interaction of collagen and proteoglycans during corneal

cross-linking. J Biol Chem 286, 13011–13022. https://doi.org/10.1074/JBC.M110.169813

Zhang, Y., Ma, K.L., Ruan, X.Z., Liu, B.C., 2016. Dysregulation of the Low-Density Lipoprotein Receptor Pathway Is Involved in Lipid Disorder-Mediated Organ Injury. Int J Biol Sci 12, 569. https://doi.org/10.7150/IJBS.14027

Zhao, M.T., Ye, S., Su, J., Garg, V., 2020. Cardiomyocyte Proliferation and Maturation: Two Sides of the Same Coin for Heart Regeneration. Front Cell Dev Biol 8. https://doi.org/10.3389/FCELL.2020.594226

Zhao, W., Zhao, J., Rong, J., 2020. Pharmacological Modulation of Cardiac Remodeling after Myocardial Infarction. Oxid Med Cell Longev 2020. https://doi.org/10.1155/2020/8815349

Zhao, X., Zhang, T., Yan, Y., Liu, F., Li, C., Fan, J., Pan, Y., Li, X., Wang, Y., 2022. Notch signaling regulates vessel structure and function via Hspg2. Gene 826, 146439. https://doi.org/10.1016/J.GENE.2022.146439

Zheng, Y.L., 2016. Some Ethical Concerns About Human Induced Pluripotent Stem Cells. Sci Eng Ethics 22, 1277–1284. https://doi.org/10.1007/S11948-015-9693-6/METRICS

Zhou, B., Ma, Q., Rajagopal, S., Wu, S.M., Domian, I., Rivera-Feliciano, J., Jiang, D., von Gise, A., Ikeda, S., Chien, K.R., Pu, W.T., 2008. Epicardial progenitors contribute to the cardiomyocyte lineage in the developing heart. Nature 454, 109. https://doi.org/10.1038/NATURE07060

Zhou, P., Pu, W.T., 2016. Recounting cardiac cellular composition. Circ Res 118, 368. https://doi.org/10.1161/CIRCRESAHA.116.308139

Zhuang, Y., Gong, Y.J., Zhong, B.F., Zhou, Y., Gong, L., 2017. Bioinformatics method identifies potential biomarkers of dilated cardiomyopathy in a human induced pluripotent stem cell-derived cardiomyocyte model. Exp Ther Med 14, 2771. https://doi.org/10.3892/ETM.2017.4850

Zhuge, Y., Zhang, J., Qian, F., Wen, Z., Niu, C., Xu, K., Ji, H., Rong, X., Chu, M., Jia, C., 2020. Role of smooth muscle cells in Cardiovascular Disease. Int J Biol Sci 16, 2741–2751. https://doi.org/10.7150/IJBS.49871

Zoeller, J.J., Whitelock, J.M., Iozzo, R. v., 2009a. Perlecan regulates developmental angiogenesis by modulating the VEGF-VEGFR2 axis. Matrix Biol 28, 284–291. https://doi.org/10.1016/J.MATBIO.2009.04.010

Zoeller, J.J., Whitelock, J.M., Iozzo, R. v., 2009b. Perlecan regulates developmental angiogenesis by modulating the VEGF-VEGFR2 axis. Matrix Biol 28, 284–291. https://doi.org/10.1016/J.MATBIO.2009.04.010